



27th Summer School and International Symposium on the Physics of Ionized Gases

August 26-29, 2014, Belgrade, Serbia

CONTRIBUTED PAPERS &

**ABSTRACTS OF INVITED LECTURES,
TOPICAL INVITED LECTURES, PROGRESS
REPORTS AND WORKSHOP LECTURES**

Editors:

Dragana Marić

Aleksandar R. Milosavljević

Zoran Mijatović



Institute of Physics, Belgrade
University of Belgrade



Serbian Academy
of Sciences and Arts

**27th Summer School and International
Symposium on the Physics of Ionized
Gases**

SPIG 2014

CONTRIBUTED PAPERS

&

ABSTRACTS OF INVITED LECTURES,
TOPICAL INVITED LECTURES, PROGRESS REPORTS
AND WORKSHOP LECTURES

Editors

Dragana Marić, Aleksandar R. Milosavljević and
Zoran Mijatović

Institute of Physics, Belgrade
University of Belgrade

Serbian Academy
of Sciences and Art

Belgrade, 2014

CONTRIBUTED PAPERS & ABSTRACTS OF INVITED
LECTURES, TOPICAL INVITED LECTURES, PROGRESS
REPORTS AND WORKSHOP LECTURES
of the 27th Summer School and International Symposium on
the Physics of Ionized Gases

August 26 – 29, 2014, Belgrade, Serbia

Editors:

Dragana Marić, Aleksandar R. Milosavljević and Zoran Mijatović

Publishers:

Institute of Physics, Belgrade
Pregrevica 118, P. O. Box 68
11080 Belgrade, Serbia

Klett izdavačka kuća d.o.o.
Maršala Birjuzova 3-5, IV sprat
11000 Belgrade

Computer processing:

Sanja D. Tošić, Nikola Škoro and Miloš Ranković

Printed by

CICERO
Belgrade

Number of copies

300

ISBN 978-86-7762-600-6

©2014 by the Institute of Physics, Belgrade, Serbia and Klett izdavačka kuća d.o.o. All rights reserved. No part of this book may be reproduced, stored or transmitted in any manner without the written permission of the Publisher.

PREFACE

This Publication contains the Contributed papers and Abstracts of Invited lectures, Topical invited lectures, Progress reports and associated Workshop lectures that will be presented at the 27th Summer School and International Symposium of the Physics of Ionized Gases – SPIG 2014. The symposium will be held at the Serbian Academy of Sciences and Arts in Belgrade, Serbia, from August 26th – 29th, 2014. It is organized by the Institute of Physics Belgrade, University of Belgrade and Serbian Academy of Sciences and Arts, under the auspices and with the support of the Ministry of Education, Science and Technological Development, Republic of Serbia.

A rare virtue of the SPIG conference is that it covers a wide range of topics, bringing together leading scientists worldwide to present and discuss state-of-art research and the most recent applications, thus stimulating a modern approach of interdisciplinary science. The Invited lectures and Contributed papers are related to the following research fields: Atomic Collision Processes (Electron and Photon Interactions with Atomic Particles, Heavy Particle Collisions, Swarms and Transport Phenomena), Particle and Laser Beam Interactions with Solids (Atomic Collisions in Solids, Sputtering and Deposition, Laser and Plasma Interaction with Surfaces), Low Temperature Plasmas (Plasma Spectroscopy and other Diagnostic Methods, Gas Discharges, Plasma Applications and Devices) and General Plasmas (Fusion Plasmas, Astrophysical Plasmas and Collective Phenomena). Additionally, the 27th SPIG encompasses three workshops that are closely related to the conference topics: the workshop on Dissociative Electron Attachment (DEA), the workshop on X-ray Interaction with Biomolecules in Gas Phase (XiBiGP) and the 3rd International Workshop on Non-Equilibrium Processes (NonEqProc). Overall, this book includes abstracts of 74 invited lectures and 114 contributed papers.

The Editors would like to thank the members of the Scientific and Advisory Committees of SPIG 2014 for their efforts in proposing the invited lectures and review of the contributed papers, as well as the chairmen of the associated workshops for their efforts and help in organizing the workshops and selection of invited talks. We particularly acknowledge the support of all members of the Local Organizing Committee for their help in the organization of the Conference. We are deeply grateful to all sponsors of the conference: SOLEIL synchrotron, RoentDek Handels GmbH, Klett izdavačka kuća d.o.o., Springer (EPJD and EPJ TI), IoP Publishing (IoP Conference Series), DEA club, Austrijski kulturni forum (Kulturforum Belgrad), Institut français de Serbie and Balassi Institute – Collegium Hungaricum Beograd.

Finally, we would like to thank all the invited speakers and participants for taking part in 27th SPIG and to wish them a pleasant stay in Belgrade, inspired and valuable moments and a very successful conference.

Editors: Dragana Marić, Aleksandar R. Milosavljević and Zoran Mijatović
Belgrade, 2014

ACKNOWLEDGEMENT

27th SUMMER SCHOOL AND INTERNATIONAL SYMPOSIUM ON THE PHYSICS OF IONIZED GASES

is organized by the

**Institute of Physics, Belgrade
University of Belgrade
Serbia**

and

**Serbian Academy of
Sciences and Arts**

under the auspices and with the support of the

**Ministry of Education, Science and Technological Development,
Republic of Serbia**

with the technical support of the
PANACOMP - Zemlja Čuda d.o.o.

and sponsored by:

**SOLEIL synchrotron
RoentDek Handels GmbH
Klett izdavačka kuća d.o.o.
Springer (EPJD and EPJ TI)
IoP Publishing (IoP Conference Series)
DEA club
Austrijski kulturni forum (Kulturforum Belgrad)
Institut français de Serbie
Balassi Institute – Collegium Hungaricum Beograd**

SPIG 2014

SCIENTIFIC COMMITTEE

Z. Mijatović (Chair), Serbia
S. Buckman, Australia
J. Burgdörfer, Austria
M. Danezis, Greece
Z. Donko, Hungary
V. Guerra, Portugal
M. Ivković, Serbia
D. Jovanović, Serbia
K. Lieb, Germany
I. Mančev, Serbia
D. Marić, Serbia
N. J. Mason, UK
A. R. Milosavljević, Serbia
K. Mima, Japan
Z. Mišković, Canada
B. Obradović, Serbia
G. Poparić, Serbia
L. C. Popović, Serbia
Z. Rakočević, Serbia
Y. Serruys, France
N. Simonović, Serbia
M. Škorić, Japan
M. Trtica, Serbia

ADVISORY COMMITTEE

D. Belić
N. Bibić
M. S. Dimitrijević
S. Đurović
N. Konjević
J. Labat
B. P. Marinković
M. Milosavljević
Z. Lj. Petrović
J. Purić
B. Stanić

ORGANIZING COMMITTEE

Institute of Physics Belgrade

D. Marić (Co-chair)
A. R. Milosavljević (Co-chair)
S. D. Tošić (Co-Secretary)
N. Škoro (Co-Secretary)
B. P. Marinković
M. Cvejić
J. Sivoš
K. Spasić
M. Ranković

Serbian Academy of Sciences and Arts

Z. Lj. Petrović
M. Ivanović

SPIG 2014 CONFERENCE TOPICS

Section 1.

ATOMIC COLLISION PROCESSES

- 1.1. Electron and Photon Interactions with Atomic Particles
- 1.2. Heavy Particle Collisions
- 1.3. Swarms and Transport Phenomena

Section 2.

PARTICLE AND LASER BEAM INTERACTION WITH SOLIDS

- 2.1. Atomic Collisions in Solids
- 2.2. Sputtering and Deposition
- 2.3. Laser and Plasma Interaction with Surfaces

Section 3.

LOW TEMPERATURE PLASMAS

- 3.1. Plasma Spectroscopy and Other Diagnostics Methods
- 3.2. Gas Discharges
- 3.3. Plasma Applications and Devices

Section 4.

GENERAL PLASMAS

- 4.1. Fusion Plasmas
- 4.2. Astrophysical Plasmas
- 4.3. Collective Phenomena

CONTENTS

Section 1. ATOMIC COLLISION PROCESSES

Invited Lectures

Dž. Belkić

The Role of High-Energy Ion-Atom/Molecule Collisions in Radiotherapy.....3

P. Swiderek and J. Warneke

The Two Sides of the Electron in Febid: Fragmentation of Molecules and Molecular Synthes.....4

M. J. Brunger, S. J. Buckman, D. B. Jones, L. Chiari, Z. Pettifer, G. B. da Silva,
M. C. A. Lopes, H. V. Duque, G. García, M. Hoshino and H. Tanaka

Recent Results for Electron Scattering from Atoms and Molecules.....5

D. B. Cassidy

Some Recent Developments in Experimental Positronium Physics.....6

P. Ranitović

Attosecond VUV Coherent Control of Molecular Dynamics and Perspectives for Using Eli-Alps User Facility.....7

Topical Invited Lectures

R. Boadle, J. Machacek, E. Anderson, L. Chiari, M. Brunger, G. Garcia, Z. Petrović,
W. Tattersall, R. White, S. Buckman and J. Sullivan

Positron Interactions with Atoms and Molecules.....8

G. A. Garcia, H. Dossmann, L. Nahon, S. Daly and I. Powis

Chirality reveals electronic/nuclear motion couplings.....9

J. D. Gorfinkiel

Latest Developments in Low Energy Electron Molecule Scattering: The R-Matrix Approach.....10

L. L. Alves

The IST-Lisbon Database on LXCAT.....11

Progress Reports

S. Maclot, R. Delaunay, D. G. Piekarski, P. Rousseau, A. Domaracka, P. Bolognesi,
L. Avaldi, S. Díaz-Tendero, L. Adoui and B. A. Huber
Stability of Nucleosides in the Gas Phase under Ionising Radiation.....12

S. Marjanović
Monte Carlo Modeling of Positron Transport in Experimental Devices and Applications.....13

R. Janečková, J. Kočíšek and J. Fedor
Electron Attachment to c-C4F8O: Dynamics and Implications for Plasmas.....14

R. Pandey, M. Ryszka, M. Dampc and S. Eden
Molecular Clusters: Radiation Induced Processes and Methods to Control Neutral Beams.....15

R. Thorman, J. Spencer, J. A Brannaka, L. McElwee-White, H. Fairbrother and
O. Ingólfsson
Low Energy Electron Interaction with Typical Focused Electron Beam Induced Deposition Precursor.....16

F. Ferreira da Silva, G. Meneses, T. Cunha, D. Almeida, G. García and
P. Limão-Vieira
Electron Transfer upon Potassium Collisions with Biomolecules.....17

J. B. Maljković
Absolute Differential Cross Sections for Elastic Electron Scattering from Small Biomolecules.....18

M. S. Rabasović
Electron – Indium Atom Scattering and Analysis of Electron and Optical Spectra.....19

N. Milojević
Single Electron Capture in Fast Ion-Atom Collisions.....20

D. Bošnjaković, Z. Lj. Petrović and S. Dujko
Simulation and Modeling of Resistive Plate Chambers.....21

Contributed Papers

1.1. M. Z. Milošević and N. S. Simonović
Complex-Rotation and Wave-Packet Calculations of the Ionization Rate for Hydrogen Atom in Electric Field.....22

1.2. I. P. Prlina and N. N. Nedeljkić <i>Effective Lifetimes of the Postselected Hydrogen Atoms</i>	26
1.3. D. A. Rostov, Ye. S. Kan, Yu. S. Krivosenko, X. O. Brykalova and A. A. Pavlychev <i>Ultrafast Dissociative Photoelectron Attachment in Photoemission from CO</i>	30
1.4. Yu. S. Krivosenko and A. A. Pavlychev <i>The Photoelectron and Neutron-Induced Recoil as Probe of Interatomic Interaction in Solids</i>	34
1.5. X. O. Brykalova, S. V. Kondratiev, D. A. Rostov, Ye. S. Kan, Yu. S. Krivosenko and A. A. Pavlychev <i>The Shape and Confinement Resonances in Photoabsorption of Free and Endohedral Molecules</i>	38
1.6. B. P. Marinković, V. Vujčić, S. Đorđević, S. Ivanović, D. B. Marinković, D. Jevremović and N. J. Mason <i>Belgrade Electron/Molecule Database Compatible with VAMDC Project</i>	42
1.7. S. D. Tošić, V. Pejčev, D. Šević, R. P. McEachran, A. D. Stauffer and B. P. Marinković <i>Integrated Cross Sections for Electron Excitation of the $4d^{10}5p$ State of the Ag Atom</i>	46
1.8. J. J. Jureta, A. R. Milosavljević and B. P. Marinković <i>High Resolution Ejected Electron Spectra of Argon at Electron Impact Energies of 303, 505, 809 and 1000 eV and Ejection Angle of 90°</i>	50
1.9. A. R. Milosavljević, C. Nicolas, M. Lj. Ranković, F. Canon, C. Miron and A. Giuliani <i>N K-Shell X-Ray Tandem Mass Spectrometry of Gas-Phase Ubiquitin Protein</i>	54
1.10. M. Lj. Ranković, J. Rackwitz, I. Bald and A. R. Milosavljević <i>Optimization of a Low-Energy Electron Gun by Electron Ray-Tracing Simulations</i> ...	58
1.11. M. M. Vojnović and D. S. Belić <i>Rate Coefficients for Electron-Impact Dissociation of O_3^+</i>	62
1.12. B. Żywicka and P. Mozejko <i>Application of Binary-Encounter-Bethe Method to Electron-Impact Ionization Cross Section Calculations for Biologically Relevant Molecules</i>	66

1.13. P. Mozejko, Cz. Szmytkowski, M. Zawadzki and E. Ptasińska-Denga <i>Total Cross Sections for Electron Scattering from Selected Hydrocarbons: The Substitutional and Additivity Effects</i>	70
1.14. S. Vogel, J. Rackwitz, R. Schürmann, J. Prinz, A. R. Milosavljević, A. Giuliani and I. Bald <i>Determination of Sequence-Specific DNA Strand Breaks Induced By VUV Radiation Using the DNA Origami Technique</i>	74
1.15. K. Regeta and M. Allan <i>Absolute Cross Sections for Electronic Excitation of Furan</i>	78
1.16. M. Ryszka, R. Pandey, M. Dampc and S. Eden <i>Experiments to Probe Electron Attachment to Stark Selected Biomolecular Clusters</i>	82
1.17. A. Ribar, E. Szymańska-Skolimowska, M. Danko, Š. Matejčík and N. Mason <i>Low Energy Electron Interactions with Nitromethane</i>	86
1.18. J. Rackwitz, J. Kopyra and I. Bald <i>Dissociative Electron Attachment to 2-Fluoroadenine</i>	90
1.19. A. R. Milosavljević, A. Domaracka, P. Rousseau and A. Giuliani <i>Highly Charged Ions Collisions with Multiply Charged Protein Anions Stored in a Linear Ion Trap</i>	94
1.20. I. Mančev and N. Milojević <i>Single Electron Capture in p- Li^+ Collisions</i>	98
1.21. T. P. Grozdanov and E. A. Solov'ev <i>Dynamical Adiabatic Potential Energy Curves of HeH^{2+} System: Crossings in Complex Plane of Internuclear Separations</i>	102
1.22. V. Yu. Lazur and V. V. Aleksiy <i>Schrodingers Formalism of Distorted-Wave Method in the Problem of Single-Electron Capture with Simultaneous Ionization</i>	106
1.23. M. M. Aoneas, M. M. Vojnović, M. M. Ristić, M. D. Vičić and G. B. Poparić <i>Electron Impact Ionization of CO in RF Electric Field</i>	110
1.24. D. Bošnjaković, Z. Lj. Petrović and S. Dujko <i>Studies of Electron Transport in Gases for Resistive Plate Chambers</i>	114

1.25. A. Banković, S. Dujko, R. D. White and Z. Lj. Petrović <i>Positron Transport in Gases in Electric and Magnetic Fields Crossed at Arbitrary Angles</i>	118
1.26. J. Mirić, O. Šašić, S. Dujko and Z. Lj. Petrović <i>Scattering Cross Sections and Transport Coefficients for Electrons in CF₃I</i>	122
1.27. J. Mirić, Z. Lj. Petrović, R. D. White and S. Dujko <i>Electron Transport in Noble-Gas Metal-Vapor Mixtures</i>	126
1.28. I. Simonović, Z. Lj. Petrović and S. Dujko <i>Third-Order Transport Coefficients for Electrons I. Structure of Skewness Tensor</i> ...	130
1.29. I. Simonović, Z. Lj. Petrović and S. Dujko <i>Third-Order Transport Coefficients for Electrons II. Molecular Gases</i>	134
1.30. Z. M. Raspopović, S. Dujko, R. D. White, T. Makabe and Z. Lj. Petrović <i>Benchmark Calculations for Spatially Resolved Electron Transport Data</i>	138
1.31. V. Stojanović, Z. Raspopović, D. Marić and Z. Lj. Petrović <i>Cross Sections and Transport Parameters of O⁻ Ions in Water Vapour</i>	142
1.32. S. Dupljanin, O. Šašić and Z. Lj. Petrović <i>Swarm Analysis of Transport Data for Electrons in Dimethyl Ether (CH₃OCH₃)</i>	146
1.33. Z. Raspopović, Ž. Nikitović, V. Stojanović, J. Jovanović and Z. Lj. Petrović <i>Modeling Of F⁻ Ions in Ar/BF₃ Mixtures</i>	150
1.34. M. Rabie, P. Haefliger and C. M. Franck <i>Obtaining Electron Attachment and Ionization Rates from Simultaneous Analysis of Electron and Ion Swarms in a Pulsed Townsend Setup</i>	154

Section 2. PARTICLE AND LASER BEAM INTERACTION WITH SOLIDS

Invited Lectures

F. Aumayr <i>What Happens at the Surface Impact Site of a Slow Highly Charged Ion?</i>	161
A. De Giacomo, M. Dell'Aglio, R. Gaudiuso, R. Elrashedy and O. De Pascale <i>Laser Ablation in Liquid during Nanoparticle Production</i>	162

Topical Invited Lectures

I. Bald, J. Rackwitz, R. Schürmann, S. Vogel and A. Keller
Low-Energy Electron-Induced Bond Cleavage Studied in DNA at a Single-Molecule Level.....163

David Duday, Nicolas Boscher, Florian Hilt and Patrick Choquet
Deposition of Innovative Coatings by DBD at Atmospheric-Pressure.....164

G. Dinescu, S. Vizireanu, T. Acsente, B. Mitu, A. Lazea, D. Stoica and V. Marascu
Plasma Synthesis and Processing of Carbon Nanowalls and Submicron Metallic Particles.....165

A. M. Ito, O. Yasuhiro, A. Takayama, S. Saito and H. Nakamura
Molecular Dynamics Simulation of Plasma-Surface Interaction for Carbon and Tungsten Materials.....166

Progress Reports

V. Prysiaznyi and M. Cernak
Treatment Effects and Its Stability on Metal Substrates after Cold Surface DBD Plasma.....167

I. Radović, D. Borka and Z. L. Mišković
Wake Effect in Graphene Due to Moving Charged Particles.....168

COST CELINA Lecture

A. Muñoz, F. Blanco, M. C. Fuss, D. Jones, M. J. Brunger and G. García
The Event By Event Modelling Procedure to Simulate Electron Beam Induced Deposition.....169

Contributed Papers

2.1. V. Borka Jovanović and D. Borka
Angular and Spatial Distributions of Protons with BN Nanotubes.....170

2.2. S. M. D. Galijaš, M. A. Mirković and N. N. Nedeljković
Beam-Foil Population of the Large-L Rydberg States of Multiply Charged Ions.....174

2.3. M. D. Majkić, S. M. D. Galijaš, I. P. Prlina and N. N. Nedeljković
Population Dynamics of the SVI, CIVII and ArVIII Ions in the Grazing Incidence on Solid Surface.....178

2.4. N. N. Nedeljković, M. D. Majkić and S. M. D. Galijaš
Effect of the Solid Work Function on the Population of the ArX Ions in the Grazing Incidence Geometry.....182

2.5. M. Milićević, A. Matković, B. Vasić and R. Gajić <i>Influence of the Electron Beam Irradiation on Graphene during Devices Production.....</i>	186
2.6. M. Nenadović, D. Kisić, D. Stojanović and Z. Rakočević <i>Optical Properties of Silver Implanted High Density Polyethylene Observed Using Spectroscopic Ellipsometry.....</i>	190
2.7. M. Novaković, M. Popović, V. Čubrović, K. Zhang and N. Bibić <i>Microstructure and Magnetic Properties of Xe Ion Irradiated Co/Si Bilayers.....</i>	194
2.8. M. Popović, M. Novaković, A. Maksić and N. Bibić <i>Structural and Optical Characterization of Tin Thin Films Implanted with High Vanadium Fluences.....</i>	198
2.9. D. K. Božanić, I. Draganić, J. Pajović, R. Dojčilović, N. Bibić and V. Djoković <i>Fabrication of Polymer Nanocomposites by Implantation with Multiple Charged Iron Ions.....</i>	202
2.10. M. Šiljegović, Z. M. Kačarević-Popović, A. N. Radosavljević, S. Korica, S. Maletić and I. Petronijević <i>Effect of Low-Energy Ion Irradiation on Optical and Dielectric Properties of Ethylene-Norbornene.....</i>	206
2.11. A. R. Milosavljević, M. Lj. Ranković, J. B. Maljković, R. J. Berczky, B. P. Marinković and K. Tökési <i>Kinetic Energy Distribution of Electrons Scattered Inside a Platinum Tube at the Incident Energy of 200 eV.....</i>	210
2.12. V. Goncharov, K. Kozadaev, A. Novikau, H. Mikithcuk and A. Migutskiy <i>Laser Deposition of Silver Nanocones at Air Pressure.....</i>	214
2.13. M. Prochazka, L. Blahova and F. Krcma <i>Thin Film Deposition of HMDSO for Barrier Applications in Archaeology.....</i>	218
2.14. J. Potočnik, M. Nenadović, M. Popović, B. Jokić and Z. Rakočević <i>Structural and Chemical Properties of the Nanostructured Ni Thin Film Obtained by GLAD Technique.....</i>	222
2.15. V. Goncharov and M. Puzyrev <i>Dynamics of Destruction Products at Influence Laser Radiation on Different Types of Graphite.....</i>	226

2.16. A. Hamdan, C. Noël, G. Henrion and T. Belmonte <i>Time-Resolved Spectroscopy of Nanosecond Discharges Created in Water between Aluminium Electrodes.....</i>	230
2.17. A. Chumakov, I. Nikonchuk and O. Kuznechik <i>Application of Pulse-Periodic Plasma Flows for Hardening of Steel Surface.....</i>	234
2.18. A. M. Petrenko, P. V. Chekan and A. N. Chumakov <i>Calibration of Pressure Sensors Using Near-Surface Laser Plasma.....</i>	238
2.19. V. S. Burakov, N. N. Tarasenko, D. A. Kotsikau, V. V. Pankov and N. V. Tarasenko <i>Laser Irradiation of Nanoparticles for Modification of Their Physical and Chemical Properties.....</i>	242

Section 3. LOW TEMPERATURE PLASMAS

Invited Lectures

A. Fridman <i>Plasma Medicine: Fundamentals and Applications.....</i>	249
G. V. Naidis <i>Modelling of Physical and Chemical Processes in Cold Atmospheric Pressure Plasma Jets.....</i>	250

Topical Invited Lectures

A. R. Ellingboe <i>A CCP-Plasma Source Operation in the High-VHF to UHF Frequencies and Scalability to Large-Area Applications.....</i>	251
F. Krcma, V. Mazankova, L. Radkova, P. Fojtikova, V. Sazavska, L. Hlochova, M. Vasicek, Z. Kozakova, R. Prikryl, M. Prochazka, L. Blahova, J. Horak and D. Janova <i>Application of Low Temperature Plasmas for Restoration/Conservation of Archaeological Objects.....</i>	252
F. Tochikubo, N. Shirai and S. Uchida <i>Liquid-Phase Reactions Induced by Atmospheric Pressure Glow Discharge with Liquid Electrode.....</i>	253
K. Kutasi <i>The Afterglow of a Surface-Wave Microwave Discharge as a Tool for Surface Process Studies.....</i>	254

M. Šimek, T. Hoder, F. C. Parra-Rojas, F. J. Gordillo-Vázquez and V. Pukner
Optical Diagnostics of Laboratory Analogue of TLE Discharges.....255

Progress Reports

S. Ptasinska
Atmospheric Pressure Plasma Jet Interactions with Liquids.....256

I. Junkar
Low Temperature Plasma for Biomedical Applications.....257

A. P. Jovanović
Electrical Breakdowns in Air: New Experiments and Statistical and Numerical Models.....258

J. Jovović
Spectroscopic Study of Plasma during Electrolytic Oxidation of Magnesium-Aluminium Alloys.....259

M. Stankov
Measurements and Models of Transient and Stationary Regimes of Glow Discharge in Argon.....260

M. Cvejić
Diagnostics of Laser Induced Plasma by Optical Emission Spectroscopy.....261

A. Derzsi, I. Korolov, E. Schüngel, Z. Donkó, and J. Schulze
Electron Heating Dynamics in Multi-Frequency Capacitive RF Discharges.....262

Contributed Papers

3.1. B. M. Obradović, S. S. Ivković, N. Cvetanović, and M. M. Kuraica
Time-Space Development of Hydrogen Balmer Alpha Line in a Barrier Hollow Cathode Discharge.....263

3.2. G. B. Sretenović, I. B. Krstić, V. V. Kovačević, B. M. Obradović and M. M. Kuraica
Experimental Study of Electric Field Development in Plasma Jet.....267

3.3. N. Cvetanović, S. S. Ivković, G. B. Sretenović, B. M. Obradović and M. M. Kuraica
Correlation Between He Line Intensity Ratio and Local Field Strength Utilized for Field Measurement.....271

3.4. I. B. Krstić, B. B. Obradović and M. M. Kuraica <i>Temporal Investigation of Population of Copper Levels in Grimm Glow Discharge for Potential UV Laser Usage.....</i>	275
3.5. I. P. Dojčinović, I. Tapalaga and J. Purić <i>Stark Broadening of Spectral Lines within Li Isoelectronic Sequence.....</i>	279
3.6. G. Lj. Majstorović, J. Jovović and N. Konjević <i>Gas Temperature Measurement in Segmented Micro Hollow Gas Discharge in Helium.....</i>	283
3.7. V. Steflekova <i>Optogalvanic Spectroscopy of Aligned/Oriented Atoms in a Glow Discharge.....</i>	287
3.8. O. Galmiz, D. Pavličák, M. Zemánek, A. Brablec and M. Černák <i>Surface Dielectric Barrier Discharge (SDBD) Between Two Liquid Electrodes.....</i>	291
3.9. F. Castillo, M. Villa, H. Martínez, O. Flores and P. G. Reyes <i>Mass Spectrometry and OES Studies of Low-Pressure Gas Mixture of He-N₂-CO₂....</i>	295
3.10. V. Prysiazhnyi, A. H. C. Ricci and K. G. Kostov <i>Preliminary Results on Electric Characterization and Emission Spectroscopy of Single Electrode Ar Plasma Jets.....</i>	299
3.11. M. T. Belmonte, J. A. Aparicio, R. J. Peláez, S. Djurović and S. Mar <i>(³P)4d²P Multiplet AR II UV Spectral Line Transition Probability Analysis.....</i>	303
3.12. S. S. Pavlović, V. M. Milosavljević, P. J. Cullen and G. B. Poparić <i>Optical Diagnostic of RF Plasma Discharges in the N₂ - Ar Gas Mixtures.....</i>	307
3.13. M. R. Gavrilović, M. Cvejić, V. Lazic and S. Jovićević <i>Single-Pulse Laser Induced Plasma in Water: Shock Wave, Bubble and Plasma Emission.....</i>	311
3.14. M. R. Gavrilović, M. Cvejić, V. Lazic and S. Jovićević <i>Dynamics and Optical Properties of the Laser Induced Bubble.....</i>	315
3.15. M. Ivković <i>Stark Shift of Several Neutral Helium Lines in Dense Low Temperature Plasma.....</i>	319
3.16. S. Djurović, Z. Mijatović, I. Savić, L. Gavanski and R. Kobilarov <i>On the Possibility of the Electron Density Estimation by Using the Intensity Ratio of Two O II Spectral Lines.....</i>	323

3.17. T. Gajo, Z. Mijatović, S. Djurović, I. Savić and R. Kobilarov <i>Stark Broadening Parameters of Li I 670.8 nm</i>	327
3.18. D. Maletić, N. Puač, G. Malović and Z. Lj. Petrović <i>Time Resolved ICCD Measurements of Asynchronous Double Plasma Jet</i>	331
3.19. Á. Kálosi, P. Dohnal, P. Rubovič, R. Plašil and J. Glosík <i>CW-CRDS Study of Recombination of H^{3+} Ions with Electrons in Stationary Afterglow Plasma</i>	335
3.20. V. S. Burakov, M. I. Nedelko, V. V. Kiris, M. M. Mardanian and N. V. Tarasenko <i>Spectroscopic Characterization of Electrical Discharge Plasma in Liquid</i>	339
3.21. A. P. Jovanović, B. Č. Popović, V. Lj. Marković, S. N. Stamenković and M. N. Stankov <i>Formative Time Delay of Electrical Breakdown in Air</i>	343
3.22. M. N. Stankov, M. D. Petković, V. Lj. Marković, S. N. Stamenković and A. P. Jovanović <i>Two-Dimensional Glow Discharge Modelling in Argon</i>	347
3.23. V. Lj. Marković, A. P. Jovanović, S. N. Stamenković, M. N. Stankov and B. Č. Popović <i>Memory Effect and Time Correlations in Air and Argon DC Breakdown Delay</i>	351
3.24. S. N. Stamenković, V. Lj. Marković, A. P. Jovanović and M. N. Stankov <i>Nonstationary Statistical Time Delay Distributions in Argon</i>	355
3.25. N. V. Ivanović, G. Lj. Majstorović, N. M. Šišović and N. Konjević <i>The Estimation of Electric Field in Cathode Fall Region of Neon Grimm Glow Discharge</i>	359
3.26. D. N. Polyakov, V. V. Shumova and L. M. Vasilyak <i>Effect of Metastable Neon Atoms in Complex Plasma of Glow Discharge</i>	363
3.27. L. M. Vasilyak, V. I. Molotkov, V. Ya. Pecherkin and S. P. Vetchinin <i>Influence of Streamer Discharge upon the Ejection of Polarization Charging Particulates from the Cathode</i>	367
3.28. T. Morávek, Z. Navrátil, J. Ráhel and J. Čech <i>Optical Diagnostics of Diffuse Helium Coplanar Barrier Discharge</i>	371
3.29. P. Kloc, V. Aubrecht and M. Bartlova <i>Scaling of the Net Emission Coefficients</i>	375

3.30. M. Ignjatovic, J. Cvetic, M. Taušanović, D. Pavlovic, R. Djuric, M. Ponjavic, D. Sumarac Pavlovic and N. Mijajlović <i>Calculation of Lightning Channel Line Charge Density Using Very Close Electric Field Measurements.....</i>	379
3.31. M. Tausanović, J. Cvetic, M. Ignjatovic, D. Pavlovic, R. Djuric, M. Ponjavic, D. Sumarac Pavlovic and N. Mijajlović <i>The Influence of the Lightning Current Reflections from the Ground on Electric Field near Channel Core.....</i>	383
3.32. J. Sivoš, D. Marić, N. Škoro, G. Malović and Z. Lj. Petrović <i>Abnormal Glow Discharge in Ethanol Vapour</i>	387
3.33. J. Sivoš, D. Marić, N. Škoro, G. Malović and Z. Lj. Petrović <i>Electrical Breakdown in Low-Pressure Methanol Vapour.....</i>	391
3.34. K. Yasserian and A. Rahbarbinesh <i>On the Electric Potential of a Dusty Plasma in the Presence of the Electronegative Gas.....</i>	395
3.35. S. Dujko, A. H. Markosyan and U. Ebert <i>Propagation of Negative Planar Streamer Fronts in Noble Gases.....</i>	399
3.36. I. Adžić, Z. Lj. Petrović and S. Dujko <i>Elementary Physical Processes of Electrons in Planetary Atmospheric Discharges.....</i>	403
3.37. A. Bojarov, M. Radmilović Radjenović and Z. Lj. Petrović <i>Particle in Cell Simulation of the Electrical Asymmetry Effect with a Realistic Model of the Ion Induced Secondary Emission.....</i>	407
3.38. M. Savić, M. Radmilović-Radjenović, M. Šuvakov and Z. Lj. Petrović <i>Modeling of the Radio Frequency Breakdown Paschen Like Curves by Monte Carlo Technique.....</i>	411
3.39. V. V. Kovačević, B. P. Dojčinović, M. M. Aonyas, M. Jović, G. B. Sretenović, I. B. Krstić, G. M. Roglić, B. M. Obradović and M. M. Kuraica <i>Hydroxyl Radical Formation in Liquid Phase of Gas-Liquid Dielectric Barrier Discharge Reactor.....</i>	415
3.40. D. Marković, S. Milovanović, M. Stamenić, B. Jokić, I. Žižović and Maja Radetić <i>The Impregnation of Corona Activated Polypropylene Non-Woven Fabric with Thymol in Supercritical Carbon Dioxide.....</i>	419

3.41. S. Ptasinska and Xu Han <i>DNA Strand Break Formation in Cells by Atmospheric Pressure Plasma Jet.....</i>	423
3.42. D. N. Polyakov, V. V. Shumova and L. M. Vasilyak <i>The Radial Balance in Dusty Plasma of Glow Discharge with Joule Heating.....</i>	427
3.43. A. Miakonkikh, K. Rudenko and A. Orlikovsky <i>In Situ OES Monitoring of Plasma Enhanced Atomic Layer Deposition of Aluminium and Hafnium Oxide.....</i>	431
3.44. K. Kuvaev, A. Miakonkikh, K. Rudenko and A. Orlikovsky <i>Sensitive OES-Technique for Endpoint Detection Applied to Plasma Etching Of W/HfO₂/Si Stack.....</i>	435
3.45. K. Spasić, N. Škoro, N. Puač, G. Malović and Z. Lj. Petrović <i>Ion Energy Distribution and Line Intensities in Asymmetrical Oxygen RF Discharge.....</i>	439
3.46. T. Mitrović, D. Maletić, N. Tomić, S. Lazović, G. Malović, T. Nenin, U. Cvelbar, Z. Dohčević-Mitrović and Z. Lj. Petrović <i>Removal of Reactive Orange 16 from Water by Plasma Needle.....</i>	443
3.47. M. Santos, J. Hung, P. Michael, E. Filipe, A. Kondyurin, Martin K. C. Ng, S. G. Wise and M. M. M. Bilek <i>Capacitively Coupled Radio-Frequency Discharges in C₂H₂-Ar-N₂ Mixtures: Enhancing the Hemocompatibility of Metallic Substrates.....</i>	447
3.48. N. Selaković, N. Puač, M. Miletić, I. Živanović, I. Dakić, G. Malović, D. Vuković and Z. Lj. Petrović <i>Methicilin Resistant Staphylococcus Aureus Inhibition Zone Areas Obtained by a Plasma Needle Treatment</i>	451
3.49. N. N. Bogachev, I. L. Bogdankevich, N. G. Gusein-zade and A. A. Ruhadze <i>Surface Wave and Operation Modes of Plasma Antenna.....</i>	455
3.50. I. Filatova, N. Chubrik and F. Truhachev <i>The Effect of a DC Electric Field on the Dynamics of Charged Submicron Particles in the Afterglow of Dusty Plasma.....</i>	459
3.51. V. I. Arkhipenko, Th. Callegari, L. V. Simonchik, J. Sokoloff and M. S. Usachonak <i>Powerful Microwave Control by the 1D EBG Plasma Structure in a Waveguide.....</i>	463
3.52. B. Tomcik, B. P. Marinkovic and B. Predojevic <i>Plasma Methods in Deposition and Evaluation of Nano-Sized Carbon Films.....</i>	467

Section 4. GENERAL PLASMAS

Invited Lectures

J. W. Sulentic, P. Marziani, D. Dultzin, M. D'Onofrio and A. del Olmo
Fifty Years of Quasars: Physical Insights and Potential for Cosmology.....473

A. Komori, T. Morisaki and LHD Experiment Group
Study of a High-Performance Plasma in the Large Helical Device.....474

Topical Invited Lectures

Ján Žabka, Miroslav Polášek, Christian Alcaraz and Véronique Vuitton
Anion Chemistry in Titan.....475

B. Predojević, V. Pejčev, D. Šević and B. Marinković
Electron Excitation and Autoionization Cross Sections for Elements of Chemically Peculiar (Cp) Stars: Study of Bismuth.....476

Progress Reports

S. Vidojević
Langmuir Waves in Interplanetary Plasma.....477

D. Stathopoulos, E. Danezis, E. Lyrtzi, A. Antoniou, L. Č. Popović, D. Tzimeas and M. S. Dimitrijević
Studying the Complex Absorption Profiles of Si IV in 21 HiBALQSO Spectra.....478

N. N. Bezuglov, M. S. Dimitrijevic, A. N. Klyucharev and A. A. Mihajlov
Dynamic Characteristics of Excited Atomic Systems.....479

V. A. Srećković, A. A. Mihajlov, Lj. M. Ignjatović and M. S. Dimitrijević
The Non-Symmetric Ion-Atom Absorption Processes in the Helium Rich White Dwarf Atmospheres in UV and EUV Region.....480

Contributed Papers

4.1. G. Jovanović
Gravity Waves in Stratified Solar Atmosphere.....481

4.2. P. Jovanović, V. Borka Jovanović and D. Borka
Shape of the Fe Ka Line Emitted from a Relativistic Accretion Disk with an Empty Gap.....485

4.3. J. Dojčinović Kovačević, L. Č. Popović
The Location of the Uv Feii Emitting Region in the Structure of The Active Galactic Nuclei.....489

4.4. A. Antoniou, E. Danezis, E. Lyratzi, L. Č. Popović, M. S. Dimitrijević and D. Stathopoulos <i>Kinematic Properties of the Nitrogen Five (N V) Region in 20 Oe-Type Stars.....</i>	493
4.5. V. M. Čadež and A. Nina <i>Comparison of Spectral Analyses of X-Radiation and Vlf Signal Amplitude During Solar X-Flare.....</i>	497
4.6. A. Nina and V. M. Čadež <i>Spectral Analyses of VLF Signal Variations and AGWs Induced by Sunrise in Low Ionosphere.....</i>	501
4.7. T. D. Tran, R. Plasil, S. Roucka, D. Mulin, S. Rednyk, D. Gerlich and J. Glosik <i>Reactions of O⁻ with H₂ at Low Temperatures.....</i>	505
4.8. D. Ilić, A. I. Shapovalova, L. Č. Popović, A. N. Burenkov, V. H. Chavushyan, A. Kovačević and W. Kollatschny <i>Long-Term Variability in the Continuum and Broad Spectral Lines of a Number of Active Galactic Nuclei.....</i>	509
4.9. N. M. Sakan, A. A. Mihajlov and V. A. Srećković <i>Inverse Bremsstrahlung Absorption Coefficients for Dense Hydrogen Plasma in Cut-Off Coulomb Potential Model.....</i>	513

The Workshop on Dissociative Electron Attachment (DEA)

J. Kopyra <i>Electron Attachment to Molecules Studied by Electron-Molecular Crossed Beam Experiment.....</i>	519
T. A. Field and T. D. Gilmore <i>Electron Attachment to Unstable Molecules.....</i>	520
K. Tanzer, L. Feketeova, B. Puschnigg, P. Scheier, E. Illenberger and S. Denifl <i>Dissociative Electron Attachment Studies with Potential Radiosensitizers.....</i>	521
M. Zlatar <i>(Time-Dependent) Density Functional Theory for Understanding Dissociative Chemistry of Organometallic Compounds.....</i>	522
R. Čurík, P. Čársky and M. Allan <i>Role of Symmetry in Electron-Impact Resonant Vibrational Excitation of Polyatomic Molecules.....</i>	523
J. Fedor, R. Janečková and J. Kočišek <i>Role of Symmetry Lowering in DEA.....</i>	524
E. Szymanska-Skolimowska, E. Krishnakumar and Nigel J. Mason <i>Velocity Slice Imaging Study on Dissociative Electron Attachment.....</i>	525

P. Papp, M. Lacko and Š. Matejčík
Dissociative Electron Attachment to Organometallic Compounds.....526

The Workshop on X-ray Interaction with Biomolecules in Gas Phase (XiBiGP)

P. Lablanquie, F. Penent, L. Andric, J. Palaudoux, P. Selles, S. Carniato, J. M. Bizau, D. Cubaynes, M. Nakano, T. P. Grozdanov, M. Žitnik, S.-M. Huttula, M. Huttula, K. Jänkälä, S. Sheinerman, E. Shigemasa, M. Tashiro, H. Iwayama, Y. Hikosaka, K. Soejima, I.H. Suzuki and K. Ito
Study of Single Photon Multiple Ionisation Processes with a Magnetic Bottle Spectrometer.....529

K. C. Prince
Synchrotron Radiation Studies of Biomolecules: Photoabsorption, and Core and Valence Photoionization530

E. Kukk
Electron-Ion Coincidence Spectroscopy as a Tool to Study Radiation-Induced Molecular Dynamics.....531

T. Schlathölter
Biomolecular Ionization and Fragmentation Dynamics Studied with Energetic Photons from Synchrotrons and Free Electron Lasers.....532

A. R. Milosavljević, C. Nicolas, F. Canon, C. Miron and A. Giuliani
Action Spectroscopy of Stored Biomolecular Ions in the Soft X-Ray Range.....533

B. Winter
Ultrafast Proton and Electron Dynamics in Core-Ionized Aqueous Solution.....534

The 3rd International Workshop on Non-Equilibrium Processes (NonEqProc)

G. Boyle, W. Tattersall, B. Philippa, R. E. Robson, M. J. Brunger, G. Garcia, S. Dujko, Z. Lj. Petrovic, R. McEachran, S. J. Buckman, J. de Urquijo and R. D. White
Non-Equilibrium Transport of Charged Particles in Gaseous and Disordered Materials.....537

Z. Donko
First Principles Calculation of the Effect of Coulomb Collisions on Electron Swarm.....538

V. Dmitrašinović and M. Šuvakov
Recent Progress in the Newtonian Three-Body Problem.....539

T. Belmonte, C. Noël and G. Henrion <i>Emission Spectroscopy of Dense Plasmas in Liquids: A Winding Road from Light to Chemistry</i>	540
J. Bredin, J. Dedrick, K. Niemi, A. West, E. Wagenaars, T. Gans and D. O'Connell <i>Picosecond-TALIF to Probe Atomic Oxygen in the Plume of an RF Driven Atmospheric Pressure Plasma Jet in Ambient Air</i>	541
S. Radovanov, H. Persing, A. Wendt, J. Boffard, C. Lin, C. Culver and S. Wang <i>VUV Emissions from Low Temperature Argon and Argon-Molecular Gas Mixtures in Inductively Coupled Plasmas</i>	542
K. Belkić and Dž. Belkić <i>Spectral Analysis for Optimization of Magnetic Resonance Spectroscopy in Early Tumor Diagnostics</i>	543
M. Allan <i>Measuring Elementary Plasma Processes: Elastic Scattering, Vibrational and Electronic Excitation, Dissociative Attachment</i>	544
N. Mason <i>Future Studies on Electron Scattering; a renaissance?</i>	545
Author Index.....	547
Post-deadline Contributions.....	

Section 1.

**ATOMIC COLLISION
PROCESSES**

THE ROLE OF HIGH-ENERGY ION- ATOM/MOLECULE COLLISIONS IN RADIOTHERAPY

Dževad Belkić

Karolinska Institute, Oncology-Pathology, Stockholm, Sweden

We review state-of-the-art quantum-mechanical theories of fast ion-atom and ion-molecule collisions with a focus on the variety of applications to hadron therapy of deep-seated tumors. The challenges for the theory are multifaceted, especially at intermediate impact energies where the otherwise powerful perturbation methods are of limited applicability. Non-perturbative methods are expected to be more adequate for this particular energy region. The other level of challenges for theoreticians encompasses collisions with participation of two and more active electrons. We present some leading classical, semi-classical and quantum-mechanical methods from ion-atom and ion-molecule collisions that could be readily extended to a wider class of bio-molecular targets of direct relevance to cancer therapy by energetic light ions. This is possible because the existing atomic collision physics methods can be adapted to bio-molecular targets without undue difficulty, by using molecular wave functions in terms of linear combinations of Slater-type orbitals. The next step would be to incorporate these methods into several powerful Monte Carlo simulations of energy losses of ions transported through tissue-like materials alongside their secondary particles (electrons and lighter nuclei). Very recently, the first results along these lines have been reported. We suggest avenues for more favorable cross-talk on a deeper and more fruitful level, especially for the benefit of patients with cancer undergoing hadron therapy.

Acknowledgements: This work is supported by Radiumhemmets-forskningsfonden, FoUU & Cancerfonden.

THE TWO SIDES OF THE ELECTRON IN FEBID: FRAGMENTATION OF MOLECULES AND MOLECULAR SYNTHESIS

Petra Swiderek, Jonas Warneke

*University of Bremen, Institute of Applied and Physical Chemistry,
Bremen, Germany
swiderek@uni-bremen.de*

Focused Electron Beam Induced Deposition (FEBID) is a very promising direct deposition technique for nanofabrication capable of producing free-standing 3D structures of sub-10 nm size. FEBID relies on electron-driven fragmentation at a surface of volatile precursor molecules. Ideally, their central metal or metalloid atoms define the nature of the deposited material while the ligands responsible for the volatility dissociate from the central atom and desorb completely from the surface. For example, the precursor $\text{Fe}(\text{CO})_5$ yields pure Fe deposits under ultrahigh vacuum conditions [1]. However, in many cases ligand material is embedded in the deposit and deteriorates its properties. As an extreme case, trimethyl(methylcyclopentadienyl)-platinum(IV) (MeCpPtMe_3) yields a deposit with composition $\text{Pt}:\text{C} = 1:8$ [2] indicating that only one methyl group becomes a volatile fragment. Loss of one methyl group also dominates dissociative electron attachment (DEA) to MeCpPtMe_3 pointing to the important role of low-energy secondary electrons in FEBID [3]. However, beside incomplete fragmentation also electron-induced formation of new bonds can lead to less volatile material. For example, the electron-induced synthesis of ethylamine from ethylene and ammonia [4] and, more relevant to FEBID, the trapping of methyl fragments by the precursor ligand acetylacetone [5] will be discussed together with potential strategies towards the development of better FEBID precursors.

Acknowledgements: This work was conducted within the framework of the COST Action CM1301 (CELINA).

REFERENCES

- [1] T. Lukasczyk, M. Schirmer, H. P. Steinrück and H. Marbach, *SMALL*, 4, 841 (2008).
- [2] J. D. Wnuk, J. M. Gorham, S. Rosenberg, W. F. van Dorp, T. E. Madey, C. W. Hagen and D. H. Fairbrother, *J. Phys. Chem. C* 113, 2487 (2009).
- [3] S. Engmann, M. Stano, S. Matejcik and O. Ingolfsson, *PCCP* 14, 14611 (2012).
- [4] E. Böhler, J. Warneke and P. Swiderek, *Chem. Soc. Rev.* 42, 9219 (2013).
- [5] J. Warneke, W.F.van Dorp, M.Stano, P.Papp, S.Matejcik, T.Borrmann, P.Swiderek, in preparation.

RECENT RESULTS FOR ELECTRON SCATTERING FROM ATOMS AND MOLECULES

M. J. Brunger^{1,2}, S. J. Buckman^{2,3}, D. B. Jones⁴, L. Chiari¹, Z. Pettifer¹,
G. B. da Silva^{1,5}, M. C. A. Lopes⁶, H. V. Duque^{1,6}, G. García⁷,
M. Hoshino⁸ and H. Tanaka⁸

¹*Centre for Antimatter-Matter Studies, CAPS, Flinders University,
GPO Box 2100, Adelaide, SA 5001, Australia*

²*Institute of Mathematical Sciences, University of Malaya,
Kuala Lumpur, Malaysia*

³*Centre for Antimatter-Matter Studies, AMPL, Australian National University,
Canberra, ACT 0200, Australia*

⁴*School of Chemical and Physical Sciences, Flinders University,
GPO Box 2100, Adelaide, SA 5001, Australia*

⁵*Universidade Federal de Mato Grosso, Barra do Garças, Mato Grosso, Brazil*

⁶*Departamento de Física, Universidade Federal de Juiz de Fora,
Juiz de Fora, MG, Brazil*

⁷*Instituto de Física Fundamental, CSIC, Madrid E-28006, Spain*

⁸*Department of Physics, Sophia University, Tokyo 102-8554, Japan*

Abstract. In this plenary lecture we present recent cross section results for low and intermediate energy electron scattering from a range of atoms and molecules. Where possible those data will be compared against corresponding results from theoretical calculations, with the relevant conclusions pertaining to the fundamental scattering behavior being drawn in each case. For each target species, the importance of the cross sections in understanding applied phenomena such as atmospheric plasmas, low-temperature laboratory plasmas, discharges and in simulating charged-particle tracks in matter will also be examined.

SOME RECENT DEVELOPMENTS IN EXPERIMENTAL POSITRONIUM PHYSICS

D. B. Cassidy

*Department of Physics and Astronomy, University College London, Gower
Street, London WC1E 6BT, UK.*

The use of a Surko-type buffer gas trap [1] has made it possible to turn ordinary neon-moderated d.c. positron beams [2] into devices that can deliver high quality cold positrons for high resolution scattering studies [3] or pulses containing up to 10^7 positrons in a ns burst [4]. The latter can be used to make a “gas” of positronium having a pressure of around 1 Torr, which in turn can be probed with pulsed lasers in much the same way as any other atomic species. The ability to create a Ps gas makes feasible a vast array of hitherto impractical or impossible experiments, such as the production of molecular positronium [5]. In this talk I will discuss some experiments in which excited atomic states of Ps can be created and studied, including Doppler-free 2-photon state-selective production of Rydberg Ps [6] and electrostatic manipulation thereof [7], measurement of the spin polarization of a positron beam via optical excitation of $n=2$ Ps states with circularly polarized light in a magnetic field, and the production of e^+A complexes via collisions with Rydberg Ps atoms [8]

Acknowledgements: This work is supported in part by the UK EPSRC (EP/K028774/1), the Leverhulme trust (RPG-2013-055) and the ERC (CIG-630119).

REFERENCES

- [1] C. M. Surko, M. Leventhal and A. Passner, Phys. Rev. Lett. 62, 901 (1989).
- [2] Positron Beams and Their Applications, edited by P. G. Coleman (World Scientific, Singapore, 2000).
- [3] S. J. Gilbert, R. G. Greaves and C. M. Surko, Phys. Rev. Lett. 82, 5032 (1999).
- [4] D. B. Cassidy, S. H. M. Deng, R. G. Greaves and A. P. Mills, Rev. Sci. Instrum. 77, 073106 (2006).
- [5] D. B. Cassidy, T. H. Hisakado, H. W. K. Tom, and A. P. Mills, Phys. Rev. Lett. 108, 133402 (2012).
- [6] T. E. Wall, D. B. Cassidy and S. D. Hogan, to be published.
- [7] S. D. Hogan and F. Merkt, Phys. Rev. Lett. 100, 043001 (2008).
- [8] C. Harabati, V. A. Dzuba, and V. V. Flambaum, Phys. Rev. A 89, 022517 (2014).

ATTOSECOND VUV COHERENT CONTROL OF MOLECULAR DYNAMICS AND PERSPECTIVES FOR USING ELI-ALPS USER FACILITY

Predrag Ranitovic^{1,2}

¹*Lawrence Berkeley National Lab, 1 Cyclotron Road, Berkeley CA, 94701*

²*ELI-HU non-profit Ltd, Dugonics ter 13, H-6720 Szeged*

Following the recent advances of the ultrafast laser technology, table-top extreme ultraviolet (XUV) sources have provided novel ways to achieve real-time manipulation of electron dynamics by means of attosecond XUV light coupled with strong laser fields in a time-resolved manner [1]. Only recently though it was realized that the multicolor VUV and XUV radiation, produced by the strong laser field in a process of high-harmonic generation (HHG), can be used as a spectroscopy tool for coherently controlling electron and nuclear wave packet dynamics on attosecond time scales [2-5].

In this talk, I will give several examples of how ultrashort laser and laser-driven XUV radiation can be used to coherently control electron and nuclear wavepacket dynamics in small atoms and molecules by means of two-pathway electron wave-packet interferences, and I will introduce the Extreme Light Infrastructure (ELI) project. In particular, I will talk about the scientific roadmap of the attosecond ELI-ALPS *user-oriented* facility currently being built in Szeged (Hungary), and prospects for using the ELI-ALPS scientific infrastructure in the future laser-driven attosecond X-Ray time-resolved experiments.

REFERENCES

- [1] F. Krausz and M. Ivanov, *Rev. Mod. Phys.* 81, (January-March 2009).
- [2] P. Johnsson et. al., *Phys. Rev. Lett.* 99, 233001 (2007).
- [3] P. Ranitovic et. al., *New Journal of Physics* 12, 013008 (2010).
- [4] P. Ranitovic et. al., *Phys. Rev. Lett.* 106, 193008 (2011).
- [5] P. Ranitovic et. al., *PNAS* 111 (3), 912-917 (2014).

POSITRON INTERACTIONS WITH ATOMS AND MOLECULES

Roisin Boadle¹, Joshua Machacek¹, Emma Anderson¹, Luca Chiari², Michael Brunger², Gustavo Garcia³, Zoran Petrovic⁴, Wade Tattersall⁵, Ronald White⁵, Stephen Buckman¹, James Sullivan¹

¹*RSPE, Australian National University, Canberra, Australia*

²*CaPS, Flinders University, Adelaide, South Australia*

³*CSIC, Madrid, Spain*

⁴*Institute of Physics, University of Belgrade, Serbia*

⁵*James Cook University, Townsville, Australia*

The availability of high-resolution, high-flux positron beams from Surko traps has transformed the positron scattering field in recent years. Absolute, state-resolved experiments are now relatively common, and accurate measurements of total and differential scattering, as well as positronium formation and annihilation cross sections and rates are available for a range of target species.

This talk will attempt to highlight some of the recent advances in the field that have been stimulated by the use of the new beam technologies. These will include absolute cross section measurements, searches for positronic complexes (resonances and bound states), interactions with biologically relevant molecules and the modeling studies that have flowed from them, and studies of channel coupling in positron scattering.

Future plans and potential applications of positron collision physics in biomedical imaging will also be highlighted.

Acknowledgements: This work is supported by the Australian, Spanish and Serbian governments.

CHIRALITY REVEALS ELECTRONIC/NUCLEAR MOTION COUPLINGS

G. A. Garcia¹, H. Dossmann¹, L. Nahon¹, S. Daly² and I. Powis²

¹ *Synchrotron SOLEIL, St Aubin BP 48, 91192 Gif sur Yvette, France*

² *School of Chemistry, University of Nottingham, NG7 2RD Nottingham, UK*

Electron/nuclei motion coupling accompanying excitation and relaxation processes is a fascinating phenomenon in molecular dynamics. A striking example of such an unexpected coupling is presented here in the context of Photoelectron Circular Dichroism (PECD) measurements on randomly-oriented, chiral methyl-oxirane[1] and trifluoro-methyl-oxirane molecules, unaffected by any continuum resonance. We show in particular that the forward/backward asymmetry in the electron angular distribution, with respect to the photon axis, that is associated with PECD, can surprisingly reverse direction according to the ion vibrational mode excited, a clear breakdown of the usual Franck-Condon assumption. A simple yet realistic model calculation is used to understand this phenomenon.

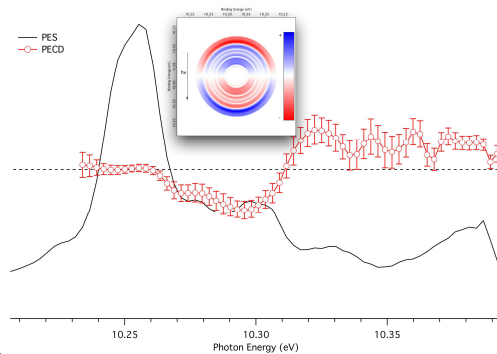


Figure 1. Photoelectron spectrum (black) and circular dichroism (red circles) measured on methyl-oxirane with circularly polarized light of 10.4 eV, corresponding to the HOMO photoionization. The inset shows the Abel inverted photoelectron dichroic image.

REFERENCES

- [1] G. A. Garcia, L. Nahon, S. Daly and I. Powis, *Nat. Commun.* 4, 2132 (2013).

LATEST DEVELOPMENTS IN LOW ENERGY ELECTRON MOLECULE SCATTERING: THE R-MATRIX APPROACH

Jimena D. Gorffnkiel

*Department of Physical Sciences, The Open University, Walton Hall,
Milton Keynes, UK*

The study of low-energy electron-molecule collisions has attracted increased interest over the last decade. Scattering data is required for the modelling of a number of physical processes and environments: from industrial plasmas to the description of the interaction of radiation with biological matter, the understanding of the formation of molecules and ions in the interstellar medium and the modelling of focused electron beam induced deposition. Data is therefore needed for more targets and more scattering processes than ever before. This need has led to the development of methodology and techniques (as well as their computational implementation) that are helping us gain a more sophisticated understanding of electron-molecule interactions.

The R-matrix method [1] has been applied to the study of low-energy electron (and positron) collisions with molecules for some time. One of its most sophisticated computational implementations is the UKRmol suite [2,3] that puts particular emphasis in the description of electronically inelastic processes and the formation of temporary negative ions (resonances) in which the electron attaches to the target molecule after electronically exciting it. In my talk, I will describe recent applications of the method (and software) to a number of processes and targets, e.g. formation of core-excited resonances in DNA bases [4]. I will discuss recent and future developments that will allow us to provide a better insight into electron and positron scattering from molecules.

REFERENCES

- [1] P.G. Burke, *R-Matrix Theory of Atomic Collisions: Application to Atomic, Molecular and Optical Processes* (Springer, 2011)
- [2] J. Tennyson, Phys. Rep. 491, 29 (2010)
- [3] J.M. Carr *et al.* Eur. Phys. J. D 66, 58 (2012)
- [4] Z. Mašín and J. D. Gorffnkiel, EPJD, 112, 68 (2014)

THE IST-LISBON DATABASE ON LXCAT

L.L. Alves

*Instituto de Plasmas e Fusão Nuclear, Instituto Superior Técnico,
Universidade de Lisboa, Av. Rovisco Pais, 1049-001 Lisboa, Portugal*

The LXCat project (www.lxcat.net) [1] is an open-access website for collecting, displaying, and downloading electron and ion scattering cross sections (also differential), swarm parameters (transport parameters and rate coefficients), interaction potentials, oscillator strengths and other data essential for modeling low-temperature plasmas. On-line tools enable importing, exporting, plotting and comparing different sets of data. The available databases have been contributed by members of the community around the world and are indicated by the contributor's chosen title. Anyone willing to contribute to this project should contact lxcat.info@gmail.com for instructions on how to take part.

At present, LXCat offers 16 databases containing sets of cross sections for electron scattering from ground-state neutral atoms and molecules, covering a range of energies from thermal up to 100's of eV and higher. The LXCat team has been making systematic inter-comparisons of cross section data and comparisons of calculated and measured swarm parameters [2-4].

This presentation will focus on the status of the data available for electrons on the IST-LISBON database with LXCat, which contains the most up-to-date electron-neutral collisional data (together with the measured swarm parameters used to validate these data) resulting from the research effort of the Group of Gas Discharges and Gaseous Electronics with Instituto de Plasmas e Fusão Nuclear, Instituto Superior Técnico, Lisbon, Portugal. Presently, the IST-LISBON database includes complete and consistent sets of electron scattering cross sections for argon, helium, hydrogen, nitrogen, oxygen and methane.

Acknowledgements: This work is partially supported by Fundação para a Ciência e a Tecnologia, under Project Pest-OE/SADG/LA0 010/2013.

REFERENCES

- [1] S. Pancheshnyi et. al., Chem. Phys. 398, 148 (2012).
- [2] L.C. Pitchford et. al., J. Phys. D: Appl. Phys. 46 334001 (2013).
- [3] L.L. Alves et. al., J. Phys. D: Appl. Phys. 46 334002 (2013).
- [4] M.C. Bordage et. al., J. Phys. D: Appl. Phys. 46 334003 (2013).

STABILITY OF NUCLEOSIDES IN THE GAS PHASE UNDER IONISING RADIATION

S. Maclot¹, R. Delaunay¹, D. G. Piekarski³, P. Rousseau¹, A. Domaracka¹,
P. Bolognesi², L. Avaldi², S. Díaz-Tendero³, L. Adoui¹ and B. A. Huber¹

¹CIMAP, CEA/CNRS/ENSICAEN/Université de Caen Basse-Normandie,
bld. Henri Becquerel, BP5133, 14070 Caen cedex 5, France

²CNR-ISM, Area della Ricerca di Roma 1, 0015 Monterotondo Scalo, Italy

³UAM, Departamento de Química - Module 13, Office 304, Facultad de
Ciencias, Cantoblanco Madrid 28049, Spain

We have studied in the gas phase the fragmentation dynamics of nucleosides following the ionisation by photons or ions. This approach allows to understand at the molecular level the mechanisms involved in the radiation damage.

Nucleosides are the building blocks of nucleic acids DNA and RNA. These are macromolecules constituted of a nucleobase and a sugar linked by the glycosidic bond. We have performed experiments with thymidine, on the one hand, interacting with low-energy multiply charged ions ($^{16}\text{O}^{6+}$ at 48 keV) at the GANIL facility in Caen (FR) applying multicoincidence mass spectrometry (Fig. 1) and, on the other hand, with VUV photons at the GASPHASE beamline of Elettra synchrotron light facility in Trieste (IT) by PEPICO measurements. The experimental studies are supported by molecular dynamics calculations provided by the UAM group in Madrid (ES).

The first results indicate a low survival rate of the intact molecule and predominantly a cleavage of the glycosidic bond accompanied with hydrogen transfers occurring between the base and sugar fragments and inside both of them. Specific fragmentation pathways are observed for nucleoside compared to separate base and sugar studies.

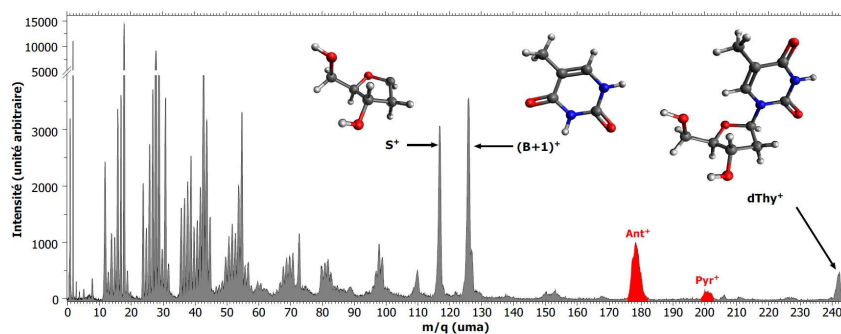


Figure 1. Mass spectrum of charged products from thymidine after the interaction with O^{6+} @48keV ions.

MONTE CARLO MODELING OF POSITRON TRANSPORT IN EXPERIMENTAL DEVICES AND APPLICATIONS

Srđan Marjanović

*Institute of Physics, University of Belgrade, Pregrevica 118, 11080 Belgrade,
Serbia*

Using our Monte Carlo simulation, we have modeled three different systems which are based on positron transport. The first model describes the operation of a standard Surko type buffer gas positron trap [1] which is the primary tool for positron research. Additionally we propose a slight change in the design, switching from N_2 as the primary trapping gas to CF_4 which is expected to provide higher positron yields. The second model investigates the mechanism behind the rotating wall compression of a trapped positron cloud in a single particle regime [2]. We also offer an explanation of the effect, which is caused by a form of resonant radial transport and we identify collision processes that contribute to the compression. The third positron application that we model is thermalization of positrons and induced secondary electrons in positron irradiated tissue. We analyze trajectories of positrons, and their products through water vapor, which simulates living tissue. We calculate profiles of energy, deposited by particles, and ranges of positrons and electrons that are relevant in determining the dosage that a patient receives during a positron tomography scan. We additionally improve the model by modifying a fraction of water molecules by adding a cross-section for dissociative attachment for CH_4 which effectively represents breaking of the C-H bond. The results show that both positrons and secondary electrons trigger this event, but at different energy and spatial range.

Acknowledgements: This work was supported by the Grants No. ON171037 and III41011 from the Ministry of Education, Science and Technological Development of the Republic of Serbia.

REFERENCES

- [1] C. M. Surko and R. G. Greaves, *Phys. Plasmas* 11, 2333 (2004).
- [2] D. B. Cassidy, S. H. M. Deng, R. G. Greaves and A. P. Mills, *Rev. Sci. Instrum.* 77, 073106 (2006).

ELECTRON ATTACHMENT TO *c*-C₄F₈O: DYNAMICS AND IMPLICATIONS FOR PLASMAS

Radmila Janečková, Jaroslav Kočišek and Juraj Fedor

*University of Fribourg, Chemistry Department, Ch. du Musée 9, CH-1700,
Fribourg, Switzerland*

The cyclic ether perfluorotetrahydrofuran (octafluorotetrahydrofuran, *c*-C₄F₈O) recently attracted lot of attention due to its electron attachment properties. This molecule can serve as a suitable substituent for plasma processing gasses. It has been already applied in Cherenkov radiation detectors [1] and it might effectively replace high voltage insulating gasses (SF₆) as it is environmentally more acceptable [2]. Since the fundamentals of *c*-C₄F₈O electron driven processes for these applications are not well known, we have performed a detailed experimental study.

We present partial absolute cross sections for negative-ion formation from electron attachment to *c*-C₄F₈O in the energy range of 0-6 eV. Besides rich fragmentation pattern from dissociative electron attachment mainly formed at electron energies around ~1.7 eV, ~2.5 eV and ~3.4 eV, we have observed long-lived parent anion (216 m/z) formed in 0.9 eV resonance. The experiment itself has been performed by the use of a quantitative DEA spectrometer with trochoidal electron monochromator in combination with ion time-of-flight (TOF) analyzer [3]. The measurements for absolute cross sections have been executed in a mixture of studied molecule *c*-C₄F₈O together with CO₂ and HCOOH used as a calibration gasses with known cross sections and positions of resonances [4].

Acknowledgements: This work has been partially supported by SCIEX NMS-CH programme of CRUS, the project NO 12.224 - IDEA, and project NO PZ00P2_132357/1 of the Swiss National Science Foundation.

REFERENCES

- [1] M. Artuso et al, Nucl. Instrum. Meth. A558, 373-387 (2006).
- [2] L. Pruette et al, in Proc. Electrochem. Soc., p. 20, (Pennington, New Jersey, 1999).
- [3] O. May et al, Phys. Rev. A 80, 012706 (2009).
- [4] R. Janečková et al., Phys. Rev. Lett. 111, 213201 (2013).

MOLECULAR CLUSTERS: RADIATION INDUCED PROCESSES AND METHODS TO CONTROL NEUTRAL BEAMS

R. Pandey, M. Ryszka, M. Dampc, S. Eden

*Department of Physical Sciences, The Open University, Milton Keynes,
MK7 6AA, United Kingdom*

Radiation induced processes in biomolecules have been investigated intensively in order to better understand the fundamental processes that can initiate DNA lesions. Measurements on hydrogen-bonded complexes, compared to studies of isolated molecules, enable closer analogies to be drawn with biological environments where different unimolecular or intermolecular reactive pathways play important roles. Our electron impact ionization and UV multi-photon ionization (MPI) experiments on gas-phase and clustered nucleobases have demonstrated strong effects of the hydrogen-bounded cluster environment on fragmentation patterns [1, 2]. Further measurements of the ions kinetic energies produced by MPI thymine clusters have provided new insights into proton transfer and dissociative ionization processes. A major challenge in analyzing radiation-induced processes in clusters is the broad distribution of sizes and configurations produced by supersonic expansion sources. To overcome this limitation we designed novel experimental setup, involving mass selection of cluster anions using quadrupole mass spectrometer. The resulting anions will be neutralized by electron photo-detachment from weakly bound anionic states, with minimal change in stability and hence dissociation [3]. Our aim is to use the method to determine absolute electron attachment cross sections and thereby investigating significant clustering effects that have been predicted theoretically [4].

REFERENCES

- [1] B. Barc, M. Ryszka, J.-C. Pouilly, E. Jabbour Al Maalouf, Z. el Otell, J. Tabet, R. Parajuli, P.J.M. van der Burgt, P. Limão-Vieira, P. Cahillane, M. Dampc, N.J. Mason, S. Eden, *Int. J of Mass Spectrom.* 365, 194 (2014).
- [2] B. Barc, M. Ryszka, J. Spurrell, M. Dampc, P. Limao-Vieira, R. Parajuli, N.J. Mason, S. Eden, *J. Chem. Phys.* 139, 244311 (2013).
- [3] J.R.R. Verlet, A.E. Bragg, A. Kammrath, O. Cheshnovsky, D. M. Neumark, *Science* 307, 93 (2005).
- [4] I.I. Fabrikant, S. Caprasecca, G.A. Gallup, J.D. Gorfinkiel, *J. Chem. Phys.* 136, 184301 (2012).

LOW ENERGY ELECTRON INTERACTION WITH TYPICAL FOCUSED ELECTRON BEAM INDUCED DEPOSITION PRECURSOR

Rachel Thorman¹, Julie Spencer², Joseph A Brannaka³, Lisa McElwee-White³,
Howard Fairbrother² and Oddur Ingólfsson¹

¹*Department of Chemistry, University of Iceland, Reykjavík, Iceland*

²*Department of Chemistry, Johns Hopkins University, Baltimore, Maryland, USA*

³*Department of Chemistry, University of Florida, Gainesville, Florida, USA*

Interactions of low energy electrons (LEEs) with precursor molecules have an important role in focused electron beam induced deposition (FEBID), in which LEEs are abundant.^[1] Due to the impact of the primary electron beam, low energy secondary electrons are emitted from the surface, both inside and outside the radius of the incident electron beam.^[2] Two candidate channels for LEE-induced molecular dissociation in FEBID are dissociative electron attachment (DEA) and dissociative ionization (DI). These processes likely contribute to adverse effects associated with FEBID, such as deposit broadening and co-deposition of ligands and ligand fragments from the organometallic precursor molecules. The ultimate goal of this research is to perform a systematic study on the role of LEEs in precursor molecule dissociation in both the gas phase and the condensed phase, and thus distinguish the dominating processes for different molecular classes. Additionally, this research looks to characterize novel organometallic compounds as potential FEBID precursors.

This progress report will discuss recent DEA, DI, and surface studies performed on one such organometallic compound, π -allyl ruthenium tricarbonyl bromide. Ultimately, a suite of gas phase, surface, and in-situ FEBID studies will be performed on this molecule, as well as several other organometallic and metal carbonyl species, in order to elucidate the role of different low-energy electron induced processes in the FEBID nanofabrication process.

Acknowledgements: This work is supported by the Icelandic Research Fund (RANNÍS) and the University of Iceland Research Fund. This work was conducted within the framework of the COST Action CM1301 (CELINA).

REFERENCES

- [1] S. Engmann, M. Stano, Š. Matečik, and O. Ingólfsson. *Phys. Chem. Chem. Phys.* 14, (2012). 14611-14618.
- [2] N. Silvis-Cividjian, C.W. Hagen, and P. Kruit. *J. Appl. Phys.* 98, (2005). 084905.

ELECTRON TRANSFER UPON POTASSIUM COLLISIONS WITH BIOMOLECULES

F. Ferreira da Silva¹, G. Meneses¹, T. Cunha¹, D. Almeida¹, G. García² and
P. Limão-Vieira¹

¹ *Laboratório de Colisões Atômicas e Moleculares, CEFITEC, Departamento de Física, Faculdade de Ciências e Tecnologia, Universidade Nova de Lisboa, Campus de Caparica, 2829-516 Caparica, Portugal*

² *Instituto de Física Fundamental, Consejo Superior de Investigaciones Científicas (CSIC), Serrano 113-bis, 28006 Madrid, Spain*

Electron driven reactions play an important role as far as biological systems are concerned. Proteins activity and functionality depends on the their structure. Depending on the biological function, proteins can act as catalysts, storage and transport of different molecules, support and shape of the cells, just to mention a few. The building blocks of the proteins are amino acids, that are in a specific sequence giving to the polipetides the compact shape that contains coils, zigzags, turns or loops. However, such can be disturbed within the physiological environment upon electron capture as a result of radiation induced processes. Understanding low-energy electrons induced decomposition, allows a proper description of the underlying molecular mechanisms. Electron transfer through the chain of amino acids can induce fragmentation leading to the loss of integrity of a protein. Electron transfer studies in potassium collisions with amino acids and simple carboxylic acids, as acetic acid, have been studied in order to understand how low energy electrons induced fragmentation via negative ion formation. [1, 2] In the present communication single amino acids as alanine, valine and tyrosine and also acetic acid decomposition upon collisions with potassium atoms will be presented in order to elucidate their fragmentation pathways.

Acknowledgements: FFS acknowledge the FCT-MEC SFRH/BPD/68979/2010, PEst-OE/FIS/UI0068/2011 and PTDC/FIS-ATO/1832/2012 grants.

REFERENCES

- [1] F. Ferreira da Silva, M. Lanca, D. Almeida, G. Garcia and P. Limao-Vieira, *Europ. Phys. J. D*, 66, 78 (2012).
- [2] F. Ferreira da Silva, J. Rafael, T. Cunha, D. Almeida and P. Limao-Vieira, *Int. J. of Mass Spectrom*, 365-366, 238-242 (2014).

ABSOLUTE DIFFERENTIAL CROSS SECTIONS FOR ELASTIC ELECTRON SCATTERING FROM SMALL BIOMOLECULES

J. B. Maljković

*Laboratory for Atomic Collision Processes, Institute of Physics Belgrade,
University of Belgrade, Pregrevica 118, 11080 Belgrade, Serbia*

E-mail: jelenam@ipb.ac.rs

The experimental investigation of electron interaction with biomolecules that are analogues to building blocks of DNA (furan, 3-hydroxytetrahydrofuran and pyrimidine) and proteins (formamide, N-methylformamide), at medium incident electron energies 40 – 300 eV, is presented. Motivation for this investigation came from the radiation damage research and a need to understand the role of secondary electrons formed by high-energy particles [1]. The accurate cross sections obtained under well-defined conditions may thus represent starting parameters in a more complex modeling. The experimental procedure includes the measurement of both relative and absolute cross sections (using the relative flow method) for elastic electron scattering from biomolecules, as well as the measurement of kinetic energy distribution of positive ions. Experimental results are compared with theory, based on a corrected form of independent atom model, Screen Corrected Additivity Rule (SCAR) [2], showing a good agreement.

Acknowledgements: The work was supported by the Ministry of Education, Science and Technological Development of Republic of Serbia (Project No. 171020) and motivated by the COST Action MP 1002 (Nano-IBCT).

REFERENCES

- [1] B. Boudaiffa, P. Cloutier, D. Hunting, M. A. Huels and L. Sanche, *Science* 287, 1658 (2000).
- [2] F. Blanco and G. García, *Phys. Lett. A* 360, 707 (2007).

ELECTRON – INDIUM ATOM SCATTERING AND ANALYSIS OF ELECTRON AND OPTICAL SPECTRA

Maja S. Rabasović

¹*Institute of Physics, University of Belgrade, Belgrade, Serbia*

Presented is an overview of experimental study of indium atom using electron and optical spectroscopy. Both experimental techniques including experimental setups [1, 2] are described. Differential and integrated cross sections on elastic and inelastic electron scattering by indium atom were measured using electron spectrometer. The measurements were performed at incident electron energies of $E_0 = 10, 20, 40, 60, 80$ and 100 eV. Optical spectra of In I and In II lines have been acquired by a streak camera [2, 3]. Plasma was generated using Nd:YAG laser. In I and In II emission lines in the time domains ranging from 500 ns to 20 μ s are presented in Fig. 1.

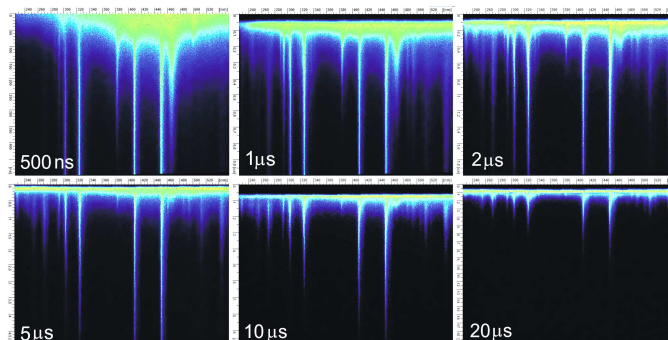


Figure 1. Time resolved LIBS streak images of pure indium sample with time range from 500 ns to 20 μ s..

Acknowledgements: This work has been done within the project MESTD RS OI 171020.

REFERENCES

- [1] D. Šević, M. S. Rabasović, V. Pejčev and B. P. Marinković, Chapter in the book *Indium: Properties, Technological Applications and Health Issues* p.241, (Nova Science, New York, 2013).
- [2] M. S. Rabasović, D. Šević, V. Pejčev, B. P. Marinković, Nucl.Instrum. Meth. B. 279, 58 (2012).
- [3] D. Šević, M. S. Rabasović and B. P. Marinković, IEEE Trans. Plasma Sci. 39 (11), 2782 (2011).

SINGLE ELECTRON CAPTURE IN FAST ION- ATOM COLLISIONS

Nenad Milojević

*Department of Physics, Faculty of Sciences and Mathematics
University of Niš, P.O.Box 224, 18000 Niš, Serbia*

Single-electron capture cross sections in collisions between fast bare projectiles and heliumlike atomic systems is investigated by means of the four-body boundary-corrected first Born (CB1-4B) approximation. The prior and post transition amplitudes for single charge exchange encompassing symmetric and asymmetric collisions are derived in terms of twodimensional real integrals in the case of the prior form and five-dimensional quadratures for the post form. The dielectronic interaction $V_{12} = 1/r_{12} = 1/[r_1-r_2]$ explicitly appears in the complete perturbation potential V_f of the post transition probability amplitude T_{if}^+ . An illustrative computation is performed involving state-selective and total single capture cross sections for the p - He (prior and post form) and He²⁺; Li³⁺; Be⁴⁺; B⁵⁺; C⁶⁺ -He (prior form) collisions at intermediate and high impact energies. We have also studied differential cross sections in prior and post form for single electron transfer from helium by protons. The role of dynamic correlations is examined as a function of increased projectile energy. Detailed comparisons with the measurements are carried out and the obtained theoretical cross sections are in reasonable agreement with the available experimental data.

SIMULATION AND MODELING OF RESISTIVE PLATE CHAMBERS

D. Bošnjaković, Z.Lj. Petrović and S. Dujko

*Institute of Physics, University of Belgrade,
Pregevica 118, 11080 Belgrade, Serbia*

Due to their excellent timing resolution and good spatial resolution, Resistive Plate Chambers (RPCs) became one of the most commonly used gaseous particle detectors, mainly for timing and triggering purposes in high energy physics experiments. Despite of their simple construction, which often consists of a single gas gap between the electrodes of highly resistive material (e.g. glass or bakelite), their modeling is not an easy task. A complete model of these devices must consider three distinct physical processes: 1) primary ionization, i.e. interaction between the high energy particle and the gas, 2) charge transport and multiplication in the gas, and 3) signal generation and electrode relaxation effects. We focus on the first two processes and discuss their effects on the main performance characteristics of an RPC such as timing resolution and detection efficiency. Then, we review different approaches in RPC modeling. Finally, we present our “microscopic” RPC model where each electron and its collisions with the gas are followed using a Monte Carlo technique. This approach demands the use of high performance computing facilities and can be considered as a nearly exact model for relatively low values of signal threshold corresponding to about 10^6 electrons in the gas gap. The results for timing resolution and efficiency of a specific timing RPC with 0.3 mm gas gap and a gas mixture of 85% $C_2H_2F_4$ + 5% iso- C_4H_{10} + 10% SF_6 are compared with experimental values [1] while taking into account different cross section sets for electron scattering in $C_2H_2F_4$. The comparison is also made with an analytical model [2] for timing distribution of electron avalanches and possible causes of slight deviations are discussed.

Acknowledgements: This work is supported by MPNTR, Serbia, under the contract number OI171037.

REFERENCES

- [1] L. Lopes, P. Fonte and A. Mangiarotti, Nucl. Instrum. Meth. A 661, S194 (2012).
- [2] W. Riegler, Nucl. Instrum. Meth. A 602, 377 (2009).

COMPLEX-ROTATION AND WAVE-PACKET CALCULATIONS OF THE IONIZATION RATE FOR HYDROGEN ATOM IN ELECTRIC FIELD

Milan Z. Milošević¹ and Nenad S. Simonović²

¹*Faculty of Science and Mathematics, University of Niš, Višegradska 33, 18000
Niš, Serbia*

²*Institute of Physics, University of Belgrade, Pregrevica 118, 11080 Belgrade,
Serbia*

Abstract. Applying two different methods, the complex rotation and the wave packet propagation method, the position and width of the lowest (resonant) state of hydrogen atom in external electric field are calculated for different field strengths. Using these results the validity of Landau formula for ionization rate in the tunneling regime is demonstrated.

1. INTRODUCTION

Ionization of the hydrogen atom in external electric field is a problem which is many times considered using different theoretical methods. Since the Hamiltonian of the system (here we use the atomic units)

$$H = \frac{p^2}{2} - \frac{1}{r} - Fz, \quad (1)$$

is separable in parabolic coordinates, for small values of the strength of electric field F it was possible to obtain approximate analytical expressions for the energy levels as functions of F , as well as the ionization rates when the atom is in the ground state (the so-called Landau formula) [1]

$$w = \frac{4}{F} \exp\left(-\frac{2}{3F}\right). \quad (2)$$

The latest expression essentially determines the probability (per unit time) of the ionization of a hydrogen atom in an electric field due to the electron tunneling through the potential barrier formed by the nuclear Coulomb potential and the constant external field (see Figure 1). A consequence of the presence of this finite barrier is that all states of the system described by Hamiltonian (1) have in fact the resonant character and formula (2) also determines the width of the lowest state.

Even today the hydrogen atom in constant electric field is frequently used as a good example for testing new theories and methods treating the problems with a perturbation which makes the spectrum continuous. Finally, within the so-called static field approximation this problem may be the first step in the analysis of ionization of atoms due to the absorption of electromagnetic radiation. Here we analyze the lowest state of the system described by Hamiltonian (1) by the use of two different methods: the complex rotation method and the wave packet propagation method.

2. COMPLEX ROTATION METHOD

A resonant state $\psi(\mathbf{r})$ can be regarded as an extension of the concept of bound state in a sense that it is an eigensolution of the Schrödinger equation which asymptotically behaves as a purely outgoing wave ($\psi(\mathbf{r})$ is not square integrable, see Figure 1) with complex eigenenergy E_{res} . The real and imaginary parts of E_{res} determine the energy (position) and the width of resonance, $E = \text{Re}(E_{\text{res}})$, $\Gamma = -2 \text{Im}(E_{\text{res}})$. The basic idea of the complex rotation method (see e.g. Ref. [2]) is to make the resonance wave function $\psi(\mathbf{r})$ square integrable by a complex rotation of the coordinate, $\psi(\mathbf{r}) \rightarrow \psi_{\theta}(\mathbf{r}) = \psi(e^{i\theta} \mathbf{r})$, where θ is a real parameter called the ‘rotation angle’. Such a ‘rotated’ state $\psi_{\theta}(\mathbf{r})$ is an eigenfunction of the so-called complex rotated Hamiltonian H_{θ} obtained from the original Hamiltonian H by the transformations $\mathbf{r} \rightarrow e^{i\theta} \mathbf{r}$, $\mathbf{p} \rightarrow e^{-i\theta} \mathbf{p}$. The spectrum of Hamiltonian (1) can be computed by diagonalizing the corresponding rotated Hamiltonian in a square integrable basis which is complete in a sense that it covers the continuous part of the spectrum, too. For this purpose we have used here the Sturmian basis [3]. Some results are shown in Table 1 as well as in Figure 2.

3. WAVE PACKET APPROACH

Alternatively the resonant states can be studied using a time dependent approach. If $\psi(\mathbf{r},0)$ is an initial wave function (wave packet) one can calculate the wave function $\psi(\mathbf{r},t)$ at an arbitrary time t by integrating the time dependent Schrödinger equation. Technically, this method reduces to the construction of a sufficiently accurate representation for the evolution operator $U(\Delta t)$, where Δt is a small time step. Then, the wave function $\psi(\mathbf{r},t)$ at a discretized time t can be obtained by integrating numerically the relation $\psi(\mathbf{r},t + \Delta t) = U(\Delta t)\psi(\mathbf{r},t)$. The energy spectrum for a given system can be obtained from the autocorrelation function $c(t)$, which is the overlap between the functions $\psi(\mathbf{r},t)$ and $\psi(\mathbf{r},0)$, by calculating its power spectrum (i.e. $|\text{FT}[c(t)]|^2$, where $\text{FT}[c(t)]$ is the Fourier transform of $c(t)$). In the power spectrum resonances appear as (approximate) Lorentzian profiles containing the information about their positions (E) and widths (Γ). In order to calculate E and Γ for the lowest state of the system determined by Hamiltonian (1), we choose for $\psi(\mathbf{r},0)$ to be the unperturbed ground state wave function of the hydrogen atom and calculate its evolution by the use of a variant of the second-order-differential scheme [4]. Since $\psi(\mathbf{r},0)$ for

$F > 0$ is not a stationary state, initially it moves periodically as a wave-packet in the potential $V = -1/r - Fz$. However, at each reflection from the potential barrier a part of the packet transmits in the outer region, and after some time (~ 100 a.u.) it reduces to an almost stationary state with well defined outgoing wave – the resonance wave function ψ (see the top of Figure 1).

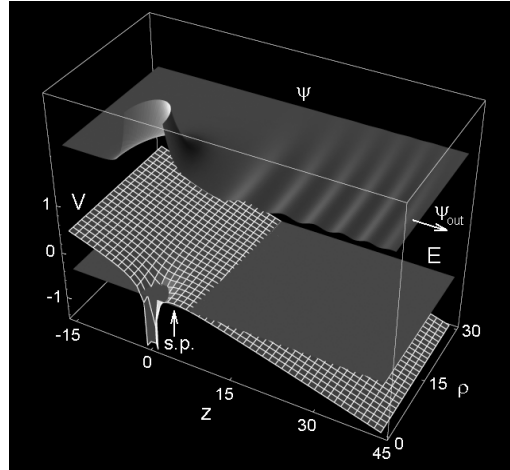


Figure 1. Bottom: The potential $V = -1/r - Fz$ (in cylindrical coordinates) for the field strength $F = 0.05$ a.u. and the corresponding lowest energy level E . The vertical arrow shows the position of the saddle point (s.p.) of the potential barrier. Top: The real part of the total wave function ψ corresponding to the lowest level.

4. RESULTS

Table 1. The positions E and widths Γ of the lowest energy level of hydrogen atom in external electric field for different field strengths F (all in atomic units) obtained using the complex rotation (CR) and the wave packet (WP) methods.

F	E (CR)	Γ (CR)	E (WP)	Γ (WP)
0	-0.5	0	-0.5	0
0.05	-0.5061	0.772E-4	-0.5061	0.66E-4
0.10	-0.5274	0.01453	-0.5276	0.01405
0.15	-0.5511	0.06004	-0.5514	0.05878
0.20	-0.5701	0.1212	-0.5694	0.1212
0.25	-0.5850	0.1895	-0.586	0.192

The values for the energy (position) E and width Γ of the lowest state at several strengths of electric field are shown in Table 1. The results obtained by the two methods are mutually in a good agreement and also in agreement with results of other authors [5]. Generally, the complex rotation method produces the

results with higher accuracy, but the time dependent method gives a better insight into dynamics of the ionization process. Roughly speaking, this process, depending on the field strength, realizes either as the tunnel ionization if $E < V_{\text{sp}}$ or as the over-barrier ionization if $E > V_{\text{sp}}$. V_{sp} is the value of the potential V at the saddle point of potential barrier (see Figure 1). It is found that $E = V_{\text{sp}}$ for $F \approx 0.065$ a.u. Finally, we have compared the numerically obtained results with Landau formula (2) (with the assumption that $w = \Gamma$) and confirmed that the formula is valid in the regime of tunnel ionization (see Figure 2).

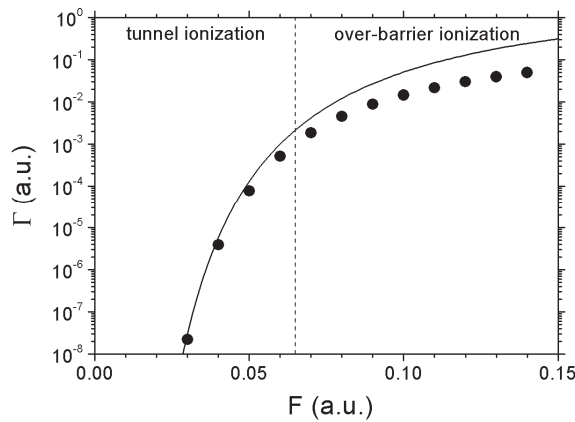


Figure 2. The comparison between numerical data (complex rotation method) for the width Γ of the lowest energy level of hydrogen atom in external electric field F (circles) and the formula (2) for the ionization rate w (full line). The vertical dashed line denotes the value of the field ($F \approx 0.065$ a.u.) when the lowest energy level is equal to the saddle point of the potential barrier.

Acknowledgements

This work is partially supported by Project No. 171020 of the Ministry of Education and Science of Serbia.

REFERENCES

- [1] L. D. Landau and E. M. Lifshitz, *Quantum Mechanics*, p. 296, (Pergamon Press, Oxford, 1991).
- [2] A. Buchleitner, B. Grémaud and D. Delande, *J. Phys. B: At. Mol. Opt. Phys.* 27, 2663 (1994).
- [3] J. Avery and J. Avery, *Generalized Sturmians and Atomic Spectra* (Singapore: World Scientific, 2006).
- [4] A. Askar and A. S. Cakmak, *J. Chem. Phys.* 68, 2794 (1978).
- [5] M. Hehenberger, H. V. McIntosh and E. Brändas, *Phys. Rev. A* 10, 1494 (1974); M. R. Hermann and J. A. Fleck, Jr., *Phys. Rev. A* 38, 6000 (1988).

EFFECTIVE LIFETIMES OF THE POSTSELECTED HYDROGEN ATOMS

I. P. Prlina and N. N. Nedeljković

University of Belgrade, Faculty of Physics, P.O.Box 368, Belgrade, Serbia

Abstract. The time symmetrized two-state vector model is adapted for postselected quantum systems with effectively non-unitary evolutions. We study the radiative decay $2p \rightarrow 1s$ of the postselected hydrogen atom. The effective lifetime $\tau_{\text{eff}}(t)$ is obtained for a model postselection, and acceleration or attenuation of the decay due to the postselection is briefly discussed, with emphases on the possible experimental applications.

1. INTRODUCTION

In recent times, some interesting systems and phenomena based on the time-symmetrized two-state vector model (TVM) [1, 2, 3, 4] have been considered theoretically; for example, the weak trace describing the past of a quantum particle [5]. The practical applications of the so called weak measurements on the postselected systems have also been demonstrated, based on their ability to enhance the measured experimental signal [6]. Some intriguing experiments based on the TVM, such as determining the "trajectories" of individual photons [8] and the wave function of the photon itself [7], have been recently performed. In the cited experiments, the weak measurements have been used, because in that case the reduction of quantum state can be avoided. The "strong" measurements, which could also produce a series of intriguing results, have not gained such attention.

In the present article we apply the TVM to the quantum decay of the postselected atomic systems. To concretize the problem, we analyze the (radiative) decay of the hydrogen atoms, considering the $2p \rightarrow 1s$ transitions. That is, we derive the time-symmetrized survival probability $\mathcal{P}_S(t)$. As a consequence of postselection, we obtain a modified "decay law" in comparison to the exponential decay $\mathcal{P}_S^{(0)}(t) = \exp(-t/\tau)$, where τ is the radiative lifetime in the absence of postselection. The survival probability $\mathcal{P}_S(t)$ decreases in time with the effective lifetime $\tau_{\text{eff}}(t)$ different than τ .

2. THEORETICAL MODEL

We assume that the atomic system is preselected at the time t_{in} in the state $\hat{\rho}_{\text{in}} = |\beta\rangle\langle\beta|$, where $|\beta\rangle$ is the first excited atomic electronic state of energy E_β ; the ground state will be denoted by $|\alpha\rangle$. For the postselection we choose the "measurement" $\hat{\Pi}_{\text{fin}} \equiv \hat{\rho}_{\text{fin}} = |\Psi_{\text{fin}}\rangle\langle\Psi_{\text{fin}}|$. We analyze the intermediate survival probability $\mathcal{P}_S(t^*)$ at the time $t = t^*$, on the postselected (teleological) ensemble.

The probability $\mathcal{P}_S(t^*)$ is given by

$$\mathcal{P}_S(t^*) = \frac{\text{Tr}(\hat{\rho}_1(t^*)\hat{\Pi}_\beta) \text{Tr}(\hat{\rho}_\beta(t_{\text{fin}})\hat{\Pi}_{\text{fin}})}{\text{Tr}(\hat{\rho}_0(t_{\text{fin}})\hat{\Pi}_{\text{fin}})}, \quad (1)$$

for $\hat{\Pi}_\beta = |\beta\rangle\langle\beta|$. In Eq. (1), $\hat{\rho}_1(t^*)$ is the result of the time evolution of the initial state $\hat{\rho}_{\text{in}}$ at the time of the intermediate measurement. By considering the radiative transitions in the atomic systems standardly as a consequence of the coupling of these systems to the field of photons, we get: $\hat{\rho}_1(t^*) = e^{-\Gamma_\beta\Delta_i}|\beta\rangle\langle\beta| + |a(\Delta_i)|^2|\alpha\rangle\langle\alpha|$, where $\Delta_i = t^* - t_{\text{in}}$ and $|a(\Delta_i)| = \sqrt{1 - e^{-\Gamma_\beta\Delta_i}}$. The quantity Γ_β has the meaning of the transition rate; the quantity $\tau = 1/\Gamma_\beta$ is the lifetime of the level E_β . For the explicit calculation of the survival probability we also need the expression $\hat{\rho}_\beta(t_{\text{fin}}) = \hat{\rho}_1(t^*)/\Delta_{i \rightarrow \Delta_f}$, where $\Delta_f = t_{\text{fin}} - t^*$. In general, the quantity $\hat{\rho}_0(t_{\text{fin}})$ in Eq. (1) depends on the particular experimental setup. In the considered case we have $\hat{\rho}_0(t_{\text{fin}}) = \exp(-\Gamma_\beta\Delta_i)\hat{\rho}_\beta(t_{\text{fin}}) + |a(\Delta_i)|^2|\alpha\rangle\langle\alpha|$.

The postselection condition requires that the state $|\Psi_{\text{fin}}\rangle$ is obtained by measurement performed on the atomic system at the final time $t = t_{\text{fin}}$. By the choice of the particular postselection, providing that the teleological ensemble could exist, we modify the dynamics of the radiative decay. We consider the following postselection:

$$|\Psi_{\text{fin}}\rangle = \frac{|\beta\rangle + \epsilon|\alpha\rangle}{\sqrt{1 + |\epsilon|^2}}, \quad (2)$$

where ϵ is a complex parameter. By this kind of postselection, via the parameter ϵ , we can choose the desired fraction (percentage) of survived excited atoms at the final time $t = t_{\text{fin}}$, and analyze their behavior in the time $t = t^* < t_{\text{fin}}$.

Finally, for the survival probability $\mathcal{P}_S(t^*)$ we have:

$$\mathcal{P}_S(t^*) = \frac{1 + |\epsilon|^2 (e^{\Gamma_\beta\Delta_f} - 1)}{1 + |\epsilon|^2 (e^{\Gamma_\beta\Delta} - 1)}, \quad (3)$$

where $\Delta = t_{\text{fin}} - t_{\text{in}}$. To simplify the presentation of our results, we express the parameter ϵ in terms of the final survival probability \mathcal{P}_{Sf} , namely we take that $\mathcal{P}_S(t_{\text{fin}}) = \mathcal{P}_{\text{Sf}}$; from this we get $|\epsilon| = \sqrt{(1/\mathcal{P}_{\text{Sf}} - 1) / (e^{\Gamma_\beta\Delta} - 1)}$.

3. EFFECTIVE LIFETIME

We define the effective decay rate $\Gamma_{\text{eff}}(t)$ by the following relation: $\Gamma_{\text{eff}}(t) = -[d\mathcal{P}_S(t)/dt]/\mathcal{P}_S(t)$; the effective lifetime can be introduced as $\tau_{\text{eff}}(t) = 1/\Gamma_{\text{eff}}(t)$. The quantity $\tau_{\text{eff}}(t)$ can be obtained in the analytic form; namely, for the survival probability given by Eq. (3), we get

$$\tau_{\text{eff}} = \tau \left[1 + e^{t/\tau} \frac{\mathcal{P}_{Sf} - \mathcal{P}_{Sf}^{(0)}}{1 - \mathcal{P}_{Sf}} \right]. \quad (4)$$

The effective lifetime can be easily controlled by choosing the \mathcal{P}_{Sf} by the appropriate postselection condition; also, the effective lifetime depends on the time of postselection t_{fin} via the probability $\mathcal{P}_{Sf}^{(0)} = \mathcal{P}_S^{(0)}(t_{\text{fin}})$.

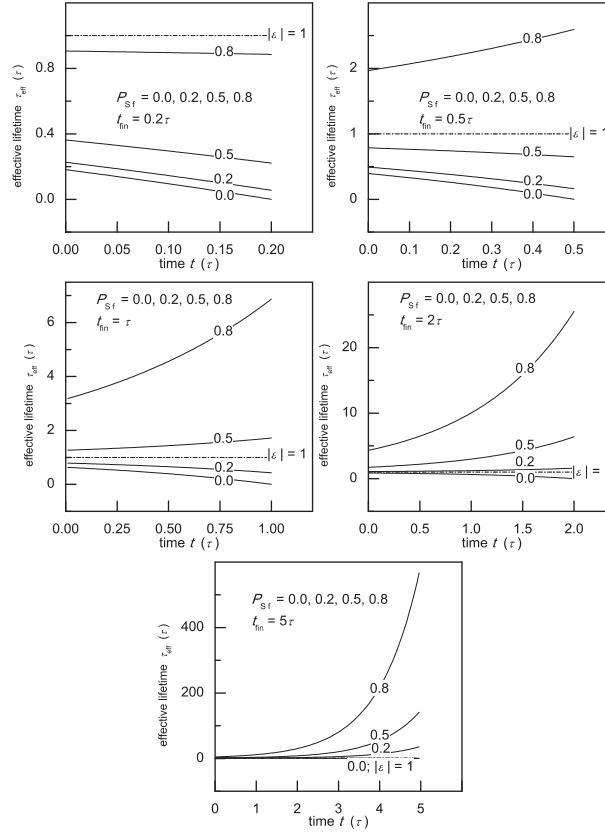


Figure 1. Effective lifetimes τ_{eff} .

In Fig. 1 we present the quantity $\tau_{\text{eff}}(t)$ obtained from Eq. (4) for the hydrogen atom postselected at different final times t_{fin} . For a given

final time, the effective lifetimes are considered for the atomic system post-selected for $\mathcal{P}_{\text{Sf}} = 0.2, 0.5$ and 0.8 , as well as for $\mathcal{P}_{\text{Sf}} = 0$, and for "natural postselection" $\mathcal{P}_{\text{Sf}} = \mathcal{P}_{\text{Sf}}^{(0)}$, i.e., for $|\epsilon| = 1$. For $\mathcal{P}_{\text{Sf}} = 1$, $\tau_{\text{eff}} = \infty$. For the natural postselection $\tau_{\text{eff}}(t) = \tau$; in other cases, the quantity $\tau_{\text{eff}}(t)$ could be less or greater than τ depending on the postselection and the final time. This circumstance can be interpreted as acceleration and attenuation of the decay, respectively, due to the postselection.

This conclusion could be of importance for the spectroscopy. That is, if the measurement of the spectral line is performed in the postselected atomic system such that $\tau_{\text{eff}} > \tau$, which is the case for $\mathcal{P}_{\text{Sf}} > \mathcal{P}_{\text{Sf}}^{(0)} = \exp(-t_{\text{fin}}/\tau)$, we could obtain more precise values of the atomic energies than in the absence of postselection, since the line width $\Gamma_{\text{eff}} < \Gamma_{\beta}$. Also, the same effect potentially allows to gain better monochromaticity of radiation, by collecting only those photons which originate from the postselected atoms. Detailed analysis of these applications requires an additional work.

Acknowledgements This work was supported in part by the Ministry of Education, Science and Technological Development, Republic of Serbia (Project 171016).

REFERENCES

- [1] Y. Aharonov, P. G Bergmann and J. L. Lebowitz, Phys. Rev. 134, B1410 (1964).
- [2] Y. Aharonov and L. Vaidman, J. Phys. A: Math. Gen. 24, 2315 (1991).
- [3] Y. Aharonov and L. Vaidman *The Two-State Vector Formalism: An Updated Review*, in: Time in Quantum Mechanics, Lect. Notes Phys. 734, edited by J.G. Muga, R. Sala Mayato and I.L. Egusquiza (Springer, Berlin Heidelberg, 2008).
- [4] N. N. Nedeljković and M. D. Majkić, Phys. Rev. A 76, 042902 (2007).
- [5] L. Vaidman, Phys. Rev A 87, 052104 (2013).
- [6] O. Hosten and P. Kwiat, Science 319, 787 (2008).
- [7] J. S. Lundeen, B. Sutherland, A. Patel, C. Stewart and C. Bamber, Nature 474, 188 (2011).
- [8] S. Kocsis, B. Braverman, S. Ravets, M. J. Stevens, R. P. Mirin, L. K. Shalm and A. M. Steinberg, Science 332, 1170 (2011)

ULTRAFAST DISSOCIATIVE PHOTOELECTRON ATTACHMENT IN PHOTOEMISSION FROM CO

D. A. Rostov¹, Ye. S. Kan¹, Yu. S. Krivosenko¹, X. O. Brykalova¹,
A. A. Pavlychev¹

¹*V.A. Fock Institute of Physics, St. Petersburg State University,
St. Petersburg, 198504, Russian Federation*

Abstract. The photoelectron–valence electrons interaction results in self-trapping of the ejected photoelectron by the remaining ion with the subsequent formation of the 2 holes – 2 electrons state. The analysis of the C 1s photoemission spectra of CO for photon energies $297 < h\nu < 305$ eV in the $\Sigma \rightarrow \Sigma$ channel revealed the ultrafast dissociation of the $\text{CO}^{**}(\text{C}1s^{-1}1\pi^{-1}2\pi^2)$ molecular state.

1. INTRODUCTION

When a core hole is created in a molecule, dissociation is very likely to occur following or during electronic relaxation. The main pathways to molecular fragmentation are a result of the core-ionized species, which are metastable and subsequently dissociate breaking chemical bonds or decay to multiply charged molecular ions. But when the dissociation occurs on the same timescale as electron decay, the process is defined as ultrafast dissociation, meaning that the molecule may fragment on the same femtosecond scale as Auger decay. The simplest molecular systems, in which core-to-valence transitions give start to the ultrafast dissociation, are core excited diatomics such as HCl, HBr and Cl₂ [1, 2]. In the present work a new process resulting in the ultrafast dissociation is considered. We show that there is an ultrafast dissociative 2 holes – 2 electrons state in CO. It is originated from the photoelectron – valence electron (PEVE) interaction leading to the attachment of the photoelectron ejected from C 1s level to the remaining molecular ion and formation the core-valence excited CO^{**} molecule. To investigate the process the spectral distribution of the C 1s $\rightarrow\sigma^*$ shape resonance in CO is inspected in more detail.

Shape resonances in X-ray absorption and inner-shell photoemission from free molecules are associated with temporary trapping of the photoelectron within the finite size potential (pseudopotential) barrier and subsequent tunneling of the photoelectron through the barrier into the continuum. Spectral distribution of oscillator strength for X-ray transitions in the shape resonance vicinity are reasonably described as a convolution of asymmetric and symmetric Lorentzian

and Gaussian line shapes [3]. The Lorentzian contributions determine the resonance lifetime that is originated by both the photoelectron trapping time and the core-hole lifetime. The experimental data analysis confirms applicability of this triple convolution approach to extract the lifetimes of the resonances in free and bound nanosystems [3].

2. MAIN RESULTS

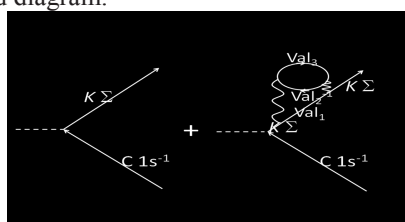
PEVE interaction [4, 5] leads to the complicated distortion of the shape resonance profile. Our attention attracts the parallel $\Sigma \rightarrow \Sigma$ transition near the C 1s shape resonance in the fixed-in-space CO molecule with emphasis on the irregular spectral behavior in the interval 297 – 305 eV. The behavior is examined in more detail in the works [6, 7]. The double core-valence excitations superimpose with the $\sigma^*(\Sigma)$ shape resonance. The double excitations are studied in detail for the perpendicular $\Sigma \rightarrow \Pi$ transitions and are practically not studied for the parallel $\Sigma \rightarrow \Sigma$ one because of the difficulties in observation of the later. To study the double excitations in the $\Sigma \rightarrow \Sigma$ channel we have analyzed more precisely the experimental spectral distribution of oscillator strength at the $\sigma^*(\Sigma)$ shape resonance.

To describe the effect of the photoelectron recapture due to PEVE interaction on the shape resonance the optical potential concept [4] is generalized. We have computed the C 1s hole creation σ^\oplus and single-hole ionization $\sigma^{+\square}$ cross sections for the $\Sigma \rightarrow \Sigma$ transition in the near-edge spectral region using the triple convolution approach [3], the optical potential concept [4] and the VDFN model [8].

Black and grey symbols in figure 1 presents the experimental photoemission spectra at the C 1s(Σ) \rightarrow $\sigma^*(\Sigma)$ shape resonance in the fixed-in-space CO. The data are taken from the works [6] and [7] respectively. As the first step to understand the complicated spectral distribution of oscillator strength of C 1s $\Sigma \rightarrow K\Sigma$ transitions for the photon energies 297 – 305 eV we have applied the triple convolution and VDFN approaches [3, 8] (see also for more detail [9]). The combination provides the description of the shape resonance in respect to the vibronic coupling. However, in the case the coupling of elastic and inelastic electron scattering effects is neglected. The dashed line in figure 1 displays the best fit of the $\sigma^*(\Sigma)$ shape resonance. We note that the dashed line describes reasonably the energy position and width of the shape resonance position but does not reproduce the complicated spectral variations observed in the low-energy side of the resonance.

To understand their origin, in the second step, we take into account PEVE interaction: the photoelectron coming through the molecular barrier interacts with valence electrons that form the barrier [4, 5]. As a result the barrier has to be regarded as deformable. According to the work [4] we introduce the optical potential $V^{\text{opt}}(k, \mathbf{r}) = W(k, \mathbf{r}) - iU(k, \mathbf{r})$. The imaginary part $U(k, \mathbf{r})$ describes the dissipation of the C 1s photoelectron through the molecular ion.

The valence electrons are excited due to the photoelectron impact. It is evident that the photoelectron impact plays particular role for the parallel transition when the photoelectron moves predominantly along the molecular axis. Using the optical potential we are able to describe the intramolecular interference of the primary and scattered photoelectron waves taking the core-valence $C1s^{-1}Val_2^{-1}Val_1Val_3$ excitations into account. This effect on the elastic scattering amplitude is described by the second diagram:



Then, to investigate the experimental cross section in figure 1 we have included the core-valence $2\sigma(C1s)^{-1}5\sigma^{-1}2\pi^2$, $2\sigma(C1s)^{-1}1\pi^{-1}2\pi^2$, $2\sigma(C1s)^{-1}5\sigma^{-1}2\pi^1Ryd^1$ ($S=1$) and $2\sigma(C1s)^{-1}5\sigma^{-1}2\pi^1Ryd^1$ ($S=0$) excited states. Their energy positions and potential curve characteristics are taken from the works [6, 10].

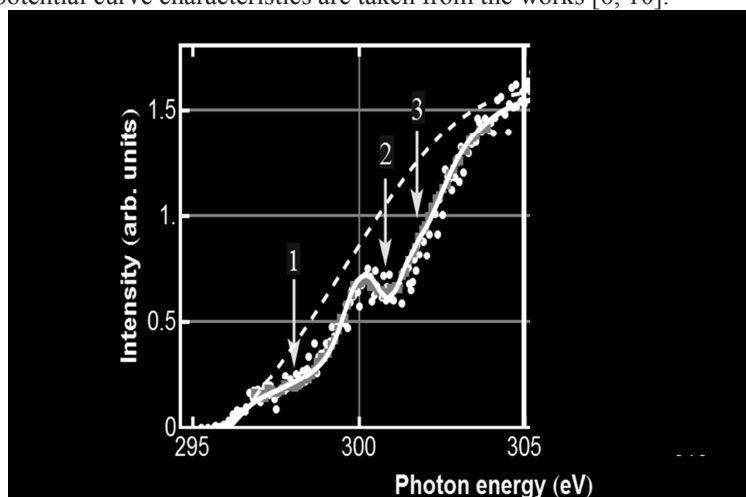
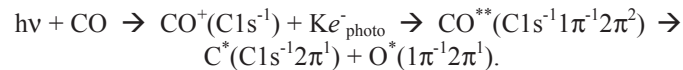


Figure 1. The experimental photoemission intensity near the $C 1s(\Sigma) \rightarrow \sigma^*(\Sigma)$ shape resonance in the fixed-in-space CO molecule, black and grey symbols are taken from the works [6] and [7] respectively. The computed cross sections with and without the photoelectron attachment are shown with \square solid and dashed lines, respectively. The arrow 1 shows the position of the $2\sigma(C1s)^{-1}1\pi^{-1}2\pi^2$ state.

The account of the triplet $2\sigma(C1s)^{-1}5\sigma^{-1}2\pi^2$, $2\sigma(C1s)^{-1}5\sigma^{-1}2\pi^1Ryd^1$ ($S=1$) and singlet $2\sigma(C1s)^{-1}5\sigma^{-1}2\pi^1Ryd^1$ ($S=0$) states (the arrows 2 and 3) allows as to reproduce the irregular behavior of the shape resonance at 301 eV (solid line in figure 1). In the work we do not discuss this spectral feature. By analyzing the computed C 1s hole creation and single-hole ionization cross

sections with the experimental spectra we conclude that *i*) the C 1s photoelectron ejected along the molecular axis with the kinetic energy $K < 2$ eV is effectively attached to $\text{CO}^+(\text{C}1\text{s}^{-1})$ with the subsequent appearance of the $\text{CO}^{**}(\text{C}1\text{s}^{-1}1\pi^{-1}2\pi^2)$ neutral molecular state, *ii*) the 2h-2e excited CO^{**} is originated by the C 1s photoelectron impact of the 1π valence shell and *iii*) the inverse lifetime of the state is ≈ 2.2 eV. Specifically, the photoemission reaction gives rise to the fast molecular dissociation. The photo- dissociative reaction is:



The quasiatomic concept [4] is used to restore the repulsive molecular potential. We also show that the C 1s photoelectron attachment plays also an important role in forming the triplet and singlet $\text{CO}^{**}(\text{C}1\text{s}^{-1}5\sigma^{-1}2\pi^1\text{Ryd}^1)$ states [8]. However, in contrast to $\text{CO}^{**}(\text{C}1\text{s}^{-1}1\pi^{-1}2\pi^2)$ the fragmentation of $\text{CO}^{**}(\text{C}1\text{s}^{-1}5\sigma^{-1}2\pi^1\text{Ryd}^1 S = 0 \text{ and } 1)$ is determined by the C 1s Auger decay.

3. CONCLUSION

In the conclusion we note that the C 1s photoelectron ejected along the molecular axis with the kinetic energy $K < 2$ eV is effectively attached to $\text{CO}^+(\text{C}1\text{s}^{-1})$ with the subsequent appearance of the $\text{CO}^{**}(\text{C}1\text{s}^{-1}1\pi^{-1}2\pi^2)$ neutral molecular state and the 2h-2e excited CO^{**} is originated by the C 1s photoelectron impact of the 1π valence shell. The photoemission reaction gives rise to the fast molecular dissociation.

Acknowledgements

The authors acknowledge St. Petersburg State University for a research grant 11.38.261.2014.

REFERENCES

- [1] P. Morin, I. Nenner, Phys.Rev.Lett., 56, 1913 (1986).
- [2] W C Stolte et al. J. Phys B 41, 145102 (2008)
- [3] R. Flesch, et al. J. Chem. Phys. 138, 144302 (2013).
- [4] A. A. Pavlychev, J. Phys. B (1999).
- [5] A. de Fanis et al. Phys. Rev. Lett. 89, 023006 (2002).
- [6] M. Kitajima, R. Püttner, S.L. Sorensen et al. Phys. Rev A 78, 033422 (2008).
- [7] E. Shigemasa et.al. Phys. Rev. A 47, 1824 (1993).
- [8] D. A. Rostov, X. O. Brykalova, Ye. S. Kan, Yu. S. Krivosenko, A. A. Pavlychev, will be published.
- [9] X. O. Brykalova et al. SPIG2014 Conference
- [10] K. Ueda et al. Phys. Rev. Lett. 94, 243004 (2005).

THE PHOTOELECTRON- AND NEUTRON-INDUCED RECOIL AS PROBE OF INTERATOMIC INTERACTION IN SOLIDS

Yu. S. Krivosenko and A. A. Pavlychev

V.A. Fock Institute of Physics, St. Petersburg State University,
St. Petersburg, 198504, Russian Federation

Abstract. Photoelectron-induced recoil effects have attracted our attention as a probe of interatomic interaction in matter. The quasi-molecular recoil (QMR) model allows restoring the interatomic potential in the bulk of solids. The model is successfully applied for the description of the recoil effects in the C 1s photoelectron spectra as well as in the neutron scattering in graphite. Our results make evident the applicability of the photoelectron and neutron spectroscopic techniques for the determination of interatomic potentials in bulk. Perspectives in further investigations of the photoelectron- and neutron-induced recoil in matter are discussed.

1. INTRODUCTION

Structure and properties of sp^2 -bonded materials are intensively studied nowadays to utilize their peculiar characteristics in nanotechnology. The most prominent examples are graphite, hexagonal boron nitride (h-BN) as well as graphene and monolayer h-BN grown on various surfaces. Interatomic potentials and strengths of chemical interactions in the materials vary substantially. Different experimental techniques as X-ray absorption spectroscopy, inner-shell photoemission and neutron scattering are successfully used to specify local electronic and atomic properties of the materials.

Recently it was shown that the $core^{-1}$ -photoelectron spectra measured in high kinetic energy regime provide a sensitive probe of interatomic interaction on surfaces and in bulk [1]. When the photoelectron kinetic energy $K > 1000$ eV and the elastically scattered photoelectrons do not contribute essentially to the $core^{-1}$ -photoelectron line the photoelectron-induced recoil dynamics controls its shape and energy position. To extract the interatomic potential the quasi-molecular recoil (QMR) model suggested in [1] is applied for the line shape analysis. Taking into account the strong dynamic core-hole localization on one of equivalent atoms in the solid the inner-shell photoemission is approximately described as occurring in a fixed-in-space quasi-molecule. Since the rotational and translational motions of the quasi-molecule can be drop out the main spectral

changes in the $core^{-1}$ -photoelectron line can be assigned with the local photoelectron-induced vibrations [1, 2]. In the framework of the QMR model the $core^{-1}$ -photoelectron line mostly contains the primary photoelectrons and can be described as

$$I(h\nu) \approx |A_{el}(core \rightarrow K)|^2 \sum_{\nu'} |A_{\nu'}(p_e)|^2 \delta(h\nu - E_{core} - K - E_{\nu'}^+), \quad (1)$$

where $h\nu, E_{core}, E_{\nu'}^+$ are the incident photon energy, the binding energy and the ν' -level vibrational energy, respectively. $A_{el}(core \rightarrow K)$ and $A_{\nu'}(p_e)$ are the amplitudes of electronic and non-Franck-Condon $0 \rightarrow \nu'$ transitions. Eq. (1) shows that the amplitudes $A_{\nu'}(p_e)$ determine the main changes in the photoelectron line under study. The amplitudes depend on both magnitude and direction of the photoelectron moment \vec{p}_e . The direction controls excitations of the different vibration modes whereas the magnitude determines their intensities [2].

In addition to the photoelectron-induced vibrations the local Franck-Condon transitions due to strong core-hole localization also accompany the electronic transition. The interplay of the non-Franck-Condon and Franck-Condon transitions is examined theoretically in the work [2]. However, there is a question: to what extent the QMR model is applicable for the quantitative description of the $core^{-1}$ -photoelectron spectra in solids. To answer this question the QMR model is directly applied both to the photoemission spectra and to the neutron scattering in HOPG measured in the work [3] at the similar recoil condition. In accordance with our expectations the QMR model reproduces both the photoemission and the neutron scattering spectra. Moreover, the later are described more precisely than the former as the former are additionally disturbed by the core-hole relaxation.

2. MAIN RESULTS

The application [1] of the QMR model to the C 1s photoelectron spectra of graphite (HOPG) measured at photon energy 7940 eV and \vec{p}_e nearly perpendicular to the basal plane has revealed that the photoelectron-induced asymmetric stretch vibrations within the quasi-molecule $C_{60}-C^+-C_{60}$ (see, figure 1) allow rationalizing the photoemission spectra. The separation energy of the vibrations is $\hbar\omega_{photo} \approx 60$ meV [1].

Figure 2 (right panel) displays the comparison of the experimental C 1s⁻¹ photoelectron line with the computed one within the $C_{60}-C^+-C_{60}$ model in supposition that $\vec{p}_e \parallel \vec{z}$ (see for detail [1]). The amplitudes $A_{\nu'}(p_e)$ are

$$A_{\nu'}(p_e) = \int \chi_{\nu'}(p+p_e) \chi_0 dp \quad (2)$$

Here χ_v and χ_0 are the eigenfunctions referring to the asymmetric vibrations in ionic and ground states [1].

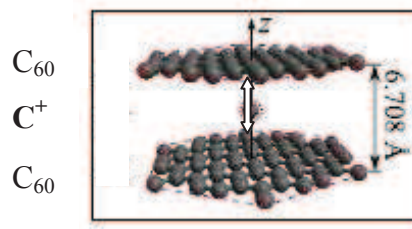


Figure 1. The hexagonal quasi-molecular unit $C_{60}-C^+-C_{60}$ in graphite is plotted. The double arrow shows the asymmetric motion of the core-ionized atom.

To have a complimentary probe of the recoil dynamics in HOPG the QMR model is directly applied to neutron scattering in the solid. In the work [3] the neutron scattering is measured at the equivalent recoil condition. The theoretical and experimental spectra of neutron scattering are shown in figure 2 (left panel). The theoretical data are computed within the QMR model.

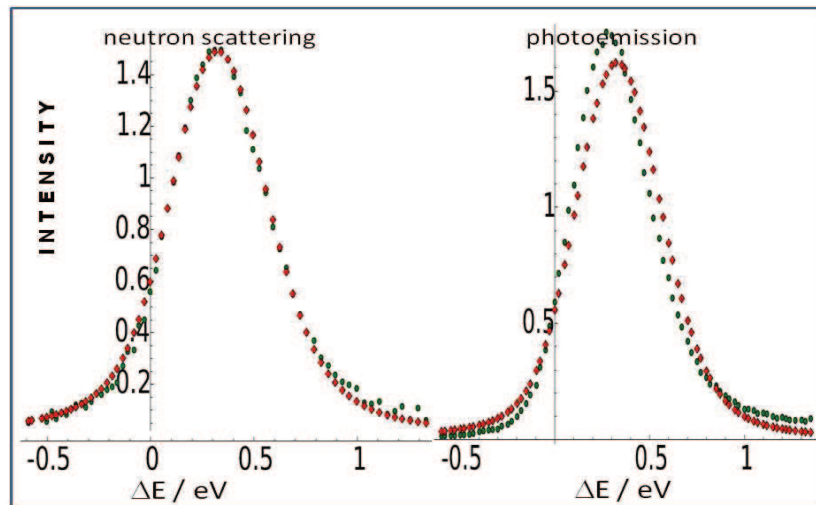


Figure 2. The experimental C 1s photoelectron line (right panel) [4] and the neutron scattering (left panel) [3] on bulk atoms in HOPG: black circles. The theoretical spectra computed within the QMR model: red diamonds. ΔE is the energy shift of the photoelectron and neutron kinetic energies, respectively.

The analysis of the computed and experimental spectra in figure 2 shows that both the photoelectron- and neutron-induced recoil effects in HOPG are reasonably reproduced in the framework of the quasi-molecular $C_{60}-C^+-C_{60}$ model. It is seen that the QMR model provides a more accurate description of the

neutron scattering spectrum. We obtained the separation energy $\hbar\omega_{neutron} \approx 55$ meV for the local neutron-induced asymmetric stretch vibrations in HOPG. The precise coincidence of the photoelectron- and neutron-induced local vibrations in HOPG supports the applicability of the QMR model for the investigation of interatomic interaction in the solid. The analysis of the photoelectron- and neutron-induced recoil effects allows determining the interatomic potential function:

$$U(z; z_{eq}) \approx \frac{1}{2} \mu \omega_{photo(neutron)}^2 (z - z_{eq})^2, \quad (3)$$

where μ is the reduced mass of the quasi-molecule and z_{eq} is the equilibrium position of the core-ionized atom. We assign the more sufficient discrepancy between the experimental and computed spectra obtained for the C 1s⁻¹ photoemission to the core-hole relaxation neglected in the calculations. Within the QMR model the main candidate to explain the difference is the symmetric stretching in the quasi-molecule.

3. CONCLUSION

The photoelectron- and neutron-induced effects on C 1s photoemission and neutron scattering on bulk atoms in graphite are examined in the framework of the QMR model. It is shown that in both cases the observed spectral changes can be mainly assigned with the excitation of local asymmetric vibrations of the quasi-molecular C₆₀-C⁺-C₆₀ unit with the separation energies $\hbar\omega_{neutron} \approx 55$ meV and $\hbar\omega_{photo} \approx 60$ meV. Their similarity confirms the applicability of the QMR model and opens new perspectives in application of the recoil effects for investigations of the interatomic interaction and chemical bonding in bulk and on surface.

Acknowledgements

The authors acknowledge RFBR grant 12-02-00999 and St. Petersburg State University for a research grant 11.38.638.2013.

REFERENCES

- [1] Yu. S. Krivosenko, A. A. Pavlychev, Chem. Phys. Lett. 575, 107 (2013).
- [2] Yu. S. Krivosenko and A. A. Pavlychev, Phys. Rev. A 89, 032517 (2014).
- [3] M. Vos et al., Phys. Rev. B 78, 024301 (2008).
- [4] Y. Takata et al., Phys. Rev B 75, 233404 (2007).

THE SHAPE AND CONFINEMENT RESONANCES IN PHOTOABSORPTION OF FREE AND ENDOHEDRAL MOLECULES

X. O. Brykalova¹, S. V. Kondratiev¹, D. A. Rostov¹, Ye. S. Kan¹,
Yu. S. Krivosenko¹, A. A. Pavlychev¹

¹ *V.A. Fock Institute of Physics, St. Petersburg State University,
St. Petersburg, 198504, Russian Federation*

Abstract. Similarity and distinctions of the shape and confinement resonances in photoabsorption and molecular photoionization are examined. Our emphasis is put on the link of the resonances with molecular dynamics. It is shown that the energy positions of the shape and confinement resonances are respectively disturbed either by the non-Franck-Condon distribution of vibrational excitations or by the effective quadratic displacement of the confined atom (or molecule). As the showcases the O 1s \rightarrow σ^* shape resonance in CO and the lowest Ar 1s confinement resonance in Ar@C₆₀ are computed and discussed.

1. INTRODUCTION

Shape resonance phenomena play a dominating role in the near edge continuum X-ray absorption and photoionization spectra of free molecular species. These resonances are associated with the temporary trap of the photoelectron ejected from molecular core within the finite-size molecular barrier and subsequent tunneling the photoelectron through the barrier into the ionization continuum [1, 2]. The trapping mechanism is usually assigned with the interference of the primary and multiply scattered electron waves when their wave length λ corresponds to quasi-stationary states inside the barrier (see, e.g. [3]). More complicated interference occurs in encapsulated molecules as the ejected electron can be additionally trapped inside the capsule. The shape resonance phenomena in endohedral systems are divided into three groups: (i) the molecular shape resonances, (ii) the confinement resonances and (iii) the window-like resonances [3]. Using the double-barrier-optical-potential model [4] Brykalova and co-authors [3] have shown that, in contrast to the window-like resonances, the origin of the molecular shape and confinement resonances is very similar. They both are related to the trapping of the photoelectron within the single finite-size molecular or capsular barrier and the subsequent tunneling through the barrier. As a result they obey the unified condition: $2k_n R + 2\delta + \varphi \cong 2\pi n$ ($n = 0, 1, \dots$) where the first term is the kinematic

phase shift, R is the radius of the barrier, δ and φ are the electron scattering phase shifts on the ionized atom and the barrier. The trapping times of the ejected electron with the wave number k_n and the core-hole lifetimes determine the resonance widths [2]. The trapping time is usually shorter than the core-hole lifetime.

The major distinctions between the shape resonances and confinement resonances are provoked by the differences in molecular and capsular sizes [5]. Indeed, the coupling of electronic and nuclear-frame motions determines the diversity in the spectral distribution of oscillator strength for X-ray transitions at the shape and confined resonances [3]. As the examples in Section 2 the O 1s \rightarrow σ^* shape resonance in CO and the lowest Ar 1s \rightarrow Ep confinement resonance in Ar@C₆₀ are computed taking the vibronic coupling into account. It is revealed that the shape resonance undergoes substantial distortion due to the non-Franck-Condon distribution of the vibrational excitations whereas the confinement resonance is strongly distorted due to the effective quadratic displacements of the confined argon in the carbonic cage. The deviations in line-shape of the resonances are discussed.

2. MAIN RESULTS

In the shape resonance vicinity the intensity of vibrational excitations demonstrates substantially non-Franck-Condon distribution that is originated by intramolecular interference of the primary and scattered electron waves [6]. According to the work [2] spectral dependence of the single-hole ionization cross section referring to the vibrational $0 \rightarrow v'$ transition is approximated

$$\sigma_{v'}^+ \approx \sigma_0^+ F_{0v'} \sum_{\Gamma} \iint L_{\Gamma}^{photo}(k'; R_{v'}^+) L^{core}(k - k') G(k' - k'') dk' dk''. \quad (1)$$

The equation describes spectral dependence of the cross section in the shape resonance vicinity. L_{Γ}^{photo} , L^{core} are the Lorentz distributions corresponding to the photoelectron trapping and core-hole decay, and G is the Gauss distribution describing the bandwidth of the light source. The amplitude of the back scattered wave ejected from molecular core determines L_{Γ}^{photo} dependent on the effective radius $R_{v'}^+ \approx \frac{1}{2}(R^+ + R_e) + v'\Delta$ of the photoelectron trapping region. Here R_e and R^+ are the equilibrium interatomic distances in ground and ionic states. Δ is the characteristic site-dependent step [6] and $F_{0v'}$ is the Franck-Condon factor. Since the effective radius of the trapping region depends on v' the resonance energy becomes also v' -dependent. This results in the non-Franck-Condon distribution of vibrational excitations at the shape resonance. To demonstrate its spectral dependence of the $0 \rightarrow v'$ excitations that accompany O 1s $\Sigma \rightarrow K\Sigma$ transition is computed for $v'=0, 1, 2$ and compared with the experimental spectra [7]. The

calculations are performed are using Eq.1 and the VDFN model [6] and plotted in figure 1. The theoretical and experimental spectra [7] agree rather precisely.

One can see the positions of the σ^* shape resonance do not coincide with one another for $v'=0, 1$ and 2 . The resonance energies increase with an increase in v' resulting in non-Franck-Condon distribution of vibrational excitations at the shape resonance. On this background the measured position of the shape resonance in the spectra cannot be directly linked with the interatomic distances in absorber.

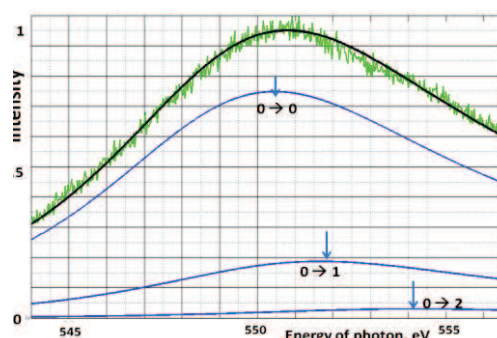


Figure 1. (Color on-line) The computed $O\ 1s^{-1}\sigma^*$ shape resonance in CO for the $v=0 \rightarrow v'=0, 1$ and 2 (blue solid lines). The arrows mark the shape resonance positions. The experimental cross section (green) is taken from the work [7].

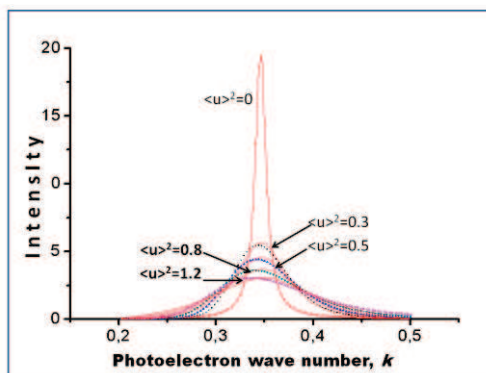


Figure 2. (Color on-line) The lowest $Ar\ 1s^{-1}$ confinement resonance in the endohedral $Ar@C_{60}$ molecule as a function of the effective quadratic displacement $\langle u \rangle^2$. The solid lines display their best Lorentzian fit.

Another situation is realized for the confinement resonance. To study the relationship between the molecular-frame motions associated and the line shape of the confinement resonance we have computed Ar 1s photoabsorption spectra of $Ar@C_{60}$. As argon is weakly bound with the cage the equilibrium

argon positions coincide in ground and ionic states. However the mean quadratic displacement playing minor role in CO, becomes dominating in Ar@C₆₀. Using eq.1 we have $\sigma^+ = \sigma_0^+ \sum_{\Gamma} M_{\Gamma}^{conf}(k)$ where

$$M_{\Gamma}^{conf}(k) = 1 + 2 \operatorname{Re} \sum_{\mu \geq 1} B^{\mu}(k; R_e) e^{-2k^2 \mu^2 \langle u \rangle^2} \quad (2)$$

In the case the summation over the multiplicity μ of the photoelectron scattering events cannot be done analytically. Symbols in figure 2 display the computed profiles of the confinement resonance located just above the Ar 1s edge in Ar@C₆₀ for the different displacements $\langle u \rangle^2$. In addition to the evident resonance broadening we see the red shift and the deviation of the resonance line shape from the Lorentzian with an increase in $\langle u \rangle^2$. The peculiarities do not correspond to the shape resonance phenomena.

3. CONCLUSION

The shape and confinement resonances in photoabsorption and photoemission spectra of free CO and endohedral Ar@C₆₀ molecules are computed and examined. It is shown that the vibronic coupling specifies the distortion in their line shape distortion. The non-Franck-Condon distribution of vibrational excitation deforms spectral distribution of oscillator strength for the σ^* shape resonance whereas the effective quadratic displacement of Ar in carbonic cage deforms essentially the line shape of the confinement resonance.

Acknowledgements

The work is supported by RFBR grant NO 12-02-00999 and St. Petersburg State University research grant NO 11.38.638.2013.

REFERENCES

- [1] J. M. Combes, et al. Commun. Math. Phys. 110, 215 (1987).
- [2] R. Flesch et al. J.Chem. Phys. 138, 144302 (2013).
- [3] X. O. Brykalova et al. J. Electron Spectrosc. Rel. Phenom. in press (2014) <http://dx.doi.org/10.1016/j.jelspec.2014.04.004>
- [4] A. A. Pavlychev et al. Phys. Chem. Chem. Phys. 8, 1914 (2006)
- [5] J. P. Connerade, V. K. Dolmatov, S. T. Manson, J. Phys. B. 33, 2279 (2000).
- [6] A. A. Pavlychev, D. A. Mistrov, J. Phys. B. 42, 055103 (2009).
- [7] R. Püttner et al. New J. Phys. 15, 033003 (2013).

BELGRADE ELECTRON/MOLECULE DATABASE COMPATIBLE WITH VAMDC PROJECT

Bratislav P. Marinković^{1,3}, Veljko Vujčić^{2,4}, Stefan Đorđević³, Stefan Ivanović³,
Dara B. Marinković⁴, Darko Jevremović² and Nigel J. Mason⁵

¹ *Institute of Physics, University of Belgrade, Pregrevica 118, P.O.Box 68,
11080 Belgrade, Serbia*

² *Astronomical Observatory, Volgina 7, P.O.Box 74 11060 Belgrade, Serbia*

³ *School of Electrical and Computer Engineering of Applied Studies, Vojvode
Stepe 283, 11000 Belgrade, Serbia*

⁴ *Faculty of Organizational Sciences, University of Belgrade, Jove Ilića 154,
11000 Belgrade, Serbia*

⁵ *The Open University, Department of Physical Sciences, Walton Hall, Milton
Keynes, MK7 6AA, United Kingdom*

Abstract. We present the progress report on the development of Belgrade electron/molecule data base which is hosted by The Institute of Physics, University of Belgrade. The data base has been developed under the standards of VAMDC project which provides a common portal for several European data bases that maintain atomic and molecular data. Belgrade data base covers collisional data of electron interactions with atoms and molecules in the form of differential (DCS) and integral (QINT, QMT, QVIS) cross sections as well as energy loss spectra. The final goal is to become a node within the VAMDC consortium and to integrate into the wider scope of radiation damage RADAM data base.

1. INTRODUCTION

Providing, maintaining and distributing the atomic and molecular data that comes from fundamental experiments and calculations based on different levels of sophistication of theoretical insights in atomic particle world, nowadays is a quest of computerized and networked society. There are so many communities which would benefit from such collections, let us just mention several ones from astrophysical and atmospheric physics [1], plasma (with all applications to industry like plasma processing [2] or lighting [3]), biomedicine/biophysics to other fundamental and applied research disciplines like spectroscopy or surface science [4]. Among data bases that cover the field of atomic and molecular physics one can distinguish those that maintain mainly bibliographic data about the published work on atomic processes (like NIST bibliographic database on Atomic Transition Probabilities [5]) or that maintain

actual data sets or evaluated and recommended values [6]. A new era of data accessibility opened with the idea of Virtual Atomic and Molecular Data Centre VAMDC [7] that creates a common portal for different data bases in the field which use the same data protocol for exchanging and representing data in the format of so called “xsams” xml files. VAMDC now provides a scientific data e-infrastructure enabling easy access to atomic and molecular data [8].

While the vast of structural and transition data are present in the current VAMDC consortium data bases, the number of collisional data bases is rather small. Our goal is to make a functional data base that would maintain data on electron/atom and molecule interactions. These data are in the form of differential and integral cross sections for elastic scattering and electronic excitation processes. Also, energy loss spectra as relative intensities of scattered electrons versus electron energy loss at the fixed impact electron energy and scattering angle are stored in the present data base.

2. BELGRADE DATABASE

The first ideas of development of Belgrade data base came with the research interests on expert and information systems that would facilitate data analysis and maintenance of the measured sets of data in electron atom/molecule interactions. The process model was defined and further developed from the context level to several hierarchical levels each of them represented by the data flow diagram [9]. Also, the relational data model was implemented and developed up to the level of recognition of all the entities.

The present data base follows the part of VAMDC data model that concerns with the collisions. Namely, processes that are under the scope of VAMDC are divided in three classes: radiative, non-radiative and collisional. In collisions there are always a reactant and a product side. In the case of our data base one of the reactants and one of the products is electron. The target in the reactant side could be either atom or molecule but it is always in the ground level state. The product after the interaction with electron could be either in the ground state, when we are talking about elastic scattering, or in the excited state, up to now only electronic state excitations are covered but also other types of inelastic processes could be easily included.

Data model of Belgrade electron/molecule data base with the entities and attributes is shown in Figure 1. Also, the relations between entities of one-to-one and one-to-many are shown. The principle adopted for data storage is that only those data that has been previously published and so had passed the refereeing procedure, should be maintained within the data base. For such reasons a part concerning the sources of data is present in the data base with all crucial entities (authors, journal, volume, pages, doi, Bibtex). Atoms and molecules are covered by the entity Species and are characterized by their state i.e. SpeciesState entity. Data itself are organized within Data Sets which include Tabulated data of cross sections or spectroscopic data.

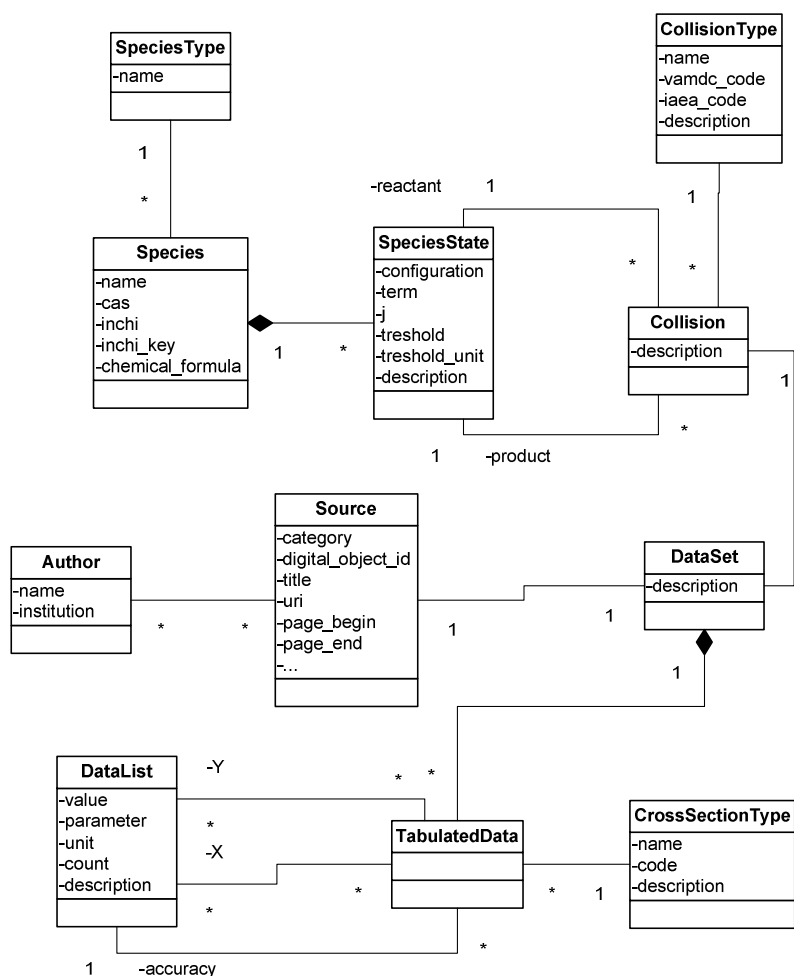


Figure 1. Data model of Belgrade electron/molecule database with entities and attributes. Relationships of one-to-one, one-to-many and many-to-many are shown.

Belgrade eMol database is generated with Django, a Python-based web framework, and runs under MySQL RDBMS. Application is hosted on a linux machine with Nginx as a web server and Gunicorn as app server. Access to data is possible via VAMDC-Tapservice protocol or via AJAX-enabled web interface (<http://emol.ipb.ac.rs>). Both queries return data in xsams format.

Connection and compatibility with VAMDC is established by written dictionary, TAP validator and xsams output form of data.

4. CONCLUSIONS AND PROSPECTS

The present Belgrade data base maintains electron/molecule interaction data published in the scientific literature and it contains unique set of data within VAMDC consortium. Its aim is also to facilitate the evaluation of data undertaken by the eMol board of experts that meets regularly and perform critical analysis of published electron/molecule data on specific molecular targets. Further more Belgrade data base is included in the wider scope of RADAM data base which covers specific needs of radiation community. RADAM data base has five distinctive sets of areas that cover complex processes met in radiation damage i.e. photon, ion, electron/positron interactions, multiscale processes and biological effects [10].

Acknowledgements

This work is partly supported by RS MESTD under the grants OI 171020 and III 44002 and by VAMDC consortium.

REFERENCES

- [1] L. Campbell and M. J. Brunger, *Plasma Sources Sci. Technol.* 22, 013002 (2013).
- [2] N. J. Mason, *J. Phys. D: Appl. Phys.* 42, 194003 (2009).
- [3] K. Bartschat and O. Zatsarinny, *Plasma Sources Sci. Technol.* 20, 024012 (2011).
- [4] R. T. Haasch, J. Patscheider, N. Hellgren, I. Petrov and J. E. Greene, *Surf. Sci. Spectra* 19, 30 (2012).
- [5] <http://physics.nist.gov/cgi-bin/ASBib1/TransProbBib.cgi>
- [6] W. L. Wiese, *Physica Scripta*. Vol. T105, 85–89, 2003. The Expanding NIST Atomic Spectra Database
- [7] <http://www.vamdc.eu/>
- [8] M.L. Dubernet, V. Boudon, J.L. Culhane, M.S. Dimitrijević, A.Z. Fazliev, C. Joblin, F. Kupka, G. Leto, P. LeSidaner, P.A. Loboda, H.E. Mason, N.J. Mason, C. Mendoza, G. Mulas, T.J. Millar, L.A. Nuñez, V.I. Perevalov, N. Piskunov, Y. Ralchenko, G. Rixon, L.S. Rothman, E. Roueff, T.A. Ryabchikova, A. Ryabtsev, S. Sahal-Bréchet, B. Schmitt, S. Schlemmer, J. Tennyson, V.G. Tyuterev, N.A. Walton, V. Wakelam, C.J. Zeppen, *J. Quant. Spec. Radiat. Transfer*, 111, 2151 (2010).
- [9] V. M. Cvjetković, B. P. Marinković, and D. Šević, *Information System in Atomic Collision Physics*, in *Advances and Innovations in Systems, Computing Sciences and Software Engineering*, Ed. Khaled Elleithy, p.485, (Springer, Dordrecht, The Netherlands, 2007).
- [10] S. Denifl, G. Garcia, B.A. Huber, B.P. Marinković, N.J. Mason, J. Postler, H. Rabus, G. Rixon, A.V. Solov'yov, E. Suraud, A.V. Yakubovich, *J. Phys.:Conf. Ser.* 438 012016 (2013).

INTEGRATED CROSS SECTIONS FOR ELECTRON EXCITATION OF THE $4d^{10}5p$ STATE OF THE Ag ATOM

S. D. Tošić¹, V. Pejčev², D. Šević¹, R. P. McEachran³, A. D. Stauffer⁴
and B. P. Marinković¹

¹*Institute of Physics, University of Belgrade, Pregrevica 118, 11080 Belgrade,
Serbia*

²*Faculty of Natural Sciences, University of Kragujevac, Radoja Domanovića 12,
34000 Kragujevac, Serbia*

³*ARC Centre for Antimatter-Matter Studies, Australian National University,
Canberra, ACT 0200, Australia*

⁴*Department of Physics and Astronomy, York University, Toronto, ON M3J 1P3
Canada*

Abstract. We have investigated the electron-impact excitation of the combined (two fine-structure levels) resonant $4d^{10}5p^2P_{1/2,3/2}$ state in silver from the ground $4d^{10}5s$ state both experimentally and theoretically. Measurements are presented for the combined level while the relativistic distorted wave (RDW) calculations were carried out for each level separately and for the combined level as well. Both the experimental and theoretical results were obtained in the incident electron energy (E_0) range from 10 to 100 eV with experimental scattering angles (θ) from 10° up to 150° . Experimental absolute differential cross sections (DCSs) were determined through normalization of the relative DCSs at 10° to our previous small angle experimental DCS values. The integrated cross sections which include integral (Q_I), momentum transfer (Q_M), and viscosity (Q_V) cross sections were determined by numerical integration of the absolute DCSs.

1. INTRODUCTION

In this paper, we continue our study of the combined resonant $4d^{10}5p^2P_{1/2,3/2}$ state of the silver atom excited from the ground state by electron impact [1]. Those results at small scattering angles show that the measured differential cross sections were generally in quite good agreement with the relativistic distorted-wave (RDW) calculations especially at higher energies and smaller scattering angles. Thus, we established the experimental DCSs at 10° as a base for the normalization of our present relative measurements of the DCSs which are extended over a wide range of scattering angles up to 150° for experiment and up to 180° for theory. The energy range remains the same (from

10 to 100 eV). In this way, we obtained absolute DCS values which were extrapolated to 0° and 180° and numerically integrated to obtain the integral (Q_I), momentum transfer (Q_M) and viscosity (Q_V) cross sections. Since the observed excited state has two fine-structure levels with total angular momentum $J = 1/2$ and $3/2$ which cannot be distinguished in the present experiment, measured results are presented for the excitation of the combined level. RDW calculations were performed for both fine-structure levels and for the combined excitation.

2. EXPERIMENT

The apparatus used is a conventional crossed-beam electron spectrometer described in more detail in our recent papers dealing with electron scattering by silver and lead atoms [1-3]. In the crossed beam arrangement the electron beam is formed in a system of cylindrical electrostatic lenses and hemispherical energy selectors. The scattered electrons are detected by a rotating analyzer that covers an angular range from -30° to 150° , in the plane perpendicular to the atomic beam. The analyzer is of the same construction as the electron monochromator except that it has a channel electron multiplier as a single-electron detector at the end.

A silver vapour beam was produced by heating a Knudsen-type oven crucible containing silver metal by two separate coaxial heaters. The working temperature was about 1300 K, the background pressure was of the order of 10^{-5} Pa, the overall energy resolution (FWHM) was typically 160 meV while the angular resolution was 1.5° . The position of the true zero scattering angle was determined before each angular distribution measurement by checking the symmetry of the scattered electrons at negative and positive scattering angles (usually from -10° to $+10^\circ$). Due to the change of effective interaction volume versus scattering angle, the effective path length correction factors V_{eff} [4] determined for the present experimental conditions were applied and corrections of the measured scattered intensities was made. The obtained relative DCSs were put on an absolute scale by normalization to the absolute DCSs for the same excitation process at 10° [1]. Our experimental integrated cross sections are obtained by the extrapolation of the absolute DCSs to 0° using our previously reported results at small angles and to 180° using the appropriate RDW calculation followed by numerical integration. Integral (Q_I), momentum transfer (Q_M) and viscosity (Q_V) cross sections are defined as:

$$Q_I = 2\pi \int_0^\pi DCS(\theta) \sin \theta \, d\theta \quad (1)$$

$$Q_M = 2\pi \int_0^\pi DCS(\theta) \left[1 - \left(1 - \frac{\omega}{E_0} \right)^{1/2} \cos \theta \right] \sin \theta \, d\theta \quad (2)$$

$$Q_V = 2\pi \int_0^\pi DCS(\theta) \left[1 - \left(1 - \frac{\omega}{E_0} \right) \cos^2 \theta \right] \sin \theta d\theta \quad (3)$$

where $DCS(q)$ is absolute differential cross section, w is excitation energy and E_0 is electron impact energy. The details of the RDW method for calculating the DCSs were given in [1] and references therein.

3. RESULTS AND DISCUSSION

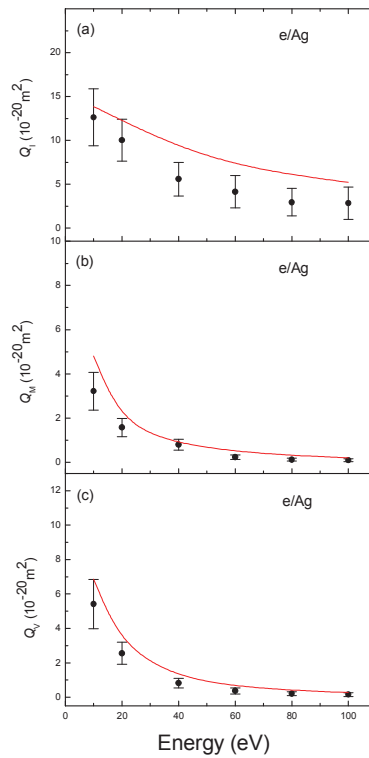


Figure 1. (a) Integral, (b) momentum transfer, and (c) viscosity cross sections for electron impact excitation of the $4d^{10}5p^2P_{1/2,3/2}$ state of the silver atom. Filled circles with error bars denote the present experimental results. The solid line shows the combined DCSs calculated by the RDW method.

In Figure 1 we show the results for the integral (Q_I) (a), momentum transfer (Q_M) (b) and viscosity (Q_V) (c) cross sections for electron excitation of the $4d^{10}5p^2P_{1/2,3/2}$ state of silver. Experiment confirms a slow decrease of Q_I , Q_M and Q_V with increasing incident electron energy as is also predicted by theory. One can see that reasonably good agreement was achieved between experiment and theory concerning the shape of the energy dependences of all integral cross

sections but theory gives slightly larger values of all integral cross sections at all electron energies though they lie within the limits of the error bars in several cases. The main reason for this behaviour is the fact that the present calculated DCSs are higher than the normalized measured ones over the whole angular range.

Considering excitation of the $4d^{10}5p^2P_{1/2,3/2}$ fine structure levels, it should be mentioned that there is also the $4d^95s^2D_{5/2}$ state with an energy of 3.749 eV which is intermediate to these fine-structure doublet (with energies of 3.664 eV and 3.778 eV, respectively). One should expect that there must be some contribution from the excitation of this level in our measurements. However, since this excitation from the 2S ground level to the 2D state belongs to the electric quadrupole transition, we suppose that its contribution to the excitation cross sections of the resonance 2P states is negligible. Also, as we already reported in our previous paper [1], the DCS for the combined levels can be represented as a sum of DCSs for excitation of the individual levels.

4. CONCLUSION

Electron impact excitation from the ground state of silver has been studied both experimentally and theoretically. Measurements have been performed at 10, 20, 40, 60, 80 and 100 eV electron energies and scattering angles from 10° to 150° . Calculations were also carried out for the same energies and scattering angles up to 180° . We conclude that good agreement is achieved between the present two sets of data especially at higher energies.

Acknowledgements

This work is supported by RS MESTD under the grant OI 171020 and it was conducted within the framework of the COST Action CM1301 (CELINA).

REFERENCES

- [1] S. D. Tošić, V. Pejčev, D. Šević, R. P. McEachran, A. D. Stauffer and B. P. Marinković, Nucl. Instr. Meth. B, 279, 53 (2012).
- [2] S. Milisavljević, M. S. Rabasović, D. Šević, V. Pejčev, D. M. Filipović, Lalita Sharma, Rajesh Srivastava, A. D. Stauffer and B. P. Marinković, Phys. Rev. A, 76, 022714 (2008).
- [3] S. D. Tošić, M. S. Rabasović, D. Šević, V. Pejčev, D. M. Filipović, Lalita Sharma, A. N. Tripathi, Rajesh Srivastava and B. P. Marinković, Phys. Rev. A, 77, 012725 (2008).
- [4] R. T. Brinkman and S. Trajmar, J. Phys. E, 14, 245 (1981).

HIGH RESOLUTION EJECTED ELECTRON SPECTRA OF ARGON AT ELECTRON IMPACT ENERGIES OF 303, 505, 809 AND 1000 eV AND EJECTION ANGLE OF 90°

J. J. Jureta, A. R. Milosavljević and B. P. Marinković

Institute of Physics, University of Belgrade, Pregrevica 118, Belgrade, Serbia

Abstract. We present high resolution ejected electron spectra of argon at several high impact electron energies from 303 to 1000 eV and the ejection angle of 90°. The spectra cover autoionization region of excitation energies from 21.26 to 38.26 eV. These spectra have been obtained by using high resolution electron spectrometer with a hemispherical analyzer and a high energy electron gun. The features have been identified as autoionizing states and resonances and their assignments and energy positions have been compared with those found in literature.

1. INTRODUCTION

Autoionizing states and resonances in argon have been studied in the past by different experimental techniques; photons [1], high energy ions [2], high energy electrons [3,4] and low energy electrons [5,6]. The studies of resonances are cited in [7]. Here we present results of our measurements of autoionizing states and resonances in argon at electron impact energies of 303, 505, 809 and 1000 eV in the region of excitation energies from 21.26 to 38.26 eV (5.50 to 22.50 eV of ejection energy), and the ejection angle of 90°. The aim of this study is to improve the understanding of a very important role of the resonances in the behavior of the autoionization states at the higher electron impact energies. This was possible due to the very high resolution obtained in the measured spectra, as demonstrated by resolving the triplet and singlet states.

2. EXPERIMENTAL SETUP

The apparatus represents a typical crossed electron-atom experiment already described earlier [8]. Here we will give a short outline. It is consisted of a high energy electron gun, high resolution hemispherical analyzer, hypodermic needle as a source of an effusive beam of target gas, a Faraday cup as a collector for incident electron beam and 7 channeltrons for detection of ejected electrons.

The background pressure was 10^{-8} mbar, while the working pressure with argon was 10^{-6} mbar. The estimated energy resolution of ejected electron spectra was below 0.080 eV. The calibration of the ejected electron energy scale was done in a mixture of argon and helium at high impact energy of 303 eV using the position of the double excited $2s2p(^1P)$ state at 60.130 eV (35.55 eV of ejected energy) [9]. The incident electron energy scale was calibrated through the elastic channel.

3. RESULTS AND DISCUSSION

Figure 1 shows four ejected electron spectra measured at the incident energies of 303, 505, 809 and 1000 eV and the ejection angle of 90° . The spectra are shown with subtracted background without normalisation. They cover energy region of ejected electrons from 5.50 to 22.50 eV i.e. the region of excitation energy from 21.26 to 38.26 eV (ionization potential for Ar is 15.76 eV). All spectra show identical form with small differences in intensities of the features

The ejected energy domain presented in the figure can be divided into three regions. In the first one from 5.5 to 9 eV, an isolated well defined peak marked “a” at the energy of 6.22 eV (21.98 eV) and two small peaks marked “b” at 7.70 eV (23.46 eV) and “c” at 8.63 eV (24.39 eV) at the impact electron energies of 303 and 505 eV are present. The first peak has been already reported previously [2,3,5,10], however only Hicks et al [5] give its energy position at 6.24 eV and propose that it comes as a result of the excitation above the second ionization potential at 40.74 eV. The present measurement gives the energy of 6.22 eV, which is in excellent agreement with reference [5]. Other two peaks “b” and “c” with low intensities are seen for the first time in the present experiment, according to our knowledge and they can be due to similar type of excitation.

The second region of ejected energies from 9 to 14 eV (24.76 to 29.76 eV of excited energies) was the subject of many experimental studies mentioned in the Introduction. It is abundant with the features in the form of well define peaks and deeps. Under these experimental conditions the figure shows double peaks and deeps separated by 0.180 eV which correspond to the triplet-singlet splitting in argon ion. The autoionizing states in this energy region have the configuration $3s3p^6(ns,np,nd)$ and not all of them are present in the previously reported experiments with electrons, depending on the experimental conditions and the resolution.

The members of the $3s3p^6np$ series are not seen in the present experiment. The first two features marked as “d” and “d'” correspond to the $3s3p^64s(^3,^1S)$ states respectively, which are present with low intensities because they represent optically forbidden transitions. The next two well defined features marked as “e” and “e'” at 11.54 eV (27.30 eV) and 11.72 eV (27.48 eV) should belong to the $3s3p^63d(^3,^1D)$ series.

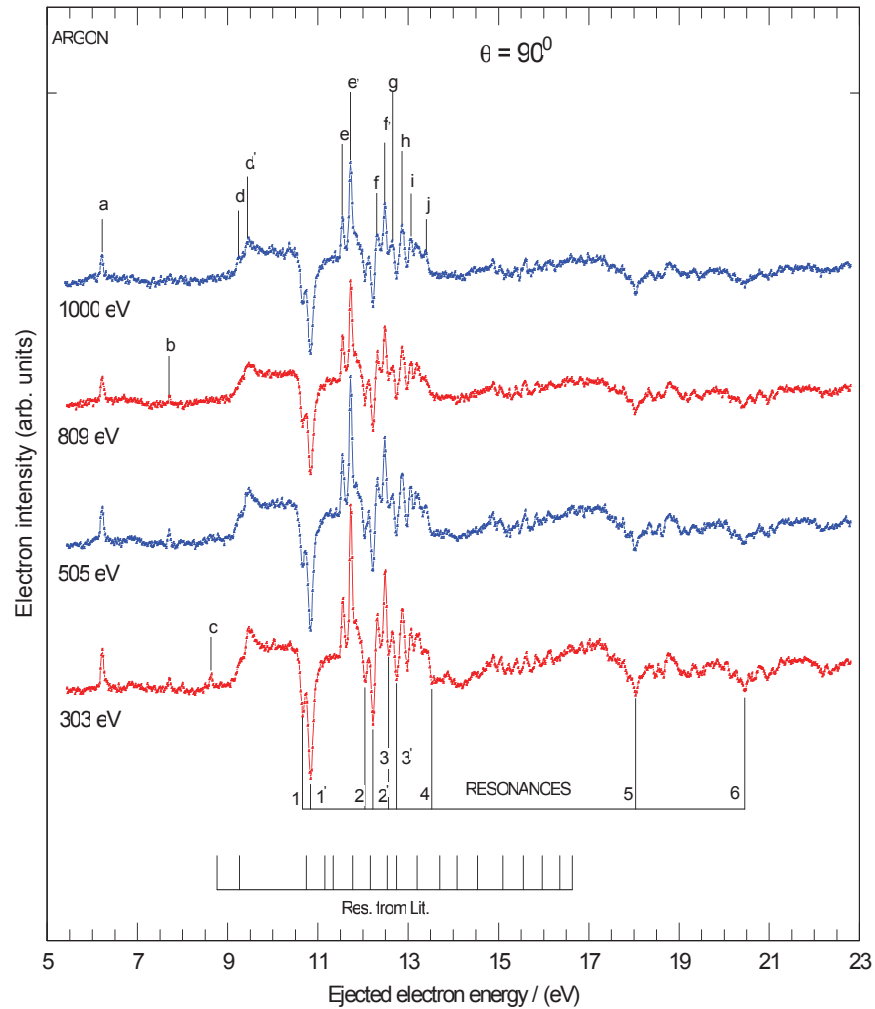


Figure 1. Ejected electron spectra of argon obtained at the ejection angle of 90° . The incident electron energies labeled on the left hand side of the figure were: 1000, 809, 505, and 303 eV respectively. The energy region for ejected electrons is from 5.50 to 22.50 eV corresponding to the region from 21.26 to 38.26 eV of excitation energies. The energy width per channel was 0.020 eV. The short vertical lines above the peaks denoted with small letters from “a” to “j” mark the position of excited states, while the vertical lines below the spectrum of 303 eV show the positions of minima or resonances marked with numbers 1 to 6. The short vertical lines at the bottom of the figure mark positions of resonances taken from the literature [7].

The next two less pronounced features in the spectra marked as “f” and “f' ” at energies 12.30 eV (28.06 eV) and 12.48 eV (28.24 eV) belong to the $3s3p^64d$ ($^3,^1D$) series. Again, the energy separation between two peaks is 0.18 eV. The two small not identified features “i” at 13.06 eV (28.82 eV) and “j” at 13.40 eV (29.16 eV) belong to the $3s3p^6$ series are the last features belonging to the single excitation from $3s$ shell. The energy region above 14 eV (29.76 eV) is due to the decay of doubly excited states $3s^23p^4 nln'l'$ to the ground state of argon ion. Under the present experimental condition the later states appear in the form of large number of features with low intensity.

Temporary negative ions (resonances) in the autoionization region of argon have been studied in the past [7]. In the present experiment they appear in the form of double resonances separated by 0.180 eV, indicating that they are formed at the threshold or very close to the threshold of singlet and triplet states. Three pairs of this type of resonances are visible on the figure. The first pair 1-1' has energy positions of 10.66 eV (26.42 eV) and 10.84 eV (26.60 eV), which correspond to $3s3p^64p$ ($^3,^1P$) states, in good agreement with references [1,4]. The second resonance pair 2-2' has energy positions of 12.04 eV (27.80 eV) and 12.22 eV (27.98 eV), respectively with the energy splitting of 0.180 eV. The position of 2' (27.98 eV) is in a good agreement with the previously reported $5p$ (1P) state [1,4] (27.996 eV and 27.994 eV, respectively), whereas the resonance 2 (27.80 eV) has not been reported in the literature. The third pair 3-3' at 12.56 eV (28.32 eV) and 12.74 eV (28.50 eV) is present with much lower intensity, but with the same splitting of 0.180 eV. The position of 3' (28.50 eV) is in a good agreement with the $6p$ (1P) state from references [1, 4] (28.509 eV). The triplet state $6p$ (3P) has not been seen in previous measurements. These two resonances coincide in energies with two resonances from literature [7] shown at the bottom of the figure 28.30 and 28.50 eV respectively.

Acknowledgements

This work has been partly supported by RS MESTD under the grant NO 171020.

REFERENCES

- [1] R. P. Madden, D. L. Ederrer and K. Codling, Phys. Rev. 177, 136 (1969).
- [2] M. E. Rudd, T. Jorgensen and D. J. Vols, Phys. Rev. 151, 28 (1966).
- [3] K. Siegbahn et al., *ESCA Applied to Free Molecules*, (North-Holland Publ. Co., Amsterdam, 1969).
- [4] S. L. Wu et al., Phys. Rev. A, 51, 4494 (1995).
- [5] P. J. Hicks et al., p. 515, *Proc. 8th ICPEAC*, (Institute Vinca, Beograd, 1973).
- [6] J. W. McConkey and J. Fryar, p. 204, *Proc. 9th ICPEAC*, (Seattle, 1975).
- [7] S. J. Buckman and C. W. Clark, Rev. Mod. Phys. 66, 539 (1994).
- [8] J. J. Jureta, A. R. Milosavljevic and B. P. Marinkovic. p. 126, *Proc. 2nd Nat. Conf. Elec. At. Mol. Photon. Phys.* (Inst. Phys, Belgrade, 2011).
- [9] K. Codling, R. P. Madden, and D. L. Ederer, Phys. Rev. 155, 26 (1967).
- [10] G. N. Ogurtsov et al., Sov. Phys. JETP, 30, 16 (1970).

N K-SHELL X-RAY TANDEM MASS SPECTROMETRY OF GAS-PHASE UBIQUITIN PROTEIN

A. R. Milosavljević¹, C. Nicolas^{2,*}, M. Lj. Ranković¹, F. Canon³, C. Miron² and A. Giuliani^{2,4}

¹*Institute of Physics, University of Belgrade, Pregrevica 118, Belgrade, Serbia*

²*Synchrotron SOLEIL, L'Orme des Merisiers, Saint-Aubin, B.P. 48, 91192 Gif-sur-Yvette, France*

³*UAR 1008 Cepia, Institut National de la Recherche Agronomique (INRA), BP 71627, 44316 Nantes Cedex 3, France*

⁴*INRA, U1008, CEPIA, Rue de la Géraudière, 44316 Nantes, France*

Abstract. We present results on the N K-shell X-ray tandem mass spectrometry of gas-phase, multiply charged ubiquitin protein. The results have been achieved by coupling a linear ion trap mass spectrometer, fitted with an electrosprayed ion source probe, to a soft X-ray synchrotron beamline. The tandem mass spectrum of the 5+ charge state precursor of ubiquitin at the activation energy of 402 eV is presented and discussed. The results show a predominant ionization channel of the protonated protein precursor, but accompanied also by losses of small neutral fragments.

1. INTRODUCTION

The controlled study of protein degradation upon exposure to X-rays is of particular importance for the radiation damage research. Additionally, this field has become highly relevant in the last few years, when it was demonstrated that short and intense X-ray pulses from the X-ray free electron lasers (XFEL) can be used for protein 3D structure determination using single-object coherent X-ray diffraction [1]. This is of special interest for membrane proteins, which are difficult to crystallize and study using conventional protein crystallography methods at synchrotrons. There has been a large effort to understand the details of radiation damage of biomaterials at the molecular level, which can also favor important medical applications such as cancer therapy [2]. With this respect, an immense number of publications have been devoted to the electron/ion/photon interaction with DNA and its components [3]; however, protein ionization/degradation and associated secondary effects were less investigated

* email: christophe.nicolas@synchrotron-soleil.fr

although equally important in damage modeling [1]. It is well known that X-ray irradiation induces strong fragmentation in amino acids and peptides [4]. Nevertheless, surprisingly, gas phase proteins appeared to be much less prone to dissociation, whereas dominant channels corresponded to ionization and losses of neutral fragments [5]. Still, it should be noted that intensive production of low-energy secondary electrons, due to direct ionization or to the normal/resonant Auger decay of the core-ionized/-excited states, can also strongly affect the degradation of the biomaterial [6]. Very recently, it has been also predicted that resonant X-ray photoabsorption can effectively produce slow electrons, through the initial inner-shell excitation triggering a resonant-Auger intermolecular Coulombic decay (ICD) cascade [7]. Although the latter study [7] has been performed for a simple ArKr model system, the authors pointed out that the process might have consequences for fundamental and applied radiation biology. With this respect, the inner-shell mass-resolved action spectroscopy of a protein can indeed resolve the dominant relaxation channels upon resonant X-ray photon absorption.

2. EXPERIMENTAL SETUP

The experimental setup and coupling of the linear quadrupole ion trap to a synchrotron beamline has been described in previous publications [5,8,9]. Briefly, the setup is based on a commercial linear quadrupole ion trap mass spectrometer (Thermo Finnigan LTQ XL) equipped with an electrospray ionization (ESI) source. The electrosprayed ions are introduced from the front side into the trap, while the soft X-ray photon beam enters the ion trap from the backside. The irradiation time (about 500 ms in the present case) of the mass-selected precursors is regulated by a special photon shutter [10]. The setup includes a differential pumping stage to accommodate the pressure difference between the beamline (10^{-9} mbar) and the LTQ (10^{-5} mbar of He in the main chamber).

The setup is connected to the soft X-ray beamline PLEIADES [11,12] of the SOLEIL storage ring in Saint-Aubin (France). The photon beam is produced by a quasi-periodic APPLE II type of undulator (80 mm period), followed by a modified Petersen plane grating monochromator with varied line spacing and varied groove depth gratings. For the present experiment, a 400 lines mm^{-1} grating was used, which provides high photon flux on the order of $1\text{--}2 \times 10^{12}$ photons $\text{s}^{-1}/0.1\%$ bandwidth for the used energy. The energy resolution used (full width at half maximum, FWHM) was about 430–460 meV. The photon energy was calibrated according to the N $1s \rightarrow \pi^*$ resonance in molecular nitrogen. Multiply protonated ubiquitin protein (Sigma Aldrich) was generated by the ESI source from a water/acetonitrile (75:25) solution at 10 μM .

3. RESULTS AND DISCUSSION

The tandem mass spectrum of the 5+ charge state ubiquitin precursor, upon resonant X-ray photon irradiation during 500 ms, below N $1s$ ionization

threshold (IT) is presented in Figure 1. The spectrum shows that the inner-shell photo-excitation of a protein dominantly leads to its ionization accompanied by losses of neutral fragments. The ionization of the photo-excited precursor at photon energies below the direct inner-shell IT is the consequence of the resonant Auger decay [7] triggered by the promotion of a core (1s) electron to an unoccupied, bound molecular orbital, forming a highly-excited state. A valence electron fills the core vacancy and the molecule decays by ejecting another (Auger) electron. It is also possible that more than one valence electron be ejected during decay leading to multiple resonant Auger decay [13].

The finding that the ionization process, accompanied by low-mass neutral fragment losses, represents the dominant relaxation channels upon X-ray absorption by ubiquitin protein is very important for the radiation damage research, imposing limitations to the widely applied building blocks approach based on the premise that the properties of complex macromolecules can be elaborated through investigation of their components. Note that the channelling of the absorbed energy into multiple electron ejection and neutral fragment losses, instead of backbone destruction, does not necessarily mean a better protection of the biological material; the secondary electrons can further produce damage [6] and neutral fragment losses from amino acids can induce mutations. However, the present results certainly bring new insights for a more accurate modelling of the complex radiation damage phenomenon. Multiple electron ejection, rather than the formation of small ions and radicals, suggests that the resonant X-ray irradiation of protein-rich regions in the cell would produce a significant number of secondary electrons.

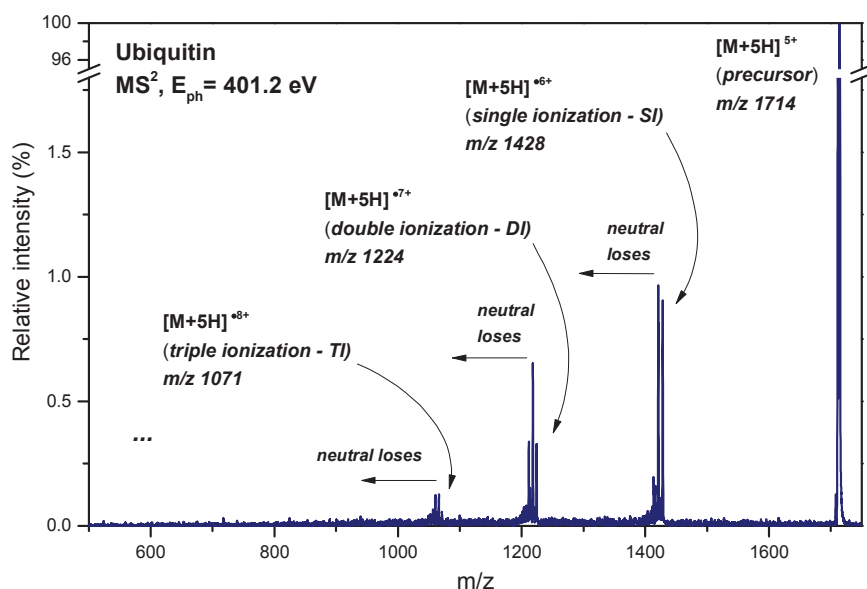


Figure 1. Tandem ESI/photoionization mass spectra of the 5+ (m/z 1714) ions of ubiquitin protein, obtained after 500 ms of irradiation at the photon energy of 401.2 eV.

Acknowledgements

Data collection was performed at the PLEIADES beamline at the SOLEIL Synchrotron (Proposal Number 20130382). This work is supported by the Agence Nationale de la Recherche Scientifique, France, under the project #BLAN08-1_348053 and motivated by ESF/COST Actions CM1204 “XUV/X-ray light and fast ions for ultrafast chemistry (XLIC)” and MP1002 “Nano-scale insights in ion beam cancer therapy (Nano-IBCT)”. A.R.M. acknowledges the support by the Ministry of education, science and technological development of Republic of Serbia under the grant NO 171020. We are grateful to E. Robert for technical assistance and the general SOLEIL staff for running the facility.

REFERENCES

- [1] H. N. Chapman, et al. *Nature* 470 73 (2011).
- [2] Nano-IBCT: Nanoscale insights into Ion Beam Cancer Therapy (Nano-IBCT). at <<http://fias.uni-frankfurt.de/nano-ibct/overview/>>
- [3] I. Baccarelli, I. Bald, F. A. Gianturco, E. Illenberger and Kopyra, *J. Phys. Rep.* 508, 1–44 (2011).
- [4] O. González-Magaña, et al. *J. Phys. Chem. A* 116, 10745–51 (2012).
- [5] A. R. Milosavljevic, et al. *J. Phys. Chem. Lett.* (2012).
- [6] B. Boudaïffa, P. Cloutier, D. Hunting, M. A. Huels and L. Sanche, *Science* (80-.). 287, 1658–1660 (2000).
- [7] K. Gokhberg, P. Kolorenč, A. I. Kuleff and L. S. Cederbaum, *Nature* 505, 661–3 (2014).
- [8] A. R. Milosavljević, C. Nicolas, J. Lemaire, C. Déhon, R. Thissen, J.-M. Bizau, M. Réfrégiers, L. Nahon, A. Giuliani, *Phys. Chem. Chem. Phys.* 13, 15432–15436 (2011).
- [9] A. R. Milosavljević, C. Nicolas, J.-F. Gil, F. Canon, M. Réfrégiers, L. Nahon, A. Giuliani, *J. Synchrotron Radiat.* 19, 174–178 (2012).
- [10] A. R. Milosavljević, C. Nicolas, J.-F. Gil, F. Canon, M. Réfrégiers, L. Nahon, A. Giuliani, *Nucl. Instrum. Methods Phys. Res., Sect. B* 279, 34–36 (2011).
- [11] J. Söderström, A. Lindblad, A. N. Grum-Grzhimailo, O. Travnikova, C. Nicolas, S. Svensson, C. Miron, *New J. Phys.* 13, 073014/1–073014/13 (2011).
- [12] C. Miron, C. Nicolas, O. Travnikova, P. Morin, Y. Sun, F. Gel'mukhanov, N. Kosugi, V. Kimberg, *Nat. Phys.* 8, 135–138 (2012).
- [13] A. P. Hitchcock, et al. *Phys. Rev. A* 37, 2448 (1988).

OPTIMIZATION OF A LOW-ENERGY ELECTRON GUN BY ELECTRON RAY-TRACING SIMULATIONS

M. Lj. Ranković¹, J. Rackwitz², I. Bald^{2,3} and A. R. Milosavljević¹

¹*Laboratory of atomic collision processes, Institute of Physics Belgrade, University in Belgrade, Pregrevica 118, 11080 Belgrade, Serbia*

²*Institute of Chemistry, University of Potsdam, Karl-Liebknecht-Str. 24-25, 14469 Potsdam, Germany*

³*BAM Federal Institute for Materials Research and Testing, Richard-Willstätter Str. 11, 12489 Berlin, Germany*

Abstract. We have performed electron ray-tracing simulations, in order to optimize a commercial low-energy electron gun used for controlled irradiation of biological samples deposited on a surface. The simulations have been performed by using SIMION program packet, for electron energies from 1 to 20 eV. The results suggest possibilities to improve the performance of the electron gun considering the stability of the focal position over the used energy domain.

1. INTRODUCTION

A novel method that allowed for the first time to visualize the electron-induced dissociation of single chemical bonds within well-defined self-assembled DNA nanostructures has been recently developed [1]. It is based on AFM imaging and quantification of low-energy-electron-induced bond dissociations within specifically designed oligonucleotide targets that are attached to DNA origami templates.

The previous electron-irradiation experiments [1] investigated the strands breaks as a function of electron fluence at fixed electron energy of 18 eV, and it was found that at the fluence of $1-5 \times 10^{12} \text{ cm}^{-2}$ the number of DNA strand breaks increased linearly with the fluence. Further experiments are presently in progress, in order to investigate the electron energy dependence of the strand breaks over a domain from 1-20 eV. In order to perform such experiment properly, the incident electron beam should be controlled to preserve an optimal electron current density at the sample. We present herein the electron ray-tracing simulations that should help obtaining the best conditions of the electron gun used in the experiment. Although the present study does not take into account all possible parameters (for example, the Earth and other stray fields), the results suggest possibilities to improve the performance of the electron gun.

2.RESULTS AND DISCUSSION

2.1 Simion

The simulation of the electron gun in the present study was conducted by using the commercial program SIMION8[1]. Briefly, a desired geometry of the electrodes of the gun is loaded into SIMION through a geometric file, written in SIMION's specific programming language. Each electrode, specified in the geometry file has its own electric potential value, which should be defined by the user. SIMION program solves the Laplace equation for a given electric potential and stores data in a potential array (*.pa#) file. By solving Laplace equation, SIMION calculates the electric field defined by gradient of electrode potential, using a method of finite differences. Additional changes of electrode potentials and starting conditions of the projectiles (electrons) have been done through "LUA" programming code, written in a separate file which controls the entire simulation. In the final step, charged particle trajectories are being displayed.

2.2 Modeling and simulation

The present electron gun consists out of five cylindrical electrodes, with the cathode being one of them. Geometry of the electrodes and a 3D model of the electron gun are displayed in Figure1.

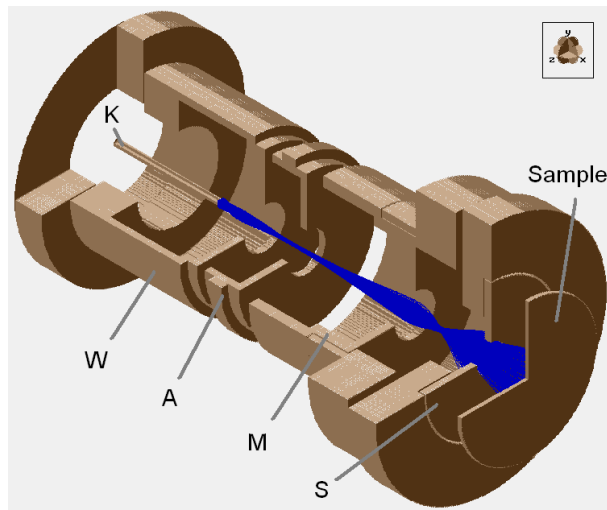


Figure1. 3D model image from SIMION8 of the electron gun. Denotations: K-cathode, W-wehnelt, A-anode, M-metal rings (gnd), S-shutter and Sample holder disk.

In the present simulations, in order to preserve a cylindrical symmetry of the whole electrode assembly, the cathode is made as a simple bar, although it is hairpin in real. This should not affect the present preliminary simulation, because the electrons are generated just in front of the cathode with 0.1eV

energy, without simulating a thermo-electronic emission, where a shape of the cathode is very important.

The present experimental setup has W, M and S (see Figure 1) set on the ground voltage, with the anode biased to a high positive voltage (500V in the simulation). The sample disk is grounded through a picoamperemeter and placed at a distance of $d=5$ mm apart from the last electrode (shutter), while cathode is set to a negative voltage which defines the electron energy. To control the irradiation time, a deceleration of all electrons is achieved by applying a small negative voltage (around 110% of the electron's energy) on the shutter electrode (S). In the simulation, 501 electrons were generated uniformly from a disk with a radius of $r=0.5$ mm, with $E_0=0.1$ eV initial energy and $\alpha_0=45^\circ$ cone divergence angle, just near the surface of the cathode. The radius of the electron beam as a function of the electron energy was recorded, with fixed anode voltage (Figure 2).

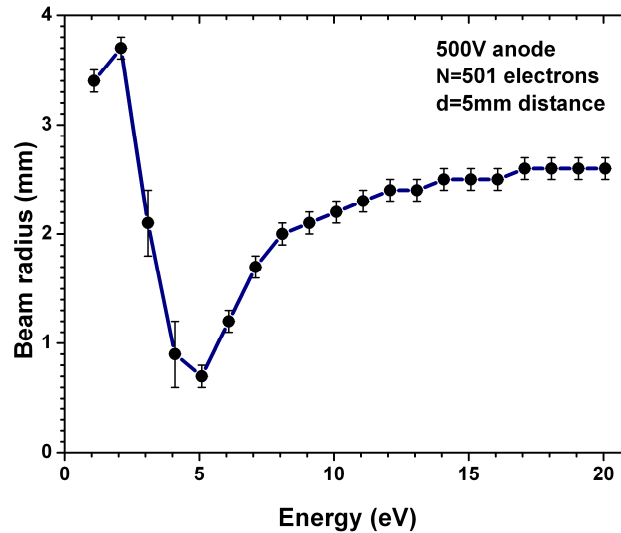


Figure2. The radius of the electron beam for different electron energies, at 5mm distance from the exit, with fixed anode voltage of 500V.

Low energy electrons (up to 5 eV) are highly scattered, with the Wehnelt electrode being grounded, because no primary extraction zone was formed. In that energy range, the transmission of electrons through the electron gun was below 50%, while the electron beam had unstable geometry. For the electron energies above 5eV, the electron beam is well defined and approaches desired 2.5 mm radius (5 mm diameter) even with the fixed anode voltage. Optimization of the anode voltage up to 5eV energy range, had no influence on the stabilization of electron beam. Experimentally obtained electron beam diameter at 10 eV is in a good agreement with the calculated value.

In order to further improve the electron transmission and better control the beam geometry, formation of the primary extraction zone as well as it's

tuning of gun's potentials as a function of the energy is needed. This was done by setting floating voltages on the wehnelt and the anode (W and A in Figure1, respectively) relative to the cathode. W was set to -4V, while A was set to 500V, both relative to K. With additional programming in "LUA" the voltage on A was adjusted in order to obtain the beam radius of $r=5$ mm at a distance of $d=5$ mm, from the shutter, for different applied electron energies. The results of this optimization are given in Figure3. Clearly, beam radius is dependent of the energy, therefore at least one (anode) voltage must be set accordingly.

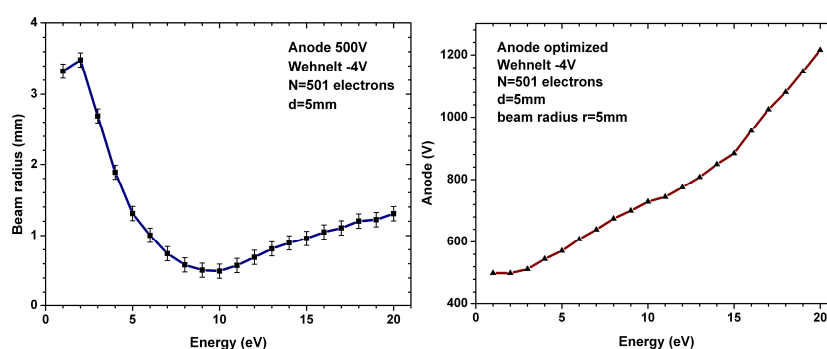


Figure3. Left: Electron beam radius at $d=5$ mm distance for fixed anode (500V) and wehnelt (-4V) voltages, relative to cathode; Right: Optimized anode voltage, to keep electron beam radius near $r=5$ mm at a distance of $d=5$ mm.

Acknowledgements

This research was supported by a Marie Curie FP7 Integration Grant within the 7th European Union Framework Programme and by the Deutsche Forschungsgemeinschaft (DFG). We acknowledge a grant by the German Academic Exchange Service (DAAD, project No. 57055766) supported by the German Federal Ministry of Education and Research, and support by the MESTD of RS (171020) and the COST Action CM1301 (CELINA).

REFERENCES

- [1] A. Keller, I. Bald, A. Rotaru, E. Cauet, K. V. Gothelf and F. Besenbacher, ACS Nano 6, 4392 (2012).
- [2] D. J. Manura and D. A. Dahl, SIMION Version 8.0, User Manual, Scientific Instruments Services, Inc. (2007).

RATE COEFFICIENTS FOR ELECTRON-IMPACT DISSOCIATION OF O_3^+

M. M. Vojnović and D. S. Belić

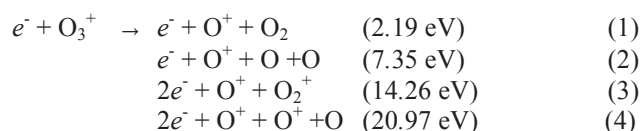
*University of Belgrade, Faculty of Physics, P.O.Box 386,
11000 Belgrade, Serbia*

Abstract. Maxwellian and non-equilibrium rate coefficients for electron-impact dissociation of O_3^+ to O^+ fragment have been calculated. Two sets of cross section data, measured recently by different experimental groups, are used. In the case of Maxwellian distribution electron energies cover the range from 0 up to 100 eV. The non-equilibrium electron energy distribution functions are adopted from the recent electron observations by the 3-D plasma and energetic particles experiment on the WIND spacecraft, for the mean electron energies from 4 eV to 72 eV. The contributions of dissociative excitation and dissociative ionization are also determined. The role of the electron-impact dissociation of O_3^+ to the Ozone layer depletion has been discussed.

1. INTRODUCTION

The problem of Ozone layer depletion in the stratosphere is attracting significant attention of researchers in the past decades. Various mechanisms which contribute to the Ozone molecule decomposition have been investigated. It has been recognized that the absorption of UV light leads to its depletion, but some molecular reactions and collisions with atoms, ions and electrons, present in the stratosphere are also found to play a role. A significant influence is attributed to the air pollutants, such as nitric oxides, and chlorine and bromine compounds, as well.

In addition to the above reactions, produced O_3^+ ions are opening a new reaction channels to the ozone destruction. In this work electron-impact dissociation of O_3^+ is investigated. Following reactions are considered:



Here, the numbers in the parentheses represent the threshold energies for the given processes. Reactions (1) and (2) are dissociative excitation (DE) processes and (3) and (4) represent dissociative ionization (DI) [1].

Absolute cross sections for electron-impact dissociation of O_3^+ to O^+ and O_2^+ fragments have been measured at ORNL by Deng et al [2] (2010). More recently cross sections for dissociation to O^+ fragments are measured at LLN (Louvain-la-Neuve) by Belić et al [1]. Both experiments used a crossed beams technique, but the results for dissociation producing O^+ fragments disagree for a factor of 3 in a wide electron energy region. This has been attributed to the broad fragment kinetic energy distribution and loss of the signal in the ORNL experiment [2]. This effect has been corrected in [1] by performing careful scans of the signal and taking into account the transmission efficiency of the experiment.

The maximum of the cross section [1] is $3.6 \times 10^{-16} \text{ cm}^2$ and unlike [2], has an average value of $3 \times 10^{-16} \text{ cm}^2$ in a wide energy range from 5 to 500 eV. Such a broad energy interval of high cross sections may result in a high rate for the considered process. Thus, we can raise the question of importance of electron-impact ozone ion dissociation in the stratosphere, relative to the other competitive mechanisms. Thus, it is possible that the electrons, originating from the Solar wind and penetrating in the stratosphere along the polar cusp, play an important role in the ozone layer depletion.

2. METHOD

Rate coefficients have been calculated by the well known expression:

$$K(\bar{E}_{el}) = \sqrt{2/m_e} \int_{\varepsilon_{thr}}^{+\infty} \sigma(\varepsilon) \sqrt{\varepsilon} \cdot f_e(\bar{E}_{el}, \varepsilon) d\varepsilon \quad (5)$$

where \bar{E}_{el} is the mean electron energy, $\sigma(\varepsilon)$ is the cross section for considered process, ε_{thr} is the threshold energy and $f_e(\bar{E}_{el}, \varepsilon)$ is the normalized electron energy distribution function (EEDF) [3]. Calculations have been performed by using numerical interpolation for experimental cross section data. In case of equilibrium conditions, the EEDF in (5) is given by the Maxwellian equation:

$$f(\bar{E}_{el}, \varepsilon) = 1 / \sqrt{2\pi} (3 / 2\bar{E}_{el})^{3/2} \sqrt{\varepsilon} \exp(-3\varepsilon / 2\bar{E}_{el}) \quad (6)$$

For non-equilibrium case EEDF for the mean electron energy values up to 71,7 eV have been adopted from measurements of the non-thermal “super-halo” component of the Solar wind electrons with the help of 3D Plasma and Energetic Particles experiment on the WIND spacecraft [4].

The cross sections, used for rate coefficient calculations, are measured by Belić et al [1] and by Deng and coworkers [2]. These are the only experimental results for electron-impact dissociation of O_3^+ to O^+ and our intention was to compare resulting rate coefficients. In reference [1] the cross sections for electron-impact dissociative excitation and dissociative ionization

are also determined and their relative contributions to the total rate coefficients are discussed.

3. RESULTS

Maxwellian rate coefficients have been calculated in the electron energy range from 0 to 100 eV, and non-equilibrium rate coefficients in the range from 0 to 72 eV of the mean electron energy. These calculations are performed for the cross section data sets of refs. [1] and [2], for comparisons. The results are presented in figure 1.

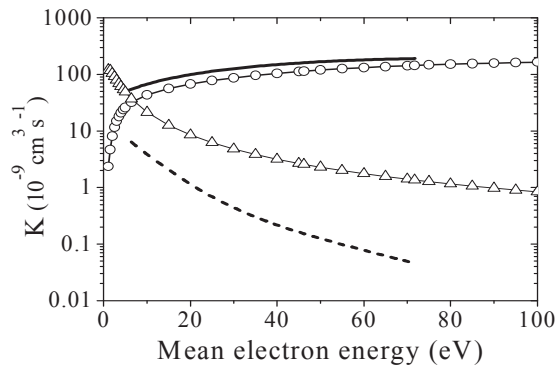


Figure 1. Rate coefficients, K , for: Maxwellian EEDF, circles [1], triangles [2]; and for non-equilibrium EEDF, solid line [1], dashed line [2].

It is clearly seen that, in particular for the high mean electron energies, for both Maxwellian and non equilibrium EEDF's, rates obtained with the LLN data [1] are significantly higher than those from ORNL [2], more than two orders of magnitude near 100 eV.

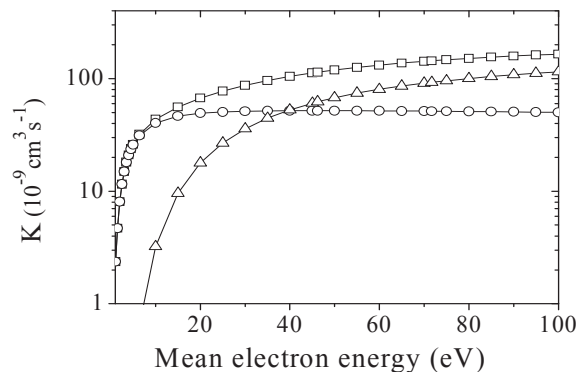


Figure 2. Total Maxwellian (circles), DE (triangles) and DI (squares) rates.

In the LLN experiment, based on the fragment kinetic energy distribution arguments, particular contributions of dissociative excitation and dissociative ionization processes are determined.

The contributions of Maxwellian rate coefficients for dissociative excitation DE and dissociative ionization DI of O_3^+ to O^+ fragments, as well as the total Maxwellian dissociation rate coefficients are given in Fig. 2. The DE rates are more important for the low mean energies and the DI is dominant for the electron energies above 40 eV.

4. CONCLUSION

Rate coefficients have been calculated for electron-impact dissociation of O_3^+ to the O^+ fragments. Experimental cross section results from Belić et al [1] and Deng et al [2] have been used. Maxwellian and non-equilibrium EEDF have been applied for the mean electron energies from threshold to 100 eV. Significantly higher rate coefficients are obtained for more recent results of Belić et al [1] since these cross sections are higher than [2]. The difference is even bigger for the non-equilibrium EEDF's. Thus, investigated processes are found to play more important role in the ozone cation dissociation, than it was previously assumed.

This demonstrates that the Solar wind electrons penetrating in the stratosphere along the polar cusp can play a significant role in the ozone layer depletion.

Acknowledgements

This work is supported in part by the Ministry of Science of the Republic of Serbia, under the contract NO 171016.

REFERENCES

- [1] D. S. Belić, X. Urbain and P. Defrance, Phys Rev A 2014, Submitted.
- [2] S. H. M. Deng, C. R. Vane, M. E. Bannister and M. Fogle, Phys. Rev. A 82, 062715 (2010).
- [3] M. Ristić, G. B. Poparić and D. S. Belić, Chem. Phys. 331, 410 (2007).
- [4] R. P. Lin, Coronal Physics from Radio and Space Observations Lecture notes in Physics 483, 93 (1997).

APPLICATION OF BINARY-ENCOUNTER-BETHE METHOD TO ELECTRON-IMPACT IONIZATION CROSS SECTION CALCULATIONS FOR BIOLOGICALLY RELEVANT MOLECULES

Bożena Żywicka and Paweł Możejko

*Atomic Physics Division, Department of Atomic, Molecular and Optical Physics,
Faculty of Applied Physics and Mathematics, Gdańsk University of Technology,
ul. G. Narutowicza 11/12, 80-233 Gdańsk, Poland*

Abstract. Electron-impact cross sections for platinum chemotherapeutic compounds, purine and pyrimidine molecules calculated using binary-encounter-Bethe model are presented as examples of possible applications of that method.

1. INTRODUCTION

It is well established now, than low- and intermediate-energy electron interactions should be taken into account in the studies of the processes induced within biological material by primary ionizing radiation [1].

One of the most important process which occurs in electron scattering from molecules is the electron-impact ionization. The maximum of efficiency of that process generally is located between 70-100 eV for large number of molecular target. The threshold for ionization process for polyatomic molecules is usually located within 7-11 eV energy range. Thus it is evident that the above energy ranges coincide with typical energies of the secondary electrons in biological media. The objective of that contribution is to show applicability of the binary-encounter method to electron-impact ionization cross section evaluation for biologically relevant targets and to present selected recent and new results.

2. THEORETICAL METHOD

Due to the binary-encounter-Bethe method (BEB) [2,3] the electron-impact ionization cross section of a given molecular orbital can be calculated according to:

$$\sigma^{BEB} = \frac{S}{t+u+1} \left[\frac{\ln t}{2} \left(1 - \frac{1}{t^2} \right) + 1 - \frac{1}{t} - \frac{\ln t}{t+1} \right], \quad (1)$$

where $u=U/B$, $t=T/B$, $S=4\pi a_0^2 NR^2/B^2$, $a_0=0.5292 \text{ \AA}$, $R=13.61 \text{ eV}$, and T is the energy of impinging electron. The total cross section for electron-impact ionization can be obtained as a sum of ionization cross sections calculated for all molecular orbitals:

$$\sigma^{ION} = \sum_i^{n_{MO}} \sigma_i^{BEB}, \quad (2)$$

Where n_{MO} is the number of the given molecular orbital. It is extremely important that in the BEB method there is no free parameter. All quantities have well defined physical meaning and can be quite precisely evaluated. The electron binding energy, B , kinetic energy of the given orbital, U , and orbital occupation number, N , should be calculated for the ground state of the geometrically optimized molecules. Such calculations can be performed with quantum chemistry computer codes like GAUSSIAN [4] using appropriate basis set. In our works we have performed calculations at the Hartree-Fock level with, if it is possible, Gaussian basis set. Obtained that way, ionization energies are not precise enough and are usually higher more than 1 eV from experimental ones. For this reason we have usually performed also outer valence Green function (OVGF) calculations of ionization potentials [5] using the GAUSSIAN code.

3. METHOD APPLICABILITY AND SELECTED RESULTS

In Figure 1 total electron-impact ionization cross sections calculated for tetrahydrofuran (C_4H_8O) molecules [6] is compared with experimental results [7].

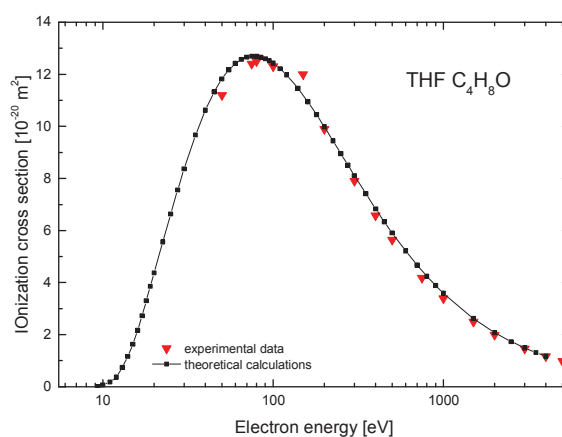


Figure 1. Comparison of total electron-impact ionization cross sections calculated [6] and measured [7] for tetrahydrofuran molecule.

The agreement between results of calculations with experimental data is quite satisfactory, especially for energies higher than 200 eV.

Having in hands such promising proof of the applicability of the BEB method we have applied that approach in the calculations of ionization cross sections for targets for which, due to its nature, measurements in the absolute scale can be extremely difficult. In Figure 2 we have compared ionization cross sections for cisplatin, carboplatin and oxaliplatin [8,9] molecules. These compounds are popular anticancer drugs, which can induce damage to tumors via their interactions with DNA. The most striking feature of ionization total cross sections for these compound is the fact that the value of the ionization cross section peak for cisplatin is about 1.9 and 1.8 times lower than those for oxaliplatin and carboplatin, respectively.

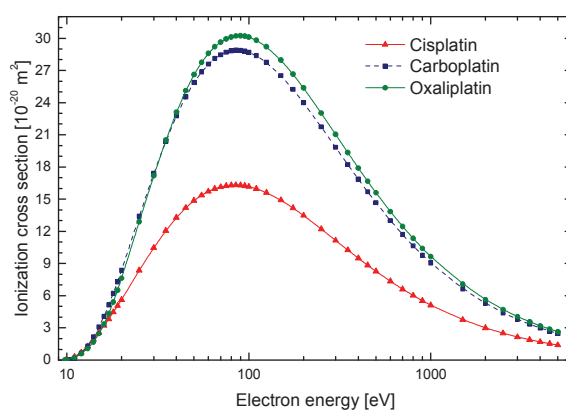


Figure 2. Comparison of total electron-impact ionization cross section calculated for platinum based chemotherapeutic compounds: cisplatin [8], carboplatin [9] and oxaliplatin [9].

In Figure 3 we have presented results of our recent calculations of electron-impact ionization cross section for pyrimidine and purine molecules. Purine molecule is one of the most occurring nitrogen-containing heterocyclic molecule and it is a base compound of guanine and adenine. Pyrimidine molecule can be regarded as base compound of cytosine, thymine and uracil. Calculations have been performed within 6-311 G basis set. The ionization threshold energies obtained with OVGf method are equal to 9.068 eV for purine and 9.151 eV for pyrimidine molecules. Ionization cross section for purine is much higher than those for pyrimidine in the whole studied energy range. For purine molecule cross section maximum of $17.53 \times 10^{-20} \text{ m}^2$ is located at 80 eV. Cross section maximum for pyrimidine of $12.47 \times 10^{-20} \text{ m}^2$ is peaked at 75 eV.

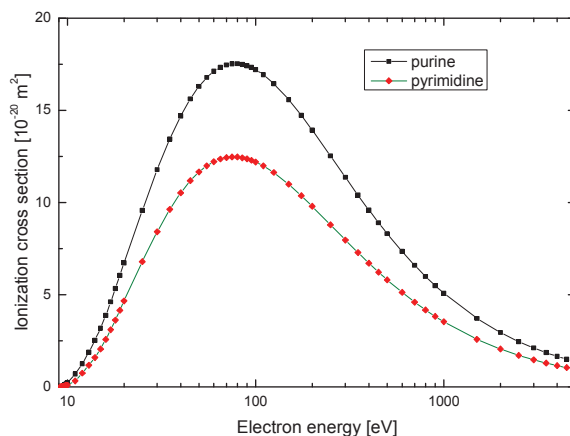


Figure 3. . Electron-impact ionization cross sections calculated for purine and pyrimidine molecules.

Acknowledgements

This work has been partially sponsored by the Polish Ministry of Science and Higher Education (MNiSzW). This work was conducted within the framework of the COST Action CM1301 (CELINA).

REFERENCES

- [1] L. Sanche, *Eur. Phys. J. D* 35, 367 (2005).
- [2] Y.-K. Kim and M. E. Rudd, *Phys. Rev. A* 50, 3954 (1994).
- [3] W. Hwang, Y.-K. Kim and M. E. Rudd, *J. Chem. Phys.* 104, 2956 (1996).
- [4] M. J. Frisch et al, *GAUSSIAN 03 Revision B.05* (Pittsburgh, Gaussian, 2003).
- [5] V. G. Zakrzewski and W. von Niessen, *J. Comp. Chem.* 14, 13 (1994).
- [6] P. Mozejko and L. Sanche, *Radiat. Phys. Chem.* 73, 77 (2005).
- [7] M. Fuss, A. Munoz, J. C. Oller, F. Blanco, D. Almeida, P. Limao-Vieira, T. P. D. Do, M. J. Brunger and G. Garcia, *Phys. Rev. A* 80, 052709 (2009).
- [8] B. Żywicka and P. Mozejko, *Eur. Phys. J. D* 66, 54 (2012).
- [9] B. Żywicka and P. Mozejko, *Eur. Phys. J. Spec. Topics* 222, 2285 (2013).

TOTAL CROSS SECTIONS FOR ELECTRON SCATTERING FROM SELECTED HYDROCARBONS: THE SUBSTITUTIONAL AND ADDITIVITY EFFECTS

Paweł Możejko, Czesław Szmytkowski, Mateusz Zawadzki and Elżbieta Ptasińska-Denga

Atomic Physics Division, Department of Atomic, Molecular and Optical Physics, Faculty of Applied Physics and Mathematics, Gdańsk University of Technology, ul. G. Narutowicza 11/12, 80-233 Gdańsk, Poland

Abstract. Total cross sections (TCS) for electron scattering from selected alkyne molecules, ethylene and its derivatives are compared. All cross sections have been measured in a wide energy range, from about 1 eV up to 370 eV, with the same electrostatic electron spectrometer. The substitutional and additivity effects are indicated and discussed.

1. INTRODUCTION

The complete knowledge of electron-molecule scattering processes is essential in understanding of the electron-driven phenomena in astrochemistry [1], biological media [2] as well as in plasmas [3]. The total cross section, which can be regarded as the sum of integrated cross sections for all scattering channels, can be determined in absolute way, without any normalization procedures. From systematic studies concerning total cross section determination for electron scattering from polyatomic molecules it is possible to notice some regularities and useful relationships like perfluorination effects [4], isomer effect [5] or group additivity rule [6]. In the present work we examine energy dependence of TCSs for selected alkyne molecules: 1-butyne, propyne and acetylene, as well as for ethylene molecule and its selected derivatives: propene, 1-butene and 1-pentene.

2. EXPERIMENTAL

All presented experimental results have been obtained with electrostatic electron spectrometer working in the linear transmission configuration. The method is based on measurements of the attenuation of the intensity of a projectile-particle beam transmitted through the volume filled with target particles. In the ideal transmission experiment, i.e. when (i) the projectile beam is monoenergetic, parallel and very narrow, (ii) the concentration of target

molecules, n , is low enough for interactions with projectiles to be single only, and (iii) only those projectiles are registered which have not interacted with target molecules, while (iv) the solid angle subtended by the detector is near zero, the TCS ($Q(E)$) is related to the attenuation of the electron beam as follows:

$$Q(E) = \left(\int_a^b n(x) dx \right)^{-1} \ln \frac{I_0(E)}{I_g(E)} \quad (1)$$

where $I_g(E)$ and $I_0(E)$ are intensities of detected transmitted electron currents of energy E in the presence or absence of the target in the scattering volume, respectively; $n(x)$ is the target density at the point x of the electron pathway, while integration is performed over the entire path of the electron beam where $n(x) \neq 0$. Accuracy of TCS measured with the transmission technique depends on electron beam resolution, electron energy, uncertainties in target pressure and temperature measurements. In experiments carried out in our laboratory systematic uncertainties are less than 10% for low collision energies and lower than 5% for intermediate energies [7].

3. RESULTS

In Figure 1 total cross sections measured for 1-butyne ($\text{HC}\equiv\text{C}-\text{CH}_2\text{CH}_3$) [8], propyne ($\text{HC}\equiv\text{C}-\text{CH}_2$) [9] and acetylene ($\text{HC}\equiv\text{CH}$) [8] are compared.

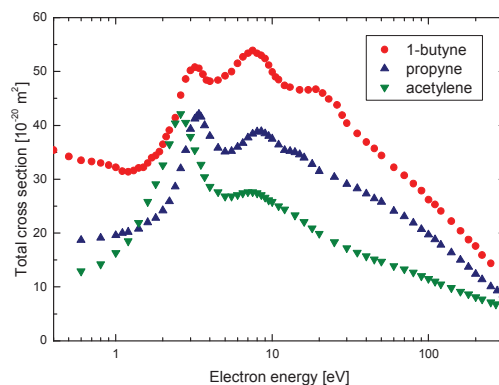


Figure 1. Comparison of total cross sections measured for selected alkyne molecules.

The shape of total cross section for 1-butyne resembles that for propyne and acetylene. Each molecule of the studied alkynes has, on one of the ends of the molecular chain, the triple carbon-to-carbon bond. In subsequent molecules of

the studied series, one hydrogen atom in the acetylene molecule is replaced with the methyl group to form propyne and with the ethyl group to form 1-butyne. Due to this substitutional effect, i.e. due to substitution of one hydrogen atom in the acetylene molecule with a functional group, the size of resulting molecule increases and, generally, it leads to the increase of the respective electron-scattering total cross section value.

In Figure 2 total cross sections for selected ethylene family, i.e. ethylene ($\text{H}_2\text{C}=\text{CH}_2$) [10], propene ($\text{H}_2\text{C}=\text{CH}-\text{CH}_3$) [5], 1-butene ($\text{H}_2\text{C}=\text{CH}-\text{CH}_2\text{CH}_3$) [11] and 1-pentene ($\text{H}_2\text{C}=\text{CH}-(\text{CH}_2)_2\text{CH}_3$) [12] molecules, are compared. It is evident that for energies higher than 3 eV the magnitude of the total cross section increases with the increase of the size of the investigated molecules.

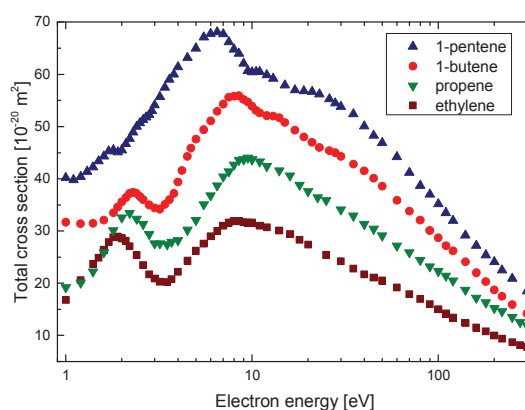


Figure 2. Comparison of total cross sections measured for ethylene and selected ethylene derivatives.

In Figure 3 we have compared total cross sections measured for 1-butyne and propyne molecules with respective estimation obtained using the simple additivity rule. Basing on the dependence of total cross sections on the molecular size, observed in Figure 1 and Figure 2, we have estimated total cross sections for propyne and 1-butyne molecules according to the following simple rules:

$$\text{TCS}(\text{C}_3\text{H}_4) = \text{TCS}(\text{C}_2\text{H}_2) + 0.5\text{TCS}(\text{C}_2\text{H}_4) \quad (2)$$

and

$$\text{TCS}(\text{C}_4\text{H}_6) = \text{TCS}(\text{C}_2\text{H}_2) + \text{TCS}(\text{C}_2\text{H}_4), \quad (3)$$

respectively; $\text{TCS}(\text{C}_2\text{H}_2)$ and $\text{TCS}(\text{C}_2\text{H}_4)$ are the experimental data [8,10]. Figure 3 shows that using such simple approximation we have obtained estimated TCSs which are, in the intermediate energy range (50-250eV), in reasonable agreement with experimental data.

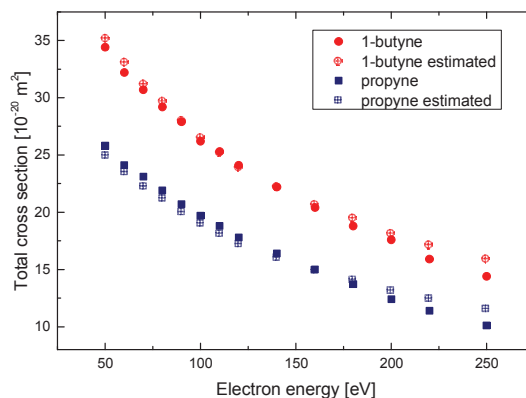


Figure 3. TCSs measured and estimated for 1-butyne and propyne molecules

Acknowledgements

This work has been partially sponsored by the Polish Ministry of Science and Higher Education (MNiSzW).

REFERENCES

- [1] N.J. Mason, B. Nair, S. Jheeta and E. Szymańska, *Faraday Discuss.* DOI:10.1039/c4fd00004h (2014).
- [2] L. Sanche, *Eur. Phys. J. D* 35, 367 (2005).
- [3] E. Böhler, J. Warneke and P. Swiderek, *Chem. Soc. Rev.* 42, 9219 (2013).
- [4] Cz. Szmytkowski and E. Ptasińska-Denga, *Vacuum* 63, 545 (2001).
- [5] Cz. Szmytkowski and S. Kwitniewski, *J. Phys. B* 35, 2613 (2002).
- [6] A. Domaracka, P. Możejko, E. Ptasińska-Denga and Cz. Szmytkowski, *Publ. Astron. Obs. Belgrade* 84, 35 (2008).
- [7] Cz. Szmytkowski and P. Możejko, *Vacuum* 63, 549 (2001).
- [8] Cz. Szmytkowski, P. Możejko, M. Zawadzki, K. Maciąg and E. Ptasińska-Denga, *Phys. Rev. A* 89, 052702 (2014).
- [9] Cz. Szmytkowski and S. Kwitniewski, *J. Phys. B* 35, 3781 (2002).
- [10] Cz. Szmytkowski, S. Kwitniewski and E. Ptasińska-Denga, *Phys. Rev. A* 68, 032715 (2003).
- [11] P. Możejko, E. Ptasińska-Denga, Cz. Szmytkowski and M. Zawadzki, *J. Phys. B* 45, 145203 (2012).
- [12] Cz. Szmytkowski, P. Możejko, M. Zawadzki and E. Ptasińska-Denga, *J. Phys. B* 46, 065203 (2013).

DETERMINATION OF SEQUENCE-SPECIFIC DNA STRAND BREAKS INDUCED BY VUV RADIATION USING THE DNA ORIGAMI TECHNIQUE

S. Vogel¹, J. Rackwitz¹, R. Schürmann^{1,2}, J. Prinz¹, A. R. Milosavljević³, A. Giuliani⁴ and I. Bald^{1,2}

¹*Institute of Chemistry, University of Potsdam, Karl-Liebknecht-Str. 24-25,
14469 Potsdam, Germany*

²*BAM Federal Institute for Materials Research and Testing, Richard-Willstätter
Str. 11, 12489 Berlin, Germany*

³*Institute of Physics Belgrade, University of Belgrade, Pregrevica 118, 11080,
Serbia*

⁴*Synchrotron SOLEIL, Gif-sur-Yvette, France*

Abstract. We have studied the sequence-specific DNA damage induced by VUV photons in an energy range from 6.5 eV to 9.5 eV on the single-molecule level. By using a novel DNA origami technique, we were able to visualize the photon-induced dissociation of single chemical bonds within complex but well-defined self-assembled DNA nanostructures, deposited on a UV transparent substrate. The method employs atomic force microscopy (AFM) to image and quantify photon-induced bond dissociations within specifically designed oligonucleotide targets that are attached to DNA origami templates. Therefore, we were able to determine quantitatively the sequence-specific DNA strand break yields in dependence of the VUV photon energy.

1. INTRODUCTION

There is a long standing effort to fully understand photon interaction with DNA and RNA molecules, which are carriers of genetic information. DNA and RNA strongly absorb in ultraviolet (UV) and far-UV spectral region [1], which should lead easily to photon-induced destruction or severe carcinogenic damage. However, it appears that there is an amazing photostability of DNA, suggested to be due to an ultra-fast de-excitation of the bases from their excited electronic state to a hot ground state, thus allowing an efficient cooling of the molecule through vibrational interactions with the environment. Nevertheless, an UV-induced ultrafast damage of oligonucleotides can occur by formation of cyclobutadiene pyrimidine dimers [2], and at photon energies higher than 8 eV DNA strand breaks in plasmid DNA have been observed [3]. All these results led

to better understanding of very complex processes triggered by energetic photon interaction with DNA, which depend on physicochemical properties of single bases, their inter-connections, solvent effects etc. [1]. However, it has not been possible so far to visualize and quantify photon-induced damage to oligonucleotides of specific nucleotide sequence on a single molecular level. Stacking interactions between the DNA nucleobases lead to a strong modification of the nucleobase's electronic properties and hence their photoinduced fragmentation dynamics [4]. Measuring the photon-induced DNA strand breaks on a single molecular level as a function of the photon energy and the flux is particularly interesting for both the studies on DNA photostability and the important field of radiation damage research [3,5].

We have recently developed a novel method that allowed for the first time to visualize the electron-induced dissociation of single chemical bonds within complex, but well-defined self-assembled DNA nanostructures [6,7]. We use AFM to image and quantify low-energy-electron-induced bond dissociations within specifically designed oligonucleotide targets that are attached to DNA origami templates thereby forming a DNA nanoarray. In electron-irradiation experiments we have used 18 eV electrons and found that at a fluence of $1 - 5 \times 10^{12} \text{ cm}^{-2}$ the number of DNA strand breaks increases linearly with the electron fluence. By using electron beams with a current of 1 – 10 nA irradiation times below 100 s are required. This novel technique enables the fast and parallel determination of DNA strand break yields with unprecedented control over the DNA's primary and secondary structure.

In the present work, we combine the DNA origami technique with the wide-energy high-brilliance VUV synchrotron source at SOLEIL, in order to perform a detailed investigation of DNA photo-radiation damage in its most natural environment and on a single molecule level.

2. EXPERIMENTAL METHOD

2.1 DNA origami samples

DNA origami nanostructures were prepared from the M13mp18 scaffold strand and a set of 208 short oligonucleotides according to a well-established procedure [6]. In brief, the DNA strands are mixed in TAE buffer with 10 mM MgCl_2 and annealed from 80°C to room temperature within 2 hours, and the non-assembled excess strands are removed by spin-filtering. The assembled structures are deposited on SiO_2/Si and CaF_2 substrates, respectively, by deposition in 10x TAE buffer with 100 mM MgCl_2 solution for 45 min. The excess solution is removed by washing with 4 mL of ethanol/water (1/1) mixture and subsequently the sample is dried with a blow of nitrogen. Then the samples are transferred into the chamber filled with Ar and irradiated with VUV photons with defined energy and fluence. After irradiation the samples are washed again with ethanol/water to remove fragmentation products and then incubated in a 50 nM solution of

streptavidin for 5 min, washed again and dried. Then the samples are analyzed with AFM.

2.2 Experimental set up

The irradiation chamber of the beamline is connected to the APEX branch of the DISCO beamline at the synchrotron SOLEIL synchrotron radiation facility. The samples were deposited on a holder attached to a Z manipulator that allowed for fine adjustment of the sample on the beam. The differential pumping system of the beamline was used to filter out the second order light. The samples were irradiated for different time to establish a dose-response curve as a function of the photon energy. The photon flux was measured using a calibrated photodiode.

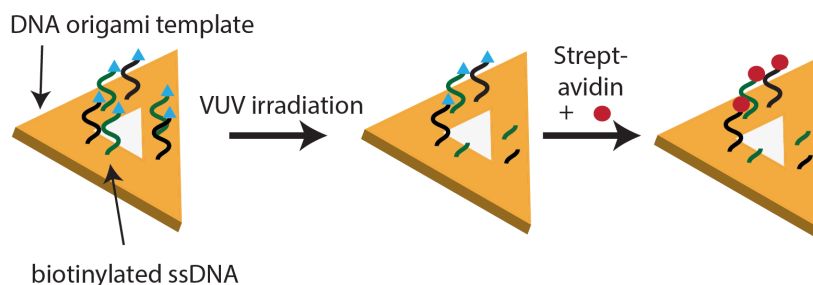


Figure 1. Scheme of the DNA origami triangles, which serve as a support of the oligonucleotide target structures. After the irradiation with VUV photons the remaining intact target structures are visualized for AFM using streptavidin.

3. RESULTS

We have irradiated DNA origami samples carrying the target sequences 5'-TT(XTX)₃TT (X = C,A) with VUV photons at 6.5 eV, 7.3 eV, 8.44 eV, 8.94 eV, 9.14 eV and 9.5 eV. By using AFM for the visualization of DNA single strand breaks in the target sequences we could observe that the relative number of DNA strand breaks increases with the photon flux. Thus, we could establish dose-response curves for all photon energies. The energies were chosen to match either resonances observed in previous experiments (6.5 eV and 7.3 eV)[9],[10], or the ionization potentials (IP) of isolated nucleobases (IP(A) = 8.44 eV, IP(C) = 8.94 eV, IP(T) = 9.14 eV), or to be right above the ionization threshold of all DNA bases (9.5 eV). By comparing the DNA strand break yield of the two target sequences at the different irradiation energies, we can deduce important information about the underlying damage mechanism.

Furthermore, we performed measurements on both SiO₂/Si substrates and VUV transparent CaF₂ to directly compare the effect of secondary electrons released from the Si substrate. All measurements have been performed at atmospheric pressure under Ar to avoid DNA damage induced by evacuation or venting of the chamber.

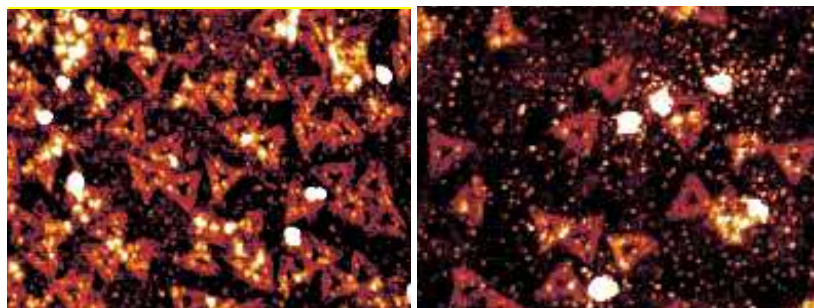


Figure 2. AFM images of DNA origami nanostructures deposited on CaF_2 irradiated at 8.44 eV for 1 min (left), and 20 min (right).

Acknowledgements

This research was supported by a Marie Curie FP7 Integration Grant within the 7th European Union Framework Programme and by the Deutsche Forschungsgemeinschaft (DFG). We are grateful to the synchrotron SOLEIL for providing beamtime and support under project no. 20131271 and to a grant by the German Academic Exchange Service (DAAD, project No. 57055766) supported by the German Federal Ministry of Education and Research. A.R.M. acknowledges support by the MESTD of RS (171020) and the COST Action MP1002 (Nano-IBCT).

REFERENCES

- [1] Middleton et al, *Annu. Rev. Phys. Chem.* 60, 217 (2009).
- [2] W. J. Schreier, T. E. Schrader, F. O. Koller, P. Gilch, C. E. Crespo-Hernandez, V. N. Swaminathan, T. Carell, W. Zinth, B. Kohler, *Science* 315, 625 (2007).
- [3] K. Hieda, *Int. J. Radiat. Biol.* 66, 561, (1994).
- [4] U. Kadhane, A.I.S. Holm, S.V. Hoffmann, S.B. Nielsen, *J. Photochem. Photobiol. A* 197, 110 (2008).
- [5] I. Baccarelli, I. Bald, F. A. Gianturco, E. Illenberger, J. Kopyra, *Phys. Rep.* 508, 1 (2011).
- [6] A. Keller, I. Bald, A. Rotaru, E. Cauet, K. V. Gothelf, F. Besenbacher, *ACS Nano* 6, 4392 (2012).
- [7] A. Keller, J. Kopyra, K. V. Gothelf, I. Bald, *New J. Phys.* 15, 083045 (2013).
- [8] Smialek et al, *Radiat. Res.* 172, 529 (2009).
- [9] Smialek et al, *J. Phys. Conf. Ser.* 101, 012020 (2008).
- [10] A. R. Milosavljević, V. Z. Cerovski, F. Canon, M. Ranković, N. Škoro, L. Nahon, A. Giuliani: *J. Phys. Chem. Lett.* 5, 1994 (2014).

ABSOLUTE CROSS SECTIONS FOR ELECTRONIC EXCITATION OF FURAN

Khrystyna Regeta and Michael Allan

*Department of chemistry, University of Fribourg, Chemin du Musée 9,
1700 Fribourg, Switzerland*

Abstract. We measured absolute differential cross sections (DCSs) for elastic scattering and for electronic excitation of furan, both as a function of scattering angle and as a function electron energy, from threshold to 14 eV. Preliminary comparison with existing calculations is given. Two bands are observed in the excitation of the lowest triplet state and assigned as valence core excited resonances.

1. INTRODUCTION

Electron-driven chemistry has many applications, including plasma-chemistry, radiotherapy and nanofabrication by Focused Electron Beam Induced Processing (FEBIP). Of the three primary electron-driven chemistry mechanisms: dissociative ionization (DI), dissociative electron attachment (DEA), and neutral dissociation (ND), the last has been the least studied experimentally because it does not produce charged products. We make a contribution to its understanding because electronic excitation (EE) is the initial step in most ND reactions.

Electronic excitation cross sections are notoriously difficult to calculate from first principles. It is therefore desirable to provide quantitative experimental data, particularly near threshold, for comparison with theory. An example of such collaboration concerns the cross sections measured for the prototype π -system ethene in our laboratory, where the input from the experiment led to improvement of theory [1]. We also measured the EE cross sections for the FEBIP precursor $\text{Pt}(\text{PF}_3)_4$ [2,3] but such data are unlikely to inspire calculations at the present time because the numerous d- and f- electrons make the task too difficult. We therefore chose a prototype molecule more complex than, but related to, the ethene case – the furan molecule. Qualitative (relative) data at 0° were already measured in our laboratory and revealed interesting resonances [4]. Absolute elastic cross sections were measured more recently by Maljkovic *et al.* [5] in the range 50-300 eV. Electron energy loss spectra were measured by Palmer *et al.* [6]. Measurements of elastic and electronically inelastic cross sections, together with first-principles

calculation relevant to our study were reported by da Costa *et al.* [7]. The present work extends the experimental results of Ref. [7] by reporting absolute measurements as a function of electron energy in the near threshold region, with fine energy spacing permitting observation of resonances, and using the magnetic angle changer to cover the entire angular range 0° - 180° . The hemispherical analyzer instrument and the relative flow normalization technique were described previously [1,3].

2. RESULTS

The EEL spectra in Fig. 1 show the excited states for which excitation cross sections were measured. The spectrum recorded under low momentum transfer conditions agrees well with the UV photoabsorption spectrum [6], the 90° and low residual energy spectrum shows the triplet states in agreement with earlier EEL spectra [6,7].

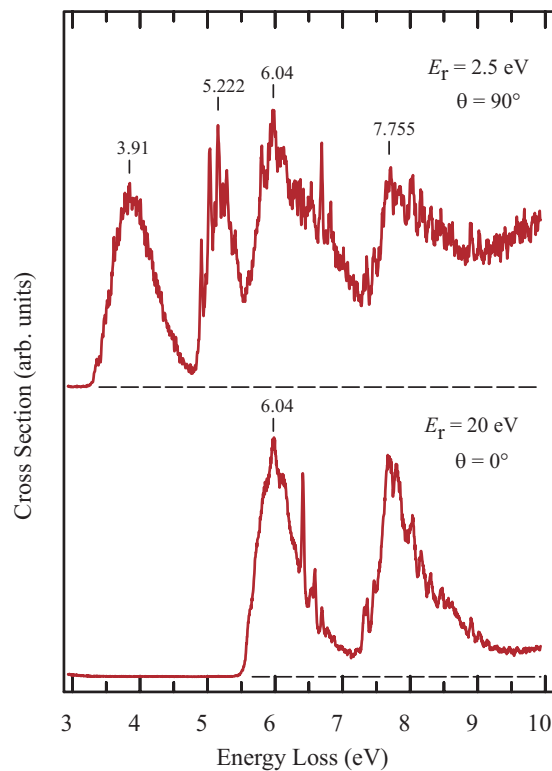


Figure 1. EEL spectra recorded at the (constant) residual energies and scattering angles indicated.

Absolute cross sections for electronic excitation were determined by integrating under energy-loss bands recorded with constant incident energies and normalizing to the elastic cross section determined by the relative flow method with He as reference gas. Excitation functions were then recorded at the peaks of the energy-loss bands, corrected for the instrumental response function, and normalized to the absolute values. Figure 2 shows examples for the two lowest triplets 3B_2 and 3A_1 , and the lowest singlet state 1B_2 , recorded at the two extreme angles of 0° and 180° .

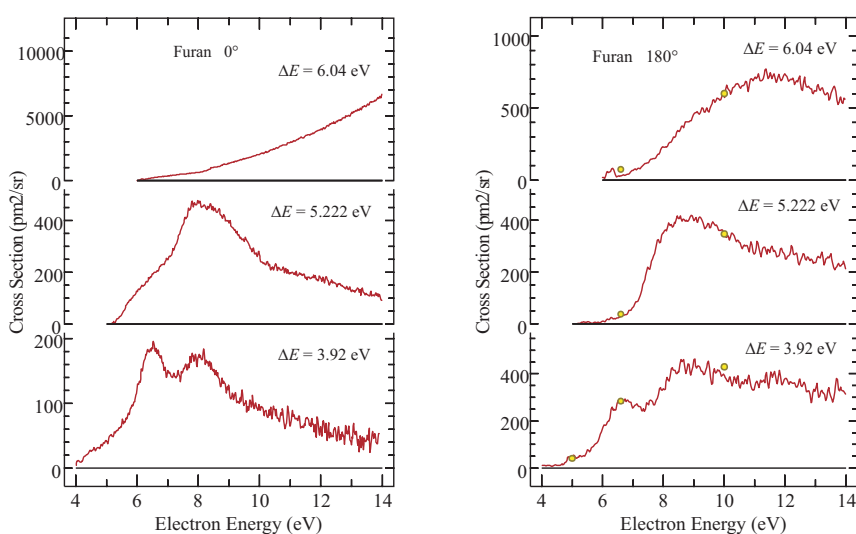


Figure 2. DCSs for electronic excitation.

The two resonances at 6.50 eV and 8.0 eV observed in the cross section for the excitation of the first triplet state confirm the earlier finding of Ref. [4]. Furan has three occupied π orbitals, π_1 , π_2 and π_3 and two empty π orbitals, π_4 and π_5 . The ground state configuration is $(\pi_1)^2(\pi_2)^2(\pi_3)^2$. We propose an assignment of the 6.5 eV resonance as $(\pi_1)^2(\pi_2)^2(\pi_3)^1(\pi_4)^2$ and the 8.0 eV resonance as $(\pi_1)^2(\pi_2)^1(\pi_3)^2(\pi_4)^2$ valence core excited shape resonances. This assignment is based on the analogy with ethene [1], where the $(\pi)^1(\pi^*)^2$ valence core excited shape resonance was prominent in the cross section for the excitation of the $^3(\pi,\pi^*)$ state, and on the suggestive fact that the separation of the 6.50 eV and 8.0 eV resonances (1.5 eV) is nearly equal to the separation of the π_2 and π_3 orbitals (1.4 eV), as revealed by the photoelectron spectrum [8]. The cross section for the excitation of the singlet state attains very large values and rises nearly linearly with energy at 0° , as expected for a spin and dipole allowed transition. The cross section is much smaller at 180° .

The cross section for excitation of the 1B_2 state at 0° in Fig. 2 has magnitudes in qualitative agreement with the differential cross sections calculated by da Costa *et al.* [9]. Our data can also be compared to the calculated (DCSs) of da Costa *et al.* [7] at 5, 6, 7.5, and 10 eV for the 1st, and at 7.5 and 10 eV for the 2nd triplet state. The agreement is reasonable near threshold (5 eV and 6 eV for the 1st triplet), but our values are substantially lower than calculated at higher energies. Similarly, there is a reasonable agreement for the 2nd triplet at 7.5 eV, but the calculation is much higher at 10 eV.

There is a qualitative agreement with the calculation of da Costa *et al.* [7] in the sense that a number of resonances are calculated in the excitation functions of triplet states, although more resonances appear in the calculation than in our experiment.

3. CONCLUSION

We measured a comprehensive set of DCSs for electronic excitation of furan. The data shows resonances in the triplet excitation. We hope that our measurements will inspire more theoretical work with the goal to reproduce these resonances. Data similar to that in Fig. 2 but at other scattering angles, and angular distributions, will be presented in a later publication.

Acknowledgements

This work was supported by the Swiss National Science Foundation under the grant No. 200020-131962/1, and the Cost Action CM1301 CELINA.

REFERENCES

- [1] M. Allan, C. Winstead and V. McKoy, *Phys. Rev. A* 77, 042715 (2008).
- [2] O. May, D. Kubala, M. Allan, *PCCP* 14, 2979 (2012).
- [3] M. Allan, *J. Chem. Phys.* 134, 204309 (2011).
- [4] K. Asmis, PhD thesis, (University of Fribourg, Switzerland, 1996).
- [5] J. B. Maljkovic, F. Blanco, R. Curik, G. Garcia, B. Marinkovic and A. Milosavljevic, *J. Chem. Phys.* 137, 064312 (2012).
- [6] M. H. Palmer, I. C. Walker, C. C. Ballard and M. F. Guest, *Chem. Phys.* 192, 111 (1995).
- [7] R. da Costa, M. Bettega, M. Lima, M. Lopes, L. R. Hargreaves, G. Serna and M. A. Khakoo, *Phys. Rev. A* 85, 062706 (2012).
- [8] E.E. Rennie, C.A.F. Johnson, J.E. Parker, D.M.P. Holland, D.A. Shaw, M.A. MacDonald, M.A. Hayes and L.G. Shpinkova, *Chem. Phys.* 236, 365 (1998).
- [9] R. F. da Costa, M. H. F. Bettega, M. T. do N. Varella and M. A. P. Lima, *J. Phys.:* Conf. Ser. 388, 012015 (2012).

EXPERIMENTS TO PROBE ELECTRON ATTACHMENT TO STARK-SELECTED BIOMOLECULAR CLUSTERS

M. Ryszka, R. Pandey, M. Dampc and S. Eden

*Department of Physical Sciences, The Open University,
Milton Keynes, MK7 6AA, United Kingdom*

Abstract. We report developments in the optimization of a new experimental setup currently being optimized at The Open University. The experiment will allow us to probe electron attachment to Stark-selected biomolecular clusters. We present preliminary results on the neutral beam deflection and selection processes.

1. INTRODUCTION

A major challenge in analyzing radiation-induced processes in clusters is the broad distribution of sizes and configurations produced by supersonic expansion sources (or alternative cluster sources, for example utilizing laser ablation). This poster summarizes our recent progress in the development of an experiment based on the irradiation of specific biomolecular isomers and clusters with electrons from a high-resolution monochromator [1] and analysis of the resultant anions by mass spectrometry. The system [2] incorporates a Stark deflector developed by Küpper and co-workers at DESY to deflect polar species in inhomogeneous electric fields in order to control the target configurations. They have recently applied the method to separate singly hydrated indole from monomers and larger clusters in a mixed beam [3].

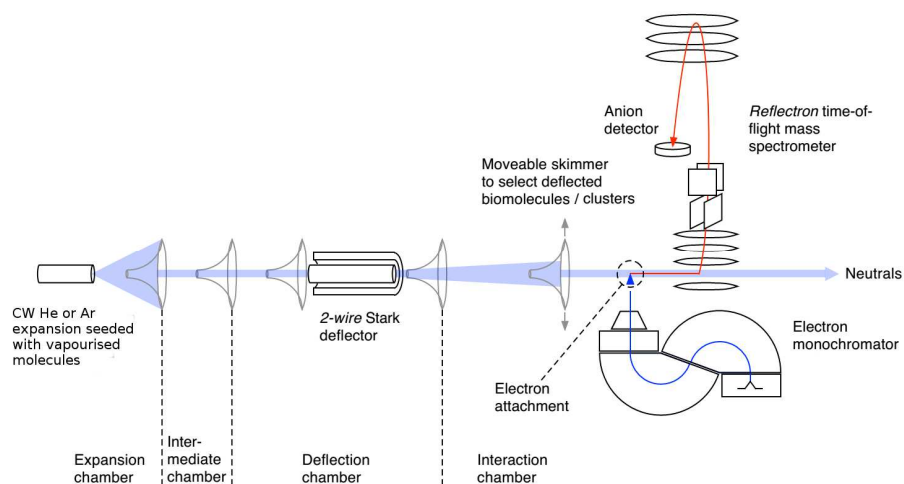


Figure 1. Experiment to probe electron attachment to Stark-selected clusters.

2. THE EXPERIMENT

The molecular beam source in the OU experiment (shown schematically in Figure 1) is based supersonic expansion of argon or helium seeded with the molecules of interest. A CW expansion is used with a TOF extraction frequency of up to 50 kHz in order to maximize the electron attachment signals. Producing molecules and clusters in low J states is essential for effective Stark selection so the expansion chamber is pumped at $>2,000 \text{ ls}^{-1}$. The experimental design involves using a moveable skimmer to select specific parts of Stark-deflected beams for electron attachment measurements. To date, comparisons of with theory have been limited by the spread of biomolecular isomers and clusters in experiments. The project is being carried out in collaboration with Gorfinkiel and Fabrikant who are innovating methods to calculate low-energy electron interactions with clusters [4].

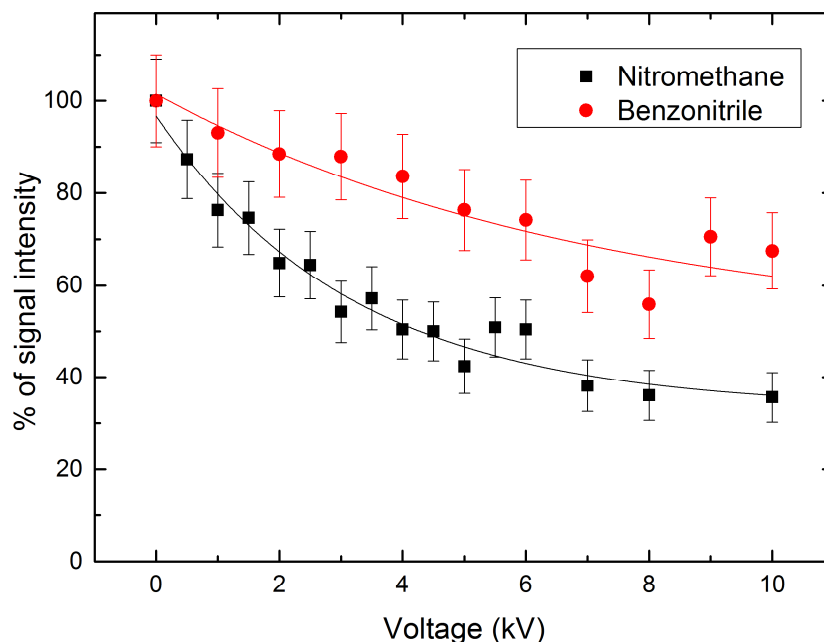


Figure 2. Percentage of signal intensity as a function of the voltage across Stark-deflector. Curves fitted to experimental data using asymptotic model.

3. PRELIMINARY RESULTS

By performing electron impact ionization experiments on water, benzonitrile, and nitromethane seeded in helium and argon beams, we have obtained evidence for signal suppression as a function of Stark-deflector voltage (Figure 2). We interpret these results as deflection of the coldest molecules out of the axis of beam by Stark deflection. Further work is in progress to recover these deflected molecules for collision experiments and independent characterization by resonance-enhanced multi-photon ionization (REMPI). These on-going experiments are based on using a moveable skimmer to select specific parts of deflected beams. Figure 3 shows a two-dimensional map of a molecular beam without a deflecting voltage applied.

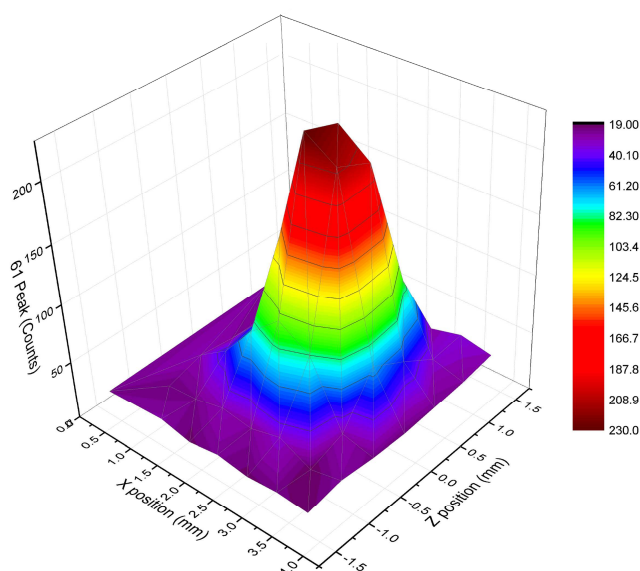


Figure 3. Molecular beam's profile, mapped in two dimensions using the movable skimmer, for the Stark-Deflector voltage of 0 kV.

Acknowledgements

We would like to acknowledge The Open University, the EU (Marie Curie Intra-European Reintegration Grant), and the EPSRC for funding M. Ryszka's studentship. The EPSRC is acknowledged for S. Eden's Post-doctoral Fellowship at the Life Sciences Interface and his current Career Acceleration fellowship. Further financial support for our work has been provided by the EU through the RADAM, ITS-LEIF, EIPAM, and nano-IBCT actions. We acknowledge the key roles of our collaborators on the project: J. Küpper (DESY), J. Gorfinkiel (OU), I. Fabrikant (Nebraska), G. Garcia (CIEMAT, Madrid), and their respective co-workers.

REFERENCES

- [1] H. Ibach, *Journal of Electron Spectroscopy and Related Phenomena*, 64/65 819-823 (1993).
- [2] S. Eden, EPSRC CAF project EP/J002577/1
- [3] S. Trippel, Y-P. Chang, S. Stern, T. Mullins, L. Holmegaard, and J. Küpper, *Phys. Rev.* 86, 033202 (2012).
- [4] I. I. Fabrikant, S. Caprasecca, G. A. Gallup, J. D. Gorfinkiel, *J. Chem. Phys.* 136, 184301 (2012).

LOW ENERGY ELECTRON INTERACTIONS WITH NITROMETHANE

Anita Ribar¹, Ewelina Szymańska-Skolimowska², Marian Danko¹, Štefan Matejčík¹ and Nigel Mason²

¹ *Department of Experimental Physics, Comenius University Bratislava,
Šafárikovo nám. 6, 818 06 Bratislava, Slovakia*

² *Department of Physical Sciences, The Open University, Walton Hall, MK7 6AA
Milton Keynes, United Kingdom*

Abstract. Time of Flight mass spectrometer using the Velocity Slice Imaging technique (GASIC) at the Open University, UK and an Electron Induced Fluorescence Apparatus (EIFA) at the Comenius University, SK were used to investigate the interactions of low energy electrons with nitromethane, CH₃NO₂. Using the GASIC apparatus we observed dissociative electron attachment (DEA) to nitromethane at impact energies in the range between 0 – 20 eV and with EIFA we examined dissociative excitation (DE) of electron induced fluorescence (EIF) from the molecule at 50 eV. The emission spectrum in range between 300 – 670 nm is presented in this paper, as well as velocity slice images of O⁻ at 6 eV and 10 eV electron impact energies.

1. INTRODUCTION

Nitromethane, CH₃NO₂, is the simplest nitro-compound and is widely used in industry as a solvent, degreaser and has characteristics typical of commonly used explosives and propellants [1]. It can also act as a human carcinogenic agent [2]. Further motivation for the research on nitromethane's interaction with low energy electrons is due to its abundance in the Earth's atmosphere, where it may influence local chemistry [3]. Extensive studies on nitromethane using mass-spectroscopy have been reported in the literature [4] and its electronic state spectroscopy characterised [5]. There have also been some studies exploring electron collisions with these molecules (e.g. elastic scattering [6] and Dissociative Electron Attachment (DEA) [7]). However, to date, there are few studies on electron induced dissociation of nitromethane, in particular there have been no recorded emission spectra from neutral fragments of nitromethane reported in the UV/VIS region, nor have the dynamics of the DEA process been studied in detail (e.g. by using the recently developed technique of velocity slice imaging (VSI) in order to understand the kinetic energy and angular distribution of the anions.

2. EXPERIMENTAL APPARATUS

Both the GASIC [8] and EIFA [9] apparatuses use cross electron/molecular beam geometries with the electron gun as the source of a monoenergetic magnetically collimated beam of electrons encountering the molecular beam derived from an effusive capillary. Operating pressures differ in orders of magnitude due to the higher efficiency of ionisation observed with GASIC (10^{-6} mbar) compared to the fluorescence of nitromethane (10^{-4} mbar). However, in both cases the single collision event condition is observed.

The GASIC experiment was used for examination of the DEA to nitromethane. DEA is a resonant process in which the incident electron is captured by the neutral molecule forming a transient negative ion (TNI), which subsequently decays into anionic and neutral fragments. Anions enter the flight tube at the end of which a positive sensitive detector (PSD) is placed. Mass spectra are collected in the pulse counting mode of the PSD and the VSI of anion distribution obtained. Electron induced fluorescence (EIF) and dissociative excitation (DE) of nitromethane was studied using EIFA. Radiative deexcitation was detected with a photomultiplier after the light has passed through an optical Czerny – Turner monochromator operating over the spectral range 180 – 700 nm. Using this apparatus we are able to obtain electron energy resolved spectra, emission cross sections for EIF and DE processes and the thresholds for these reactions for both ionic and neutral fragments.

3. EXPERIMENTAL RESULTS AND DISCUSSION

Using the GASIC apparatus we obtained anionic mass spectra for nitromethane at several electron energies. The anion yield of O^- was measured and two resonances at 6 eV and 10 eV (Fig. 1.). The O^- ion distribution occurs as big ‘spot’ without any anisotropic structure. The large radius of the ‘spot’ suggests a high kinetic energy of the product anions.

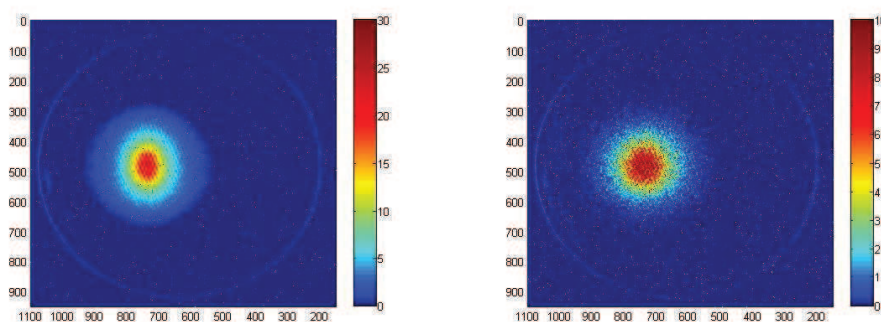


Figure 1. The VSI of O^- from CH_3NO_2 obtained at 6 eV (left) and 10 eV (right).

The major advantage of VSI measurements compared to other turn table techniques is its ability to measure the angular distribution in the whole range from 0 – 180°. The lack of anisotropy in angular distribution provides us with clear information about the TNI symmetry. From the radius of the Newton sphere on the image, the initial kinetic energy and the internal energy of the anions can be determined (Table 1). High kinetic energy anions are detected.

Table 1. The kinetics of DEA channels leading to the formation of O^- based on thermochemical data. The bond energy (D_{AB-C}) and electron affinity (EA_C) were taken from Sailer et al. [10]. The incident electron energy (E_e) was taken from our results. All values are given in eV.

Negative ion channel	EA_C	D_{AB-C}	$E_{\text{threshold}}$	E_e (max peak)	E_{KER}	m_{AB}/m_{ABC}	E_{max}
$O^- + CH_3NO$	1.46	4.76	3.3	6 10	2.7 6.7	0.7377	1.9918 4.9426

An emission spectrum of nitromethane in the region 300 – 670 nm was obtained at 50 eV electron energy impact using EIFA operating with a resolution of ~ 0.8 nm (Fig. 2)

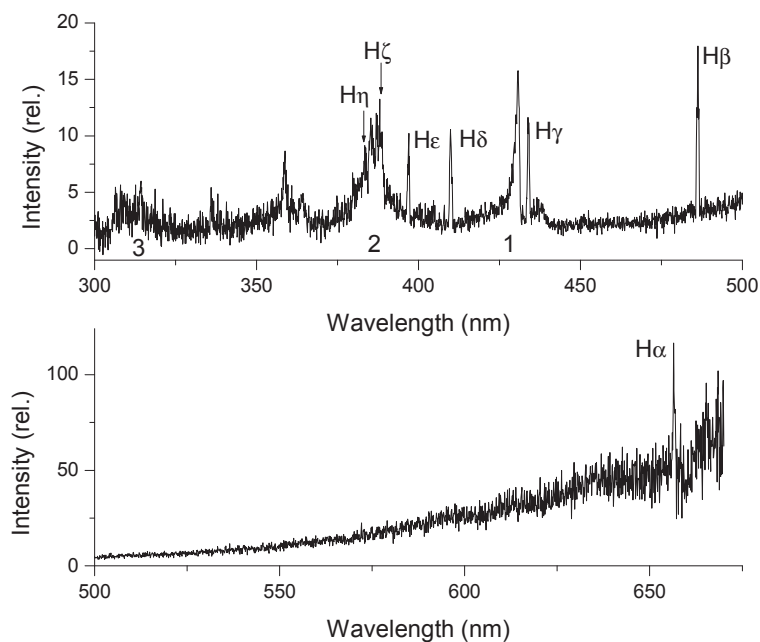


Figure 2. The emission spectrum of CH_3NO_2 obtained at 50 eV electron impact with the most intense transitions determined. Balmer lines are marked and three wide bands of mixed CH and CN electronic-vibrational transitions.

4. CONCLUSIONS

The angular distribution and kinetic energy of O^- anionic fragments, formed through scattering resonances has been reported. The emission spectrum of the nitromethane in the range between 300 – 670 nm with EIFA was recorded and the most intense lines and bands were identified, namely hydrogen Balmer lines, CH bands and CN violet band. Further work with the molecule is planned in the future in order to obtain more detailed information on the electron energy levels, threshold energies and DE cross-sections.

Acknowledgements

This work was partially supported by the Slovak Research Agency, project Nr. APVV-0733-11, DO7RP-0025-11 and Grant UK Nr. UK/140/2014 and EU FP7 projects Lassie (ITN) and SUP@VAMDC and ARGENT (ITN).

REFERENCES

- [1] S. Klezenberg, N. Eisenreich, W. Eckl and V. Weiser, *Prop., Expl., Pyrot.* 24, 189 (1999).
- [2] A. Takeuchi, Y. Nishimura, Y. Kaifuku, T. Imanak, S. Natsumeda, H. Ota, S. Yamada, I. Kurotani, K. Sumino and S. Kanno, *J. Occup. Health* 52, 194 (2010).
- [3] W. D. Taylor, T. D. Allston, M. J. Moscato, G. B. Fazekas, R. Kozlowski and G. A. Takacz, *Int. J. of Chem. Kin.* 12, 231 (1980).
- [4] A. Di Domenico, J. L. Franklin, *Int. J. Mass Spectrom. Ion Phys.* 9, 171 (1972).
- [5] D. J. Goebbert, K. Pichugin, and A. Sanov, *J. Chem. Phys.* 131, 164308 (2009)
- [6] S. L. Lunta, D. Fieldb, J. P. Zieselc, N. C. Jonesd, R. J. Gulleye, *Int. J. Mass Spec.* 205, 197 (2001).
- [7] E. Alizadeh, F. Ferreira da Silva, F. Zappa, A. Mauracher, M. Probst, S. Denifl, A. Bacher, T. D. Mark, P. Limao-Vieira, P. Scheier *Int. Jour. of Mass Spec.* 271, 15 (2008).
- [8] D. Nandi, V. S. Prabhudesai, E. Krishnakumar and A. Chatterjee, *Rev. Sci. Instrum.* 76, 053107 (2005).
- [9] M. Danko, J. Orszag, M. Durian, J. Kocisek, M. Daxner, S. Zottl, J. B. Maljkovic, J. Fedor, P. Scheier, S. Denifl and S. Matejcik, *J. Phys. B: At. Mol. Opt. Phys.* 46, 045203 (2013).
- [10] W. Sailer, A. Pelc, S. Matejcik, E. Illenberger, P. Scheier and T. D. Märk, *J. Chem. Phys.* 117, 7989 (2002).

DISSOCIATIVE ELECTRON ATTACHMENT TO 2-FLUOROADENIN

Jenny Rackwitz¹, Janina Kopyra² and Ilko Bald^{1,3}

¹*Department of Chemistry, University of Potsdam, Potsdam, Germany*

²*Department of Chemistry, Siedlce University, Siedlce, Poland*

³*BAM Federal Institute of Materials Research and Testing, Berlin, Germany*

Abstract. To reveal fundamental mechanisms of DNA radiation damage and to understand the mode of action of potential radiosensitizers used in tumor radiation therapy, we have studied the dissociative electron attachment to 2-Fluoroadenine in the energy regime 0 – 12 eV. For this, we irradiated the gaseous sample with low-energy electrons and detected the resulting fragment anions with a quadrupole mass spectrometer. We could observe various fragment anions, among them the (M-H)⁻ ion which is formed via several overlapping resonances between 0.5 and 2.5 eV. We compare the results with DEA data from non-fluorinated adenine and we identified novel fragmentation pathways opening up in 2-fluoroadenine. In general we observed that the low-energy resonances of 2-fluoroadenine result in more effective fragmentation than in adenine.

1. INTRODUCTION

Low-energy electrons (0-20 eV) belong to the most important intermediates in DNA damage by high-energy radiation since DNA strand breaks can be induced by dissociative electron attachment (DEA). During the last decade research on DEA was focused on small DNA building blocks and especially the question of where the extra electron can initially localize and which anion states can lead to a DNA strand break. In 2002 it was proposed that an initial capture of a 1 eV electron by the π^* orbital of a nucleobase leads to a subsequent transfer of the negative charge to a σ^* orbital of the DNA backbone and results in a DNA backbone cleavage at the phosphodiester bond [1]. Different studies have shown that electrons down to 0 eV can also attach to the sugar D-ribose [2, 3] and the phosphate group [4, 5] resulting in a multitude of dissociation reactions, each representing a DNA strand break.

Fluorination at different parts of DNA building blocks increases the sensitivity towards low-energy electrons, resulting in a more efficient DEA [6]. Therefore, fluorinated nucleobase derivatives are currently being used in tumor radiation therapy to enhance the sensitivity of tumor tissue towards radiation. Within a broad effort to understand the mode of action of existing therapeutics for tumor radiation therapy and to explore potential and improved radiosensitizers, we have

studied recently the radiosensitizer gemcitabine [6]. Gemcitabine is a derivative of deoxycytidine, which is fluorinated at the sugar moiety. The DEA study on gemcitabine revealed that fluorination can selectively enhance DEA cross sections associated with the exact position of fluorination within the molecule. Here, we extend our DEA studies on potential radiosensitizers and analyze DEA to 2-fluoroadenine (2FA). A comparison of the DEA process in 2FA with the respective processes in non-fluorinated adenine (A) reveals details about modification of specific dissociation processes.

2. EXPERIMENTAL SETUP

DEA to 2-fluoroadenine was measured with a crossed molecular/electron beam setup (Figure 1) [7]. A trochoidal electron monochromator delivered an electron beam of 200-250 meV energy resolution. The substance sublimated by thermal evaporation at 150-190 °C. Anions were formed by electron attachment and the anionic products were analyzed with a quadrupole mass spectrometer. The intensity of each individual fragment anion was recorded as a function of the electron energy in the range of 0-12 eV.

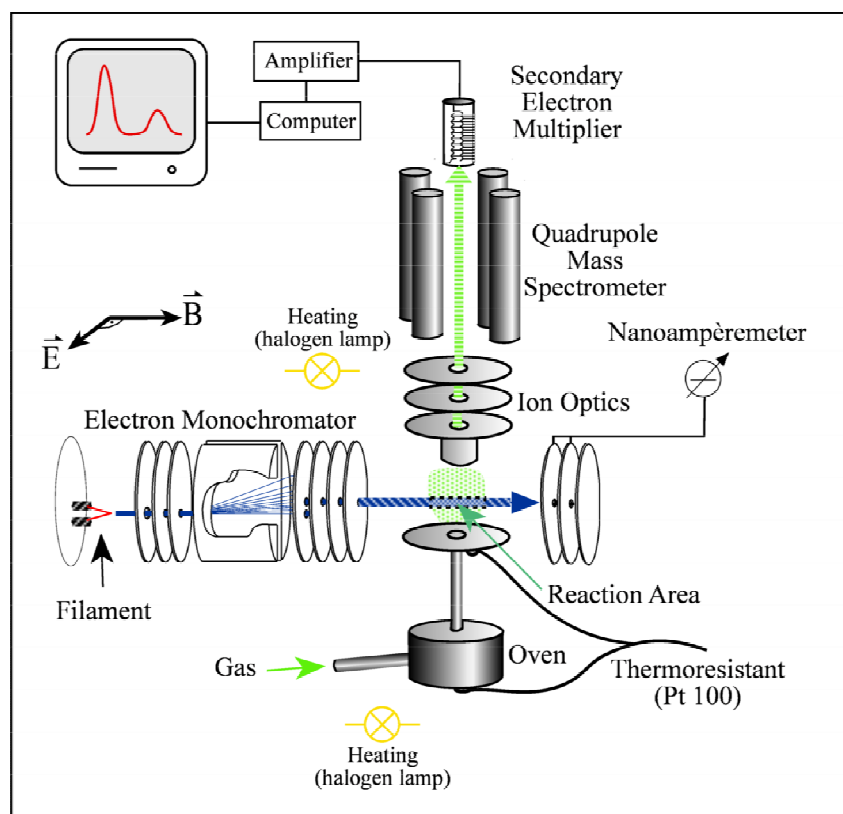


Figure 1. Experimental setup for DEA to 2-fluoroadenine.

3. RESULTS

Fragment ions resulting from DEA to 2-Fluoroadenine have been detected with different intensities at 152, 133, 132, 98, 96, 82, 80, 59, 45 and 26 amu. Some of them are comparable with the non-fluorinated adenine [8, 9], yet few reveal different resonance energies. The fragment ion at 152 amu shows the highest signal intensity and can be ascribed to the dehydrogenated parent anion (M-H)⁻. The loss of H proceeds through different and strongly overlapping resonances between 0 and 3 eV. The fragment ions (M-HF)⁻ and (M-HF-H)⁻ at 133 and 132 amu are mainly created through higher energy resonances between 4 and 7 eV. The second strongest signal at 45 amu has been attributed to the (FCN)⁻ ion. The (FCN)₂⁻ ion was detected at 59 amu with lower intensity. A small amount of CN⁻ (26 amu) was created through a resonance close to 0 and 2 eV. In contrast to adenine no CN⁻ could be observed at 6 eV from the fluorinated analogue. At 96 amu a small signal is generated at 0 eV (Eq. 1), which can be ascribed to (C₄HFN₂)⁻ (Figure 2).



For adenine no comparable fragment could be detected. 2FA has a higher dipole moment than A. Hence, it is suggested that the fragment at 96 amu is formed via a vibrational Feshbach resonance around 0 eV. The near 0 eV resonance creates further anionic fragments with different masses.

In conclusion, we observed anionic fragments formed through different DEA mechanisms such as vibrational Feshbach resonances, shape and core excited resonances.

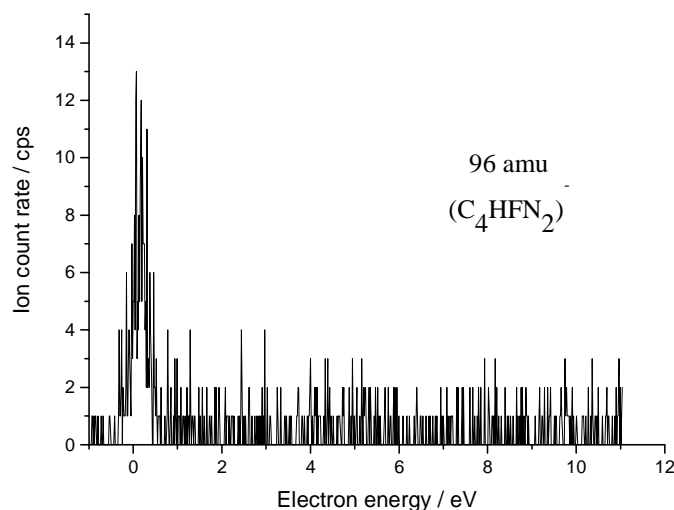


Figure 2. Ion yield curve of (C₄HFN₂)⁻ formed via DEA to 2-Fluoradenine measured with quadrupole mass spectrometer.

Acknowledgements

This research was supported by the COST Action MP1002 (Nano-IBCT).

REFERENCES

- [1] R. Barrios, P. Skurski and J. Simons, *J. Phys. Chem. B* 106, 7991 (2002).
- [2] I. Bald, J. Kopyra and E. Illenberger, *Angew. Chem. Int. Ed.* 45, 4851 (2006).
- [3] I. Baccarelli, F. A. Gianturco, A. Grandi, N. Sanna, R. R. Lucchese, I. Bald, J. Kopyra and E. Illenberger, *J. Amer. Chem. Soc.* 129, 6269 (2007).
- [4] C. König, J. Kopyra, I. Bald and E. Illenberger, *Phys. Rev. Lett.* 97, 018105 (2006).
- [5] I. Bald, I. Dabkowska and E. Illenberger, *Angew. Chem. Int. Ed.* 47, 8515 (2008).
- [6] J. Kopyra, A. Keller and I. Bald, *RSC Adv.* 4, 6825 (2014).
- [7] I. Bald, J. Langer, P. Tegeder and O. Ingolfsson, *Int. J. Mass Spectrom.*, 277, 4 (2008).
- [8] H. Abdoul-Carime, J. Langer, M.A. Huels and E. Illenberger, *Eur. Phys. J. D* 35, 399 (2005).
- [9] D. Huber, M. Beikircher, S. Denifl, F. Zappa, S. Matejcik, A. Bacher, V. Grill, T.D. Märk and P. Scheier, *J. Chem. Phys.* 125, 084304 (2004).

HIGHLY CHARGED IONS COLLISIONS WITH MULTIPLY CHARGED PROTEIN ANIONS STORED IN A LINEAR ION TRAP

A. R. Milosavljević^{1*}, A. Domaracka², P. Rousseau^{2,3}, and A. Giuliani^{4,5}

¹*Institute of Physics, University of Belgrade, Pregrevica 118, Belgrade, Serbia*

²*CIMAP, UMR 6252 CEA-CNRS-ENSICAEN-Unicaen, boulevard Henri
Becquerel, 14070 Caen, France*

³*Université de Caen Basse-Normandie, Esplanade de la Paix, 14032 Caen,
France*

⁴*Synchrotron SOLEIL, L'Orme des Merisiers, Saint Aubin, B.P. 48,
91192 Gif-sur-Yvette, France*

⁵*INRA, U1008, CEPIA, Rue de la Géraudière, 44316 Nantes, France*

Abstract. We have investigated 375 keV Xe²⁵⁺ ions collisions with cytochrome *c* (≈ 12.5 kDa) and BPTI (≈ 6.5 kDa) gas-phase protein anions of selected charge states. The experiment has been performed by coupling a linear quadrupole ion trap mass spectrometer, equipped with the electrosprayed ions probe, to the highly charged ions (HCIs) beamline. We report the first results on HCI interaction with stored protein anions, showing a multiple electron capture accompanied by neutral losses, as dominant relaxation channels.

1. INTRODUCTION

There is a large interest to study high-energy particles (electrons, photons, ions) collisions with biopolymers (proteins and DNA) isolated and maintained under well-defined conditions in the gas phase. Such studies can improve our understanding of the basic physicochemical properties of biomolecules, as well as the interplay between these properties and their function [1]; lead to important new applications such as novel methods for protein sequencing [2]; and support research on radiation damage and novel medical methods such as ion-beam cancer therapy [3]. However, it is experimentally very challenging to bring large biomolecules such as proteins and DNA intact into the gas phase and perform standard collisional experiments under well-defined conditions.

We have recently developed an experimental setup [4] that couples a linear ion trap with the synchrotron beam, thus allowing to perform controlled

* email: vraz@ipb.ac.rs

investigation on energetic photon (VUV and X-ray) interaction with large multiply charged biopolymers and to study, for the first time structure and charge-state dependence of the gas-phase VUV ionization of proteins [1] and X-ray inner-shell excitation/ionization of proteins [5].

Most recently, we have extended our study to collision with ions, in order to investigate highly charged ions interactions with multiply charged protein ions stored in a linear ions trap. Particularly, we have studied the interaction of 375 keV Xe^{25+} ions with cytochrome *c* (≈ 12.5 kDa) and BPTI (≈ 6.5 kDa) gas-phase protein ions of selected charge states as a function of the precursor charge state.

2. EXPERIMENTAL SETUP

The experimental setup is based on a commercial linear quadrupole ion trap (“Thermo scientific LTQ XL”), equipped with an electrospray ion source (ESI), which has been coupled to the ARIBE beamline, the low-energy ion beam facility of the GANIL in Caen, France [9]. A detailed description of the experimental setup, which has been previously coupled to synchrotron beamlines, is given elsewhere [4,6]. Briefly, the target ions were produced by ESI and introduced from the front side into the ion trap; after isolation of the desired precursor, the Xe^{25+} ion beam was introduced into the trap through the back lens of the LTQ XL spectrometer. The vacuum manifold with a turbo pumping stage has been designed to accommodate pressure difference between the beamline (10^{-8} mbar) and LTQ (10^{-5} mbar).

Multiply deprotonated cytochrome *c* and BPTI (Sigma Aldrich) molecules were generated by the ESI source from water/acetonitrile (75 : 25) solution at 10 mM. Negative protein precursors have been isolated in the gas phase in the ion trap and submitted to 375 keV Xe^{25+} . The mass spectra have been repeatedly recorded for a specific precursor, after an irradiation time of about 1 s. For each charge state, the background signal (both without the incident ion beam and without the targets ions in the trap) has been recorded, as well.

3. RESULTS AND DISCUSSION

Cytochrome *c* has been investigated previously in our work on X-ray interaction with trapped biopolymers [5] and very recently in collisions of 96 keV Xe^{8+} ions [7]. The present contribution presents results for a selected -11 charge state precursor. BPTI protein has been investigated further, representing a complex biopolymer, which should not unfold in the gas phase (until some degree of protonation) due to disulfide bridges [1].

Figure 1 shows tandem mass spectra upon Xe^{25+} ion activation of deprotonated cytochrome *c* (a) and BPTI (b) proteins. Except the dominant peak corresponding to the precursor ion, additional peaks at higher m/z , which correspond to the electron capture by the highly positively charged Xe projectile, are clearly seen. The electron capture, i.e. electron detachment from the precursor protein ion to one Xe^{25+} orbital, is accompanied by intensive neutral

losses. In both cases, the dominant loss corresponds to the mass of about 44 Da, thus suggesting a possible loss of CO_2 ; however, neutral losses from the amino acids cannot be excluded, therefore more detailed measurements with higher mass resolution are needed in order to perform an accurate analysis. Still, it is interesting to note that the dominant reaction channels upon highly charged ion collisions with trapped proteins anions represent the electron detachment (captured by the incident projectile) accompanied by neutral losses, whereas backbone fragmentation is less abundant. This might be regarded as a surprise considering previous results with amino acids [10] and peptides [8], however, this is actually in line with our most recent study on soft X-ray [5]. Indeed, the susceptibility of proteins biopolymers to energetic ion bombardment is significantly different in comparison with their monomer units (amino acids), suggesting that a so-called building blocks approach may not be relevant in this particular case.

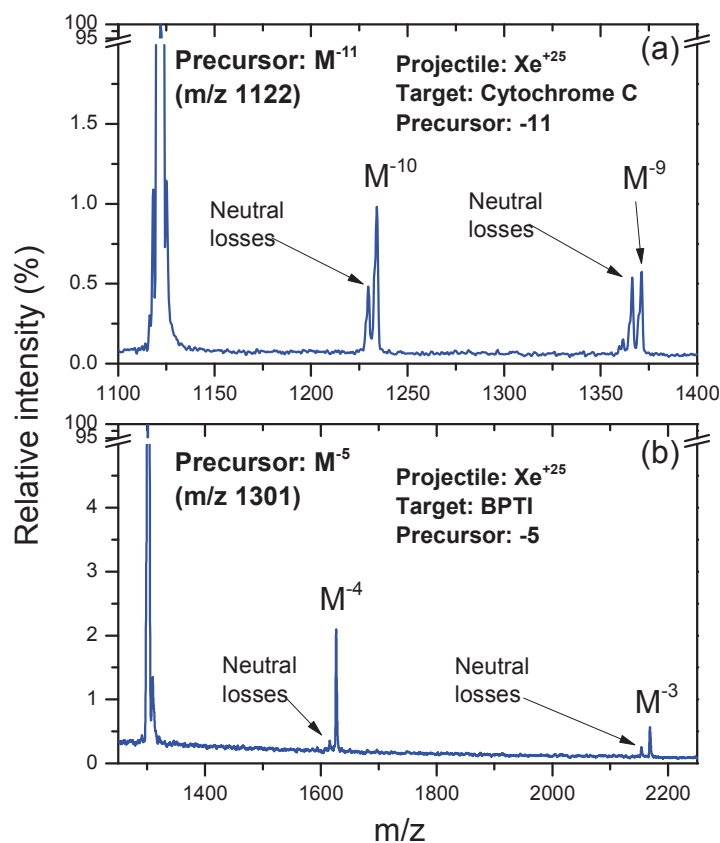


Figure 1. Tandem mass spectra of -11 charge state precursor of cytochrome *c* protein (a) and -5 charge state precursor of BPTI protein (b) upon activation by 375 keV Xe^{+25} projectiles.

Acknowledgements

This work is supported by the Agence Nationale de la Recherche Scientifique, France, under the project #BLAN08-1_348053. A.R.M. acknowledges the support for a short term scientific mission from ESF/COST Action CM1204 “XUV/X-ray light and fast ions for ultrafast chemistry (XLIC)” and partly by the Ministry of education, science and technological development of Republic of Serbia under the grant NO 171020. The work is also motivated by the ESF/COST Action MP1002 “Nano-scale insights in ion beam cancer therapy (Nano-IBCT)”. The experiments have been performed in GANIL in the framework of the interdisciplinary program advisory committee. We are grateful to Fabien Noury, Thierry Been and Stéphane Guillous for the technical support and for the preparation of the ion beam.

REFERENCES

- [1] A. Giuliani, A. R. Milosavljević, C. Hinsen, F. Canon, C. Nicolas, M. Réfrégiers, L. Nahon, *Ang. Chem. Int. Ed.* 51, 9552 (2012)
- [2] F. Canon, A. R. Milosavljević, G. van der Rest, M. Réfrégiers, L. Nahon, P. Sarni-Manchado, V. Cheynier, and A. Giuliani, *Angewandte Chemie International Edition* 52, 8377 (2013).
- [3] ESF/COST Action MP1002 (Nano-IBCT) <http://fias.uni-frankfurt.de/nano-ibct/?page=home>
- [4] A. R. Milosavljević, C. Nicolas, J. Lemaire, C. Déhon, R. Thissen, J.-M. Bizau, M. Réfrégiers, L. Nahon, and A. Giuliani, *Phys. Chem. Chem. Phys.* 13, 15432 (2011).
- [5] A. R. Milosavljević, F. Canon, C. Nicolas, C. Miron, L. Nahon and A. Giuliani, *J. Phys. Chem. Letters* 3, 1191 (2012).
- [6] A. R. Milosavljević, C. Nicolas, J.-F. Gil, F. Canon, M. Réfrégiers, L. Nahon and A. Giuliani, *J. Synchrotron Radiat.* 19, 174 (2012).
- [7] S. Martin, C. Ortega, L. Chen, R. Brédy, A. Vernier, P. Dugourd, R. Antoine, J. Bernard, G. Reitsma, O. Gonzalez-Magana, R. Hoekstra, and T. Schlathölter, *Phys. Rev. A* 89, 012707 (2014).
- [8] S. Bari, R. Hoekstra, and T. Schlathölter, *Phys. Chem. Chem. Phys.* 12, 3376 (2010).
- [9] V. Bernigaud, O. Kamalou, A. Ławicki, M. Capron, R. Maisonnny, B. Manil, L. Maunoury, J. Rangama, P. Rousseau, J.-Y. Chesnel, L. Adoui, B. A. Huber, *Publ. Astron. Obs. Belgrade* 84, 83 (2008).
- [10] M. Capron, S. Díaz-Tendero, S. Maclot, A. Domaracka, E. Lattouf, A. Ławicki, R. Maisonnny, J.-Y. Chesnel, A. Méry, J.-C. Poully, J. Rangama, L. Adoui, F. Martín, M. Alcamí, P. Rousseau, B. A. Huber, *Chem. Eur. J.* 18, 9321 (2012).

SINGLE ELECTRON CAPTURE IN $p - \text{Li}^+$ COLLISIONS

Ivan Mančev and Nenad Milojević

*Department of Physics, Faculty of Sciences and Mathematics,
University of Niš, P.O.Box 224, 18000 Niš, Serbia*

Abstract. We report theoretical state-selective and total single-capture cross sections for $p - \text{Li}^+$ collisions by using the four-body boundary-corrected first Born (CB1-4B) approximation for impact energies between 50 and 1500 keV. The calculated results are found to be in good agreement with experimental findings.

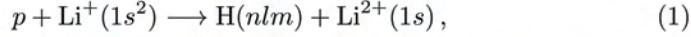
1. INTRODUCTION

Charge exchange process in fast heavy particle collisions with atomic and molecular targets is very important in various branches of physics such as astrophysics and plasma physics. The data of these collisions processes are in great need in plasma diagnostics for fusion research. This work is focused on the theoretical investigation of single electron capture in the $p - \text{Li}^+$ collisions by using the four-body boundary-corrected first Born (CB1-4B) approximation. The CB1-4B method is a fully quantum mechanical four-body formalism, since it explicitly considers each individual particle and all the interactions among them in the collision under investigation. This method strictly preserves the correct Coulomb boundary conditions in both collisional channels [1, 2]. In the CB1-4B model, the proper connection between the long-range Coulomb distortion effects and the accompanying perturbation potentials is accomplished according to the well-established principles of scattering theory [2]. As evidenced in abundant applications, imposing the correct Coulomb boundary conditions in the entrance and exit channels is of crucial importance, particularly for ion-atom(ion) collisions [3, 4].

In the present work the CB1-4B approximation is applied to calculate state-selective and total cross section for single electron capture in $p - \text{Li}^+$ collisions. Atomic units will be used throughout unless otherwise stated.

2. THEORY AND RESULTS

We consider single electron capture in collisions of a proton with a lithium ion:



where nlm is the usual set of three hydrogen quantum numbers. Let \vec{s}_1 and \vec{s}_2 (\vec{x}_1 and \vec{x}_2) be the position vectors of the first and second electron (e_1 and e_2) relative to the proton (target nucleus), respectively. Further, let \vec{R} be the position vector of target nucleus with respect to projectile.

The prior form of the transition amplitude for process (1) in the CB1-4B approximation reads as [5]:

$$T_{if}(\vec{\eta}) = \int \int \int d\vec{x}_1 d\vec{x}_2 d\vec{R} \varphi_{nlm}^*(\vec{s}_1) \varphi_{\text{T}}^*(\vec{x}_2) \left(\frac{2}{R} - \frac{1}{s_1} - \frac{1}{s_2} \right) \times \varphi_i(\vec{x}_1, \vec{x}_2) e^{-i\vec{\alpha} \cdot \vec{R} - i\vec{v} \cdot \vec{x}_1} (vR - \vec{v} \cdot \vec{R})^{-i\xi}, \quad (2)$$

where $\xi = -1/v$ while \vec{v} is the incident velocity vector. The momentum transfer $\vec{\alpha}$ is defined by: $\vec{\alpha} = \vec{\eta} - (v/2 - \Delta E/v)\hat{v}$, where $\Delta E = E_i - E_f$ with E_i being the binding energy of the two-electron target and $E_f = -1/(2n^2) - 3^2/2$. The transverse component of the change in the relative linear momentum of a heavy particle is denoted by $\vec{\eta} = (\eta \cos \phi_\eta, \eta \sin \phi_\eta, 0)$ and has the property $\vec{\eta} \cdot \vec{v} = 0$. The function $\varphi_i(\vec{x}_1, \vec{x}_2)$ denotes the two-electron ground state wave function of the $\text{Li}^+(1s^2)$ ion. The functions $\varphi_{nlm}(\vec{s}_1)$ and $\varphi_{\text{T}}(\vec{x}_2)$ in Eq. (2) represent the bound state wave functions of the hydrogen-like atomic systems $\text{H}(nlm)$ and $\text{Li}^{2+}(1s)$ respectively.

As shown in Ref. [5], the original nine-dimensional integral for transition amplitude from Eq. (2) can be reduced to a two-dimensional integral over real variables from 0 to 1, whereas for computations of the total cross sections, three-dimensional quadratures are needed. An extensive analytical study of the post version of the transition amplitude for electron capture into the arbitrary nlm final states of the projectile was carried out in Ref. [6]. The post form of the transition amplitude was derived in terms of five-dimensional real integrals for numerical computations.

In the present work, we have used the two parameter wave-function of Silverman *et al.* [7] for the ground state of lithium ion: $\varphi_i(\vec{x}_1, \vec{x}_2) = (N/\pi)(e^{-\alpha_1 x_1 - \alpha_2 x_2} + e^{-\alpha_2 x_1 - \alpha_1 x_2})$, where $N^{-2} = 2[(\alpha_1 \alpha_2)^{-3} + (\alpha_1/2 + \alpha_2/2)^{-6}]$ with $\alpha_1 = 3.294909$, $\alpha_2 = 2.078981$ and $E_i = -7.248748$. The total cross section is given by: $Q_{if}(\pi a_0^2) = \frac{1}{2\pi^2 v^2} \int_0^\infty d\eta \eta |T_{if}|^2$. The total cross sections for capture into any states for reaction (1), can be obtained by means of following formulae according to the Oppenheimer $(n)^{-3}$ scaling law: $Q_{\text{tot}} \simeq Q_1 + Q_2 + Q_3 + 2.56124Q_4$.

The results of our computations of the state-selective and the total cross sections for reaction (1) in prior form are summarized in Table

at impact energies 50-1500 keV. The cross sections are obtained by means of the two-parameter wave function of Silverman *et al.* [7] for the ground state of the Li^+ target. The results from Table 1 indicate that $Q_{ns} > Q_{np}$, $Q_{np} > Q_{nd}$ and $Q_{nd} > Q_{nf}$ at all the considered energies. All numerical integrations are performed by means of the Gauss-Legendre quadrature. The numbers of the Gauss-Legendre quadrature points are varied until convergence to two decimal places has been attained for state-selective and total cross sections.

In Figure 1. we compare our theoretical results for prior total cross sections for $p - \text{Li}^+$ collisions with the available experimental data. The full line shows the results obtained by means of the two-parameter wave function of Silverman *et al.* [7], whereas dashed line represents the cross sections obtained by using uncorrelated one-parameter Hylleraas wave function.

Final state nl	Energy (keV)				
	50	70	100	150	200
1s	2.57[-17]	1.78[-17]	1.12[-17]	5.57[-18]	2.99[-18]
2s	2.20[-18]	1.66[-18]	1.14[-18]	6.29[-19]	3.57[-19]
2p	1.27[-18]	7.32[-19]	3.81[-19]	1.63[-19]	7.96[-20]
3s	6.08[-19]	4.63[-19]	3.25[-19]	1.83[-19]	1.05[-19]
3p	4.09[-19]	2.42[-19]	1.28[-19]	5.53[-20]	2.73[-20]
3d	1.43[-20]	8.16[-21]	3.83[-21]	1.43[-21]	6.43[-22]
4s	2.50[-19]	1.92[-19]	1.35[-19]	7.65[-20]	4.40[-20]
4p	1.77[-19]	1.05[-19]	5.59[-20]	2.43[-20]	1.21[-20]
4d	8.26[-21]	4.77[-21]	2.25[-21]	8.43[-22]	3.82[-22]
4f	7.51[-23]	4.38[-23]	1.92[-23]	6.30[-24]	2.66[-24]
Q_{tot}	3.13[-17]	2.17[-17]	1.37[-17]	6.86[-18]	3.70[-18]

Final state nl	Energy (keV)				
	300	500	700	1000	1500
1s	1.03[-18]	1.99[-19]	5.72[-20]	1.33[-20]	2.19[-21]
2s	1.29[-19]	2.57[-20]	7.40[-21]	1.73[-21]	2.83[-22]
2p	2.35[-20]	3.43[-21]	7.77[-22]	1.36[-22]	1.55[-23]
3s	3.82[-20]	7.65[-21]	2.21[-21]	5.15[-22]	8.43[-23]
3p	8.15[-21]	1.20[-21]	2.73[-22]	4.78[-23]	5.47[-24]
3d	1.68[-22]	1.97[-23]	3.67[-24]	5.04[-25]	4.19[-26]
4s	1.61[-20]	3.23[-21]	9.34[-22]	2.18[-22]	3.59[-23]
4p	3.61[-21]	5.34[-22]	1.22[-22]	2.13[-23]	2.43[-24]
4d	1.00[-22]	1.18[-23]	2.20[-24]	3.02[-25]	2.52[-26]
4f	6.33[-25]	6.09[-26]	9.44[-27]	1.02[-27]	6.27[-29]
Q_{tot}	1.28[-18]	2.47[-19]	7.06[-20]	1.63[-20]	2.68[-21]

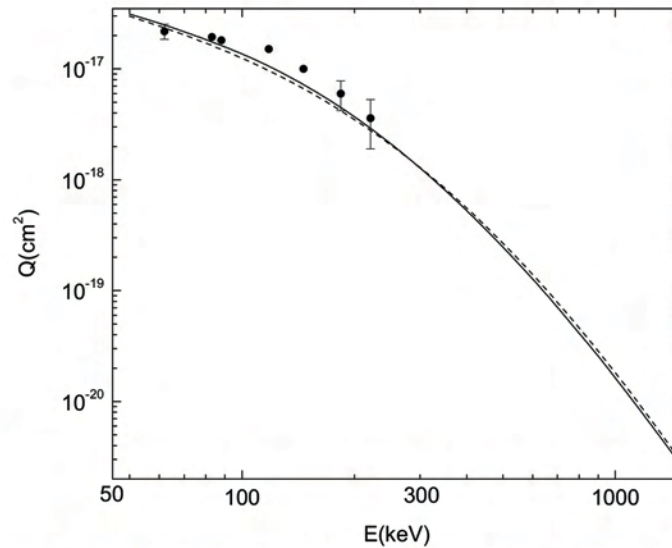


Figure 1. Total cross section for reaction (1). Full line: the CB1-4B results with Silverman *et al.* [7] function, dashed line: CB1-4B results with Hylleraas wave function. Experimental data: • Sewell *et al.* [8]

Acknowledgements Authors thank the Ministry of Education, Science and Technological Development of the Republic of Serbia for support through Project No. 171020.

REFERENCES

- [1] Dž. Belkić, R. Gayet and A. Salin, Phys. Rep. **56**, 279 (1979); D. Dollard, J. Math. Phys. **5**, 729 (1964).
- [2] Dž. Belkić, *Principles of Quantum Scattering Theory* (Institute of Physics, Bristol, 2004).
- [3] Dž. Belkić, *Quantum Theory of High-Energy Ion-Atom Collisions* (Taylor & Francis, London 2008).
- [4] Dž. Belkić, I. Mančev and J. Hanssen, Rev. Mod. Phys. **80**, 249 (2008).
- [5] I. Mančev, N. Milojević and Dž. Belkić, Phys. Rev. A **86**, 022704 (2012).
- [6] I. Mančev, N. Milojević and Dž. Belkić, Phys. Rev. A **88**, 052706 (2013).
- [7] J.N. Silverman, O. Platas, F.A. Matsen, J. Chem. Phys. **32**, 1402 (1960).
- [8] E.C. Sewell, G.C. Angel, K.F. Dunn and H.B. Gilbody, J. Phys. B: At. Mol. Phys. **13**, 2269 (1980).

DYNAMICAL ADIABATIC POTENTIAL ENERGY CURVES OF HeH^{2+} SYSTEM: CROSSINGS IN COMPLEX PLANE OF INTERNUCLEAR SEPARATIONS

T. P. Grozdanov¹ and E. A. Solov'ev²

¹*Institute of Physics, University of Belgrade,
Pregrevica 118, 11080 Belgrade, Serbia*

²*Bogoliubov Laboratory of Theoretical Physics,
Joint Institute for Nuclear Research,
141980 Dubna, Moscow region, Russia*

Abstract. Inelastic transitions in slow ion-atom(ion) collisions $\text{He}^{2+} + \text{H}$ or $\text{He}^+ + \text{H}^+$ are determined by properties of the quasi-molecule HeH^{2+} . Assuming straight-line trajectories of the heavy particles one can define dynamical adiabatic potential energy curves (DAPEC) which depend on internuclear separation R and an additional parameter $\omega = \rho v$ - product of the impact parameter and relative collision velocity. We study the analytic continuations of DAPEC into the complex R -plane. Probabilities of the non-adiabatic transitions are determined by the positions of the branch points connecting various DAPEC surfaces. We investigate how the positions of various branch points change with the variation of the parameter ω .

1. INTRODUCTION

The crossings of electronic adiabatic eigenvalues (potential energy curves (PEC)) in the complex plane of internuclear separations R , play the key role in the standard (separable) one-electron two-Coulomb-center problem (see review paper [1]). They can be verified only by direct numerical calculation in the complex R -plane as branch points R_b connecting two PEC $\varepsilon_i(R)$ and $\varepsilon_f(R)$ of the same symmetry - $\Delta\varepsilon_{if}(R) \sim \sqrt{R - R_b}$. If the distance from the real R -axis to the branch point R_b is proportional to \hbar it is named *hidden crossing*, whereas if it is exponentially small with respect to the inverse of Planck constant \hbar it is named *avoided crossing*. In fact, $\varepsilon_i(R)$ and $\varepsilon_f(R)$ are different branches of a single (multivalued) analytic function $\varepsilon(R)$. If we adopt the impact-parameter method for description of

a collision problem, that is assume that nuclei follow classical trajectories defined by the given function $R = R(t, \rho, v)$ of time t , impact parameter ρ , and asymptotic relative collision velocity v , then the "single pass" electron transition probability via crossing is determined by expression

$$p_{if}(\rho, v) = \exp\left(-\frac{2}{\hbar} \left| \text{Im} \int_L \varepsilon(R) \frac{dR}{v_R(R, \rho, v)} \right| \right), \quad (1)$$

where $v_R(R, \rho, v) = dR/dt$ is the radial collision velocity. The contour L in complex R -plane starts at any real R_1 where $\varepsilon(R_1) = \varepsilon_i(R_1)$ goes around complex branch point R_b and ends up back on any real R_2 where $\varepsilon(R_2) = \varepsilon_f(R_2)$.

The transitions caused by the rotation of the internuclear axis which are known to be localized in the regions of degeneracies (exact crossings) of PEC corresponding to states with different symmetries, in the standard adiabatic approach can be taken into account only by numerical close-coupling calculations.

2. DYNAMICAL ADIABATIC THEORY

We consider a collision system consisting of a single electron and two bare nuclei of charges Z_A and Z_B travelling along the straight-line trajectories in the (x, y) -scattering plane, so that $\mathbf{R}(t) = \mathbf{R}_B(t) - \mathbf{R}_A(t) = vt\hat{\mathbf{x}} + \rho\hat{\mathbf{y}}$. We next modify the electronic time-dependent Schrödinger equation (for details see Ref.[2]): the electronic coordinates (x, y, z) are divided by the internuclear separation $R(t)$ and subsequently transformed to the rotating (molecular) coordinate system (q_1, q_2, q_3) with the q_1 axis directed along the internuclear axis. Finally, one arrives at the eigenvalue problem for DAPEC:

$$H(R, \omega)\Phi_j(\mathbf{q}, R, \omega) = E_j(R, \omega)\Phi_j(\mathbf{q}, R, \omega), \quad (2)$$

with (we use atomic units throughout)

$$H(R, \omega) = -\frac{1}{2}\Delta_q - R \left(\frac{Z_A}{|\mathbf{q} + \alpha\hat{\mathbf{q}}_1|} + \frac{Z_B}{|\mathbf{q} - \beta\hat{\mathbf{q}}_1|} \right) + \omega L_3 + \frac{1}{2}\omega^2 q^2 \quad (3)$$

where $\hat{\mathbf{q}}_1$ is the unit vector along q_1 axis, α and β ($\alpha + \beta = 1$) define the position of the coordinate origin on the internuclear axes and L_3 is the operator of the projection of the electronic angular momentum onto the direction perpendicular to the scattering plane. The parity $\Pi_3(q_3 \rightarrow -q_3)$ is the only conserved symmetry.

The general properties of DAPEC $E_j(R, \omega)$ for the complete range of real internuclear separations $R \in (0, +\infty)$ have been studied in our recent work [2]. An example for $\omega = 1$ in the case of HeH^{2+} system is show in Fig.1. Note, that any DAPEC $E_j(R, \omega)$ is related to the usual PEC $\varepsilon_j(R)$ of the two-Coulomb center problem by relation $E_j(R, 0) = \varepsilon_j(R)R^2$.

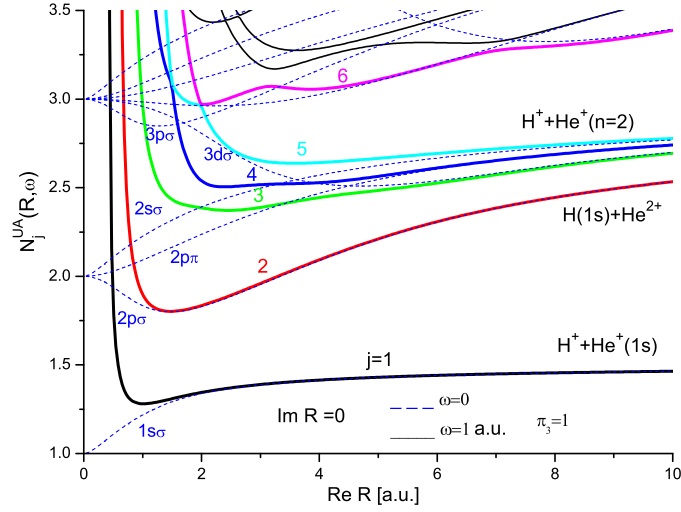


Figure 1. Solid lines are low-lying scaled DAPEC represented in terms of "effective united atom principal quantum number" $N_j^{UA}(R, \omega) = (Z_A + Z_B)[-2E_j(R, \omega)/R^2]^{-1/2}$. Dashed lines correspond to standard PEC of the $(\text{HeH})^{2+}$ molecular ion labeled by united-atom quantum numbers

3. RESULTS

Here, we are interested in analytic continuations of DAPEC into the complex R -plane, i.e. the solutions of the eigenvalue problem Eq.(2) for complex values of R . The numerical method used is the same as described in our previous work [2] for real values of R . The solutions enable us to detect the various branch points $R_b(i, f; \omega)$ connecting the pairs of complex DAPEC $E_i(R, \omega)$ and $E_f(R, \omega)$. The single-pass electron transition probabilities will be given by Eq.(1) with substitution: $\varepsilon(R) \rightarrow E(R, \omega)/R^2$.

In dynamical adiabatical representation the rotational transitions are transformed into radial transitions through the operator L_3 in Eq.(3), generating the so called L_3 - *crossings*. Two examples of the L_3 -crossings are shown in Fig.2. At $\omega \rightarrow 0$ they correspond to $2p\sigma - 2p\pi$ or $(i, f) = (2, 3)$ and $2s\sigma - 2p\pi$ or $(i, f) = (3, 4)$ rotational coupling in the united-atom limit. However, as ω increases, one can notice the transformations: $R_b(2, 3; 0.3) \rightarrow R_b(2, 4; 0.5)$ and $R_b(2, 4; 0.75) \rightarrow R_b(2, 5; 0.8)$. This kind of transformations are caused by the relative motion of other branch points in the complex R -plane. For example, the first of these transformations occurs due to the change of position of the branch points in the other shown L_3 -trajectory, namely due to the fact that $\text{Re } R_b(3, 4; 0.3) < \text{Re } R_b(2, 3; 0.3)$

and $\text{Re } R_b(3, 4; 0.5) > \text{Re } R_b(2, 4; 0.5)$. Also shown in Fig.2 as full squares in the limited region are hidden crossings labeled as $\omega = 0 - 1(1 - 2), (1 - 5)$ which at $\omega \rightarrow 0$ correspond to $1s\sigma - 2p\sigma$ (i.e. $(j=1 - j'=2)$ -radial coupling between the ground and the first excited state. As detailed calculations show they undergo the transition $R_b(1, 2; 0.75) \rightarrow R_b(1, 5; 0.8)$ which can be explained by the positions of the branch points from the L_3 - trajectory just below them: $R_b(2, 4; 0.75) < \text{Re } R_b(1, 2; 0.75)$ and $\text{Re } R_b(2, 5; 0.8) > \text{Re } R_b(1, 5; 0.8)$. Additional types of branch points and their transformations will be discussed at the conference.

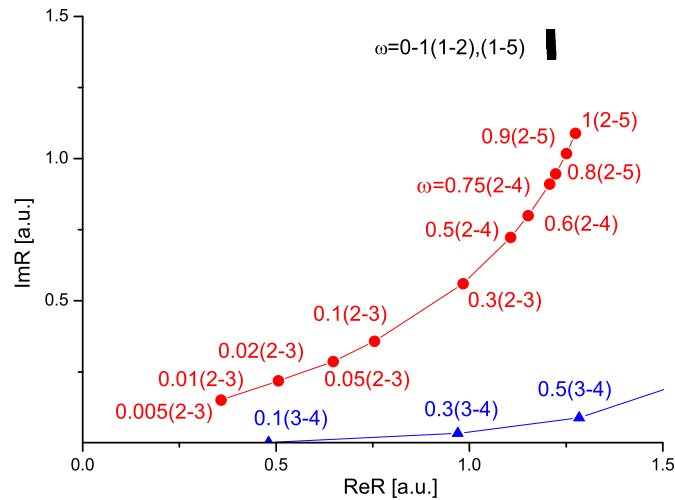


Figure 2. Each branch point $R_b(i, f; \omega)$ is labeled as $\omega(i - f)$. Full circles are L_3 -crossings which undergo transformations $R_b(2, 3; 0.3) \rightarrow R_b(2, 4; 0.5)$ and $R_b(2, 4; 0.75) \rightarrow R_b(2, 5; 0.8)$. Full triangles are part of the L_3 -crossings trajectory $R_b(3, 4; \omega)$. Full squares labeled $\omega = 0 - 1(1 - 2), (1 - 5)$ are the hidden crossings.

Acknowledgements

This work was partly supported by Serbia-JINR collaboration program and by the Ministry of Education, Science and Technological Development of the Republic of Serbia through the project No. 171020.

REFERENCES

- [1] E. A. Solov'ev, J. Phys. B: At. Mol. Opt. Phys., 38, R153 (2005)
- [2] T. P. Grozdanov and E. A. Solov'ev, Phys. Rev. A 88, 022707 (2013)

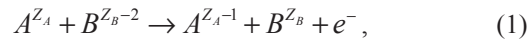
SCHRODINGER'S FORMALISM OF DISTORTED- WAVE METHOD IN THE PROBLEM OF SINGLE- ELECTRON CAPTURE WITH SIMULTANEOUS IONIZATION

V. Yu. Lazur and V. V. Aleksiyy

*Uzhhorod National University, 88000, Uzhhorod, Voloshin Str., 54.
e-mail: volodymyr.lazur@uzhnu.edu.ua.*

Abstract. The Schrodinger formalism of the continuum-distorted-wave method is used for the analysis of capture with ionization in the region of intermediate and high particle-collision rates. The proposed formalism is tested on the example of the capture cross section with ionization of the collision of a helium atom with protons. The results obtained are shown to be in good agreement with experimental data.

Methods of describing elementary processes in the region of intermediate and high particle-collision rates are developing especially intensely [1]. Methods taking into account possible multi-step reaction mechanisms may be mentioned as among the most successful approaches to the solution of this problem. One may include in these methods the continuum-distorted-wave (CDW) approximation method [2, 3], which, as studies have shown [3, 4], gives a qualitatively correct description of second-order effects. This method has been used for calculation of total and differential cross sections of "pure" charge-exchange processes [3] and "pure" ionization [4]. We considered the charge-exchange (capture) with simultaneous ionization of



constituting a two-electron transition, where one of the electrons of "target-atom" B^{Z_B-2} is captured by incident particle A^{Z_A} , while a second one of its electrons passes into the continuous spectrum. The successes attained in the study of charge-exchange and ionization processes based on the CDW method have prompted us to work out the Schrodinger formalism of the continuum-distorted-wave method to describe the capture process with ionization (1). We will the relative motion of the nuclei of the colliding particles is thereby described by the straight-line trajectory $\vec{R}(t) = \vec{\rho} + \vec{v}t$, where \vec{R} is the vector joining the nuclei of the system, $\vec{\rho}$ is the target parameter, and \vec{v} is the relative velocity of motion of the nuclei of the colliding particles. We will assume that in reaction (1) the core electrons of the A^{Z_A} and B^{Z_B} ions do not change their state. The total electronic Hamiltonian of the system in this case has the form ($e = \hbar = m = 1$):

$$H = H_0 + V; H_0 = -\frac{1}{2} \sum_{j=1}^2 \Delta_j; V = -\sum_{j=1}^2 \left(\frac{Z_A}{s_j} + \frac{Z_B}{x_j} \right) + \frac{1}{r_{12}} + \frac{Z_A Z_B}{R}, \quad (2)$$

where Z_A, Z_B are the effective charges of the atomic cores of A^{Z_A}, B^{Z_B} ; $\vec{x}_\kappa, \vec{s}_\kappa, \vec{r}_\kappa$ describe the position of the j electron with respect to the ion B^{Z_B} , the incident particle A^{Z_A} , and the center of line segment R . The essence of the CDW method consists in separation of the total Hamiltonian of the system into two parts:

$$H = H_i + v_i; H_i = H_0 + V_i; v_i = V - V_i; V_i = -\sum_{j=1}^2 \frac{Z_B}{x_j} + \frac{1}{r_{12}}, \quad (3)$$

$$H = H_f + v_f; H_f = H_0 + V_f; v_f = V - V_f; V_f = -Z_A/s_1. \quad (4)$$

One of them - $H_i (H_f)$ (usually called the channel Hamiltonian) - defines the bound states in the system, while the other - $v_i (v_f)$ - gives the remainder not containing the bound-state contribution. We also introduce wave functions $\Psi_i^+(t), \Psi_f^-(t)$, which are exact solutions of the Schrodinger equation

$$\left(H - i \frac{\partial}{\partial t} \right) \Psi_{i,f}^\pm(t) = 0, \quad (5)$$

but satisfy different boundary conditions for large $|t|$ [5]. We introduce the wave function $\chi_i^+ (\chi_f^-)$ (the distorted wave), appearing as the solution of the nonstationary Schrodinger equation in some potential $U_i (U_f)$:

$$\left(H_i + U_i - i \frac{\partial}{\partial t} \right) \chi_i^+ = 0, \quad \left(H_f + U_f - i \frac{\partial}{\partial t} \right) \chi_f^- = 0. \quad (6)$$

It is necessary to solve these equations with the boundary conditions $\chi_i^+(t) \xrightarrow{t \rightarrow -\infty} \Phi_i^B \exp[i\sigma_i(t)], \chi_f^-(t) \xrightarrow{t \rightarrow \infty} \Phi_f^A \exp[-i\sigma_f(t)]$, where σ_i and σ_f are the Coulomb phase [5].

We construct the distorting potentials U_i, U_f in the following form:

$$W_i = v_i - U_i = Z_A \left(\frac{1}{R} - \frac{1}{s_2} \right) - \sum_{\kappa=1}^2 \varphi_i^B(\vec{x}_1, \vec{x}_2) \times \vec{\nabla}_\kappa [\varphi_i^B(\vec{x}_1, \vec{x}_2)]^{-1}, \quad (7)$$

$$W_f = v_f - U_f = Z_\alpha \left(\frac{1}{R} - \frac{1}{s_2} \right) - \frac{1}{x_{12}} - \frac{1}{x_1} - \vec{\nabla}_1 \varphi_f^A(\vec{s}_1) \vec{\nabla}_1 [\varphi_f^A(\vec{s}_1)]^{-1}. \quad (8)$$

With this choice of $U_i (U_f)$, equation (6) allows separation of variables, and its solution is expressed in terms of the degenerate hypergeometric functions:

$$\begin{aligned} \chi_i^+ &= \Phi_i^B L_i^+, & \chi_f^- &= \Phi_f^A L_f^-, \\ L_i^+ &= N(v_A) \exp \left\{ i \frac{Z_A(Z_B-1)}{v} \ln(vR - v^2 t) \right\} \times F(i v_A, 1, i v s_1 + i \vec{v} \vec{s}_1); \\ L_f^- &= N^*(v_B) \exp \left\{ -i \frac{Z_A(Z_B-1)}{v} \ln(vR + v^2 t) \right\} \times \varphi_k^-(\vec{x}_2) F(i v_B, 1, i v x_1 + i \vec{v} \vec{x}_1). \end{aligned} \quad (9)$$

Taking into account the condition $\lim_{t \rightarrow \infty} \langle \Phi_f^A \exp[-i\sigma_f(t)] | \chi_i^+ \rangle = \lim_{t \rightarrow \infty} \langle \Psi_f^- | \chi_i^+ \rangle = 0$ imposed on U_i , we shall represent the desired amplitude of the capture process with ionization in the "prior" formalism in the following form:

$$\mathcal{A}_{if}^-(\vec{\rho}) = \lim_{t \rightarrow \infty} \langle \Psi_f^- | \Phi_i^B \exp[i\sigma_i(t)] \rangle = \lim_{t \rightarrow \infty} \langle \Psi_f^- | \chi_i^+ \rangle = -i \int_{-\infty}^{\infty} dt \iint d\vec{r}_1 d\vec{r}_2 \Psi_f^{*-} W_i \chi_i^+. \quad (10)$$

Using the expressions (99) for functions χ_i^+ and χ_f^- present \mathcal{A}_{if}^- in the form:

$$\begin{aligned} \mathcal{A}_{if}^-(\vec{\rho}) &= -i(2\pi)^{-3/2} (\rho v)^{2\nu} N(v_A) N(v_B) N(\xi_B) \int_{-\infty}^{\infty} dt \iint d\vec{r}_1 d\vec{r}_2 e^{-i(\vec{v}\vec{\eta} + \vec{k}\vec{x}_2 - \Delta E t)} G_i G_f, \quad (11) \\ G_f &= \varphi_f^{A*}(\vec{s}_1) F(iv_B, 1, iv x_1 + i\vec{v}\vec{x}_1) F(i\xi_B, 1, ik x_2 + i\vec{k}\vec{x}_2); \nu = Z_A(Z_B - 1)/v; \\ G_i &= \vec{\nabla}_{\vec{x}_1} \varphi_i^B(\vec{x}_1, \vec{x}_2) \vec{\nabla}_{\vec{s}_1} F(iv_A, 1, iv s_1 + i\vec{v}\vec{s}_1); \quad \Delta E = E_k + E_f^A - E_i^B. \quad (12) \end{aligned}$$

The most convenient way to calculate the capture cross section with ionization is with the help of the well known Fourier transform method [3]. In the limit $\mu \rightarrow \infty$ the quantum mechanical transition amplitude \mathfrak{R}_{if}^- is the Fourier transform of the quasiclassical analog of the transition amplitude \mathcal{A}_{if}^- [3, 6]:

$$\mathfrak{R}_{if}^-(\vec{\eta}) = (2\pi)^{-1} \int d\vec{\rho} \exp(-i\vec{\eta}\vec{\rho}) \mathcal{A}_{if}^-(\vec{\rho}), \quad (13)$$

where $\vec{\eta}$ is a two-component vector perpendicular to v : $\vec{\eta} \cdot \vec{v} = 0$. Taking (11) into account, equation (13) is easily transformed into the form

$$\begin{aligned} \mathfrak{R}_{if}^-(\vec{\eta}) &= N_{AB}(\vec{I} \cdot \vec{J}), \quad (14) \\ \vec{J} &= \iint d\vec{x}_1 d\vec{x}_2 \exp\{i(\vec{p}\vec{x}_1 - \vec{k}\vec{x}_2)\} F(iv_B, 1, iv x_1 + i\vec{v}\vec{x}_1) F(i\xi_B, 1, ik x_2 + i\vec{k}\vec{x}_2) \times \\ &\times \vec{\nabla}_{\vec{s}_1} \varphi_i^B(\vec{x}_1, \vec{x}_2); \quad N_{AB} = \frac{(2\pi)^{-3/2}}{2\pi i v} N(v_A) N(v_B) N(\xi_B); \quad \vec{p} = -\vec{\eta} + \left(\frac{\Delta E}{v} - \frac{v}{2}\right) \hat{v}; \\ \vec{I} &= \int d\vec{s}_1 \exp(i\vec{q}\vec{s}_1) \varphi_f^{A*}(\vec{s}_1) \vec{\nabla}_{\vec{s}_1} F(iv_A, 1, iv s_1 + i\vec{v}\vec{s}_1); \quad \vec{q} = \vec{\eta} - \left(\frac{\Delta E}{v} + \frac{v}{2}\right) \hat{v}. \quad (15) \end{aligned}$$

Below we shall use the free-electron approximation for the description of the bound states of the active electrons and shall present the two-electron wave function in the form $\varphi_i^B(\vec{x}_1, \vec{x}_2) = \varphi_i^B(\vec{x}_1) \varphi_i^B(\vec{x}_2)$. Setting up the problem as explained above leads to factorization of the matrix element (15), in which integration over \vec{x}_1 and \vec{x}_2 is carried out independently:

$$\begin{aligned} \vec{J} &= \vec{J}_1 \cdot \vec{J}_2; \quad \vec{J}_1 = \int d\vec{x}_1 \exp(i\vec{p}\vec{x}_1) F(iv_B, 1, iv x_1 + i\vec{v}\vec{x}_1) \vec{\nabla}_{\vec{s}_1} \varphi_i^B(\vec{x}_1); \\ \vec{J}_2 &= \int d\vec{x}_2 \exp(-i\vec{k}\vec{x}_2) F(i\xi_B, 1, ik x_2 + i\vec{k}\vec{x}_2) \varphi_i^B(\vec{x}_2). \quad (16) \end{aligned}$$

Choosing $\varphi_i^B(\vec{x}_1)$, φ_f^A in the form of very simple variation functions with effective charges $\lambda = Z_B^*$ and Z_A and applying Nordsieck's method of contour integration [8], we find that the matrix elements \vec{J}_1 , \vec{J}_2 , \vec{I} can be expressed in the form:

$$\begin{aligned}
\bar{J}_1 &= -8\pi i \lambda N_\lambda (\lambda^2 + p^2)^{-2} (1 - \mathcal{R}_1)^{-iv_B} \left[(1 - iv_B) \bar{p} - iv_B \bar{q} (1 - \mathcal{R}_1)^{-1} \right]; \\
J_2 &= 8\pi N_\lambda (\lambda^2 + k^2)^{-2} (1 - \mathcal{R}_2)^{-i\xi_B} \left[\lambda (1 - i\xi_B) + i\xi_B (\lambda - ik) (1 - \mathcal{R}_2)^{-1} \right]; \\
\bar{I} &= -8\pi v_A v N_{Z_\alpha} (Z_\alpha^2 + q^2)^{-2} (1 - \mathcal{R})^{-iv_A-1} (v_A \bar{v} + i\bar{q}); \\
\mathcal{R} &= 2 \frac{iZ_\alpha v - \bar{q} \bar{v}}{Z_\alpha^2 + q^2}; \quad \mathcal{R}_1 = 2 \frac{i\lambda v - \bar{p} \bar{v}}{\lambda^2 + p^2}; \quad \mathcal{R}_2 = 2 \frac{i\lambda k + k^2}{\lambda^2 + k^2}. \quad (17)
\end{aligned}$$

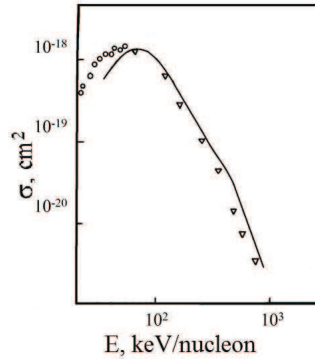


Figure 1. Capture cross section with ionization for collision of a He atom with protons. Theory: solid line – CDW method. Experiment: ∇ - [9], O - [10].

The total capture cross section with ionization (1) is expressed by the formula

$$\sigma_{if}^- = 8\pi^2 \int_0^\infty dk \cdot k^2 |N_{AB}(k)|^2 \int_0^\infty d\eta \cdot \eta \left| (\bar{I} \cdot \bar{J}_1) J_2 \right|^2. \quad (18)$$

Results of calculations of total capture cross sections with ionization of $p + \text{He}(1S^2) \rightarrow \text{H}(1S) + \text{He}^{++} + e^-$ are presented in Fig. 1 along with experimental data [9, 10].

REFERENCES

- [1] V. I. Lendel, V. Yu. Lazur, M. I. Karbovanets and R.K. Janev, *Introduction to the theory of atomic collisions*, p. 192 (Vysshaya shkola, Lvov, 1989).
- [2] V. Yu. Lazur and M. V. Khoma, *Adv. in Quantum Chemistry*, 65, 363 (2013).
- [3] Dz. Belkic, R. Gayet and A. Salin, *Phys. Rep.*, 56, No. 6, 279 (1979).
- [4] Dz. Belkic, *J. Phys. B*, 11, No. 20, 3529 (1978).
- [5] V. Yu. Lazur, V. V. Aleksiy, M. V. Khoma, *Scientific Herald of Uzhhorod University. Series Physics. Issue 34* (2013).
- [6] D. S. F. Grothers and J. F. McCann, *J. Phys. B*, 16, 3229 (1983).
- [7] L. R. Dodd and K. R. Greider, *Phys. Rev.*, 146, 675 (1966).
- [8] A. Nordsieck, *Phys. Rev.*, 93, 785 (1954).
- [9] V. V. Afrosimov, Yu. A. Mamaev, et al, *Zh. Tekh. Fiz.*, 39(1), 159 (1969).
- [10] M. B. Shah and H. B. Gilbody, *J. Phys. B*, 18, 899 (1985).

ELECTRON IMPACT IONIZATION OF CO IN RF ELECTRIC FIELD

M. M. Aoneas¹, M. M. Vojnović¹, M. M. Ristić², M. D. Vičić¹
and G. B. Poparić¹

¹*Faculty of Physics, University of Belgrade, P.O. Box 44,
11000 Belgrade, Serbia*

²*Faculty of Physical Chemistry, University of Belgrade, P.O. Box 137,
11000 Belgrade, Serbia*

Abstract. Rate coefficients for electron-impact ionization of CO molecules in the presence of radio-frequency (RF) electric field have been calculated. Monte Carlo method has been applied to obtain non-equilibrium electron energy distribution functions within one cycle of the electric field. The results have been obtained for frequency values of 50, 100 and 500 MHz, at reduced electric field amplitude value of 200 Td (1 Td = 10^{-21} Vm²). Time-dependent behavior of electron mean energy and ionization rate coefficients under the influence of frequency change was studied and it is presented in this paper.

1. INTRODUCTION

The study of electron-carbon monoxide collision processes is of great importance for practical applications such as chemical detectors and laser devices [1]. Investigation of electron-impact processes in the molecular gas under the influence of radio-frequency electric field is necessary for technologies such as RF plasma reactors, or RF excited gas lasers, based on the use of radio frequency electric signal for excitation of gas molecules. One of the most investigated types of lasers in the past decades is RF excited CO laser [2-4]. Modeling of these devices is significant for better understanding of excitation and ionization mechanisms involved when an external time-varying electric field is applied.

The aim of this work is to analyze the time dependent characteristics of electron-impact ionization of CO under the action of external RF electric field.

2. MONTE CARLO SIMULATION

Monte Carlo simulation developed for electron transport through CO gas molecules, previously described in [5], was modified for the case when time-dependant electric field is present:

$$\vec{E}(t) = \sqrt{2}(E/N)\vec{k} \cos(2\pi\nu t) \quad (1)$$

where E/N is effective reduced field strength, ν is frequency of the RF field and \vec{k} is the unit vector in the field direction. For solving differential equations of electron motion Eq. (1), we have used Runge Kutta method [6].

Electron position and velocity is determined after each time step (Δt) in the simulation. When the steady state is reached, the electron energy is sampled in each Δt within one period, resulting with the time modulated non-equilibrium electron energy distribution function (EEDF) [7].

Experimentally measured electron-impact cross sections for elastic and non-elastic scattering processes have been used for simulation and for rate coefficients calculation.

The simulation algorithm and the used cross section data set have been successfully tested by comparison with experimentally measured transport properties in DC field to those obtained by described simulation.

3. RESULTS AND DISCUSSION

Results have been obtained at E/N of 200 Td, for RF electric field frequencies of 50, 100 and 500 MHz.

The initial electron kinetic energy was 5 eV. The gas pressure was 1 Torr (133.3 Pa). The non-equilibrium EEDF was sampled in order to calculate the rate coefficients for considered process at specific time (t), given by the following equation:

$$K(\langle \varepsilon, t \rangle, t) = \sqrt{2/m_e} \int_{\varepsilon_{thres}}^{+\infty} \sigma(\varepsilon) \sqrt{\varepsilon} \cdot f_e(\langle \varepsilon, t \rangle, \varepsilon, t) d\varepsilon \quad (2)$$

where $\langle \varepsilon \rangle$ is the mean electron energy, $\sigma(\varepsilon)$ is the excitation cross section for the given process, ε_{thres} is the threshold energy for observed process $f_e(\langle \varepsilon, t \rangle, \varepsilon, t)$ is the normalized EEDF. The Figure 1. presents the change of mean electron energy during one cycle of electric field at 200 Td, for different values of frequency.

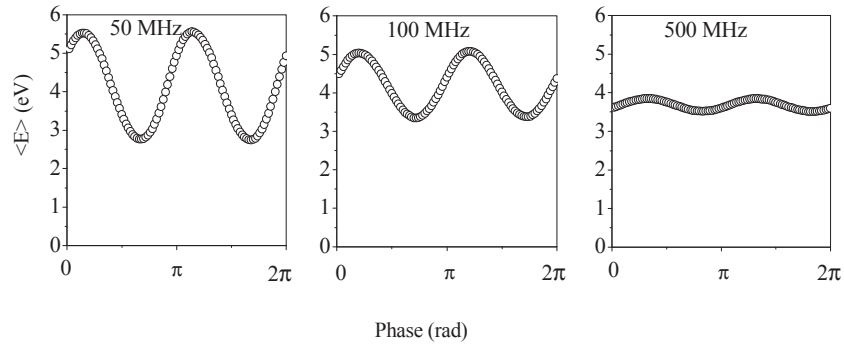


Figure 1. Mean electron energy values at 200 Td at various RF field frequencies (indicated).

With increasing frequency the mean electron energy decreases. This is caused by the phase delay between mean energy and electric field oscillations, since it becomes more difficult for electrons in the CO gas to follow the changes of the external electric field as the frequency is increasing. At 500 MHz oscillations start to diminish.

Rate coefficients for electron-impact ionization of CO for the E/N value of 200 Td at frequencies: 50, 100 and 500 MHz during one cycle are shown on Figure 2.

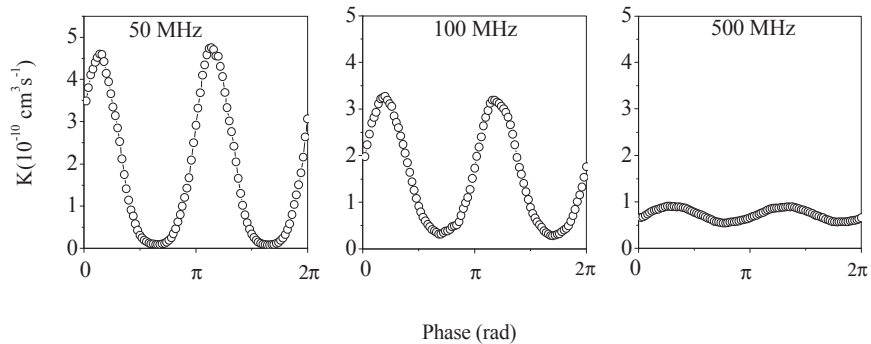


Figure 1. Ionization rate coefficients for frequencies: 50, 100 and 500 MHz at 200 Td.

The decrease of ionization rate coefficients with increasing frequency is noticeable, just as with mean electron energy, due to incapability of electrons in the CO gas to follow the change of electric field. Generally, because of changes that appear in EEDF's at high energy, the variation of ionization rate coefficients with frequency in one period is more pronounced than it is the case with the mean electron energy [7].

4. CONCLUSIONS

Set of rate coefficients for electron-impact ionization of CO gas under the influence of RF electric field are obtained. By means of Monte Carlo simulation, EEDF's has been sampled within one phase of the electric field. An insight into time-modulated properties of the mean electron energy and ionization rate coefficients is given.

Acknowledgements

This work is partially supported by the Ministry of Education and Science of the Republic of Serbia under the grant NO 171016.

REFERENCES

- [1] M. Vojnović, M. Popović, M. M. Ristić, M. M. Vičić and G. B. Poparić, *Chem. Phys.* 423, 1(2013).
- [2] G. N. Pearson and D. R. Hall, *Optics Communications* 68, 52(1988).
- [3] H. Zhao, H. J. Baker and D. R. Hall, *Appl. Phys. Lett.* 59, 1281 (1991).
- [4] A. A. Ionin, *IEEE Journal of Quantum Electronics* 45, 215 (2009).
- [5] M. Ristić, G. B. Poparić and D. S. Belić, *Chem. Phys.* 331, 410 (2007).
- [6] R. Morrow, *J. Comp. Phys.* 43, 1 (1981).
- [7] M. P. Popović, M. M. Vojnović, M. M. Aoneas, M. M. Ristić, M. D. Vičić and G. B. Poparić, *Physics of Plasmas*. 21, 063504 (2014).

STUDIES OF ELECTRON TRANSPORT IN GASES FOR RESISTIVE PLATE CHAMBERS

D. Bošnjaković, Z.Lj. Petrović and S. Dujko

*Institute of Physics, University of Belgrade,
Pregrevica 118, 11080 Belgrade, Serbia*

Abstract. We study the electron transport in gases used by Resistive Plate Chambers in ALICE, ATLAS and CMS experiments at CERN. Particularly, we identify and discuss the electron transport phenomena in these gases using the Boltzmann equation analysis and spatially resolved Monte Carlo calculations. The understanding of electron transport phenomena and its implications is necessary for correct implementation of transport data in modeling of these devices.

1. INTRODUCTION

Resistive Plate Chambers (RPCs) were introduced in 1980s as a practical alternative to spark counters with localized discharge [1,2]. Today, they are one of the most frequently used particle detectors in large high energy physics experiments owing to their outstanding timing resolution, good spatial resolution and low cost per unit volume while the electrodes of highly resistive material (e.g. glass or bakelite) make them resilient to destructive discharges [3]. They also found their way in other areas such as geophysics and medical imaging [4].

There were many approaches in modeling of RPCs. Being analytical, fluid or Monte Carlo based [5], they all require the knowledge of electron transport data in gases which are used as input parameters. Also, a matter of particular importance which had practically no attention in the particle detector community is the correct implementation of these data with respect to duality of transport coefficients. For example, in fluid modeling of these devices one must use the flux data but in models where electron avalanche is treated as a whole, bulk data must be used. In this work, we calculate the electron transport parameters and study the associated kinetic phenomena in gas mixtures used by RPCs in ALICE, ATLAS and CMS experiments at CERN.

2. THEORETICAL METHODS

Electron transport coefficients are calculated from the solution of the non-conservative Boltzmann equation (BE). Instead of the conventional two term approximation for solving the Boltzmann equation, we have used a

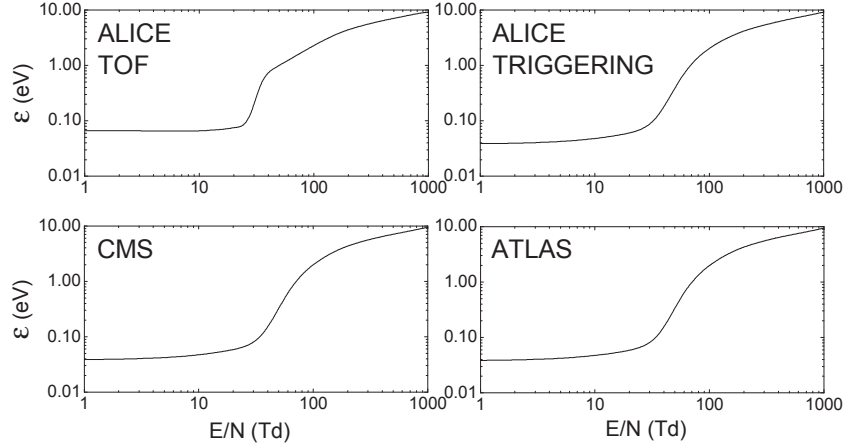


Figure 1. Variation of the mean energy with E/N for RPCs used in ALICE, CMS and ATLAS experiments at CERN.

contemporary multi term approach [6]. In addition to Boltzmann equation, a Monte Carlo technique is used to sample spatially resolved transport data; for more details the reader is refer to [7].

3. RESULTS AND DISCUSSION

The results in this section are calculated for the following RPC gas mixtures of $C_2H_2F_4$ /iso- C_4H_{10} / SF_6 , used at CERN: (1) ALICE timing RPC, 90/5/5; (2) ALICE triggering RPC, 89.7/10/0.3; (3) CMS triggering RPC, 96.2/3.5/0.3; and (4) ATLAS triggering RPC, 94.7/5/0.3. We use the cross section set for $C_2H_2F_4$ developed by our group [8], cross section for iso- C_4H_{10} taken from MAGBOLTZ 2.7.1 code developed by S. Biagi [9], and cross sections for SF_6 taken from Itoh et al. [10]. The reduced electric field E/N is given in Td ($1 \text{ Td} = 1 \times 10^{-21} \text{ Vm}^2$).

Figure 1 shows mean electron energies over a range of E/N values, for different RPC gas mixtures used at CERN. We may observe a very small change of mean energy up to about 30 Td where the rapid rise begins. The small change of electron energy is due to the rising collision frequency for vibrational excitations in $C_2H_2F_4$. This effect can be named as *inelastic cooling* since the electrons loose considerable energy in inelastic collisions. At about 30 Td cross sections for vibration excitation begin to drop and electron energy starts to rise rapidly. In addition to inelastic cooling, for ALICE TOF mixture with higher SF_6 concentration, one can also observe that in the same E/N range the mean energy is significantly higher than the thermal value of 0.038 eV. This is a typical example of *attachment heating* [11] which takes place since electrons with lower energies are consumed in thermal attachment by the SF_6 molecules.

Calculations of drift velocities (Figure 2) reveal another interesting phenomenon: the bulk drift velocity in case of ALICE TOF mixture exhibits a

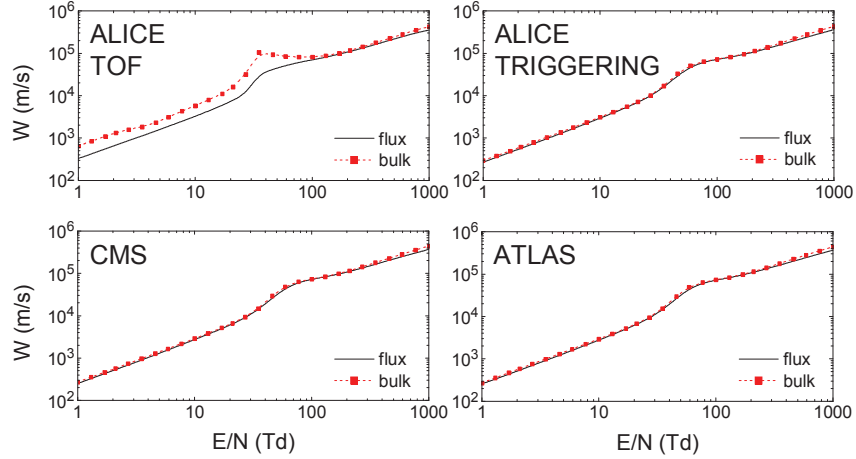


Figure 2. Variation of the bulk and flux drift velocities with E/N for RPCs used in ALICE, CMS and ATLAS experiments at CERN.

prominent negative differential conductivity (NDC) while this effect is not present in the flux component or in any other gas mixture. NDC is a kinetic phenomenon defined as a decrease of drift velocity with increasing electric field strength [12]. It arises from a certain combination of elastic and inelastic cross sections and is usually present in both flux and bulk components of drift velocity but it was argued whether it can be present only (or dominantly) in the bulk component when non-conservative collisions are present [13]. Here it is clear that the NDC is induced by electron attachment since it is not present in the flux component and the electron energies are well below the threshold for ionization. The occurrence of NDC can be understood in terms of spatially dependent (resolved) mean energy and attachment rate. It is well-known that the mean energy is not constant along the swarm because the electrons at the front of the swarm have higher energies than those at the back. This follows from the fact that electrons at the front gain more energy from the electric field as they are accelerated through a higher potential. As a consequence, the attachment rate coefficient is not uniform because the cross sections for attachment are energy dependent as well. In our case, the bulk drift velocity explicitly depends on the spatial profile of the attachment rate. Since the attachment rate is greater at the back of the swarm than at the front, the center of mass of the swarm shifts forward which results in an increase of bulk component of drift velocity over the flux component. This increase roughly depends on the spatial gradient (slope) of the attachment rate coefficient. Figure 3 shows the spatial profiles of attachment rate coefficients, for different E/N values, calculated using a Monte Carlo technique. One must bear in mind that calculations were performed for a stationary gas ($T = 0$ K) and thus the values are shifted with respect to those obtained from BE so that the onset of NDC (the peak in the bulk drift velocity) corresponds to $E/N = 10$ Td. Indeed, one can see that the slope is at its maximum for $E/N = 10$ Td. With increasing E/N the slope drops and so does the NDC.

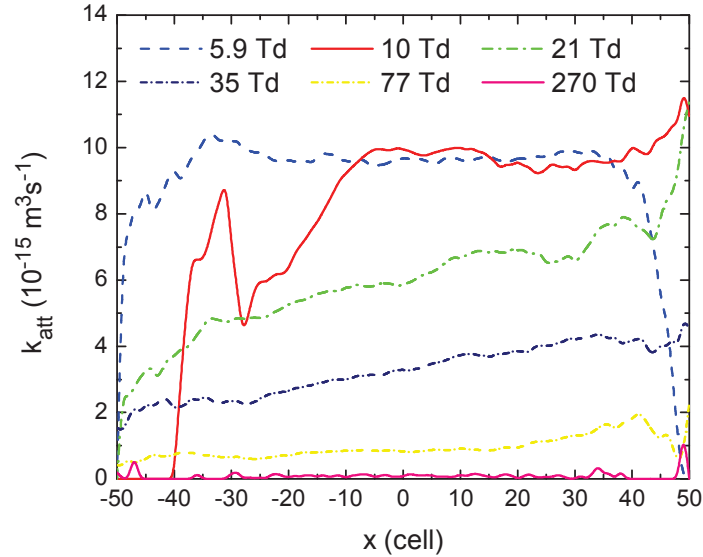


Figure 3. Spatially resolved attachment rate coefficient for a range of E/N in ALICE timing RPC. ($t = 1$ ns)

Acknowledgements

This work is supported by MPNTR, Serbia, under the contract number OI171037.

REFERENCES

- [1] R. Santonico and R. Cardarelli, Nucl. Instrum. Meth. 187, 377 (1981).
- [2] R. Santonico et al., Nucl. Instrum. Meth. A 263, 20 (1988).
- [3] P. Fonte, IEEE Trans. Nucl. Sci. 49, 881 (2002).
- [4] M. Couceiro et al., Nucl. Instrum. Meth. A 661, S156 (2012).
- [5] W. Riegler and C. Lippmann, Nucl. Instrum. Meth. A 518, 86 (2004).
- [6] S. Dujko et al., Phys. Rev. E 81, 046403 (2010).
- [7] Z. M. Raspopović et al., IEEE Trans. Plasma Sci. 39, 2566 (2011).
- [8] O. Šašić et al., J. Phys. D: Appl. Phys. 46, 325201 (2013).
- [9] S. Biagi, Nucl. Instrum. Meth. A 421, 234 (1999).
- [10] H. Itoh et al., J. Phys. D: Appl. Phys. 26, 1975 (1993).
- [11] R. E. Robson and K. F. Ness, Phys. Rev. A 33, 2068 (1986).
- [12] Z. Lj. Petrović, R. W. Crompton and G. N. Haddad, Aust. J. Phys. 37, 23 (1984).
- [13] S. B. Vrhovac and Z. Lj. Petrović, Phys. Rev. E 53, 4012 (1996).

POSITRON TRANSPORT IN GASES IN ELECTRIC AND MAGNETIC FIELDS CROSSED AT ARBITRARY ANGLES

A. Banković¹, S. Dujko¹, R. D. White², Z. Lj. Petrović¹

¹*Institute of Physics, University of Belgrade, Pregrevica 118, POB 68, Zemun, Serbia*

²*ARC Centre for Antimatter-Matter Studies, School of Engineering and Physical Sciences, James Cook University, Townsville 4810, QLD, Australia*

Abstract. In this work we apply a multi term solution of the Boltzmann equation to investigate various aspects of positron transport in gases under the influence of electric and magnetic fields crossed at arbitrary angles. Calculations are performed over a range of E/n_0 and B/n_0 values, and angles between the fields for positrons in N_2 and H_2 . Values of mean energy, drift velocity components, diffusion tensor components and rate coefficient for positronium (Ps) formation are discussed in this work. It is found that the angle between the fields can be used to efficiently control the behavior of positron transport properties.

1. INTRODUCTION

In the standard Surko positron trap, the initial positron beam, guided by electric and magnetic fields and by collisions with neutral buffer gas, rapidly develops into a swarm-like distribution [1]. Positrons accumulated in the trap are then used for different kinds of experiments in atomic, molecular and material physics. Therefore, it is of great importance to have a full control over the positron transport properties and over the process of positron accumulation. In this paper, we extend our previous work on positron transport in a crossed field configuration [2], by considering positron transport properties in N_2 and H_2 when electric and magnetic fields are crossed at arbitrary angles. Results presented in this work represent the first multi term solution of the non-conservative Boltzmann equation for positrons in varying configurations of electric and magnetic fields.

2. THEORETICAL METHOD

All information on the drift and diffusion of positrons in gases is contained in the positron phase-space distribution function $f(\mathbf{r}, \mathbf{c}, t)$, where \mathbf{r}

represents the spatial coordinate of a positron at time t , and \mathbf{c} denotes its velocity. This function is determined by solving Boltzmann's equation:

$$\left[\partial_t + \mathbf{c} \cdot \nabla_{\mathbf{r}} + \frac{e}{m} [\mathbf{E} + \mathbf{c} \times \mathbf{B}] \cdot \nabla_{\mathbf{c}} \right] f(\mathbf{r}, \mathbf{c}, t) = -J(f, f_0), \quad (1)$$

where ∂_t , $\nabla_{\mathbf{r}}$, and $\nabla_{\mathbf{c}}$ are the gradients with respect to time, space and velocity, while e and m are the charge and mass of the positron and \mathbf{E} and \mathbf{B} are electric and magnetic fields. The right-hand side of Eq. (1) $J(f, f_0)$ denotes the linear positron-neutral molecule collision operator, accounting for elastic, inelastic and nonconservative (e.g. Ps formation and/or annihilation) collisions. The directional dependence of $f(\mathbf{r}, \mathbf{c}, t)$ in velocity space is represented by an expansion in terms of spherical harmonics:

$$f(\mathbf{r}, \mathbf{c}, t) = \sum_{l=0}^{\infty} \sum_{m=-l}^l f_m^{(l)}(\mathbf{r}, \mathbf{c}, t) Y_m^{[l]}(\hat{\mathbf{c}}), \quad (2)$$

where $\hat{\mathbf{c}}$ denotes angles of \mathbf{c} . It is important to note that no restriction has been placed on the number of spherical harmonics $Y_m^{[l]}(\hat{\mathbf{c}})$. All calculations are performed assuming hydrodynamic conditions; thus the spatial and explicit time-dependences are treated by the density gradient expansion. The speed dependence of $f(\mathbf{r}, \mathbf{c}, t)$ is treated by an expansion in terms of Sonine polynomials about a Maxwellian at an internally determined temperature. Applying these expansions and finite truncation of Sonine polynomials and spherical harmonics, the Boltzmann equation is converted to a hierarchy of coupled algebraic equations for the moments of f which are related to the positron transport properties. For more details on the applied theory and associated computer code the reader is referred to [3] and references therein.

In this paper we discuss the behavior of the mean energy and drift velocity as well as the behaviour of individual elements of the diffusion tensor, using the cross section data for H_2 and N_2 described in our previous work [4]. For an arbitrary field configuration, the drift velocity vector and diffusion tensor are full and there are no symmetries that can be exploited.

3. RESULTS AND DISCUSSION

In $\mathbf{E} \times \mathbf{B}$ configuration and for a fixed electric field, the mean energy of positrons is a decreasing function of B/n_0 [2]. This effect is known as magnetic cooling. Here we examine how the angle between the fields influences this effect. Fig. 1a shows the mean energy for positrons in H_2 for $B/n_0=1000\text{Hx}$, as a function of E/n_0 and the angle between electric and magnetic fields, ψ . For increasing ψ we observe that the mean energy becomes less sensitive to the details of collisions and that magnetic field starts to dominate the behavior of the swarm. Also, for a fixed value of E/n_0 , an increase in ψ leads to a decrease in the mean energy – the magnetic cooling effect is enhanced as the component of magnetic field perpendicular to electric field is increased. Therefore, for a fixed

E/n_0 , the mean energy can be controlled either by varying the strength of magnetic field or the angle between the fields.

In a crossed field configuration, magnetic field nullifies the negative differential conductivity (NDC) effect in the bulk drift velocity. When fields are crossed at an arbitrary angle, the angle can also be used to control this effect. For example, for positrons in H_2 (Fig. 1b), the bulk drift velocity for 1000Hx shows NDC for low values of ψ ($0^\circ < \psi < 65^\circ$). With an increasing component of the magnetic field perpendicular to the electric field, the NDC effect is first reduced and then entirely removed from the profile of bulk drift velocity. At $\psi \approx 85^\circ - 90^\circ$ there is no sign of NDC in the bulk drift velocity. The disappearance of NDC for large angles is more pronounced for $B/n_0 = 2000Hx$.

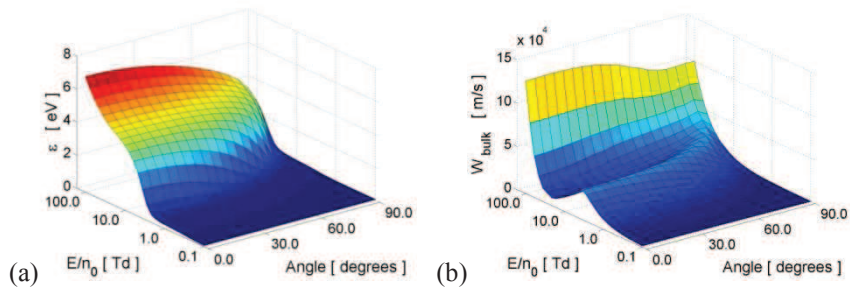


Figure 1. Mean energy (a) and bulk drift velocity (b) for positrons in H_2 as a function of E/n_0 , and the angle between the fields ($B/n_0 = 1000 Hx$).

In this section we illustrate how the angle between the fields affects the behavior of the diffusion coefficients. There are three diagonal elements of diffusion tensor and they all respond in a different way to the magnetic field, the non-conservative nature of Ps formation, collisions and the angle between fields. The longitudinal diffusion coefficient $n_0 D_{zz}$ (it is assumed that the electric field vector lies along the z -direction while magnetic field is on y - z plane making an angle ψ with the z -axis), is a decreasing function of angle ψ for a fixed E/n_0 . The same applies for $n_0 D_{xx}$ which describes diffusion along the $\mathbf{E} \times \mathbf{B}$ direction. On the other hand $n_0 D_{yy}$ increases with ψ . The off-diagonal elements of the diffusion tensor also show different sensitivity to magnetic field, collisions and the angle, and are of the same order of magnitude as diagonal elements. This suggests their careful consideration in prospective models of positron traps. Off-diagonal elements are not directly experimentally measurable quantities, but sums of appropriate pairs are; a typical example is the Hall diffusion coefficient in a crossed field configuration. It is interesting to note that some of the off-diagonal elements of the diffusion tensor are negative. This “negativity” decreases with increasing magnetic field.

In the Surko trap, electric and magnetic fields are both in axial direction. For parallel fields, the mean energy and longitudinal diffusion are not affected by magnetic field. For a fixed E/n_0 the transverse diffusion coefficient is a decreasing function of magnetic field, which is evident from figure 2a for

positrons in N_2 . In order to illustrate the explicit effects of Ps formation on positron transport properties, in figure 2b, we show the relative difference between the bulk and flux values for transverse diffusion coefficient. These results can be used to find the optimal values of electric and magnetic fields in the Surko trap in order to minimize losses to the walls.

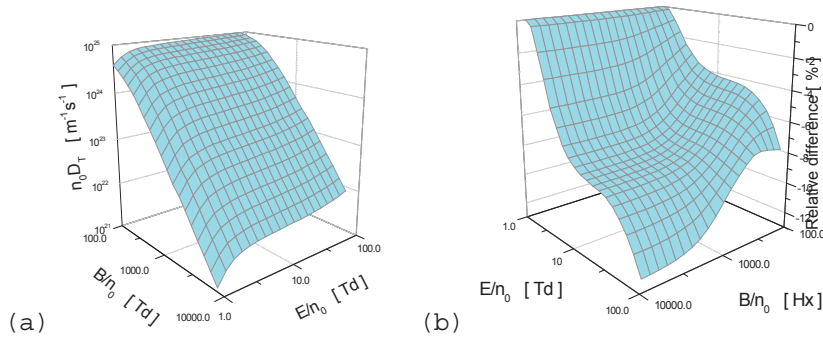


Figure 2. Transverse diffusion coefficient (a) and relative difference between the bulk and flux values of the transverse diffusion coefficient (b) as function of E/n_0 and B/n_0 for positrons in N_2 in parallel field configuration.

In conclusion, by varying the angle between electric and magnetic fields we get a new method of controlling the properties of positron swarm. This can be of great importance in experimental setups where accumulating a huge number of these positrons is one of the crucial issues.

Acknowledgements

This work was supported by the MPNTRS Grants No. ON171037 and III41011 and Australian Research Council.

REFERENCES

- [1] S. Marjanović, M. Šuvakov, A. Banković, M. Savić, G. Malović, S. J. Buckman and Z. Lj. Petrović, IEEE Trans. Plasma Sci. 39 (2011) 2614
- [2] A. Banković, S. Dujko, R. D. White, J. P. Marler, S. J. Buckman, S. Marjanović, G. Malović, G. Garcia, Z. Lj. Petrović, New J. Phys. 14, 035003 (2012).
- [3] S. Dujko, R. D. White, Z. Lj. Petrović and R. E. Robson, Phys. Rev. E 81, 046403 (2010).
- [4] Z. Lj. Petrović, A. Banković, S. Dujko, S. Marjanović, G. Malović, J. P. Sullivan and S. J. Buckman, AIP Conf. Proc. 1545, 115 (2013).

SCATTERING CROSS SECTIONS AND TRANSPORT COEFFICIENTS FOR ELECTRONS IN CF₃I

J. Mirić¹, O. Šašić^{1,2}, S. Dujko¹ and Z.Lj. Petrović¹

¹*Institute of Physics, University of Belgrade, Pregrevica 118, 11080 Belgrade, Serbia*

²*Faculty of Transport and Traffic Engineering, University of Belgrade, Vojvode Stepe 305, 11000, Belgrade, Serbia*

Abstract. Scattering cross sections for electrons in CF₃I are discussed using the swarm method. Electron drift velocity, effective ionization coefficient and diffusion coefficients are calculated using a Monte Carlo simulation technique and from solution of the non-conservative Boltzmann equation. Calculated data for pure CF₃I and its mixtures with rare gases, N₂ and SF₆ are compared with those measured experimentally under both the time-of-flight and pulsed-Townsend conditions. Among many important phenomena observed in electron transport we note the existence of negative differential conductivity in the profile of the bulk drift velocity with no signs of the same phenomenon in the profile of flux drift velocity.

1. INTRODUCTION

Trifluoroiodomethane (CF₃I) is a processing gas employed for plasma etching of various materials. Due to its short atmospheric lifetime (1.8 days), low GWP (0.4 times than of CO₂) and high critical electric field (437 Td) CF₃I shows a promise for application as an alternative refrigerant to commonly used fluorocarbons such as CF₄ [1], and as a potential high voltage insulator, both on its own and mixed with N₂ and CO₂ in high-voltage insulation technology [2]. In spite of these important applications of CF₃I, still there is a lack of reliable sets of cross sections for electron scattering and associated electron transport coefficients.

In this work we discuss the existing sets of cross sections for electron scattering in CF₃I. Using the swarm method, our initial set of cross sections is constructed from other available sets, and data for individual scattering channels. Calculated transport data are then compared with those measured in experiments and if the agreement is not enough, then cross sections are modified. This process is repeated until some preset agreement between theoretically calculated and experimentally measured data is achieved. Increasing the accuracy of the set of

cross sections, the electron transport is investigated using the multi term approach for solving the Boltzmann equation where particular emphasis was placed upon the explicit effects of non-conservative collisions on the drift and diffusion.

2. CROSS SECTIONS FOR ELECTRON SCATTERING IN CF_3I

The initial set of cross sections in this work was developed by Kimura and Nakamura [3], and is presented by solid curves in Figure 1. Due to disagreement between experimentally measured swarm data and those obtained in theoretical calculations, we have concluded that there are some internal inconsistencies in the set proposed by Kimura and Nakamura. Similar conclusions have been recently found by Kawaguchi *et al.* [4].

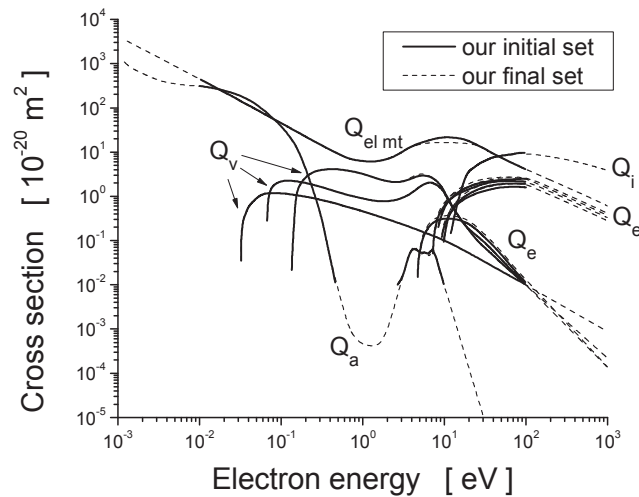


Figure 1. Cross sections for electron scattering in CF_3I from Kimura and Nakamura (solid curves) [3] and from our work (broken curves).

In this work the cross sections were extended in energy up to 1000 eV so that calculated data may cover the region between a few Td and few thousands of Td. This is of great importance having in mind the high critical field of CF_3I . The logarithmic extrapolation was used for electronic excitation with the lowest threshold and for all vibrational excitations as well as for the electron attachment. The Born-Bethe approximation was used to extrapolate the cross sections for momentum transfer in elastic collisions and for the cross sections for electronic excitation. The cross section for ionization was modified as follows: in the energy range up to 45 eV we have used the cross section from [3] while for higher energies than 45 eV we have included the theoretically calculated cross section developed by Anthony *et al.* [5]. Using the data

suggested by Christophorou [6], the cross section for attachment between 0.5 and 3 eV was reconstructed.

Cross section for momentum transfer in elastic collisions in the energy region between 4 and 20 eV was modified together with the cross section for vibrational excitation with the highest threshold in order to fit the drift velocity from experimental measurements of Kimura and Nakamura [3]. The ionization coefficient was fitted through the modification of cross sections for electronic excitations having in mind the large uncertainties associated with the magnitudes of these cross sections. Our final set of cross sections for electron scattering in CF_3I is shown in Figure 1. This set of cross sections provides much better agreement between theoretically calculated and experimentally measured swarm transport data as discussed below.

3. TRANSPORT COEFFICIENTS FOR ELECTRONS IN CF_3I

In Figure 2 we compare our results for the electron drift velocity with experimental data obtained under the time-of-flight [3] and pulsed-Townsend conditions [2]. The calculated values of W are initially lower than those measured in experiments. After modification of cross sections the calculated values of W are in a good agreement with experimental measurements obtained under the time-of-flight conditions. Our flux drift velocity is calculated by the two-term approximation (TTA) for solving the Boltzmann equation and using a Monte Carlo simulation technique.

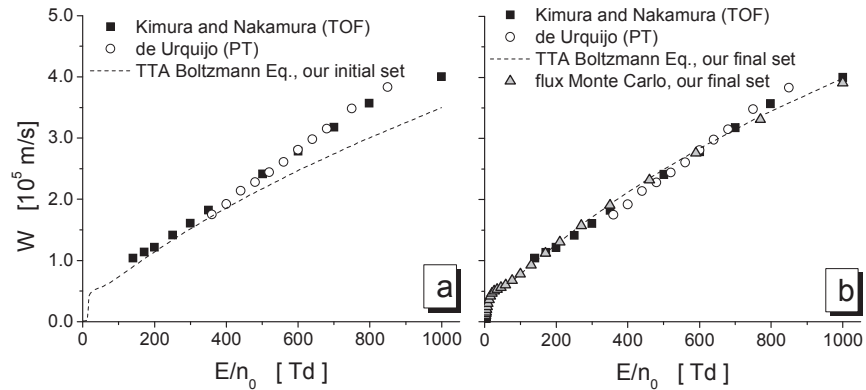


Figure 2. Variation of the drift velocity with E/n_0 for electrons in CF_3I . Our TTA results are compared with those obtained in experiments for (a) our initial set of cross sections and (b) our final set of cross sections.

Figure 3 shows the calculated values of effective ionization coefficient $(\alpha-\eta)/n_0$ using the initial set of cross sections (a) and our final set of cross sections (b). Values of $(\alpha-\eta)/n_0$ measured by Kimura and Nakamura [3] and de

Urquijo *et al.* [2] are also plotted. In Figure 3 (a), calculated values of $(\alpha-\eta)/n_0$ are higher than the measured data for higher E/n_0 . Calculated values using our final set of cross sections agree well with the measured data in a wide range of E/n_0 except for E/n_0 less than approximately 200 Td where the effects of attachment are dominant.

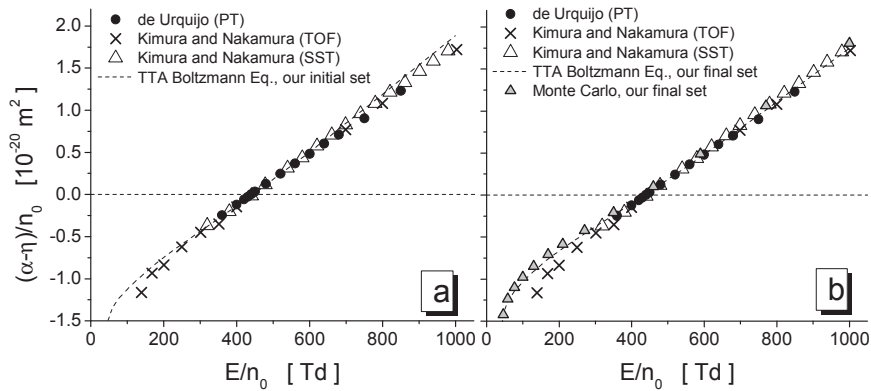


Figure 3. Variation of the effective ionization coefficient with E/n_0 for electrons in CF_3I . Our TTA results are compared with those obtained in experiments for (a) our initial set of cross sections and (b) our final set of cross sections.

Other transport properties including diagonal elements of the diffusion tensor, mean energy and rate coefficients are also calculated using a Monte Carlo simulation technique and from multi term solutions of the Boltzmann equation. Bulk values of the drift velocity and diffusion coefficients are evaluated and explicit effects of the electron attachment and/or ionization are examined.

Acknowledgements

This work was supported by MPNTRRS Projects OI171037 and III41011.

REFERENCES

- [1] Y.T. Duan, L. Shi, L.Q. Sun, M.S. Zhu and L.Z. Han, *Int. J. Thermophys.* 21, 393 (2000).
- [2] J. de Urquijo, A. M. Juarez, E. Basurto and J. L. Hernandez-Avila, *J. Phys. D* 40, 2205 (2007).
- [3] M. Kimura and Y. Nakamura, *J. Phys. D: Appl. Phys.* 43, (2010).
- [4] S. Kawaguchi, K. Satoh and H. Itoh, *Eur. Phys. J. D* 68, 100 (2014).
- [5] B. K. Antony, K. N. Joshipura and N. J. Mason, *J. Phys. B: At. Mol. Opt. Phys* 38, 189 (2005).
- [6] L. G. Christophorou and J. K. Olthoff, *J. Phys. Chem. Ref. Data* 29, 553 (2000).

ELECTRON TRANSPORT IN NOBLE-GAS METAL-VAPOR MIXTURES

J. Mirić¹, Z.Lj. Petrović¹, R.D. White² and S. Dujko¹

¹*Institute of Physics, University of Belgrade,
Pregrevica 118, 11080 Belgrade, Serbia*

²*ARC Centre for Antimatter-Matter studies, James Cook University,
School of Electrical Engineering and Physical Sciences, 4810 Townsville,
Australia*

Abstract. Electron transport coefficients required for the modeling of light sources are calculated from the multi term solution of the non-conservative Boltzmann equation. Calculations are performed over a range of E/n_0 values (ratio of the electric field, E , to the neutral number density n_0), gas temperatures and metal vapor concentrations relevant to lamp discharges. Values and general trends of mean energy, drift velocity, diffusion tensor and rate coefficients are presented in this work.

1. INTRODUCTION

The progress and further improvements of light sources based on low or high pressure electrical gas discharges require the most accurate modeling of charged particle transport processes in noble-gas-metal-vapor mixtures [1]. In particular, modern high intensity discharge lamps are usually filled with noble gas at high pressure (0.1 to 12 bar) and metallic salts. Noble gas provides light during the initial warm-up phase of the operation while metallic salts take over light emission after they have evaporated [2]. Our work has been motivated, in part, by recent suggestions that highly accurate data for transport coefficients required as input in fluid models of lamp discharges may significantly improve the existing models. Current models of such lamps require knowledge of the plasma electrical conductivity, which can be calculated from the cross sections for electron scattering in noble-gas-metal-vapor mixtures and mobility coefficients presented in this work.

In this work we investigate electron transport in mixtures of noble gases (He, Ne, Ar, Kr and Xe) and metal vapors (Na, K, Cs, Mg and Hg)

under swarm conditions using a multi term theory for solving the Boltzmann equation [3]. In section 2, we give a brief discussion of the theoretical multi term solution of the Boltzmann equation under non-conservative conditions while in section 3 we present a few examples of our systematic study of electron transport in noble-gas-metal-vapor mixtures.

2.THEORETICAL METHODS

Electron transport coefficients are determined by solving the non-conservative Boltzmann's equation under the hydrodynamic conditions for electrons drifting and diffusing through the noble-gas-metal-vapor mixtures under the influence of spatially homogeneous electric field. In brief, the solution of Boltzmann's equation is found by expanding the distribution function as sums of products with the directional dependence of \mathbf{c} contained in spherical harmonics $Y_l^{(m)}(\hat{\mathbf{c}})$ (where \mathbf{c} is the electron velocity), the spatial distribution contained in $G_\mu^{(s\lambda)}$, the s -th application of the spatial gradient operator operating on $n(\mathbf{r}, t)$, and the speed distribution contained in an expansion discussed below [3]. Thus, we have

$$f(\mathbf{r}, \mathbf{c}, t) = \sum_{l=0}^{\infty} \sum_{m=-l}^l \sum_{s=0}^{\infty} \sum_{\lambda=0}^s \sum_{\mu=-\lambda}^{\lambda} f(lm|s\lambda\mu) Y_l^{(m)}(\hat{\mathbf{c}}) G_\mu^{(s\lambda)} n(\mathbf{r}, t). \quad (1)$$

The coefficients $f(lm|s\lambda\mu)$ are functions of the speed c and are obtained by the expansion

$$f(lm|s\lambda\mu) = \omega(T_b, c) \sum_{\nu=0}^{\infty} F(\nu lm|s\lambda\mu) R_{\nu l}(T_b, c), \quad (2)$$

where $\omega(T_b, c)$ is a Maxwellian distribution at a temperature T_b . T_b is not equal to the neutral gas temperature and serves as an adjustable parameter to optimize the convergence. $R_{\nu l}$ are related to a Sonine polynomial of order (ν, l) while the coefficients $F(\nu lm|s\lambda\mu)$ are the so-called moments that are relatively simply related to transport coefficients. The classical two term approximation (TTA) for solving the Boltzmann equation covers only the range in l of 0 and 1, which is not sufficient for good accuracy in noble-gas metal-vapors. Using the above decomposition of f (1), the Boltzmann equation is converted to a hierarchy of doubly infinite set of coupled algebraic equations for the moments. The resulting coefficient matrix is sparse and direct numerical inversion procedure is used to calculate the moments.

3.RESULTS AND DISCUSSIONS

The transport coefficients shown below are functions of E/n_0 and are expressed using the unit townsend ($1 \text{ Td} = 10^{-21} \text{ Vm}^{-1}$). In this work

we will cover a range of E/n_0 up to 1000 Td. The temperature of Hg vapor is varied between 0 and 8000 K. The internal states are assumed to be governed by a Maxwell-Boltzmann distribution which essentially places all metal-vapor atoms in the ground state for the temperatures considered. The effects of dimmers are not included. Cross sections for electron scattering in Na, K and Cs are taken from [4] while for Hg and Mg are taken from the Lxcat database [5].

In figure 1 (a) we show the variation of the mean energy with E/n_0 and gas temperature T , for electrons in Hg vapor. For lower E/n_0 the mean energy is different for different gas temperatures and only for $T = 8000$ K the electrons are in thermal equilibrium with the Hg vapor. This means that the electron velocity distribution is approximately thermal-Maxwellian. For increasing E/n_0 the effects of the gas temperature are less pronounced; the electron velocity distribution is non-equilibrium and non-Maxwellian though transport properties are still dependent on T . In the limit of higher E/n_0 , the electron swarm is far from thermal-equilibrium and the influence of the Hg vapor temperature can be neglected.

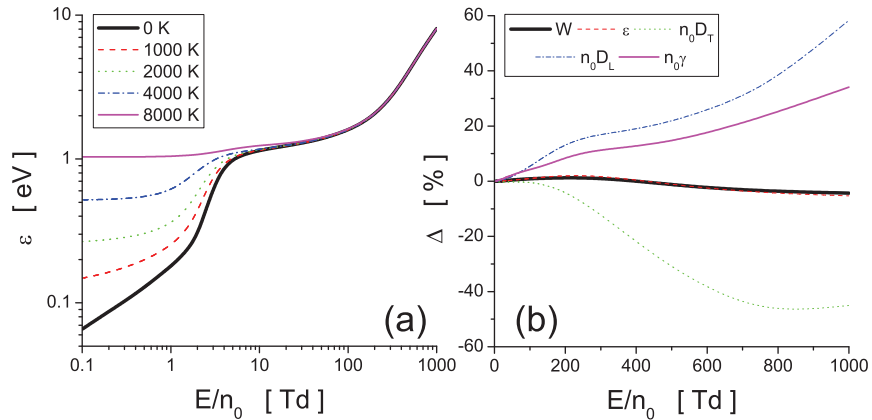


Figure 1. (a) Variation of the mean energy with E/n_0 and gas temperature T for electrons in Hg vapor. (b) Percentage difference between the two term and multi term results for various transport properties. The gas temperature is set to 293 K.

In figure 1 (b) we illustrate the errors associated with the TTA for solving the Boltzmann equation for electrons in Hg vapor. We observe that increasing E/n_0 deteriorates the accuracy of the TTA. For the chosen set of conditions, the mean energy and drift velocity have the errors of the order of 5% while the errors of the diffusion coefficients are much higher and are of the order of 50 %.

Figure 2 (a) shows the variation of the mean energy and drift ve-

locity with E/n_0 for electrons in various metal-vapors. For lower E/n_0 , we observe that the electrons are in thermal-equilibrium only with the K-vapor. The properties of the cross sections are reflected in the profiles of the mean energies. When elastic collisions are dominant, the mean energy grows very fast. Much slower rise of the mean energy is a consequence of the large energy loss of the electrons as the inelastic channels become important. Except for very low E/n_0 the mean energy in Hg vapor dominates the mean energies of electrons in other vapors.

From figure 2 (b) we see that for $E/n_0 \geq 6$ Td the drift velocity in Hg vapor dominates the drift velocities of electrons in other vapors. This suggests that plasma electrical conductivity will be the highest for Hg vapor.

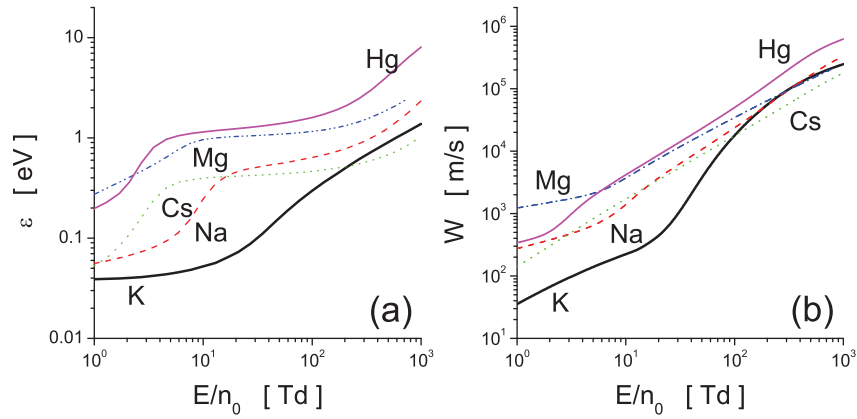


Figure 2. Variation of the mean energy (a) and drift velocity (b) with E/n_0 for electrons in metal-vapors. The gas temperature is $T = 298$ K.

REFERENCES

- [1] G.G. Lister, J.E. Lawler, W.P. Lapatovich and V.A. Godyak, Rev. Mod. Phys. 76 541 (2004)
- [2] A. Sobota, F. Manders, E.M. van Veldhuizen, J. van Dijk, and M. Haverlag, IEEE Trans. Plasma Sci. 38, 2289 (2010).
- [3] S. Dujko, R.D. White, Z.Lj. Petrović and R.E. Robson, Phys. Rev. E 81, 046403 (2010).
- [4] Al-Amin S A J, Lucas J, J. Phys. D: Appl. Phys. 21, 1261 (1988).
- [5] <http://fr.lxcat.net/home/>

THIRD-ORDER TRANSPORT COEFFICIENTS FOR ELECTRONS I. STRUCTURE OF SKEWNESS TENSOR

I. Simonović, Z.Lj. Petrović and S. Dujko

*Institute of Physics, University of Belgrade,
Pregrevica 118, 11080 Belgrade, Serbia*

Abstract. Third-order transport properties are calculated through a Monte Carlo simulation for electrons moving in an infinite gas under the influence of spatially homogeneous electric and magnetic fields. The structure of the skewness tensor and symmetries along individual elements are studied by means of a group projector technique.

1. INTRODUCTION

Electron transport in gases under the influence of electric and magnetic fields has long been of interest, with many scientific and technological applications. These applications have been usually modeled assuming hydrodynamic conditions, in which the electron flux was analyzed in terms of drift and diffusion terms. The truncation of the electron flux to low order transport coefficients, e.g., to the drift velocity and diffusion tensor, may be invalid for a number of reasons, such as the presence of sources and sinks or physical boundaries. Before applying the strict non-hydrodynamic treatment, it is desirable to analyze the high-order transport coefficients and it is important to develop methods for their calculations. This issue has been addressed by several authors in the context of an electric field only case. The semi-quantitative momentum transfer theory developed by Vrhovac *et al.* [1] and Monte Carlo simulation performed by Penetrante and Bardsey [2] were used to analyze the skewness tensor for electrons in rare gases. A three-temperature treatment of the Boltzmann equation and molecular dynamics simulation were used by Koutselos to calculate the third order transport coefficients of ions in atomic gases [3].

In this work we apply the group projector method [4] to investigate the structure of the skewness tensor and symmetries along its individual

elements when both the electric and magnetic fields are present. Using a Monte Carlo simulation technique, the longitudinal and transverse skewness coefficients are calculated for the ionization model of Lucas and Saelee [5].

2. THEORETICAL METHODS

The starting point in our analysis is the flux gradient relation

$$\mathbf{\Gamma}(\mathbf{r}, t) = \sum_{k=0}^{\infty} \Gamma^{(k+1)}(t) \odot (-\nabla)^k n, \quad (1)$$

and diffusion equation

$$\frac{\partial n(\mathbf{r}, t)}{\partial t} = \sum_{k=0}^{\infty} \omega^{(k)}(t) \odot (-\nabla)^k n. \quad (2)$$

where $n(\mathbf{r}, t)$ is the electron density while $\mathbf{\Gamma}(\mathbf{r}, t)$ is the electron flux. $\Gamma^{(k+1)}(t)$ are time dependent tensors of rank k and \odot denotes a k -fold scalar product.

As pointed out in [1] one should make a difference between microscopic and macroscopic transport coefficients. Microscopic bulk transport coefficient of an order k , $\omega^{(k)}(t)$, is a tensor of rank k , which multiplies the k -th gradient of concentration, in (2). Microscopic flux can be obtained from microscopic bulk by subtracting the term associated with the explicit effects of non-conservative collisions. Macroscopic flux transport coefficient of order k , $\Gamma^{(k)}(t)$, is a tensor of rank k , which in the flux gradient relation (1), multiplies the $(k - 1)$ -th gradient of concentration. These tensors are, starting from rank 3, symmetric by every permutation of indices, that does not change position of the first index, because all indices, except the first, are contracted with partial derivatives of concentration.

In this work, we consider a co-ordinate system in which the z -axis is defined by the electric field \mathbf{E} while the magnetic field \mathbf{B} lies along the z -axis (parallel field configuration) or along the y -axis (an orthogonal field configuration) or makes an angle ψ with \mathbf{E} and lies in the $y - z$ plane (an arbitrary field configuration). Using the method based on group projectors and identifying the symmetries along the individual elements of the skewness tensor we have determined the following structures of the tensor depending on the field configuration:

1. Electric field only configuration ($\mathbf{E} = E e_z$):

$$\begin{aligned} Q_{x|ij} &= \begin{pmatrix} 0 & 0 & Q_{xxz} \\ 0 & 0 & 0 \\ Q_{xxz} & 0 & 0 \end{pmatrix}, & Q_{y|ij} &= \begin{pmatrix} 0 & 0 & 0 \\ 0 & 0 & Q_{xxz} \\ 0 & Q_{xxz} & 0 \end{pmatrix}, \\ Q_{z|ij} &= \begin{pmatrix} Q_{zxx} & 0 & 0 \\ 0 & Q_{zxx} & 0 \\ 0 & 0 & Q_{zzz} \end{pmatrix}. \end{aligned} \quad (3)$$

2. Parallel field configuration ($\mathbf{E} = E\mathbf{e}_z$, $\mathbf{B} = B\mathbf{e}_z$):

$$\begin{aligned} Q_{x|ij} &= \begin{pmatrix} 0 & 0 & Q_{xxz} \\ 0 & 0 & Q_{xyz} \\ Q_{xxz} & Q_{xyz} & 0 \end{pmatrix}, & Q_{y|ij} &= \begin{pmatrix} 0 & 0 & -Q_{xyz} \\ 0 & 0 & Q_{xxz} \\ -Q_{xyz} & Q_{xxz} & 0 \end{pmatrix}, \\ Q_{z|ij} &= \begin{pmatrix} Q_{zxx} & 0 & 0 \\ 0 & Q_{zxx} & 0 \\ 0 & 0 & Q_{zzz} \end{pmatrix}. \end{aligned} \quad (4)$$

3. Crossed field configuration ($\mathbf{E} = E\mathbf{e}_z$, $\mathbf{B} = B\mathbf{e}_y$):

$$\begin{aligned} Q_{x|ij} &= \begin{pmatrix} Q_{xxx} & 0 & Q_{xxz} \\ 0 & Q_{xyy} & 0 \\ Q_{xxz} & 0 & Q_{xzz} \end{pmatrix}, & Q_{y|ij} &= \begin{pmatrix} 0 & Q_{yxy} & 0 \\ Q_{yxy} & 0 & Q_{yyz} \\ 0 & Q_{yyz} & 0 \end{pmatrix}, \\ Q_{z|ij} &= \begin{pmatrix} Q_{zxx} & 0 & Q_{zxx} \\ 0 & Q_{zyy} & 0 \\ Q_{zxx} & 0 & Q_{zzz} \end{pmatrix}, \end{aligned} \quad (5)$$

where $i, j = x, y, z$. For an arbitrary field configuration, $Q_{ijk} = Q_{ikj}$ for any individual element of the skewness tensor.

3. RESULTS AND DISCUSSIONS

In the hydrodynamic regime the skewness tensor is given by

$$\mathbf{Q}_{abc} = \frac{1}{3!} \frac{d}{dt} \langle \mathbf{r}_a^* \mathbf{r}_b^* \mathbf{r}_c^* \rangle, \quad (6)$$

where (a, b, c) take values from the set $\{x, y, z\}$ while the angular brackets $\langle \rangle$ denote ensemble averages in configuration space and $\mathbf{r}^* = \mathbf{r} - \langle \mathbf{r} \rangle$. From (3) it is clear that \mathbf{Q} has seven non-vanishing elements, three of which are independent, Q_{zzz} , $Q_{zxx} = Q_{zyy}$ and $Q_{xzx} = Q_{xxz} = Q_{yzy} = Q_{yyz}$. Due to direct sampling of swarm dynamic properties in our Monte Carlo code only two independent components of the skewness tensor can be isolated, the longitudinal skewness coefficient $Q_L = Q_{zzz}$ and transverse skewness coefficient $Q_T = Q_{zxx} + Q_{xzx} + Q_{xxz} = Q_{zyy} + Q_{yzy} + Q_{yyz}$.

In Fig. 1 we show the variation of $n_0^2 Q_L$ with E/n_0 for the ionization model of Lucas Saelee. We see that $n_0^2 Q_L$ monotonically decreases with increasing E/n_0 and/or with increasing parameter F . For the conservative case ($F = 0$) gas model is reduced to elastic and excitation cross sections and no ionization occurs while for non-conservative case ($F = 1$) the gas model consists of elastic and ionization cross sections and no excitation occurs. In this model, for increasing E/n_0 the collision frequency for inelastic collisions is also increased while the collision frequency for the momentum transfer in elastic collisions remains unaltered. This suggests that for increasing E/n_0 inelastic collisions tend to reduce $n_0^2 Q_L$. A decrease

in $n_0^2 Q_L$ with increasing F is a clear sign that the skewness coefficients are more sensitive than the lower order transport coefficients with respect to small variation in the distribution function induced by the ionization cooling.

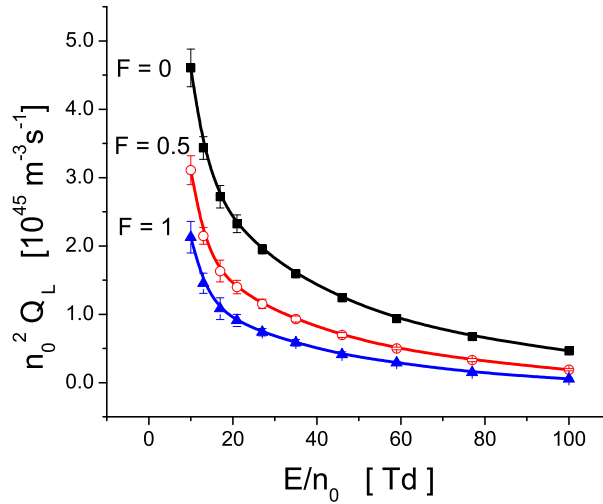


Figure 1. Variation of the longitudinal skewness coefficient with E/n_0 for three different ionization models as indicated on the graph.

Acknowledgments

This work was supported by MPNTRRS Projects OI171037 and III41011.

REFERENCES

- [1] S.B. Vrhovac, Z.Lj. Petrović, L.A. Viehland and T.S. Santhanam, *J. Chem. Phys.* 110, 2423 (1999).
- [2] B.M. Penetrante and J.N. Bardsley, in *Non-equilibrium Effects in Ion and Electron Transport*, edited by J.W. Gallagher, D.F. Hudson, E. E. Kunhardt, and R.J. Van Brunt, (Plenum, New York, 1990), p. 49.
- [3] A.D. Koutselos, *Chem. Phys.* 315, 193 (2005).
- [4] A.O. Barut and R. Raczka, *Theory of group representations and applications* (World Scientific, Singapore, 1986).
- [5] J. Lucas and H. Saelee, *J. Phys. D: Appl. Phys.* 8, 640 (1975).

THIRD-ORDER TRANSPORT COEFFICIENTS FOR ELECTRONS II. MOLECULAR GASES

I. Simonović, Z.Lj. Petrović and S. Dujko

*Institute of Physics, University of Belgrade,
Pregrevica 118, 11080 Belgrade, Serbia*

Abstract. A Monte Carlo simulation technique is used to calculate the third-order transport coefficients for electrons and positrons in molecular gases. Values and general trends of the longitudinal and transverse skewness coefficients as a function of the reduced electric field in N_2 , CH_4 and CF_4 are reported here. We investigate the way in which the skewness transport coefficients are influenced by the energy dependence of cross sections for electron/positron scattering. Correlations between the skewness and diffusion coefficients have been found and studied.

1. INTRODUCTION

Studies of third-order transport coefficients for charged particles in gases are very useful under conditions when transport is greatly affected by non-conservative collisions and/or under conditions when the truncation of the charged particle flux to low order transport coefficients is not sufficient for accurate description of transport phenomena. There is a huge body of data for electrons (and ions), and since recently even for positrons, when it comes to low order transport coefficients, including the drift velocity and diffusion tensor, and rate coefficients. In contrast, little is known about high-order transport coefficients, particularly for electrons and positrons. This is understandable having in mind that the traditional swarm experiments have been interpreted without the consideration of high order transport [1], though it has been suspected to influence the motion of the electrons [2] and ions [3]. Third-order transport coefficients are most likely to be measured in the near future and hence it is of great importance to develop methods for their theoretical calculations. Such information can help in the design of future experiments as well as in the interpretation of their results.

The aims of this work are (1) to provide Monte Carlo calculations of the skewness transport coefficients for electrons and positrons in molecular gases, (2) to investigate the correlations between skewness and low order transport coefficients (e.g., the drift velocity and diffusion tensor), and (3) to study the explicit and implicit effects of non-conservative collisions on the skewness transport properties. In section 2 we give a brief discussion of our Monte Carlo method while in section 3 we present a few examples of our results for electrons in N_2 .

2. THEORETICAL METHODS

The Monte Carlo code applied in this work follows a large number of particles (usually 10^7 and sometimes even more) moving in an infinite gas under the influence of spatially homogeneous electric field. Particles (positrons or electrons) gain energy from the electric field and dissipate this energy through binary collisions with background neutral particles. The charged particle interactions are neglected since the transport is considered in the limit of low charged-particle density. All calculations are performed at zero gas temperature. For more details about our Monte Carlo simulation code see recent reviews [4, 5].

Skewness transport coefficients are determined after relaxation to steady state. The bulk values are calculated using the following formulas:

$$Q_L^{(B)} = \frac{1}{3!} \frac{d}{dt} (\langle z^3 \rangle - 3\langle z \rangle \langle z^2 \rangle + 2\langle z \rangle^3), \quad (1)$$

$$Q_T^{(B)} = \frac{1}{3!} \frac{d}{dt} (\langle zy^2 \rangle - \langle z \rangle \langle y^2 \rangle), \quad (2)$$

while the corresponding flux components are determined as follows:

$$Q_L^{(F)} = \frac{1}{3!} (3\langle z^2 V_z \rangle - 3\langle V_z \rangle \langle z^2 \rangle - 6\langle z \rangle \langle z V_z \rangle + 6\langle V_z \rangle \langle z \rangle^2), \quad (3)$$

$$Q_T^{(F)} = \frac{1}{3!} (\langle y^2 V_z \rangle + 2\langle zy V_y \rangle - \langle y^2 \rangle \langle V_z \rangle - 2\langle z \rangle \langle y V_y \rangle), \quad (4)$$

where indices B and F refer to *bulk* and *flux*. We consider a coordinate system in which the electric field lies along the z -axis.

3. RESULTS AND DISCUSSIONS

In figure 1 we show the variation of the longitudinal and transverse skewness coefficients, $n_0^2 Q_L$ and $n_0^2 Q_T$, respectively, with E/n_0 for electrons in N_2 . In order to understand the correlation between skewness and diffusion coefficients, on the same figure we show the variation of the longitudinal and transverse, $n_0 D_L$ and $n_0 D_T$, diffusion coefficients with E/n_0 . For lower E/n_0 , less than 40 Td, we observe that $n_0 D_L$ is a decreasing function

of E/n_0 . For the same E/n_0 , $n_0^2 Q_L$ decreases markedly. For $E/n_0 \geq 40$ Td, $n_0 D_L$ is a monotonically increasing function of E/n_0 while $n_0^2 Q_L$ increases with increasing E/n_0 , reaching a peak, and then it starts first to decrease and then again to increase. If we take a careful look, we see that after reaching the peak, $n_0^2 Q_L$ is decreased when the profile of $n_0^2 Q_L$ is changed from a typical convex to a more concave profile. This illustrates high sensitivity of $n_0^2 Q_L$ with respect to the collisional process that control the behavior of diffusion along the field direction. For $E/n_0 \geq 400$ Td both $n_0 D_L$ and $n_0^2 Q_L$ are monotonically increasing functions of E/n_0 . From the profile of $n_0^2 Q_T$, we see that the transverse skewness coefficient is correlated very well with both $n_0 D_L$ and $n_0 D_T$. This applies for electrons in N_2 ; for electrons in CF_4 we have identified the regions of E/n_0 where $n_0^2 Q_T$ exhibits better correlation with $n_0 D_T$ than with respect to $n_0 D_L$.

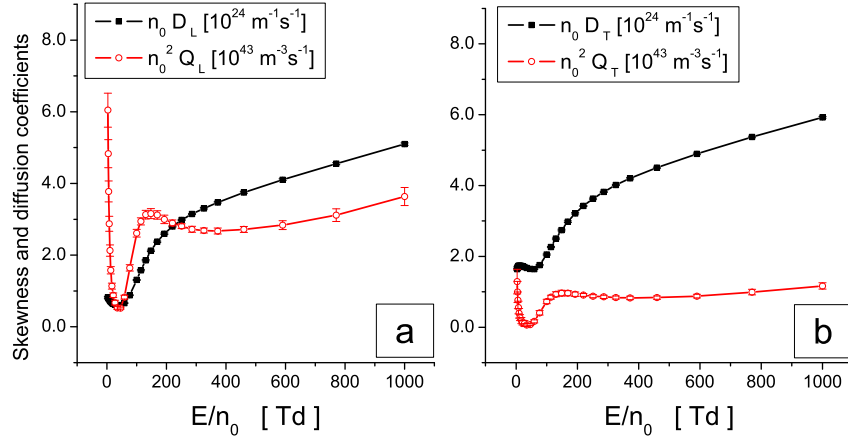


Figure 1. Variation of the longitudinal skewness and longitudinal diffusion coefficients with E/n_0 (a) and variation of the transverse skewness and transverse diffusion coefficients with E/n_0 (b) for electrons in N_2 .

Figure 2 displays the variation of the bulk and flux values of $n_0^2 Q_L$ (a) and $n_0^2 Q_T$ (b) with E/n_0 for electrons in N_2 . Increasing E/n_0 results in a more pronounced distinction between bulk and flux values. The explicit effects of ionization on the skewness properties become clearly evident for $E/n_0 \geq 150$ Td. For both $n_0^2 Q_L$ and $n_0^2 Q_T$ the bulk values overestimate the corresponding flux values and this is exactly what has been previously observed for the drift and diffusion in N_2 [6]. The differences between bulk and flux values do not exceed 60% for both $n_0^2 Q_L$ and $n_0^2 Q_T$ for E/n_0 considered in this work. Better understanding of the explicit effects of ionization on the skewness transport properties requires knowledge of the spatially resolved data along the swarm, particularly those associated with the high-order variations of the average energy.

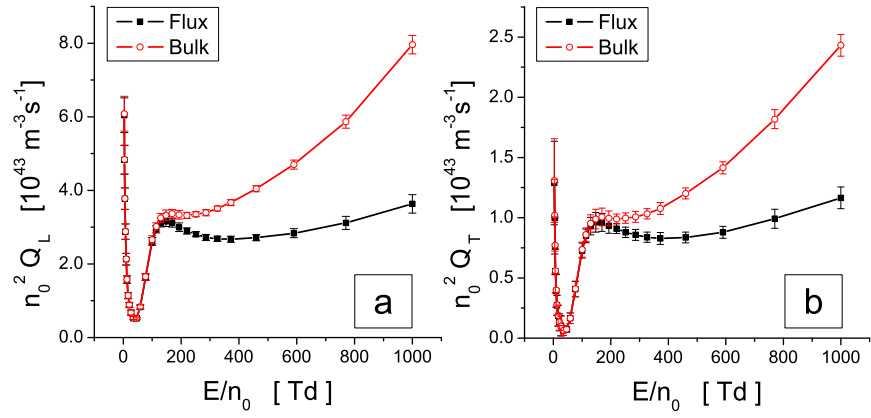


Figure 2. Variation of the bulk and flux longitudinal (a) and transverse (b) skewness coefficients with E/n_0 for electrons in N_2 .

Acknowledgments

This work was supported by MPNTRRS Projects OI171037 and III41011.

REFERENCES

- [1] L.G.H. Huxley and R.W. Crompton, *The Drift and Diffusion of Electrons in Gases* (New York: Wiley Interscience, 1973).
- [2] B.M. Penetrante and J.N. Bardsley, in *Non-equilibrium Effects in Ion and Electron Transport*, edited by J.W. Gallagher, D.F. Hudson, E. E. Kunhardt, and R.J. Van Brunt, (Plenum, New York, 1990), p. 49.
- [3] A.D. Koutselos, *Chem. Phys.* 270, 165 (2001).
- [4] S. Dujko, Z.M. Raspopović and Z.Lj. Petrović, *J.Phys.D: Appl. Phys.* 38, 2952 (2005).
- [5] S. Dujko, R.D. White and Z.Lj. Petrović, *J.Phys.D: Appl. Phys.* 41, 245205 (2008).
- [6] S. Dujko, U. Ebert, R.D. White and Z.Lj. Petrović, *Jpn. J. Appl. Phys.* 50, 08JC01 (2011).

BENCHMARK CALCULATIONS FOR SPATIALLY RESOLVED ELECTRON TRANSPORT DATA

Z.M. Raspopović¹, S. Dujko¹, R.D. White², T. Makabe³ and Z.Lj. Petrović¹

¹*Institute of Physics, University of Belgrade, Pregrevica 118, 11080 Belgrade, Serbia*

²*ARC Centre for Antimatter-Matter Studies, School of Electrical Engineering and Physical Sciences, James Cook University, 4810 Townsville, Australia*

³*Faculty of Science and Technology, Keio University, Yokohama 223-8522, Japan*

Abstract. A Monte Carlo simulation technique is used to produce accurate benchmark calculations for spatially resolved electron transport data in model and real gases in the presence of electric and magnetic fields. The spatial variation of the swarm parameters is investigated under conditions when electron transport is greatly affected by magnetic field and non-conservative collisions. The results of Monte Carlo simulations for the averaged energy and coefficients in its density gradient expansion are in a very good agreement with those predicted by a multi term solution of Boltzmann's equation.

1. INTRODUCTION

Studies of charged-particle swarms moving in an infinite gas in electric and magnetic fields is a topic of great interest both as a problem in basic physics and as a problem important for many technological applications. One of the major challenges in these investigations is an accurate representation of temporal and spatial relaxation of charged-particle swarms in gases when both the electric and magnetic fields are present. Relaxation and transient processes of a swarm of charged particles are related to various problems of gaseous electronics such as modeling of non-equilibrium plasma discharges, high-speed switching technique and physics of gas lasers [1].

In this work we apply a Monte Carlo simulation technique to follow spatiotemporal development of electron swarms acted upon by electric and magnetic fields. The aims of this work are (1) to provide accurate benchmark calculations for spatially resolved swarm data, (2) to investigate transient effects in both time and space during the process of relaxation, and (3) to study the synergism of magnetic fields and non-conservative collisions on spatiotemporal swarm development. In Section 2 we briefly discuss the sampling technique implemented in our Monte Carlo code and basic elements of a theory for solving

the Boltzmann equation. Benchmarks and associated discussions are presented in Section 3.

2. THEORETICAL METHODS

In this paper, we apply a Monte Carlo simulation code that follows a large number of particles (typically 10^6 – 10^7) through a neutral gas under the influence of uniform and crossed electric and magnetic fields. In order to sample the spatially resolved transport data in our Monte Carlo simulations, the computational domain is restricted to 6σ where σ is the standard deviation of the Gaussian distribution in space. This domain is divided into cells. Every cell contains 100 points and these points are used as exact locations where swarm properties are sampled. The spatially resolved swarm parameters are determined by counting the electrons and their properties in every cell.

In particular, in this work we present comparison between our Monte Carlo simulations and Boltzmann equation analysis for the averaged energy and coefficients in its density gradient expansion calculated by Monte Carlo method and Boltzmann equation. The average energy plays an important role in understanding various phenomena associated with the drift and diffusion. Under hydrodynamic conditions, the density gradient expansion of the average energy is given by

$$\varepsilon(\mathbf{r}, t) = \sum_{k=0}^{\infty} \varepsilon_k (-\nabla)^k n(\mathbf{r}, t) = \varepsilon_0 + \boldsymbol{\gamma} \cdot \frac{\nabla n}{n} + \dots,$$

where $n(\mathbf{r}, t)$ is the electron number density, ε_0 is the spatially homogeneous mean energy and $\boldsymbol{\gamma}$ is the energy gradient vector. The components of $\boldsymbol{\gamma}$ are calculated from the moments of the distribution function in our Boltzmann equation analysis. Explicit expressions for the moments and basic elements of a theory for solving the Boltzmann equation are given in [2]. The same quantities are determined from our Monte Carlo simulations as a slope of the average energy along the swarm and/or by direct sampling. The explicit expressions for sampling in Monte Carlo simulations are given in [3]. In a crossed field configuration, $\boldsymbol{\gamma}$ has two independent components, one along the electric field direction and another one along the $\mathbf{E} \times \mathbf{B}$ direction.

3. RESULTS AND DISCUSSION

In figure 1 we show the spatial profile of electrons and spatially resolved averaged energy along the electric field direction, the $\mathbf{E} \times \mathbf{B}$ direction and along the magnetic field direction for the instants 0.1, 10 and 100 ns. Calculations have been performed by our Monte Carlo simulation code for the Reid ramp model [4].

In the early stage of relaxation and the instant of time 0.1 ns, from the spatial profiles of electrons we observe that the swarm is localized in space due to the explicit orbital effects which act to inhibit diffusion in a plane

perpendicular to the magnetic field. Local peaks in the profiles are induced by the magnetic field. Likewise, from the profile of the average energy along the electric field direction, we see that magnetic field controls the low-energy electrons. The profile along the magnetic field direction is parabolic although the Lorentz force does not act along this direction.

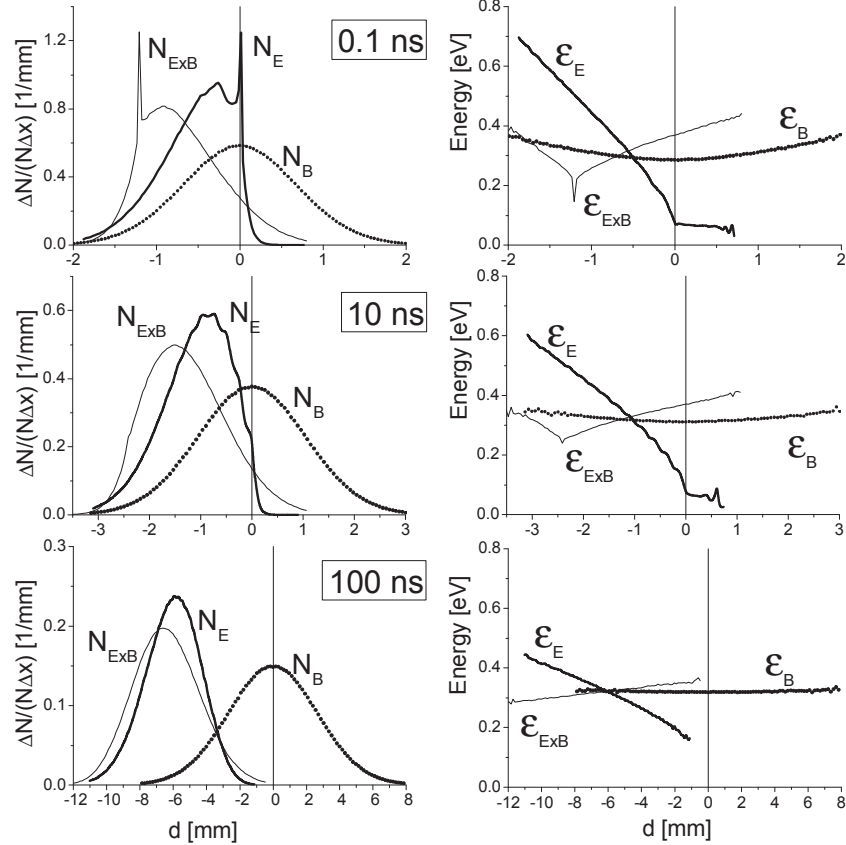


Figure 1. Spatially resolved profiles of the electrons (left column) and spatially averaged energy (right column) for electrons in the Reid ramp model at times 0.1, 10 and 100 ns. The applied reduced electric and magnetic fields are, 24 Td and 200 Hx, respectively ($1 \text{ Td} = 10^{-21} \text{ Vm}^2$; $1 \text{ Hx} = 10^{-27} \text{ Tm}^3$).

For the instant 10 ns, the existence of oscillatory feature in the profile of spatial distribution of electrons along the electric field is clearly evident. The nature of these oscillations is similar to those observed in the steady-state Townsend and Franck-Hertz experiments [3]. There are no oscillations along the $\mathbf{E} \times \mathbf{B}$ direction, nor along the magnetic field direction. The spatial profiles of electrons are asymmetric. The profile along the electric field direction is narrower and higher than the profile along the $\mathbf{E} \times \mathbf{B}$ direction and hence more localized in space.

For the instant 100 ns, the swarm parameters are fully relaxed. There are no oscillations in the spatial profile of electrons along the electric field direction. The profiles of the averaged energy along the electric field and $\mathbf{E} \times \mathbf{B}$ directions have characteristic slopes while the distribution of the average energy along the magnetic field direction is uniform as Lorentz force does not act along this direction. It is important to note that the slope of the average energy along the electric field direction is much higher than the slope of the average energy along the $\mathbf{E} \times \mathbf{B}$ direction.

In Table 1 we show comparison of the energy gradient vector components for the Reid ramp model using the Monte Carlo simulations and Boltzmann equation analysis. The agreement is very high, validating the theoretical basis and numerical integrity of our Monte Carlo code and multi term code for solving the Boltzmann equation.

Table 1. A comparison of the energy gradient vector components for the Reid ramp model using Monte Carlo simulations and a Boltzmann equation analysis. The applied reduced electric field is 12 Td and we consider a crossed field configuration.

B/n ₀ (Hx)	MC	BE	δ (%)	MC	BE	δ (%)
	$n_0 \gamma_E$ (kgs ⁻²)	$n_0 \gamma_E$ (kgs ⁻²)		$n_0 \gamma_{E \times B}$ (kgs ⁻²)	$n_0 \gamma_{E \times B}$ (kgs ⁻²)	
50	-0.3576	-0.3551	0.7	-0.0358	-0.0369	3.0
200	0.2637	0.2634	0.1	-0.0740	-0.0739	0.1
500	-0.0874	-0.0872	0.2	-0.0086	-0.0087	1.1

Acknowledgements

This work was supported by MPNTRRS Projects OI171037 and III41011, and by Australian Research Council.

REFERENCES

- [1] S. Dujko, R.D. White, Z.M. Raspopović and Z.Lj. Petrović, Nucl. Instr. Meth. B 279 84 (2012).
- [2] S. Dujko, R.D. White, Z.Lj. Petrović and R.E. Robson, Phys. Rev. E 81 046403 (2010).
- [3] S. Dujko, R.D. White and Z.Lj. Petrović, J. Phys. D: Appl. Phys. 41, 245205 (2008).
- [4] I. Reid, Aust. J. Phys. 32, 231 (1979).

CROSS SECTIONS AND TRANSPORT PARAMETERS OF O^- IONS IN WATER VAPOUR

V. Stojanović, Z. Raspopović, D. Marić and Z. Lj. Petrović

Institute of Physics, University of Belgrade, Pregrevica 118, Serbia

Abstract. The transport properties of O^- ions in water vapour in DC fields were obtained by using Monte Carlo simulation technique with the scattering cross section sets assembled on the basis of Nanbu's technique and available experimental data. In this work we present the mean energy and the reduced mobility for the conditions of low to moderate reduced electric fields E/N (N -gas density) accounting for the non-conservative collisions.

1. INTRODUCTION

Interest in application of plasmas in medicine, nanotechnologies and environmental remediation [1-5] has drawn attention to studies of discharges in water and in proximity to water [6]. Current studies show that in such systems, discharge is produced in water vapour either from evaporating liquid electrode or in bubbles created by an induced phase transition within the liquid. More generally, all atmospheric discharges contain some degree of water vapour. It is therefore of increased interest to determine how discharges are created in water [7-9]. Until recently it has been thought that discharges can only be formed in water vapor resulting from an induced phase transition. Therefore an initial point must be to have accurate knowledge of the electrical properties of water vapor and in particular its breakdown potential [10,11]. Complicated chemistry and poor data for a range of processes of particles interacting with gas and surface require further insights and more data. In this work our intention is to study energy dependent scattering probabilities of O^- ions in H_2O gas and to explore effects of non- conservative processes on transport properties of the O^- ions.

2. CROSS SECTION SETS

The scattering cross sections of O^- on H_2O molecule, measured by Hasted and Smith [12] for electron detachment (DET) and Lifshitz [13] for other low energy processes, are presented in Fig. 1.a) (thick lines) and listed in Table 1. A simple cross section set (S1) is completed based on these experimental data and applying appropriate linear extrapolations [see thin lines in Fig. 1.a)]. Note that in our extrapolations we have taken into account that polarisation and dipole

forces are expected to be important over the energy range from 20 meV to few eV.

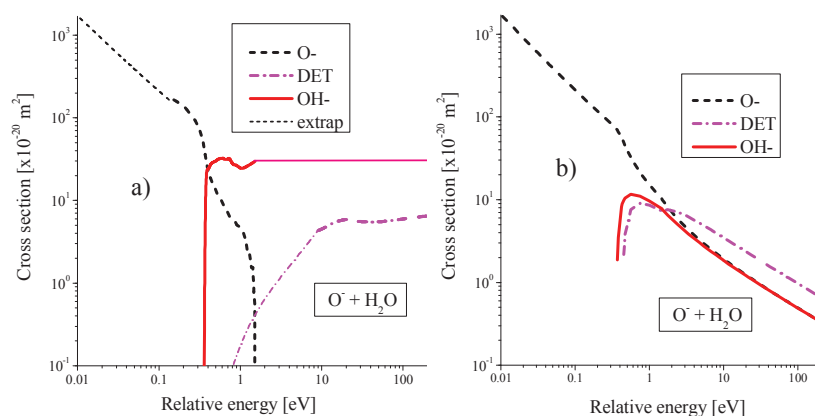


Figure 1. Cross section set of O^- ions in H_2O based on a) available experimental data (S1) with extrapolations, b) Nanbu theory (S2).

We have also calculated a cross section set by using Nanbu's theory [14-15] (S2) which is modified to treat endothermic reactions with polar molecules by the locked dipole model [16]. In Nanbu's theory reactive collision is treated by selecting the thermodynamic threshold energy and branching ratio according to the Rice-Rampersperger-Kassel (RRK) theory [14]. Obtained cross sections were corrected to fit reduced mobility obtained by SACM (Statistical Adiabatic Channel Model) approximation [Fig. 1.b)].

We have used data for polarizability and dipole moment of H_2O as used by Clary [17] and selected heats of formation and electron affinities from Ref. [18]. Threshold for electron detachment (DET) has been taken from Ref. [19].

The most probable reaction paths are shown in Table 1. We found them relevant for the selected domain of low O^- energies in water vapour.

Table 1. The list of products and the corresponding thermodynamic threshold energies Δ for reaction $O^- + H_2O$.

No	Reaction products	Δ (eV)
1	$O^- + H_2O$ (EL)	0.0
2	$OH^- + OH$	-0.36
3	$H_2O_2 + e^-$ (DET)	-0.43
	$O + H_2O + e^-$	-1.46

Moreover the usually applied procedure would be to unfold the cross sections from the measured transport coefficients and thermo-chemical data in a separate drift tube experiment but to our knowledge no such data are available.

Monte Carlo technique was applied to perform calculations of transport parameters as well as rate coefficients in DC electric fields. In this paper we have used a Monte Carlo code that properly takes into account the thermal collisions [20].

3. RESULTS AND DISCUSSION

Bulk values of drift velocity [15] are used to obtain the reduced mobility for two selected cross section sets as shown in Fig. 2.a) for a range of reduced electric fields E/N (E -electric field, N -gas density) including the range where the effects of the charge transfer collisions take place. As expected, excellent agreement is achieved for the lowest field reduced mobility where the same trend for both cross section sets exists. Reactive processes with low thresholds gradually split the two curves. At the end of our E/N scale the difference appears as a consequence of very different total cross sections at highest energies. We also show the mean energy, a parameter which cannot be directly measured in experiments but a mean energy as a function of E/N may be used directly to provide the input data in fluid models especially when the local field approximation fails. The mean energies for two cross section sets overlap up to 100 Td where slow rise of energy is obtained due to the disappearance of the O^- in the process of producing OH^- . As shown in Figure 2.b) mean energy increase with E/N from about 20 Td at room temperature. Significant increase of mean energy with E/N for the S2 with respect to the S1 is due to a significant fall of the reactive cross section with energy for S2.

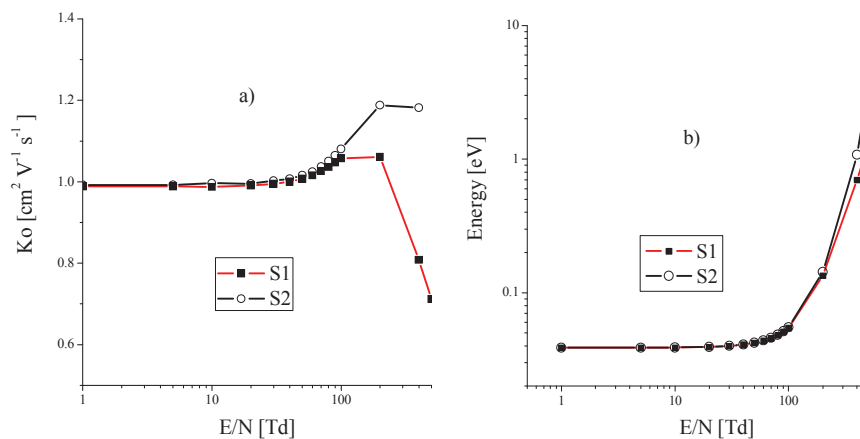


Figure 2. a) Reduced mobility, and b) mean energy, for O^- ions in water vapour as a function of E/N obtained by Monte Carlo simulation at $T=300$ K.

Acknowledgements

This work is partly supported by MESTD of Republic Serbia projects No's 171037 and 410011.

REFERENCES

- [1] K. R. Stalder, G. Nersisyan and W. G. Graham, *J. Phys. D: Appl. Phys.* **39** 3457 (2006).
- [2] T. Makabe and Z. Petrović *Plasma Electronics: Applications in Microelectronic Device Fabrication* (Boca Raton, FL: Taylor&Francis, 2006)
- [3] M. Laroussi, *Plasma Process. Polym.* **2**, 391 (2005).
- [4] S. Lazović, N. Puač, M. Miletić, D. Pavlica, M. Jovanović, D. Bugarski, S. Mojsilović, D. Maletić, G. Malović, P. Milenković, and Z. Lj. Petrović, *New J. Phys.* **12**, 083037 (2010).
- [5] K. Kutasi and J. Loureiro, *J. Phys. D* **40**, 5612 (2007).
- [6] P. Bruggeman, D. Schram, M. Á. González, R. Rego, M. G. Kong, and C. Leys, *Plasma Sources Sci. Technol.* **18**, 025017 (2009); P. Bruggeman and C. Leys, *J. Phys. D: Appl. Phys.* **42** 053001 (2009).
- [7] G. Ruíz-Vargas, M. Yousfi, and J. de Urquijo, *J. Phys. D* **43**, 455201 (2010).
- [8] Y. Itikawa and N. Mason, *J. Phys. Chem. Ref. Data* **34**, 1 (2005).
- [9] R. E. Robson, R. D. White, and K. F. Ness, *J. Chem. Phys.* **134**, 064319 (2011).
- [10] N. Škoro, D. Marić, G. Malović, W. G. Graham, and Z. Lj. Petrović, *Phys. Rev. E* **84**, 055401(R) (2011).
- [11] M. Radmilović-Radenović, B. Radenović, Ž. Nikitović, Š. Matejčik and M. Klas, *Nucl. Instr. Meth. in Phys. Res. B* **279** 103 (2012).
- [12] J.B. Hasted, R.A. Smith, *Proc. Roy. Soc. Lond. A*, Vol. 235, No.1202 349 (1956).
- [13] C. Lifshitz, *J. Phys. Chem.* **86**, 3634 (1982).
- [14] K. Denpoh and K. Nanbu, *J. Vac. Sci. Technol. A* **16** 1201 (1998).
- [15] Z.Lj. Petrović, Z.M. Raspopović, V.D. Stojanović, J.V. Jovanović, G. Malović, T. Makabe, J. De Urquijo, *Appl. Surf. Sci.* **253** 6619 (2007).
- [16] J.V. Dugan and J.L. Magee, *J. Chem. Phys.* **47** 3103 (1967).
- [17] D.C. Clary, *Chem. Phys. Lett.* **232** 267 (1995).
- [18] UMIST RATE12 astrochemistry.net \ape.jb.man.ac.uk\.
- [19] F. C. Fehsenfeld and E. E. Ferguson, *J. Chem. Phys.*, **61** 3181 (1974).
- [20] Z. Ristivojević and Z.Lj. Petrović, *Plasma Sources Sci. Technol.* **21** 035001 (2012).

SWARM ANALYSIS OF TRANSPORT DATA FOR ELECTRONS IN DIMETHYL ETHER (CH₃OCH₃)

Snježana Dupljanin^{1,2}, Olivera Šašić^{2,3} and Zoran Lj. Petrović²

¹*University of Banja Luka, Faculty of Science, M. Stojanovica 2, Banja Luka, Bosnia and Herzegovina*

²*University of Belgrade, Institute of Belgrade, PO Box 86, 11080 Zemun, Serbia*

³*University of Belgrade, The Faculty for Traffic and Transport Engineering, Vojvode Stepe 305, 11000 Belgrade, Serbia*

Abstract. In this paper we present a set of electron scattering cross sections with dimethyl ether (CH₃OCH₃, DME) molecule, obtained by the standard swarm procedure. Experimental data for drift velocity (W) and the density normalized ionization coefficient (α/N) for the pure gas as well as for its mixtures with Ar and Ne available from the literature are compared with the numeric solution of the Boltzmann equation and with the results of Monte Carlo simulations over the wide range of reduced electric fields (E/N). Analysis shows that the initial cross section set, which is used as an input in our calculations, has to be modified in order to fit experimental data.

1. INTRODUCTION

Dimethyl ether is an organic molecule that has extensive applications primarily in the industry, as an alternative fuel for diesel engines and substitute for propane. Beside that, DME is one of the largest organic molecules in the interstellar space with a significant concentration in the star-forming regions [1]. Also, it is used for particle detectors, especially for the micro-strip gas chambers (MSGC) [2,3] for detection of weakly ionizing particles, i.e. as a tracker in high energy physics [4]. Therefore, a database of the transport properties and cross sections for electron-DME interaction would help in selection of the gas mixture composition required for optimal performance of tracking detectors through detailed modeling of discharge in such gas. However, review of the existing literature shows that such data sets are scarce. There are few measurements of the drift velocity in pure DME and its mixtures with He and Ar obtained by the Time of Flight [5, 6] and by the Pulsed Townsend [7, 8] technique, as well as for the Townsend ionization coefficient [8, 9]. As to our knowledge, the only available set of cross sections is that of S. Biagi [10]. Since the cross sections of Biagi were not documented in a published paper so little is known what was used to produce them.

Our work is an attempt to provide a cross section set by using the swarm procedure for determining the cross sections and available transport data. Swarm procedure is an iterative process of adjusting the initially selected cross sections in order to achieve their consistency with the measured transport parameters. This technique proved to be exceptionally accurate for the low energy electrons [11]. It is also applicable in the range of moderate and high electron energies if the experimental results for ionization coefficients exist. Namely, the sensitivity of the high-energy tail of the electron energy distribution function to energy losses below the ionization threshold [12] allows one to renormalize the excitation cross sections.

1.1 Numerical techniques and the input data

Transport coefficients presented in this paper were calculated by using two computer codes. The first one (*Elendif*, [13]) solves the Boltzmann equation in a version of the two-term approximation (TTA). Despite the fact that there are many controversies concerning the applicability of this approximation [14, 15] it is proved to be a very useful tool in numerous trials of adjusting cross sections. The second code provides the results without the limit in accuracy and it is based on the Monte Carlo (MC) technique. The MC code used here is fully developed and well tested on numerous benchmark models [16, 17].

As an initial input in both codes, we have used the following cross section sets for: DME- the set developed by S. Biagi [10], Argon- the set of Hayashi [18] and Ne- set by Morgan [18]. The compositions of the mixtures were 20% and 50% of DME in Ar, and 50% of DME in Ne. The density of the background gas was chosen to be $3.54 \times 10^{22} \text{ m}^{-3}$ or 1 Torr (133.3 Pa) at the gas temperature of 273 K but the results are not dependent on the gas density, only on E/N. The initial number of electrons in each MC simulation was 2.5×10^5 , the E/N was varied over a range defined by the available transport data (from 1 to 300 Td, $1 \text{ Td} = 10^{-21} \text{ Vm}^2$). All electron scattering was assumed to be.

It is important to emphasize that in each cycle of adjusting the cross sections we calculated both drift velocity and ionization coefficients for the case of pure gas, as well as for the mixtures with Ar and Ne, in order to achieve the best fit to experimental results for all cases simultaneously.

2. RESULTS AND CONCLUSIONS

In this paper we show only few results that we have obtained. All the calculated cross sections, transport and rate coefficients for individual processes will be available at <http://mail.ipb.ac.rs/~cep/ipb-cnp/ionsweb/index.htm>.

Figure 1 shows the comparison of the initial cross sections with the final set of cross sections that is the result of our investigation. As it can be seen, we have modified the elastic momentum transfer cross section, the vibrational excitation with the threshold energy of 0.349 eV, and the lower electronic excitations (7.7 eV). One can see (Figure 2) that modified set provides a better agreement between calculated and measured data than the initial set. Our study

showed that while alterations in drift velocity appear to be small, the ionization coefficient needed a revision especially having in mind its key role in applications.

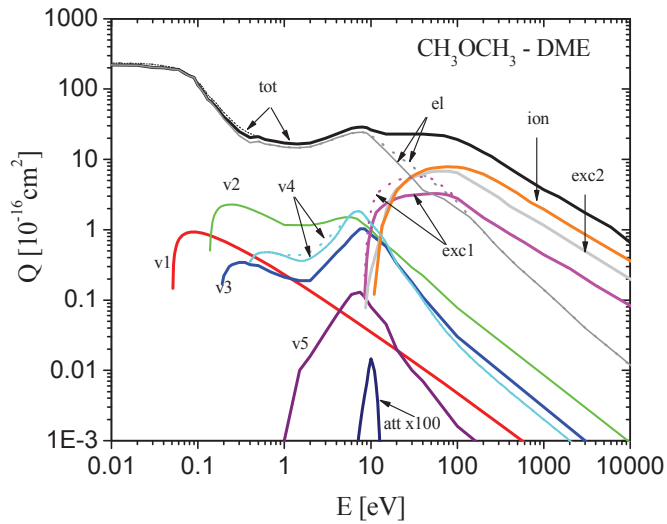


Figure 1. The cross section set for electrons in Dimethyl ether. Dotted lines: the initial set [10], solid lines: the present set.

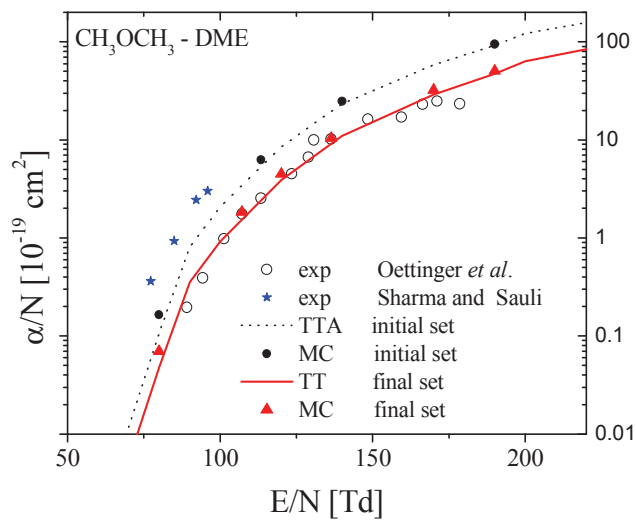


Figure 2. The comparison between calculated and measured ionization coefficients in pure DME.

Acknowledgements

This work was supported by Projects ON 171037 and II 41011.

REFERENCES

- [1] Z. Peeters, S. D. Rodgers, S. B. Charney, L. Schriver-Mazzuoli, J. V. Keane and P. Ehrenfreund, *Astronom. Astrophys.* 445, 197 (2006).
- [2] J. Miyamoto and I. P. J. Shipsey, *Nuclear Physics B* 78, 695 (1999).
- [3] F. Angelini *et al.*, *Nucl. Instr. and Meth. In Phys. Research A* 343, 441 (1994).
- [4] F. Angelini, R. Bellazzini, A. Brez, M. M. Massai, G. Spandre and M. R. Torquati, *Nucl. Instr. and Meth. In Phys. Research A* 283, 755 (1989).
- [5] F. Villa, *Nucl. Instr. And Meth.* 217, 273 (1983).
- [6] T. L. Cottrell and I. C. Walker, *Trans. Faraday. Soc.* 61, 1585 (1965).
- [7] V. Cindro, H. Kolanoski, A. Lange, D. Lauterjung, F. Müller, T. Siegmund, W. Söder and H. Thurn, *Nucl. Instr. and Meth. In Phys. Research A* 309, 411 (1991).
- [8] E. Oettinger, M. Hilderbrandt and B. Schmidt, *Nucl. Instr. and Meth. In Phys. Research A* 412, 355 (1998).
- [9] A. Sharma and F. Sauli, *Nucl. Instr. and Meth. In Phys. Research A* 323, 280 (1992).
- [10] <http://consult.cern.ch/writeup/magboltz/magboltz-10.0.2.f>
- [11] R. W. Crompton, M. T. Elford and R. L. Jory, *Aust. J. Phys.* 20, 369 (1967).
- [12] Z. Lj. Petrović, M. Šuvakov, Ž. Nikitović, S. Dujko, O. Šašić, J. Jovanović, G. Malović, V. Stojanović, *Plasma Sources Sci. Technol.* 16, S1 (2007).
- [13] W. L. Morgan and B. M. Penetrante, *Comput. Phys. Commun.* 58, 127 (1990).
- [14] Z. Lj. Petrović, S. Dujko, D. Marić, G. Malović, Ž. Nikitović, O. Šašić, J. Jovanović, V. Stojanović and M. Radmilović-Radenović, *J. Phys. D: Appl. Phys.* 42, 194002 (2009).
- [15] R. E. Robson, R. D. White and M. A. Morrison, *J. Phys. B: At. Mol. Opt. Phys.* 36, 4127 (2003)
- [16] Z. Lj. Petrović, Z. M. Raspopović, S. Dujko and T. Makabe, *Appl. Surf. Sci.* 192 1 (2002)
- [17] Z. M. Raspopović, S. Sakadžić, S. Bzenić and Z. Lj. Petrović, *IEEE Trans. Plasma Sci.* 27, 1241 (1999).
- [18] <http://www.lxcat.laplace.univ-tlse.fr>

MODELING OF F- IONS IN Ar/BF₃ MIXTURES

Z. Raspopović¹, Ž. Nikitović¹, V. Stojanović¹, J. Jovanović² and Z. Lj. Petrović¹

¹*Institute of Physics, University of Belgrade, Pregrevica 118, 11080 Belgrade, Serbia*

²*Faculty of Mechanical Engineering, University of Belgrade, Kraljice Marije 16, 11000 Belgrade, Serbia*

Abstract. Transport parameters of F⁻ ions in mixtures Ar/BF₃ in DC fields were calculated using Monte Carlo simulation technique assuming the scattering cross section set assembled on the basis of Nanbu's technique separating elastic from reactive collisions. In this work we present characteristic energy and drift velocity for low and moderate reduced electric fields E/N (N -gas density) and accounting for the non-conservative collisions.

1. INTRODUCTION

Negative ions are abundant in plasmas in fluor containing molecules that are also relevant for a wide range of applications. One should bear in mind that electron affinity of F atom is the largest of all atoms and also that electronegative plasmas containing F⁻ ions are highly reactive. Knowledge of the plasma chemistry and behavior of negative ions in plasmas is thus necessary in order to model plasma processing devices. Additionally, recent progress of discharge modeling and simulation have made contributions to a deeper understanding of the discharge phenomena and to the optimization of reactor design or finding operating conditions. One such example is plasma implantation where Boron dopant penetration in silicon is achieved by a pulsed DC plasma system (PLAD) most widely employing BF₃ gas [1, 2].

Uniform plasma and implantation with normal ion incidence are the main goals in this technological process. Control over the number density of negative ions, in this case F⁻ and BF₄⁻, increase efficiency of implantation. Modeling of such plasmas requires knowledge of transport parameters of all abundant particles [3].

2. EQUATIONS

The cross sections for scattering of BF₄⁻ ions on Ar and BF₃, and for F⁻ ions on BF₃ are calculated by using Nanbu's theory [4, 5] separating elastic from detachment collisions. The cross sections for F⁻ on Ar [5] were used to calculate

rate coefficients for detachment. The dipole polarizability of $3.31 \cdot 10^{-30} \text{ m}^3$ [6] and $1.64 \cdot 10^{-30} \text{ m}^3$ [7] is used for BF_3 and Ar target respectively. Monte Carlo technique of Ristivojević and Petrović [8] was used to calculate transport parameters as a function of E/N .

According to the Nanbu's theory, elastic and reactive endothermic collisions are separated and treated by accounting for the thermodynamic threshold energy and branching ratios according to the Rice–Rampersperger–Kassel (RRK) theory [4]. Within the RRK theory an excited molecular complex is treated as an excited activated complex where the internal energy is distributed among s equivalent vibrational modes of the complex.

The cross section for exothermic reaction (EXO) forming a super halogen molecular ion BF_4^- is commonly represented by ion capture cross section:

$$\sigma_{exo} = \beta \sigma_L \quad (1)$$

where σ_L is the orbiting cross-section [9] and β is the probability of a specific exothermic reaction.

3. DISCUSSION AND RESULTS

The transport coefficients include drift velocity, diffusion coefficients, ionization and attachment coefficients and chemical reaction coefficients for ions [3]. Excitation coefficients are also measured but seldom used in modeling.

Swarm parameters are generally applied in plasma modeling and simulations. At the same time, the non-equilibrium regime in discharges is well represented under a broad range of conditions by using Monte Carlo simulation scheme.

In this work we use Monte Carlo technique that accounts for a finite gas temperature of the background gas particles [5] to calculate swarm parameters of F^- ions in gas for temperature $T=300 \text{ K}$.

In Figure 1 we show the characteristic energies (diffusion coefficient normalized to mobility eD/K in units of eV) based on longitudinal (D_L) diffusion coefficients. We also show the mean energy, a parameter which cannot be directly measured in experiments but a map of mean energy versus E/N may be used directly to provide the data in fluid models especially when the local field approximation fails. As seen in Figure 1, the mean energy increases from about 10 Td. The Monte Carlo code [8] gives good results in which for all mixtures Ar/ BF_3 the mean energy converges to the thermal mean energy $3/2 kT = 0.038778 \text{ eV}$, while the thermal $eD/K = kT$ converges to 0.025852 eV (longitudinal (DL) and transverse (DT) diffusion coefficients).

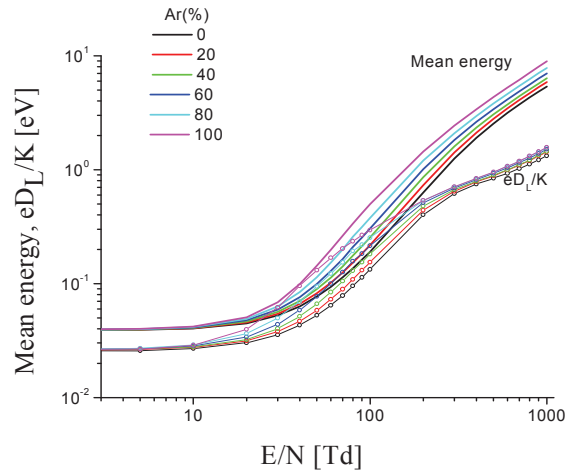


Figure 1. Mean and characteristic energy of F^- ions in BF_3 gas as a function of E/N at $T = 300$ K.

The bulk and flux drift velocities for F^- in Ar/BF_3 as a function of E/N are given in Figure 2. The drift velocities obtained by Monte Carlo simulation are calculated in real space (bulk) and in velocity space (flux) values and are obtained as $\langle v \rangle$ and dx/dt , respectively. The bulk and flux values of the drift velocity begin to differ above 100 Td but very little.

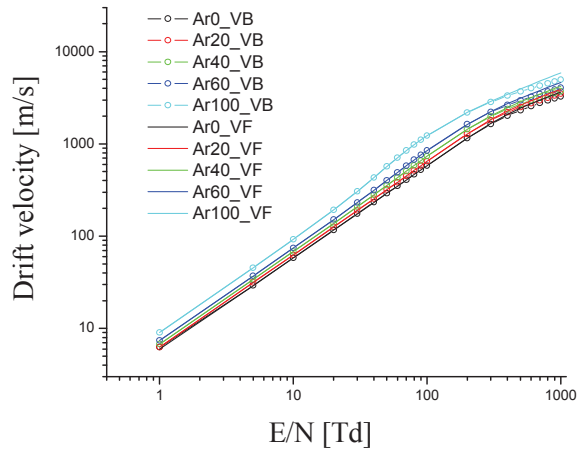


Figure 2. The bulk and flux drift velocity of F^- ions in Ar/BF_3 as a function of E/N at $T=300$ K.

4. CONCLUSION

In this paper we show transport properties for the F- in mixtures Ar/BF₃ which do not exist in the literature. The complete cross section set has been determined by extending Nanbu's theory.

The results are believed to be a good base for modeling, which could be further improved when measured values of transport coefficients become available and then perform the analysis again.

Acknowledgements

Results obtained in the Laboratory of Gaseous Electronics Institute of Physics University of Belgrade under the auspices of the Ministry of Education, Science and Technology, Projects No. 171037 and 410011.

REFERENCES

- [1] B.-W Koo, Z. Fang, L. Godet, S. B. Radovanov, C. Cardinaud, G. Cartry, A. Grouillet and D. Lenoble, *IEEE Trans. Plasma Sci.*, 32, 456 (2004).
- [2] Ž. Nikitović, S. Radovanov, L. Godet, Z. Raspopović, O. Šašić, V. Stojanović and Z. Lj. Petrović, *EPL* 95, 45003 (2011).
- [3] Z. Lj. Petrović, S. Dujko, D. Marić, G. Malović, Ž. Nikitović, O. Šašić, J. Jovanović, V. Stojanović and M. Radmilović-Radenović, *J. Phys.D: Appl. Phys.* 42, 194002 (2009).
- [4] K. Denpoh and K. Nanbu, *J. Vac. Sci. Technol. A*16, 1201(1998).
- [5] Z. Lj. Petrović, Z. M. Raspopović, V. D. Stojanović, J. V. Jovanović, G. Malović, T. Makabe and J. De Urquijo, *Appl. Surf. Sci.* 253, 6619 (2007)
- [6] C. Szmytkowski, M. Piotrowicz, A. Domaracka, L. Klosowski, E. Ptasinska-Denga and G. Kasperski, *J. Chem. Phys.* 121, 1790 (2004).
- [7] E.W Mc Daniel, *Atomic Collisions : Electron and Photon Projectiles*, John Willey & Sons, Inc. 655 (1989).
- [8] Z. Ristivojević and Z. Petrović, *Plasma Sources Sci. Technol.*, 21, 035001 (2012).
- [9] E. W. McDaniel, V. Čermak, A. Dalgarno, E. E. Ferguson and L. Friedman, *Ion-Molecule reactions*, Willey-Interscience (1970).

OBTAINING ELECTRON ATTACHMENT AND IONIZATION RATES FROM SIMULTANEOUS ANALYSIS OF ELECTRON AND ION SWARMS IN A PULSED TOWNSEND SETUP

M. Rabie, P. Haefliger and C.M.Franck

*Power Systems and High Voltage Laboratories, ETH Zurich, 8092 Zurich,
Switzerland*

Abstract. We present a procedure to obtain electron attachment and ionization rates in a pulsed Townsend experiment. Temporal drift currents for electrons and ions are analyzed using electron and ion current models. Measurements are performed in a highly automated pulsed Townsend setup in CO₂ to determine electron attachment and ionization rates as well as ion drift velocities of positive and negative ions for different reduced electric field strengths.

1. INTRODUCTION

The net production of electrons per unit time on pre-breakdown conditions is determined by the effective reaction rate. However, for electro-negative gases the net production of electrons is in general the sum of at least two types of non-conservative collisions: ionization and (dissociative) attachment.

In a Pulsed Townsend experiment positive and negative ions are created during the electron transit due to ionization and attachment. The measured current is the superposition of drifting electrons, positive and negative ions. The current that is measured during the electron transit is mainly governed by the electrons, since ion drift velocities are typically two to three orders of magnitude smaller than electron drift velocities. The analysis of this electron current provides the effective reaction rate

$$\nu_{\text{eff}} = \nu_i - \nu_a \quad , \quad (1)$$

which is the ionization minus the attachment rate. However, with a detailed analysis of the ion-dominated post-current, which starts after the electron

transit time T_e , the individual rates ν_i and ν_a might be determined separately. In addition, the drift velocities of positive and negative ions v_p and v_n can be obtained.

2. METHODS

2.1 Pulsed Townsend Method

The experimental procedures applied in this work have been described previously [1]. A short laser pulse (1.5 ns FWHM) releases $10^6 - 10^7$ start electrons from a photo cathode. The swarm parameter measurements were made in CO_2 at room temperature 293 to 300 K, at a pressure of $p = 10.5$ kPa and at electrode spacings d between 11 and 17 mm. The transport parameters depend on the reduced field strength E/N , given in Townsend (1 Td = 10^{-21} Vm²). Here, E is the electrical field strength and N is the number density of the gas.

2.2 Electron current

Measured swarm currents have been evaluated on the basis of an electron swarm model [1], in order to obtain the electron drift velocity $v_e = d/T_e$, the initial current I_0 at time T_0 , and the effective reaction rate ν_{eff} . The latter is determined by means of linear regression in the interval $[T_1, T_2]$, see Fig 1.

2.3 Ion current

In general, the ion current is the sum of all positive and negative ion currents. In the following we assume only one species of positive and one species of negative ions. No ion conversion reactions or ion clustering during the ion drift will be taken into account. The drift velocities $v_p = d/T_p$ and $v_n = d/T_n$ of positive and negative ions are assumed to be much smaller than v_e , corresponding to $T_p, T_n \gg T_e$. Then, when neglecting electron and ion diffusion, the currents of positive and negative ions after the electron transit can be expressed as a function of time $\mathbf{t}' = \mathbf{t} - T_0$ [2]:

$$\mathbf{I}_p = I_0 \frac{T_e}{T_p} \frac{\nu_i}{\nu_{\text{eff}}} (e^{\nu_{\text{eff}} T_e} - e^{\nu_{\text{eff}} \frac{T_e}{T_p} \mathbf{t}'}) . \quad (2)$$

$$\mathbf{I}_n = I_0 \frac{T_e}{T_n} \frac{\nu_a}{\nu_{\text{eff}}} (e^{\nu_{\text{eff}} T_e (1 - \frac{\mathbf{t}'}{T_n})} - 1) . \quad (3)$$

We seek a minimum number of fit parameters, in order to perform an efficient fit of the measured current \mathbf{I} to the ion current model. Here, the fit minimizes the L^2 -norm $\|\mathbf{I} - \mathbf{I}_p - \mathbf{I}_n\|$. The initial electron current I_0 , the effective rate ν_{eff} and the time T_e are already known from the electron current analysis (section 2.2). For the ion current analysis they are treated

as constant terms. After eliminating ν_a by Eq. (1) three unknown parameters remain: ν_i , T_p and T_n . Note, that \mathbf{I}_p and \mathbf{I}_n linearly depend on ν_i . We therefore rewrite the norm $\|\mathbf{I} - \mathbf{I}_p - \mathbf{I}_n\|$, using Eq. (2) and Eq. (3), to the form $\|\mathbf{a} - \nu_i \mathbf{b}\|$, where

$$\mathbf{a} = \mathbf{I} + I_0 \frac{T_e}{T_n} (e^{\nu_{\text{eff}} T_e (1 - \frac{t'}{T_n})} - 1) . \quad (4)$$

$$\mathbf{b} = I_0 \frac{T_e}{\nu_{\text{eff}}} \left(\frac{e^{\nu_{\text{eff}} T_e} - e^{\nu_{\text{eff}} \frac{T_e}{T_p} t'}}{T_p} + \frac{e^{\nu_{\text{eff}} T_e (1 - \frac{t'}{T_n})} - 1}{T_n} \right) . \quad (5)$$

Thus, for the final fit only two independent fit parameters remain, which are T_p and T_n . The remaining unknown parameter ν_i that minimizes $\|\mathbf{a} - \nu_i \mathbf{b}\|$ is then given by the linear inversion $\nu_i = \mathbf{a} \cdot \mathbf{b} / \mathbf{b}^2$, with the constraint $\nu_i \geq \nu_{\text{eff}}$.

The spatial ionization and attachment coefficients are obtained from the temporal reaction rates using $\alpha = \nu_i / v_e$ and $\eta = \nu_a / v_e$.

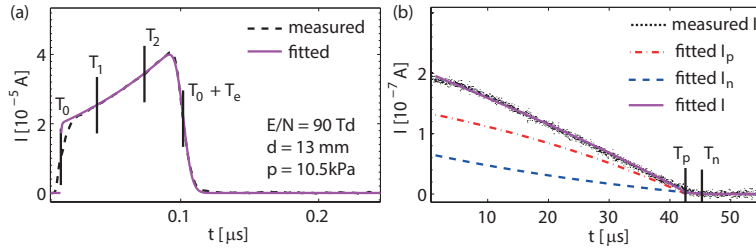


Figure 1. (a) Measured electron drift current in CO_2 and fit of the electron current model. (b) Measured ion drift current, fitted positive, negative and total ion current model, given by Eq. (2) and Eq. (3).

3. RESULTS/DISCUSSION

The electron and ion currents were measured and analyzed, according to sections 2.1, 2.2 and 2.3. The results for the reaction rates are presented in Fig. 1(a). The obtained values for α and η are in good agreement with Bolsig+ [3,4,5] and Ref. [6]. Fig. 2(b) shows the obtained ion drift velocities. For the CO_2^+ ions v_p is in very good agreement with Ref. [7]. We assume, that in our pressure range O^- is instantly converted by a three-body reaction to CO_3^- , as described e.g. in [8]. Our measured values for v_p and v_n are consistent with the general relation for ion drift $v \propto 1/\sqrt{m}$, where m is the ion mass, see Fig. 2(b). Here, v_n is given by $v_n/v_p = \sqrt{m(\text{CO}_2)/m(\text{CO}_3)}$, showing good agreement with our results. For v_n there is a discrepancy of the measured values and the data of Ref. [7].

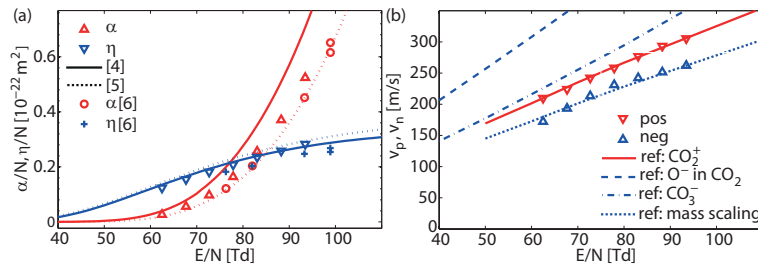


Figure 2. (a) Measured density reduced reaction rates in CO_2 vs reduced field E/N , and reference data [4,5,6]. (b) Measured drift velocities of positive v_p and negative v_n ions in CO_2 vs E/N , and reference data [7].

4. CONCLUSION

We presented a method of evaluating electron and ion currents in a pulsed Townsend experiment. The ionization and attachment rate as well as the drift velocities of positive and negative ions were obtained by fitting electron and ion models to the measured currents. The method was demonstrated for CO_2 over a E/N -range of 60 - 95 Td.

Acknowledgements

This work is financially supported by Alstom (Schweiz) AG, Pfiffner AG and ABB Switzerland.

REFERENCES

- [1] D. A. Dahl et al., J. Phys. D: Appl. Phys. 45, 485201 (2012).
- [2] T. Aschwanden, Ph.D. dissertation ETH Zurich, Diss. ETH Nr. 7931. Rep. 112, 319 (1985).
- [3] G.J.M. Hagelaar et al., Plasma Sources Sci. Technol. 14, 722-733 (2005).
- [4] Morgan database, <http://www.lxcat.net>, retrieved on July 5, (2014).
- [5] Phelps database, <http://www.lxcat.net>, retrieved on July 5, (2014).
- [6] D. K. Davies, Journal of Applied Physics 49, 127 (1978).
- [7] L. A. Viehland et al., Int. J. Mass Spectrom. Ion Proc. 149/150 555 (1995).
- [8] T. D. Fansler et al., The Journal of Chemical Physics 66, 3246 (1977).

Section 2.

PARTICLE AND LASER BEAM INTERACTION WITH SOLIDS

WHAT HAPPENS AT THE SURFACE IMPACT SITE OF A SLOW HIGHLY CHARGED ION?

Friedrich Aumayr

*Institute of Applied Physics, TU Wien – Vienna University of Technology,
Wiedner Hauptstr. 8-10/E134, 1040 Vienna, Austria, EU*

Various types of surface nanostructures such as nanosized hillocks, pits or craters have so far been observed after the impact of individual slow highly charged ions (HCI) on different materials [1–4]. Their topography, appearance, and long-time stability seem to depend sensitively on the material properties as well as on the potential energy (charge state) and kinetic energy of the incident ion (for a recent review see Ref. [5]). Surprisingly, even for very similar prototypical wide-band-gap insulators, ionic crystals of alkali halides and alkaline earth halides, vastly different and seemingly contradictory results have been found. Irradiation of KBr single crystals by individual highly charged Xe ions leads to the formation of pits of one atomic layer depth [2] while irradiation of CaF₂ single crystals produces nano-meter high hillocks protruding from the surface [1]. We have recently found the missing pieces to this puzzle [6] and are now able to construct a phase diagram as a function of kinetic and potential energies for the formation of different nanosized defect structures in CaF₂. We have reasons to believe that this scenario should also hold for other halide crystals as well.

We have also started to investigate the effect of individual slow highly charged ion bombardment of thin, freestanding carbon nano-membranes (CNM) of 1 nm thickness [7]. After irradiation by slow HCI we find nanoscopic holes (3 - 30 nm in diameter) in the CNM, the size of which depends on the potential and kinetic energy of the impinging ion. The number density of these nanopores corresponds well with the incident ion fluence, indicating that about every HCI produces a nano-hole in the CNM.

REFERENCES

- [1] A. S. El-Said, et al., Phys. Rev.Lett. 100, 237601 (2008).
- [2] R. Heller, et al., Phys. Rev.Lett. 101, 096102 (2008).
- [3] M. Tona, et al. Phys. Rev. B 77, 155427 (2008).
- [4] R. Ritter et al., EPL 97, 13001 (2012).
- [5] F. Aumayr, et al., J.Phys.: Cond.Mat. 23, 393001 (2011).
- [6] A. S. El-Said, et al., Phys. Rev.Lett. 109, 117602 (2012).
- [7] C. Nottbohm et al., Ultramicroscopy 108, 885 (2008).
- [8] R. Ritter et al., Appl. Phys. Lett. 102, 063112 (2013).

LASER ABLATION IN LIQUID DURING NANOPARTICLE PRODUCTION

A. De Giacomo^{1,2}, M. Dell'Aglio², R. Gaudiuso², R. Elrashedy¹ and
O. De Pascale²

¹*Department of Chemistry, University of Bari, Via Orabona 4, 70125 Bari-Italy*
²*CNR-IMIP, Via Amendola 122/D, 70126 Bari-Italy*

Experiments of single and double pulse Laser Ablation in Liquids (LAL) were carried out for studying the production of nanoparticles (NPs) in water, which revealed the fundamental role of plasma evolution and relaxation, as well as cavitation bubble dynamics produced by the laser plasma itself, in the formation of nanostructure and in their corresponding properties. Different techniques were used for studying the phenomena occurring during LAL at different conditions (single pulse [1], double pulse and external pressure [2]). These include Optical Emission Spectroscopy and fast camera shadowgraph for studying the laser induced plasma characteristics and other shadowgraph-like experiments for the cavitation dynamics and material ejection, and combination of spectroscopic and microscopic techniques for investigating the correlation between the ablation process and the produced nanoparticles.

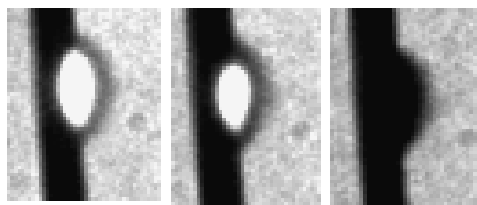


Figure 1. Temporal evolution of laser induced plasma under water.

REFERENCES

- [1] A. De Giacomo, M. Dell'Aglio, A. Santagata, R. Gaudiuso, O. De Pascale, P. Wagener, G. C. Messina, G. Compagnini and S. Barcikowski, *Physical Chemistry Chemical Physics*, 15, 3083 (2013).
- [2] A. De Giacomo, A. De Bonis, M. Dell'Aglio, O. De Pascale, R. Gaudiuso, S. Orlando, A. Santagata, G. S. Senesi, F. Taccogna, R. Teghil, *Journal of Physical Chemistry C* 115 (12) (2012).

LOW-ENERGY ELECTRON-INDUCED BOND CLEAVAGE STUDIED IN DNA AT A SINGLE- MOLECULE LEVEL

I. Bald^{1,2}, J. Rackwitz¹, R. Schürmann^{1,2}, S. Vogel¹, A. Keller³

¹*Institute of Chemistry, University of Potsdam, Germany*

²*BAM Federal Institute for Materials Research and Testing, Berlin, Germany*

³*Chemical Engineering and Macromolecular Chemistry, University of
Paderborn, Germany*

Secondary low-energy electrons are considered one of the main sources of DNA damage induced by ionizing radiation. First experimental observations suggested that the DNA sequence may have an influence on the type and yield of the damage, which would be highly relevant for the understanding of existing and the development of novel radiosensitizers used in radiation chemotherapy. However, this issue could up to now not be tackled in a satisfying manner because of severe limitations of conventional chemical and biochemical analytical tools. The recent groundbreaking advances in DNA nanotechnology enable now a systematic and efficient sequence-specific detection of DNA radiation damage using DNA origami templates.[1,2]

Here it is demonstrated that DNA origami templates can be used as a versatile tool to determine the absolute cross sections of electron induced DNA strand breaks of different DNA sequences. We find unexpectedly that 5'-TT(ATA)3TT sequences have a higher damage cross section than 5'-TT(GTG)3TT sequences. Furthermore, we find that the reactivity of the radiosensitizer 5-Bromouracil depends on the nucleobase sequence in which it is embedded.

Acknowledgements: This research was supported by a Marie Curie FP7 Integration Grant within the 7th European Union Framework Programme and by the Deutsche Forschungsgemeinschaft (DFG).

REFERENCES

- [1] A. Keller, I. Bald, A. Rotaru, E. Cauet, K. V. Gothelf and F. Besenbacher, ACS Nano 6, 4392 (2012).
- [2] A. Keller, J. Kopyra, K. V. Gothelf and I. Bald, New J. Phys. 15, 083045 (2013).

DEPOSITION OF INNOVATIVE COATINGS BY DBD AT ATMOSPHERIC-PRESSURE

David Duday, Nicolas Boscher, Florian Hilt and Patrick Choquet

CRP Gabriel Lippmann, SAM, 41 rue du Brill L-2422 Belvaux, Luxembourg

Despite Dielectric Barrier Discharges (DBD) were discovered in the 19th century, their efficient use for coating deposition is still limited due to several technological problems. A way to overcome these problems is to take advantage of the recent developments in high voltage electronics to better coupled generator and reactor, and to ensure conventional polymerization pathways at atmospheric pressure for the fast deposition of polymer thin films. Another way to generate innovative DBD coatings is to use new families of precursors, or even better, monomers specifically designed for DBD processes. In this work, a plane-to-plane electrodes configuration is used and liquid precursors are vaporized into the discharge using a bubbler system. Chopped ac and nanosecond pulse dc waveforms are alternatively applied to high voltage electrodes to deposit plasma polymers. Glycidyl MethAcrylate (GMA) and DiEthylAllylPhosphate (DEAP) coatings are deposited on flat Si wafers for chemical characterization and complex shape substrates (patterned Si wafer and polymer textile) for conformability studies. Coating depositions are carried out in both static and dynamic modes for a better understanding of coating growth mechanisms. Effect of different plasma parameters such as duty cycle, t_{on} and t_{off} durations, electrical excitation frequency, power density dissipated in the discharge, precursor concentration and gas process composition on the deposition rate, coatings chemistry, structure and conformability are discussed for both applied electrical signals. Coatings were shown to be homogenous and adherent on all studied substrates. A radical polymerization initiated by plasma leading to a higher retention of monomer pattern is shown for different precursors when nanosecond pulsed dc discharge is generated. By adding low contents of N_2 in the Ar gas process, a new family of plasma initiated conventional polymers with addition of N-containing group on the monomer unit is elaborated. Finally, the evolution of the plasma physico-chemistry with the two different electrical signals is presented and differences in deposition rate and growth mechanisms are discussed for the different conditions.

PLASMA SYNTHESIS AND PROCESSING OF CARBON NANOWALLS AND SUBMICRON METALLIC PARTICLES

G. Dinescu, S. Vizireanu, T. Acsente, B. Mitu, A. Lazea, D. Stoica, V. Marascu

*National Institute for Laser, Plasma and Radiation Physics, Atomistilor Street
409, Magurele-Bucharest, 077125, Romania*

In the presentation we consider two material classes obtained by plasma: carbon nanowalls and metallic particles. We focus on their synthesis and on the control of their properties in view of applications. Carbon nanowalls (CNW) layers are synthesised by downstream deposition in low pressure radiofrequency plasma jet. We show that the layers consists of vertically oriented, interconnected walls having graphene based structure, with thickness in the nanoscale range and length/height in the micron scale [1]. The layers present nano-micro topography, open architecture, high porosity, large specific surface area, chemical inertness and large heat conductivity. Such properties can be tailored by changing conditions: RF plasma power, substrate position, substrate temperature, geometry of plasma source. In view of applications the growth on silicon, quartz, titanium, alumina is demonstrated, while the transfer on polymers is possible by laser induced forward transfer. Surface chemistry can be easily tailored by surface functionalization. The applications of the CNW points out to batteries or supercapacitors [2], superhydrophobic or superhydrophylic surfaces, supports for catalytic particles, platforms for cells growth [3]. In addition, approaches describing the synthesis of metallic particles with plasmas at low and atmospheric pressure are presented.

Acknowledgements: This work was supported by a grant from the Romanian Ministry of National Education, CNCS-UEFISCDI, code PN-II-ID-PCE-2012-4-0629.

REFERENCES

- [1] S Vizireanu, S. D. Stoica, C. Luculescu, L. C Nistor, B. Mitu and G. Dinescu, *Plasma Sources Science and Technology*, 19, 034016 (2010).
- [2] Z. González, S. Vizireanu, G. Dinescu, C. Blanco and R. Santamaría, *Nano Energy*, 1, 833 (2012).
- [3] E. C. Stancu, A. M. Stanciuc, S. Vizireanu, C. Luculescu, L. Moldovan, A. Achour and G. Dinescu, *J. Phys. D: Appl. Phys.*, 47 (26) 265203 (2014).

MOLECULAR DYNAMICS SIMULATION OF PLASMA-SURFACE INTERACTION FOR CARBON AND TUNGSTEN MATERIALS

Atsushi M. Ito¹, Oda Yasuhiro¹, Arimichi Takayama¹, Seiki Saito³, Hiroaki Nakamura^{1,2}

¹*National Institute for Fusion Science, 322-6 Oroshi-cho, Toki 509-5292, Japan*

²*Nagoya University, Furo-cho, Chikusa-ku, Nagoya 464-8603, Japan*

³*Kushiro National College of Technology, Kushiro, Hokkaido 084-0916, Japan*

In this paper, we introduce simulation approaches to plasma-material/surface interaction (PMI/PSI) problems in fusion science and plasma application.

In the research field for fusion science, tungsten material will be used as a divertor material in ITER. However, there is a problem that the surface of tungsten is changed into a fuzzy nanostructure by helium irradiation[1]. The formation process of the fuzzy nanostructure is divided into the following four-step process. In the first step, the penetration of helium into the surface is analyzed by binary collision approximation (BCA), which is a legacy method and has been extended with recent computer resources. In the second step, the diffusion and agglomeration of helium in tungsten material is clarified by using quantum chemical calculation based on density functional theory (DFT). In the third step, the growth of a helium bubble is demonstrated by using molecular dynamics (MD) and kinetic Monte-Carlo (kMC). In the fourth step, fuzzy nanostructure formation is represented by the newly developed MD-MC hybrid simulation for the first time.

By these works, the possibility and limitation of each simulation method are clarified. Hybrid and combination methods extend the possibility of simulation approaches for the PMI. Then, we introduce other hybrid methods, BCA-MD hybrid simulation[2], for carbon materials. In addition, we also introduce the downfolding method[3], which is a method to develop a high-quality potential model for MD by comparison with the results from DFT. We suggest the advance of fusion science and plasma application by cooperation with material science.

Acknowledgements: Our work was supported by the National Institute of Natural Science (NINS) Program for Cross-Disciplinary Study and by Grants-in-Aid for Scientific Research (No. 23710135) from the Ministry of Education, Culture, Sports, Science, and Technology, Japan.

REFERENCES

- [1] S. Takamura, et. al., Plasma Fusion Res. 1, 051 (2006).
- [2] S. Saito, et.al, J. Nucl. Mater. 415, S208 (2011).
- [3] A. M. Ito, et. al., Phys. Scr. T159, 014062 (2014).

TREATMENT EFFECTS AND ITS STABILITY ON METAL SUBSTRATES AFTER COLD SURFACE DBD PLASMA

Vadym Prysiashnyi^{1,2} and Mirko Cernak¹

¹*R&D Centre for Low-Cost Plasma and Nanotechnology Surface Modifications
(CEPLANT), Brno, Czech Republic*

²*Faculty of Engineering (FEG), State University of Sao Paulo (UNESP),
Guaratingueta, Brazil*

In-line atmospheric pressure plasma treatments are in the focus of applied and industrial plasma research nowadays. The reason for high interest in plasma processing is due to environmental, functional and economic benefits. Due to enhancement of chemical reactions by high energy plasma particles, the trends to replace conventional processes involving hazardous chemicals by plasma are stimulated. The typical examples of in-line plasma treatments of metal surfaces are cleaning and activation prior to subsequent application of surface coatings.

Plasma treatments of metallic substrates have been studied for a long time. There are number of effects, such as surface cleaning, oxidation or oxide removal that can be efficiently done using plasma. A significant increase of surface hydrophilicity of metallic substrates after air plasma treatments was reported by few research groups in different laboratories. Also, it was observed that the effect of atmospheric pressure air plasma treatment of metallic surface is not permanent since the wettability of treated surface is decreasing in time, similar to the well-known aging effect observed on air-plasma treated polymer surfaces.

The present work was motivated by our belief that a more deep study is necessary to understand the processes on the surface after atmospheric pressure plasma treatments including the aging effect. As far as metallic substrate is concerned, it was decided to perform a study on few metals. The choice was given to aluminium, copper, steel and chromium as these metals have wide range of applications in different areas.

WAKE EFFECT IN GRAPHENE DUE TO MOVING CHARGED PARTICLES

Ivan Radović¹, Duško Borka¹ and Zoran L. Mišković²

¹*VINČA Institute of Nuclear Sciences, University of Belgrade, P.O. Box 522, 11001 Belgrade, Serbia*

²*Department of Applied Mathematics, and Waterloo Institute for Nanotechnology, University of Waterloo, Waterloo, Ontario, Canada N2L 3G1*

We study the wake effect induced by external charged particles [1-4] and electric dipoles [5,6] that move parallel to a supported graphene layer. In the case of fast projectiles (moving at speeds $v > v_B$, the Bohr velocity), we use one-fluid [1] and two-fluid [2] hydrodynamic models for the dielectric response of graphene's valence electrons, whereas for slow projectiles [3-6] (moving at speeds $v < v_B$), we use a polarization function within the random phase approximation, which is based on a linear approximation for graphene's π electron bands. We find that, when the projectile speed exceeds a threshold value, oscillatory wake patterns develop both in the induced density of charge carriers and the electrostatic potential in the regions of graphene trailing the projectile. Qualitative properties of the wake are strongly affected by: the speed of the particle, its distance from graphene, the size of the graphene-substrate gap, the coupling strength of the electron gas in graphene, the damping rate of graphene's π electrons, the excitation of surface phonons in the substrate, and the dipole moment orientation.

Acknowledgements: This work is supported by the Ministry of Education, Science and Technological Development of the Republic of Serbia (Project No. 45005). Z.L.M. also acknowledges support from the Natural Sciences and Engineering Research Council of Canada.

REFERENCES

- [1] I. Radović and D. Borka, Phys. Lett. A 374, 1527 (2010).
- [2] I. Radović and D. Borka, Nucl. Instrum. Methods B 268, 2649 (2010).
- [3] I. Radović, D. Borka and Z. L. Mišković, Phys. Lett. A 375, 3720 (2011).
- [4] I. Radović, V. Borka Jovanović, D. Borka and Z. L. Mišković, Nucl. Instrum. Methods B 279, 165 (2012).
- [5] I. Radović, D. Borka and Z. L. Mišković, Phys. Rev. B 86, 125442 (2012).
- [6] I. Radović, D. Borka and Z. L. Mišković, Phys. Lett. A 377, 2614 (2013).

EVENT BY EVENT MODELLING PROCEDURE TO SIMULATE ELECTRON BEAM INDUCED DEPOSITION

A. Muñoz¹, F. Blanco², M. C. Fuss³, D. Jones⁴, M. J. Brunger⁴ and G. García³

¹*Universidad Complutense de Madrid, Ciudad Universitaria 28040 Madrid, Spain*

²*Centro de Investigaciones Energéticas Medioambientales y Tecnológicas, Avenida Complutense 22, 28040 Madrid, Spain*

³*Consejo Superior de Investigaciones Científicas, Serrano 113 bis, 28006 Madrid, Spain*

⁴*Flinders University; Adelaide, SA, Australia*

In the last few years we have developed a Monte Carlo code (LEPTS) to simulate low energy electron and positron tracks in biologically relevant materials [1], both in the gas and condensed phases. Figure 1 shows an example of single electron tracks in (a) water and (b) pyrimidine. In this study we combine our LEPTS procedure for low energy particles with GEANT-4 (supported by the GAMOS architecture) for high energy particles to obtain a powerful simulation tool suitable for gaseous, liquid and solid media over a broad energy range. The capability of such a tool to simulate electron beam induced deposition on solid substrates will be discussed.

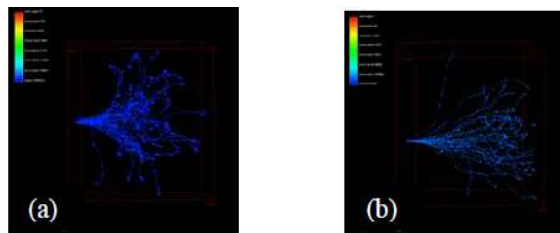


Figure 1. Single electron tracks in (a) water and (b) pyrimidin.

Acknowledgements: This work is partially supported by MINECO (FIS2012-31230), COST (MP1002, CM1301) and ARC (DP140102854).

REFERENCES

- [1] F. Blanco, A. Muñoz, D. Almeida, F. Ferreira da Silva, P. Limão-Vieira, M. Fuss, A. G. Sans and G. García, *Eur. Phys. J. D* 67, 199 (2013).
- [2] <http://geant4.cern.ch/>
- [3] <http://fismed.ciemat.es/GAMOS/>

ANGULAR AND SPATIAL DISTRIBUTIONS OF PROTONS WITH BN NANOTUBES

Vesna Borka Jovanović and Duško Borka

*Atomic Physics Laboratory (040), Vinča Institute of Nuclear Sciences,
University of Belgrade, P.O. Box 522, 11001 Belgrade, Serbia*

Abstract. In this paper we study the angular and spatial distributions of 10 and 20 MeV protons channeled through the straight (10, 10) single-wall boron-nitride (BN) nanotubes. The angular and spatial distributions of channeled protons were generated by the computer simulation method. We also varied proton incident angle to demonstrate that we can get a significant rearrangement of the propagating protons within the BN nanotube. This investigation may be used for proton beam guiding, for creating nanosized proton beams in materials science, biology and medicine.

1. INTRODUCTION

Boron nitride nanotubes were theoretically predicted in 1994 [1] and experimentally discovered in 1995 [2]. They can be imagined as a rolled up sheet of boron nitride. Structurally, it is a close analog of the carbon nanotube, except carbon atoms are alternately substituted by nitrogen and boron atoms. The carbon nanotubes can be metallic or semiconducting depending on the rolling direction and radius, but BN nanotube is an electrical insulator with a bandgap of ~ 5.5 eV, basically independent of nanotube geometry [3]. Also, layered BN structure is much more thermally and chemically stable than a graphitic carbon structure [4, 5].

2. THEORY

We adopt the right Cartesian coordinate system with the $-z$ axis coinciding with the nanotube axis, the origin is in the entrance plane of the nanotube, and the x and y axes are the horizontal and vertical axes, respectively. The initial proton velocity, v , is taken to lie in the xz plane and makes an angle α with the z axis, i.e. α is the proton incident angle. The length of the BN nanotube is assumed to be large enough to allow us to ignore the influence of the nanotube edges, and, at the same time, small enough to neglect the energy losses of channeled protons. It is assumed

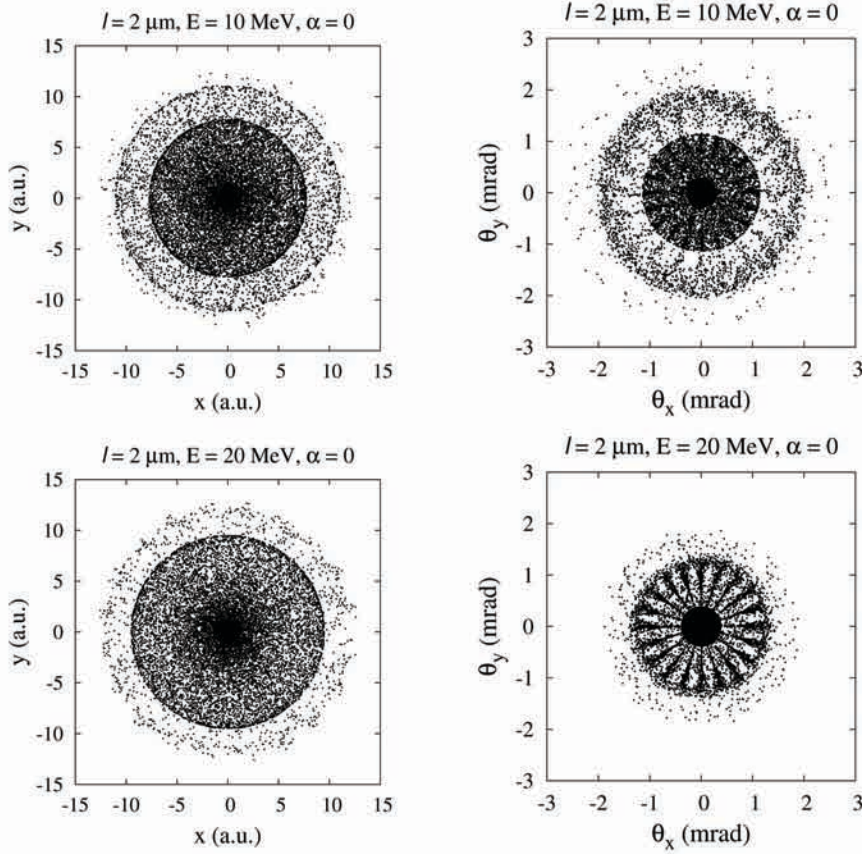


Figure 1. (left) The spatial and (right) angular distributions of protons channeled in the (10, 10) BN nanotubes in the scattering positions and scattering angle plane. The proton incident angle is $\alpha = 0$, proton energy is 10 MeV (top panel) and 20 MeV (bottom panel) and nanotube length is $2 \mu\text{m}$.

that the interaction of the ion and nanotubes can be treated classically [6, 7]. The interaction of the ion and a nanotube's atom is described by an Molière approximation of the Thomas-Fermi interaction potential and we apply continuum approximation [8, 9]. Applying continuum approximation along z axis [9] we get two types of atomic strings (strings of B atoms and strings of N atoms). Total potential is the sum of potentials of B and N atomic strings. The equations of motion are solved numerically [9, 10, 11, 12]. The spatial and angular distributions of transmitted protons are generated using a Monte Carlo computer simulation code. The components of the proton impact parameter, x_0 and y_0 , are chosen randomly from a uniform distribution within the cross-sectional area of the entrance plane of the BN nanotube.

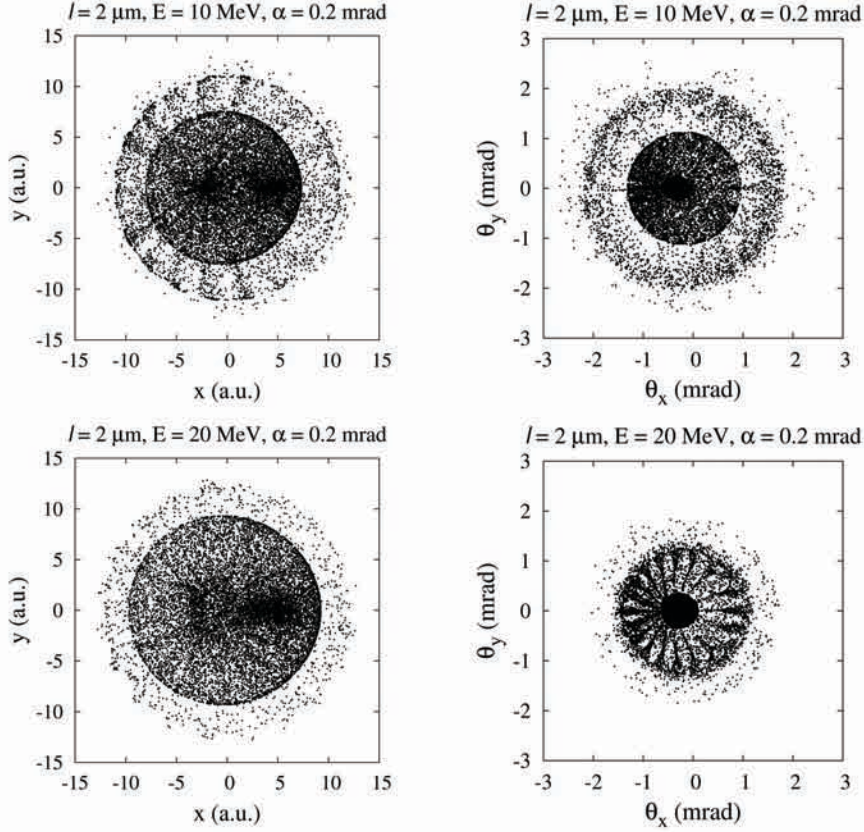


Figure 2. The same as in Fig. 1, but for $\alpha = 0.2$ mrad.

3. RESULTS AND DISCUSSION

The spatial and angular distributions of protons channeled in the (10, 10) BN nanotubes in the scattering positions and scattering angle plane for $\alpha = 0$ and for $\alpha = 0.2$ mrad are presented in Fig. 1 and Fig. 2, respectively. We can see that for $\alpha = 0.2$ mrad central maximum in position plane is shifted toward nanotube wall at the distance of about 5 a.u. along x -axis from the center. In angular plane for $\alpha = 0.2$ mrad central maximum is shifted in position ~ -0.3 mrad along Θ_x -axes. Also, spatial and angular distributions for different energies differ a lot.

We have presented a theoretical investigation of the angular and spatial distributions of protons channeled through BN (10, 10) nanotubes. Like in carbon nanotubes, spatial and angular distributions of channeled protons are very sensitive on initial proton energy and initial proton incident angle. Changing of these two parameters we can achieve a significant rearrangements of the propagating protons within BN nanotube. Our anal-

ysis shows that the BN nanotubes have very similar guiding properties like carbon nanotubes [8, 9, 10, 11, 12], but because they are more thermal and chemical stable [4, 5] they presented even better candidates for future channeling experiments.

Acknowledgements

This work is supported by the Ministry of Education, Science and Technological Development of the Republic of Serbia through the project 45005 "Functional, functionalized and improved nano materials".

REFERENCES

- [1] A. Rubio, J. L. Corkill, and M. L. Cohen, *Phys. Rev. B* 49, 5081 (1994).
- [2] N. G. Chopra, R. J. Luyken, K. Cherrey, V. H. Crespi, M. L. Cohen, S. G. Louie and A. Zettl, *Science* 269, 966 (1995).
- [3] X. Blasé, A. Rubio, S. G. Louie, and M. L. Cohen, *Europhys. Lett.* 28, 335 (1994).
- [4] W.-Q. Han, W. Mickelson, J. Cumings, and A. Zettl, *Appl. Phys. Lett.* 81, 1110 (2002).
- [5] D. Golberg, Y. Bando, C. C. Tang, and C. Y. Zhi, *Adv. Mater.* 19, 1845 (2007).
- [6] J. Lindhard, *K. Dan. Vidensk. Selsk., Mat.-Fys. Medd.* 34, 1 (1965).
- [7] D. S. Gemmell, *Rev. Mod. Phys.* 46, 129 (1974).
- [8] X. Artru, S. P. Fomin, N. F. Shulga, K. A. Ispirian, and N. K. Zhevago N. K., *Phys. Rep.* 412, 89 (2005).
- [9] D. Borka, S. Petrović, and N. Nešković, Nova Science Publishers, ISBN 978-1-61122-050-6, New York, 2011, p. 1-77
- [10] D. Borka, S. Petrović, N. Nešković, D. J. Mowbray, and Z. L. Mišković, *Phys. Rev. A* 73, 062902 (2006).
- [11] D. Borka, V. Lukić, J. Timko, and V. Borka Jovanović, *Nucl. Inst. Meth. B* 279, 169 (2012).
- [12] D. Borka, V. Lukić, J. Timko, and V. Borka Jovanović, *Nucl. Inst. Meth. B* 279, 198 (2012).

BEAM-FOIL POPULATION OF THE LARGE- l RYDBERG STATES OF MULTIPLY CHARGED IONS

S. M. D. Galijaš¹, M. A. Mirković² and N. N. Nedeljković¹

¹ *University of Belgrade, Faculty of Physics, P. O. Box 368, Belgrade, Serbia*

² *University College of Civil Engineering and Geodesy, Belgrade, Serbia*

Abstract. The population distributions of the large- l Rydberg states ($n \gg 1, l = n - 1$) of multiply charged ions ($Z = 12, 18, 24$) escaping solid surfaces are calculated using the recently developed dynamically generalized two-state vector model. We found that obtained resonance-like structures are in qualitative agreement with simulated experimental signal, i.e., we are able to explain observed resonances in decay of the beam-foil excited 2p and 2s states at very large times.

1. INTRODUCTION

We use the recently developed dynamically generalized two-state vector model (TVM) [1] in order to discuss in more detail the appearance of the resonance structure in the X-ray spectra at different delay times on the large time scale (50-3000 ps) in the beam-foil experiments with fast ions [2]. In the experiment, the 6.95 KeV line has been considered, which was assigned to the unresolved 2p \rightarrow 1s and 2s \rightarrow 1s electron transition in H-like Fe ions ($Z = 26$), after the 164 MeV Fe¹²⁺ ion beam passage through the carbon foil (90 μ g/cm²). The decay curve, which represents the photon intensity, can be effectively explained by taking into account the population of the state 2p by cascading down from Rydberg states ($n \gg 1, l \gg 1$) of the ion with core charge $Z = 26$ as the main mechanism [2]. For this reason, in Ref. [1] the population probability P_{nl} for $Z = 26$ and ionic velocity $v = 10$ a.u. has been considered within the framework of the TVM. The qualitative agreement with the population distribution predicted by experiment has been obtained for $Z = 26$ and the particular choice of the surface parameters.

However, at the backside of the foil various charge states of the Fe-ions can be obtained, and also the other ions can be considered, with other velocities. The main aim of the present paper is to present the population probabilities P_{nl} for the core charges Z and velocities v different than those considered in Ref. [1].

2. THEORETICAL MODEL

We study the formation of the large- l Rydberg states of highly charged ions escaping a solid along the direction orthogonal to the surface at velocity $v = dR/dt \gg 1$, where R is the ion-surface distance at the time t . The basic idea is to examine the process of neutralization (population) within the dynamically generalized TVM [1] which can be applied for large ionic velocities $v \approx 10$ a.u. The model is based on the TVM developed in Ref. [3, 4] for the intermediate ionic velocities $v \approx 1$ a.u. The electron exchange between the foil and the ion is described simultaneously by two wave functions: $\Psi_1(\vec{r}, t)$ which evolves from the initial electronic state characterized by the energy $-\gamma^2/2$ and the parabolic quantum numbers n_{1M} and m_M of the foil conduction band and $\Psi_2(\vec{r}, t)$, which evolves toward the final spherical Rydberg state $\nu_A = (n, l, m)$. Within the model, the potential energy of the electron interaction with ionic core image $U_{AM}(\vec{r}, R)$ is dynamically generalized: $U_{AM}^I(\vec{r}, R; v) = f_{AM}U_{AM}(\vec{r}, R)$.

The modified TVM is based on the mixed flux through the Firsov plane S_F , which is given by [1]

$$I_{nlm}^\gamma(t) = \frac{i}{2} \left(\frac{2}{2-g} \right)^{\frac{Z}{\gamma}(1-f)} \int_{S_F} \left[\gamma + \gamma_{A0} \frac{a}{r_A} + iv \left(1 - 2 \frac{da}{dR} \right) \right] \chi dS, \quad (1)$$

where $\chi = \Phi_{A,\nu_A}^{(2)*} N_M e^{-\gamma z} e^{-S_A^* - S_M} e^{iwt}$, $w = (\gamma^2 - \gamma_{A0}^2)/2 - v^2(1 - 2a/R)/2$ and the kinematic factor $g = a/R$ is defined in Ref. [5]; velocity dependent form of the factor $f_{AM} = f + \gamma_{A0} \ln v/Z$, with $\gamma_{A0} = Z/n$, is used in Eq. (1). Normalization constant N_M and eigenfunction $\Phi_{A,\nu_A}^{(2)}$ remain the same as in Ref. [3] and the factors S_A and S_M can be obtained by transformation $Z \rightarrow fZ$ in the corresponding expression of Ref. [3]. The population probability for the electron captured into the subshell (n, l) at the final time t_{fin} is given by

$$P_{nl} = \int_{\gamma_\phi}^{\gamma_{U_0}} \sum_{n_{1M}, m_{MM}} \sum_m \left| \int_{t_g}^{t_{fin}} I_{nlm}^\gamma \right|^2 d\gamma, \quad (2)$$

where $\phi = \gamma_\phi^2/2$ is the solid work function and $U_0 = \gamma_{U_0}^2/2$ is the depth of the conduction band in Sommerfeld model.

3. RESULTS AND DISCUSSION

In Fig. 1 we analyze the importance of dynamic generalization. We consider the difference between the values P_{nl} and comparable probability obtained in quasistationary image case P_{nl}^{qs} [3]. We note that TVM is comparable in magnitude with the wake field model [6], see discussion in Ref. [1]. The huge difference is oscillatory character of the TVM population distribution while the WFM distribution is the bell shaped.

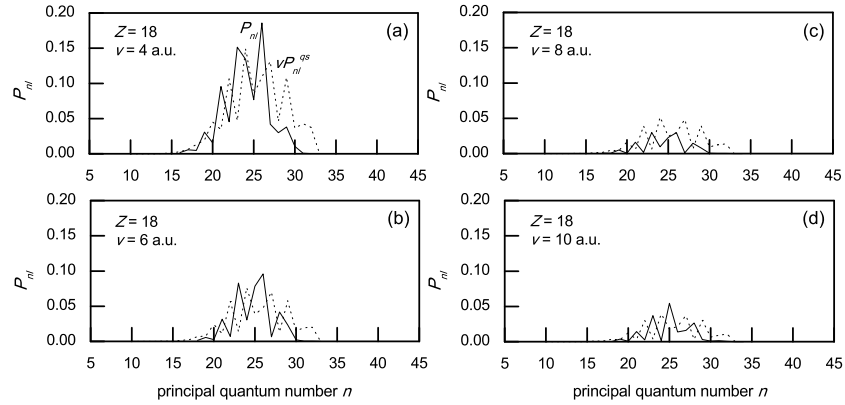


Figure 1. Population probabilities P_{nl}

In Fig. 2 we present the final population probabilities P_{nl} for the Rydberg states $n, l = n - 1$ of the ions with $Z = 12, 18$ and 24 , escaping surfaces at velocity $v = 10$ a.u. We also present the "experimental" results P_{nl}^{expt} [2] normalized to the value 0.06. We note that the population probabilities P_{nl}^{expt} are obtained for $Z = 26$, in order to estimate the occupancy of the $n = 2$ level (by cascading down from the level $n, l = n - 1$) of H-like Fe ions, which is in accordance with experiment.

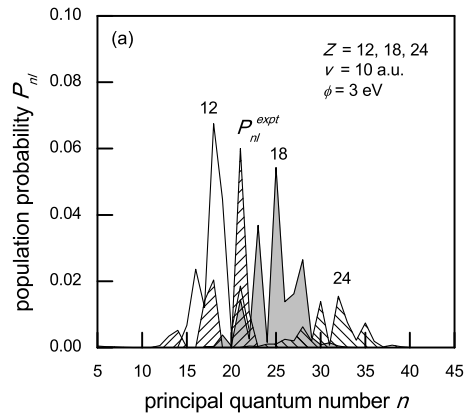


Figure 2. Population probabilities P_{nl} .

As shown in Fig. 2, several resonances in population probability distributions P_{nl} can be distinguished. On the other hand, the P_{nl}^{expt} distribution has a prominent peak at $n_{\text{res}} = 21$ (and slightly less pronounced at $n_{\text{res}} = 18$) positioned between the probability distribution obtained for $Z = 12$ and $Z = 18$. The obtained qualitative agreement requires further

theoretical and experimental investigation. It is an open question whether the resonances in the intensity of radiation could be recognized for other spectral lines, different than those considered under the assumption that the FeXII ions after passing through the carbon foil are fully stripped [2]. We note that the resonance-like structure of the population distribution has been also recognized for low- l case, at intermediate ionic velocities [7, 8].

Acknowledgements This work was supported in part by the Ministry of Education, Science and Technological Development, Republic of Serbia (Project 171016).

REFERENCES

- [1] N. N. Nedeljković, S. M. D. Galijaš and M. A. Mirković, *J. Quant. Spectrosc. Radiat. Transfer* 134, 46 (2014).
- [2] A. P. Mishra, T. Nandi and B. N. Jagatap, *J. Quant. Spectrosc. Radiat. Transfer* 120, 114 (2013).
- [3] N. N. Nedeljković, Lj. D. Nedeljković and M. A. Mirković, *Phys. Rev. A* 68, 012721 (2003).
- [4] M. A. Mirković, N. N. Nedeljković and D. K. Božanić, *J. Phys: Conf. Series* 257, 012010 (2010).
- [5] N. N. Nedeljković, Lj. D. Nedeljković, S. B. Vojvodić and M. A. Mirković, *Phys. Rev. B* 49, 5621 (1994).
- [6] M. Day and M. Ebel, *Phys. Rev. A* 19, 3434 (1979).
- [7] S. M. D. Galijaš, N. N. Nedeljković and M. D. Majkić, *Surf. Sci.* 605, 723 (2011).
- [8] S. M. D. Galijaš, N. N. Nedeljković and M. D. Majkić, *J. Phys: Conf. Series* 399, 012008 (2012).

POPULATION DYNAMICS OF THE SVI, CIVII AND ArVIII IONS IN THE GRAZING INCIDENCE ON SOLID SURFACE

M. D Majkić, S. M. D. Galijaš, I. P. Prlina and N. N. Nedeljković

University of Belgrade, Faculty of Physics, P.O.Box 368, Belgrade, Serbia

Abstract. We apply the two-state vector model recently adapted to the grazing incidence geometry to investigate the population dynamics of the SVI, CIVII and ArVIII ions interacting with solid surface. We calculate the corresponding intermediate population probabilities and rates, as well as the neutralization distances. The effect of the ionic core polarization is demonstrated: the magnitude of the population probability maxima increases and the neutralization distances decrease in respect to the point-like ionic core case. The population probabilities for the grazing incidence are shifted toward the smaller ion-surface distances compared to the escaping geometry.

1. INTRODUCTION

Recently, the population dynamics of the multiply charged ions ArVIII, KrVIII and XeVIII impinging the conducting solid surface in the grazing incidence geometry has been analyzed within the framework of the two-state vector model (TVM) [1, 2]. The effective modification of the Fermi-Dirac distribution of the electron momenta in solid due to the parallel ionic velocity v_{\parallel} has been taken into account. The results have been used to produce a complete quantum explanation of the classical trajectory of these ions during the cascade neutralization in the interaction with the solid surface. The ions ArVIII, KrVIII and XeVIII have the same ionic core charge $Z = 8$; their difference originated from different polarization of their cores.

In the present article we use the TVM to investigate the population of the Rydberg states of the SVI, CIVII and ArVIII ions under the grazing incidence. The intermediate population probabilities for these ions are known only for the ions escaping solid surfaces in the perpendicular direction [3], for small velocities $v = v_{\perp} \ll 1$ a.u. The ions SVI, CIVII and ArVIII have different core charges $Z = 6, 7$ and 8 , and different core polarizations. The effect of the parallel velocity, observed for the ions ArVIII, KrVIII and XeVIII is also expected for the ions SVI and CIVII.

2. POPULATION PROCESS IN THE SCATTERING GEOMETRY

The TVM is the time-symmetrized quantum model of the postselected systems: characteristic feature is the use of the two state vectors for describing the state of a single active electron. In the process of population of the Rydberg states of the considered ions, the first state vector evolves from the given initial state (electron in solid in the kinematically modified state μ'_M at the time $t = t_{in}$) toward the future. Simultaneously, the second state vector evolves toward the given final state (electron captured by the ion in a given ionic state $\nu_A = (n_A, l_A, m_A)$). The TVM population probabilities for the grazing geometry and for the ions escaping the surface perpendicularly are based on the same general expressions; however, the parallel velocity has a nontrivial effect [1, 2]. Within the framework of the TVM the intermediate population probability $P_{\nu_A}(t)$ is defined for the electron capture by the ion at the time t , when the ion is at the distance $R = R(t)$. The possibility that the captured electron can be recaptured by the solid is taken into account.

The basic physical quantity of our TVM is the so called mixed flux $I_{\mu'_M, \nu_A}$ [1, 4]. Using the mixed flux, we directly calculate the intermediate transition probability per unit energy parameter γ'_M at the time t

$$T_{\mu'_M, \nu_A}(t) = \left| \int_{t_{in}}^t I_{\mu'_M, \nu_A}(t') dt' \right|^2, \quad (1)$$

and the corresponding (velocity dependent) transition probability $T_{\nu_A}(t)$. We note that the energies $E'_M = -\gamma'^2_M/2$ are shifted due to the parallel velocity $v_{\parallel} \neq 0$. This shift can be calculated by applying the necessary Galilean transformations. Finally, we get the neutralization and population probabilities, which can be expressed as

$$P_{\nu_A}(t) = 1 - \exp[-T_{\nu_A}(t)]. \quad (2)$$

3. RESULTS

In Fig. 1 we present the population probabilities of the ions SVI, CIVII and ArVIII, for the polarized ionic cores and in the absence of core polarization (thick- and thin-solid curves, respectively). In the same figure we also present the corresponding rates $\Gamma_{\nu_A} = dP_{\nu_A}(t)/dt$. The population probabilities with polarized cores are positioned closer to the surface in comparison to the same quantities obtained in the point-like core approximation; the same effect has been observed in the case of normal escaping geometry in Ref. [3]. Population probabilities exhibit maxima at the distance $R = R_{max}$. The decrease of these probabilities closer to the surface is a consequence of the reionization process (electron recapture by the solid).

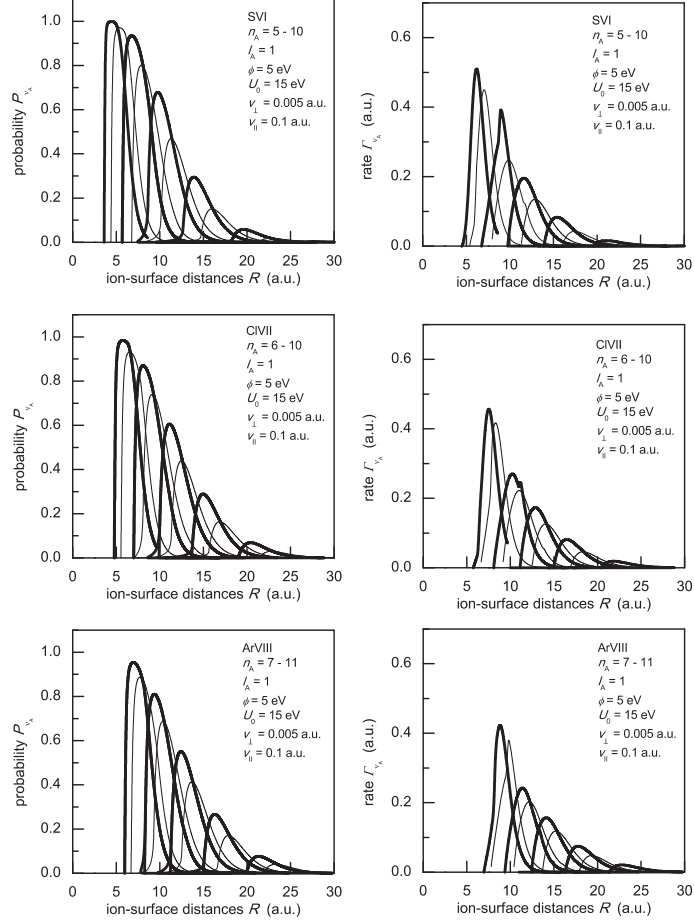


Figure 1. Population and neutralization probabilities and rates.

Neutralization distances R_c^N represent the position of maxima of the population rates Γ_{ν_A} ; these distances can be considered as distances at which the population process is mainly localized.

In Fig. 2 we present the neutralization distances R_c^N of the considered ions (obtained from the population rates) as a function of principal quantum number n_A (thick-solid curves), and compare the results with those obtained in Ref. [3] for the normal escaping geometry (dashed curves). The neutralization distances in the point-like case are presented by thin-solid curves. We see that the neutralization distances corresponding to the same ion and the same quantum state obtained in the present article in the case of grazing geometry are smaller in comparison to normal escaping geometry case. This means that the effect of the parallel velocity shifted the process

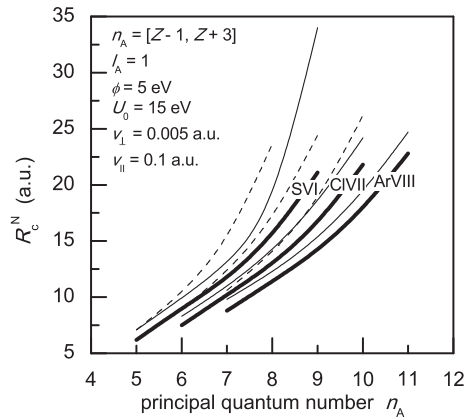


Figure 2. Neutralization distances R_c^N .

closer to the surface. This effect is more pronounced for greater quantum numbers.

From Fig. 2 we also recognize that the neutralization distances for polarized cores are smaller than in the case of point-like core approximation.

Acknowledgements This work was supported in part by the Ministry of Education, Science and Technological Development, Republic of Serbia (Project 171016).

REFERENCES

- [1] N. N. Nedeljković, M. D. Majkić and S. M. D. Galijaš, *J. Phys. B: At. Mol. Opt. Phys.* 45, 215202 (2012)
- [2] M. D. Majkić, N. N. Nedeljković and S. M. D. Galijaš, *J. Phys: Conf. Series* 399, 012009 (2012)
- [3] N. N. Nedeljković, M. D. Majkić, S. M. D. Galijaš and S. B. Mitrović, *App. Surf. Sci.* 254, 7000 (2008)
- [4] N. N. Nedeljković and M. D. Majkić, *Phys. Rev. A* 76, 042902 (2007).

EFFECT OF THE SOLID WORK FUNCTION ON THE POPULATION OF THE ArX IONS IN THE GRAZING INCIDENCE GEOMETRY

N. N. Nedeljković, M. D. Majkić and S. M. D. Galijaš

University of Belgrade, Faculty of Physics, P.O.Box 368, Belgrade, Serbia

Abstract. We use the two-state vector model to investigate the intermediate stages of the population process of the Rydberg states of the ArX ion interacting with the conducting surfaces, under grazing incidence geometry. The effect of the solid work function on the population process is analyzed in details. The solid work function has influence on the position and the magnitude of the population probabilities. At higher ionic velocities, the larger n_A Rydberg states are populated only in the interaction with solid surfaces of the sufficiently low work function. By the increase of the solid work function, the neutralization distances increase as well.

1. INTRODUCTION

The population dynamics of the multiply charged ArX ion impinging the conducting solid surface in the grazing incidence geometry has been analyzed within the framework of the two-state vector model (TVM) in Refs. [1, 2]. In the cited references, the effect of parallel velocity on the population probabilities and neutralization distances has been analyzed in details. On the other hand, only the Al surface with work function $\phi = 5eV$ has been considered.

In the present article, the TVM is used to analyze the influence of the solid work function on the population process of the Rydberg states of the Ar X ions in the grazing incidence geometry. That is, we analyze the "population histories" for the considered quantum states, for different solid surfaces. The first state of the TVM carries the information about the initial condition (preselection) $|\Psi_1(t_{in})\rangle = |\mu_M\rangle = |\gamma_M, n_{1M}, m_M\rangle$, while the second state carries the information about a condition that has to be met in the future (postselection) $|\Psi_2(t_{fin})\rangle = |\nu_A\rangle = |n_A, l_A, m_A\rangle$. At the initial time, $t = t_{in}$, the ion has been at the distance $R \rightarrow \infty$ from the surface, and at final time the ion-surface distance is $R = R_{fin}$.

2. FORMATION OF THE INTERMEDIATE RYDBERG STATES IN THE GRAZING GEOMETRY

The TVM, adapted to the grazing incidence case [1, 2] is in many details the same as in the normal emergence case [4]. The transition probability $T_{\mu'_M, \nu_A}(t)$ per unit energy parameter γ'_M (transition probability density) is defined by the same expression as in [4]. The corresponding intermediate transition probability $T_{\nu_A}(t)$, in which the overall effectively extended conduction band participate, represents a "sum" over μ'_M :

$$T_{\nu_A}(t) = \int \sum_{n_{1M}, m_M} \langle f \rangle_{\Omega_{\vec{k}'}} T_{\mu'_M, \nu_A}(t) d\gamma'_M. \quad (1)$$

The intermediate population probability of the Rydberg state that will evolve into the final state $|\nu_A\rangle$ (probability of the formation of intermediate Rydberg state) is given by $P_{\nu_A}(R)$, which follows directly from Eq. (1). In (1) the quantity $\langle f \rangle_{\Omega_{\vec{k}'}} = \int_{4\pi} f d\Omega_{\vec{k}'}/4\pi$ is the angle averaged Fermi-Dirac distribution $f = I_{[0, E_F]}(k^2/2)$, where $E_F = U_0 - \phi$ is the Fermi energy; by this expression we introduce the solid work function ϕ as a parameter of the TVM; by U_0 we denoted the depth of the potential well in solid. The quantity $T_{\mu'_M, \nu_A}(t)$ is defined for the energy parameter $\gamma'_M = \sqrt{2U_0 - k'^2}$, where $\vec{k}' = \vec{k} - \vec{v}_{\parallel}$.

We consider the population probability $P_{\nu_A}(t) = 1 - \exp(-T_{\nu_A}(t))$. Due to the presence of the factor $\langle f \rangle_{\Omega_{\vec{k}'}}$ in the expression (1), the probability P_{ν_A} first increases with decreasing R , exhibits maximum $P_{\nu_A}^{\max}$ at $R = R_{\max}$, and after that decreases with further decreasing of R .

3. RESULTS

In Fig. 1 we present the population probabilities of the Rydberg states ($n_A = 8-18, l_A = 1$) for ArX ion ($Z = 8$) impinging a solid surface at grazing incidence. For the perpendicular and parallel velocity components we used the values $v_{\perp} = 0.005$ a.u. and $v_{\parallel} = 0.1$ a.u., respectively, and analyze the effect of the solid work function taking the values from $\phi = 2.8$ eV to $\phi = 5.2$ eV.

We see that the positions and the magnitudes of the population probabilities vary with ϕ in a controllable way. The population of all the considered Rydberg states of the ArX ion is possible in the case of the solids with work function $\phi = 2.8$ eV and $\phi = 3.5$ eV, such as W(110). However, for $\phi = 4.3$ eV; Al(111) and for $\phi > 4.3$ eV the population of some Rydberg states becomes practically impossible. The number of the states which can be populated decreases with the increase of ϕ . That is, the magnitude of the population probability maxima of the Rydberg states for higher value of the principal quantum number ($n_A > Z + 4$) decreases with further increase of the solid work function. The value of the solid work function $\phi = 5.2$

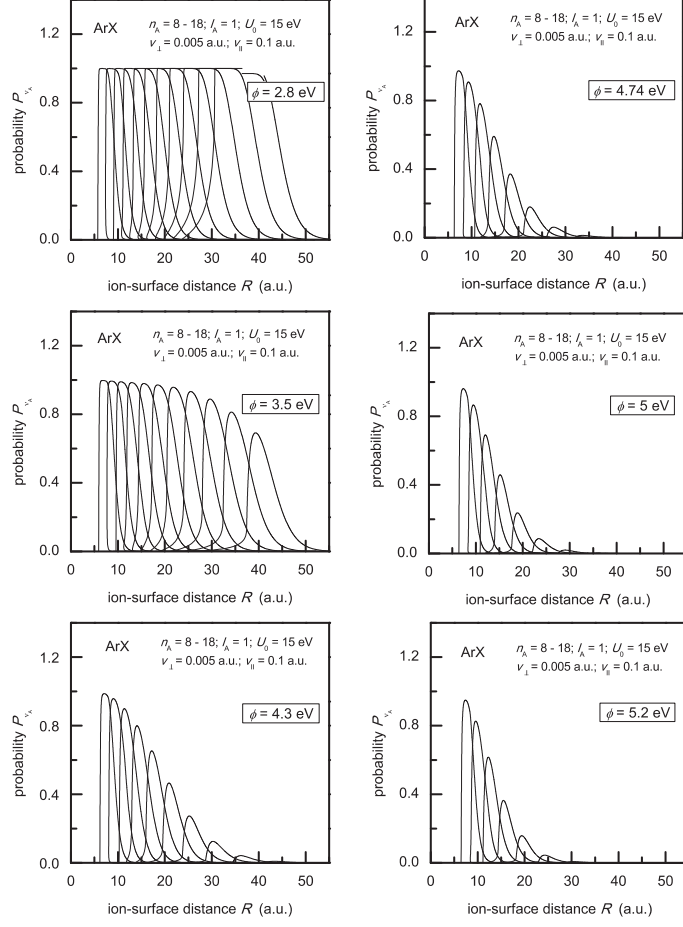


Figure 1. Population probabilities $P_{\nu_A}(t)$.

eV for the considered values of the v_{\perp} and v_{\parallel} , "allows" only the population states $n_A \in [Z - 2, Z + 1]$.

We note that the population of the higher Rydberg states becomes possible (for the same work function) for higher values of the parallel velocity component. For example, the population of the states $n_A = Z + 5$ for the $\phi = 5.2$ eV (Ni(111)) is possible for the parallel velocity component $v_{\parallel} = 0.15$ a.u. Thus, the population of the Rydberg states with higher values of the principal quantum number requires an increase of the solid work function and/or an increase of the v_{\parallel} .

In Fig. 2 we present the neutralization distances R_c^N via work function ϕ for the ArX ion, for the same ion-surface characteristics as in Fig. 1. From the figure we can conclude that the neutralization distances for

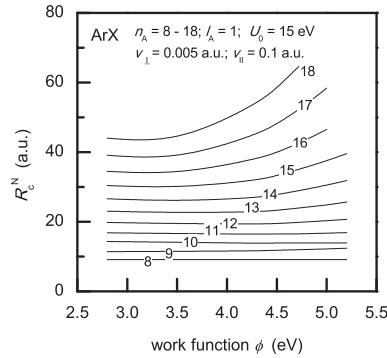


Figure 2. Neutralization distances R_c^N via solid work function ϕ .

the population of the states $n_A \in [Z - 2, Z + 1]$ are practically independent on the solid work function. The most probable ion-surface distances for the population of the Rydberg states with higher values of the n_A become different for different surfaces. With increase of the solid work function ϕ the neutralization distances R_c^N (for these Rydberg states) also increase.

The population rule can be established based on the analysis of the present paper. At lower values of the solid work function and for smaller values of the parallel ionic velocities all Rydberg states can be populated. At higher ionic velocities v_{\parallel} the states with greater values of the principal quantum number n_A can be populated only if the solid work function is sufficiently low.

Acknowledgements This work was supported in part by the Ministry of Education, Science and Technological Development, Republic of Serbia (Project 171016).

REFERENCES

- [1] N. N. Nedeljković, M. D. Majkić and S. M. D. Galijaš, J. Phys. B: At. Mol. Opt. Phys. 45, 215202 (2012)
- [2] M. D. Majkić, N. N. Nedeljković and S. M. D. Galijaš, J. Phys: Conf. Series 399, 012009 (2012)
- [3] N. N. Nedeljković, M. D. Majkić, S. M. D. Galijaš and S. B. Mitrović, App. Surf. Sci. 254, 7000 (2008)
- [4] N. N. Nedeljković and M. D. Majkić, Phys. Rev. A 76, 042902 (2007).

INFLUENCE OF THE ELECTRON BEAM IRRADIATION ON GRAPHENE DURING DEVICES PRODUCTION

Marijana Milićević, Aleksandar Matković, Borislav Vasić and Radoš Gajić

Institute of Physics, University of Belgrade, Pregrevica 118, 11080 Belgrade, Serbia

Abstract. We examine the influence of the electron beam irradiation on single and few layer graphene samples, introduced during e-beam lithography process, commonly used for fabrication of contacts and various graphene devices. For this purpose two point probe (2PP) field effect transistors (FET) with graphene channel, as well as clean graphene samples are exposed to electron beam irradiation, with varied beam energy and exposure time. Techniques such as micro-Raman spectroscopy, DC transport, atomic force microscopy (AFM), Kelvin probe force microscopy (KPFM) and electrostatic force microscopy (EFM) measurements are employed to determine the influence of the electron beam irradiation of graphene. Critical parameters for the electron beam irradiation of graphene are obtained. These allow fabrication of graphene devices without introducing damage and defects through the process of the electron beam irradiation.

1. INTRODUCTION

Graphene's ability to efficiently conduct current and heat, together with its single atomic layer thickness and optical transparency led to the great research activity [1] and efforts to make next-generation nano-devices [2]. These are in most cases fabricated using electron beam lithography (EBL), technique that has been employed both for making various contact geometries and for patterning of graphene. Also imaging of the devices is done using scanning electron microscopy (SEM) and transmission electron microscopy (TEM). In both cases, energetic electrons lead to irradiation of the material, giving rise to damage and disordering of graphene lattice [3]. This may result on lowering of graphene device performances by influencing carrier mobility and doping. In this work we present such investigation focusing on single and few layer graphene samples.

2. SAMPLE PREPARATION AND IRRADIATION

2.1 Preparation

Graphene samples are obtained by micro-mechanical exfoliation of highly ordered pyrolytic graphite (HOPG) on Si-wafer with 300 nm thick layer of SiO₂. Graphene flakes are identified using optical microscope (Figure 1.c and Figure 2.a) and then confirmed with Raman spectroscopy. 2PP FET-s are fabricated using UV photo-lithography (see Figure 1). Afterwards, a 200 nm thick layer of poly(methyl methacrylate) (PMMA) is spin-coated on top of FETs, in the same way as it would be done for EBL. By doing so, it is possible to see the influence of the electron beam on graphene in conditions most commonly present in practice.

2.2 Irradiation

Samples with and without PMMA coating are placed in a SEM and exposed to the electron beam of various energies (1 keV, 10 keV, 20 keV, 30 keV, shown in Figure 1.b and 1.c) and exposure times (1min, 10min, 30 min, 60 min), resulting with the different accumulated irradiation dosages. Figure 2.b shows SEM image obtained by applying irradiation of 1keV on graphene for 10 min. For AFM measurements the devices with PMMA coating are soaked in Iso-propyl alcohol-MIBK 1:1 mixture after exposure, in order to remove this layer.

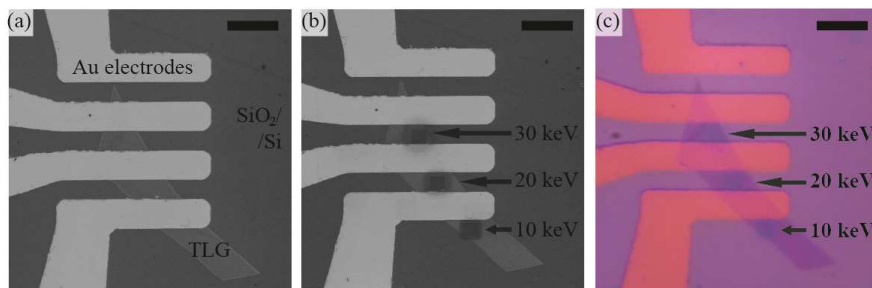


Figure 1. (a) shows SEM images of a tri-layer graphene (TLG) with 15 nm thick evaporated gold contacts, made by UV photo-lithography. (b) and (c) show SEM and optical microscopy images of the same device after three expositions to the electron beam (exposed areas of 4x4 μm², exposition time of 10 minutes) with energies of 10 keV, 20 keV and 30 keV. Scale bars (in top right) are 10 μm long.

3. RESULTS

Before and after exposure the devices are examined by room-temperature Raman spectroscopy, DC electrical measurements, AFM, KPFM and EFM. The changes in Raman spectra under irradiation such as broadening of

G and 2D peaks, as well as change in relation of intensities of defect D and G Raman mode $I(D)/I(G)$, are indicative of the disorder and defects [4]. These changes are increased with larger electron dosages. Defect mode D and amorphous carbon mode G^* of various intensities are observed after different irradiation dosages. Sample's topography (Figure 2.c) and material contrast (Figure 2.d) are obtained by AFM. Afterwards, KPFM and EFM measurements (Figures 1.e – 1.h) are used to investigate the interaction between the sample and the electron beam.

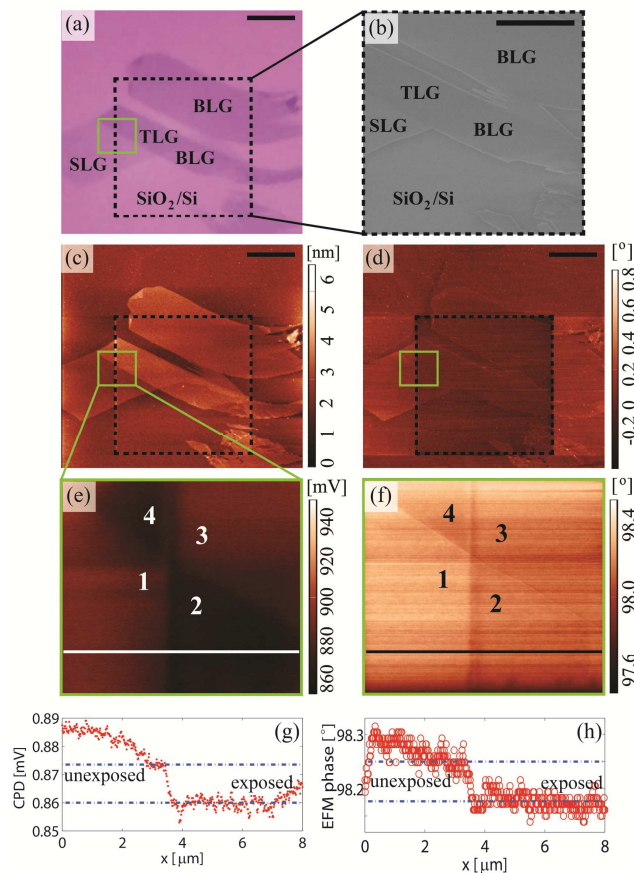


Figure 2. (a) shows optical microscopy image of the sample. (b) shows SEM image of the exposed area. (c) and (d) show AFM topography and phase, respectively. Scale bars in (a) to (d) are 10 μm . Dashed (black) square in (a), (c) and (d) marks the area exposed to the electron beam, while solid (green) square marks the area used for KPFM and EFM measurements. (e) and (f) show KPFM and EFM maps of $8 \times 8 \mu\text{m}^2$ area. Here, numbers 1 to 4 indicate unexposed SLG, exposed SLG, exposed TLG and unexposed TLG areas, respectively. Solid horizontal lines in (e) and (f) indicate height profiles shown in (g) and (h), respectively.

The difference between the exposed and unexposed areas of the sample, seen both in KPFM and EFM, are a combination of the trapped charges in the SiO₂ and the change of graphene's work function. The latter is a consequence of both sample damage and the electric field doping introduced by the trapped charges. 2PP transport measurements give possibility to observe changes in resistivity as a function of a back-gate voltage. These measurements allow for an unambiguous separation of the effects as the decrease in electron mobility (defects in graphene structure) and change in charge neutrality point (accumulated trapped charges) [1].

4. CONCLUSION

In this study we examine the influence of electron beam irradiation on graphene devices using Raman spectroscopy, DC transport measurements, AFM, KPFM and EFM in order to obtain critical parameters for EBL and SEM imaging both with and without top PMMA layer. Results show presence of certain disorder in graphene lattice and of amorphous carbon for almost all electron dosages.

Acknowledgements

This work is supported by the Serbian MPNTR through Projects OI 171005, III 45018, and by Qatar NRF through Project NPRP 7-665-1-125 .

REFERENCES

- [1] A. H. Castro Neto, F. Guinea, N. M. R. Peres, , K. S. Novoselov and A. K., Geim, *Rev. Mod. Phys.* 81, 1 (2009).
- [2] Q. Bao and K. Ping Loh, *ACS Nano* 6, 5 (2012).
- [3] I. Childres, L. A. Jauregui, M. Foxe, J. Tian, R Jalilian, I. Jovanovic and Y. P. Chen, *Appl. Phys. Lett.* 97, 173109 (2010).
- [4] A. C. Ferrari and J. Robertson, *Phys. Rev. B* 61, 14095 (2000).

OPTICAL PROPERTIES OF SILVER IMPLANTED HIGH DENSITY POLYETHYLENE OBSERVED USING SPECTROSCOPIC ELLIPSOMETRY

Miloš Nenadović, Danilo Kisić, Danka Stojanović and Zlatko Rakočević

*INS Vinca, Laboratory of Atomic Physics, University of Belgrade, Mike Alasa
12-14, 11001 Belgrade, Serbia*

Abstract. High density polyethylene (HDPE) has been modified by Ag^+ ion implantation with the energy of 60 keV. The doses of implanted silver ions were 1×10^{15} , 5×10^{15} and 1×10^{16} ions/cm². The changes in refractive index (n) and extinction coefficient (k) were observed using spectroscopic ellipsometer. Increasing the implantation dose leads to moving the maximum of refractive index and extinction coefficient towards higher wavelengths. This is a consequence of optical activation of the polymer, caused by different concentrations of silver ions in the polymer matrix.

1. INTRODUCTION

Polymeric solid materials have been applied to many fields ranging from everyday life to low- and high-technology engineering due to their many unique advantages such as light weight, mold ability, ability to form complicate shapes, corrosion resistance, versatile electronic and optical properties, and low manufacturing cost [1,2]. It has been proven recently that ion implantation technology is very attractive for modifying the surface properties of polymeric materials. The structural changes caused by high energy ions give improvements in optical properties, surface chemical activity, and potential applications in sensor systems [3,4].

2. EXPERIMENTAL PROCEDURE

Commercial 2 mm thick table of HDPE (BASF, 0.945g/cm³) was mechanically polished with 4000 grade polishing paper, cleaned in ultra-sonic bath in ethanol solution and rinsed with 18.2 M Ω deionised water. Initial HDPE samples (1 cm \times 1 cm) were implanted by Ag^+ ions with the energy of 60 keV in the ion implanter chamber. The working pressure in the chamber was 1×10^{-6} Pa. The source of Ag^+ ions was the preheated AgCl salt (Fluka, p.a.), with the assistance of argon as a carrier gas.

Characterization of the optical properties was carried out by measuring refractive index (n) and extinction coefficient (k) using HORIBA Jobin Yvon UVISEL iHR320 ellipsometer. Monochromator wavelength range was from 200 to 2200 nm, or from 0.6 to 4.8 eV. All optical spectra were recorded under the same conditions with a step of 0.1 eV. The obtained optical spectra were further analyzed using the software package Delta Psi2.

3. RESULTS AND DISCUSSION

Figure 1a shows the dependence of refractive index (n) on wavelength. For the untreated HDPE sample, refractive index shows no dependence on wavelength, and remains constant at the value of 1.5. This suggests the existence of homogeneity in the structure of HDPE because there is no significant change in the speed of light through the polymer. Increase of silver ions implantation dose, causes refractive index maximum position to shift towards higher values of wavelength (420, 482 and 596 nm). The maximum values of refractive index increase, too (1.94, 2.15 and 2.32). This is a consequence of the amount of implanted silver ions in the polymer matrix. A higher concentration of silver ions in the polymer is a greater obstacle to the propagation of light through the material and therefore the value of refractive index increases with increasing implantation dose.

The dependence of extinction coefficient (k) on wavelengths is presented in figure 1b. Extinction coefficient of the untreated HDPE doesn't show dependence on wavelength. Its value remains constantly close to zero, regardless of the light wavelength. This indicates a high degree of transparency of pure high density polyethylene in the entire wavelength range. Increase of silver ions implantation dose, causes extinction coefficient maximum position to shift towards higher values of wavelength (304, 323, and 389 nm). The maximum value of extinction coefficient increases too (0.41, 0.59, and 0.79). These changes of extinction coefficient are in agreement with refractive index changes, and confirm optical activation of high density polyethylene.

Extinction coefficient is a measure of optical absorption of the material. In the case of implantation of silver ions with different doses, there is the increase of absorption with the increase of implantation dose. This is consistent with the expected results because the amount of implanted material is proportional to the degree of absorption.

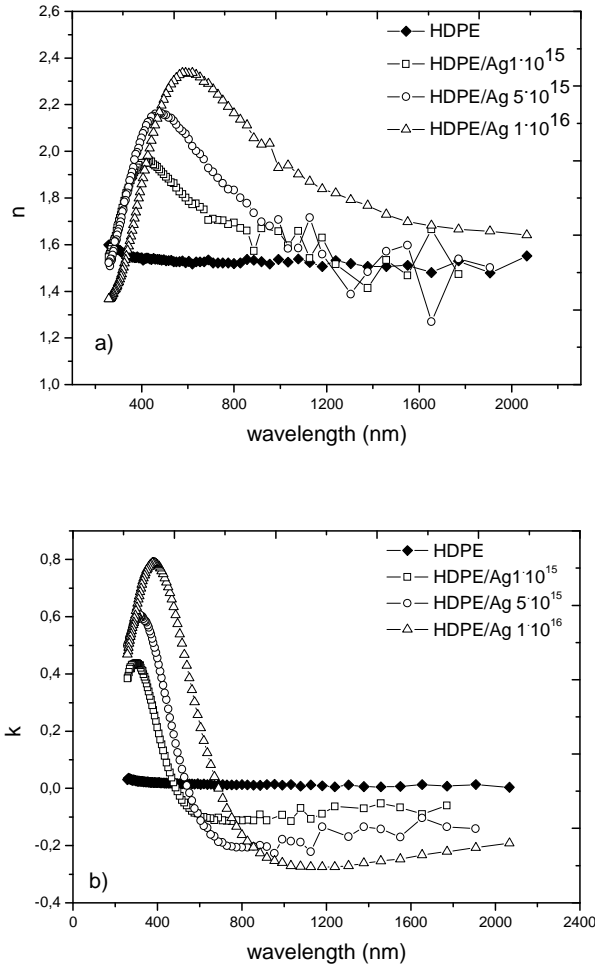


Figure 1. Optical spectra of the HDPE/Ag system implanted with doses 1×10^{15} , 5×10^{15} and 1×10^{16} ions/cm²: a) dependence of refractive index (n) on wavelength b) dependence of extinction coefficient (k) on wavelength.

4. CONCLUSIONS

High density polyethylene has been modified by Ag⁺ ion implantation with the energy of 60 keV and with the doses of 1×10^{15} , 5×10^{15} and 1×10^{16} ions/cm². As a result of ion implantation, significant optical changes on HDPE

surface region are observed. The polymer is optically activated due to the changes of refractive index and degree of absorption (extinction coefficient) in the material, after silver ions implantation. Shifts of the refractive index and extinction coefficient peaks positions, together with the changes of the values of refractive index and extinction coefficient are directly related to the amount (concentration) of implanted ions.

Acknowledgements

This work was financially supported by the Ministry of Education and Science of the Republic of Serbia (project no. III45005).

REFERENCES

- [1] J. M. Charrier, *Polymeric Materials and Processing: Plastics, Elastomers and Composites*, Hanser Publishers, Munich, New York, 1991.
- [2] D. Fink, *Fundamentals of ion-irradiated polymers*, Springer, 2004.
- [3] V.B. Odzhaev, I.P. Kozlov, V.N. Popok, D.B. Sviridov, *Ion Implantation of Polymers*, Belorussian State University, Minsk, 1998.
- [4] M. Nenadovic, J. Potocnik, M. Ristic, S. Strbac, Z. Rakocevic, *Surf. Coat. Technol.* 206 (2012) 4242.

MICROSTRUCTURE AND MAGNETIC PROPERTIES OF Xe ION IRRADIATED Co/Si BILAYERS

M. Novaković¹, M. Popović¹, V. Čubrović², K. Zhang³, N. Bibić¹

¹*VINČA Institute of Nuclear Sciences, University of Belgrade, 11001 Belgrade, Serbia*

²*Faculty of Physics, University of Belgrade, 11001 Belgrade, Serbia*

³*II. Physikalisches Institut, Georg-August-Universität Göttingen, Friedrich-Hund-Platz 1, 37077 Göttingen, Germany*

Abstract. Evolution of the microstructure of Co/Si bilayers during Xe⁺ ions irradiation has been studied and the same is correlated with magnetic properties. Thin cobalt films were deposited by electron beam evaporation method on (100) Si wafer, to a thickness of 50 nm. After deposition the layers were irradiated with 400 keV Xe⁺ ions to the fluences in the range of 2-30×10¹⁵ ions/cm². Analyses by Rutherford backscattering spectroscopy and transmission electron microscopy provided information on the implanted Xe profiles as well as thickness and the microstructure of ion-induced mixed regions. Magnetic properties of the layers were analyzed by using in-plane magneto-optical Kerr effect. In as deposited layer we found predominantly uniaxial magnetic anisotropy. After irradiation a mixed region at the interface was observed and magnetic anisotropy was lost.

1. INTRODUCTION

Ion irradiation of ferromagnetic films, tens of nm thick, can dramatically modify their microstructural and magnetic properties. Based on the need to tailor shallow CoSi₂ junctions as contact metallization, the Co–Si system has been investigated in much detail, with respect to thermal and ion-induced mixing [1,2], implantation through metal doping [3], nano-patterning via focused ion beams [4], and low-energy and swift heavy-ion mixing [5,6]. Nonetheless, the correlations existing between the microstructural properties of ion-irradiated or ion-mixed metal/silicon bilayers and their magnetic properties (in the case of 3d elements) is far from being understood.

The present work outlines the influence of the Xe⁺ ion irradiation on the structural and magnetic properties of Co/Si bilayer induced by intermixing processes. The present paper refers to a small selection of the results obtained so far, which will be presented and discussed in more detail in a forthcoming article.

2. EXPERIMENTAL

Cobalt thin films were prepared on crystalline (100) silicon wafers, by using electron beam evaporation method. The films were deposited to a thickness of 50 nm, under the vacuum of 1×10^{-4} Pa. After deposition the samples were irradiated with a beam of 400 keV Xe^+ ions to the fluences of 2, 4, 6, 8, 10, 15, 20 and 30×10^{15} ions/cm². The pressure during implantations was about 2×10^{-5} Pa. According to SRIM calculations [7] a mean ion range of 400 keV Xe^+ ions in Co–Si system is 80 nm, with the maximum energy deposited at the Co/Si interface.

Compositional characterization of samples was performed with Rutherford backscattering spectroscopy (RBS), using the 900 keV He^{++} ion beam. The backscattering spectra were taken at normal incidence and the changes in the concentration profiles of the Co/Si components were analyzed with the Data Furnace WiNDF software [8]. Cross-sectional transmission electron microscopy (XTEM) was performed on PHILIPS CM30 microscope, operated at 300 kV, and we also used micro-diffraction (MD) and fast Fourier transformation (FFT) analyses. The magnetic properties of the samples were characterized at room temperature by in-plane magneto-optical Kerr effect (MOKE) measurements. Angle-dependent magnetic remanence obtained from the MOKE hysteresis curves gave information about magnetic anisotropy in the films.

3. RESULTS AND DISCUSSION

Fig. 1 illustrates the deduced Co and Si depth profiles in Co/Si bilayers irradiated with 400 keV Xe^+ ions, for various ion fluences.

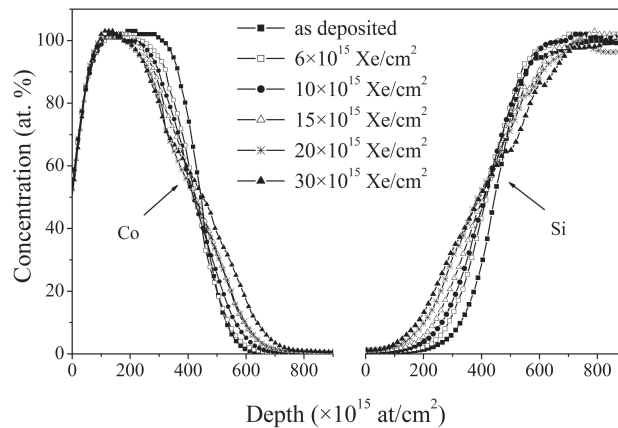


Figure 1. Variation of Co and Si concentration profiles in Co/Si bilayers irradiated with 400 keV Xe^+ ions.

For the sake of clarity, the spectra corresponding to the samples irradiated with 2, 4 and 8×10^{15} Xe/cm² were omitted from the figure. The presented profiles clearly illustrate that even for the lower irradiation fluences the ion irradiation induces intermixing of the bilayer components. Both Co and Si signals exhibit diffusion-like concentration profiles, with a progressive broadening of the Co/Si interface for increasing Xe-ion fluence. It was found that the intermixed region increases almost linearly with the ion fluence [9].

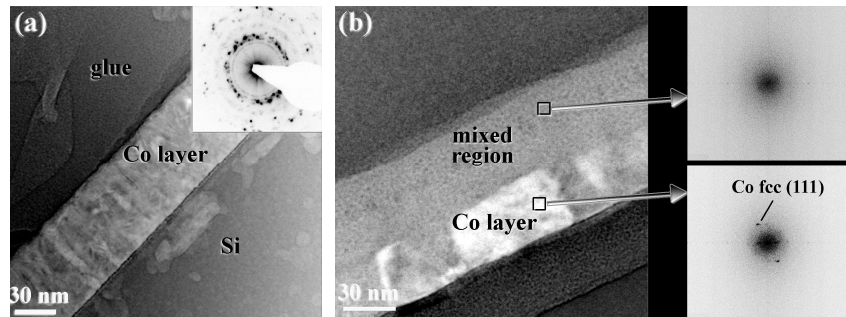


Figure 2. Cross-sectional TEM analysis of Co/Si bilayers: (a) as deposited Co/Si sample; (b) Co/Si layer irradiated to 20×10^{15} Xe/cm².

Additional information about the layer structure was gained from cross-sectional TEM, shown in Fig. 2. Bright-field image of as deposited sample (a) shows 50-nm-thick Co layer, well separated from the Si substrate. The Co layer grows in the form of a columnar structure. The obtained ring-like diffraction pattern indicates a very fine polycrystalline structure of the layer. TEM image shown in (b) was taken from Co/Si bilayer after irradiation to 20×10^{15} Xe/cm². Note the high contrast between the Si substrate and the mixed region. The wide of intermixed region is ~ 50 nm and based on the corresponding Fourier transform it is evident that this region is amorphous. At the same time, the crystallinity of the rest of Co layer is preserved.

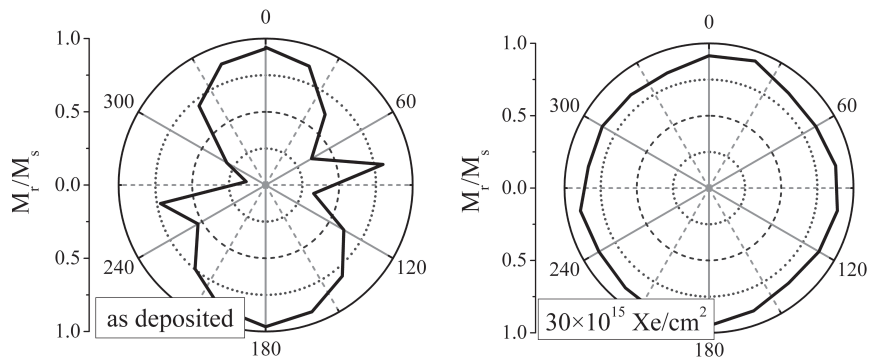


Figure 3. Angular dependence of the relative remanence M_r/M_s of as deposited and 30×10^{15} ions/cm² Xe⁺ irradiated Co/Si films, measured with MOKE.

Information about magnetic anisotropy in the layers was obtained from the MOKE measurements of relative magnetic remanence M_r/M_s , the parameter M_s being the saturation magnetization. The angular dependence of relative magnetization on the ion fluence is illustrated in Fig. 3. The as deposited Co layer show uniaxial anisotropy, with a rather small fourfold components of magnetization. After irradiation to the fluence of 30×10^{15} ions/cm² the isotropic contribution becomes dominant component of magnetization in Co/Si layers. This is probably due to the changes of the internal stresses induced by ion irradiation, but needed further clarification.

4. CONCLUSION

The structural and magnetic properties of polycrystalline 50-nm-thick Co films irradiated by 400 keV Xe⁺ ions has been investigated. It was observed that Xe⁺ ions irradiation leads to the formation of amorphous intermixed region at the Co/Si interface. As for the magnetic properties, it was found very strong effect of Xe⁺ ions irradiation. In as deposited Co layer a coupling of uniaxial and fourfold anisotropies has been occurred. But, after irradiation with Xe⁺ ions the isotropic contribution becomes dominant component of magnetization.

Acknowledgements

This work was supported by the Ministry of Education and Science of the Republic of Serbia (Project No. III 45005) and by Deutsche Forschungsgemeinschaft (Project 436 SER 113/2).

REFERENCES

- [1] W. Xia, C. A. Hewett, M. Fernandes, S. S. Lau and D. B. Poker, *J. Appl. Phys.* 65, 2300 (1989).
- [2] S. Dhar, Y. N. Mohapatra and V. N. Kulkarni, *Phys. Rev. B* 54, 5769 (1996).
- [3] L. Niewohner and T. Jager, *Proceedings of the Eighth IEEE VLSI Multilevel Interconnection Conference*, p.329 (1991).
- [4] M. M. Mitan, D. P. Pivin, T. L. Alford and J. W. Mayer, *J. Vacuum Sci. Technol. B* 19, 2525 (2001).
- [5] J. M. Fallon, C. A. Faunce, P. J. Grundy and H. J. Blythe, *J. Appl. Phys.* 87, 6833 (2000).
- [6] D. Bhattacharya, S. K. Srivastava, P. K. Sahoo, G. Principi, D. Kabiraj, T. Som, V. N. Kulkarni and D. K. Avasthi, *Surf. Coat. Technol.* 158/159, 59 (2002).
- [7] J. F. Ziegler, J. P. Biersack and U. Littmark, *The Stopping and Range of Ions in Solids*, (Pergamon Press, New York, 1984); <http://www.srim.org>.
- [8] N. P. Barradas, C. Jaynes and R. P. Webb, *Appl. Phys. Lett.* 71, 291 (1997).
- [9] M. Novaković, K. Zhang, M. Popović, N. Bibić, H. Hofsäss and K.P. Lieb, *Nucl. Instrum. Methods B* 269, 881 (2011).

STRUCTURAL AND OPTICAL CHARACTERIZATION OF TiN THIN FILMS IMPLANTED WITH HIGH VANADIUM FLUENCES

Maja Popović, Mirjana Novaković, Aleksandar Maksić, Nataša Bibić

*VINČA Institute of Nuclear Sciences, University of Belgrade, 11001 Belgrade,
Serbia*

Abstract. Polycrystalline titanium nitride (TiN) film deposited by d.c. reactive sputtering on Si(100) wafer was irradiated with 80 keV vanadium ions up to the fluence of 2×10^{17} ions/cm². Rutherford backscattering spectrometry, cross-sectional (high-resolution) transmission electron microscopy (TEM/HRTEM) and spectroscopic ellipsometry were carried out in order to study structural and optical properties of TiN/Si samples. From cross-sectional TEM observations of implanted sample it was found that the TiN film was damaged inside of 120-170 nm and the traces of VN was identified. It is also observed that the vanadium ions caused the optical changes in TiN film.

1. INTRODUCTION

Transition metal nitrides such as titanium nitride present highly covalent bonds in simple, usually cubic structures, which give them an extreme hardness, high corrosion resistance and excellent mechanical and high-temperature stability [1,2]. Due to their excellent tribological characteristics, TiN films have been widely used in industry ranging from hard coatings, coatings for corrosion and wear resistance, to diffusion barriers in microelectronic devices. To further improve the properties of TiN coatings ion implantation technology is found to be an effective method to modify structural, electrical and optical properties of the TiN films. Therefore, many studies have been carried out on the effects of the implantation of different ions into TiN coatings [3,4].

In this paper, high dose (up to 2×10^{17} ions/cm²) vanadium-ion implantation has been performed on the TiN films deposited on Si wafers, and the microstructural and optical changes induced by this ion were investigated.

2. EXPERIMENTAL DETAILS

Titanium nitride films were deposited on Si (100) wafers by dc reactive sputtering from a Ti target of 99.9% purity, using sputtering (Ar) and reactive

(N₂) gases. The films had a thickness of 240 nm as verified by TEM. Then, the samples were implanted with 80 keV V⁺ ions to the fluences of 1×10^{17} and 2×10^{17} ions/cm². The chosen V-ion energy guaranteed that the average projected range, $R_p = 38$ nm, and full width at half maximum (FWHM), $\Delta R_p = 14$ nm, estimated with the SRIM2010 [5].

The Rutherford backscattering analysis (RBS) was performed with a 900 keV He⁺⁺ ion beam and the concentration profiles of the various components were analyzed with the WIN-DF code [6]. Microstructure of the samples was investigated using cross-sectional (high resolution) transmission electron microscopy at a Philips CM200-FEG microscope operated at 200 keV. In order to investigate the structure of crystalline regions, the image was analyzed by fast Fourier transformation (FFT). Ellipsometry measurements were conducted over the spectral range from 260 – 2100 nm at an angle of incidence of 70 degrees using a HORIBA – Jobin Yvon UVIS ellipsometer.

3. RESULTS AND DISCUSSION

The Ti, V, O and Si concentration profiles of as deposited TiN sample and sample irradiated with 2×10^{17} V/cm² deduced from RBS are presented in Fig. 1. Firstly, we note an increase in total layer thickness, which most probably is due to surface oxidation and overcomes the expected reduction in layer thickness due to sputtering. Secondly, we observe inhomogeneous concentration of Ti almost in the whole layer especially in the vanadium-enriched zone. It was found that the vanadium ions are stopped at 60 nm from the surface which is deeper than the SRIM calculation predicted ($R_p=38$ nm), with the maximum concentration of 20 at %.

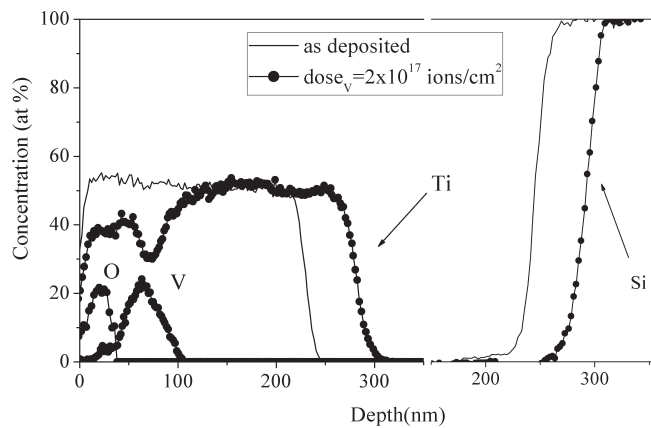


Figure 1. Ti, V, O and Si depth profiles in as deposited and vanadium irradiated TiN films to the fluence of 2×10^{17} ions/cm².

A bright-field TEM image, a high-resolution TEM image, and the Fourier transforms corresponding to several regions of the damaged sublayer of a

TiN/Si sample after implantation of 2×10^{17} V-ions/cm² are presented in Figures 2a,b. In the bright-field image (a) a 20-30 nm amorphous (oxidized) surface layer can be discerned, followed by a 120-170 nm thick damaged layer containing the V atoms (as proven via RBS, Figure 1), as well as the remaining TiN sublayer of columnar structure, which was not affected by ion implantation. As shown in the lower part of Figure 2, the FFT patterns taken from three different parts of damaged region, shown in HRTEM image in (b) revealed, besides the expected TiN(111), (200) and (220) reflexes, traces of VN(111) and VN(200) reflexes.

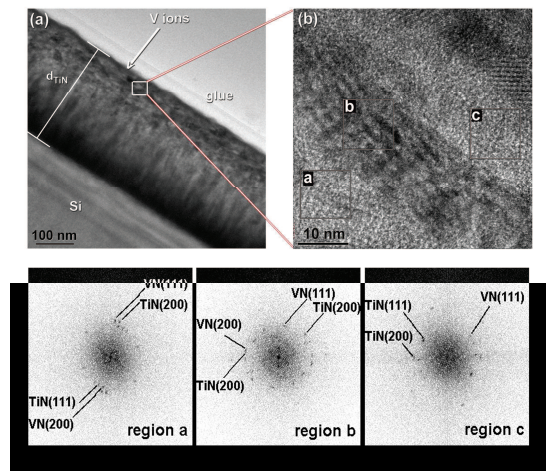


Figure 2. TEM analysis of TiN/Si bilayers implanted with 2×10^{17} V-ions/cm²: (a) TEM bright field image; and (b) HRTEM image of the damaged region indicated in (a) and Fourier transforms from the labeled regions.

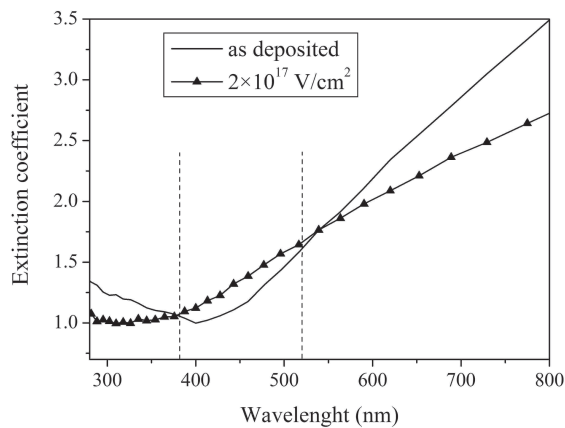


Figure 3. The obtained extinction coefficient (k) as a function of wavelength for as deposited and vanadium implanted TiN sample to the fluence of 2×10^{17} ions/cm².

Using spectroscopic ellipsometry complex refractive index (real part (n) and imaginary part (k)) as a function of wavelength was calculated. Fig. 3 shows k values for as deposited sample (solid line) and vanadium implanted TiN sample to the fluence of 2×10^{17} ions/cm² (triangles) in the range of 280-800 nm. The as deposited sample exhibits a minimum of k value in the visible part of the spectrum and almost linear increase with increasing wavelength which is similar to that previously reported for TiN films [7]. Qualitatively, we observed a considerable change in slope after V ion implantation. The presence of vanadium atoms in the TiN films leads to the higher values of k in the spectral range where pure vanadium adsorbs (380-520 nm).

4. CONCLUSIONS

We have studied the effects of vanadium ion implantation on the structural and optical properties of TiN thin film. It was found that the vanadium ion implantation to the fluence of 2×10^{17} ions/cm² rearranges the crystalline structure of the layer, breaks up the columns and induces the growth of nanocrystals of VN phase. Also, the extinction coefficient of implanted sample was changed due to the presence of vanadium atoms in TiN film.

Acknowledgements

This work was supported by the Ministry of Education and Science of the Republic of Serbia (Project No. III 45005) and by Deutsche Forschungsgemeinschaft (Project 436 SER 113/2).

REFERENCES

- [1] B. Bushan, B. K. Gupta, *Handbook of Tribology*, (McGraw-Hill, New York, 1991).
- [2] R. F. Bunshah (Ed.), *Handbook of Hard Coatings: Deposition Technologies, Properties and Applications*, (Noyes Publications, Norwich, New York, 2001).
- [3] P. H. Mayrhofer, A. Hörling, L. Karlsson, J. Sjöln, T. Larsson, Ch. Mitterer and L. Hultman, *Appl. Phys. Lett.* 83, 2049 (2003).
- [4] K. E. Davies, B. K. Gan, M. B. Taylor, D. R. McKenzie, M. M. M. Bilek, D.G. McCulloch and B.A. Latella. *J. Phys.: Cond. Matter* 16, 7947 (2004).
- [5] J. F. Ziegler, J. P. Biersack and U. Littmark, *The Stopping and Range of Ions in Solids*, Pergamon Press, New York, 1985; code SRIM2010: <http://www.srim.org>
- [6] M. Uhrmacher, K. Pampus, F. J. Bergmeister, D. Purschke and K. P. Lieb, *Nucl. Instr. Meth. B* 9, 234 (1985).
- [7] J. Pflüger, J. Fink, W. Weber and K.P. Bohnen, *Phys. Rev. B* 30, 1155 (1984).

FABRICATION OF POLYMER NANOCOMPOSITES BY IMPLANTATION WITH MULTIPLE CHARGED IRON IONS

D. K. Božanić¹, I. Draganić¹, J. Pajović², R. Dojčilović¹, N. Bibić¹ and
V. Djoković¹

¹ *Vinča Institute of Nuclear Sciences, University of Belgrade, P.O. Box 522,
11001, Belgrade, Serbia*

² *Faculty of Physics, University of Belgrade, P.O. Box 368, 11001 Belgrade,
Serbia*

Abstract. Ethylene vinyl acetate copolymer nanocomposites were prepared by implantation with Fe⁶⁺ ions. The ions were produced by metal-ions-from-volatile-compounds (MIVOC) method with the M1 machine of FAMA, at the Vinča institute. The changes in the surface morphology and physical properties of the films upon irradiation were followed up by transmission electron microscopy (TEM), UV-vis spectroscopy and electrical resistivity measurements.

1. INTRODUCTION

Metal ion implantation with has been widely reported as a tool for the fabrication of polymer nanocomposite structures [1,2]. Polymers are considered as good implantation substrates since they can be easily processed into desired shapes and usually exhibit long term dimensional stability. On the other hand, by a selection of ion energy and ion dose, it is possible to modify the properties of the host polymer matrices as well as to control the size and spatial distribution of the particles formed. In this way, it is possible to obtain a multifunctional material that combines the advantageous properties of both components.

In this paper, we report preliminary results on preparation of the surface nanocomposite of ethylene vinyl acetate copolymer (EVA) through irradiation with Fe⁶⁺ ions. So far, various polymers were used as substrates for implantation with Fe ions [1-5]. Typical ion beam energies were 100-150 eV, while the ion doses went up to 1×10^{17} ions/cm². It was found that the morphology of the obtained iron particles partially depends on the type of the polymer. In most of the cases, the implantation results in spherical particles but, when polyethylene terephthalate (PET) was used as the substrate, the needle- and worm-like structures were obtained [5]. Also, the properties of the composites depended on the hardness of the substrate. For example, effective magnetization of the composite increases if the viscous silicon were used instead solid silicon substrate

[3]. EVA copolymer (used as a matrix in the present investigations) is inherently flexible, tough, and transparent material. It is proved solution for footwear, wire and cable insulation, as well as photovoltaic sheets applications. In order to prepare the EVA based nanocomposites, we irradiated the copolymer substrates with various doses of Fe^{6+} ions and investigate the morphological and physical properties of the obtained films.

2. EXPERIMENTAL

2.1 Preparation of copolymer substrates

EVA copolymer with 9% vinyl acetate (VA) content and a density of $\rho = 0.93 \text{ g}\cdot\text{cm}^{-3}$ was supplied by Plastamid, South Africa. The isotropic EVA sheets were prepared by compression moulding. The EVA pallets were kept at 5 min at 150 °C for 10 minutes and then 1.75 MPa pressure was applied for another 5 min. After that, the sheets were quenched in water at 20 °C. The obtained sheets had thickness of 200 μm .

2.2 Irradiation with Fe^{6+} ions

EVA samples, 1 cm in width and 2 cm in length, were placed in the interaction chamber of the C2 channel of the facility for modification and analysis of materials with ion beams (FAMA), at the Vinča Institute [6]. The ions produced with the M1 machine of FAMA, being an electron cyclotron resonance ion source, were directed onto the target substrate. The scheme of the experimental setup is shown in Figure 1.

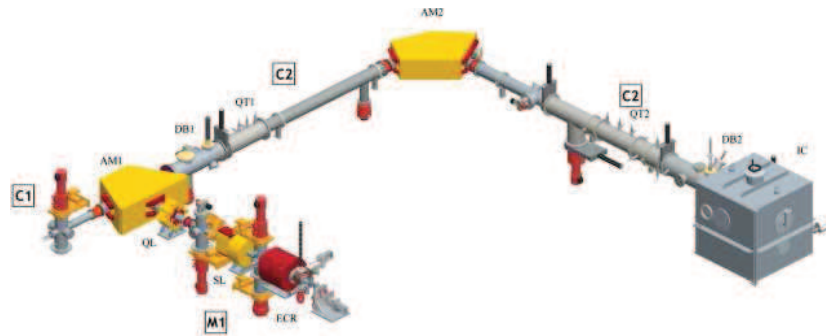


Figure 1 The scheme of the experimental setup.

At the mVINIS Ion Source, mini-oven technique is adequate for the solid materials with low melting point (the maximum oven temperature is 900 °C). For this reason, metal-ions-from-volatile-compounds (MIVOC) method was applied to produce iron ions [7]. The well-known ferrocene powder $\text{Fe}(\text{C}_5\text{H}_5)_2$ was used for the extraction of the multiple charged iron ion beam spectrum [7], while Fe^{6+} ions were selected to interact with substrate. The irradiation doses were 1×10^{15} , 5×10^{15} , 1×10^{16} , 1×10^{17} ions/cm². The beam energy and current were 90 keV and 64 μA , respectively.

2.3 Methods

For transmission electron microscopy (TEM) measurements, the Fe⁶⁺ ion irradiated EVA films were embedded in a resin and microtomed into electron beam transparent films using a Reichert-Jung Ultracut. TEM measurements were performed using a Phillips CM10 transmission electron microscope at 100 kV.

The changes in the optical absorption properties with changes in absorbed dose of Fe⁶⁺ ions were investigated by using Perkin-Elmer Lambda 5 UV–vis spectrophotometer.

The changes in the surface resistivity of the films after irradiation with Fe⁶⁺ ions was studied on a Agilent 4339B high-resistance meter, calibrated with Keithley 5155 standards (10^8 – 10^{13} Ω , $\Delta R/\Delta V = -0.03\%$ V^{-1}) for all voltage ranges. The samples were in the form of disks 13 mm in diameter.

3. RESULTS

Figure 2 shows the TEM image of the cross section of the EVA film irradiated with 1×10^{17} ions/cm². A large number of nanostructured particles were formed after irradiation. Their size is approximately 2 nm and they are mostly located about 150 nm beneath the surface of the film. They form a strip about 80 nm wide. The results clearly show that the irradiation with multiple charge ions is a convenient method for fabrication of the surface nanocomposite structures.

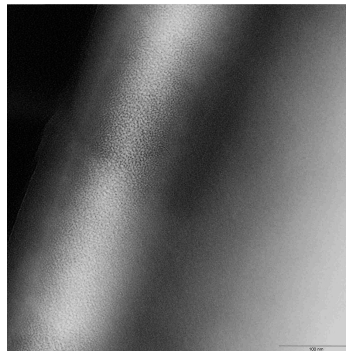


Figure 2. TEM image of the cross section of the EVA film irradiated with 1×10^{17} ions/cm² (bar 100 nm).

The multiple charged ions affect also the surface properties of the matrix itself. The interaction of ions with EVA macromolecules induces the formation of free radicals and their subsequent crosslinking. As a result there are changes in the optical transparency and surface resistivity of the films. The results in Table 1 show that the surface resistivity values of the EVA films significantly decrease with an increase in irradiation dose.

Table 1. Surface resistivity of the EVA films for various does of Fe⁶⁺ ions

Irradiation dose [cm ⁻²]	0	1×10^{15}	5×10^{15}	1×10^{16}	1×10^{17}
Surface resistivity [Ω]	$2.1 \cdot 10^{14}$	$3.1 \cdot 10^{11}$	$2.6 \cdot 10^{11}$	$1.7 \cdot 10^9$	$3.2 \cdot 10^7$

Figure 3 shows UV-vis absorption spectra of the as prepared EVA films and EVA films irradiated with 1×10^{15} and 1×10^{16} ions/cm². Irradiation with multiple charge iron ions obviously leads to the increase the optical absorption of the copolymer. This effect is again the consequence of the processes of oxidation and crosslinking induced by multiple charge ions.

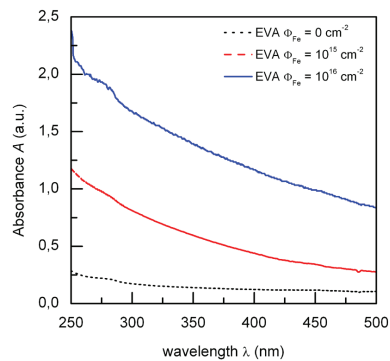


Figure 3 UV-vis spectra of the as prepared and irradiated EVA films

Acknowledgements

The work was supported by the Ministry of Education and Science of Republic of Serbia (Project Nos. 172056 and 45020).

REFERENCES

- [1] A. L. Stepanov and R. I. Khaibullin, *Rev. Adv. Mater. Sci.* 7, 108-125 (2004).
- [2] V. N. Popok, *Rev. Adv. Mater. Sci.* 30, 1-26 (2012).
- [3] R.I. Khaibullin, *Nucl. Instrum. Meth. B* 148, 1023-1028 (1999).
- [4] K. Ogawa, *U.S. Pat.* 4,751,100 (1988).
- [5] C. Okay, et al. *Phys. Stat. Sol. (a)* 203, 1525-1531 (2006).
- [6] Dobrosavljević A, Milosavljević M, Bibić N and Efremov A *Rev. Sci. Instrum.* 71, 786 (2000).
- [7] I. Draganić, T. Nedeljković, J. Jovović, M. Šiljegović and A. Dobrosavljević *Journal of Physics: Conference Series* 58, 427–430 (2007).

EFFECT - OF LOW ENERGY ION IRRADIATION ON OPTICAL AND DIELECTRIC PROPERTIES OF ETHYLENE-NORBORNENE

M. Šiljegović¹, Z. M. Kačarević-Popović¹, A. N. Radosavljević¹, S. Korica¹,
S. Maletić² and I. Petronijević²

¹*University of Belgrade – Vinča Institute of Nuclear Sciences, PO Box 522,
11001 Belgrade, Serbia*

²*Faculty of Physics, University of Belgrade, Studentski trg 12-14, 11000
Belgrade, Serbia*

Abstract. Ethylene-norbornene (TOPAS 6017S-04) copolymer films were irradiated in vacuum with 100 keV N⁵⁺ ions to fluences ranging from 10¹⁴ to 10¹⁶ cm⁻². Changes in optical and dielectric properties were analyzed by ultraviolet–visible and dielectric relaxation spectroscopies. The indirect energy gap values were determined from the absorption edge in the 180–900 nm region using Tauc’s relation. The energy gap of ethylene–norbornene copolymer decreases with increasing the fluence of N⁵⁺ ions. Significant changes in the dielectric β- and γ-relaxation were observed in the case of N⁵⁺ irradiated TOPAS 6017S-04 samples.

1. INTRODUCTION

Ion irradiation has become a highly developed tool for modifying the surface properties of different materials. When applied to polymers, energetic ions can induce many processes, such as sputtering, bond breaking and creation of double bonds, emission of small molecular groups, creation of carbonaceous clusters and the production of primary and secondary radicals. These radicals are responsible for most of the observed transformations. The structural modifications occurring in the irradiated layer may induce various improvements to the mechanical, electrical and optical properties of polymers [1]. This produces opportunities for the use of ion irradiation as a method for the fabrication of special polymer materials for optical, electronic and sensor applications.

Polymers with a high glass transition temperature, low optical propagation loss and low water absorption are especially well-suited for outdoor electronic and optical applications. During the last two decades, completely amorphous ethylene-norbornene copolymers have attracted increasing attention because of their unique combination of optical, electrical and thermal properties [2]. This cycloolefin copolymer family is characterized by excellent transparency, low birefringence, very low water absorption and high heat decomposition temperatures. TOPAS 6017S-04, with the highest glass transition temperature

among the TOPAS family, is a particularly suitable material for the fabrication of optical waveguides, biosensors and optoelectronic systems for high-temperature environments.

2. MATERIALS AND METHODS

TOPAS 6017S-04 films ($T_g = 178$ °C, $\rho = 1.02$ g/cm³), 50 μ m thick, were purchased from TOPAS Advanced Polymers (USA). The samples of size 2 cm \times 2 cm were homogeneously irradiated in vacuum with 100 keV N⁵⁺ ions to fluences of 10^{14} , 10^{15} and 10^{16} cm⁻².

Ultraviolet–visible (UV–Vis) spectroscopy was employed to investigate the variation in the optical energy gap with the ion fluence. The UV–Vis spectra of TOPAS films were obtained using Shimadzu UV-3600PC UV/Vis/Near-IR spectrophotometer in the range of 180–900 nm.

The dielectric losses ($\tan \delta$) of TOPAS films were measured using the Precision LCR Meter (Agilent 4285A). The samples in the form of discs, 13 mm in diameter, were placed in a stainless steel cell with an ac signal of 1 V applied across the cell. Control of the sample temperature in the range of 50–400 K was achieved using the CTI-Cryogenics Cryodyne closed loop system and Lake Shore 340 temperature controller.

3. RESULTS

The transmittance spectra of pristine and ion irradiated TOPAS 6017S-04 films in the wavelength range 180–900 nm are shown in the Fig. 1 as a function of N⁵⁺ ion fluences. The reduction in optical transmittance due to

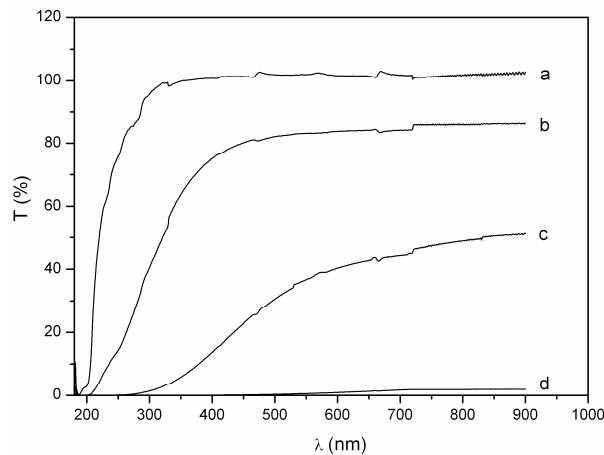


Figure 1. Transmittance spectra of (a) pristine and 100 keV N⁵⁺ irradiated TOPAS samples for the fluence of (b) 10^{14} , (c) 10^{15} and (d) 10^{16} cm⁻².

irradiation may result from the delocalized electron states generation in the forbidden gap of the copolymer and formation of localized states of defects the number of which increases with the increase of the applied fluence.

Using Tauc's model [3], the optical band gap for the indirect electronic transitions can be obtained by plotting $(\alpha h\nu)^{1/2}$ as a function of photon energy $h\nu$. The variation of band gap as a function of ion fluence is shown in Fig. 2. The estimated value of the energy gap for pristine sample is 2.40 eV and is reduced to 1.95, 1.85 and 0.55 eV for films irradiated with the fluence of 10^{14} , 10^{15} and 10^{16} cm^{-2} , respectively. The decrease in the energy gap values is due to formation of carbon enriched clusters after the ion bombardment of TOPAS samples. Bombardment with N^{5+} ions leads to the hydrogen release, to crosslinking and double bond formation in the irradiated copolymer. Overlapping of π -orbitals of the conjugated C=C bonds results in appearance of delocalized π -electrons, whose energy gap, between π and π^* bands, decreases with the length of conjugation.

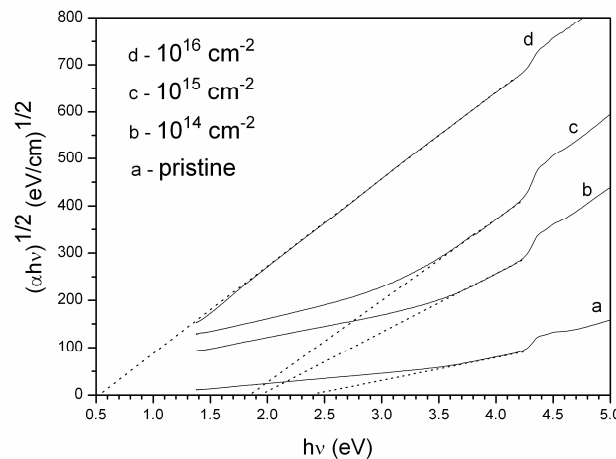


Figure 2. The dependences of $(\alpha h\nu)^{1/2}$ on photon energy $h\nu$ for TOPAS films irradiated with N^{5+} ions.

The results of dielectric measurements for TOPAS in the temperature range from 50 to 400 K at 10 MHz are shown in Fig. 3. The peak at 291 K in Fig. 3a corresponds to the amorphous molecular relaxation (β -relaxation) of the copolymer [4]. After irradiation with the fluence of 10^{15} cm^{-2} several peaks of β -relaxation in the range of 240-310 K and a new feature of γ -relaxation at 210 K are observed (Fig. 3c). Significant decrease of intensities of β -relaxation in the samples irradiated with 10^{16} cm^{-2} is caused by the amorphous nature of β -relaxation and by carbon cluster formation (with ordered graphite-like structures)

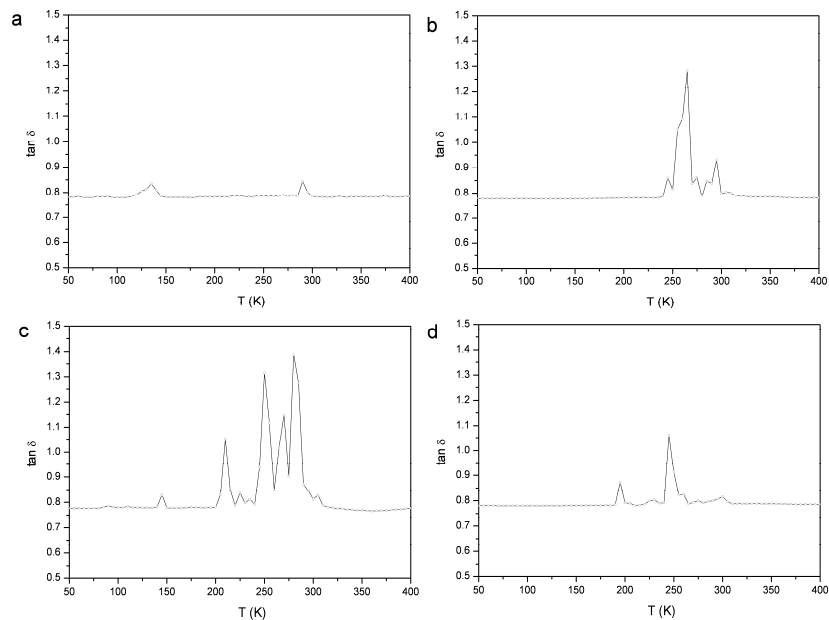


Figure 3. Temperature dependence of $\tan \delta$ at 10 MHz for (a) pristine and 100 keV N^{5+} irradiated TOPAS samples for the fluence of (b) 10^{14} , (c) 10^{15} and (d) 10^{16} cm^{-2} .

at fluences higher than 10^{15} cm^{-2} . These changes in the β - and γ -relaxation indicate structural changes in amorphous regions of the copolymer and great sensitivity of TOPAS 6017S-04 to N^{5+} irradiation.

Acknowledgements

We acknowledge the support to this work provided by the Ministry of Education, Science and Technological Development of Serbia through project *Physics and Chemistry with Ion Beams*, no. III45006 and project no. III45005.

REFERENCES

- [1] Z. Kačarević-Popović, N. Tjapkin, M. Šiljegović, I. Draganić, Nucl. Instr. and Meth. in Phys. Res. B 236, 594 (2005).
- [2] M. Blochowiak, T. Pakula, H. J. Butt, M. Bruch and G. Floudas, J. Chem. Phys. 124, 134903-1 (2006).
- [3] F. Abeles, *Optical Properties of Solids*, p. 277, (North-Holland Publ., Amsterdam, 1972).
- [4] D. I. Bower, *An Introduction to Polymer Physics*, p. 266, (Cambridge Univ. Press, Cambridge, 2002).

KINETIC ENERGY DISTRIBUTION OF ELECTRONS SCATTERED INSIDE A PLATINUM TUBE AT THE INCIDENT ENERGY OF 200 eV

A. R. Milosavljević^{1,*}, M. Lj. Ranković¹, J. B. Maljković¹, R. J. Berezky²,
B. P. Marinković¹ and K. Tőkési²

¹*Institute of Physics, University of Belgrade, Pregrevica 118, Belgrade, Serbia*

²*Institute for Nuclear Research, Hungarian Academy of Sciences, H-4001 Debrecen, Hungary, EU*

Abstract. We have measured the kinetic energy distribution of electrons escaping a macroscopic platinum (Pt) tube (3.3 mm diameter and 40.8 mm length). The 200 eV incident electron beam of about 800 nA was directed into the capillary entrance at a large tilt angle of 5.5°, with respect to the capillary axis. The results show a dominant fraction of elastically scattered electrons, accompanied by inelastic losses.

1. INTRODUCTION

Insulating micro- and nano-capillaries made of different materials have been extensively used to investigate the so-called *guiding* phenomenon, which was first revealed with the pioneering work of Stolterfoht and coauthors in 2002 [1]. Briefly, the beam of charged particles, particularly highly charged ions (HCI), dynamically deposit charge on the inner capillary surface, thus providing a Coulomb field that deflects the particles and efficiently guides them towards the capillary exit. Large attention has been devoted to this phenomenon due to both an interesting physics and possible applications, such as the possibility to introduce a micro/nano HCI beam directly into a biological object [2]. The first results on electron guiding through insulating capillaries have been reported more recently [3,4], followed by a more detailed investigations [5,6]. A comprehensive review on the subject can be found in the recent paper by Lemell et al. [7].

In contrast to the HCI, the electron transmission through insulating capillaries appeared to be much more complex [5,6,7]. Particularly, electrons can be closely elastically scattered from the surface (not only deflected by deposited charge), inelastically scattered and can produce secondary electrons (which thus affect the Coulomb interaction). Moreover, it has been suggested that even metallic (conductive) capillaries could be used for the electron guiding [6].

In the present work, we investigate electron transmission through metallic macroscopic capillaries. Our aim is both to learn about fundamental properties of the electron guiding by metallic capillaries, governed by electron-surface interaction, and to investigate the potential application of metallic high-aspect ratio capillaries as a robust, spatially well-determined, low-energy electron carrier/source, which could be efficiently applied to study electron driven molecular processes under different environmental conditions. We started investigation with a large-diameter Pt tube, in order to compare the obtained results to the electron interaction with a plane Pt surface and theoretical simulations. In the present work, we have investigated transmission of 200 eV incident electrons through a single Pt macrocapillary (3.3 mm diameter and 40.8 mm length – the aspect ratio of about 12.4). The intensity of the outgoing electron current has been measured as a function of both the incident beam angle with respect to the capillary axis (tilt angle) and the kinetic energy of outgoing electrons.

2. EXPERIMENTAL SETUP

The experiment has been performed in the Laboratory for Atomic Collision Processes, at the Institute of Physics Belgrade (IPB) by using the electron spectrometer UGRA [8], which has been modified to perform the present experiment. The electron gun produces a well collimated electron beam, with a diameter and an angular divergence estimated to be approximately 1 mm and 1° at 200 eV of the incident energy, and with an energy spread of about 0.5 eV. The Pt tube has been fitted inside the entrance electron lens system (see Figure 1), in front of the electron gun, which can be rotated around the capillary entrance in the angular domain of about -15 to $+15$ degrees. The angle between the capillary axis and incident electron beam direction is denoted as the tilt angle.

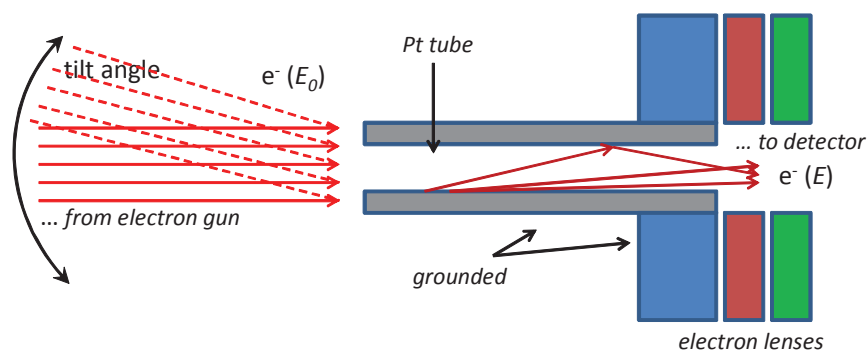


Figure 1. Schematic drawing of the experimental setup.

The electrons escaping the capillary were focused by an electrostatic lens (Figure 1) into a double cylindrical mirror energy analyzer (DCMA), followed by a single channel multiplier used as a detector. Since the entrance lens of the analyzer is fixed to have its axis parallel to the capillary axis, the observation angle is fixed at 0° and the acceptance angle also depends on the focal properties of the entrance lens. The kinetic energy distribution of the electrons escaping the capillary was measured by recording the electron current at the detector (count rates) as a function of the retarding potential at the entrance of the DCMA that worked in a constant pass-energy mode, thus providing a constant energy resolution over the whole scanned energy domain [8]. Still, it should be noted that the recorded kinetic energy distribution can be affected by the transmission of the entrance lens [8].

3. RESULTS

The preliminary obtained kinetic energy distribution of electrons escaping the Pt tube at the tilt angle of about 5.5° and for the incident electron energy of 200 eV is shown in Figure 2.

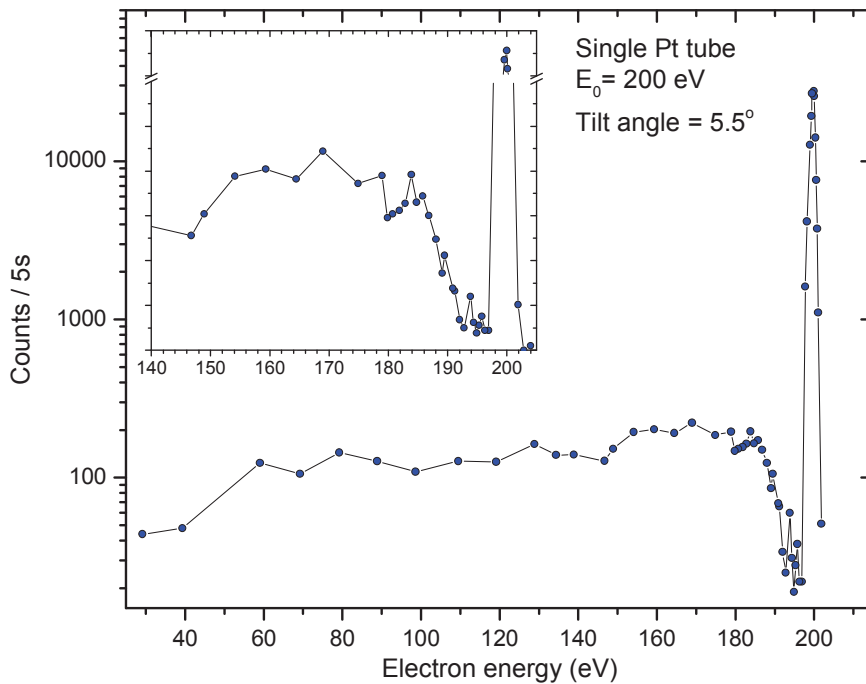


Figure 2. The kinetic energy distribution of electrons escaping the Pt tube at the tilt angle of 5.5° and the incident electron energy of 200 eV.

The aspect ratio of the Pt tube defines the tilt angle of 4.6° as a maximum angle to transmit the direct electron beam. Moreover, even at smaller tilt angles down to only a few degrees, the electron detection should not be possible due to the aspect ratio of the entrance lens stack and the DCMA (see Figure 1), which also depends on the electrostatic field. Therefore, the present results suggest that 200 eV electrons can be directed and transmitted along the metallic Pt tube. The dominant fraction of the transmitted electrons seems to suffer only elastic surface collisions. Inelastically scattered electrons are also detected and further work is in progress to compare the present results with the electron scattering from a plane Pt surface and calculations that include cylindrical geometry.

Acknowledgements

The work was supported by the Ministry of education, science and technological development of Republic of Serbia under the grant OI 171020, by the Hungarian SRF OTKA No. NN 103279, and by the Bilateral Cooperation Program between the Hungarian and Serbian Academies. The work is also motivated by ESF/COST Action CM1301 "Chemistry for Electron-Induced Nanofabrication (CELINA).

REFERENCES

- [1] N. Stolterfoht, J. - H. Bremer, V. Hoffmann, R. Hellhammer, D. Fink, A. Petrov and B. Sulik, *Phys. Rev. Lett.* 88, 133201 (2002).
- [2] T. Ikeda, T. M. Kojima, T. Kobayashi, W. Meissl, V. Mäckel, Y. Kanai and Y. Yamazaki, *J. Phys. Conf. Series* 399, 012007 (2012).
- [3] A. R. Milosavljević, Gy. Viktor, Z. D. Pešić, P. Kolarž, D. Šević, B. P. Marinković, S. Matefi-Tempfli, M. Matefi-Tempfli and L. Piraux, *Phys. Rev. A* 75, 030901 (2007).
- [4] S. Das, B. S. Dassanayake, M. Winkworth, J. L. Baran, N. Stolterfoht and J. A. Tanis, *Phys. Rev. A* 76, 042716 (2007).
- [5] A. R. Milosavljević, K. Schiessl, C. Lemell, K. Tokési, M. Mátéfi-Tempfli, S. Mátéfi-Tempfli, B. P. Marinković and J. Burgdörfer, *Nucl. Instrum. Meth. B* 279, 190 (2012).
- [6] K. Schiessl, K. Tókési, B. Solleder, C. Lemell and J. Burgdörfer, *Phys. Rev. Lett.* 102, 163201 (2009).
- [7] C. Lemell, J. Burgdörfer and F. Aumayr, *Prog. Surf. Sci.* 88, 237 (2013).
- [8] A. R. Milosavljević, S. Madžunkov, D. Šević, I. Čadež and B. P. Marinković, *J. Phys. B* 39, 609 (2006).

LASER DEPOSITION OF SILVER NANOCONES AT AIR PRESSURE

Victor Goncharov, Konstantin Kozadaev, Andrew Novikau, Helena Mikithcuk
and Alex Migutskiy

*Belarusian State University, 4 Nezavisimosty str., 220030 Minsk, Belarus
e-mail: kozadaeff@mail.*

Abstract. The present work is dedicated to the development of formation method for Ag cone-shaped surface nanostructures on silicon layer. For the formation of Ag nanoparticles fluxes the method of laser synthesis at air pressure is proposed. By the deposition of Ag nanostructures on solid layers, the cone-shaped surface nanostructures of Ag can be obtained.

1. INTRODUCTION

At present, nanotechnologies are considered to be one of the most promising directions of science and technology development. The high practical interest to nanostructures is based on specific features (physical, chemical, biological), which are not character to massive objects consisting of the same materials. This allows, for example, modifying the traditional media with metal nanostructures, thus improving their physical and chemical parameters. An example of such a problem is the obtaining of surface nanostructures consist of noble metals. Such nanostructures are actively used in petroleum chemistry, organic chemistry, polymer chemistry, as well as in the optical industry.

2. LASER EROSION OF SILVER TARGETS BY NANOSECOND PULSES AT AIR PRESSURE

In the process of exposure of massive silver planes to intense nanosecond laser pulses part of the irradiation is absorbed by free conduction electrons in thin surface layer ($\sim 1 \mu\text{m}$). Initially high coefficient of reflection of optical radiation by smooth silver surface ($R = 0.97$ for a light wavelength of 1000 nm) under intense laser action can significantly decrease, enhancing the integral dose of pulse energy absorbed by the target to 50% of the total optical energy reaching the target surface [1].

In case of nanosecond pulse (even with duration ~ 10 ns) action the leading edge time of laser pulse (10^{-9} s) becomes comparable with the characteristic time of electron-ion thermal relaxation in metals ($>10^{-10}$ s). So the absorbed optical energy can not penetrate deep into the target material due to

only electronic thermal conductivity, therefore the irradiative thermal conductivity became dominant. As a result a macro-layer of the “solid–vapor” phase transition almost without a liquid phase is formed under the influence of excess energy in the thin ($\sim 5\text{--}10\ \mu\text{m}$) surface layer of the target [2]. This macro-layer can be comparable with an explosive layer, which detonation process is followed by two basic physical effects: formation of the metal vapor-plasma plume (rapidly expands to outer space) and generation of the intensive shock wave (propagates deep into the target). This model of laser erosion of metals is called a “hydrodynamic” model, since it is precisely the hydrodynamic plasma motion that determines the basic regularities of interaction [3].

At the initial stage of its formation the vapor-plasma plume (due to the inverse breaking effect) begins to actively absorb the optical energy of the acting laser pulse, so increasing the internal energy of plasma and rapidly propagating in the atmosphere (according to the evaluations of [2] the initial velocity of vapor-plasma plume of silver is 7 km/s). After the finishing of the laser pulse, adiabatic expansion of the vapor-plasma plume continues, which leads to its gradual cooling. So in the plasma cloud, there appear local density fluctuations which subsequently turn to silver drop-liquid particles due to the condensation processes. The result average sizes of silver particles lie in the nanometric range (40–50 nm). This condensed phase of silver in the form of nanodrops is present in the surface region of the target over a rather long period: 500–600 μs from the laser action [4].

Substantial roughness on the target surface (in the form of longitudinal scratches with transverse dimensions of $\sim 50\text{--}100\ \mu\text{m}$) increase the concentration of nanodrops in the erosion plume by 2 to 3 orders (up to $10^{13}\ \text{cm}^{-3}$) of magnitude compared to the smooth target surface (with irregularities of $\sim 1\ \mu\text{m}$). This effect is based on the increasing of the effective interaction area of the rough surfaces and to the presence of numerous gas-formation centers. In the case of multiple laser action without changing the localization of the focal spot we have observed the effect of a decrease in the concentration of metallic nanodrops in the erosion plume for each subsequent pulse. After 4–5 actions of this kind, the efficiency of nanoparticle formation is no different from the case of a smooth target neglecting of the initial level of roughness. The indicated regularity is character to the process of smoothing out of the irregularities of the surface relief by a train of laser pulses [4].

3. EXPERIMENT

In the present work to form the layer of silver cone-shaped nanostructures we used an Nd:YAG ($\lambda = 1064\ \text{nm}$) laser generating pulses of duration 20 ns with a mean energy of 200 mJ, whose focusing into a spot with 3 mm diameter permitted obtaining a power density of $\sim 0,1\ \text{GW}/\text{cm}^2$. The pulse repetition frequency was 5 Hz. The characteristic exposure time for obtaining samples containing silver cone-shaped nanostructures was chosen to be equal to 2 min for one sample (600 pulses). The synthesis process proceeded in an air medium with subsequent deposition of formed silver nanocones on silicon layer.

For the target, we used massive plate from Ag, which chemical homogeneity has been confirmed by a state certificate.

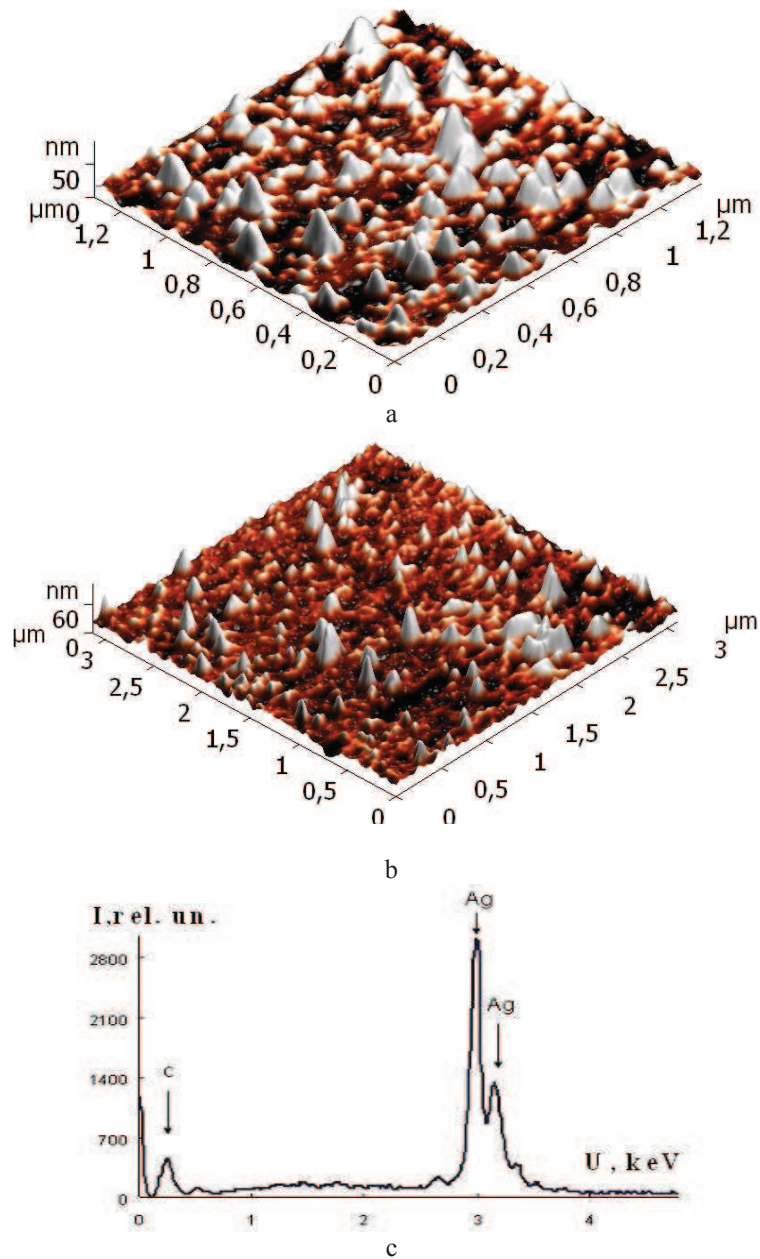


Figure 1. Results of investigation: AFM images (a, b), characteristic spectrum of nanocones (c).

For an investigation we used the following direct methods of diagnosing the parameters of the ultradisperse metal phase: atomic-force microscopy (AFM) and recording of the characteristic spectra of nanoobjects under their excitation by a sharply focused electron beam (electron probe). The results of investigation of the samples using AFM (Fig. 1 a, b) have shown the presence of cone-shaped nanoobjects. The spectrum of characteristic radiation of the particles on the carbon substrate (Fig. 1 c) points to the fact that the material of these structures corresponds to the material of the target, i.e. to Ag.

4. CONCLUSIONS

On the basis of the method of laser synthesis, an industrial technology of silver nanodrops fluxes formation can be developed. By the deposition of nanodrops on solid layers the silver cone-shaped surface nanostructures can be obtained. The chief advantages of the given technological approach are the ease of the technological realization of the process, the low production cost, and high rates of synthesis of Ag nanostructures.

REFERENCES

- [1] V. K. Goncharov, K. V. Kozadaev, V. V. Makarov and D.V. Shechrykovich, *J. Engineering. Phys. and Thermophys.* 86, 798 (2013).
- [2] K. V. Kozadaev, *Information Opt.* 23, 6 (2014).
- [3] S. I. Anisimov, B. S. Luk'yanchuk, *Adv. Phys. Sc.* 45, 293 (2002).
- [4] V. K. Goncharov, K. V. Kozadaev, V. V. Makarov and D.V. Shechrykovich, *J. Engineering. Phys. and Thermophys.* 86, 805 (2013).

THIN FILM DEPOSITION OF HMDSO FOR BARRIER APPLICATIONS IN ARCHAEOLOGY

M. Prochazka, L. Blahova and F. Krcma

*Faculty of Chemistry, Brno University of Technology, Purkynova 464/118,
612 00 Brno, Czech Republic*

Abstract. Thin film chemical vapour deposition technique has been used for more than 50 years. Introducing organosilicones as precursors, e.g. hexamethyldisiloxane (HMDSO) or tetraethyl orthosilicate (TEOS), brought new possibilities to this method. Barrier properties of thin films have become an important issue, especially for army and emergency services as well as for food and drink manufacturers. Our work is focused on deposition of protective HMDSO thin films via plasma enhanced chemical vapour deposition for encapsulating cleaned archaeological artefacts, preventing preventing these historical objects from destructive corrosion objects.

1. INTRODUCTION

Chemical vapour deposition has been used for thin film production for more than 50 years. We can find many successful applications in different industry branches, e.g. in automotive, food industry or in medicine. During 1980's, this deposition technique has been improved by adding plasma to the process. Plasma enhanced chemical vapour deposition (PECVD) or plasma assisted chemical vapour deposition (PACVD) allow using many new types of precursors, especially organosilicones.

Organosilicones offer several advantages. Organic groups have nearly infinite options for proper control of deposited layers. Additionally, they are compatible with other organic compounds and provide elasticity, preventing the layer to crack. Silicon atoms support binding to inorganic substrates including glass [1]. Hexamethyldisiloxane (HMDSO) and tetraethyl orthosilicate (TEOS) are used as PECVD precursors very often [2]. Main applications of organosilicone precursors are in microelectronics [3], automotive and food industry [4].

There are also other fields which can benefit from this type of precursors. Archaeology is one of them. Some organosilicone thin films have good barrier properties which make them suitable candidates for archaeological artefacts preservation. The aim of this work is to examine thin films based on HMDSO for possible application in archaeology.

2. EXPERIMENTAL PROCEDURES

Thin films were deposited simultaneously on several sample substrates: pure silicon substrate, iron plates, glass and polypropylene foil (PP, 20 μm).

PECVD was carried out in a glass bell-jar type reactor using capacitively coupled plasma generated by a RF source (13.56 MHz). HMDSO was used as the precursor. Reaction mixture (HMDSO+O₂) total flow rate of 10 sccm remained constant during all experiments. The whole device was pumped continuously by a rotary oil pump to maintain constant processing pressure of 15 Pa. The optical emission spectrometer Jobin Yvon Triax 550 with a 1200 gr/mm grating and a CCD detector was used for plasma diagnostics.

Deposited thin films were analyzed by various methods, including infrared spectrometry, thin film thickness measurements and barrier properties evaluation. Barrier properties are the most important parameters for the desired application. They can be tested in a corrosion chamber where salt fog and elevated temperature simulate the most frequent factors causing corrosion. Another approach is to measure permeability of deposited layers. Oxygen transmission rate (OTR) measurement is a standard method for gas permeability determination [5]. It measures the amount of oxygen passed through the thin film over time.

Oxygen transmission rate was measured for PP foils after the deposition. Infrared (IR) spectra of prepared layers were obtained after the deposition as well. Thin film thickness was monitored in situ by a quartz crystal monitor and verified on finished thin film by interference microscopy. Thickness of all films was 40–50 nm. It is known that thinner films do not form compact layers reliably. Thicker films crack on these substrates due to different thermal expansion coefficients.

3. RESULTS AND DISCUSSION

First, barrier properties of deposited thin films were tested. Gas permeability of organosilicone-based thin films is highly dependent on deposition parameters. This was confirmed by preliminary experiments. We prepared thin films with very different barrier properties. Oxygen transmission rate varied from 120 to 1500 $\text{cm}^3 \text{m}^{-2} \text{atm}^{-1} \text{day}^{-1}$. We focused on films with low OTR only, optimizing the parameters of the experiment to obtain as low OTR as possible. Dependences of oxygen transmission rate on supplied power and on composition of reaction mixture (O₂ content in gas mixture of HMDSO+O₂) are shown in Fig. 1 and Fig. 2. Both dependences show minima corresponding to the best barrier properties achieved. Low supplied power does not enable sufficient ionization and fragmentation of the precursor. On the other hand, too high power causes excessive fragmentation. Composition of thin films was analyzed by X-ray photoelectron spectroscopy and infrared spectroscopy. Both techniques indicate composition similar to SiO₂. Because Si-O bonds are required, destroying these bonds by high power leads to lower SiO_x layer formation.

Infrared spectra (Fig. 3) show decreasing carbon content in the thin film with increasing O_2 content in the reaction mixture. This also corresponds to the decrease of CH fragment concentration in optical emission spectra. All that means less carbon incorporated in the deposited thin film. The lower the carbon content is, the better barrier properties can be achieved. However, certain amount of carbon is needed to maintain elasticity which is vital for deposition on flexible substrates.

Barrier properties of deposited films depend on surface morphology, too. The smoother the surface is, the better barrier properties of the thin film are. Several tests were run to explore the option of cleaning the substrate by argon and oxygen plasma before the thin film deposition. Argon plasma pre-treatment decreased OTR of deposited film from $120 \text{ cm}^3 \text{ m}^{-2} \text{ atm}^{-1} \text{ day}^{-1}$ to $80 \text{ cm}^3 \text{ m}^{-2} \text{ atm}^{-1} \text{ day}^{-1}$. Oxygen pre-treatment caused OTR increase to about $160 \text{ cm}^3 \text{ m}^{-2} \text{ atm}^{-1} \text{ day}^{-1}$. Oxygen plasma probably grafted reactive species (e.g. radicals of atomic oxygen, O_2 , OH) to the surface of the substrate instead of cleaning it.

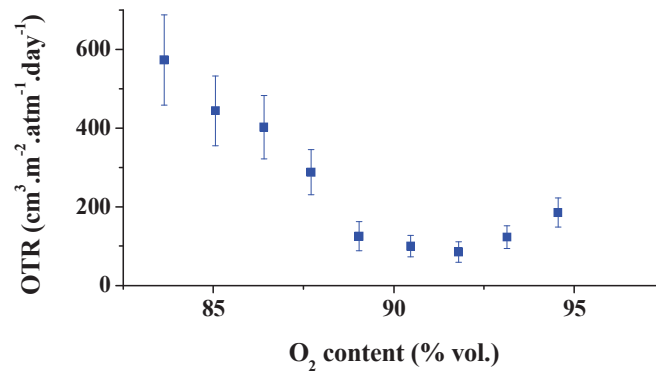


Figure 1. Dependence of oxygen transmission rate on O_2 content in reaction mixture (HMDSO+ O_2).

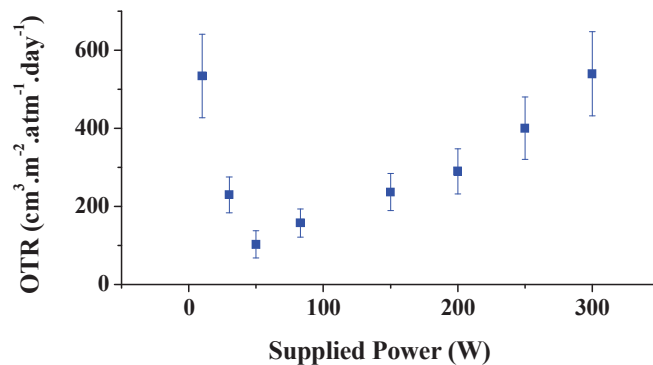


Figure 2. Dependence of oxygen transmission rate on supplied power.

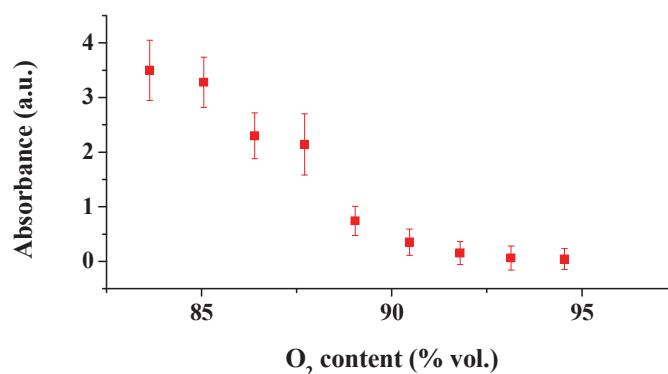


Figure 3. Dependence of absorbance of Si-C on O₂ content in reaction mixture

4. CONCLUSIONS

SiO₂-like thin films were tested for possible application in archaeology artefacts conservation. Thin films were deposited via low pressure PECVD using HMDSO as a precursor.

Deposited films have good barrier properties. Best barrier properties were achieved for 50 W of supplied power and 92 % of O₂ in reaction mixture (O₂+HMDSO). Oxygen transmission rate of these thin films was approximately 120 cm³ m⁻² atm⁻¹ day⁻¹. Argon plasma pre-treatment before the thin film deposition decreased OTR of the thin film to 80 cm³ m⁻² atm⁻¹ day⁻¹. Thin films have very low carbon content determined by infrared spectrometry.

Further research will focus on multi-layer systems as well as on temperature influence on substrates made of different materials.

Acknowledgements

This research has been supported by the Ministry of Culture of the Czech Republic, project no. DF11P01OVV004.

REFERENCES

- [1] V. Cech, A. Knob, H. Hosein, A. Babik and L. Drzal, Proc. Int. Conf. Composite Interfaces (Interface 21), 1 (2012).
- [2] R. Barni, S. Zanini and C. Riccardi, Adv. Phys. Chem., 2012 (2012).
- [3] C. H. Lin, H. L. Chen and L. A. Wang, Microelectron. Eng., 57-58, 555 (2001).
- [4] R. Morent, N. De Geyter, S. Van Vlierberghe, P. Dubruel, C. Leys, L. Gengembre, E. Schacht and E. Payen, Prog. Org. Coat. 64, 304 (2009).
- [5] ASTM Standard F1927 – 07, DOI: 10.1520/F1927-07

STRUCTURAL AND CHEMICAL PROPERTIES OF THE NANOSTRUCTURED NICKEL THIN FILM OBTAINED BY GLAD TECHNIQUE

J. Potočnik¹, M. Nenadović¹, M. Popović¹, B. Jokić², Z. Rakočević¹

¹University of Belgrade, INS Vinča, Laboratory of Atomic Physics, Mike Alasa
12-14, 11001 Belgrade, Serbia

²University of Belgrade, Faculty of Technology and Metallurgy, Karnegijeva 4,
11000 Belgrade, Serbia

Abstract. A columnar structure of nickel thin film has been obtained using Glancing Angle Deposition technique. Thickness of the deposited thin film was 370 nm with glass substrate positioned 15 degrees with respect to the nickel vapor flux. The nickel thin film was characterized by X-ray Photoelectron Spectroscopy, Scanning Electron Microscopy and Atomic Force Microscopy. It was found that the thin film consists of 80.8 at.% of nickel. The diameter of the columns was 43 nm.

1. INTRODUCTION

Glancing Angle Deposition (GLAD) is a technique for the deposition of columnar nanostructures [1]. Obtained columnar nanostructures are inclined toward the direction of the incident particle flux and may take a form of slanted and vertical posts [2,3], helices [4] or zig - zag [5] structures. GLAD technique is compatible with variety of materials, which increases its combinatorial power [6]. Schematic illustration of the growth of columnar nanostructures is given in Figure 1. The formation of the nucleus from the arriving particle flux is a random process. Nuclei grow into columns giving rise to the development of the shadowing.

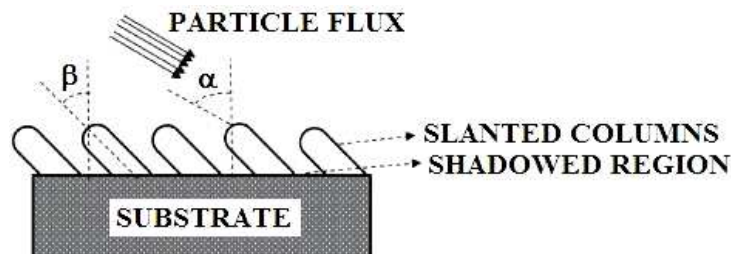


Figure 1. Schematic view of GLAD growth [7].

The column tilt angle (β) is smaller than the incident particle flux angle (α) (Figure 1). Its value can be obtained using equation [8]:

$$\beta = \alpha - \arcsin\left(\frac{1 - \cos \alpha}{2}\right) \quad (1)$$

In this work, GLAD method designed and assembled in our laboratory was used for the deposition of nickel thin film with columnar structure.

2. EXPERIMENTAL

Nickel thin film was deposited using GLAD technique by evaporating nickel onto glass substrate. The base pressure of the system was 4×10^{-5} Pa. Emission current was constant and its value was 170 mA. The duration of the deposition was 1 hour and 30 minutes.

Prior to deposition, glass substrate was cleaned in ethanol solution in ultra – sonic bath and rinsed with 18.2 M Ω deionised water. After that, substrate was also cleaned by the ozone (NovaScan PSD-UVT) and then attached to substrate holder in the chamber. After the preparation glass sample was positioned at the angle of 15 degrees with respect to the nickel vapor flux.

X-ray Photoelectron Spectroscopy (SPECS Systems, PHOIBOS 100/150) was used to determine the chemical composition of the deposited thin film and the presence of possible contaminants. Concentrations of elements present in the film were obtained using CASAXPS software. To remove the surface impurities, as well as in order to perform depth analysis, the sample was sputtered with argon ions.

Field Emission Scanning Electron Microscope, Mira XMU (TESCAN, Czech Republic) at 20 kV was used for morphology studies. Prior to the FESEM analysis, the sample was sputter coated with Au-Pd alloy. Cross sectional SEM image of the sample was used to determine the thickness of the film.

The obtained nickel thin film was also characterized using Multimode Quadrex SPM with Nanoscope IIIe controller (Veeco Instruments, Inc.). In this work, AFM was operated in the tapping mode. Surface topography and diameter of the columns were observed.

3. RESULTS AND DISCUSSION

XPS analysis was performed after 80 sec of sputtering with argon ions (Figure 2). It was found that the layer consists of 6.0 at.% of oxygen, 13.2 at.% of carbon and 80.8 at.% of nickel. The presence of carbon is probably due to the absorption from the ambient atmosphere, since we found the deposited film has a porous structure.

The cross section image of the sample was obtained by SEM technique at 20 kV. The columns are densely packed and uniformly tilted with respect to

the substrate surface as illustrated in Figure 3. It can be noticed the presence of small particles on the surface of the sample. These particles originate from Au-Pd alloy coating, which was deposited on the cross sectional sample. In this case, the conductivity of glass substrate was achieved.

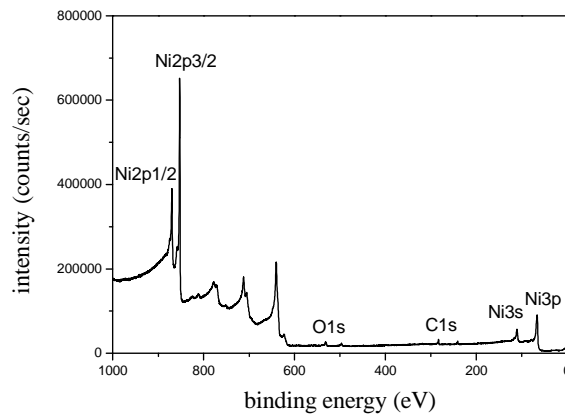


Figure 2. XPS spectra of the nickel thin film.

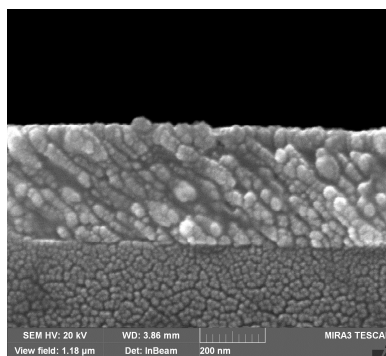


Figure 3. SEM cross section image of the nickel thin film.

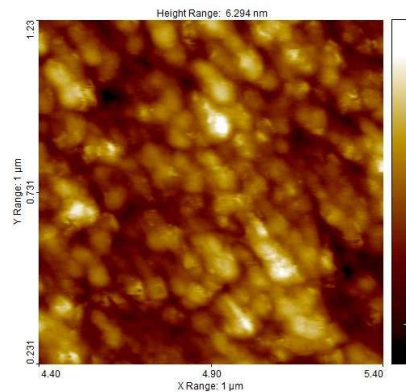


Figure 4. Topographic AFM image of the nickel thin film.

Based on a cross sectional image it can be seen that the thickness of a nickel thin film is (370 ± 10) nm. The columns are tilted at the angle of $\beta = (55 \pm 3)$ degrees, which is in a good agreement with the theoretically obtained value of $\beta = 54$ degrees.

Figure 4 shows the surface topography of the sample. It can be seen that the diameter of the columns found to be (43 ± 5) nm. Also, surface roughness value was determined to be (0.74 ± 0.04) nm.

4. CONCLUSION

We have demonstrated that the deposition of nickel thin film with a columnar structure can be achieved using GLAD technique. It was found that the thin film consists of 80.8 at.% of nickel, as confirmed by XPS analysis. SEM cross section image analysis have shown that the thickness of the nickel thin film is 370 nm. The columns of the thin film are tilted at the angle of approximately 55 degrees with respect to the substrate surface. According to AFM analysis it was found that the diameter of the columns is 43 nm and the surface roughness value is 0.74 nm.

Acknowledgements

This work was financially supported by the Ministry of Education and Science of the Republic of Serbia; project no. III45005.

REFERENCES

- [1] B. Dick, M. J. Brett, T. J. Smy, M. R. Freeman, M. Malac, R. F. Egerton, J. Vac. Sci. Technol. A18, 1838 (2000).
- [2] R. Messier, T. Gehrke, C. Frankel, V. C. Venugopal, W. Otano, A. Lakhtakia, J. Vac. Sci. Technol. A15, 2148 (1997).
- [3] K. Robbie, M. J. Brett, J. Vac. Sci. Technol. A15, 1460 (1997).
- [4] Y. P. Zhao, D. X. Ye, G. C. Wang, T. M. Lu, NanoLett. 2, 351 (2002).
- [5] R. Messier, V. C. Venugopal, P. D. Sunal, J. Vac. Sci. Technol. A18, 1528 (2000).
- [6] M. T. Tachuk, M. M. Hawkeye, M. J. Brett in Handbook of Deposition Technologies for Films and Coatings – Science, Applications and Technology, third edition 621 (2010).
- [7] M. H. Ehsani, H. Rezagholipour Dizaji, S. Azizi, S. F. Ghavami Mirmahalle, F. Hosseini Siyanaki, Phys. Scr. 88, 025602 (2013).
- [8] R. N. Tait, T. Smy, M. J. Brett, Thin Solid Films 226, 196 (1993).

DYNAMICS OF DESTRUCTION PRODUCTS AT INFLUENCE LASER RADIATION ON DIFFERENT TYPES OF GRAPHITE

V. Goncharov, M. Puzyrev

*Institute of Applied Physics Problems, Belorussian State University
7 Kurchatov St., 220045, Minsk, Belarus
e-mail: puzyrev@bsu.by*

Abstract. Temporary and spatial characteristics of an erosive flame of a graphite target are determined. The target was irradiated by YAG:Nd³⁺ laser impulses with a wavelength $\lambda = 1064$ nm and a pulse duration $\tau = 20$ ns. The repetition frequency of laser impulses was 5 Hz. It is shown that irradiation time of a target surface influence on characteristics of an erosive laser flames. The additional zone of a luminescence has been defined in space.

1. INTRODUCTION

Diamondlike carbon films differ exclusively high mechanical and tribological characteristics. One of effective ways of such films formation is the method of a pulse laser deposition [1]. The pulse laser deposition allows producing continuous superthin films of various materials and multilayered structures on their basis, with a wide range of properties [2].

Various factors: parameters of laser radiation, pressure of residual gases (vacuum), material target parameters, kinetic energy of ions, etc. [3] influence on film formation process and its properties (type of a crystal structure, the size of crystals, adhesion, an epitaxy, etc.).

Properties of the deposited films depend on plasma parameters. We can control properties of deposited films if to monitor spatial and temporary plasma parameters.

2. EXPERIMENT

The LOTIS-TII pulsed YAG:Nd³⁺ laser with a wavelength $\lambda = 1064$ nm and a pulse duration $\tau = 20$ ns (full width at half maximum FWHM) was used for the experiments. The repetition frequency of laser impulses was 5 Hz. Laser radiation was focused on graphite target, placed in vacuum chamber under 2.6×10^{-3} Pa. The target was mounted at a 45° with respect to the laser beam and was constantly rotated to provide fresh surface for ablation. The laser intensity

was $5.7 \times 10^8 \text{ W/cm}^2$. The laser beam diameter was kept constant (about 2 mm). Films deposition was carried out at room temperature. Two different types of carbon targets were used.

CCD array image sensor ICX415AL was used for spatial distribution of a laser flame luminescence. The measurement of temporary parameters of a flame luminescence was made with an employment lenses system and the optical fiber. The determinate zone image of a flame was transferred by optical fiber on Silicon photomultiplier detectors sensor (SPM 10020). This sensor measured temporary of a plasma luminescence. The signal from this sensor transferred Tektronix TDS2022B oscillograph.

3. RESULTS

The structure of a graphite target is a parameter, which influence on a plasma flame formation, and on deposited films properties.

The target N1 was made from highly oriented pyrolytic graphite (HOPG). This graphite has high density close to a theoretical limit 2.25 g/sm^3 , and has diffraction of x-ray beams close to monocrystal natural graphite.

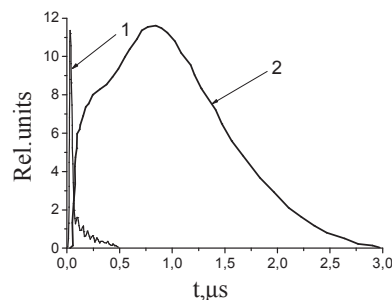


Figure 1. Temporary plasma luminescence near a surface of a graphite target (distance 0.5 mm): 1 – laser impulse; 2 – plasma luminescence.

The target N2 was made from pure fine-grained synthetic graphite (MG1). This type of graphite is isotropic. Average density of this material is about 1.65 g/sm^3 . The porosity of graphite MG1 is $25 \div 26 \%$. The porous graphite can contain significant amount of physically and chemically adsorbed gas impurity. The target was exposed additional annealed in vacuum $\sim 10^{-2} \text{ Pa}$ at 2273 K during 2 hours to purify from gas. The influence of high temperature vacuum annealing on the content of hydrogen in graphite targets was estimated by secondary ions mass spectrometer (SIMS) on radicals CH and CH₂ emissions. The SIMS have shown the content of the hydrogen impurity in initial graphite MG1 is about 4 at.%. After vacuum annealing the CH- and CH₂-radicals emissions decreases in $25 \div 30$ times.

The irradiation of the laser single impulse on a graphite target begins to the plasma luminescence at its surface. Its duration is $\sim 3.0 \mu\text{s}$ (figure 1).

It was measured a spatial luminescence of a laser flame. Experiments showed that spatial dimensions of plasma is ~ 8 mm at distance of 5 mm from a target surface (figure 2).

It also was experimentally revealed that at distance ~ 3.8 cm are the area consisting of graphite particles (figure 2, area 2). It is well visible if before a lens of the CCD sensor to locate the IR7 filter (figure 3). This filter allows reducing a plasma luminescence (from 300 nm up to 900 nm). It also is visible that these graphite particles are and near a laser target surface (figure 3, area 1).

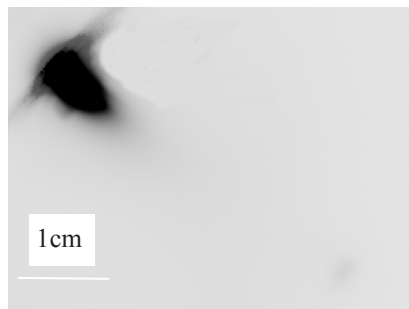


Figure 2. Spatial plasma luminescence near a surface of a graphite target (distance 0.5 mm).

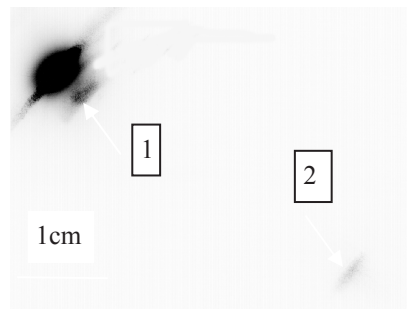


Figure 3. Spatial plasma luminescence near a surface of a graphite target (distance 0.5 mm) with the IR7 filter.

The measurement of temporary characteristics of this flame luminescence at distance of 3.8 cm confirms the presented area (figure 4). Using temporary characteristics erosive plasma flame it is possible to calculate the speed of plasma spread, and carbon particles. These sizes are ~ 100 km/s and ~ 7 km/s respectively.

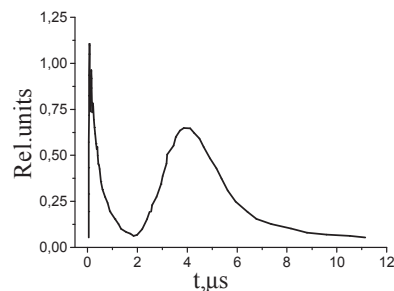


Figure 1. Temporary plasma luminescence at distance 3.8 cm from a surface of a graphite target.

The destruction of the pyrolytic graphite target of with repetition frequency of laser impulses 5 Hz (figure 5) depends on the total irradiated time a happens as follows. Graphite particles eject out from a target surface substantially until 1 minute (figure 5 a). In the 2 minutes, the quantity of particles decreases (figure 5 b). In the 10 minutes of a particle practically are absent (figure 5 c). The MG1

graphite destruction happens similarly. Graphite particles eject out from a target surface in the 5 minutes decreases, but does not stop that is connected with porous structure of graphite despite its annealing in vacuum (figure 5 d).

4. CONCLUSIONS

Experiments showed that deposition of diamondlike films with the contents more than 50% of sp^3 - bonds should be carried out in the 5 minutes after the beginning of the irradiation of a graphite target surface. The additional zone of a luminescence is determined at distance 3.8 cm from target surface. This zone can be explained by a formation of the carbon chains with the bond energy release.

The speeds of plasma spread of destruction products in an erosive laser flame are experimentally determined. The spread speed of carbon plasma is $\sim 100\text{km/s}$, graphite particles $\sim 7\text{km/s}$.

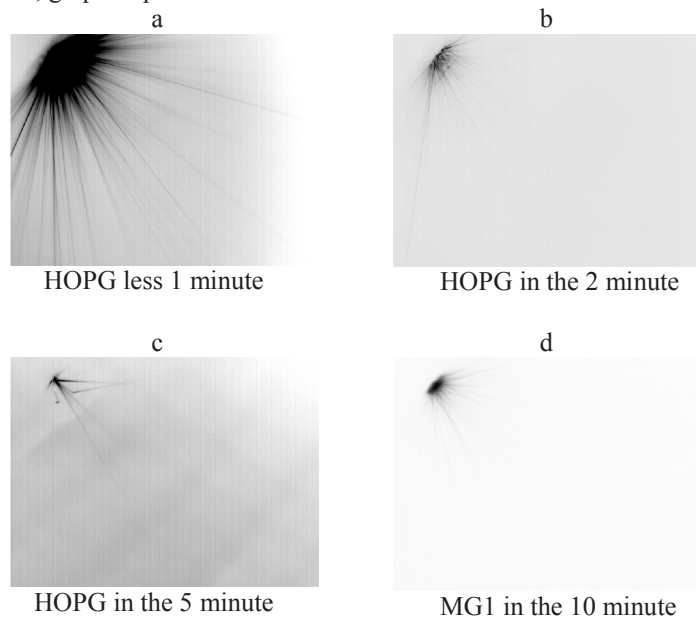


Figure 5. Spatial plasma luminescence of the laser erosion flame versus total time irradiated target for different type graphite.

REFERENCES

- [1] S. Yasuda, T. Chikyow, S. Inoue, N. Matsuki, K. Miyazaki, S. Nishio, M. Kakihana, H. Koinuma, Appl. Phys. A. 69, 925 (1999).
- [2] R. Eason, Pulsed laser deposition of thin films: Applications-LED growth of functionäal materials. 682 p (Hoboken. N.J. :Wiley-Interscience, 2007).
- [3] K. L. Saenger, J. Appl. Phys. 70, 5629 (1991).

TIME-RESOLVED SPECTROSCOPY OF NANOSECOND DISCHARGES CREATED IN WATER BETWEEN ALUMINIUM ELECTRODES

A. Hamdan¹, C. Noël^{1,2}, G. Henrion^{1,2} and T. Belmonte^{1,2}

¹*Université de Lorraine, Institut Jean Lamour, UMR CNRS 7198, NANCY, F-54011 France*

²*CNRS, Institut Jean Lamour, UMR CNRS 7198, NANCY, F-54011, France*

Abstract. Time-resolved optical emission spectroscopy is used to characterize nanosecond-pulsed discharges in water. Two aluminium electrodes, in a pin-to-pin configuration, serve as source material to produce nanoparticles. At the beginning of the spark, a strong background emission dominates the visible spectrum. Al I and Al II lines appear 200 ns after breakdown, exactly when the current stops. O I lines, observed 50 ns later, are followed after 150 ns by the emissions of H α and the blue-green system of AlO. Some very specific features characterize all the optical transitions. Correlated with TEM observations of nanoparticles, optical measurements show that the two existing types of nanoparticles are made by different mechanisms involving two different gaseous precursors.

1. INTRODUCTION

High-yield production of nanoparticles with controlled size distributions is a major stake in many potential scopes of application. For instance, producing high amounts of silicon nanocrystals with narrow distributions centred on ~5-10 nm could favour their widespread utilization in such diverse application areas as optoelectronics, solid-state lighting or fluorescent agents for biological applications [1].

Discharges in liquids are characterized by high production yields [2, 3] but they are difficult to control [4] because of their stochastic behaviour. The advent of nanosecond-pulsed discharges made it possible to have breakdown on demand with a high reproducibility level. Thus, it is possible to resort to time-resolved optical emission spectroscopy (OES) to better understand how nanoparticles are synthesized during the spark discharge. In this work, we investigate by OES discharges in water between aluminium electrodes in pin-to-pin configuration and correlate the as-performed measurements to the different types of nanoparticles dispersed in the liquid.

2. EXPERIMENTAL SETUP

The experimental set-up is described in detail elsewhere [4]. Briefly, aluminium rods were used as electrodes (diameter: 2.0 mm; 100 μm in curvature radius at apex). The distance between electrodes was $100 \pm 10 \mu\text{m}$. A high DC voltage power supply (Technix SR15-R-1200 – 15 kV – 80 mA) fed a high voltage solid-state switch (Behlke HTS-301-03-GSM) that delivered a maximum current of $2 \times 30 \text{ A}$ under a voltage up to $2 \times 30 \text{ kV}$. Pulsed High Voltage (PHV), +15 kV, was controlled by a low-frequency signal generator (Thurlby Thandar Instruments (400 MHz) TGA 1242 Arbitrary/Function Generator) and applied to the power electrode, the second electrode being grounded. One pulse is characterized by its on-time (200 ns). The operating frequency of the PHV was 3 Hz typically.

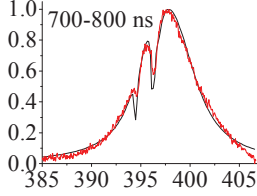
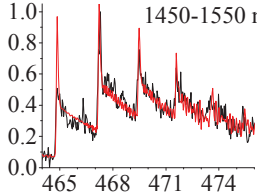
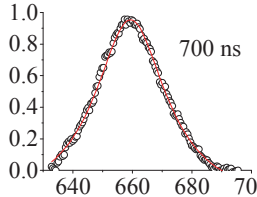
Optical emission spectroscopy was performed with a 550 mm focal length monochromator (Jobin-Yvon TRIAX 550) equipped with a 100 gr mm^{-1} grating for overall spectra in the [250-900 nm] visible range and strongly broadened lines like $\text{H}\alpha$, and a 1800 gr mm^{-1} grating for recording of specific transitions requiring high spectral resolution. Both of them were coupled with an HORIBA Jobin-Yvon i-Spectrum Two iCCD detector. Each measurement is averaged over 20 spectra recorded in boxcar mode with an exposure time of 50 ns.

3. RESULTS AND DISCUSSION

In Table 1, the emission lines observed until 1600 ns after breakdown are listed. These lines were modelled as follows. We used the data by Descoedres *et al.* [5] inspired from the data by Gigoso and Cardenoso [6] to describe the $\text{H}\alpha$ line. For self-absorbed aluminium lines, we used the model of Sakka *et al.* [7]. It is based on the description of the optical paths of the collected light where the emitting and absorbing atoms are continuously distributed in the plasma region. Effects of position-dependent Stark shift and Stark broadening due to the spatially distributed plasma electrons are thus taken into account. The most intense AIO transitions of the blue-green system of AIO (i.e. $\Delta v = -1, 0$ and $+1$ bands) were fitted to access rotational temperatures. O I and Al II lines were not exploited.

The electron density determined either from $\text{H}\alpha$ broadening, $\text{H}\alpha$ shift in wavelength or by self-absorption of Al I lines give similar trends. It is about 10^{19} cm^{-3} and decays down to 10^{18} cm^{-3} after $\sim 1 \mu\text{s}$ typically. Stark broadening is the main broadening source for every lines. No $\text{H}\beta$ line is found, because of the lowering of the ionization energy caused by high pressure levels (~ 100 bars typically). Rovibrational fits of AIO bands are satisfactory but far from being accurate anyway. They give comparable trends where the rotational temperature evolves typically from 6000 K to 3000 K from $1 \mu\text{s}$ to $1.6 \mu\text{s}$ (unrealistic higher values are predicted between 0.8 and $1 \mu\text{s}$, likely because of the weakness of these lines, hardly emerging from the background emission).

Table 1. Main emission lines observed between 0 and 1600 ns. Theoretical positions are given in column 2. w, m, s, vs stand for weak, medium, strong and very strong (used to qualify the lines maximal intensity). Examples of transitions (in black) with the modelled profiles (in red) are provided.

Transition	Wavelength (nm)	Examples of transition
Al I ($3s^23p-{}^1Snd$)	256.80 ^w ; 257.51 ^w	
Al I ($3s^23p-2s^25s$)	265.25 ^w ; 266.04 ^w	
Al I ($3s^23p-2s^23d$)	308.22 ^{vs} ; 309.27 ^w ; 309.28 ^w	
Al I ($3s^25d-2s^24d$)	308.70 ^{vs}	
Al I ($3s^23p-2s^24s$)	394.40 ^{vs} ; 396.15 ^{vs}	
Al II ($3s3p-3s4s$)	281.62 ^m	
Al II ($3s3d-3s4f$)	358.66 ^m ; 358.75 ^m	
AlO($B^2\Sigma^+-X^2\Sigma^+$) $\Delta v=-2$	533.70 ^w	
AlO($B^2\Sigma^+-X^2\Sigma^+$) $\Delta v=-1$	507.94 ^m	
AlO($B^2\Sigma^+-X^2\Sigma^+$) $\Delta v=0$	484.22 ^m	
AlO($B^2\Sigma^+-X^2\Sigma^+$) $\Delta v=+1$	464.81 ^m	
AlO($B^2\Sigma^+-X^2\Sigma^+$) $\Delta v=+2$	447.04 ^w	
H α	656.28 ^s	
O I ($2p^33s-2p^33p$)	777.19 ^s -777.41 ^s -777.54 ^s	
O I ($2p^33s-2p^33p$)	844.62 ^s -844.64 ^s -844.68 ^s	

One of the most striking features of these lines is their time evolutions. They are reproduced in figure 1. The emission of the background light, produced by electron-ion recombination mainly, but also by bremsstrahlung in the near-infrared region, dominates until the end of the plasma, ca. 220 ns (determined from unreported electrical characteristics). Next, atomic lines (Al I, Al II and O I, 50 ns later) appear. The H α line is only visible 150 ns after O I emission. It is very interesting to see that this transition appears together with rovibrational bands of the AlO blue-green system.

This shift is likely due to pressure exerted by the plasma towards the liquid. This phenomenon was nicely analysed by Sano *et al.* [8]. It is based on the existence of a gas film, likely made of H₂O, in the gas phase zone adjacent to the gas-liquid interface. According to these authors, “even if the thickness of this

H₂O gas film is thin in normal gravity, the existence of this film should play an important role to determine the product structures. This is because the H₂O gas film may block the reaction of carbon vapor with the liquid H₂O at the gas–liquid interface. This blocking effect brings about an inhibiting effect for the formation of the products which can be expected from the reaction at the gas–liquid interface.” So, we can assume that a large part of the available aluminium atoms produced by electrode erosion cannot be oxidized because of this blocking effect at the beginning of the spark, but only after about 450 ns in our conditions.

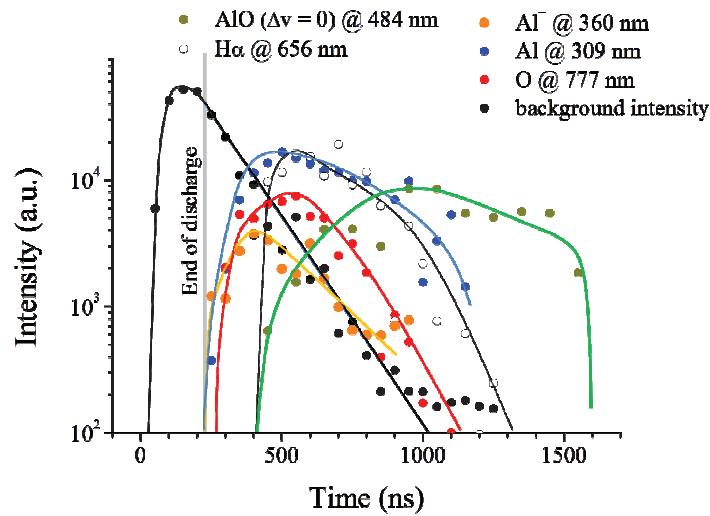


Figure 1. Time evolution of selected transitions.

REFERENCES

- [1] L. Mangolini, E. Thimsen and U. Kortshagen, *Nano Lett.* 5, 655 (2005).
- [2] N. Sano, H. Wang, I. Alexandrou, M. Chhowalla, K. B. K Teo, G. A. J. Amaratunga and K. J. Iimura, *Appl. Phys.* 92, 2783 (2002).
- [3] C. H. Lo, T. T. Tsung, L. C. Chen, C. H. Su and H. M. Lin, *J. Nanopart. Res.* 7, 313 (2005).
- [4] A. Hamdan, C. Noël, J. Ghanbaja, S. Migot-Choux and T. Belmonte, *Mater. Chem. Phys.* 142, 199 (2013).
- [5] A. Descoeur, C. Hollenstein, R. Demellayer and G. Walder, *J. Mater. Process. Technol.* 149, 184 (2004).
- [6] M. A. Gigoso and V. Cardenoso, *J. Phys. B: At. Mol. Opt. Phys.* 29, 4795 (1996).
- [7] T. Sakka, T. Nakajima and Y. H. Ogata, *J. Appl. Phys.* 92, 2296 (2002).
- [8] N. Sano, O. Kawanami, T. Charinpanitkul and W. Tanthapanichakoon *Thin Solid Films* 516, 6694 (2008)

APPLICATION OF PULSE-PERIODIC PLASMA FLOWS FOR HARDENING OF STEEL SURFACE

A. Chumakov¹, I. Nikonchuk¹, O. Kuznechik²

¹*B.I. Stepanov Institute of Physics of the NASB,
68 Nezavisimosti Ave., Minsk, 220072 Belarus,
e-mail: chumakov@imaph.bas-net.by*

²*Powder Metallurgy Institute,
41 Platonova Str., Minsk, 220072 Belarus*

Abstract. The pulsed-plasma device generating air plasma flows with a frequency of 10 Hz, velocity of 4 km/s and temperature of 12 000 K, used for modification of steel surface at atmospheric pressure. The device is based on the formation of high-energy pulsed-periodic plasma flows in stationary plasma channel with a temperature of 2000-4000 K. Treatment of structural steel (0.42% C, 0.5% Mn, 0.25% Cr) by pulse-periodic plasma flows with a frequency of 2 Hz provided a threefold increase of the microhardness with depth of the modified layer over 300 μm .

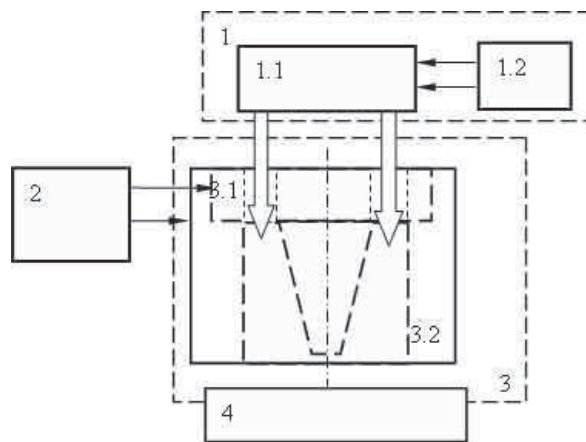
1. INTRODUCTION

Increasing the wear resistance of instruments by surface hardening of their materials and coatings is an important problem of mechanical engineering. This problem can be solved using the method of the pulse-plasma treatment in air at atmospheric pressure, which is implemented [1] with the aid of the devices including a facility for preparing and feeding the gas mixture, detonation and acceleration chambers, and pulse high-voltage power supply and control. The main shortcomings of existing equipment are high level of acoustic noise and complexity of the preparation and maintenance of plasma-forming medium. Our purpose was to create a pulsed-plasma device for surface modification of metals at atmospheric pressure air devoid of these shortcomings.

2. PULSE-PLASMA DEVICE AND DIAGNOSTIC EQUIPMENT

Created pulse-plasma device uses air as plasma-forming substance (Fig. 1) [2]. The construction of pulse-plasma device has such structural elements as source of constant-acting air plasma 1, high-voltage power supply and control unit 2, and accelerating chamber 3 whose structural features are an

evolutional continuation of pulse-periodic plasmatron [3]. Air plasma continuously fed through the plasmatron 1.1 in the working area of the ionizer 3.1 (Fig. 1). High-voltage discharge in the air plasma is creating when power supply and control unit 2 gives a high voltage pulse on accelerator 3.2. The special construction of the accelerator provides heating and accelerating of the plasma, which treats the surface of the target 4. The temperature generated by the air plasma flows at the output of the accelerator chamber reaches $\sim 10^4$ K, pressure reaches 60 bar, plasma velocity $1\div 4$ km/s, and the frequency of repetition of plasma flows in the range 0.1–10 Hz [2].



1 – source of the constantly acting air plasma: 1.1 – plasmatron, 1.2 – facility for feeding a plasma-forming gas and electric current; 2 – high-voltage power supply and control unit; 3 – accelerating chamber: 3.1 – ionizer, 3.2 – accelerator; 4 – treated surface

Figure 1. Scheme of the pulsed-plasma device.

The hardware-diagnostic complex to study the features of plasma formation and determine its characteristics consists of a calibrated high-speed photodetectors, pulse pressure sensors, double-channel spectrometer SL40-2-2048USB (SOLAR TII, Ltd, Belarus), optical pyrometer based on CCD SONY I415AL (B.I. Stepanov Institute of Physics of the NASB, Belarus), digital oscillograph Bordo-424 (BSU, Belarus).

3. RESULTS AND ANALYSIS

Measurement of the radiation intensity of high-energy plasma flow (Fig. 2a) showed a pulsed nature of the brightness temperature changes. The pulse duration of the plasma radiation corresponded to duration of current pulses of high voltage discharge (Fig. 2b). Every current discharge was accompanied by a generation of four plasmoid with the time interval $T \sim 200 \mu\text{s}$. Amplitude of plasma light flux pulsation decreases from the third pulse. Such dependence is

due to the fact that the electric current and the magnetic field in the accelerator reach their peak in the first half period of high-voltage discharge (Fig. 3b). During this time period, the maximum luminous flux of plasma is reached (Fig. 3a).

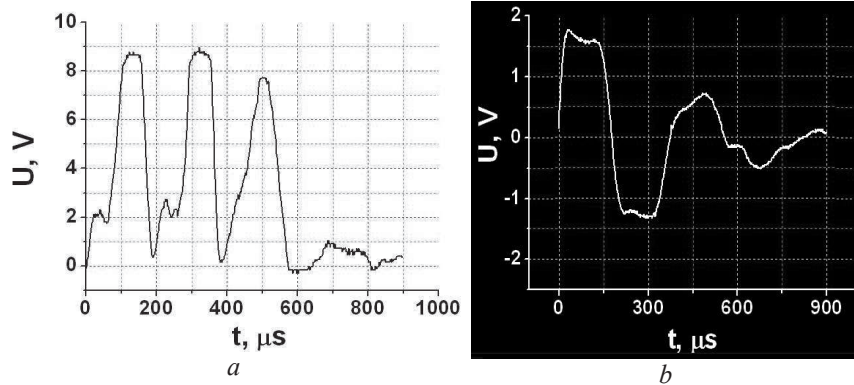


Figure 2. Oscillograms of luminous flux of plasma (a) and discharge current in the accelerator chamber (b, sensitivity of the current sensor is 4.58 kA/V).

Performed measurements of the brightness temperature of plasma flows suggest that its maximum values reach $1.5 \cdot 10^4$ K.

Pressure measurements of repetitively pulsed plasma flows were performed using piezoelectric sensor of pulse pressure. The results of pressure measurements in air pulse plasma jet shown in Fig. 2.

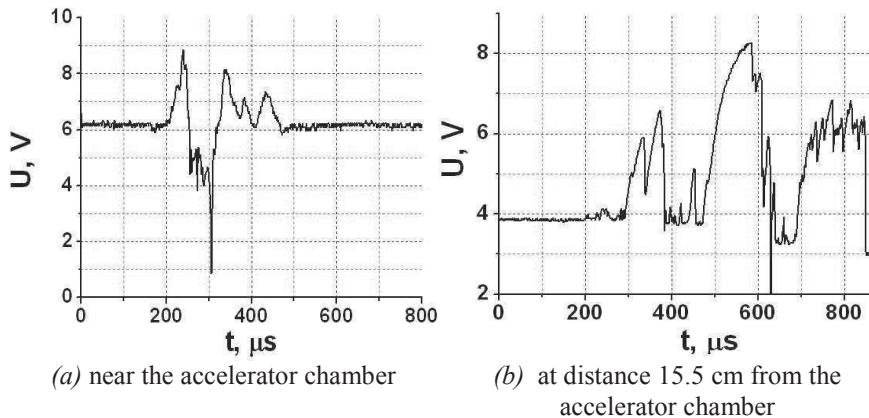


Figure 3. Oscillograms of plasma stream pressure at different distance from the accelerator chamber (sensitivity of the pressure sensor is 8.4 bar/V).

Maximum pressure of plasma flows reach values of 60 bar. Waveform analysis showed that the pressure pulsations in the pulsed plasma jet correlate with the brightness of its glow only at a distance from the accelerator chamber. Should be noted that the work of the pulse-plasma source is accompanied with a relatively low noise level (it does not exceed 80-110 dB at a distance of 1 m).

Treatment of structural steel (0.42% C, 0.5% Mn, 0.25% Cr) was performed in air by pulse-periodic plasma flows with a frequency of 2 Hz. The microhardness of surface layers was determined using the instrument MPT-3. Analysis of the results showed that the interaction of pulsed plasma flows with the surface of tool steel causes the formation of hardening structures. The results of microhardness measurements are shown in Fig. 4. The microhardness of the initial samples is about 2 GPa. After the impact of the air plasma flows on steel samples, the microhardness increases to the values 6 GPa (Fig. 4), gradually decreasing during the deepening of 1000 μm almost to baseline values (2 GPa).

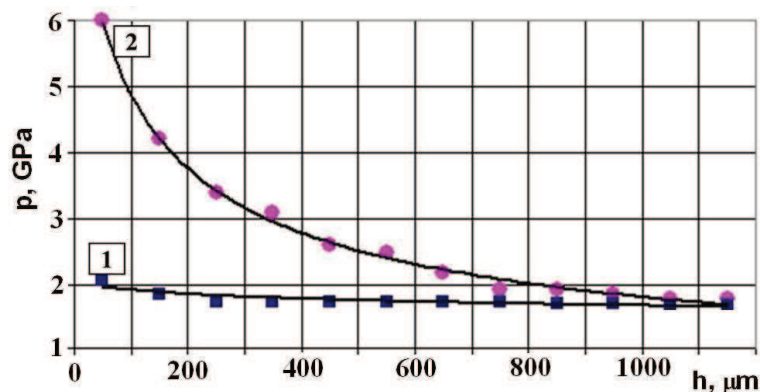


Figure 4. Microhardness distribution in the surface layer (initial sample (1) and sample after pulse-plasma treatment (2)).

4. CONCLUSIONS

Presented pulsed-plasma device provides the generation of pulsed air plasma flows characterized by frequency 0.1–10 Hz, pressure 5.0–6.5 MPa, temperature up to 10000–12000 K, velocity up to 1–4 km/s and maximum level of acoustic noise up to 110 dB (duration of noise does not exceed about 1–2 ms).

Pulsed-plasma device that generates air plasma can be used for the surface treatment of materials and coatings of tools and machine parts, allowing the hardening in the open air.

REFERENCES

- [1] A.D. Pogrebnyak and Yu.N. Tyurin, *Phys.-Usp.* 48, 487 (2005).
- [2] Yu.A. Chivel, O.O. Kuznechik, D.V. Minko, I.S. Nikonchuk, A.N. Chumakov, K.E. Belyavin, *Journal of Engineering Physics and Thermophysics.* 84(5), 1108-1113 (2011).
- [3] Pulse-periodic plasmatron: patent 2343651 Russia, MPK H 05H 1/26, B 23K 10/00 / Yu.A. Chivel, I.S. Nikonchuk, D.V. Minko, O.O. Kuznechik; publ. 2009.10.01.

CALIBRATION OF PRESSURE SENSORS USING NEAR-SURFACE LASER PLASMA

A.M. Petrenko, P.V. Chekan and A.N. Chumakov

*B.I. Stepanov Institute of Physics, National Academy of Sciences of Belarus,
Minsk, Belarus*

e-mail: a.chumakov@dragon.bas-net.by

Abstract. Calibration of pulse pressure sensors by a spherical shock wave generated by near-surface laser plasma in the air is proposed. The method is based on the analytical description of dynamics of the laser-initiated shock wave.

1. INTRODUCTION

A number of methods are used for calibrations of pressure sensors in the laboratory practice [1–4]. The common important drawback of these calibration methods is the poor efficiency.

This work demonstrates that it is possible to apply the Sadowski formula, obtained for the mass chemical blast, for describing the shock wave attenuation of the pulse near-surface laser air breakdown. Based on the such description of dynamics of the laser-initiated shock wave (SW), the new pressure sensor calibration method is proposed and experimentally substantiated [5].

2. EXPERIMENTAL

The measurement geometry during the calibration of a single sensor is shown in Fig. 1. Calibrated sensor 9, electrically connected to oscilloscope 10, is placed at the given distance R from optical breakdown region 7. The distance R should be at least an order of magnitude longer than the radius of the entrance window of the sensor. In this case, the distances from the edge and from the center of the entrance window of the sensor to the center of the breakdown differ by less than 0.5%. In these conditions, the curvature of the spherical SW front does not influence the sensor readings.

The breakdown can be carried out near the solid-state target surface. In this case the laser radiation power density $q \geq 10^8 \text{ W/cm}^2$ is sufficient for the near-surface breakdown, allowing one to vary the initiating laser pulse energy within wide limits. In these conditions the acting laser radiation is completely absorbed on the target surface in the laser plasma, and the SW time formation ($\sim 10^{-7}$ s) exceeds the laser pulse duration. Such optical breakdown is similar to a

blast, and the SW becomes spherical at a distance from the breakdown place that exceeds the size of the focus region by an order of magnitude. In this form, it reaches the sensitive element of calibrated sensor 9. As a result of the SW action, calibrated sensor 9 generates an electric signal, the shape of which is unambiguously connected to the time profile of the shock peak.

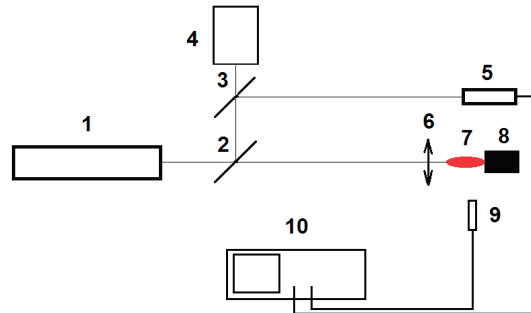


Figure 1. Measurement geometry: 1 – laser; 2,3 - beam splitters; 4 - laser-pulse energy meter; 5 – photodetector; 6 – lens; 7 – optical breakdown region; 8 – target; 9 – calibrated sensor; 10 - oscilloscope.

The corresponding oscillogram is recorded by oscilloscope 10. Based on this oscillogram, one can determine the amplitude of signal ΔU_f , unambiguously related to the pressure amplitude ΔP_f of the transmitted shock peak. The sought calibration coefficient is determined by the ratio:

$$K = \frac{\Delta P_f}{U_f}, \quad (1)$$

The value ΔP_f can be obtained by the calculation method or determined using the earlier calibrated pulse pressure sensor.

4. RESULTS AND DISCUSSION

The SW amplitude at a specified distance from the breakdown place was obtained by numerically calculating the laser blast in a spherically symmetrical arrangement [6] and can be used for calibration of pulse pressure sensors. But it is more preferable to perform analytical calculations of the SW, based, e.g., on the Sadowski formula [7]. The Sadowski formula well describes the spherical SW attenuation, which is caused by a chemical blast. It was obtained for a spherical blast of trinitrotoluene (TNT) in air. For other explosive materials there is the special procedure for recalculating coefficients of the Sadowski formula [8]. The analysis of the experimental data [6] gives grounds to assume that the Sadowski formula is also applicable to a laser blast. Applying the above coefficient recalculation procedure for laser blast conditions, the Sadowski formula can be written in the following form suitable for the analysis:

$$\Delta P_f = A \frac{E}{R^3} + B \frac{E^{2/3}}{R^2} + C \frac{E^{1/3}}{R}, \quad (2)$$

where ΔP_f , bar, is the pressure drop; E , is the blast energy; R , cm, is the SW radius; and A , B , and C are the coefficients equal to:

$$A = 1.699; B = 1.0572; C = 0.5307 \quad (3)$$

The experimental check of applicability of formula (2) with coefficients (3) was fulfilled using a pulse Nd:YAG laser in the Q-switching mode ($E_1 = 75$ mJ, $\lambda = 1.064$ μm , and $\tau = 20$ ns). The comparison of the obtained experimental data and those calculated from formula (2) with coefficients (3) showed the noticeable excess of the calculated values ΔP_f over the experimental data.

Only modified coefficients A , B , and C gave the quantitative agreement between formula (2) and experimental data. The following values were obtained for these coefficients by the least-squares method:

$$A = 0.7143; B = 0.9604; C = 0.3595 \quad (4)$$

With these coefficient values, formula (2) approximates the experimental data with an error that does not exceed 6%.

The shock wave in the air was initiated by the near-surface optical breakdown, obtained using the neodymium laser in the Q-switching mode (the pulse energy $E_2 = 1.37$ J, $\tau = 75$ ns, the radiation was focused by lens with a focal distance of 100 mm on the end wall of a brass rod into a 2.5-mm-diameter spot). At the distances from 1 to 80 cm from the breakdown region, pressure amplitudes of shock waves were measured with the calibrated sensor. At the same points, pressure amplitudes (in bars) were calculated from formula (2) with modified coefficients (4). For a point, 60 cm from the breakdown region, the calibration coefficient $K = 0.137$ bar/V was obtained. The calibrated readings of the sensor were calculated by the formula (1).

No p.	$R, \text{ cm}$	$U_f, \text{ V}$	$\Delta P_d, \text{ bar}$	$\Delta P_f, \text{ bar}$	$\Delta, \%$
1	5	0.94	0.129	0.134	3.9
2	8	0.518	0.071	0.0703	-0.98
3	10	0.396	0.0543	0.0528	-2.8
4	20	0.179	0.0245	0.023	-6.1
5	40	0.081	0.0111	0.0107	-3.6
6	60	0.0505	0.00692	0.00692	0.0
7	70	0.0398	0.00545	0.00595	9.2
8	80	0.0359	0.00492	0.00518	5.3

The above table lists initial values ΔU_f and calibrated readings of the sensor ΔP_d , the calculation results of ΔP_f by the formula (2), and their difference. It is clear from the table that the calibrated readings of the sensor are in good agreement with the values calculated from formula (2) with modified coefficients (4) for distances ≥ 5 cm. The deviation maximum was 9.2%. This indicates that the Sadowski formula with coefficients (4) describes the pressure amplitude of

the pulse laser breakdown with the accuracy sufficient for practical applications, if the energy of the laser pulse varies from 7.5×10^{-2} to 1.37 J and its duration changes from 20 to 75 ns. The measurement and calculation results of the pressure amplitude of the laser air breakdown as functions of the SW distance from the breakdown place are shown in Fig. 2. The differences in sensor readings at $R < 5$ cm are due to comparability of sizes of the sensor receiving window and the radius of SW curvature near the breakdown region.

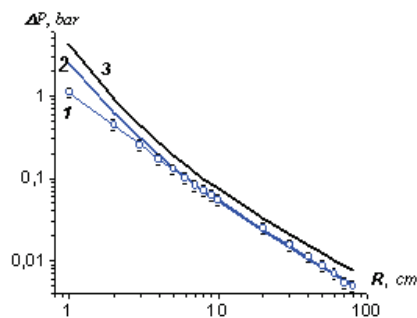


Figure 2. Dependences of experimentally measured and calculated SW amplitude values on its radius: (1) SW amplitude, measured by the sensor, calibrated by the proposed method; (2) calculation results by formula (2) with modified coefficients (4); and (3) calculation results by formula (2) with initial coefficients (3).

4. CONCLUSIONS

Calibration of pressure sensor by spherical shock wave initiated at laser near-surface air breakdown does not require the usage of standard, pre-calibrated sensors, and in this sense it is standardless method.

REFERENCES

- [1] V. A. Voitenko and L. I. Kuznetsov, *Prib. Tekh. Eksp.*, no. 4, 189 (1992).
- [2] E. M. Fedyakov, V. K. Koltakov and E. E. Bagdat'ev, *Izmerenie peremennykh davlenii* (Measurement of Variable Pressures), Moscow: Nauka, 1982.
- [3] I. I. Krivonosov and A. N. Merkur'ev, USSR Inventor's Certificate no. 1255881, *Byull. Izobret.*, 1986, no. 33, p. 162.
- [4] Yu. A. Chivel', Rep. Belar. Patent no. 6749, *Afits. Byull.*, no. 4, 182 (2004).
- [5] A. M. Petrenko et al. RF Patent no. 2469284, *Byull. Izobret.*, 2012, no. 34.
- [6] A. N. Chumakov et al. *J. Engin. Phys. Thermophys.*, 75(3), 725 (2002).
- [7] M. A. Sadovskii, *Geophysics and Physics of Explosion*, Moscow: Nedra, 1999.
- [8] G. I. Pokrovskii, *Vzryv* (Explosion), Moscow: Nedra, 1980.

LASER IRRADIATION OF NANOPARTICLES FOR MODIFICATION OF THEIR PHYSICAL AND CHEMICAL PROPERTIES

V.S.Burakov¹, N.N.Tarasenka¹, D.A. Kotsikau², V.V.Pankov², N.V.Tarasenko¹

¹*B. I. Stepanov Institute of Physics, National Academy of Sciences of Belarus,
68 Nezalezhnasti Ave., 220072 Minsk, Belarus*

²*Chemical department, Belarusian State University, Nezalezhnasti Ave. 4,
220002 Minsk, Belarus*

Abstract. Laser irradiation has been applied for modification of the morphology, change of the inner structure and synthesis of compound nanoparticles through the photoinduced processes of heating, fragmentation, phase transitions and chemical interactions. The temperature control of the laser heated particles has been shown to be achieved based on the measurement and analysis of the emitted blackbody-like radiation from the hot nanoparticles.

1. INTRODUCTION

Last decades laser-induced modification of nanoparticles (NPs) has received much attention for targeted changes of their properties. In particular, laser irradiation of NPs can result in a change of their morphology through the fragmentation and aggregation processes, can lead to the defects removal and crystallinity improvement, as well as to the phase transitions, that change a composition and inner structure of the particles. The result of the laser irradiation depends on the exposure conditions (laser fluence, laser pulse duration, exposure time, etc.) and kinetics of the relaxation processes in the surrounding medium. Because of the selectivity of the light absorption by particles, the efficiency of laser excitation is expected to be dependent on the laser wavelength.

It should be noted that the result of laser modification of NPs is mostly determined by the temperature that is reached during the irradiation. Exact knowledge of the particle temperature during pulsed laser irradiation is important for the correct interpretation of observed phenomena. Therefore it is important to develop a method of the particles temperature control during laser irradiation. It is possible to determine the temperature of the heated nanoparticles based on the analysis of the emission spectra of the heated particles [1].

In the present work laser induced modification of metal (Au, Ag, Cu), oxide (ZnO, (α,γ -Fe₂O₃, Fe₃O₄)) and mixtures of gadolinium, silicon and germanium NPs produced by laser ablation in liquid has been studied with control

of the temperature of laser heated particles by means of analysis of the emitted blackbody-like radiation from the hot NPs.

2. EXPERIMENTAL

The initial colloids were prepared by laser ablation in ethanol or water. The colloids were subjected to laser irradiation with the second harmonic of the Nd: YAG laser (wavelength 532 nm, pulse duration 10 ns) with fluence of 230 and 400 mJ/cm².

The emission of the heated particles was displayed by a lens ($F = 61$ mm) in 1:1 scale on the entrance slit of the polychromator with the diffraction grating with 600 lines/mm, 1:4.9 aperture and focal length of 380 mm. For the detection of radiation a gateable CCD detector (1024 x 256 pixels) was used. In order to reduce the noise introduced by the radiation fluctuations the signal was averaged for 10 laser pulses. For the calibration of the optical detection system a tungsten strip calibration lamp was used. To determine the temperature of the nanoparticles based on their thermal radiation, the calibrated spectra were fitted by a Planck curve, taking into account the emissivity function of NPs and that the CCD detector counts the photon numbers.

3. RESULTS AND DISCUSSION

3.1 Temperature determination of laser irradiated colloidal nanoparticles

It has been demonstrated that the detection of black body radiation can be used for fast non-contact measurements of particle temperature. It is known that thermal emission of the black body is described by the Planck's law:

$$I = \frac{hc^2}{\lambda^5} \frac{1}{e^{\frac{hc}{\lambda k_B T}} - 1} \quad (1)$$

where I denotes the photon number in the $(\lambda, \lambda + \Delta\lambda)$ spectral region, λ is the wavelength, T is the absolute temperature, c is the speed of light, h is the Planck constant, k_B – is the Boltzmann constant.

Taking into account the emissivity of NPs ε (W/cm²) (for small NPs with the diameter less than the wavelength of the emitted light) the expression (1) can be written as:

$$I \propto \varepsilon(r, \lambda) \frac{1}{\lambda^5} \exp\left(-\frac{hc}{\lambda k_B T}\right) \quad (2)$$

According to the Mie theory, the emissivity of the small nanoparticle is [2]:

$$\varepsilon = \frac{8\pi N_m r}{\lambda} \operatorname{Im}\left(\frac{m^2 - 1}{m^2 + 2}\right) \quad (3)$$

where N_m is the refraction index of the surrounding medium, $m = N_p/N_m$, where N_p is the refraction index of the particle material and r is the particle diameter.

By fitting the measured and then corrected emission spectrum of the NPs by the theoretical curves (2) it was possible to estimate the temperature of the particles in solution excited by the laser pulses.

For instance, analysis of the emission spectrum of gold nanoparticles prepared by laser ablation in ethanol and additionally irradiated by the second harmonic of the YAG:Nd³⁺ laser allowed to conclude that at the laser fluence of 0.4 J/cm² the particles are heated up to 1700 K that exceeds the melting point of gold (1337.6 K). Consequently, laser irradiation can cause changes in both size and shape of the particles.

1.2 Laser-induced modification of NPs morphology

The properties of the NPs were found to be sensitive to the additional laser irradiation. For instance, plasmon peak position of as-prepared gold NPs was around 542 nm indicating formation of particles with dimensions of 60 nm. The blue shift of the SPR maximum in the absorption spectra and narrowing of the red tail of the plasmon resonance band after 532 nm irradiation can be attributed to the depletion of the particle aggregates and fragmentation of parent NPs into smaller ones by the additional laser irradiation. These spectra findings are in agreement with TEM data and results of particle temperature determination (Fig.1).

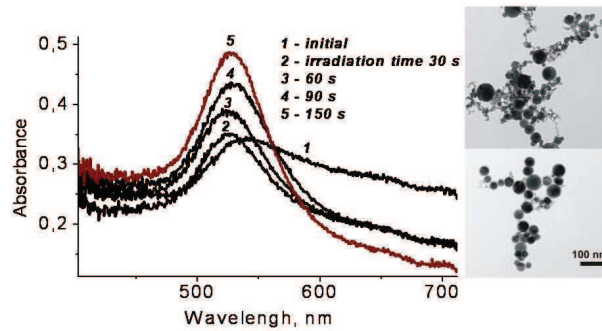


Figure 1. Temporal variation of the absorption spectra of gold NPs in water during irradiation with the nanosecond 532 nm laser and TEM images of the as-prepared Au NPs (top) and after the 150 s irradiation with the 80 mJ 532 nm laser beam (bottom).

TEM images show that the initial nanoparticles were loosely agglomerated, some presented as chains of small clusters. Laser irradiation by the 532 nm laser beam resulted in formation of well-separated near-spherical particles with an average diameter of 30 nm and the narrower size distribution.

1.3 Synthesis of compound NPs

Laser irradiation of the mixture of colloids formed after the sequential ablation of silicon, gadolinium and germanium targets in ethanol was shown to be suitable for a formation of gadolinium silicides and germano-silicides compound nanoparticles. Higher purity $Gd_5Si_2Ge_2$ sample with improved crystallinity was achieved by additional laser treatment of as-prepared colloids. Magnetization was found to increase after laser irradiation of samples due to ordering in the grain structure and the magnetic moments at the surface.

1.4 Doping of NPs

For a synthesis of doped ZnO NPs we used two step process which involved a sequential ablation of Zn and Ag targets in the 0.01M ammonium nitrate solution followed by the additional laser irradiation of the formed colloid with the second harmonic of the Nd:YAG laser (532 nm, 90 mJ).

The analysis of SAED patterns of the as-prepared sample showed that it is composed of the ZnO NPs in zincite structure and of cubic Ag. Laser irradiation of NPs results in the distortion of the lattice and disappearing of Ag reflections that may be the consequence of doping of ZnO or alloying of Ag and Zn NPs.

1.4 Laser induced phase-structure changes in iron oxide NPs

Laser irradiation of the colloidal and powder iron oxide NPs resulted in the ordering of crystal structure and partial removal of adsorbed and structural hydroxyl groups from the particle surface. The morphology of NPs changed from the irregularly shaped particles to spherical ones with diameters close to the initial particle sizes (50-90 nm). Besides, a fraction of small NPs with sizes in the range of 5-8 nm has been observed after laser modification. It was found that laser heating of α - Fe_2O_3 phase in non-equilibrium conditions resulted in the formation of spinel phases of iron oxide (γ - Fe_2O_3 , Fe_3O_4) while single-phase γ - Fe_2O_3 sample undergoes a partial thermo stimulated phase transition to the thermodynamically stable α - Fe_2O_3 phase.

Acknowledgements

This work is partially financed by the Belarusian Foundation for Fundamental Researches under grant No. F 14SRB-008.

REFERENCES

- [1] V. Poborchii, T. Tada, and T. Kanayama, J. of Appl. Phys., 97, 104323-1, (2005)
- [2] P.Heszler, K. Elihn, L. Landstrom, and M. Boman, Smart Materials and Structures, 11, 631 (2002).

Section 3.

**LOW TEMPERATURE
PLASMAS**

PLASMA MEDICINE: FUNDAMENTALS AND APPLICATIONS

Alexander Fridman

Drexel University, Drexel Plasma Institute, Philadelphia, USA

General principles of applications of non-thermal plasmas for medicine are discussed in the presentation, including physical and bio-chemical mechanisms of non-thermal plasma interaction with living tissues, plasma assisted sterilization, blood coagulation, and healing different diseases. Physics and engineering of different discharges used in plasma medicine is considered. Both in-vitro and in-vivo plasma-medical experiments are discussed. From all variety of modern plasma-medical applications, this presentation is focused mostly on plasma-assisted treatment of wounds, on plasma-stimulated tissue regeneration, plasma treatment of cancer and cardio-vascular diseases.

Technological developments have resulted recently in many important medical advances. Such medical technologies include applications of ionizing radiation, lasers, ultrasound, magnetism and others. Plasma technology is a relative newcomer to the field of medicine. Experimental work conducted at several major universities, research centers and hospitals around the world over the recent decade demonstrates that non-thermal plasma can provide breakthrough solutions of challenging medical problems. The non-thermal plasma is clearly a promising new tool to be provided to medical doctors for solving medical problems previously unsolved.

Between different non-thermal discharges applied today in plasma medicine, this presentation is focused on physics and engineering of the different modifications of the floating-electrode nanosecond and microsecond-pulsed dielectric barrier discharges FE-DBD, as well as different modifications of plasma jets.

MODELLING OF PHYSICAL AND CHEMICAL PROCESSES IN COLD ATMOSPHERIC PRESSURE PLASMA JETS

G.V. Naidis

Joint Institute for High Temperatures RAS, 125412 Moscow, Russia

Non-thermal (cold) atmospheric-pressure plasmas have attracted a lot of attention in the past decade due to new biomedical and chemical applications. Among various sources of cold plasma, atmospheric-pressure plasma jets formed by pulsed discharges in flows of noble gases (pure or with molecular admixtures) and emerged into ambient air are a topic of great interest. It has been revealed that at pulse repetition frequencies in kilohertz range plasma jets are composed of bullet-like plasma volumes travelling with high velocities. Numerous experiments and simulations have demonstrated that the plasma bullets are ionization waves – streamers propagating along plasma jets. Chemically active species (excited atoms and molecules, radicals, charged species) are produced, by streamers, not only in discharge regions close to electrodes but along the whole jets. Due to this property, the plasma jets operating in the plasma bullet mode are capable to deliver fluxes of various active species, including those with short lifetimes, directly to treated objects. Knowledge of composition of active species generated in plasma is of crucial importance for applications. Available experimental information on gas composition in kilohertz range plasma jets is rather scarce, so that elaboration of computational approaches is of great interest.

In the talk, a review of observed properties of plasma jets will be given. Results of numerical simulations of the dynamics and structure of streamers propagating along plasma jets will be presented. An approach used for evaluation of chemical composition of plasma generated by repetitive streamers in plasma jets will be discussed, and evaluated densities of produced active species will be given. The calculated results will be compared with available experimental data.

**A CCP-PLASMA SOURCE OPERATION IN THE
HIGH-VHF TO UHF FREQUENCIES AND
SCALABILITY TO LARGE-AREA APPLICATIONS**

Albert R. Ellingboe

*Plasma Research Laboratory, School of Physical Sciences and NCPST, Dublin
City University, Dublin, Ireland*

APPLICATION OF LOW TEMPERATURE PLASMAS FOR RESTORATION/CONSERVATION OF ARCHAEOLOGICAL OBJECTS

Frantisek Krcma, Vera Mazankova, Lucie Radkova, Petra Fojtikova, Vera Sazavska, Lenka Hlochova, Michal Vasicek, Zdenka Kozakova, Radek Prikryl, Michal Prochazka, Lucie Blahova, Jakub Horak, Drahomira Janova

*Brno University of Technology, Faculty of Chemistry, Purkynova 118, 612 00
Brno, Czech Republic*

The plasma chemical treatment of archaeological artifacts by RF hydrogen low pressure plasma is applied in practice since mid 80's [1]. The corrosions as well as their removal are a very complex problem. The application of low pressure plasmas can be much more effective in contrary to the classical conservation procedures, but the mechanism of corrosion removal induced by plasma is not fully understood yet, and optimal conditions are not known well. As each archaeological object is original with its unique composition of corrosion layers as well as corrosion history, it is necessary to study influence of processes and discharge conditions on corrosion removal using the model corroded samples. Various plasma conditions are applied based on low pressure RF hydrogen-argon plasma. The conditions are optimized for selected most frequent materials of original metallic archaeological objects (iron, bronze, copper, and brass).

Application of this low pressure plasma on glass and ceramic objects is nearly impossible due to induced high temperature stress. Very recently, we developed a new plasma jet generated in liquids. The first results of its application on selected non-metallic materials are presented here, too.

The last plasma application in the conservation field is deposition of thin layers protecting the objects from secondary corrosion. Organosilicone and parylene thin films are applied. The deposition conditions and thin films characteristics are discussed separately [2].

Acknowledgements: This work is supported by Ministry of Culture of the Czech Republic under project No. DF11P01OVV004.

REFERENCES

- [1] S. Veprek, J. Patscheider and J. Elmer, Plasma Chem. Plasma Process., 5, 201 (1985).
- [2] M. Prochazka, L. Blahova, F. Krcma, Proc. SPIG XXVII, 2014.

LIQUID-PHASE REACTIONS INDUCED BY ATMOSPHERIC PRESSURE GLOW DISCHARGE WITH LIQUID ELECTRODE

Fumiyoshi Tochikubo, Naoki Shirai and Satoshi Uchida

*Department of Electrical and Electronic Engineering, Tokyo Metropolitan
University, 1-1, Minami-Osawa, Hachioji, Tokyo 192-0397, Japan*

There are many kinds of nonthermal plasmas in contact with liquid. DC atmospheric pressure glow discharge (APGD) with liquid electrode is an easy method to obtain simple and stable plasma-liquid interface[1]. When we focus attention to liquid-phase reaction, the discharge system is considered as an electrolysis with plasma electrode instead of metal electrode. The plasma electrode will supply electrons or positive ions to the liquid surface in a different way from the conventional metal electrode. In this work, we studied some of liquid-phase reaction induced by electron or positive-ion irradiation from dc glow discharge to the liquid surface. The plasma-induced liquid-phase reaction was applied to the formation of metallic nanoparticles (NPs) in the liquid.

Electron irradiation to liquid surface generated OH^- in liquid and pH of the liquid changed from initial pH of 7 to 10 while positive-ion irradiation generated H^+ and pH of the liquid became roughly 3, even without the dissolution of nitrogen oxides from gas. OH radical generation in liquid was also confirmed both by electron irradiation and positive-ion irradiation. The generation efficiency of OH radical was better with positive-ion irradiation. Both Ag NPs in AgNO_3 solution and Au NPs in HAuCl_4 solution were synthesized by electron irradiation while Au NPs were also generated by positive-ion irradiation[2]. We also succeeded in the generation of Fe_3O_4 particles in FeCl_2 solution by electron irradiation.

Acknowledgements: This work was supported financially in part by Kakenhi (No 2111007), Japan

REFERENCES

- [1] N. Shirai, K. Ichinose, S. Uchida and F. Tochikubo, *Plasma Sources Sci. Technol.* 20, 034013 (2011).
- [2] N. Shirai, S. Uchida and F. Tochikubo, *Jpn. J. Appl. Phys.* 53, 046202 (2014).

THE AFTERGLOW OF A SURFACE-WAVE MICROWAVE DISCHARGE AS A TOOL FOR SURFACE PROCESS STUDIES

Kinga Kutasi

*Wigner Research Centre for Physics of the HAS, Institute for Solid State Physics
and Optics, Konkoly Thege M. út 29-33, H-1121 Budapest, Hungary*

The afterglow system here presented is based on a surface-wave microwave discharge generated in flowing gas (typically of 1000 sccm gas flow rate) in a 5 mm inner diameter quartz tube, with 2.45 GHz frequency microwave. The pressure in the discharge tube is typically 100-700 Pa. The quartz discharge tube is connected to a further tube or chamber [1-3], where a charge free afterglow plasma rich in active neutrals can build up. This region can be used for surface treatments and to study the interaction of active species with polymer surfaces, biological samples or complex molecules, such as biomolecules [1,3]. The advantage of the system is that the composition of the afterglow in the studied region can be easily tuned – e.g. by either varying the distance between the discharge region and the treatment/interaction region, or the gas flow rate – since the different active species have different relaxation or recombination times depending on the pressure and gas composition [4,5]. In the case of a large afterglow chamber a connecting tube can be also used, which allows an easier tuning of the afterglow composition [2]. The density of active species can be further tuned by controlling the losses on the system's walls.

The exact composition of the plasma in the different part of the system and the controlling possibilities can be easily determined by means of modelling. The possibilities offered by this afterglow system will be discussed through the modelling results.

Acknowledgements: The work has been supported by the Hungarian Science Foundation OTKA, through project K-104531.

REFERENCES

- [1] D. Duday et al., Plasma Process. Polym. 10, 864-879 (2013).
- [2] M. Moisan et al., Eur. Phys. J. Appl. Phys. 63, 10001-p1-p46 (2013).
- [3] M. Mafra et al., Plasma Process. Polym. 6, S198 (2009).
- [4] K. Kutasi et al., Plasma Process. Polym 5, 840 (2008).
- [5] K. Kutasi et al., Plasma Sources Sci. Technol. 20, 035006 (2011).

OPTICAL DIAGNOSTICS OF LABORATORY ANALOGUE OF TLE DISCHARGES

M. Šimek¹, T. Hoder^{1,2}, F. C. Parra-Rojas³, F. J. Gordillo-Vázquez³
and V. Prukner¹

¹*Institute of Plasma Physics, Academy of Sciences of the Czech Republic,
Za Slovankou 3, 18200 Prague, Czech Republic*

²*Leibniz Institute for Plasma Science and Technology - INP,
Felix-Hausdorff-Str. 2, 17489 Greifswald, Germany*

³*Instituto de Astrofísica de Andalucía (IAA – CSIC), Glorieta de la Astronomía
s/n, 18008 Granada, Spain*

The transient luminous events (TLEs) are large scale discharges occurring above thunderclouds in the upper atmosphere. The red-sprite TLE is driven by the quasi-electrostatic field in the mesosphere following a positive cloud-to-ground lightning flash produced below. The studies performed through imaging instruments with high frame rates have discovered the existence of complex streamer downward/upward propagating structures with propagation velocities between 10^6 and 10^8 m/s and provided basic information on associated optical emission. However, detailed investigation of sprites based on optical emission is quite difficult due to their stochastic nature and very long distances of the diagnostic instrumentation from the TLE's. In addition, the most important characteristics of red-sprite TLE's is that they propagate vertically over large distances surpassing altitudes of ~ 35 to ~ 85 km above sea level characterised by very different pressures, between ~ 3 and $\sim 10^{-2}$ mbarr, and gas temperatures between -10 and -75 °C. Benchmark studies of equivalent laboratory discharges are therefore of interest in order to correctly understand spectrometric fingerprints of real TLE's. Because it is difficult to scale-down a whole red-sprite event maintaining at the same time such large pressure/temperature gradients, we performed an investigation of filamentary streamers propagating in a DBD gap instead, fixing pressure/temperature conditions which are characteristic for various altitudes covering whole range of red sprite occurrence. In this work, triggered single streamer events were produced in volume DBD geometry under TLE conditions (synthetic air, pressure, temperature) and associated emission waveforms were studied with high spatio-temporal resolutions. Basic characteristics, such as streamer morphology or dynamics of radiative species, will be presented and discussed in the light of published real red-sprite data.

Acknowledgements: This work is supported by the AV ČR under collaborative project M100431201 between the IPP and IAA.

ATMOSPHERIC PRESSURE PLASMA JET INTERACTIONS WITH LIQUIDS

Sylwia Ptasinska

*Radiation Laboratory and Department of Physics, University of Notre Dame,
Notre Dame, 46556 IN, USA*

Atmospheric pressure plasma jet is an emerging area of contemporary technology that bridges many science fields to bear on important medical and industrial problems.

Many experimental studies have been conducted which showed that results of plasma treatment strongly depend on doses delivered to biological tissue or other materials. Generally, a plasma dose is associated with treatment duration.

A broad spectrum of different APPJ sources is used but with a very limited comparability and a reliable estimate of the plasma dose still remains to be one of the open questions!

In our laboratories we have built two APPJ sources, which were successfully used for studies on damage to DNA and cancer cells [1-4] and for the growth of silicon nitride films [5]. For medical applications, an APPJ interacts directly with liquid, which contains a biological sample. However, the dose delivered at the interface of plasma/liquid is difficult to estimate. In this study, the use of Fricke solution dosimetry, a common technique in radiation-chemistry, is proposed. This type of dosimetry is widely accepted because of its advantages of the accuracy, reproducibility and linear dependence of its response as a function of doses. In order to obtain dosage at the interface, the Fricke solution was placed in containers with a different height and diameter and then irradiated by the APPJ. Obtained results were extrapolated and dosage rate estimated.

Acknowledgements: The research described herein was supported by the Division of Chemical Sciences, Geosciences and Biosciences, Basic Energy Sciences, Office of Science, United States Department of Energy through grant number DE-FC02-04ER15533. This project has been performed in collaboration with Harper Cancer Research Institute at the University of Notre Dame.

REFERENCES

- [1] X. Han et al, APL 102, 233703 (2013).
- [2] M. Klas and S. Ptasinska, PSST 22, 025013 (2013).
- [3] X. Han et al, EPJD 68, 46 (2014).
- [4] S. Ptasinska et al, PCCP 12, 7779 (2010).
- [5] X. Zhang and S. Ptasinska. JPD 47, 14520 (2014).

LOW TEMPERATURE PLASMA FOR BIOMEDICAL APPLICATIONS

Ita Junkar

Jozef Stefan Institute, Jamova 39, 1000 Ljubljana, Slovenia

It is of primary importance to appropriately condition the surface of biomedical device for desired biological response. In the biomedical field plasma treatment techniques are becoming widely used, as plasma enables activation of relatively inert biomedical devices, which are usually made from polymers. Creating blood compatible material is highly complex and still poorly understood as so far not enough knowledge on the effects of surface characteristics and blood compatibility exist.

In the scope of our work we studied the effects of low temperature plasma treatment on surface properties and biological response of biomedical devices in contact with blood. The effects of plasma treatment on surface chemistry were determined by X-ray photoelectron spectroscopy (XPS) and Secondary ion mass spectrometry (SIMS). Changes in morphology and surface roughness were observed with atomic force microscopy (AFM) and scanning electron microscopy (SEM). The biological response was determined *in vitro* by assessing the number of attached cells. Our results indicate that low temperature plasma is an appealing method for treatment biomedical devices in contact with blood.

ELECTRICAL BREAKDOWNS IN AIR: NEW EXPERIMENTS AND STATISTICAL AND NUMERICAL MODELS

Aleksandar P Jovanović

*Department of Physics, Faculty of Sciences and Mathematics, University of Niš,
Višegradska 33, P.O. Box 224, 18001 Niš, Serbia*

The electrical breakdowns and discharges in air are of great significance for science and technology due to wide applications in surface treatment, for plasma actuators, in medicine or for vehicle re-entry. Besides the breakdown itself, the pre-breakdown phenomena and relaxation after the breakdown are also of great significance. In this report the analysis of DC glow discharge and its relaxation processes is discussed by measuring the time delay to electrical breakdown. Statistical analysis of time delay distributions is presented [1] and the statistical model based on the mixed distribution is applied to experimental data measured with different electrodes from which electron yield is calculated. The appearance of mixed distributions is physically described based on analysis of the cathode surface by SEM, EDX and AFM measurements. Also, by analyzing the memory curve measured in synthetic air the early and late relaxation of DC discharge are discussed. The processes responsible for the memory effect are identified and corresponding rate coefficients are determined. In order to confirm that the correct particles are identified, the 2D numerical model for relaxation is developed. The stationary densities in DC discharge in air that are used as initial densities for the model for relaxation are calculated by the 1D numerical model which is verified by modeling the Paschen's curve as well as current and voltage waveforms [2].

Acknowledgements: This work is supported by Ministry of Education, Science and Technological development of the Republic of Serbia under the grant ON 171025.

REFERENCES

- [1] V. Lj. Marković, A. P. Jovanović, S. N. Stamenković and B. Č. Popović, EPL, 100, 45002 (2012).
- [2] A. P. Jovanović, M. N. Stankov, V. Lj. Marković and S. N. Stamenković EPL, 104, 65001 (2013).

SPECTROSCOPIC STUDY OF PLASMA DURING ELECTROLYTIC OXIDATION OF MAGNESIUM- ALLUMINIUM ALLOYS

Jovica Jovović

*University of Belgrade, Faculty of Physics, Studentski trg 12-16, 11001
Belgrade
E-mail:jjovica@ff.bg.ac.rs*

Plasma electrolytic oxidation (PEO) is high-voltage anodizing technique of lightweight metals above the dielectric breakdown voltage when thick, highly crystalline oxide coating with high corrosion resistance, high wear resistance, and other desirable properties is formed. PEO leads to the local generation of plasma in the form of micro-arc discharges expanding from the metal surface through dielectric layer. In order to assess in more detail the process of plasma ejection from micro-channel, an optical emission spectroscopy study of PEO on magnesium-aluminium alloys is carried out. Plasma electron number density (N_e) diagnostics is performed either from the H_β line shape or from the width or shift of non-hydrogenic ion lines of aluminium and magnesium. The line profile analysis of the H_β revealed the presence of two types of discharges characterized by relatively low electron number density $N_e \approx (10^{15} - 10^{16}) \text{ cm}^{-3}$, while the third discharge process with larger electron density $N_e = (1-2) \times 10^{17} \text{ cm}^{-3}$ is detected from the width and shift of aluminium and magnesium singly charged ion lines. These PEO micro-discharges are induced by 1. breakdown at the surface of dielectric, 2. breakdown of dielectric and 3. an ejection of metal plasma through micro hole generated in dielectric by process number 2. On the basis of present and other results it was shown that low N_e discharges do not depend upon anode material or electrolyte composition. During the course of this study, difficulties in the analysis of spectral line shapes are encountered and the ways to overcome some of the obstacles are demonstrated.

Acknowledgements: The author gratefully acknowledges the discussions with N.Konjević and S. Stojadinović. This work is supported by the Ministry of Education, Science and Technological Development of the Republic of Serbia under Project 171014.

MEASUREMENTS AND MODELS OF TRANSIENT AND STATIONARY REGIMES OF GLOW DISCHARGE IN ARGON

Marjan Stankov

*Department of Physics, Faculty of Sciences and Mathematics, University of Niš,
Višegradska 33, PO box 224, 18001 Niš, Serbia*

Measurements and modelling of stationary DC glow discharge, as well as transient regimes of discharge inception and afterglow relaxation in argon are reported. Fluid models are widely applicable for glow discharge modelling and they are used most common for determination of particle number densities, intensity of electrical field and mean electron energy. In this work, the fluid models were applied for tracking the glow discharge establishment, calculation of the static breakdown voltage U_s and Paschen curve $U_s(pd)$ (pressure times inter-electrode distance). The measurements of the static breakdown voltage and current-voltage ($I-U$) characteristics were carried out on the gas tube with a plane-parallel electrode system made from OFHC copper for different values of pd and the results were compared to those from different fluid models. The applicability of fluid models for modelling of $I-U$ characteristics at different values of pd is tested. The current and voltage waveforms are also modeled and compared to ones measured by oscilloscope. From statistically based measurements of electrical breakdown time delay t_d , the statistical and formative times are determined under different conditions. The formative times calculated from [1D] and [2D] fluid models are compared to those obtained from experiment. The measurements of time delay were performed for different relaxation times τ in afterglow and the memory curve $\overline{t_d}(\tau)$ is presented. For the analysis of afterglow, the analytical and numerical models were applied and diffusion coefficients of atomic and molecular argon ions are determined, extending from ambipolar to free diffusion limits.

Acknowledgements: This work is supported by Ministry of Education, Science and Technological development of Republic of Serbia under the grant ON 171025.

DIAGNOSTICS OF LASER INDUCED PLASMA BY OPTICAL EMISSION SPECTROSCOPY

M. Cvejić

Institute of Physics, University of Belgrade, Serbia

We describe the procedure for diagnostics of laser induced plasma (LIP) by optical emission spectroscopy technique. LIP was generated by focusing Nd:YAG laser radiation (1.064 nm, 50 mJ, 15 ns pulse duration) on the surface of a pellet containing aluminum, magnesium and lithium. Details of the experimental setup and experimental data processing are presented. High speed plasma photography was used to study plasma evolution and decay. From those images optimum time for plasma diagnostics is located. The electron number density, N_e is determined by fitting profiles of Mg and Li lines using available Stark broadening data while electron temperature, T_e , was determined from relative intensities of Li I lines using Boltzmann plot (BP) technique. All spectral line recordings were tested for the presence of self-absorption and then if optically thin, Abel inverted and used for plasma diagnostic purposes.

Acknowledgements: This work is supported by the Ministry of Education, Science and Technological Development of Republic Serbia under Project No. 171014.

REFERENCES

- [1] M. Cvejić, M. R. Gavrilović, S. Jovićević and N. Konjević, *Spectrochim. Acta Part B* 85 20–33 (2013).

ELECTRON HEATING DYNAMICS IN MULTI-FREQUENCY CAPACITIVE RF DISCHARGES

A. Derzsi¹, I. Korolov², E. Schüngel², Z. Donkó¹, and J Schulze²

¹*Wigner Research Centre for Physics, Hungarian Academy of Sciences,
Budapest, Hungary*

²*Department of Physics, West Virginia University, Morgantown, USA*

We perform a systematic investigation of the electron heating dynamics in capacitively coupled radio frequency (RF) plasmas operated at multiple consecutive harmonics in argon by PIC/MCC simulations, extending the parameter range covered in previous studies [1]. We focus on the effect of modifying the driving voltage waveform on the electron heating and ionization dynamics as well as the independent control of the ion flux and mean ion energy at the electrodes. The driving voltage waveform is shaped by adding maximum 4 consecutive harmonics of 13.56 MHz with specific harmonics' amplitudes and phases. Based on the Electrical Asymmetry Effect, a dc self-bias voltage is generated in multi-frequency discharges that can be controlled by the harmonics' phases and is enhanced by adding more harmonics. Changing the driving voltage waveform, the electron heating and ionization dynamics are affected, influencing also the control of ion properties at the electrodes. We find that, depending on the mode of discharge operation, customizing the voltage waveform has different impact on the control of ion properties [2]: (i) At low pressures, where the discharge is operated in α -mode, increasing the number of harmonics leads to stronger sheath expansion heating, this way the ion flux can be increased, but the mean ion energy does not remain constant for high voltage amplitudes. At low pressures, the mean ion energy can be controlled at constant ion flux by adjusting the harmonics' phases. (ii) At high pressures and assuming a high secondary electron emission coefficient, where the discharge operates in γ -mode, both the ion flux and mean ion energy changes by adjusting the harmonics' phases. Under these conditions, increasing the number of harmonics leads to a decrease of the ion flux and a change of the mean ion energy.

REFERENCES

- [1] T. Lafleur et al., Appl. Phys. Lett. 101, 124104 (2012); T. Lafleur and J. P. Booth, J. Phys. D 45, 395203 (2012); T. Lafleur et al., Appl. Phys. Lett. 100, 194101 (2012); P. A. Delattre et al., J. Phys. D 46, 235201 (2013).
- [2] A. Derzsi, I. Korolov, E. Schüngel, Z. Donkó, and J. Schulze, Plasma Sources Sci. Technol. 22, 065009 (2013).

TIME-SPACE DEVELOPMENT OF HYDROGEN BALMER ALPHA LINE IN A BARRIER HOLLOW CATHODE DISCHARGE

B. M. Obradović, S. S. Ivković, N. Cvetanović, and M. M. Kuraica

University of Belgrade, Faculty of Physics, 11000 Belgrade, Serbia

Abstract. Simultaneous electrical and spectroscopic investigations of the development of barrier hollow cathode discharge in hydrogen have been performed. By analyzing the shape of excessively broadened Balmer alpha line profiles, during the discharge development, different phases in the discharge establishing can be resolved.

1. INTRODUCTION

Energetic hydrogen atoms have been detected via large Doppler broadening of hydrogen Balmer lines in different types of discharges. Hydrogen lines are broadened to a great extent with far wings corresponding to kinetic energies of several hundreds of electron volts, i.e., orders of magnitudes higher than gas temperatures. Shapes of Balmer line profiles depend on the direction of observation, indicating anisotropy of motion of fast hydrogen atoms. Highly asymmetric broad line profiles were observed along the electric field. For generation of energetic H atoms, a detailed model was given by Phelps and co-workers in Ref. 1 and 2. According to this, three types of hydrogen ions, H^+ , H_2^+ and H_3^+ are accelerated in the electric field and undergo charge exchange reactions with H_2 creating energetic H atoms. These charge exchange processes produce fast hydrogen atoms moving toward the cathode, i.e. in the field direction. It was shown earlier that the overall hydrogen line profile is comprised of three components: narrow and middle width component (coming from electronic excitation) and wide component (coming from excitation of energetic atoms) [3]. Large Doppler broadening in a hollow cathode discharge was reported in a number of papers [4 – 6]. At low pressures, in so called high voltage hollow cathode regime, the negative glow is extracted from the cathode cylinder and cathode fall fills the gap to the anode ring, making the electric field vector coincide with the central axis of the cathode cylinder.

2. EXPERIMENT

Experimental set-up is presented in Fig. 1. The discharge tube is a glass cylinder with diameter of 20 mm. One electrode is another closed glass cylinder set at one side of the tube - sealed by microscopic glass and filed with transparent electrolyte. The other electrode is a steel mesh cylinder which is positioned inside the glass tube, see Fig. 1. The discharge tube was evacuated down to 10^{-2} mbar first, and then filled with hydrogen at 1.1 mbar pressure. The discharge was driven by an AC voltage with frequency of 20 kHz. The sinusoidal voltage signal from a HP MODEL function generator was amplified using an audio amplifier (400 W) and transformed to a high voltage. The applied voltage was measured via a 1:1000 P6015A Tektronics voltage probe; the total current was monitored by a current probe (ipc cm-100-m). The applied voltage and the discharge current were monitored by Tektronics TDS 3032 (300 MHz bandwidth, 2 Gsamples/s) oscilloscope. The discharge image was projected by a lens to the entrance slit of an Echelle-type spectrograph equipped with an ICCD (PI MAX2, Princeton Instruments) – instrumental FWHM = 0.02 nm. ICCD is triggered with a time delayed pulse, initially generated by the discharge current pulse. The gate duration was 50 ns during the measurements of the H_{α} line development. The hollow cathode configuration was chosen to obtain ICCD triggering with a minimal jitter. This was possible only in a barrier discharge arrangement, where seed electrons on the barrier facilitate the breakdown in the next half-period.

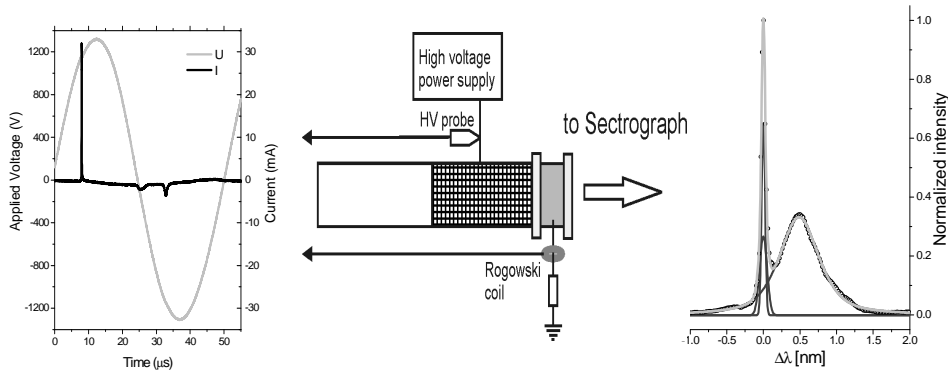


Figure 1. Experimental set-up with current and voltage oscilograms (left) and recorded hydrogen Balmer alpha line fitted with three peak functions (right).

3. RESULTS AND DISCUSSION

An example of recorded H_{α} line profile presented on Fig. 1, shows two distinct peaks: narrow („core“), unshifted, caused by electronic excitation, and broad („wing“), shifted, caused by heavy particle collisions. Fig. 2a gives H_{α}

line profiles recorded at different times during the development of the discharge, with the shifts given in velocity values of hydrogen atoms. Referent time instant, indicated as 0 ns, is the time of maximal current, see Fig.3. Analyzing smoothed profiles of broad peaks, which here are used for clarity; one can conclude that maxima of these peaks are shifted towards lower values. Recorded line profiles we were used for analysis of the excited atoms energy distribution and fraction of heavy particle processes in the total excitation, as in Ref. 6. Energy distributions of excited fast atoms, see Fig. 2b, are obtained from the red wing of the profiles. Distributions are obtained by simple histogram transformation from wavelength (velocity) distribution to energy distribution and normalization to the integral of $f(\epsilon)$. Energies on the abscissa are “detected” energies, i.e., kinetic energies in the direction of observation.

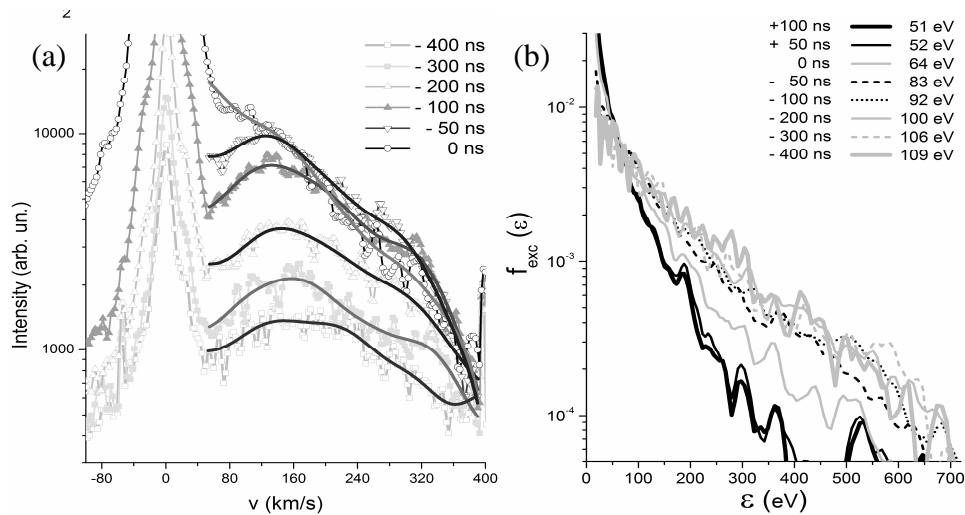


Figure 2. (a) H_{α} line profiles recorded during the discharge development. (b) Energy distribution of excited fast H atoms obtained from the H_{α} line wings.

Development of the core and wing intensity, and the hydrogen atoms mean energy are presented in Fig. 3 together with the development of the discharge voltage and current. One can see from the graphs that core and wing intensities increase during the discharge development i.e. during the current increase, and they decrease during the falling edge of the current pulse i.e. during the extinguishing phase of the discharge. Analyzing the figure one can conclude that the ratio of core and wing intensities start to increase with start of current step increase, and time dependence of core to wing intensity ratio clearly follows the current development. As we mentioned earlier, core of the line profile is formed due to electronic excitation, so, rapid increase of the core intensity is evidence of increasing of electron density in the discharge. Similarly to this behavior, it was demonstrated in a pulse high voltage hollow cathode discharge, experimentally and theoretically, that steep increase of the discharge current during the

breakdown phase is caused by rapid density increase of low-energy electrons produced in the process of secondary electron emission from the cathode [7, 8].

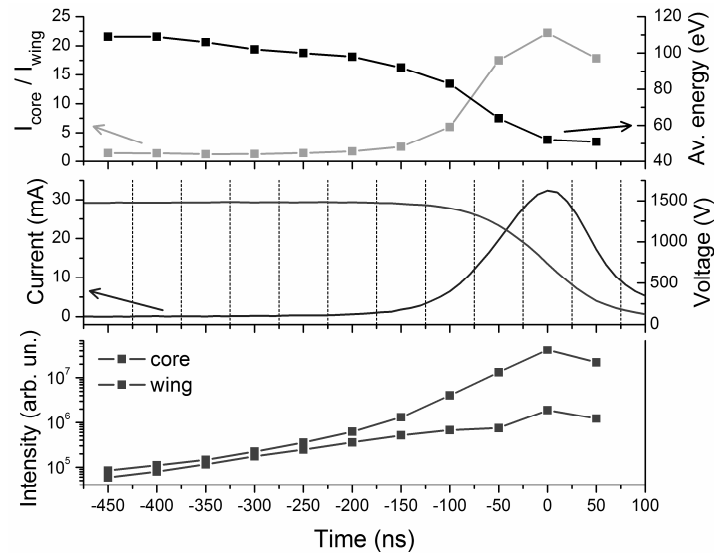


Figure 3. (Top) Intensity ratio and H atom mean energy. (Middle) Discharge voltage and current signals. (Bottom) Core and wing intensities.

Acknowledgements

This work is supported by the Ministry of Education and Science of the Republic of Serbia through the Project No. 171034 and the Project No. 33022.

REFERENCES

- [1] Z. Lj. Petrović, B. M. Jelenković and A. V. Phelps, *Phys. Rev. Lett.* 68, 325 (1992).
- [2] A. V. Phelps, *Phys. Rev. E* 79, 066401 (2009).
- [3] N. Cvetanović, B. M. Obradović, and M. M. Kuraica, *J. Appl. Phys.* 97, 033302 (2005).
- [4] B. P. Lavrov and A. S. Mel'nikov, *Opt. Spectrosc.* 79, 842 (1995).
- [5] N. M. Sišović, G. Lj. Majstorović, and N. Konjević, *Eur. Phys. J. D* 32, 347 (2005).
- [6] N. Cvetanović, B. M. Obradović, and M. M. Kuraica, *J. Appl. Phys.* 110, 073306 (2011).
- [7] J. P. Boeuf and L. C. Pitchford, *IEEE Trans. Plasma Sci.* 19, 286 (1991)
- [8] M. Favre, H. Chuaqui, E. Wyndham, and P. Choi, *IEEE Trans. Plasma Sci.*, 20, 53 (1992).

EXPERIMENTAL STUDY OF ELECTRIC FIELD DEVELOPMENT IN PLASMA JET

Goran B. Sretenović, Ivan B. Krstić, Vesna V. Kovačević,
Bratislav M. Obradović and Milorad M. Kuraica

University of Belgrade, Faculty of Physics, P.O. Box 44, 11001 Belgrade, Serbia

Abstract. The focus of the presented article is on the spatially and temporally resolved measurements of the electric field in the atmospheric pressure plasma jet operating in helium. Maximal values of the electric field strength reach 20 kV/cm. Electric field measurements are accompanied by the electrical and spectroscopic diagnostics of the discharge evolution.

1. INTRODUCTION

Non-thermal plasma jets in noble gases consist of luminous traces which propagate very similar to the cathode directed streamers in air [1]. These luminous traces, known as plasma bullets are governed with one order of magnitude lower electric field than in case of the air streamer [2].

This paper is devoted to the spatio-temporal development of the plasma jet in helium. Here we present temporally resolved measurements with the focus on the quantitatively obtained values of the electric field.

2. EXPERIMENTAL SETUP

Dielectric barrier discharge (DBD) plasma jet in helium has been investigated. It consists of 1 cm wide copper electrode wrapped around the glass tube, 1 cm above the tube's end. This electrode is connected to the high voltage. The other, grounded copper electrode was placed 2 cm downstream from the nozzle, see Fig. 1. The glass tube has inner diameter of 2 mm and outer diameter of 4 mm. The flow of helium (99.996%) through the tube is controlled by mass flow controller and it was kept at 2.6 L min⁻¹. Custom made power source is used to supply jet with 12.65 kHz of sinusoidal voltage signal with the amplitude of 4 kV. After one hour of discharge conditioning, the temporal stability of the current was better than 10 ns. The schematic overview of the spectroscopic measurements is presented in Fig. 1. More details about these measurements can be found in our previous papers [3–5]. Plasma jet was projected on the entrance slit of a 1-m spectrometer with 1200 g/mm diffraction grating. As a detector of the radiation an ICCD (PI-MAX2, Princeton Instruments) is used. The pixel to pixel resolution of spectral apparatus was 0.0108 nm/pixel. Due to the very low

intensity of spectrally resolved radiation, the entrance slit for all measurements was kept at $70\ \mu\text{m}$, which resulted in the instrumental line profile full width at half maximum of $0.044\ \text{nm}$.

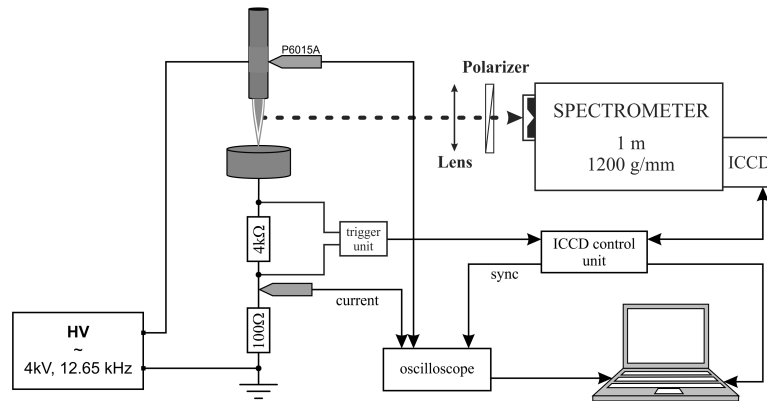


Figure 1. Schematic overview of the jet construction with a sketch of the spectroscopic measurements arrangement.

3. RESULTS AND DISCUSSION

Fig. 2 shows contour plot of He ($2^3\text{P}-3^3\text{S}$) line at $706.5\ \text{nm}$ for plasma jet in helium. It represents spatio-temporal evolution of discharge for the positive half cycle of plasma jet. The setup of the jet with the grounded electrode allows elongated lifetime of the jet emission in one halfcycle. As can be seen in this figure, discharge progression can be divided into two phases. The first phase is equivalent to the cathode directed ionization wave – streamer propagation, with the mean propagation velocity of $20\ \text{km/s}$. At the moment when the bullet reaches the cathode the anode glow has developed and discharge current starts to rise. The second phase continues with the development of some kind of positive column just as in case of a transient glow discharge. Further, the decay of the discharge occurs and follows the discharge current signal. Such plasma jet evolution is completely equivalent to the microdischarge development in N_2/O_2 mixtures [6]. The difference between plasma jet and microdischarge development is in the time scale, which is probably the consequence of the gas composition and applied voltage values. While the microdischarge in air lasts approximately $20\ \text{ns}$ [6], the lifetime of the observed plasma jet phenomenon is longer for three orders of magnitude i.e. about $18\ \mu\text{s}$. This is very motivating conclusion and further investigations in this direction would be desirable.

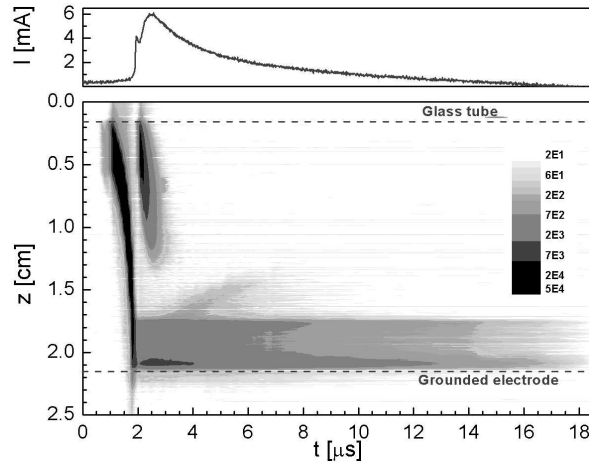


Figure 2. Contour plots of the He I 706.5 nm line emissions in plasma jet. Upper figure represents corresponding discharge current.

Plasma bullet velocity is obtained from the ICCD images. The bullet velocity dependence on the position is presented in Fig. 3. The velocity of the bullet rises with the distance from the tube end. Such velocity behavior is also the feature of the microdischarge in air [6]. In the immediate vicinity of the cathode (grounded electrode), velocity of the bullet reach the maximal value of ~ 40 km/s and starts to decrease slightly.

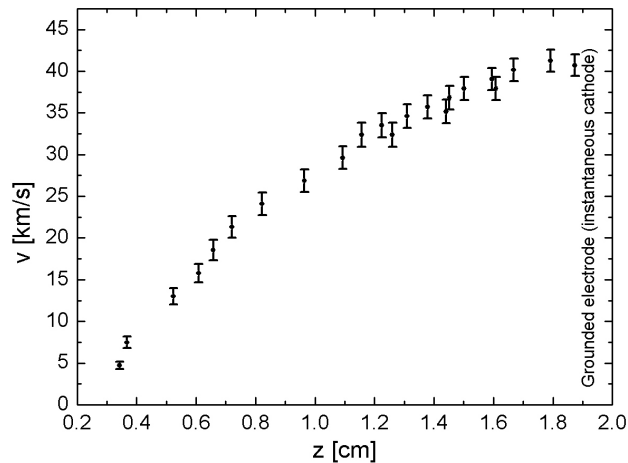


Figure 3. Plasma bullet velocity in plasma jet.

Using the non-perturbing, spectroscopic method based on the Stark polarization spectroscopy spatially and temporally resolved measurements of the axial electric field have been performed. The electric field rises almost linearly in

the space and time, and reaches the plateau 3 mm in front of the cathode, Fig. 4. Presented measurements are in line with recent theoretical predictions [2].

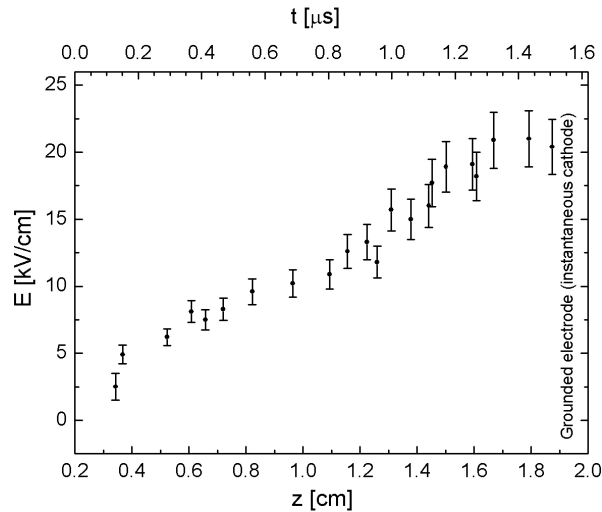


Figure 4. Electric field strength development in plasma jet.

Acknowledgements

This work was supported by the Ministry of Education and Science of the Republic of Serbia through Project 171034 and Project 33022. Acknowledgements

REFERENCES

- [1] M. Teschke, J. Kedzierski, E. G. Finantu-Dinu, D. Korzec, and J. Engemann, *IEEE Trans. Plasma Sci.* 33, 310 (2005).
- [2] X. Lu, G. V. Naidis, M. Laroussi, and K. Ostrikov, *Phys. Rep.* in press (2014).
- [3] G. B. Sretenović, I. B. Krstić, V. V Kovačević, B. M. Obradović, and M. M. Kuraica, *Appl. Phys. Lett.* 99, 161502 (2011).
- [4] G. B. Sretenović, I. B. Krstić, V. V Kovačević, B. M. Obradović, and M. M. Kuraica, *IEEE Trans. Plasma Sci.*, 40, 2870 (2012).
- [5] G. B. Sretenović, I. B. Krstić, V. V Kovačević, B. M. Obradović, and M. M. Kuraica, *J. Phys. D: Appl. Phys.* 47, 102001 (2014).
- [6] R. Brandenburg, M. Bogaczyk, H. Höft, S. Nemschokmichal, R. Tschiersch, M. Kettlitz, L. Stollenwerk, T. Hoder, R. Wild, K.-D. Weltmann, J. Meichsner, and H.-E. Wagner, *J. Phys. D: Appl. Phys.*, 46, 464015 (2013).

CORRELATION BETWEEN HELIUM LINE INTENSITY RATIO AND LOCAL FIELD STRENGTH UTILIZED FOR FIELD MEASUREMENT

N. Cvetanović¹, S. S. Ivković², G. B. Sretenović², B. M. Obradović², M. M. Kuraica²

¹*University of Belgrade, Faculty of Transport and Traffic Engineering, Vojvode Stepe 305, 11000 Belgrade, Serbia*

²*University of Belgrade, Faculty of Physics, Studentski trg 12, 11001 Belgrade, Serbia*

Abstract. A novel spectroscopic method for measuring electric field in atmospheric pressure discharges is presented. It based on the dependence of He I 667.8 nm and 728.1 nm line intensity ratio on the local electric field strength. Line ratio dependence on local field strength was firstly examined by measuring field via an established method of Stark polarization spectroscopy (He I 492.2 nm line). Collisional-radiative model was developed for the involved singlet levels to explain and confirm the field dependence. The results of the model were compared to experiment and satisfactory agreement was obtained.

1. INTRODUCTION

Knowledge of cathode fall development and electric field distribution in the cathode region is essential for understanding the gas discharge formation and production of charged particles. In that respect, non-invasive spectroscopic methods for electric field measurement are important for experimental verification of the discharge models. In our previous papers, electric field was measured in atmospheric pressure dielectric barrier discharge (DBD) using Stark polarization spectroscopy of He I 2^1P-4^1D 492.19 nm line and its forbidden counterpart [1, 2]. Even though this method is independent of plasma conditions due to its *ab initio* basis, it suffers from relatively low intensity of helium lines with forbidden counterparts. Additionally, at atmospheric pressure, measurement of low field values is limited due to the overlap of the atomic line and its forbidden component caused by pressure broadening. These limitations disable investigations of regions with lower field strength and at time instances with lower current and consequent lower light intensity.

Therefore, a simpler and a more robust method for electric field measurements in the cathode region of a low temperature atmospheric pressure

discharges would be useful. The new method, suggested here, uses intensity ratio of two helium singlet lines: He I 2^1P-3^1D at 667.8 nm and He I 2^1P-3^1S at 728.1 nm. We have firstly experimentally observed dependence of the line ratio on the electric field strength in helium DBD. To exclude the influence of self-absorption on line ratio, the standard self-absorption test was performed and also, measured line profile shape is explicated according to broadening mechanisms.

The dependence of line ratio on local field strength can be explained as a consequence of the change in the excitation rate which is induced by change in the electron energy distribution (EEDF). This is a direct correlation between the electric field strength and line intensity ratio – similar connection was used to measure the field in molecular gases [3]. Therefore, to postulate the method, the condition that EEDF is determined by local field strength is necessary. Furthermore, it is well known that in the case of atmospheric pressure discharges, the relaxation time of the EEDF is short enough for electrons to be in equilibrium with the local field; even in the case of high field gradients i.e. local field approximation is valid [4].

2. RESULTS

To obtain the functional dependence of the line ratio on the local electric field strength a simple collisional-radiative model was developed. Namely, a system of time dependent balance equations for all sublevels of singlet helium $n=3$ and radiatively connected $n=4$ level was numerically solved:

$$\frac{dN(i)}{dt} = \sum_k Rp_{ki} + \sum_j Rd_{ji} \quad (1)$$

where $N(i)$ is the density of a sublevel i , while Rp_{ki} and Rd_{ji} are rates for specific populating and depopulating processes respectively. The included populating processes are electron impact excitations from the ground level and metastable 2^1S and 2^3S levels. The excitation transfers $3P \leftrightarrow 3D$ are also taken into account with cross section taken from the article [5]. The levels are depopulated through spontaneous emission with transition probabilities taken from [6], and also via associative ionization, common in high pressure discharges. The coefficients for the non-radiative depopulating processes are taken from [5]. Rate constants for electronic excitation, at a given reduced field value (E/N), were calculated using the BOLSIG+ Boltzmann equation solver [7]. Sets of electron impact cross sections were taken from [8] for collisions with ground level atom, and from [9] for excitation from metastable levels. In solving the equations, the quasi-steady-state approximation was not applied to verify that steady level densities are reached in short time periods typical for DBD.

The line intensity ratio is then from level density as:

$$\frac{I_{667}}{I_{728}} = \frac{h\nu_{667} A_{667} N(3^1D)}{h\nu_{728} A_{728} N(3^1S)} \quad (2)$$

where A and ν are the transition probabilities and frequencies of the two spectral lines in question. The obtained curve for line intensity ratio, together with experimental values is shown in Fig. 1 for several values of the He 2^1S metastable densities, with gas temperature set to 310 K. Experimental points were obtained via the mentioned method of Stark polarization spectroscopy (He I 492.2 nm) in the helium DBD at atmospheric pressure. Sinusoidal voltage of 1.75 kV was applied to configuration similar to [2].

By analyzing the graph function in Fig. 1 it can be seen that agreement with experimental results is satisfactory and curve exhibits almost linear dependence above the field of 4 kV/cm, up to 40 kV/cm (maximum value of the calculation), regardless of metastable density. Most importantly, model calculation has shown that the line ratio curve is independent of electron density in the entire electric field range, due to the equal influence of electron numbers to all excitation rates. At lower field values (<4 kV/cm), the excitation from metastable levels becomes important due to the fact that energy of the electrons is too low for electronic excitation from the ground level. The change of the curve shape with metastable density at lower field is the main cause of method uncertainty in this region and disables the use of the method below 3 kV/cm, without the explicit knowledge of metastable density. The ratio increase with decreasing field is absent when metastables are excluded from the model and the curve monotonically extends to low field values.

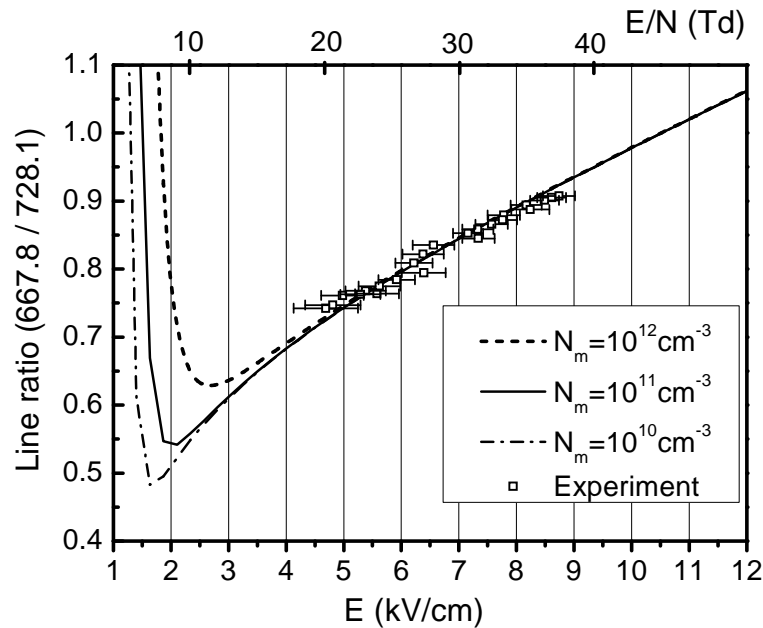


Figure 1. Line ratio dependence on the local electric field strength - comparison between the model and experiment.

The line ratio method enabled more detailed measurement of discharge development. Namely, electric field evolution with DBD discharge development was investigated and it was found that discharge transforms from subnormal to glow-like with current increase, concurring with model [10].

3. CONCLUSION

A novel method for measurement of electric field strength in the cathode region of a dielectric barrier discharge in helium is suggested and tested. The method is based on line intensity ratio of two singlet atomic lines of helium: He I 667.8 nm and 728.1 nm. In summation, the line ratio method may be used only for high pressure (e.g. atmospheric) discharges where the local field approximation is valid and at regions with considerable electric field strength (>3 kV/cm) where excitation from metastables is negligible. Verification with the Stark method is recommended in the field regions where both methods are applicable.

REFERENCES

- [1] B. M. Obradović, S. S. Ivković and M. M. Kuraica, *Appl. Phys. Lett.* 92 191501 (2008).
- [2] S. S. Ivković, B. M. Obradović, N. Cvetanović, M. M. Kuraica and J. Purić, *J. Phys. D: Appl. Phys.* 42 225206 (2009).
- [3] K. V. Kozlov, Wagner H-E, Brandenburg R and Michel P *J. Phys. D: Appl. Phys.* 34 3164–76 (2001).
- [4] F. Massines, N. Gherardi, N. Naudé and P. Ségur *Plasma Phys. Control. Fusion* 47 B577–B588 (2005).
- [5] B. Dubreuil, A. Catherinot *Phys. Rev. A* 21 188 (1980).
- [6] W. L. Wiese, J. R. Fuhr, *J. Phys. Chem. Ref. Data* 38 565 (2009).
- [7] G. J. M. Hagelaar, L. C. Pitchford, *Plasma Sources Sci. Technol.* 14 722 (2005).
- [8] Biagi - v8.9 database, <http://www.lxcat.laplace.univ-tlse.fr>
- [9] Yu.V. Ralchenko et al., *Impact Processes*, NIFS-Data-59 (Nagoya, Japan: NIFS) (2000).
- [10] T. Martens, W. J. M. Brok, J. van Dijk, A. Bogaerts, *J. Phys. D: Appl. Phys.* 42 122002 (2009).

TEMPORAL INVESTIGATION OF POPULATION OF COPPER LEVELS IN GRIMM GLOW DISCHARGE FOR POTENTIAL UV LASER USAGE

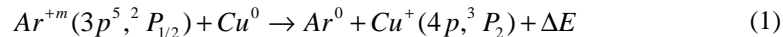
I. B. Krstić¹, B. B. Obradović¹ and M. M. Kuraica¹

¹*University of Belgrade – Faculty of Physics, Studentski trg 12-16, 11000
Belgrade*

Abstract. Resonant energy transfer from metastable argon ions to copper atoms in argon glow discharge is very efficient due to small difference between the energy levels of Ar II ($3p^5, ^2P_{1/2}$) and Cu II ($4p, ^3P_2$). During their relaxation copper ions emit photons of wavelength 224.7 nm. Since the intensity of this copper ion line depends on the sputtering of cathode material, which in turn depends on the discharge current, the pulse generator was constructed. Its role was to enable high current pulses, thereby increasing the population of excited levels of copper ions. In order to find the best possible conditions for obtaining an inverse population of the involved copper ion level temporal studies were performed for lines Cu II 224.7 nm, Cu II 221.8 nm and Cu II 224.2 nm.

1. INTRODUCTION

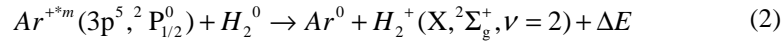
Various measurements in Grimm glow discharge [1] and a modified Grimm glow discharge [2, 3] showed that the charge exchange between argon ions and sputtered copper atoms is very intense [4, 5]. This unusual high intensity some of the emitted lines from this system is due to charge exchange resonant energy transfer between the metastable state of argon ions and copper atoms in their ground states. This reaction can be represented in standard notation as:



In the charge exchange process (1) energy difference ΔE is 0.02eV. The small energy difference produces increase of the population of ionized copper atom at level 3P_2 , which is upper level of Cu II 224.70 nm spectral line. Therefore the intensity of mentioned line is increased compared to some other lines with similar upper level, e.g. Cu II 221.8 nm [4, 6]. It can be concluded that the charge exchange process (1) can be efficiently used for increasing Cu II 224.70 nm line intensity and eventually for achieving inverse population.

It has been also shown that intensity of the Cu II 224.70 nm line was dramatically decreased with small addition of H₂ (3%) in working gas in

comparison with line intensity in pure argon (99.999%) [4]. This can be regarded as a competition of two processes, the charge exchange reactions between the Ar^{+m} and Cu (1), and quenching of Ar^{+m} by H_2 which can be described by the following reaction [4]:



The higher efficiency of the process (2) than the process (1) is the reason of very small intensity of Cu II 224.7nm line with addition of hydrogen. This is because the energy difference in the process (2) is one order of magnitude less than in the process (1) and has value $\Delta E=0.002eV$.

2. EXPERIMENTAL SETUP

The modified Grimm plasma source used in this experiment has already been described in more details elsewhere [2, 6]. Therefore only some details will be given here for the sake of completeness. The hollow anode 50 mm long with inner diameter of 8.00 mm has longitudinal slot (10 mm long and 1.5 mm wide) for plasma observation. The water-cooled cathode holder has exchangeable copper electrode 5.00 mm long and 7.60 mm in diameter which screws into holder to provide good electrical and thermal contact.

During the experiment the pressure in the chamber was maintained at 5.8 mbar. To run the discharge, a stabilized laboratory made pulse high voltage power supply (HVPS) was used. Current was measured using a Rogowski coil and simultaneously with voltage probe attached to 50 Ω non-inductive resistor whose role is current limitation. Experimental setup is shown in Fig. 1.

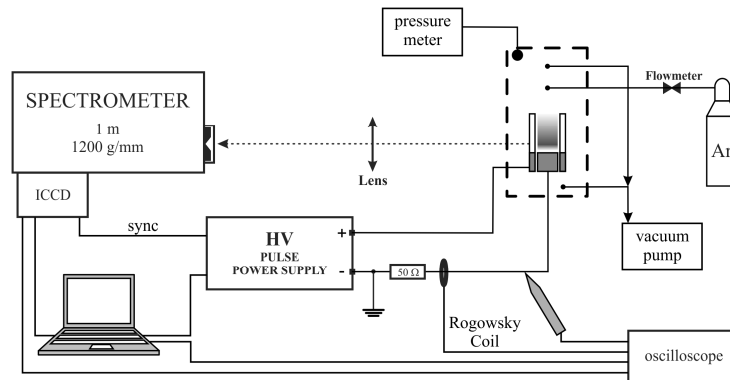


Figure 1. Schematic diagram of an experimental setup

It was shown previously that intensity of the Cu II 224.70 nm line strongly depends on the discharge current [4, 6]. On the other hand, direct current supply (DC) has the limitation of small value of discharge current. To overcome this limitation i.e. to obtain higher discharge current, and also to reduce power consumption, mentioned adjustable pulse HVPS was used in this

experiment. HVPS has control over frequency from 0.1 Hz to 500 kHz and pulse width from 10ns to 98% of a period. Power supply has capability to ensure 0.15 J per pulse up to 15 kHz, which are five orders of magnitude higher than needed to run the discharge in DC regime with the same current. Rising and falling time at the edge of the voltage pulse on a test resistor is less than 200 ns.

A Tektronix TDS 2024B digital storage oscilloscope (200 MHz, 2 GS/s) was employed to monitor and record voltage and current signals as well signal for synchronization of an ICCD camera. For a space-time resolved emission measurements, projection optics were used to image the whole glow discharge onto the entrance slit of a 1 m spectrometer. ICCD was triggered with a TTL generated from power supply as shown in Fig. 1. The jitter between mentioned TTL and gate recording of an ICCD is less than 5ns. Pulse width is set to 6 μ s and period of a repetition rate is 200 μ s. To study the temporal development of the discharge and the afterglow, spectroscopic recordings in 1 μ s steps, with 1 μ s gate duration, were used.

3. RESULTS AND DISCUSSIONS

It is known that intensity of lines emitted by sputtered atoms and ions has a nonlinear dependence on the discharge current [1]. The same is the case for Cu II 224.7 nm line. That is because the mentioned asymmetric charge exchange process is the dominant process i.e. 99.99% of the upper level density is exited through this channel [7]. To obtain higher intensity of this line and possibly the expected effect of population inversion the pulse mode of Grimm glow discharge is used. Although, increased pressure decreases the metastable Ar⁺ density [6], the pressure of 5.8 mbar was chosen to achieve higher current, thereby increasing the density of copper atoms in the discharge.

By changing the pulse width in the range 1–50 μ s it was found that the optimal pulse width value is 5-10 μ s. Pulse width of 6 μ s and period of 5kHz was used during the experiment performed here.

Time dependences of line intensities are studied and for several of Cu II lines results are presented in Fig. 2. All intensities are normalized to their maxima for comparison. Here it must be mentioned that intensity of line Cu II 224.7 nm is more than ten times greater than intensity of other represented lines, so that is the reason for small fluctuations of intensity of other Cu II lines. The lines Cu II 221.8 nm and Cu II 224.2 nm are selected because of smallest but yet one order of magnitude higher energy difference than needed for charge transfer for Cu II 224.7 nm line. Because of that they have different population mechanisms compared to Cu II 224.7 nm line. Namely, Cu II 221.8 nm and Cu II 224.2 nm are populated by electron impact excitation [7] consequently having much smaller intensity. From figure 2 one can see, that after the voltage pulse there is a rapid decrease of every Cu II line except Cu II 224.7 nm. This is due to reduced energy input leading to reduced electron impact excitation. The line Cu II 224.7 nm has prolonged intensity due to charge transfer excitation with metastable Ar⁺ (eq. 1). Different decay is also consequence of this transfer. In our opinion this effect can be used for inverse population. This time of

afterglow of Cu II 224.7 nm line can be used to confirm the charge transfer, and to investigate possibility for increase population of this line as well as detection of population inversion of the involved levels.

It was found that upper level of Cu II 224.7 nm line can be increased almost by factor of two using two successive pulses [8], with delay of couple of pulse widths. This process will be investigated further.

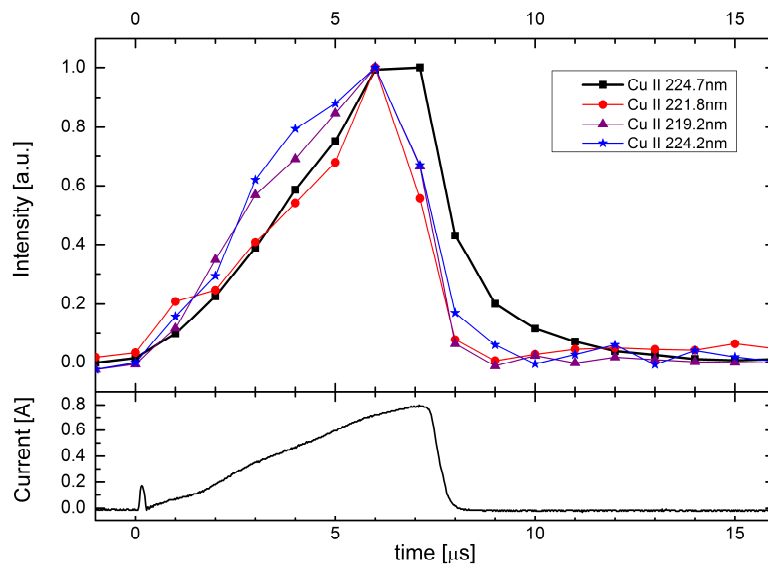


Figure 2. Comparison of intensity of Cu II lines 219.2 nm, 221.8 nm, 224.2 nm and 224.7 nm during the 6 μ s pulse at $U=710V$ and pressure of 5.8mbar.

REFERENCES

- [1] W. Grimm, *Spectrochimica Acta*, 23B, 443 (1967).
- [2] M. M. Kuraica and N. Konjević, *Phys. Rev. A* vol.46, 4429 (1992).
- [3] N. P. Ferreira, H. G. C. Human, and L. R. P. Butler, *Spectrochim. Acta*, 35B, 285 (1980).
- [4] M. M. Kuraica and N. Konjević, *Physica Scripta*. vol.50, 487 (1994).
- [5] Edvard B. M. Steers and Richard J. Fielding, *Jour. Of Anal. At. Spec.*, vol.2, 239 (1987).
- [6] M. K. Levy, D. Serxner, A. D. Angstadt, R. L. Smith and K. R. Hess, *Spectrochimica Acta*, 46B, 253 (1991).
- [7] A. Bogaerts, R. Gijbels, *Jour. Of Anal. At. Spec.*, vol.13, 721 (1998).
- [8] Chenglong Yang, Eric Oxley and W. W. Harrison, *J. Anal. At. Spectrom.*, 16, 1131 (2001).

STARK BROADENING OF SPECTRAL LINES WITHIN Li ISOELECTRONIC SEQUENCE

I. P. Dojčinović, I. Tapalaga and J. Purić

*University of Belgrade, Faculty of Physics, P. O. Box 44, 11000 Belgrade,
Serbia*

Abstract. This paper analyses Stark broadening of spectral lines within lithium like elements (Li I, Be II, B III, C IV and N V). Strong correlation exists between Stark broadening and the upper level ionization potential. A functional dependence of Stark broadening on rest core charge of the emitter has been observed.

1. INTRODUCTION

Recently published papers devoted to a study of Stark parameter regularities of multiply charged ion spectral lines originating from the same transition array [1] and checking the dependence on the upper level ionization potential of electron impact widths using quantum mechanical calculations [2] have shown that these dependences can be used for enlarging number of Stark widths data of astrophysical interest.

After a series of papers [3-8] that analyzed Stark broadening (ω) dependence on the upper level ionization potential (χ), it was established that this dependence has a form of $\omega[\text{rad} \cdot \text{s}^{-1}] = a \cdot (\chi[\text{eV}])^{-b}$ (where a and b are independent constants).

The purpose of this paper is to present the results that were found concerning Stark broadening dependence on the core charge that affects the electron in spectral transition (Z). For neutral atoms $Z = 1$, for singly charged ions $Z = 2$ and so on. For this purpose five ions from lithium isoelectronic sequence have been analyzed. The data for (ω) has been taken from [9]. Atomic data was taken from [10].

2. THEORY

As predicted in theory and described in [11], the Stark broadening is Z dependent, but the exact formula has not been found so far. Stark broadening (ω) is given by:

$$\omega = N_e \cdot f(T) \cdot a \cdot Z^c \cdot \chi^b \quad (1)$$

It is intuitive that Stark broadening depends on surrounding charge due to electric field generation, but it is difficult to find the total charge that generates local electric field. Effective charge was the first logical choice, but it showed low correlation with Stark broadening. On the other hand Z (as defined above) showed better results. Detailed presentation of all results is beyond the scope of this paper.

The Stark broadening ω has to be given in *rad/s* due to physical connection between transition energy and electric field. The conversion is done by:

$$\omega = \frac{2\pi c}{\lambda^2} \Delta\lambda \quad (2)$$

In order to investigate different Stark parameter regularities, an accurate set of theoretical and experimental data, being normalized to the particular electron density (N_e) and temperature (T), is necessary. The normalization to the same N_e can be done by linear scaling due to the linear dependence of Stark widths on N_e . However, Stark width dependence on the T is different from one spectral line to another for all spectra. Therefore, the correction to temperature dependence has to be done with great care for every spectral line separately as described in [3].

3. RESULTS

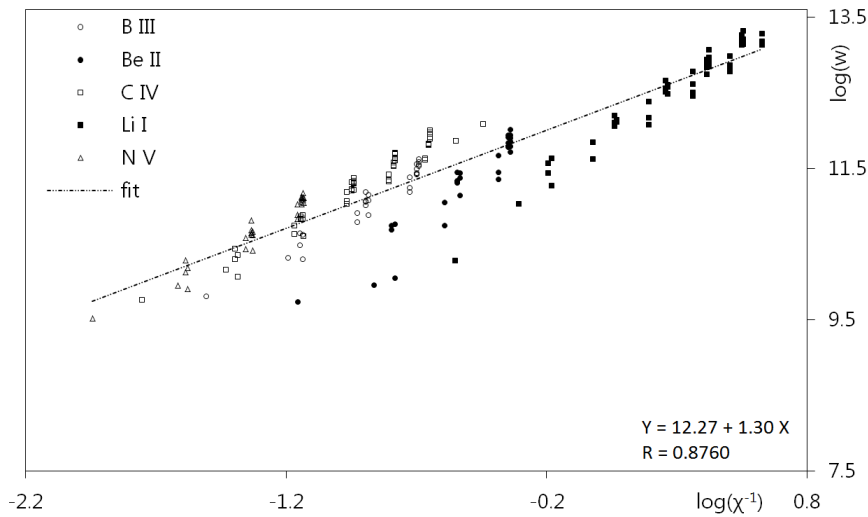


Figure 1. Stark broadening dependence on the upper level ionization potential in log-log scale for lithium like ions.

The data taken from Stark B and NIST database has been shown in Figure 1. The only modification of source data was in conversion from $\Delta\lambda$ to ω as described in Equation (2). All data is normalized to temperature $T = 100000$ K and electron concentration of $N_e = 10^{17} \text{cm}^{-3}$. These environmental parameters were chosen because both neutral atoms and highly ionized ions can exist in environment with those parameters or in very similar environment so that a small extrapolation is necessary. The correlation factor for this data is low which shows that proposed model is not good and that corrections must be made.

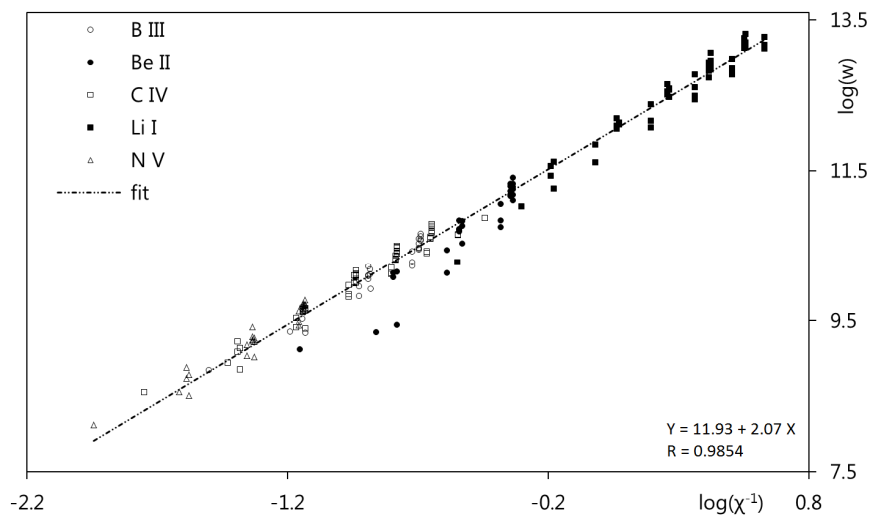


Figure 2. The rest core charge (Z) correction of Stark broadening dependence on the upper level ionization potential in log-log scale for lithium like ions.

In Figure 2 a corrected model has been used. Instead of showing ω it was divided by Z^2 . In this case the correlation factor was improved as shown. The definition of Z was also the subject of our investigation, but this definition showed best results. With Z defined as shown above, parameter c from Equation (1) was varied and the results were best for $c = 2$. With the exception of beryllium spectral lines, other ions fit theoretical model.

4. CONCLUSION

The results of Stark broadening regularities within lithium isoelectronic sequence are presented in this paper. It is shown that the core charge that affects the electron in spectral transition Z affects the intensity of Stark broadening. The exact form of this influence is given by Equation (1) in which the parameter $c=2$. Based on this theoretical model, predictions can be made for lithium like ions with high ionization stage that were not been measured experimentally or

calculated theoretically so far. Such data are used in the analyses of relative abundances of chemical elements, opacity calculations, radiative transfer through stellar atmospheres of some classes of stars, line profiles and their effects on synthetic spectra [12,13].

Acknowledgements

This work is financially supported by the Ministry of Education, Science and Technological development of the Republic of Serbia within the project 171034.

REFERENCES

- [1] J. Purić, I. P. Dojčinović, M. Nikolić, M. Šćepanović, B.M. Obradović, M. M. Kuraica, *ApJ* 680, 803 (2008).
- [2] H. Elabidi, S. Sahal-Bréchet, *Eur. Phys. J. D* 61, 285 (2011).
- [3] I. Tapalaga, I. P. Dojčinović, J. Purić, *Mon. Not. R. Astron. Soc.* 415, 503 (2011).
- [4] I. Tapalaga, I. P. Dojčinović, M. K. Milosavljević, J. Purić, *Publ. Astron. Soc. Aust.* 29, 20 (2012).
- [5] I. P. Dojčinović, I. Tapalaga, J. Purić, *Publ. Astron. Soc. Aust.* 28, 281 (2011).
- [6] I. P. Dojčinović, I. Tapalaga, J. Purić, *Mon. Not. R. Astron. Soc.*, 419, 904 (2012).
- [7] D. Jevtić, I. P. Dojčinović, I. Tapalaga, J. Purić, *Bull. Astr. Soc. India* 40, 151 (2012).
- [8] I. P. Dojčinović, I. Tapalaga, J. Purić, *Mon. Not. R. Astron. Soc.*, 429, 2400 (2013).
- [9] S. Sahal-Bréchet, M. S. Dimitrijević, N. Moreau, 2012. Stark-B database, [online]. Available: <http://stark-b.obspm.fr> [Feb 13, 2012]. Observatory of Paris, LERMA and Astronomical Observatory of Belgrade
- [10] Yu. Ralchenko, A. E. Kramida, J. Reader, and NIST ASD Team (2012). NIST Atomic Spectra Database (ver. 4.1.0), [Online]. Available: <http://physics.nist.gov/asd> [2012, January 17]. National Institute of Standards and Technology, Gaithersburg, MD
- [11] J. Purić, M.H. Miller, A. Lesage, *ApJ* 416, 825 (1993).
- [12] Y. Takeda, D.-I. Kang, I. Han, B.-C. Lee, K.-M. Kim, S. Kawanomoto, N. Ohishi, *Publ. Astron. Soc. Japan* 64, 38 (2012).
- [13] H. W. Zhang, K. Butler, T. Gehren, J. R. Shi, G. Zhao, *A&A* 453, 723 (2006).

GAS TEMPERATURE MEASUREMENT IN SEGMENTED MICRO HOLLOW GAS DISCHARGE IN HELIUM

G. Lj. Majstorović¹, J. Jovović² and N. Konjević²

¹*University of Defence, Military Academy, 11105 Belgrade, Pavla Jurišića
Šturma 33, Serbia*

e-mail: gordana.majstorović@va.mod.gov.rs

²*University of Belgrade, Faculty of Physics, 11001 Belgrade, P.O. Box 368,
Serbia*

Abstract. Emission spectroscopy technique is used to measure gas temperature in segmented micro hollow gas discharge (SMHGD) source operating in helium at atmospheric pressure. The rotational temperature of $\sim (900 \pm 50)$ K is determined from nitrogen ion bands belonging to first negative system using Boltzmann plot technique while the vibrational temperature of $\sim (3500 \pm 200)$ K is obtained from integral intensity ratio of two consecutive vibrational bands of the same sequence. Under our experimental conditions, translational gas temperature is equal to rotational temperature of nitrogen molecules.

1. INTRODUCTION

Gas discharge generated in discharge volume having dimensions ranging from several tens up to thousand micrometers and operating at medium or high pressure is often called micro hollow gas discharge (MHGD). Electrode geometries, modes of operation, plasma parameters and some applications of MHGD are reported in [1].

The characterization of MHGD is generally done by using emission and absorption spectroscopy techniques. For standard Optical Emission Spectroscopy (OES), plasma broadened hydrogen lines (usually the H_β line) are employed for N_e and T_g diagnostics. The OH, N_2 and N_2^+ bands are used for T_g measurement while relative intensities of atomic or ionic lines are employed for electron temperature T_e diagnostics, see e.g. [2,3]. Short overview of spectroscopic techniques for N_e and temperatures measurements is given in [4]. In this study, OES technique is used to measure gas temperature in segmented gas discharge source with micro hollow electrodes (SMHGD) in helium at atmospheric pressure. For that purpose, several bands belonging to the first negative and second positive system of nitrogen are recorded and analyzed.

2. EXPERIMENTAL

A detailed description of SMHGD source is given in [5] and thus only few important details will be mentioned here. The discharge channel consists of five water cooled metal discs separated by alumina. Three central discs are made of copper while stainless steel was used for the cathode and anode. The length of the channel is 7.8 mm while central hole diameter is 1 mm. The discharge was driven in helium (99.996%) at 80 mA current and cathode-anode voltage of 445 V. The digital volumetric flow controller (0-500 sccm) was used to measure gas flow rate through the discharge. Spectroscopic measurements were performed axially (end-on) through the cathode center with 2 m focal length spectrometer (reflection grating 651 grooves/mm, reciprocal dispersion 0.74 nm/mm in the first diffraction order). Thermoelectrically cooled CCD (2048 × 506 pixels, pixel size 12 × 12 μm, -10 °C) was used as radiation detector. The discharge image was projected to the entrance slit of spectrometer with two times magnification using an achromatic lens (focal length 75.8 mm). A standard coiled-coil tungsten halogen lamp was used for wavelength sensitivity calibration of the spectrometer-detector system.

3. RESULTS AND DISCUSSION

Several intensive nitrogen molecular bands are observed in helium SMHGD where N₂ as an impurity is always present. The recorded rotational bands of the first negative (1⁻) system of nitrogen (B²Σ_u⁺ - X²Σ_g⁺) shown in Fig. 1 are used for rotational temperature (T_{rot}) measurement using Boltzmann plot (BP) technique, see Fig. 2. This technique is applied here since the variation of R branch lines intensity with rotational quantum number K is defined by the thermal population of the rotation emission levels [6]. The rotational constant for the upper states (from B²Σ_u and v[']=0) is taken from [7]. It is important to mention that N₂⁺ band at 427.8 nm is well resolved, see Fig 1b, what makes this band more reliable for T_{rot} measurement than N₂⁺ band at 391.4 nm, see Fig. 1a. Nevertheless, the difference between rotational temperatures obtained from BPs in Fig. 2 is within experimental uncertainty. In atmospheric pressure discharges, due to high collision frequencies, T_{rot} determined from N₂ rotational bands is close to the gas temperature [8]. From the intensity ratio of two consecutive vibrational bands of the same sequence, see Fig. 3, the vibrational temperature (T_{vib}) was determined. For the procedure of T_{vib} measurement see e.g. [9]. Molecular data for nitrogen bands in Fig. 3 are taken from [7]. One should notice that in helium SMGHD, $T_{vib} > T_{rot}$ what is characteristic for non-thermal plasmas created by externally applied electric field [8].

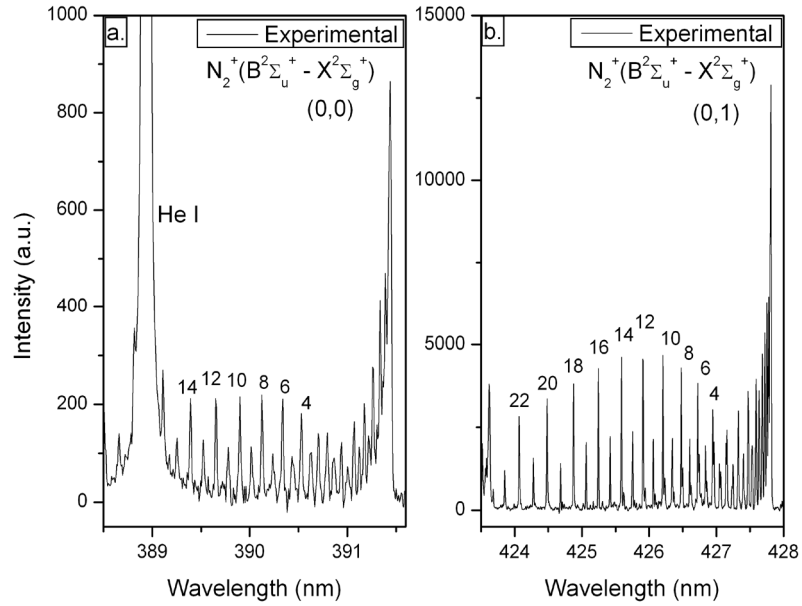


Figure 1. The recording of a. $N_2^+(B^2\Sigma_u^+, 0 - X^2\Sigma_g^+, 0)$ band in the first and b. $N_2^+(B^2\Sigma_u^+, 0 - X^2\Sigma_g^+, 1)$ band in the second order of diffraction grating.

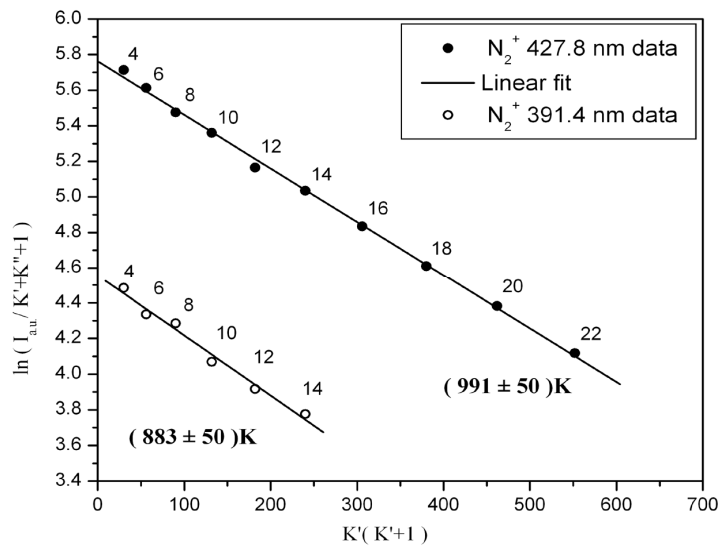


Figure 2. Boltzmann plots of N_2^+ lines presented in Fig. 1 and linear fits through data points.

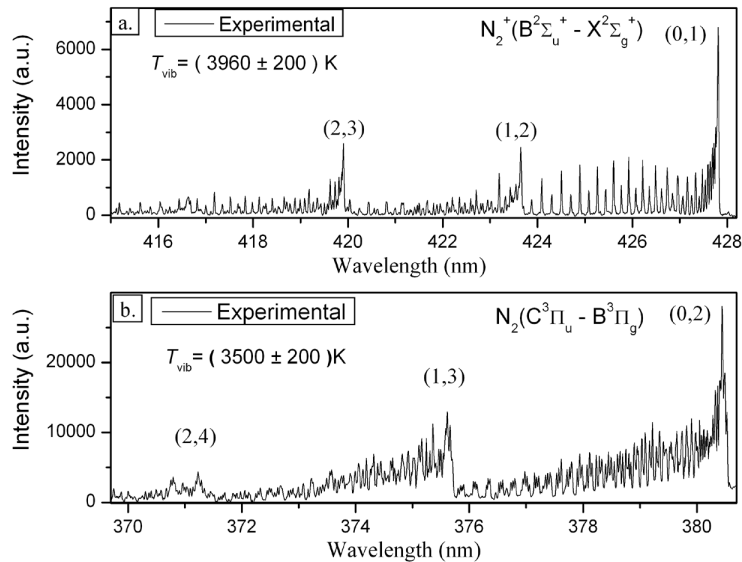


Figure 3. The spectra of a. first negative system nitrogen bands and b. second positive system nitrogen bands recorded in the first order of diffraction grating.

Acknowledgements

This work is supported by the Ministry of Education, Science and Technological Development of the Republic of Serbia under Project 171014.

REFERENCES

- [1] K. H. Becker, U. Kogelschatz, K. H. Schoenbach and R. J. Barker, *Non-Equilibrium Air Plasmas at Atmospheric Pressure*, p. 682, (UK: IOP Publishing Ltd 2005).
- [2] B. N. Sismanoglu, K. G. Grigorov, R. Caetano, M. V. O. Rezende and Y. D. Hoyer, *Eur. Phys. J. D* 60, 505 (2010).
- [3] P. Bruggeman, G. Cunge and N. Sadeghi, *Plasma Sources Sci. Technol.* 21, 035019 (2012).
- [4] M. Cvejić, Dj. Spasojević, N. M. Šišović and N. Konjević, *J. Appl. Phys.* 110, 033305 (2011).
- [5] J. Jovović and N. Konjević, *Eur. Phys. J. D* 68, 60 (2014).
- [6] G. Herzberg, *Molecular Spectra and Molecular Structure, Spectra of Diatomic Molecules* Vol. 1 (Krieger Publishing Co, Malabar FL 1989).
- [7] A. Lofthus and P. H. Krupenie, *J. Phys. Chem. Ref. Data* 6, 113 (1977).
- [8] D. Staack, B. Farouk, A. Gutsol and A. Fridman, *Plasma Sources Sci. Technol.* 17, 025013 (2008).
- [9] G. Lj. Majstorović, N. M. Šišović, N. Konjević, *Plasma Sources Sci. Technol.* 16, 750 (2007).

OPTOGALVANIC SPECTROSCOPY OF ALIGNED/ORIENTED ATOMS IN A GLOW DISCHARGE

V. Stefleková

*Institute of Solid State Physics – BAS
72, Tzarigradsko Chaussee Blvd., 1784 Sofia, Bulgaria
Email: vasilka@issp.bas.bg*

Abstract. The technique of optogalvanic spectroscopy is used the conductivity of both aligned and oriented ensemble of atoms to be compared. The waveform of the time resolved signals are observed to depend on the polarization of the light absorbed.

1. INTRODUCTION

The atomic magnetic state m is known to manifest itself in optical spectroscopy. Recently two types of coherent ensembles, i. e. aligned ($\Delta m=0, \pm 2$) and oriented ($\Delta m=\pm 1$) ones were compared in their light induced conductivity Ref. [1].

In this work the galvanic manifestation, including the time of decay T of one and the same ensemble of atoms aligned/oriented, is compared. The objects are NeI buffers in a hollow cathode discharge (HCD). The measurements are based on light induced coherences. The time resolved optogalvanic technic is used.

2. EXPERIMENT

Figure 1 shows the used experimental set-up.

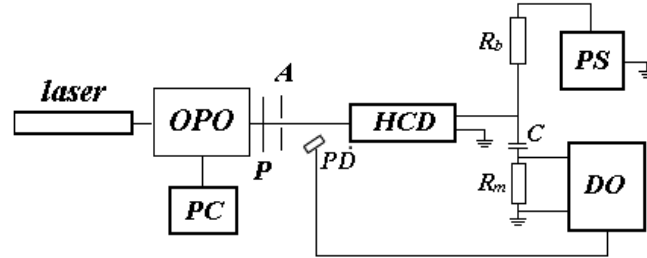


Figure 1. Schematic diagram of the experiment: *HCD* – hollow cathode discharge, *OPO* – optical parametric oscillator system, *P* – polarizer (linear or achromatic wave plate $\lambda/4$, 450-800 nm), *A* – aperture, *PD* – photo detector, *C* – decoupling capacitor, *R_b* - ballast resistor, *R_m* = 20 k Ω – measuring resistor, *PC* – personal computer, *PS* – power supply, *DO* – digital oscilloscope.

The trademarked HCD lamps Ne/Li (Narva) and Ne/CaBa (Cathodeon Inc.) were used. The discharge was produced by applying a highly stable dc voltage and was operated in a negative glow regime. A standard experimental scheme for TROGS detection was employed. TROGSs were induced by irradiating the HCD with an OPO system, which delivered a pulse of duration 4 ns FWHM at a repetition rate of 10 Hz and an average output power of 25 mW and were detected across $R_m = 20 \text{ k}\Omega$ with a digital oscilloscope. The RC constant was chosen low enough to detect TROGS $\Delta U(t)$.

3. RESULTS AND DISCUSSIONS

Generally, the measured time resolved optogalvanic signals (TROGSs) $\Delta U^{OG}(t)$ (Fig. 2 - contain certain general regularities: *i*) the signal is composed by a fast rising peak followed by an exponential decay to either base line or signal with an opposite sign, which returns to the base line; *ii*) the discharge current I stimulates extending the waveforms $\Delta U^{OG}(t)$; *iii*) as expected, the signal on the transitions NeI ($2p_{10} \rightarrow 5d_3$) is smaller in amplitude than signal on the transition NeI ($1s_5 \rightarrow 2p_{10}$).

There are various models concerning the channels of the plasma TROG reaction Refs. [2-4]. Ultimately, they are reduced to changes of electron number density Δn_e and/or electron drift velocity Δv_e , i.e. $\Delta j = c_1 \Delta n_e + c_2 \Delta v_e$. vs. the conductivity change Δj . These terms define also the characteristic decay time T of evolution $\Delta U^{OG}(t)$ at sufficiently short light pulse. Within these frames the evolutions $\Delta U^{OG}(t)$ induced by plane $\Delta U^{OG}(t)^{align}$ – and circularly polarized light pulse $\Delta U^{OG}(t)^{orient}$ are compared here.

First of all the above evolutions are not similar in shape. It excludes a possible effect of non-uniform absorption of either plane- or circularly polarized

light. Moreover, it should be noted that the measured signals due to either of circular/linear polarization in each of the pairs of Figs. 2 (a₁, a₂ and b₁, b₂) differ from one another. In order to precise the comparison we have made best fit to the exponent part of TROGS in Figs. The approximation $y = A_I * \exp(-x/T_I)$ is used.

The signals in the two polarizations depend on the operating discharge current I so, that the relation $T^{\text{align}}/T^{\text{orient}}$ changes within the frames $1 \geq T^{\text{align}}/T^{\text{orient}} \geq 1$ vs. value of I . This ratio is particularly sensitive to I - value on the transition $1s_5-2p_{10}$. It is due to higher OG efficiency of plane polarized light (Fig. 2 (b₂)).

Really, the TROGSs due to plane- and circularly polarized light represent time resolved evolution of aligned and oriented ensembles of atoms. The found inequalities $T^{\text{align}} \neq T^{\text{orient}}$ mean that ones and the same processes of relaxation are of specific rate constants within the frames of one and the same optical transition. These constants depend on the coherent state of the transition.

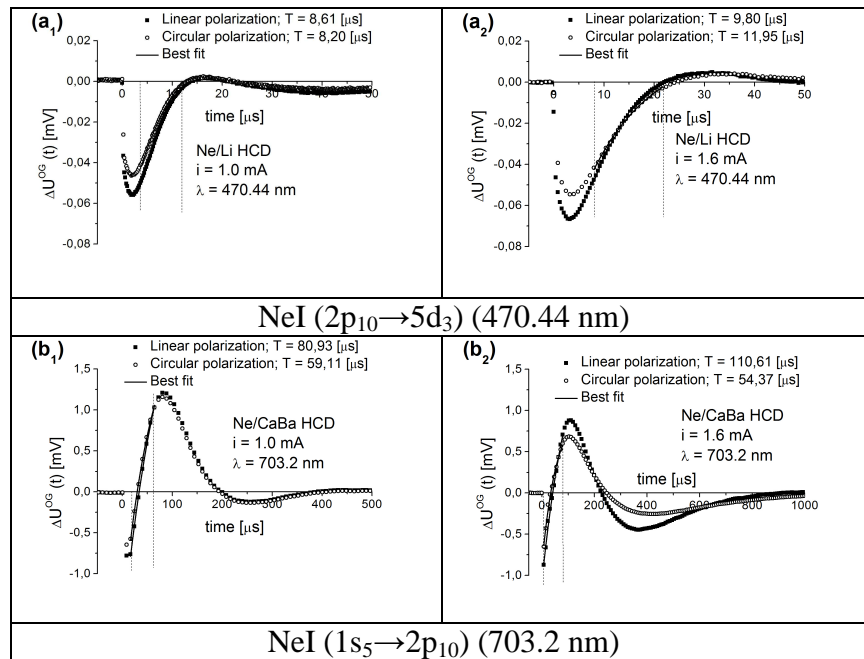
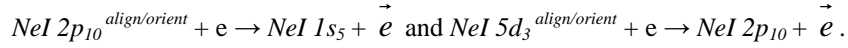


Figure 2. Experimental TROGSs from *aligned* (linear polarization) and *oriented* (circular polarization) NeI transitions $2p_{10}-5d_3$ (a₁, a₂) and $1s_5-2p_{10}$ (b₁, b₂) states in Ne/Li HCD and Ne/CaBa lamps. Broken lines point the time interval Δt [μs] of the fitting: a₁-[3.8÷12.0] μs ; a₂-[6.4÷24.0] μs ; b₁-[16.4÷64.4] μs ; b₂-[7.2÷79.2] μs ;

Therefore, the coherent state of the excited atom's ensemble adds some specific coherent conductivity to the conventional one.

According to Ref. [5] the only reason for this difference may be the specific rate constants of superelastic interaction



Our results suggest, that non thermalized electrons \vec{e} are of different density depending on the coherences *align/orient*. These electrons stimulate the steeplike excitation/ionization as a specific contribution to the gas discharge conductivity.

4. CONCLUSIONS

The TROGSs $\Delta U^{OG}(t)$ induced by plane- and circular polarized light pulse distinguish in waveform parameters.

The best fit made to the exponent part of TROGS reveals different decay of the either of aligned or oriented atoms. It means different rate of the collisional interaction dependent on the coherence *alignment/orientation*. Ultimately, the produced non thermal electrons contribute to the conductivity by the additional excitation/ionization.

Therefore TROGSs describe a specific conductivity of one and same ensemble of atoms that are *aligned* \leftrightarrow *oriented* selectively.

Acknowledgements

This work is partially supported by the EU project - Research Potential (REGPOT 316309 INERA) and bilateral project between Bulgarian Academy of Sciences and Serbian Academy of Sciences and Arts.

REFERENCES

- [1] V. Steflekova and D. Zhechev, J. Phys.: Conf. Ser. 514 (1), 012053 (2014).
- [2] B. Barbieri, N. Beverini and A. Sasso, Rev. Mod. Phys. 62, 603 (1990).
- [3] D. Zhechev and S. Atanassova, Opt. Commun. 156 (4-6), 400 (1998).
- [4] S. Mahmood, M. Anwar-ul-Haq, M. Riaz and M. A. Baig, Eur. Phys. J. D. 36 (1), 1 (2005).
- [5] S. N. Khvorostovsky, D. Z. Zhechev, Spectr. Lett. 23 (7), 911 (1990).

SURFACE DIELECTRIC BARRIER DISCHARGE (SDBD) BETWEEN TWO LIQUID ELECTRODES

O. Galmiz¹, D. Pavliňák¹, M. Zemánek¹, A. Brablec¹ and M. Černák¹

¹*CEPLANT - R&D Center for Low-Cost Plasma and Nanotechnology Surface Modifications, Dept. of Physical Electronics, Masaryk University, Kotlarska 2, 61137 Brno, Czech Republic*

Abstract. In this work a new type of surface dielectric barrier discharge is presented where the plasma is generated on the surface of dielectric wall between water (liquid) electrodes. An apparatus using such discharge is very attractive, besides other things, for industrial treatment of hollow dielectric objects of different sizes or it could be used for treatment of heat sensitive materials. The appearance of the plasma as well as its structure was observed by means of high-speed camera while basic characteristics of the discharge were obtained by optical emission spectroscopy and by current and voltage measurements. Here, preliminary results as to the new discharge are presented.

1. INTRODUCTION

Nowadays in literature a lot of attention is paid to discharges generated in water or other liquids or in contact with them [1 – 3]. The advantages of such discharges for wastewater treatment, surface modification and treatment of heat sensitive materials were already discussed [4 – 6]. The aim of the presented research was preferentially the development of methods for surface treatment of different hollow dielectric objects at atmospheric pressure. It was found that new type of surface dielectric barrier discharge (SDBD) with liquid electrodes fulfills these requirements. In this configuration the generated plasma covers visually quite homogeneously the treated dielectric wall. We assume that due to the extremely high electric field generated by the triple point effect [7] along common boundary between air, liquid and dielectric surfaces the „positive corona effect“ takes place which supports the formation of plasma.

2. EXPERIMENTAL SETUP

The schematic drawing of the SDBD is shown in Fig.1a while in Fig. 1b the photos of the reactor and plasma are presented. The discharge was generated along the boundary of air, dielectric and the 5% oxalic acid solution in distilled water. The discharge was powered by high voltage power supply unit LIFETECH with sinusoidal voltage output driven at 20 kHz (tuned to the

resonance for each discharge conditions). The discharge generated results in bluish coloured homogeneous plasma observable with the naked eye

Basic parameters of the discharge plasma (composition, rotational and vibrational temperature, etc) were determined by optical emission spectroscopy (OES) recording the spectra by Horiba Jobin-Yvon FHR 1000 monochromator (2400 gr/mm^{-1} and 3600 gr/mm^{-1}), the Symphony CCD detector and quartz optical fiber.

The time resolved optical imaging of studied discharge was performed using intensified interline CCD camera Princeton Instruments PI-MAX3: 1024i-SR-46 (ICCD camera. The sequence of 200 photos with the gate exposure time of 200 ns was recorded. In this way the whole pulse period was captured.

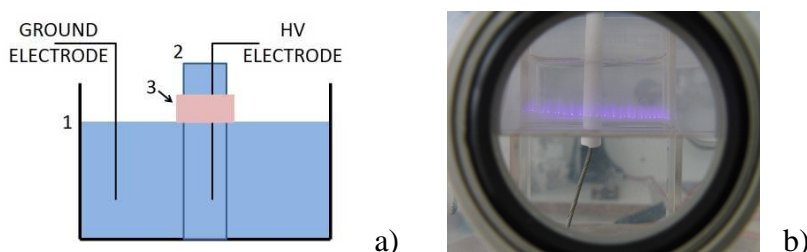


Figure 1. a) schematic drawing of the SDBD reactor: 1 - PP reactor with 5% oxalic acid solution, 2 - glass quevette with 50 ml 5% oxalic acid solution (conductivity 50 mS/cm , 3 – plasma region, b) photo of the reactor and the discharge SDBD (applied power is 20 W).

4. RESULTS AND DISCUSSIONS

The emission spectra were recorded in the spectral range of 250 – 750 nm. It was found that in the emission spectra of the discharge generated in air at atmospheric pressure and influenced by water and water vapours one can identify the most intensive bands belongs to the second positive system of nitrogen $\text{C}^3\Pi_u(v') \rightarrow \text{B}^3\Pi_g(v'')$ (for estimation of rotational and vibrational temperature, Fig. 2), the 306.3 nm system of OH radicals (the R1 branch $\text{A}^2\Sigma^+ \rightarrow \text{X}^2\Pi$ was used for estimation of rotational temperature, Fig.2) and first negative system N_2^+ ($\text{FNS}, \text{B}^2\Sigma_u \rightarrow \text{X}^2\Sigma_g$).

It is known that the rotational temperature estimated from nitrogen is always significant smaller than the rotational temperature determined from the OH which correlates with the values measured for other types of surface DBDs in ambient air [9 - 11].

Typical current and voltage waveforms of the SDBD are shown in Fig.3. Note that current waveform is not symmetrical and that appearance of positive and negative polarities differs. The current maximum peaks for the positive polarity are much bigger and in general the time during which the

plasma discharge exists is longer. With increasing of power the current peaks also increase.

Although the plasma appears to be visually diffuse the fast camera pictures shown complicated structure as shown in Fig. 4. Discharge consists of short microdischarges which randomly appear and disappear. The appearance of the discharge in each half cycle of the applied voltage is different. Applying positive polarity filaments are not linear and have a tendency for branching while in the negative polarity they propagate upwards as one channel. The intensities of branches differs one from another which also correlates with Fig. 3.

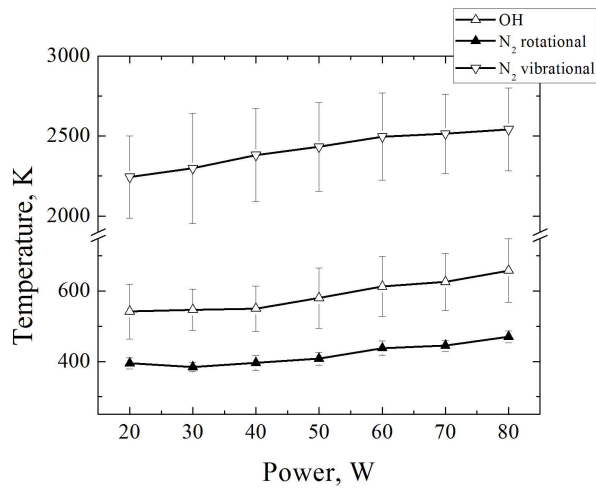


Figure 2. Rotational and vibrational temperature vs. applied voltage.

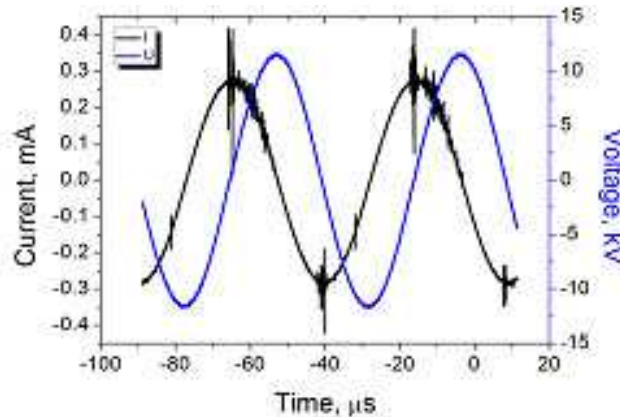


Figure 3. Typical current and voltage waveforms of the SDBD, power of 80 W.

For higher powers the number of filaments is practically the same as well as their length. The photos were taken with the gate exposure of 200 ns and 50 accumulations. The accumulation number was 50 because of weak intensity of the discharge.

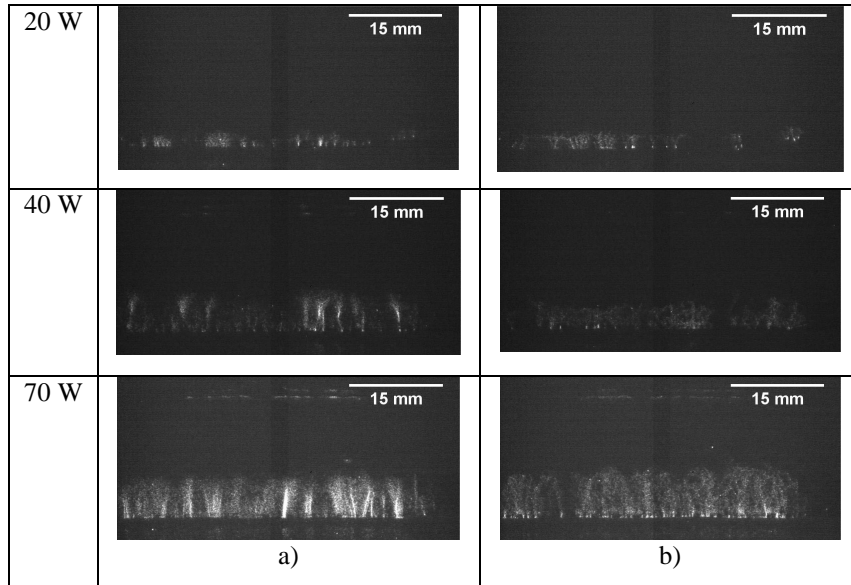


Figure 4. Photos of the plasma discharge: a) negative polarity, b) positive polarity.

Acknowledgements

This research has been supported by the project R&D centre for low-cost plasma and nanotechnology surface modifications CZ.1.05/2.1.00/03.0086 funded by European Regional Development Fund.

REFERENCES

- [1] B. Jiang et al, *Chemical Eng. J.*, 348 – 368, 236 (2014).
- [2] R. P. Joshi et al, *Plasma Chem. and Plasma Processing*, 1, 33, (2013).
- [3] P. Bruggeman, Ch. Leys, *J. Phys. D: Appl. Phys.* 42 (2009).
- [4] A. Brablec et al, *Czech. J. Phys.* 2002, 52, Suppl. D, 491.
- [5] A. Nikiforov, C. Leys, *Plasma Chem. Plasma Processing*, 26, 415 (2006).
- [6] R. S. Joshi, J. F. Friedrich, M. H. Wagner, *Eur. Phys. J. D* 54, 249 (2009).
- [7] N. M. Jordan et al, *J. Appl. Phys.*, 102, 033301 (2007).
- [8] P. Bruggeman et al, *Plasma Processes and Polymers* 6, 751 (2009).
- [9] M. Cernaak et al, *Plasma Phys. Control. Fusion* 53, 124031 (2011).
- [10] I. Biganzoli et al, *Plasma Sources Sci. Technol.*, 22, 025009 (9pp) (2013).
- [11] S. J. Pendleton et al, *IEEE Trans. on Plasma Sci.*, 39, 2072 (2011).

MASS SPECTROMETRY AND OPTICAL EMISION SPECTROSCOPY STUDIES OF LOW-PRESSURE GAS MIXTURE OF He-N₂-CO₂

F. Castillo¹, M. Villa², H. Martínez¹, O. Flores¹ and P.G. Reyes²

¹*Laboratorio de Espectroscopia, Instituto de Ciencias Físicas, Universidad Nacional Autónoma de México, Apartado Postal 48-3, 62251, Cuernavaca, Morelos, Mexico.*

²*Facultad de Ciencias, Universidad Autónoma del Estado de México, Estado de México, México*

Abstract. Optical emission spectroscopy and mass spectrometry measurement were used to study a gas mixture glow discharge of He-N₂-CO₂ at total pressure of 1.0 and 2.0 Torr, a flow of 20 l/min. The emission bands were measured in the wavelength range of 200 to 1100 nm. The species observed were N₂⁺, C, C⁺, O, O⁺, N, N⁺, He, CO, CO₂, C₂O, CN, N₂ and N₂⁺, and He, which agree with mass spectrometry measurement. The electron temperature and ion density were determined by a double Langmuir probe. The electron temperature was of T_e = 3.35±0.34 eV, for 1.0 Torr and T_e=3.85±0.39 eV, for 2.0 Torr, and the ion density in the order of 10¹⁰ cm⁻³.

1. INTRODUCTION

Many plasma studies have been directed towards the possibility of decomposing CO₂ from industrial and energy exhausts, thus contributing to the pollution abatement [1]. These studies have clearly shown that CO₂ can be efficiently decomposed in CO and O₃ under the application of non-thermal plasmas [2]. Additionally, the efficiency of the decomposition process can be altered using mixtures of CO₂ with other gases, which also opens the possibility of generating additional species of industrial interest [3]. Although the application of DC discharges in pure molecular gases and their mixtures has been increasing in recent years, full quantitative understanding of the chemistry in such systems has not yet been reached. The principal reasons for this situation are the lack of reliable data for many physical-chemical reactions and surface processes. In previous studies [4], we performed an experimental characterization of DC He-N₂ mixture plasma using optical emission spectroscopy and mass spectrometry. Following this direction, this paper is intended to acquire knowledge of emission spectroscopy, and to carry out

measurements of electron temperature and ion density in a gas mixture glow discharge of CO₂-He-N₂, at a total pressure of 1.0 and 2.0 Torr.

2. EXPERIMENTAL DETAILS

The schematic diagram of the experimental setup is identical to that described in previous work [4, 5]. The discharge cell consists of two parallel electrodes enclosed in stainless steel vacuum chamber. The two electrodes were made of stainless steel disc, with 30 mm in diameter. The electrodes are positioned at the center of the reaction chamber with 10 mm gap spacing. The plasma chamber was pumped down by a vacuum system to a base pressure of 10⁻⁶ Torr. A continuous dynamic flow of CO₂-He-N₂ gas mixture was let in the system through needle valves at the desired pressures. A DC glow discharge was produced between the two electrodes. A lateral flange was a quartz window, used to monitor the active species generated in the glow discharge by plasma emission spectroscopy; the optical spectroscopy measurements (OES) were carried out by using a high-resolution Ocean Optics Inc. Spectrometer HR2000CG-UV-NIR. The grating has a spectral response in the range of 200 to 1100 nm.

A quadrupole mass spectrometer (QMS) is connected via cutoff and needle valves to the recipient for process gas analysis by in situ MS. The process gas composition and its changes during CO₂-N₂-He plasma are measured using Faraday cup detection mode at a pressure of 5.0 x 10⁻⁵ Torr inside the analyzer of the mass spectrometer.

The double Langmuir probe employed in this work is identical to that described in previous work [4, 5].

3. RESULTS AND DISCUSSION

A typical optical emission spectroscopic of CO₂/He/N₂ glow discharge plasma at a pressure of 1.0 and 2.0 Torr is displayed in Fig. 1. This allowed analysis of the most luminous area, which corresponds to the negative glow near the cathode dark space. The species observed were C, C⁺, O, O⁺, N, N⁺, He, CO, CO₂, C₂O, CN, N₂ and N₂⁺, this would imply that the main process for the production of these species is the electron impact excitation, ionization or dissociation. From the gas phase CO₂/He/N₂, excited neutral molecules as well as the primary radicals O, O⁺, C, C⁺, CO, N and N⁺ in their ground and excited states, are generated by electron processes.

However, some species are not only produced by an excited neutral CO₂ and N₂ molecules, another reaction mechanics that has the possibility of occurring is a recombination: C + CO → C₂O and C + N₂ → CN₂.

The intensities of the emission lines and bands for 2.0 Torr are most intense than that of 1.0 Torr (see Fig. 1). This dependence can be explained due to the mean free path decreases as the pressure is increased, this leads to larger number of excited particles, therefore to an increase in the signal detected for most of the emission bands.

From the measured experimental current-voltage characteristic probe at a pressure of 1.0 and 2.0 Torr, we got an electron temperature of $T_e = 3.35 \pm 0.34$ eV and an ion density of $n_i = (9.27 \pm 1.14) \times 10^{10} \text{ cm}^{-3}$, for 1.0 Torr and $T_e = 3.85 \pm 0.39$ eV and an ion density of $n_i = (9.21 \pm 1.11) \times 10^{10} \text{ cm}^{-3}$, for 2.0 Torr.

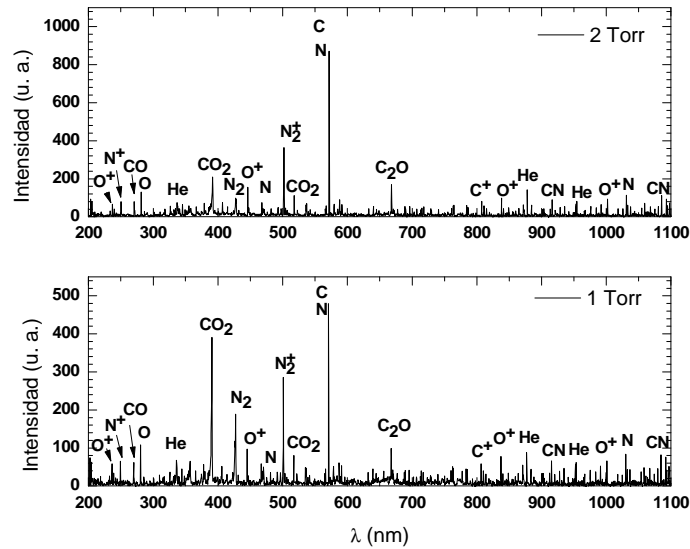


Figure 1. Emission spectra of N_2 -He plasma.

In this study, the MS parameters were optimized to provide the best possible sensitivity and better spectra. Figure 2 shows the mass spectra at two total pressures of the gas mixture.

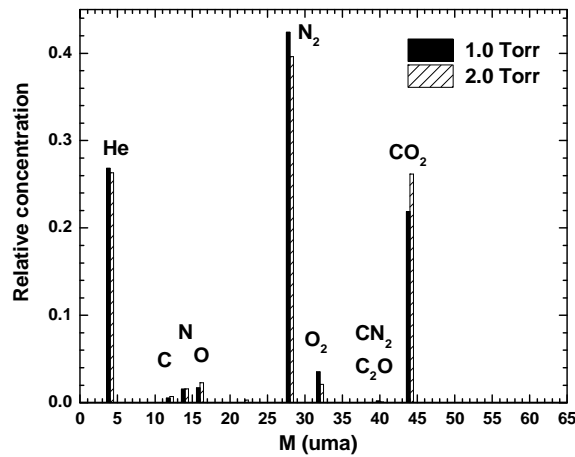


Figure 2. Mass spectra as a function of the total pressure of the gas mixture.

The MS spectra show eight masses at 4, 12, 14, 16, 28, 32, 40 and 44, corresponding to the presence of He, C, N, O, N₂, O₂, C₂O or CN₂ and CO₂ species, respectively. The high intense peaks correspond to He, CO₂ and N₂, while the intensity of the peak corresponding to the CN₂ and CO₂ molecules is relatively low. Comparing Figures 1 and 2, the results of mass spectroscopy were found to be consistent with the OES measurements.

4. CONCLUSIONS

In this study, we analyzed the plasma formed during low-pressure (1.0 and 2.0 Torr) glow discharge of N₂/CO₂/He by using optical emission spectroscopy and mass spectrometry.

The species observed were C, C⁺, O, O⁺, N, N⁺, He, CO, CO₂, C₂O or CN₂, CN, N₂ and N₂⁺, and He, consistent with the results of mass spectrometry.

It was shown that the species observed are generated in the He- CO₂-N₂ mixture, predominantly by electron impact excitation, ionization or dissociation.

The formation of C₂O or CN₂ molecules, as observed in MS, could be attributed to the recombination process, which leads to the formation of these species.

Acknowledgements

This work is partially supported by DGAPA IN101613 and CONACyT under the grant No.128714.

REFERENCES

- [1] L. Chang-Jun, X. Gen-hui and W. Timing, Fuel Processing Technology 58, 119 (1999).
- [2] G. Horvath, J. D. Skalny and N. J. Mason, Journal of Physics D: Applied Physics 41, 225207 (2008).
- [3] L. M. Zhou, B. Xue, U. Kogelschatz and B. Eliasson, Energy Fuels 12, 1191 (1998).
- [4] O. Flores, F. Castillo, H. Martinez, M. Villa, S. Villalobos and P. G. Reyes, Physics of Plasmas 21, 053502 (2014).
- [5] P. G. Reyes, C. Torres and H. Martinez, Radiation Effects and Defects in Solids 169, 285 (2014).

PRELIMINARY RESULTS ON ELECTRIC CHARACTERIZATION AND EMISSION SPECTROSCOPY OF SINGLE ELECTRODE AR PLASMA JETS

Vadym Prysiashnyi¹, Alonso H. C. Ricci¹ and Konstantin G. Kostov¹

¹*Faculty of Engineering (FEG), State University of Sao Paulo (UNESP), Guaratingueta, Brazil*

Abstract. The surface modifications using Ar plasma jets were studied with special focus on the plasma properties. The dynamics of current peaks, dissipated power values and emission spectroscopy depending on the dielectric substrate material were measured. It has been shown that the plasma properties strongly depend on the substrate when the plasma is in direct contact with it. Analysis of the normalized emission line intensities shows that the effect of the substrate can be measured not only in its proximity, but at the jet nozzle.

1. INTRODUCTION

Recently research community addresses the study of plasma jets [1,2]. Both plasma properties and its effects on the surface properties are studied. However, we found lack of information about the studies on the influence of the treated substrate onto the plasma properties. Some comments were given by Hao et al. [3], but we believe this study should be done more extensive. It was decided to use small plasma jet (with jet diameter of 1 mm) for localized treatment applications. Electrical characterization and optical emission spectroscopy was utilized to study the plasma properties.

2. EXPERIMENTAL

Plasma jets were produced and blown out from polypropylene tube complemented with metal bar electrode. The dielectric tube has a conical form to limit the gas flow and generate thin plasma column. To eliminate numerous effects of gas mixture, it was decided to work only with analytical Ar (99.999%) as a carrier gas. Glass, polystyrene, acrylic plastic and cellulose (paper) was in contact with plasma jet. Electrical characteristics were studied by measuring the current waveforms, Lissajous figures and dissipated power calculations. Emission spectroscopy was acquired using Andor Shamrock 303i emission

spectrometer through an optical fiber located perpendicularly to the plasma channel. Due to low plasma emission the slit width was varied from 150 μm to 200 μm . Emission spectra were recorded when a fiber was pointed to the jet nozzle and close to the substrate.

The high voltage was generated using a commercial power supply Minipuls 4 (GBS Elektronik, Germany). It was developed to generate high AC voltages up to 40kVp-p with operation frequency from 5 kHz to 40 kHz. Due to a specific coupling between the transformer cascade and the plasma jet at frequency of 19 kHz the output signal is a combination of two sine-like waves (one with higher amplitude and one with lower). Such signal waveforms contributes for the generation of cold plasma with less tube heating.

3. RESULTS

The study of current peaks (directly related with the number of Ar filaments) showed that when plasma is touching the substrate the number, amplitude and peak occurrence strongly depends on the substrate material, as, for example, it is presented in Table 1.

Table 1. Current peaks occurrence when the plasma is touching the dielectric substrate. Applied voltage 18 kVp-p, gas flow 0.8 L/min.

<i>Material</i>	<i>Positive current peaks</i>	<i>Negative current peaks</i>	<i>Frequency of occurrence</i>	<i>Average amplitude, mA</i>
Glass	4	2	Not in each period	10
Acrylic	6	3	In each period	5
Polystyrene	2	2	Almost each period	12
Paper	5	2	Almost each period	18

Figure 1 shows the dependences of the dissipated power depending on the nozzle-substrate distance. For large distances when plasma jet are not touching the substrate, the power values are same as expected, but when plasma jet approach the surface, the slopes of power dependences are different for different material.

It was decided to find out if the emission of the plasma changes depending on the substrate type. Typical emission spectrum of Ar plasma jet is presented in Figure 2. It contains emission of Ar I lines, second positive system of N_2 and OH band. Near the jet nozzle the Ar lines are more intense, while at the substrate the intensity of Ar lines are weak, while the light is mostly emitted through de-excitation of nitrogen molecules.

The normalized intensities of selected lines depending on the substrate material are presented in Figure 3. As it can be seen, the substrate is not only

affecting the relative ratio of emission lines measured close to the substrate, but measured at the jet nozzle also.

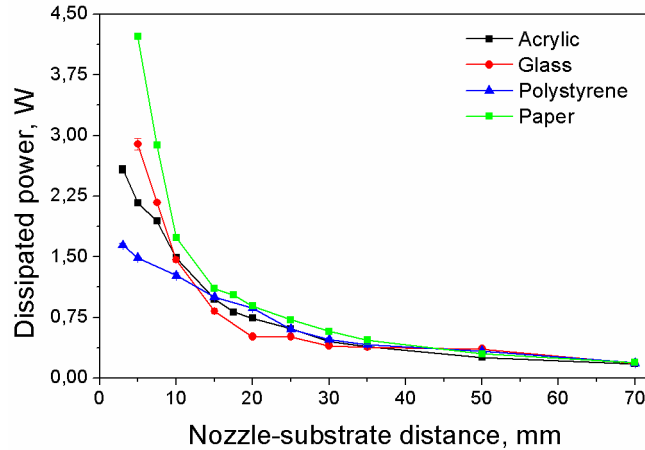


Figure 1. Dissipated power as a dependence of the nozzle-substrate distance. Ar gas flow 0.8 L/min, applied voltage 15 kVp-p.

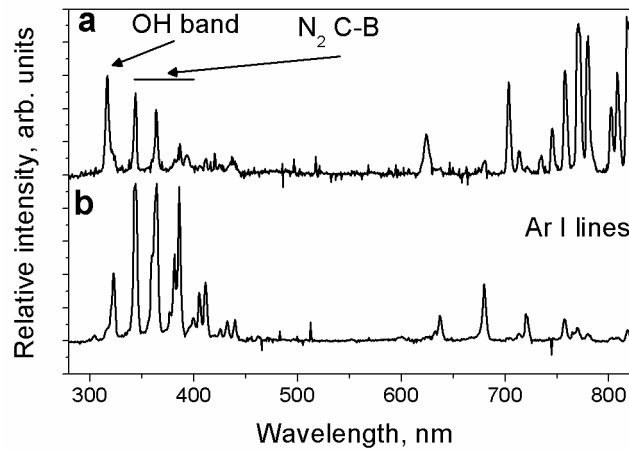


Figure 2. Emission spectra for Ar plasma jet touching the dielectric substrate measured (a) at the nozzle, (b) at the substrate. Ar gas flow 0.8 L/min, applied voltage 15 kVp-p, nozzle-substrate distance 10 mm, substrate material: glass.

The obtained data shows the importance of the substrate material on the plasma jet operation. Further research is necessary to perform in order to explain the phenomena, though it is certain that the dielectric properties of the substrate material as well as the ability to save the surface charge are playing important role [4].

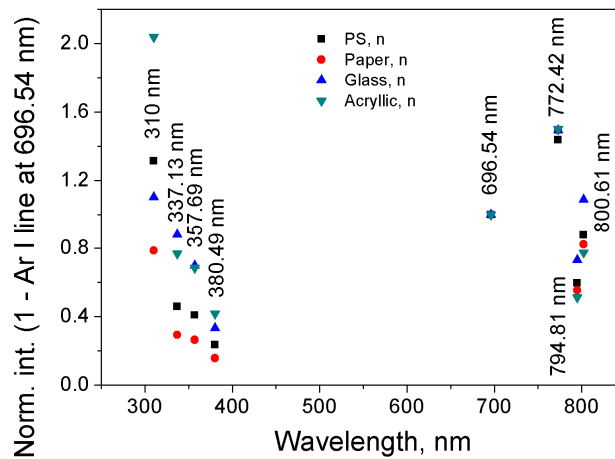


Figure 3. Normalized line intensities measured from Ar plasma jet touching the dielectric substrate measured at the jet nozzle. Ar gas flow 0.8 L/min, applied voltage 15 kVp-p, nozzle-substrate distance 10 mm.

4. CONCLUSIONS

It has been shown that electrical characteristics and light emission of the single electrode Ar plasma jet is strongly depending on the dielectric substrate. The number and frequency of current peaks as well as their amplitudes are dependent on the material. The difference in the dissipated power values can be explained by different dielectric properties of the substrate material. The analysis of the selected nitrogen, OH and Ar lines showed that the relative ratio of lines is different when the dielectric material is changed not only the spectra obtained near the substrate, but at the nozzle exit also. More deep study is necessary to elucidate the reasons of the observed phenomena.

Acknowledgements

This research was supported by Fundação de Amparo à Pesquisa do Estado de São Paulo (FAPESP; grant No. 2013/06732-3) and Conselho Nacional de Desenvolvimento Científico e Tecnológico (CNPq; project No. 470995/2013-0).

REFERENCES

- [1] M. Laroussi, T. Akan, *Plasma Process. Polym.* 9, 777 (2007).
- [2] K.-D. Weltmann et al., *J. Phys. D: Appl. Phys.* 41, 194008 (2008).
- [3] Z. Hao, S. Ji, A. Qiu, *IEEE T. Plasma Sci.* 40, 2822(2012).
- [4] R. Wild et al., *J. Phys. D: Appl. Phys.* 47,042001 (2014).

(³P)4d²P MULTIPLET AR II UV SPECTRAL LINE TRANSITION PROBABILITY ANALYSIS

M. T. Belmonte¹, J. A. Aparicio¹, R. J. Peláez², S. Djurović³ and S. Mar¹

¹ *Departamento de Física Teórica, Atómica y Óptica, Universidad de Valladolid, Paseo de Belén 7, 47011 Valladolid, Spain*

² *Laser processing Group, Instituto de Óptica, CSIC, C/ Serrano 121, 28006 Madrid, Spain*

³ *Faculty of Sciences, Department of Physics, Trg Dositeja Obradovića 4, 21000 Novi Sad, Serbia.*

Abstract. This work reports six relative atomic transition probabilities of Ar II lines from the multiplet (³P)4d²P in the spectral region 320–339 nm, all of which were measured in an emission experiment. The spectral lines were emitted by a low-pressure-pulsed plasma. Electron temperatures of 19000–22000 K were determined from the Boltzmann-plot of 11 Ar II spectral lines available from sources cited in the bibliography. Electron densities of $(3.5\text{--}9.0) \times 10^{22} \text{ m}^{-3}$ were determined by a two-wavelength interferometry method. The transition probabilities measured were compared with those given by NIST, to reveal some systematic disagreement.

1. INTRODUCTION

Argon plasmas have been extensively studied over the last fifty years due to their desirable characteristics [1] and the suitability of their spectral lines to work as a tool for temperature diagnostics [2]. However, despite all the efforts made to assemble an accurate set of transition probabilities (A_{ki}) [3], some of the data recommended by NIST [4] for Ar II spectral lines in the UV region [5] have uncertainties of around 50%.

In this experiment, some relative A_{ki} -values for UV Ar II spectral lines coming from the multiplet (³P)4d²P have been carefully measured, trying to reduce the uncertainty of the values given by the bibliography. The electron temperature has been measured using A_{ki} -values from 11 lines [6, 7], 5 of which are qualified with B by NIST [6]. In addition, the existing data for those lines [5, 8-10] have been carefully studied, finding a systematic disagreement worth analyzing.

2. EXPERIMENT AND PLASMA DIAGNOSTICS

The experimental set-up shown in Figure 1 has been described in detail in previous articles [11] and therefore, only the most relevant aspects will be summarized here for completeness. Measurements were carried out using a low-pressure-pulsed plasma source.

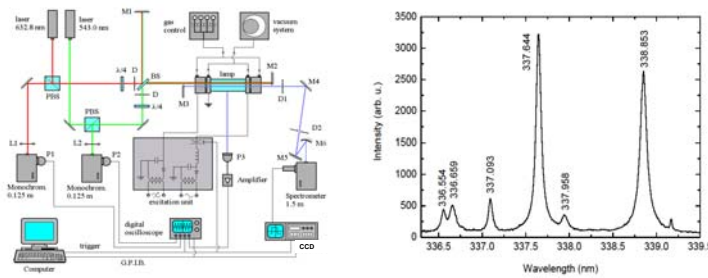


Figure 1. Left) Experimental set-up. Right) Example of one of the spectra recorded.

The plasma was produced inside a cylindrical tube of Pyrex, 175 mm in length and 19 mm in interior diameter. Argon at a pressure of 500 Pa was continuously introduced at a rate of $1 \text{ cm}^3 \text{ min}^{-1}$. The pressure of argon was adjusted to obtain minimal self-absorption and maximum intensity. The plasmas were created by discharging a capacitor bank of $20 \mu\text{F}$ charged up to 7.5 kV. The gas in the tube was preionized by a continuous current of several mA in order to ensure plasma reproducibility. In these conditions, the plasma emission lasted for $150 \mu\text{s}$.

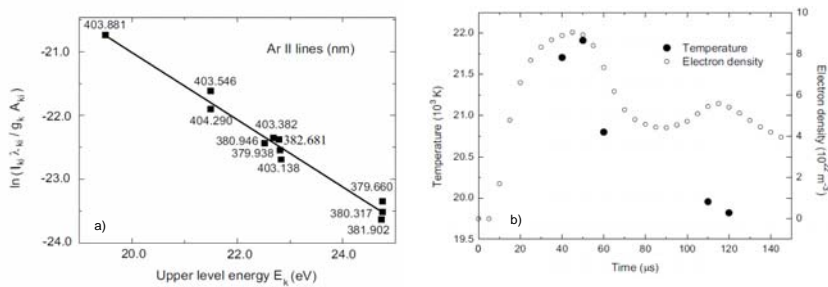


Figure 2. a) Example of Ar II Boltzmann-plot corresponding to the $50 \mu\text{s}$. b) Temperature and electron density evolution over the plasma life.

Plasma **electron temperature** was determined by using the Boltzmann-plot technique for 11 Ar II spectral lines (Fig. 2a) for which the transition probabilities were well known [6, 7], all of them belonging to the spectral interval of 379-405 nm. The criteria to select the reference data was to use the data from Bennett et al. [6] when they exist and their accuracy was B

and from Aparicio et al. [7] in the other cases. The interval of the upper energy levels considered is 19-25 eV. To determine the **electron density**, a two-laser interferometry method [12] was used. Temporal evolution of these plasma parameters is shown in Fig 2b).

3. RESULTS AND CONCLUSIONS

Figure 3 compares the transition probability values taken from Bennett et al. [6] and from Rudko & Tang [5], henceforth A_B and A_R respectively, with those measured in this experiment, A_{TW} . As can be seen from Fig. 3a), the A_{ki} -values reported by [6] show very good agreement with A_{TW} , having the line of fit a y-intercept of 0.022 ± 0.015 and a slope of 1.011 ± 0.037 . It is possible to observe how the A_{ki} -values in Fig 3a) are randomly distributed along the unit-slope line, giving a R-square value of 0.980.

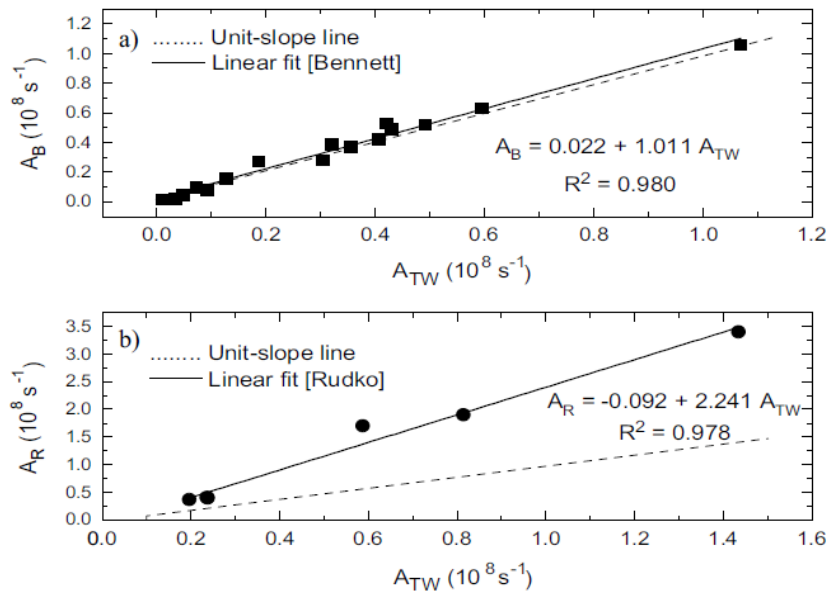


Figure 3. Comparison of the transition probabilities measured in this experiment (A_{TW}) with those from Bennett et al. [6] (A_B) and Rudko & Tang [5] (A_R).

In opposition, as is shown in Fig. 3b), the line of fit for A_R -values has a y-intercept of -0.092 ± 0.124 and a slope of 2.241 ± 0.170 with a R-square value of 0.978, which shows that the A_R values are 2.2 times larger than A_{TW} on average. In Table 1 we present the measured transition probabilities ordered according to the upper and lower state, the wavelength for every transition and the A_R and A_{TW} values with their accuracy, as well as the ratio between them.

Table 1. Transition probabilities of Ar II spectral lines measured in this work (A_{TW}) in units of 10^8 s^{-1} . For the comparison, available data from [5] is given (A_R), as well as their ratio with the measured values. For both A_{TW} and A_R the accuracy in percentage has been included in brackets, with D representing uncertainties between 41- 50%.

Upper state	Lower state	λ (nm)	A_{TW}	A_R	A_R / A_{TW}
$(^3P)4d^2P_{3/2}$	$(^3P)4p^2S^{\circ}_{1/2}$	338.853	0.81 (12)	1.9 (D)	2.35
	$(^3P)4p^2P^{\circ}_{3/2}$	329.364	0.59 (17)	1.7 (D)	2.88
	$(^3P)4p^2D^{\circ}_{3/2}$	320.432	0.24 (12)	0.4 (D)	1.67
$(^3P)4d^2P_{1/2}$	$(^3P)4p^2P^{\circ}_{1/2}$	330.723	1.43 (12)	3.4 (D)	2.38
	$(^3P)4p^2P^{\circ}_{3/2}$	336.659	0.24 (17)	0.41 (D)	1.71
	$(^3P)4p^2D^{\circ}_{3/2}$	327.332	0.20 (16)	0.37 (D)	1.85

The present analysis shows how our measurements have a good agreement with the most accurate ones from [6], whereas values recommended by NIST from [5] are systematically 2.2 ± 0.4 times larger than ours.

Acknowledgements

We thank S González for his work on the experimental device. M.T. Belmonte thanks the University of Valladolid for her PhD scholarship and R.J. Peláez acknowledges the grant JCI-2012_13034 from the Juan de la Cierva program. S. Djurović thanks the Ministry of Education, Science and Technological Development of the Republic of Serbia for support via Project 171014.

REFERENCES

- [1] W. L. Wiese, J. Quant. Spectrosc. Radiat. Transfer 40, 3, 421 (1988)
- [2] K. Behringer and P. Thoma, J. Quant. Spectrosc. Radiat. Transfer 16, 605 (1976)
- [3] V. Vujnović and W. L. Wiese, J. Phys. Chem. Ref. Data 21, 5 (1992)
- [4] http://physics.nist.gov/PhysRefData/ASD/lines_form.html
- [5] R. I. Rudko and C. L. Tang, J. Appl. Phys. 38, 4731 (1967)
- [6] W. R. Bennett Jr., P. J. Kindlmann and G. N. Mercer, Chemical Lasers: Applied Optics Supplement 2, 34 (1965)
- [7] J. A. Aparicio, M. A. Gigosos and S. Mar, J. Phys. B: At. Mol. Opt. Phys. 30, 3141 (1997)
- [8] R. I. Rudko and C. L. Tang, J. Appl. Phys. 39, 4046 (1968)
- [9] H. Statz, F. A. Horrigan, S. H. Koozekanani, C. L. Tang and G. F. Koster, J. Appl. Phys. 36, 2278 (1965)
- [10] G. F. Koster, H. Statz, F. A. Horrigan and C. L. Tang, J. Appl. Phys. 39, 4045 (1968)
- [11] S. Djurović, S. Mar, R. J. Peláez, J. A. Aparicio, Mon. Not. R. Astron. Soc. 414, 1389 (2011)

OPTICAL DIAGNOSTIC OF RF PLASMA DISCHARGES IN THE N₂ - Ar GAS MIXTURES

Sanja S. Pavlović¹, Vladimir M. Milosavljević^{2,3} Patrick J. Cullen³
and Goran B. Poparić²

¹*Belgrade Polytechnic, Brankova 17, 11000 Belgrade, Serbia*

²*Faculty of Physics, Studentski trg 12, 11000 Belgrade, Serbia*

³*Bio-plasma Research group, Dublin Institute of technology,
Dublin 1, Ireland*

Abstract. An optical diagnostic on the radio frequency (RF) plasma discharges in N₂ - Ar gas mixtures have been conducted. A number of gas flow rates for N₂ and Ar gas mixes were used in the experiment. A standard 13.56 MHz RF power supplier was employed. The power generator operated from 60 to 100 W. The optical diagnostic was conducted by measuring the relative intensities of Argon atomic spectral lines for different gas ratios of argon and nitrogen, as well as for a different RF discharge powers. The results of measurements and the short analyses of RF plasma discharges conditions are presented in this work.

1. INTRODUCTION

The nitrogen molecule plays an important role in various aspects of technology or/and environmental physics. Nitrogen is also important for astrophysics, because of the fact that it comprises a significant fraction of extraterrestrial space. It is also found in the atmospheres of Mars, Venus, Titan and Triton. Industrial physics use electron impact excitation and ionization of N₂ in many plasma and discharge technologies and applications. Diffuse discharge switches [1], plasma etching [2] and laser devices are based on these processes. In chemistry, processes in the plasma polymerization [3] and chemical detectors are related to the nitrogen molecule. Excitation and ionization of nitrogen are also important processes in various surface and coating technologies [4]. Plasma nitriding [5], a well-known surface hardening technique is related with gas mixtures where the presence of nitrogen is necessary. Argon gas also plays an important role in the nitrogen gas mixtures and in the above mentioned plasma technologies. Argon as a noble gas is very resistant to chemical reaction in plasma gas mixtures and very often serves as buffer gas. The argon atom is also very useful in plasma diagnostic due to sharp optical spectral lines in its optical spectrum.

2. EXPERIMENTAL SETUP

For the purpose of diagnostic RF plasma discharges, a cylindrical 304 stainless steel vessel was used to serve as a plasma chamber. The length of the cylinder is 400 mm and its diameter is 100 mm. In the center of the cylinder is an electrode from copper which diameter 6 mm. From the side of the chamber, there is a quartz view port which is used for optical measurements. In order to control gas mixture purity, a vacuum system with mass gas flow meters was used. The high purity of N_2 and Ar gases were introduced in the previously evacuated plasma's chamber by a vacuum pump, enabling control of the desired ratios in the gas mixtures and limiting impurity. The high voltage RF generator was connected to the central electrode of the chamber, while the ground was connected to the outer body of the chamber. The standard 13.56 MHz frequency was applied for RF discharges. The power which was used during plasma discharges was in the range from 60 W to 100 W.

The optical system which enabled our optical measurements was consisted of a collimated lens, long optical path spectrometer with high resolution grating connected to a step-motor and a photomultiplier. The focusing lenses were adjusted to focus the spectral radiation of plasma discharges which took place at distance of 40 mm from the anode of the cylindrical tube system. High resolution optical spectrometer was used to record spectral lines from 300 to 790 nm. The resolution of recorded spectrums was 0.01 nm, which was achieved by using a high resolution grating and long optical path of spectrometer of about 4 meters. The photomultiplier tube operated in continuous mode and the photoelectron current was measured for every angular position of grating with the spectra recorded using in-house software.

3. RESULT AND DISCUSSION

The optical spectra of the RF plasma discharges in N_2 - Ar gas mixtures were measured under varying experimental conditions, including discharge power, which was controlled by the current limitation of RF high voltage generator and the ratios of gas participation in the mixtures by tuning the gas flow rates. The optical measurements were performed in the spectral range from 300 nm to 795 nm. Beside argon atomic spectral lines, many nitrogen vibration spectral lines were observed in the spectra (see Fig 1.).

For the purpose of diagnostics, we chose to analyze the relative intensities of the argon atomic spectral lines for different ratios of the gas participation in the mixtures, as well as for different discharge powers. The most intense argon atom spectral lines were chosen where spectral noise is the smallest thereby limiting the influence of experimental error. The chosen spectral lines had high energy of the upper atomic states, which help in determining the shape of tail region of electron energy distribution functions and enabling an estimation of the mean electron energies during the different condition of discharges. The chosen spectral lines are presented in table 1.

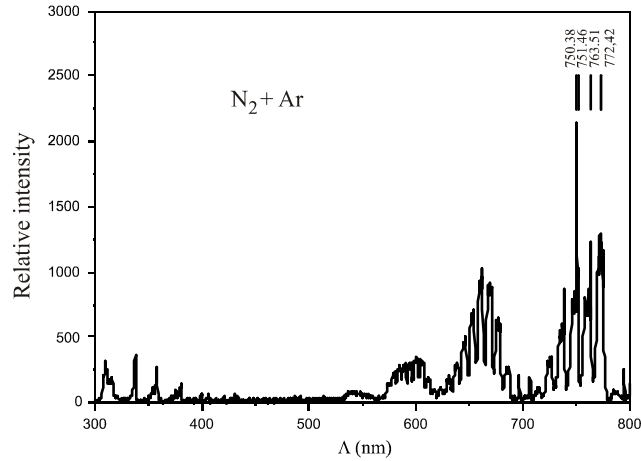


Figure 1. An optical spectrum of the N_2+Ar plasma gas mixture.

Table 1. Argon atom spectral lines chosen for plasma diagnostic.

λ (nm)	Upper level	Energy of up. level (eV)	Rel. Intensity (NIST [6])
750.38	$3s^23p^5(^2P^{\circ}_{1/2})4p\ 2[1/2]\ 0$	11.827	20000
751.46	$3s^23p^5(^2P^{\circ}_{3/2})4p\ 2[1/2]\ 0$	11.623	15000
763.51	$3s^23p^5(^2P^{\circ}_{3/2})4p\ 2[3/2]\ 2$	11.548	25000
772.42	$3s^23p^5(^2P^{\circ}_{3/2})4p\ 2[1/2]\ 1$	11.723	10000

The relative intensity of the argon spectral lines for different flow ratios with nitrogen are given in table 2. From table 2 it can be concluded that the argon spectral lines are most intense in the case when the percentage of nitrogen in the gas mixtures was the lowest. It is considerable bearing in the mind that nitrogen in this case takes only small part of electron energy. When the participation of nitrogen is greater, relative intensities of the spectral lines decrease as the nitrogen over takes the greater amount of electron energy through collision processes. It should be noted that with a further increase of nitrogen concentration, a small increase in the intensities of the spectral lines can be observed again.

This behavior of relative intensities of argon spectral lines could be explained by the changing shape of electron energy distribution function when the ratio of participation gases in gas mixtures is changed. The required detailed analysis would include theoretically predicted electron energy distribution functions and an estimation of the rate coefficients for the excitation of the argon atom in the upper electronic states of analyzed spectral lines. Also, the branching

into the lower electronic states during de-excitation and radiation should also be included in the more detailed analysis.

Table 2. Relative intensity of argon atom spectral lines for different flow ratios in the mixtures with nitrogen

λ (nm)	Rel. Intensity Rel. flow ratio (2/10)	Rel. Intensity Rel. flow ratio (2/30)	Rel. Intensity Rel. Flow ratio (2/60)
750.38	0.2398	0.0761	0.08636
751.46	0.0874	0.0108	0.04658
763.51	0.0970	0.0608	0.02484
772.42	0.0565	0.0115	0.01519

4. CONCLUSIONS

Optical diagnostic of radio frequency plasma discharges in N₂ and Ar gas mixtures was performed in the work. Several ratios of gas mixtures of N₂ and Ar gases were analyzed. The standard 13.56 MHz frequency was used in the plasma discharges. The power of discharge ranged from 60 to 100 W. The optical diagnostic was conducted by measuring the relative intensities of Argon atomic spectral line emissions for different ratios of gas mixtures and RF discharge powers.

Acknowledgements

This work was supported in part by the Ministry of Education and Science of the Republic of Serbia by the Projects No. 171006 and No. 171016.

REFERENCES

- [1] S. R. Hunter and J. G. Carter, *J. Appl. Phys.* 58, 3001 (1985).
- [2] W. Z. Collison, T. Q. Ni and M. S. Barnes, *J. Vac. Sci. Technol. A* 16, 100 (1998).
- [3] H. Yasuda and T. Hsu, *J. Polym. Sci. Polym. Chem. Ed.* 15, 81 (1977).
- [4] S. Gredelj, A. R. Gerson, S. Kumar and G. P. Cavallaro, *Appl. Surf. Sci. A* 199, 183–194 (2002).
- [5] E. Guiberteau, G. Bonhomme, R. Hugon and G. Henrion, *Surf. Coat. Technol.* 97, 552–556 (1997).
- [6] <http://physics.nist.gov/>

SINGLE-PULSE LASER INDUCED PLASMA IN WATER: SHOCK WAVE, BUBBLE AND PLASMA EMISSION

M. R. Gavrilović^{1,2}, M. Cvejić¹, V. Lazic³; S. Jovićević¹

¹*Institute of Physics, University of Belgrade, 11080 Belgrade, Serbia*

²*Faculty of Electrical engineering, University of Belgrade, 11120 Belgrade, Serbia*

³*ENEA (UTAPRAD-DIM), Via. E. Fermi 45, 00044 Frascati (RM), Italy*

Abstract. We report the results of the laser induced underwater breakdown study on Al and Si targets. Breakdown is induced with single nanosecond laser pulse. Shock wave evolution is recorded and analyzed using schlieren imaging technique. Spectral emission is studied by optical emission spectroscopy at different delay times after laser plasma initiation.

1. INTRODUCTION

Laser induced breakdown (LIB) in liquids is a complex process initiated by multi-photon absorption or by cascade ionization, and it was extensively studied in the past years. This interest was mainly driven by emerging laser applications in medicine [1,2]. The most important difference between plasma formation inside gaseous environment and liquid comes from plasma confinement and vapor bubble formation, accompanied by a high local pressure and mechanical effects much stronger than those observed in a gaseous surrounding [3,4]. Experimental investigation of these processes is a complicated issue, since they occur on short timescale and in very small volume. Therefore, a high temporal and spatial resolution survey is required.

In this work mechanical and optical properties of single pulse LIB on submerged solid target in distilled water are studied by means of fast schlieren photography and optical emission spectroscopy.

2. EXPERIMENTAL

Experimental setup used in this study is presented schematically in Fig.1. Nd:YAG laser source operated at 1064 nm, with 20 ns pulse duration and 50 mJ energy was used for the plasma initiation. Laser beam was focused using two lenses, where the second lens was built in the chamber wall directly, see Fig 1. Lenses were aligned in the manner that the laser beam induces breakdown on

the surface of solid target placed vertically inside a chamber filled with distilled water. Two chambers of different sizes were used: in the first one, optical path length in the water was $l = 3$ cm and in the second $l = 5$ cm. Both chambers were equipped with two quartz windows, see Fig 1. Pure Al and Si targets used in this study were placed in target holders and moved after each laser shot.

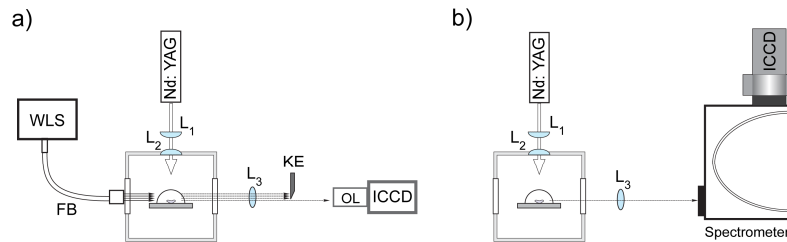


Figure 1. Experimental setup for a) schlieren photography b) optical emission spectroscopy. Nd:YAG laser $\lambda = 1064$ nm, 20 ns pulse duration, energy 50 mJ, WLS-white light source, FB-fiber bundle, L_1, L_2, L_3 -lenses, KE-knife edge, OL-objective lens

Schlieren imaging was performed using setup depicted in Fig 1a. Area above the target was illuminated with the white light source (WLS) light guided through the fiber bundle placed closely to the chamber lateral window. Back-illuminated area above the sample was further imaged with the lens L_3 placed after the chamber exit window. Vertically mounted knife-edge was positioned in the focus of the lens to monitor refractive index gradients perpendicular to the sample. Final image was formed using objective lens mounted on the iCCD camera. Plasma emission was recorded using setup in Fig 1b. Image of the plasma plume was projected onto the entrance slit (10 μm width and 2.5 mm height) of the spectrometer (Shamrock sr-303i, Czerny-Turner type, focal length 303 mm, with the grating of 1200 grooves/mm.) using lens L_3 . The plasma radiation was recorded with the iCCD detector mounted on the exit slit plane of the spectrometer. The ICCD was operated by a pulse generator (DG-535, Stanford Research Systems), allowing the choice of gate width and delay time for time resolved data acquisition.

3. RESULTS AND DISCUSSION

Following the laser induced breakdown in the liquid shock wave (SW) emerges, as a result of the disturbance induced by the pressure developed during plasma formation [5]. Apart from the clearly distinguishable shock waves in Fig. 2, one can also observe intense plasma emission and vapor bubble when plasma emission is not of too high intensity. Using the dimensionally calibrated sequence of schlieren images recorded with different delay times, the shock wave velocity can be estimated, see Fig 2, bottom row. Due to lower intensity of plasma emission with Si target, shock wave velocity can be estimated at earlier delay times compared to Al target. At 150 ns delay time estimated shock wave velocity for Si target is approximately 4.2 km/s which is three times higher than

normal sound speed in water. Subsequent slowing down of the shock wave is a consequence of the energy losses in the shock front. Based on the estimated average shock wave velocity u_s , an average pressure of the shock wave front can be inferred using equation (1) from [5]:

$$p_s = c_1 \rho_0 u_s \left(10^{(u_s - c_0)/c_2} - 1 \right) + p_{\text{stat}} \quad (1)$$

c_0 , c_1 , c_2 , ρ_0 , p_{stat} are taken from [5]. For accurate pressure measurements however, more sophisticated methods are needed that can assess SW velocity precisely and in the close vicinity of the target surface [5]. Apart from the initial shock wave formation, example of the second shock wave released after the collapse of the vapor bubble is also presented in the Fig 2, last images in the first two rows.

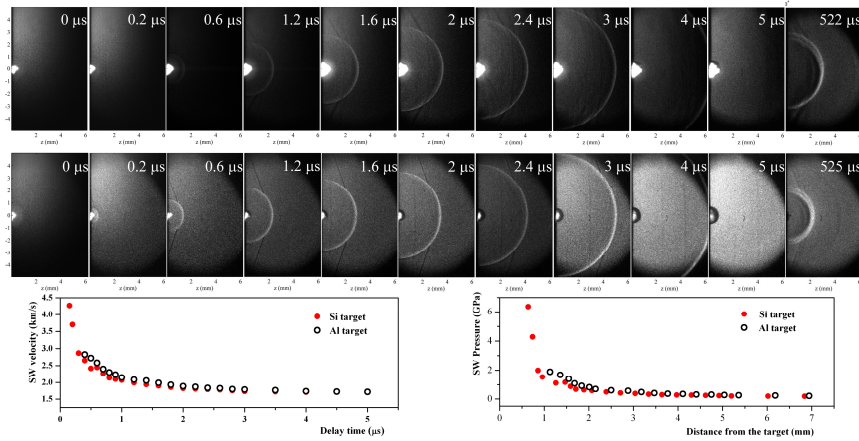


Figure 2. Time evolution of the shock wave for Al target (first row) and Si target (second row) for $l=3$ cm. The last image in the both sequences represents second shock wave. Bottom row shows calculated average shock wave velocity and pressure as a function of delay time after the laser pulse and distance from the target, respectively.

Spectral recordings of the single pulse LIB on solid target in water are shown in Fig 3. Spectra were recorded for the three delay times after the laser pulse 0.5, 1 and 2 μs , averaged over 20 laser shots. They are dominated by the intense continuum emission, especially at early delay times when spectral lines are broad and merged with continuum. At later delay times continuum intensity decreases but then usually only lines from low excitation energy levels can be detected. In the case of Al sample two resonance lines belonging to the $3s^23p-3s^24s$ ($^2P^0-^2S$) transition are clearly detected. Apart from Al I resonance lines, strong emission of molecular band was also observed, and it was identified as $B^2\Sigma^+ \rightarrow X^2\Sigma^+$ AlO (0,0) band. For Si sample, the recorded line profile of highest quality in the sense of signal to noise and signal to continuum ratio belongs to the $3s^23p^2-3s^23p4s$ ($1S-1P^0$) transition. Visible plasma radiation for Si sample lasted shorter than in

the case of Al target and consequently it was recorded for only two delay times 0.1 and 1 μ s after the laser pulse. Apart from the lines originating from target material emission from the elements present in water was also detected. Example is given in Fig 3d.

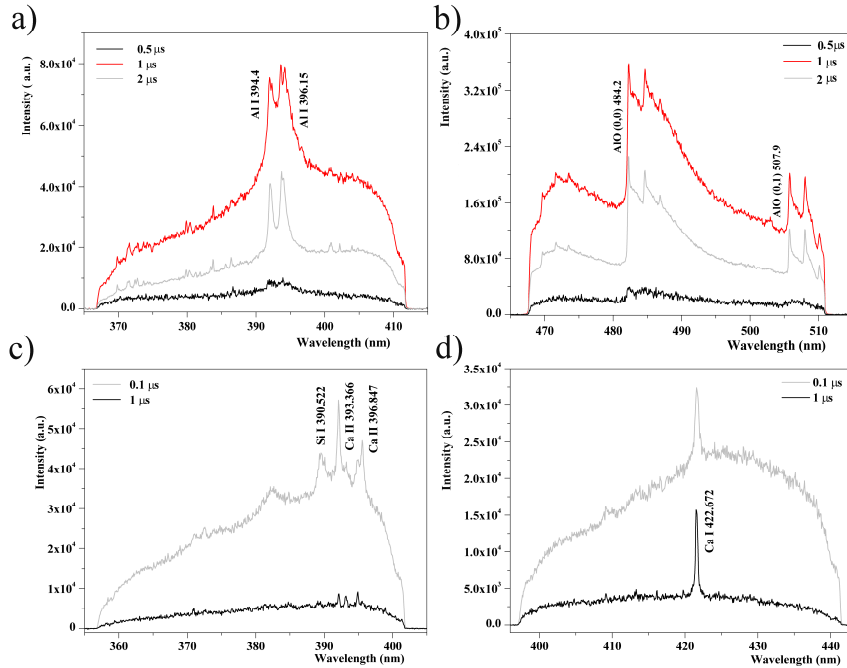


Figure 3. Single-pulse laser induced emission spectra in distilled water for a) b) Al sample c) d) Si sample

Acknowledgements

This work is supported by Ministry of Science, Education and Technological development under the grant NO 171014.

REFERENCES

- [1] P. K. Kennedy, D. X. Hammer, B. A. Rockwel, *Prog. Quantum Electron.* 21, 155–248, (1997).
- [2] A. Vogel, V. Venugopalan, *Chem. Rev.* 103, 577–644, (2003).
- [3] V. Lazić, J. J. Laserna, S. Jovičević, *Spectrochim. Acta Part B*, 82, 48–49, (2013).
- [4] A. De Giacomo, M. Dell'Aglio, O. De Pascale, M. Capitelli, *Spectrochimica Acta Part B* 62, 721–738, (2007).
- [5] W. Lauterborn, A. Vogel, *Bubble Dynamics and Shock Waves*, p 75 (Springer Berlin Heidelberg, 2013)

DYNAMICS AND OPTICAL PROPERTIES OF THE LASER INDUCED BUBBLE

M. R. Gavrilović^{1,2}, M. Cvejić¹, V. Lazic³; S. Jovićević¹

¹*Institute of Physics, University of Belgrade, 11080 Belgrade, Serbia*

²*Faculty of Electrical engineering, University of Belgrade, 11120 Belgrade, Serbia*

³*ENEA (UTAPRAD-DIM), Via. E. Fermi 45, 00044 Frascati (RM), Italy*

Abstract. In the present paper we focus our attention to laser induced bubble emerging after laser ablation of solid target in the liquid. The dynamics of bubble evolution and optical properties are studied with fast shadowgraphy and with scattering and transmission measurements.

1. INTRODUCTION

Formation of the laser induced bubble and its subsequent evolution has attracted a lot of attention in recent years. The interest is caused by numerous applications in different research fields [1]. Detailed knowledge of bubble dimensions and optical properties is important for optimal delivery of subsequent laser pulses. The reason is that the bubble affects transmission of laser pulses during expansion and cooling, and can lead to beam defocusing. Further experimental and theoretical investigation is still needed, especially in the case of laser induced bubble on the solid target inside liquid [2].

2. EXPERIMENTAL

Experimental setup used in this study is described schematically in Fig.1. Nd:YAG laser operated at 1064 nm, with 20 ns pulse duration and 50 mJ energy was used for the plasma initiation. Laser beam was focused using two lenses, where the second lens was built in the chamber wall. Lenses were adjusted in the manner that the laser beam induces breakdown on the surface of metallic target placed vertically inside a chamber filled with distilled water. Two chambers of different sizes were used: in the first one, optical path length in the water was $l = 3$ cm and in the second one $l = 5$ cm. Both chambers were equipped with two quartz windows, see Fig 1. Pure Al and Si targets used in this study were placed in target holders and moved after each laser shot.

Transmission measurements were performed under illumination of HeNe laser, Fig 1a. The laser was expanded to ~5 mm diameter and sent through chamber windows parallel to the target surface. On the opposite side of the chamber

photomultiplier tube (PMT) with interferential filter (IF) for He-Ne wavelength was placed and used for the detection of transmitted radiation. For the scattering measurements probe was green laser diode beam sent through the beam expander and directed on the target with incidence angle of $\sim 60^\circ$, Fig1b. The scattered light was collected through chamber window and focused with lens L_3 onto the entrance slit of PMT equipped with suitable IF.

For the shadowgraphy measurements, area above the target surface was illuminated with the white light source (WLS). The light was guided through the fiber bundle placed closely to the chamber lateral window, Fig 1c. Back-illuminated area above the sample was further imaged with the lens L_3 placed after the chamber exit window. Final image was formed using objective lens mounted on the iCCD camera.

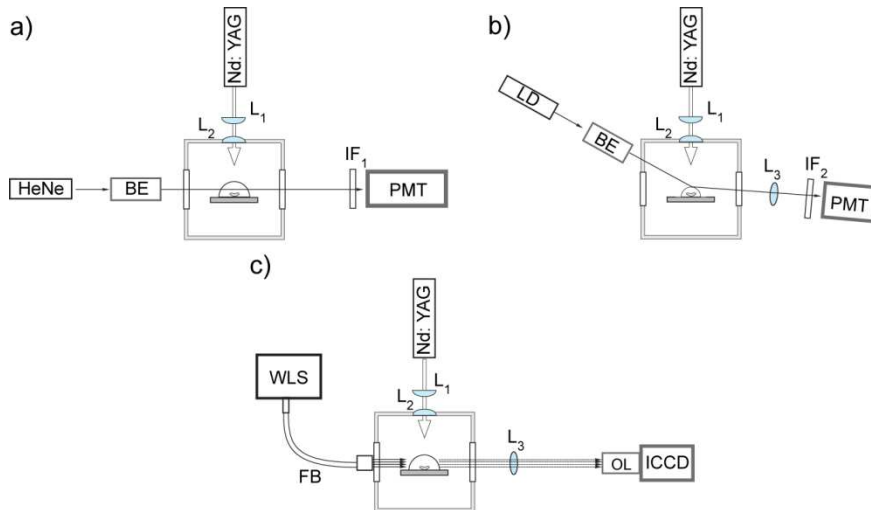


Figure 1. Experimental setup for a) transmission b) scattering c) shadowgraphy measurements. Nd:YAG laser $\lambda = 1064$ nm, 20 ns pulse duration, energy 50 mJ, L_1, L_2, L_3 -lenses, BE-beam expander, HeNe-helium-neon laser, LD – green laser diode, IF_1, IF_2 -interference filters, PMT – photomultiplier tube, WLS-white light source, FB-fiber bundle OL-objective lens

3. RESULTS AND DISCUSSION

Using Beer-Lambert law estimated laser energy delivered to the target surface was 60% and 43 % of the incident laser energy for the optical path lengths in water $l = 3$ and $l = 5$ cm, respectively. For the calculation of laser energy absorption through water column value $\alpha = 0.072$ cm^{-1} was used [1]. Based on the crater dimensions on the target surface estimated fluences were in the range 7 - 8 J/cm^2 (0.35 - 0.4 GW/cm^2) for $l = 5$ cm, and 14.5 - 18 J/cm^2 (0.72 - 0.9 GW/cm^2) for $l = 3$ cm. Except for the decrease in energy losses through water absorption, craters on the target were smaller and more regular when using $l = 3$ cm thus producing higher fluences on the target surface.

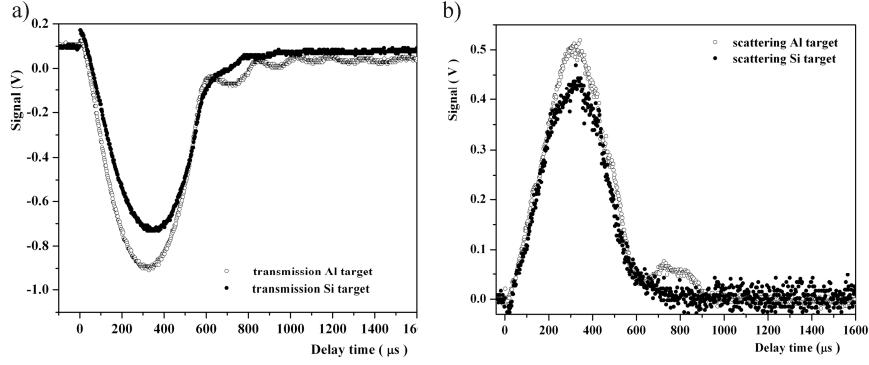


Figure 2. Comparison of optical signals for Al and Si targets as a function of the delay time after the laser pulse a) transmitted HeNe laser beam b) scattered LD beam. Optical path length in water was $l = 5\text{cm}$

The result of transmission and scattering measurements are presented in Fig 2. The transmission signal shows for the case of Al target several cycles of bubble growth and decay. For the Si target only first bubble can be seen while successive bubble rebounds are not clearly discernible. This situation is even more pronounced in the case of scattering signal, where only for Al the second bubble could be detected.

The bubble evolution in the sense of its size and shape were studied with fast shadowgraphy. Example is given in Fig. 3 for the case of Al and Si target with $l = 5\text{ cm}$. From dimensionally calibrated images bubble size was determined. In Fig 3 both bubble dimensions (height and width) are shown for both studied target materials. Differences between two bubble dimensions were minor for the first bubble, i.e. the observed bubble had almost hemispherical shape. After bubble collapse formation of new shockwave and bubble occurred [3]. These newly formed bubbles had very irregular shapes and sizes. With fast shadowgraphy two or three bubble cycles were detected in first millisecond after the laser pulse for both targets and both focusing conditions. Applying approximate formula (1) widely used in literature [2], energy contained in the first bubble can be estimated from the maximum radius:

$$E_b = \frac{2}{3} \pi R_{\max}^3 (p_{\text{stat}} - p_v) \quad (1)$$

where difference between static pressure in liquid and pressure of the vapor inside the bubble ($p_{\text{stat}} - p_v$) is inferred using (2)

$$T_c = 1.83 \cdot R_{\max} \sqrt{\frac{\rho}{p_{\text{stat}} - p_v}} \quad (2)$$

T_c represents first bubble collapse time. Results are summarized in Table 1.

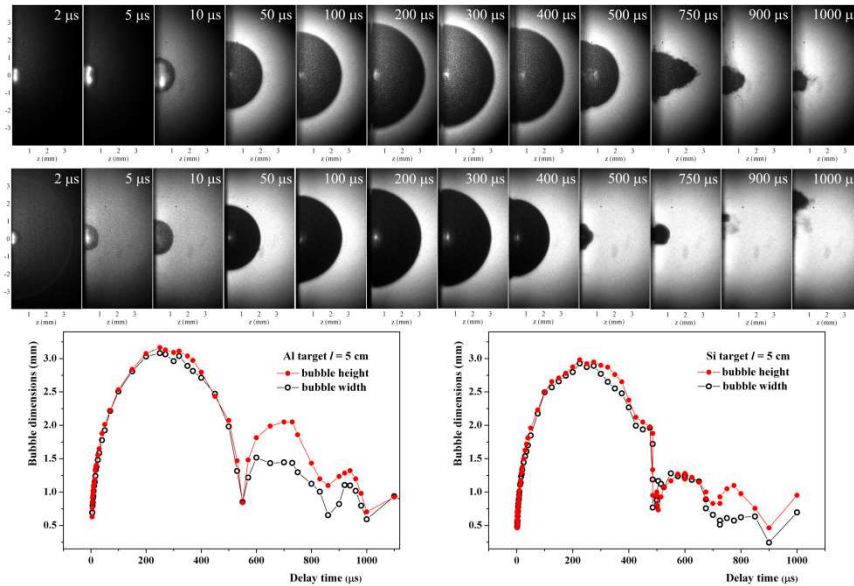


Figure 3. Bubble evolution and decay recorded with fast shadowgraphy measurements for Al (upper row) and Si target (bottom row). Optical path length in water was $l = 5$ cm. Bubble dimensions determined from image sequences above are shown on graphs for Al target (left) and Si target (right).

Table 1. Calculated bubble energies E_b for Al and Si target

		R_{\max} (mm)	T_c (μ s)	E_b (mJ)
Al	$l = 5$	3.16	540	7.56
	$l = 3$	3.15	520	8.03
Si	$l = 5$	2.98	505	6.45
	$l = 3$	2.95	525	5.67

Acknowledgements

This work is supported by the Ministry of Education, Science and Technological Development of Republic Serbia under Project No. 171014.

REFERENCES

- [1] V. Lazic, S. Jovićević, M. Carpanese, Appl. Phys. Lett. 101, 054101, (2012).
- [2] G. Cristoforetti, M. Tiberi, A. Simonelli, P. Marsilli, F. Giammanco, Appl. Opt, 51, B30, (2012).
- [3] V. Lazic., J.J. Laserna, S. Jovićević, Spectrochim. Acta Part B, 82,42-49, (2013).

STARK SHIFT OF SEVERAL NEUTRAL HELIUM LINES IN DENSE LOW TEMPERATURE PLASMA

M.Ivković

Institute of Physics, University of Belgrade, P.O.Box 68, 11080 Belgrade, Serbia

Abstract. Stark shift of the neutral helium spectral lines $2p^1P^o - 3d^1D$ at 667.8 nm and $2p^3P^o - 3s^3S$ at 706.5 nm are measured in the plasma of a linear low pressure pulsed arc. Plasma electron density in the range $9 - 60 \times 10^{22} \text{ m}^{-3}$ is determined from the wavelength separation between allowed He I 447.1 nm ($2p^3P^o - 4d^3D$) line and its forbidden component ($2p^3P^o - 4d^3F^o$). Plasma electron temperature in the range 26 000 – 34 000 K is determined from several Si II lines. Measured spectral line shifts are compared with results of several theoretical calculations.

1. INTRODUCTION

Helium is present in plasma sources used for many applications. The use of helium isolated spectral line shapes is very popular techniques for electron density, N_e diagnostics of these plasmas. In order to establish physical background great effort was devoted to study He I spectral lines shapes theoretically [1, 2] and experimentally [3-5]. Recently, theoretical studies of He I lines in dense plasmas with the inclusion of dynamic screening [6] and mutual interaction between particles [7] have been published. The difference between line shift values at N_e in [6] and [7] and lack of experimental data in relevant N_e region motivated us to perform this experiment. Study was limited to the line shifts only, since the line widths are affected by self-absorption in our experimental conditions.

2. EXPERIMENT

In this He I line shape study, linear low pressure pulsed discharge already described in [8] was used as a plasma source, see Figure 1. Therefore, only minimum details are given here for completeness. A pulsed discharge has the tungsten electrodes mounted inside quartz tube (inner diameter 8 mm). Both electrodes have 0.6 mm diameter central openings to enable spectroscopic measurements along the axis of plasma column. Continuous flow of helium or helium with 3% of hydrogen (initial gas pressure in the discharge tube: 120 mbar) was used. A typical current shape measured by Rogowski coil and recorded with an oscilloscope is shown in Figure 2. The discharge was driven by

the low inductance 15 μF capacitor charged up to 9 kV. The pulse-to-pulse current reproducibility, significantly improved by dc glow preionization, was better than 1%.

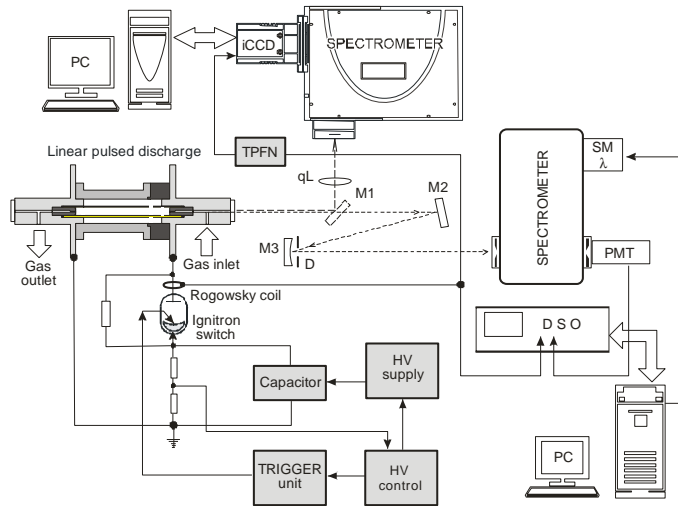


Figure 1. Experimental setup

For data recording and acquisition two systems were used. One based on a 0.3 m Shamrock 303 spectrometer equipped with Andor ICCD camera DH724 and another based on scanning 1m McPherson monochromator equipped with photomultiplier and digital storage oscilloscope. A 1:1. axial image of plasma source was projected on the entrance slits of both spectrometers by means of corresponding folding mirrors and quartz focusing lens or focusing mirror. The recording systems were synchronized with the pulse from Rogowsky coil.

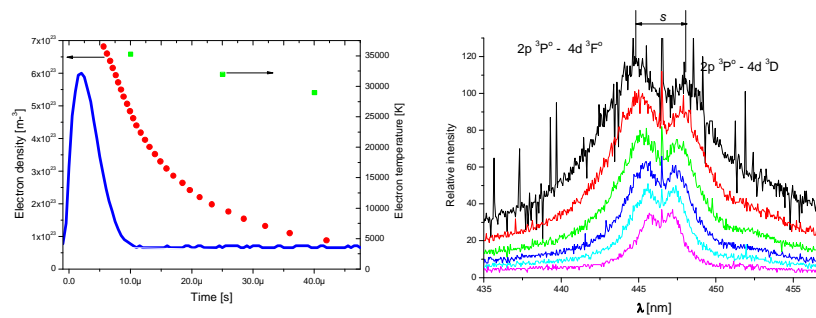


Figure 2. a) Current pulse, electron density and electron temperature decay. b) The overall shape of the He I 447 nm lines during plasma decay.

The electron temperature was determined from lines at 386.26, 412.805, 413.089, 597.756, 597.893, 634.71 and 637.136 nm during plasma decay, see Figure 2a.

Plasma electron density was determined from the wavelength separation between allowed He I 447.1 nm ($2p^3P^o - 4d^3D$) line and its forbidden component ($2p^3P^o - 4d^3F^o$) recorded during plasma decay (at different times after current maximum, see Figure 2, and evaluated using approximate formula [8])

$$\log_{10}(N_e) = 21.5 + \log_{10} \left(\left(\frac{s}{0.1479} \right)^{b(T_e)} - 1 \right) \quad (1)$$

where $b(T_e) = 1.46 * 8380 / T_e$ and T_e is shown in Figure 2a.

3. RESULTS AND DISCUSSIONS

The shape of hydrogen Balmer alpha as well as profiles of neutral helium lines 667.8 and 706.5 nm recorded at different moments of plasma decay are presented in Figure 3. The narrow peaks visible in the vicinity of all line profiles originate from the low electron density plasma jet. The plasma jet is formed due to rapid plasma expansion through the small (0.6 mm diameter) openings located at the end parts of electrodes, see Fig.1.

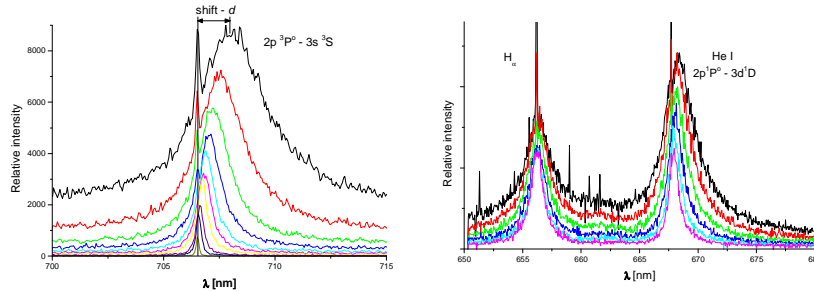


Figure 3. Shapes of the He I lines at 706.5 and 667.8 nm (together with hydrogen Balmer alpha line) at different times of plasma decay.

The side-on observation study of this jet was not possible to perform due to mechanical construction of the discharge tube. From the end-on observation of emitted radiation one can conclude that: a) narrow peaks were observed in close vicinity of all maxima of recorded lines, b) the wavelength of each line peak was the same for all recordings during plasma decay and coincide with position of corresponding spectral line maximum recorded at very late time of plasma decay, see lowest profile in Figure 3a. In addition, line widths of those narrow peaks were close to the instrumental half-width and the wavelength difference between narrow peaks of the hydrogen Balmer alpha line and neutral helium line 667.8

nm corresponds to wavelength separation between unshifted lines evaluated from wavelength tables. Therefore, the line shifts were determined as wavelength separation between line maximum and corresponding narrow peak. Measured line shifts, theoretical and other experimental data are presented in Figure 4

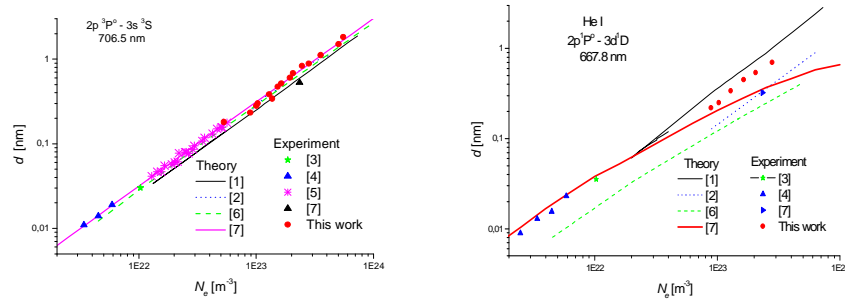


Figure 4. The comparison of the theoretical and experimental data for the shift of the He I lines at: a) 706.5 nm and b) 667.8 nm.

As can be seen from Figure 4, characteristic deviation from the straight line of line shift dependence for N_e greater than 10^{23} m⁻³ was not detected in our experiment. In order to resolve this discrepancy at larger N_e additional measurements progress.

Acknowledgements

This work is partially supported by Ministry for education, science and technology under the grant IO 171014 and III 045016.

REFERENCES

- [1] H. R. Griem *Spectral line broadening by plasmas*, (New York, 1974).
- [2] M. S Dimitrijević and S. Sahal-Brechot, *Astr. & Astrophysics* 82, 519 (1990).
- [3] D. E. Kelleher, *J. Quant. Spectrosc. Radiat. Transfer* 25, 191 – 220 (1981)
- [4] Z. Mijatović, N. Konjević, M. Ivković and R. Kobilarov, *Phys. Rev. E* 51, 4891 (1995).
- [5] C. Pérez, J. A. Aparicio, I. de la Rosa, S. Mar and M. A. Gigosos, *Phys. Rev. E* 51, 3764 (1995).
- [6] B. Omar, S. Günter, A. Wierling and G. Röpke, *Phys. Rev. E* 73, 056405 (2006).
- [7] M. Gigosos, S. Djurovic, I. Savic, D. Gonzalez-Herrero, Z. Mijatovic and R.Kobilarov, *Astronomy & Astrophysics* 561, 135 (2014).
- [8] M. Ivković, M. A. Gonzalez, S. Jovičević, M. A. Gigosos and N.Konjević, *Spectrochimica Acta B* 65, 234 (2010)

ON THE POSSIBILITY OF THE ELECTRON DENSITY ESTIMATION BY USING THE INTENSITY RATIO OF TWO O II SPECTRAL LINES

S. Djurović, Z. Mijatović, I. Savić, L. Gavanski and R. Kobilarov

University of Novi Sad, Faculty of Sciences, Department of Physics, Trg Dositeja Obradovića 4, 21000 Novi Sad, Serbia

Abstract. In this work we would like to show the possibility of the electron density determination by using the intensity ratio of O II 441.491 nm and O II 441.697 nm line. The experiment performed in plasma produced in a small electromagnetic shock T-tube showed that the intensity ratio between the two mentioned ionized oxygen spectral lines is sensitive to electron density changes.

1. INTRODUCTION

The possibilities and methods for plasma electron density determination are always of interest for scientific purposes as well as for plasma applications. It is well known that, in optical spectroscopy, hydrogen and helium spectral lines are the most suitable lines for electron density determination. If the plasma does not contain hydrogen or helium, other lines can be used for plasma diagnostic purposes. Namely, in cases where the relation between theoretical and experimental Stark parameters, halfwidths and shifts, is well established, these parameters can be used for electron density determination. In this case we would like to present the possibility of the electron density determination by using the intensity ratio of O II 441.491 nm and O II 441.697 nm lines.

2. EXPERIMENT

In this experiment we used a small electromagnetically driven T-tube as a plasma source. More details can be found in [1,2]. Here, some details will also be given for the sake of completeness. The T-tube is made of glass with the inner diameter of 27 mm. The brass reflector is placed at 140 mm from the discharge electrodes. The filling gas was pure helium at pressures of 200, 300 and 400 Pa. Ionized oxygen and silicon also appear as a very small impurity of the helium plasma. They originate from the glass T-tube walls. The T-tube was energized by

using a 4 μF capacitor bank charged up to 20 kV. The scheme of the experimental arrangement is the same as is given in [3] (Figure 1). The discharge was initiated by the 11 kV trigger pulse via the spark-gap.

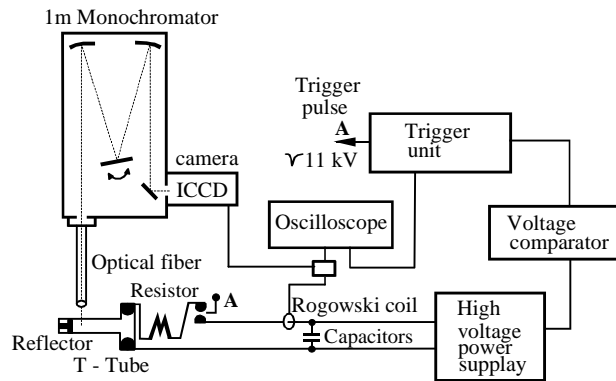


Figure 1. Block diagram of the optical and electrical arrangement of the T-tube experiment.

The discharge current was monitored by a Rogowski coil and an oscilloscope. Spectroscopic observations of plasma were made by a 1-m monochromator and an ICCD camera. The signal from the Rogowski coil was also used as the trigger signal for the ICCD camera. The observation point was fixed at 20 mm in front of the reflector. The exposure time was 0.5 μs . The optical signal was led to the entrance of the monochromator by optical fiber. The monochromator is equipped with a 1200 g/mm^{-1} grating, with 0.833 nm/mm^{-1} inverse linear dispersion.

Every experimental line profile is obtained as an average profile from 25 shots. The whole system, monochromator, ICCD camera and oscilloscope, was controlled by a personal computer.

Special attention was paid to the self-absorption checking test. The standard test, with the an external mirror behind the plasma, shows that the self-absorption effect is completely negligible under used experimental conditions.

3. RESULTS AND CONCLUSIONS

The example of the part of the spectrum which contains the mentioned O II lines and He I 447.148 nm line is shown in Fig. 2. The lines with smaller intensities, which appear over the helium line profile, are mostly other O II lines.

He I 447.148 nm line is used for electron density, N_e , determination. Two methods were applied. One method uses the peak separation, $\Delta\lambda$, while the other uses the halfwidth, w , of the helium line. For the electron density determination by using $\Delta\lambda$ we used the formula given in Ivković et al [4] and in

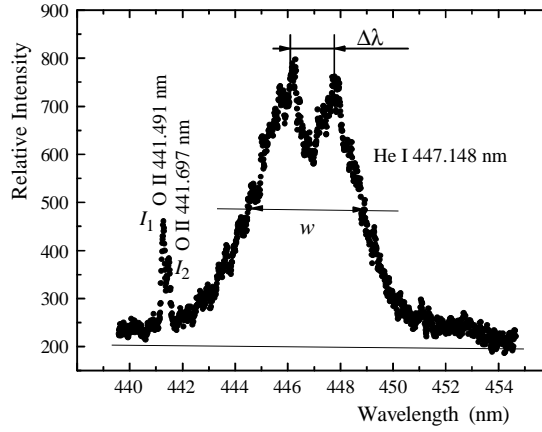


Figure 2. Part of the spectrum with the spectral lines of interest. The parameters of the helium line are also indicated.

Pérez et al [5] and halfwidth data given in Pérez et al [5]. The results are given in Table 1 and shown in Fig . 3. It is obvious that the ratio between intensities of the O II 441.491 nm (I_1) and O II 441.697 nm (I_2) line changes if the electron density changes. The electron temperature was estimated from the Boltzmann plot of several Si II lines.

Table 1. The results of the intensity measurements

T_e (K)	Ref.	Method	N_e (m^{-3})	I_1/I_2
14000	Ivković et al [4]	peak separation $\Delta\lambda$	$1.18 \cdot 10^{23}$	1.76
	Pérez et al [5]	peak separation $\Delta\lambda$	$1.05 \cdot 10^{23}$	
	Pérez et al [5]	halfwidth w	$1.15 \cdot 10^{23}$	
14000	Ivković et al [4]	peak separation $\Delta\lambda$	$1.30 \cdot 10^{23}$	1.75
	Pérez et al [5]	peak separation $\Delta\lambda$	$1.16 \cdot 10^{23}$	
	Pérez et al [5]	halfwidth w	$1.25 \cdot 10^{23}$	
15000	Ivković et al [4]	peak separation $\Delta\lambda$	$2.22 \cdot 10^{23}$	1.62
	Pérez et al [5]	peak separation $\Delta\lambda$	$2.12 \cdot 10^{23}$	
	Pérez et al [5]	halfwidth w	$1.90 \cdot 10^{23}$	
16000	Ivković et al [4]	peak separation $\Delta\lambda$	$2.67 \cdot 10^{23}$	1.50
	Pérez et al [5]	peak separation $\Delta\lambda$	$2.74 \cdot 10^{23}$	
	Pérez et al [5]	halfwidth w	$2.60 \cdot 10^{23}$	
16000	Ivković et al [4]	peak separation $\Delta\lambda$	$2.84 \cdot 10^{23}$	1.35
	Pérez et al [5]	peak separation $\Delta\lambda$	$3.00 \cdot 10^{23}$	
	Pérez et al [5]	halfwidth w	$2.70 \cdot 10^{23}$	

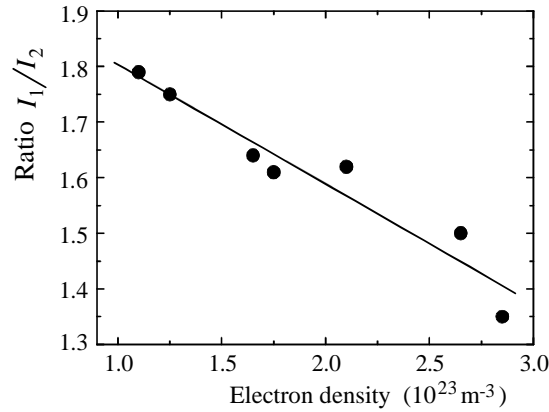


Figure 3. The intensity ratio dependence on electron density

Small changes in temperature have no significant influence on electron density determination. This can be seen from the formula given in Ivković et al [4].

Here, only preliminary measurements are presented. From Figure 1 it can be seen that there were difficulties in determining the parameters $\Delta\lambda$ and w . Namely, several O II lines which are superimposed on the He I 447.148 nm line make the determination of the parameters less accurate. This influence was not analyzed in this preliminary measurement. Our intention is just to pay attention to the sensitivity of O II 441.491 nm and O II 441.697 nm line intensity ratio to changes of plasma electron density. In order to use this parameter for diagnostic purposes it is necessary to provide more precise measurements and extend the electron density interval.

Acknowledgements

This work is partially supported by Ministry of education, science and technological development of Republic of Serbia under the grant NO 171014.

REFERENCES

- [1] S. Djurović, D. Nikolić, I. Savić, S. Sörge and A. V. Demura, *Phys. Rev. E* 71, 036407 (2005).
- [2] S. Djurović, M. Ćirišan, A. V. Demura, G. V. Demchenko, D. Nikolić, M. A. Gigosos and M. Á. González, *Phys. Rev. E* 79, 046402 (2009).
- [3] M. A. Gigosos, S. Djurović, I. Savić, D. González-Herrero, Z. Mijatović and R. Kobilarov, *Astron. Astrophys.* 561, A135 (2014).
- [4] M. Ivković, M. A. González, S. Jovičević, M. A. Gigosos and N. Konjević, *Spectrochim. Acta B* 65, 234 (2010).
- [5] C. Pérez, I. de la Rosa, J. A. Aparicio, S. Mar and M. A. Gigosos, *Jpn. J. Appl. Phys.* 35, 4073 (1996).

STARK BROADENING PARAMETERS OF Li I 670.8 nm

T. Gajo, Z. Mijatović, S. Djurović, I. Savić and R. Kobilarov

*University of Novi Sad, Faculty of Sciences, Department of Physics
Trg Dositeja Obradovića 4, 21000 Novi Sad, Serbia
E-mail: dorag@uns.ac.rs*

Abstract. Stark width and shift of Li I resonant doublet at 670.8 nm is reported. As plasma source, electromagnetically driven T-shaped shock tube was used. Measurements were done at plasma electron density of $8.85 \cdot 10^{22} \text{ m}^{-3}$ and plasma temperature of 16000 K. Obtained results are compared with the theoretical and available experimental results.

1. INTRODUCTION

Stark broadening parameters of Li I spectral lines have been rarely measured. There are a small number of papers devoted to this subject and only three [1-3] were selected in critical review [4] and only one devoted to Li 670.8 nm spectral line [5] (mentioned in [6]). Actually, lithium can be found in the star's atmosphere, laser produced lithium plasmas, Lithium Tokamak Experiments (LTX) and other tokamaks and plasmas. In all of these plasmas lithium lines can be used for plasma diagnostics purposes, especially for plasma electron density determination. Great interest in Li I spectral lines appeared in the last period (see for example Ref. 7 and reference therein).

Here, we report results of measured Stark broadening parameters (width and shift) of Li I 670.8 nm resonant spectral line. This line is actually consisted of two close spectral lines at 670.776 nm and 670.791 nm of the multiplet $2s^2S - 2p^2P^0$. Measurements were done using electromagnetically driven T-shaped shock wave tube as a plasma source.

2. EXPERIMENT AND DATA PROCESSING

Experimental set up is shown in Fig. 1. Radiation from the T-tube is led through an optical fiber to the entrance slit of 1-m monochromator equipped with 1200 g/mm diffraction grating (McPherson 2061). The spectra were recorded by fast ICCD camera (Stanford Research 4 Quik Edig). The view angle of optical fiber is 2 deg. This provided satisfactory spectral intensities. It is well known that T-tube plasmas are homogeneous along the radius. The working gas was helium

under the pressure of 200 Pa. The reflector (see Fig. 1.) was covered with LiCl. The Shock wave, developed during discharge, caused the ejection of Li atoms and formation of plasmas containing Li.

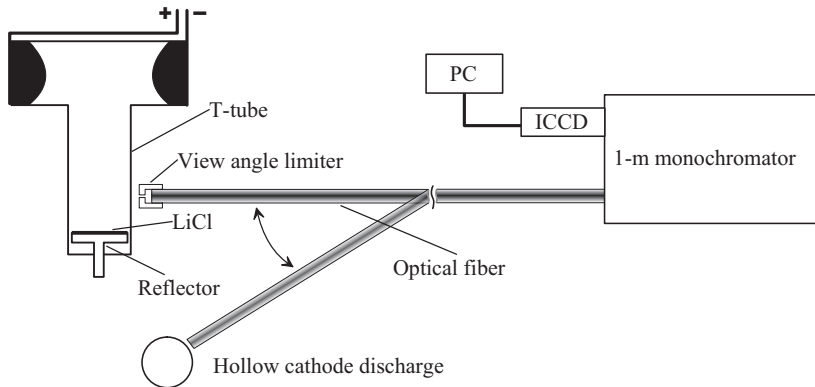


Figure 1. Experimental set up.

The spectral range covered by spectroscopic system was between 663.7 nm and 674.2 nm. This enabled simultaneous recordings of He I 667.8 nm spectral line and radiation of Li I at 670.8 nm. As a result of plasma ablation from glass walls some Si lines also appeared. Recorded spectrum is shown in Fig. 2 as an average from 50 shots. This number of shots is chosen in the way that standard deviation of the average spectral recordings (in the range of spectral lines) was inside 2-3 %. For the shift measurements two Ne I spectral lines emitted from hollow cathode discharge at 667.8276 and 671.7043 nm were used.

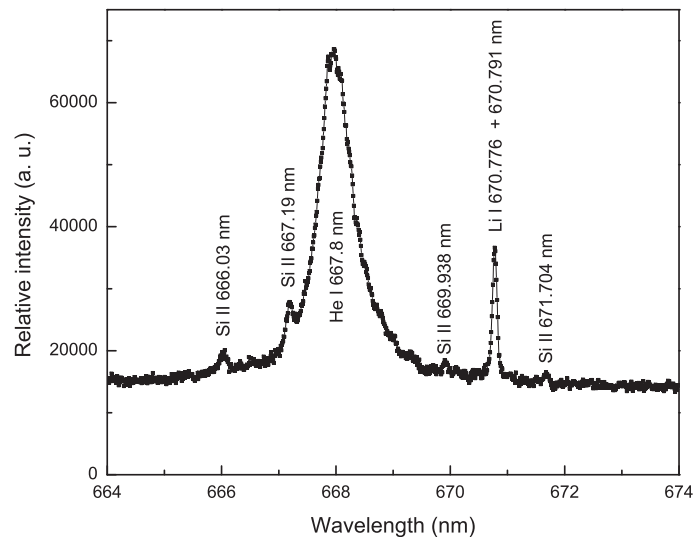


Figure 2. Recorded spectrum.

Since the plasma was practically pure helium plasma the method of line-to-continuum ratio was applied for plasma temperature determination using He I 667.8 nm spectral line [8]. Plasma electron density was determined from the Stark width of the same line in conjunction with the theoretical predictions [9] and results from [10]. In these procedures deconvolution of $j_{A,R}(x)$ profile (inherent to neutral spectral lines) and Gaussian (consisting of instrumental and Doppler component) was applied. It is well known that T-tube plasmas are in LTE and that gas and electron temperatures are equal. This is confirmed through mentioned deconvolution procedure when one of the entering parameter was gas temperature (Doppler width). Later it was also confirmed through the processing of Li I lines. From the previous measurements at similar experimental conditions [11] it was shown that even He I lines are not self absorbed, so such a small amount of lithium cannot cause self absorption. Obtained values for plasma electron density and temperature are $8.85 \cdot 10^{22} \text{ m}^{-3}$ and 16000 K, respectively.

Investigated Li I spectral lines are separated 0.015 nm but belong to the same multiplet. This means that they have the same Stark broadening parameters. Accordingly to NIST Atomic Data Base [12] these lines are of the same intensity. This fact simplifies the simultaneous procedures of separation and deconvolution of the profiles. Another facilitating fact is that these lines are weakly influenced by ions, i.e. the profiles are almost pure Lorentzian [9]. Having this in mind, the experimental profile of Li I spectral recordings corrected on underlying continuum were fitted on two Voigt profiles separated by 0.015 nm. As fixed input parameters measured values of instrumental halfwidth (0.054 nm), plasma electron density and plasma temperature (Doppler width 0.0587 nm) are taken into account. In Fig. 3 experimental profile corrected to underlying continuum together with the fitted profile is presented.

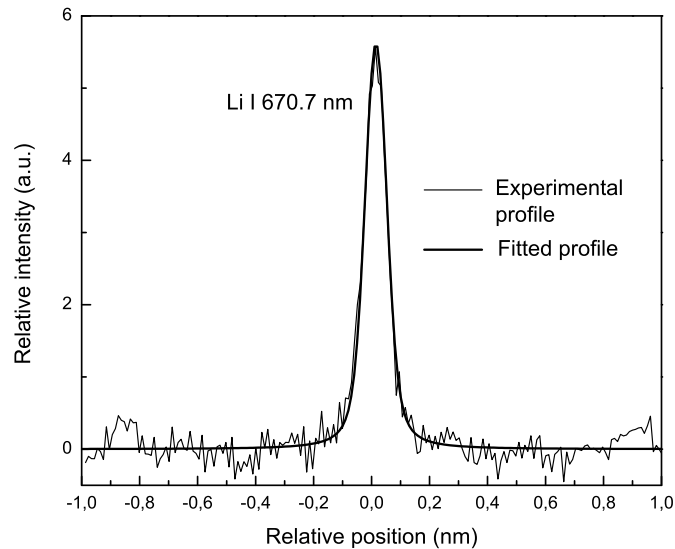


Figure 3. Experimental and fitted profile of Li I 670.7 nm line.

3. RESULTS AND CONCLUSIONS

After separation and deconvolution procedures it was found that Stark width of Li lines was 0.0350 nm. Estimated error, including errors for all measured values found to be about less than 10 %. Obtained Stark width was compared with the value predicted by [9] scaled to measured plasma electron density and temperature. It was found that ratio of measured and theoretical value is 0.989. The only available experimental results [5] gives this ratio of 1.03-1.04. The measured shift of the Li I lines was -0.0198 nm what gives the ratio to the theoretical value [9] of 3.09, while that ratio from [5] is 0.86.

Obtained Stark width in this work is in good agreement with the theoretical and experimental results. In this work the deconvolution and separation of the Li I profiles were applied, while in [5] such procedures were not reported. On the other hand, considerable disagreement between measured shift in this work and both, theory [9] and experiment [5] is found. It must be noted that the shift of the investigated lines is very small and different methods for shift determination were applied in this work and in [5] where position of investigated lines at late time of plasma decay was used as referent position of unshifted line. Of course, much more advanced techniques applied in this work, than those applied in [5], should be taken into account.

Acknowledgements

This work is supported by Ministry of education, science and technological development under the grant NO 171014.

REFERENCES

- [1] R. von der Heide and H. J. Kusch, *Z. Astrophys.* 68, 1 (1968).
- [2] B. Ya'akobi, *Phys. Rev.* 176, 227 (1968).
- [3] V. A. Zhirnov, Yu. A. Tetyukhin, *Zh. Prikl. Spektroskop.* 18, 596 (1973).
- [4] N. Konjević and J. R. Roberts, *J. Phys. Chem. Ref. Data* 5, 209 (1976).
- [5] J. Purić, J. Labat, Lj. Ćirković, I. Lakićević and S. Djeniže, *J. Phys. B: Atom. Molec. Phys.* 10, 2375 (1977).
- [6] N. Konjević and M. S. Dimitrijević, *J. Phys. Chem. Ref. Data* 13, 619 (1984).
- [7] I. P. Dojčinović, I. Tapalaga and J. Purić, *MNRAS* 429, 2400 (2013).
- [8] H. R. Griem, *Plasma Spectroscopy*, (McGraw Hill, New York, 1964).
- [9] H. R. Griem, *Spectral Line Broadening by Plasmas*, (Academic Press, New York and London, 1974).
- [10] Z. Mijatović, N. Konjević, M. Ivković and R. Kobilarov, *Phys. Rev E* 51, 4891 (1995).
- [11] M. A. Gigosos, S. Djurović, I. Savić, D. González-Herrero, Z. Mijatović and R. Kobilarov, *Astron. Astrophys.* 561, A135, p. 1-13 (2014).
- [12] http://physics.nist.gov/PhysRefData/ASD/lines_form.html

TIME RESOLVED ICCD MEASUREMENTS OF ASYNCHRONOUS DOUBLE PLASMA JET

Dejan Maletić¹, Nevena Puač¹, Gordana Malović¹ and Zoran Lj. Petrović¹

¹*Institute of Physics, University of Belgrade, Pregrevica 118, 11080 Belgrade*

Abstract. In this paper we investigate behaviour of double plasma jet device by using electrical and time resolved optical emission measurements. Our plasma jet system is consisted of two single jets put in parallel with 20 mm distance between the glass tubes. Applied voltage was around 7 kVpp and power transmitted to the plasma was 1.8 W. Target made of plastic was placed at the distance of 15 mm from both jet nozzles. Here we will show time resolved ICCD images of double jet system. From the images it is clear that the plasma jets are not time and space synchronized despite the same power supply. The delay between appearances of the plasma packages outside the glass tubes of the jets is approximately 1.6 μ s.

1. INTRODUCTION

Plasma jets are nowadays most common laboratory plasmas because of its simple construction and relatively low price. They are powered with high voltage signals, sine wave or pulsed, produced by a power supply that is usually custom made [1, 2]. Noble gas flow is used for obtaining stable glow discharge, decreasing breakdown voltage and for transport of reactive species to the sample surface. Plasma jets are relatively small in diameter, only few millimetres, but rich with chemical reactive species like radicals (N, O), ions (N^+ , O^+ , N_2^+ , O_2^+ , He^+) and molecules (O_3 , NO) [3, 4]. Small size of single plasma jet is suitable for precise treatment, but for covering larger areas jets can be arranged in 1 D or 2 D arrays [5-7]. One the most common application field of plasma jet, as a single or in array, is in medicine because of disinfection efficiency, wound healing, tooth bleaching, caries removal, etc. [8, 9]. Strong jet to jet interaction, coupling between them and with the electrical circuit are a key factors for understanding homogeneity and behaviour of the array. In this paper we will present results of asynchronous behaviour of two parallel plasma jets obtained by using time resolved ICCD measurements.

2. EXPERIMENTAL SETUP

Double plasma jet (see figure 1) used in this research is made of two glass tubes (inner diameter 4 and outer diameter 6 mm). The distance between the centres of the jets is 2 cm. Two pair of electrodes made of copper foil (9 mm

in diameter) are wrapped around the tubes. Powered electrodes are closer to the edge of the tube. The gap between the grounded and powered electrode is 15 mm in both jets. Plastic target is placed at the distance of 15 mm from the both edges of the glass tubes. Behind the target adhesive copper foil is placed and connected to the resistor of 100 k Ω in the grounded branch of the circuit. For powering plasma jet we use wave generator, custom made amplifier and high voltage transformer. The powering system is adjusted with variable inductance for the operation frequency of 80 kHz. 660 k Ω resistors are placed between power supply and powered electrodes and between grounded electrodes and resistor of 100 k Ω . Helium was used as a working gas and the flow rate was 4 slm.

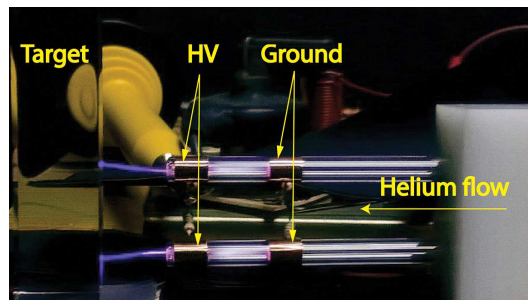


Figure 1. Experimental setup

3. RESULTS AND DISCUSSION

Current and voltage waveforms with the triggering positions are presented on figure 2. Peak to peak voltage is about 7 kVpp and the current is about 5 mA_{pp}. When plasma is ignited both signals are almost in phase with voltage slightly lagging the current signal. Triggering positions are marked with letters (A-P) from 0 to 12.0 μ s with a step 0.4 μ s. Calculated power transmitted to the plasma was 1.8 W.

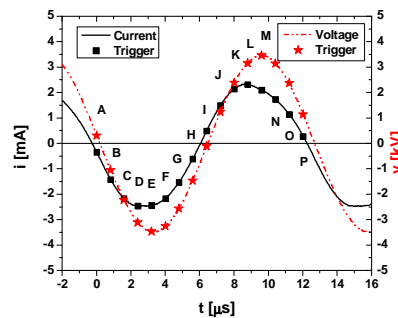


Figure 2. Current and voltage signals with labelled trigger positions

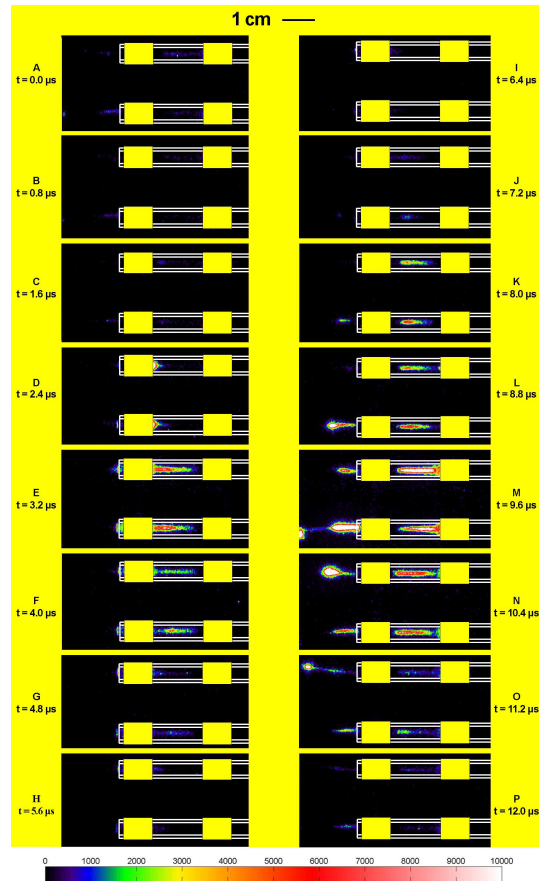


Figure 3. Time resolved ICCD images for double plasma jet, helium flow 4 slm, and applied power 1.8 W

ICCD images are presented in figure 3. In first triggering position A ($0 \mu\text{s}$) current is slightly below and voltage above zero. For this position light emission is very low with the afterglow from previous period when plasma package was travelling between the edge of the glass tube and target. At position D ($2.4 \mu\text{s}$) plasma is starting to ignite at the right edge of the powered electrode. For this triggering position voltage and current are at the negative minimum. With the increase in the current and voltage signal plasma is expanding towards the grounded electrode (triggering position E-G). In the positive slopes of the current and voltage signals light emission is almost absent until the triggering point K ($8.0 \mu\text{s}$). Now current signal has reached maximum and electrical field is sufficient for the plasma bullet precursor formation, but only in the lower jet. At the same time plasma precursor is not formed in the second jet (upper jet in figure 1.). At position M ($9.6 \mu\text{s}$) plasma reaches target in first and at position O ($11.2 \mu\text{s}$) in the second jet. The average speed of plasma packages in both jets

is about 6.4 km/s. This is much lower than 17.5 km/s obtained in case of single plasma jet without target and about the same for the inter electrode speed 5 km/s [1]. Delay between the formations of the plasma packages outside the glass tube for both plasma jets is approximately 1.6 μ s. Also, from the images it can be seen that there is some repulsion between two positive plasma channels.

4. CONCLUSION

Here we presented results of double plasma jet system. By using time resolved ICCD measurements we have detected asynchronous behaviour of the jets. Asynchronous behaviour of the plasma jets are not yet fully understood phenomenon and it needs further investigation. Fine time tuning of the jets in array can open new possibilities in plasma application. Also different jets can use different gas mixtures especially in thin film multi-layer and nano coating deposition.

Acknowledgements

This research has been supported by the Ministry of Education and Science, Serbia, under projects ON171037 and III41011.

REFERENCES

- [1] N. Puač, D. Maletić, S. Lazović, G. Malović, a. Orević, and Z. L. Petrović, *Appl. Phys. Lett.* 101, 024103 (2012).
- [2] A. V. Nastuta, I. Topala, C. Grigoras, V. Pohoata, and G. Popa, *J. Phys. D. Appl. Phys.* 44, 105204 (2011).
- [3] J.-S. Oh, Y. Aranda-Gonzalvo, and J. W. Bradley, *J. Phys. D. Appl. Phys.* 44, 365202 (2011).
- [4] N. Selaković, N. Puač, G. Malović, and Z. L. Petrović, GD2014 conference proceedings, Orlean, France, to be published (2014).
- [5] M. Ghasemi, P. Olszewski, J. W. Bradley, and J. L. Walsh, *J. Phys. D. Appl. Phys.* 46, 052001 (2013).
- [6] Q. Y. Nie, Z. Cao, C. S. Ren, D. Z. Wang, and M. G. Kong, *New J. Phys.* 11, 115015 (2009).
- [7] J. T. Hu, X. Y. Liu, J. H. Liu, Z. L. Xiong, D. W. Liu, X. P. Lu, F. Iza, and M. G. Kong, *Phys. Plasmas* 19, 063505 (2012).
- [8] G. Y. Park, S. J. Park, M. Y. Choi, I. G. Koo, J. H. Byun, J. W. Hong, J. Y. Sim, G. J. Collins, and J. K. Lee, *Plasma Sources Sci. Technol.* 21, 043001 (2012).
- [9] S. Lazović, N. Puač, M. Miletić, D. Pavlica, M. Jovanović, D. Bugarski, S. Mojsilović, D. Maletić, G. Malović, P. Milenković, *New J. Phys.* 12, 83037 (2010).

CW-CRDS STUDY OF RECOMBINATION OF H_3^+ IONS WITH ELECTRONS IN STATIONARY AFTERGLOW PLASMA

Ábel Kálosi¹, Petr Dohnal¹, Peter Rubovič¹, Radek Plašil¹ and Juraj Glosík¹

¹*Department of Surface and Plasma Science, Faculty of Mathematics and Physics, Charles University in Prague, Czech Republic*

Abstract. The experimental study of H_3^+ ion recombination with electrons is presented. The use of continuous wave cavity ring-down spectroscopy enabled in situ determination of abundances, the rotational and the translational temperatures of the recombining ions. We monitored the population of three rotational states of the ground vibrational state, corresponding to para and ortho nuclear spin states, in the discharge and the afterglow plasma. From time resolved number density measurements we determined the effective recombination rate coefficient of the ion-electron recombination at various experimental conditions.

1. INTRODUCTION

The study of the dissociative recombination of the simplest triatomic ion H_3^+ has challenged experimentalists and theorists for many years [1]. Because of the high hydrogen abundance in the universe, the process of binary recombination of H_3^+ plays a pivotal role in the chemical evolution of interstellar clouds, and also in hydrogen-containing plasmas. A successful quantum mechanical description of H_3^+ recombination was developed relatively recently [2]. Storage ring experiments with cold ion sources obtained a binary recombination rate coefficient in good agreement with this description [3,4]. One important part of the study of H_3^+ recombination with electrons was the difference between the recombination rate coefficients measured in plasma-type experiments and storage ring experiments. Experiments in helium buffered afterglow plasmas showed very fast helium assisted ternary recombination, which leads to enhanced deionization of the plasma [5]:



where α_{eff} is the effective coefficient of recombination, defined as the apparent binary rate coefficient (for details see Ref. [6]). This process eliminated many remaining discrepancies in H_3^+ recombination studies. A prominent exception to this is Amano's spectroscopic study [7] in pure H_2 buffered afterglow plasma,

which gave even higher recombination rate coefficient that was independent on H_2 number density. We report preliminary results of experiments conducted using SA-CRDS (stationary afterglow with cavity ring-down spectrometer) apparatus in helium buffered afterglow plasma. The dependence of effective recombination rate coefficient on H_2 number density at 300 K was investigated.

2. EXPERIMENT

The SA-CRDS apparatus is described in detail elsewhere (see e.g. Refs. [6,8]), so only a short description will be given here. In the experiment, the plasma is formed in a pulsed microwave discharge in a mixture of He/Ar/ H_2 (with typical composition 10^{17} , 10^{14} , $10^{14} - 10^{17} \text{ cm}^{-3}$). The power from the microwave generator is cut off by an external high voltage switch within a fall time of $< 30 \mu\text{s}$. The fused silica discharge tube (inner diameter $\sim 1.5 \text{ cm}$) is cooled by liquid nitrogen or pre-cooled nitrogen gas in the range of 77–300 K. To avoid the excessive heating of the gas during the discharge a fairly low microwave power is used (in the range 5–15 W).

The ion density measurement is based on cavity ring down spectroscopy in the continuous wave modification (cw-CRDS), for details see Refs. [8,9]. The light source is a distributed feedback (DFB) laser diode with central wavelength of 1381.55 nm, linewidth $< 2 \text{ MHz}$ and maximum optical output power of 20 mW. The wavelength is measured absolutely by EXFO WA-1650 Wavemeter and relatively by Fabry-Perot etalon. The light signal exiting the optical cavity is detected by InGaAs avalanche photodiode. A schematic picture of the apparatus is shown in Fig. 1.

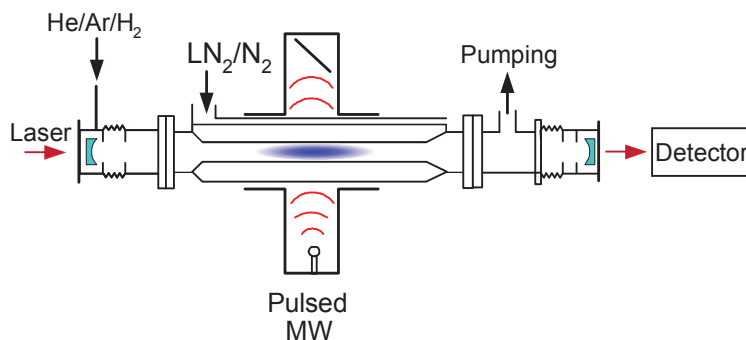


Figure 1. Schematic diagram of the Stationary Afterglow apparatus with cw-CRDS absorption spectrometer. The discharge tube at the centre (containing a He/Ar/ H_2 gas mixture in this case) is immersed in liquid or pre-cooled gaseous nitrogen. The plasma is ignited periodically by pulsed microwave discharge (MW) in the optical cavity, formed by two highly reflective mirrors. The light signal exiting the optical cavity is detected by an InGaAs avalanche photodiode.

The time resolved densities of three of the lowest rotational states of the ground vibrational state of the H_3^+ ion were measured using the second overtone

transitions $3v_2^1(2,1) \leftarrow 0v_2^0(1,1)$, $3v_2^1(2,0) \leftarrow 0v_2^0(1,0)$ and $3v_2^1(4,3) \leftarrow 0v_2^0(3,3)$, corresponding to a para and two ortho states (for details on spectroscopic notation see Ref. [10]). The overall number density of H_3^+ ions is then calculated under assumption of thermal population of states. The effective recombination rate coefficients are evaluated from the H_3^+ ion density decay in the afterglow of the discharge. For details on data analysis see Ref. [6]. The kinetic temperature of the ions in the discharge and the afterglow plasma is determined from the Doppler broadening of the absorption lines. Example of measured absorption line profiles is plotted in Fig. 2. The rotational temperature is evaluated from the relative population of probed states. Both kinetic and rotational temperature of the H_3^+ ions is close to the temperature of the discharge tube (T_{wall}) within a few Kelvins. For thorough discussion on thermalization of H_3^+ dominated plasma see Ref. [6].

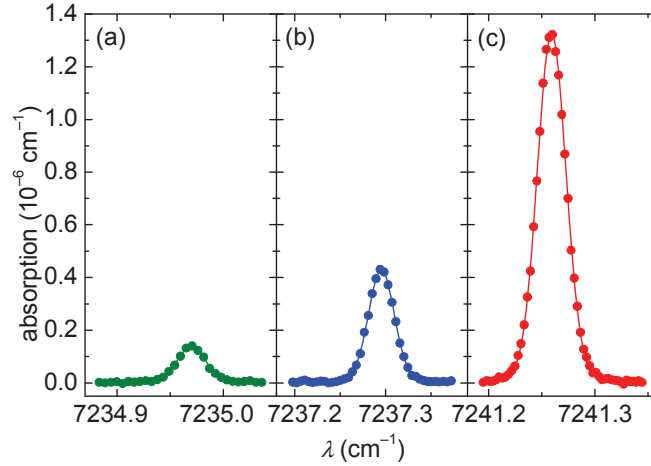


Figure 2. Example of absorption line profiles of the H_3^+ ion measured in 850 Pa of helium, (a) transition $3v_2^1(4,3) \leftarrow 0v_2^0(3,3)$, (b) transition $3v_2^1(2,1) \leftarrow 0v_2^0(1,1)$, (c) transition $3v_2^1(2,0) \leftarrow 0v_2^0(1,0)$. The mean value of the kinetic temperatures evaluated from the Doppler broadening of the absorption lines is $T_{\text{kin}} = (115 \pm 10)$ K.

3. EXPERIMENTAL DATA AND RESULTS

The dependence of effective recombination rate coefficient on H_2 number density was studied at temperature of $T_{\text{wall}} = 300$ K and for H_2 number densities in the range of $10^{14} - 3 \times 10^{16} \text{ cm}^{-3}$. The results are plotted in Fig. 3. As can be seen from Fig. 3, the value of effective recombination rate coefficient increases with increasing H_2 number density for $[H_2] < 8 \times 10^{15} \text{ cm}^{-3}$ and then saturates at a value of $\alpha_{\text{eff}} \approx 2 \times 10^{-7} \text{ cm}^3 \text{ s}^{-1}$. This is in good agreement with the values obtained by Amano [7] in pure H_2 that are indicated by dashed line in Fig. 3.

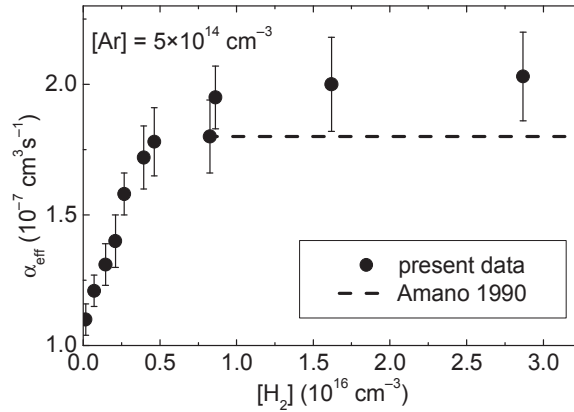


Figure 3. Measured dependence of α_{eff} on H_2 number density at $T_{\text{wall}} = 300$ K and $P = 900$ Pa of He in a He/Ar/ H_2 mixture. The values measured by Amano [7] in pure H_2 are indicated by dashed line.

4. SUMMARY AND CONCLUSIONS

The preliminary results of experimental study of H_3^+ recombination with electrons at temperature of $T_{\text{wall}} = 300$ K were presented. A nontrivial dependence of effective recombination rate coefficient on H_2 number density was observed, linear dependence at lower number densities and saturation in the interval studied by Amano. The results are summarized in Fig. 3. Further experiments are in progress.

Acknowledgements

This work was partly supported by GACR P209/12/0233, GACR 14-14649P and by GAUK 692214.

REFERENCES

- [1] M. Larsson and A. E. Orel, *Dissociative Recombination of Molecular Ions*, (Cambridge University Press, Cambridge, 2008).
- [2] V. Kokoouline, C. H. Greene and B. D. Esry, *Nature* 412, 891 (2001).
- [3] B. J. McCall et al., *Phys. Rev. A* 70, 052716 (2004).
- [4] H. Kreckel et al., *Phys. Rev. Lett.* 95, 263201, (2005).
- [5] J. Glosik et al., *Phys. Rev. A* 79, 052707 (2009).
- [6] P. Dohnal et al., *J. Chem. Phys.* 136, 244304 (2012).
- [7] T. Amano, *J. Chem. Phys.* 92, 6492 (1990).
- [8] P. Macko et al., *Int. J. mass Spectrom.* 233, 299 (2004).
- [9] D. Romanini et al., *Chem. Phys. Lett.* 264, 316 (1997).
- [10] C. M. Lindsay and B. J. McCall, *J. Mol. Spectrosc.* 210, 60 (2001).

SPECTROSCOPIC CHARACTERIZATION OF ELECTRICAL DISCHARGE PLASMA IN LIQUID

V. S. Burakov, M. I. Nedelko, V. V. Kiris, M. M. Mardanian, N. V. Tarasenko

*B. I. Stepanov Institute of Physics, National Academy of Sciences of Belarus,
68 Nezalezhnasti Ave., 220072 Minsk, Belarus*

Abstract. In this study, a pulsed electrical discharge in liquid has been used for production of semiconductor nanoparticles (NPs), in particular silicon nanocrystals and ternary chalcogenide compounds of copper. The NPs preparation conditions have been optimized using optical emission spectroscopy (OES) in the visible and near ultraviolet regions. The elements present in the plasma were identified. The electron density and temperature were determined from the analysis of the Stark broadening of the spectral lines and the Boltzmann distribution of the excited atoms, respectively.

1. INTRODUCTION

Electrical discharge assisted synthesis of nanomaterials is a new and exciting technique which provides rapid reaction rates, high energy efficiencies, and environmental safety. We have developed this method for synthesis of semiconductor silicon and multicomponent copper indium diselenide (CuInSe_2) nanoparticles [1,2]. Plasmas in liquids provide extremely rapid chemical reactions due to a presence of activated species and radicals under high pressure. The final size and composition of resultant particles are defined by the thermodynamic conditions of plasma (its temperature, density of atoms and ions). Accurate diagnostics of plasma parameters are important for a better understanding of the chemistry of this type of plasma. Although the plasmas produced in liquids are characterized by intense continuum emission spectra, spectroscopic techniques can be useful for plasma characterization and optimization of conditions in reactive plasma for composite NPs formation.

In the present paper optical emission spectroscopy technique has been developed and applied to evaluate parameters of the electrical discharge plasma in liquid (EDL). According to the experimental results, it has been revealed that electrical discharge plasma produced in liquid is rather dense because of the confinement effect of the ambient liquid, and has a high temperature. Parameters of plasmas in liquids, such as densities of atoms and electrons have been determined and capabilities of the formation of semiconductor NPs have been demonstrated.

2. EXPERIMENTAL

For synthesis of NPs two types of reactor cell design were constructed: the reactor containing two electrodes submerged into the liquid was used for generation of silicon nanoparticles and a funnel-shaped plastic cell with two coaxial vertically orientated electrodes made of a refractory metal was used for the synthesis of CuInSe_2 nanoparticles from the stoichiometrical mixture of copper, indium and selenium micropowders. Conical shape of the cell prevented removal of particles from the discharge zone. The power supply provided an alternating current (ac) spark discharge with a repetition rate of 100 Hz. The discharge was initiated by applying a high-frequency voltage of 8.5 kV. The optimal distance between the electrodes was 0.3-0.5 mm and 15-20 mm for the discharge chambers, shown in Figure 1a and 1b, respectively. The peak current of the pulsed spark discharge was 60 A with a pulse duration of 30 μs . With the purpose of determination the component composition of the electrical discharge plasma in liquid and optimization of the NPs formation process spectroscopic investigation has been performed since the erosion and atomization of the electrode material are largely responsible for the formation of particles in the discharge. Spectroscopic studies of plasma were performed using diffraction spectrograph (grating 1200 lines/mm) equipped with a CCD linear array.

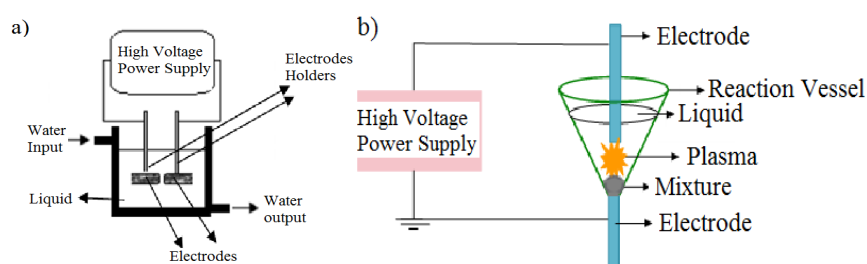


Figure 1. Schematic diagram of the discharge chambers for synthesis of NPs (a) and plasma processing of micropowders (b).

3. RESULTS AND DISCUSSION

Analysis of optical emission spectra allowed determining several parameters of discharge plasmas created in liquids. The emission spectra of EDL plasma consisted of lines corresponding to excited neutral and singly ionized species coming from the electrodes and products of liquid decomposition (OH radicals, atomic hydrogen (Balmer lines) and oxygen).

In case of Si-Si discharge in water and ethanol, the observed spectral lines were dominated by H_α and H_β hydrogen spectral lines, atomic and ionic lines of the silicon. The most intense lines in this spectra were Si I 288.157 nm, Si II 385.602 nm and Si I 390.552 nm. These spectral lines were used to

determine the electron temperature of the plasma. The electron density of the electrical discharge plasma were determined based on analysis of the shape of the recorded hydrogen H_α spectral line, assuming the dominant contribution comes from Stark broadening. For Si-Si discharge plasma, electron temperature was estimated to be around 1.03 and 0.88 eV for discharge in water and ethanol, respectively. The electron density in the plasma formed in water was significantly bigger than that produced in ethanol.

Fig.1 illustrates the emission spectrum of the plasma generated between the tungsten electrodes submerged in the suspension with copper, indium and selenium particles in ethanol. In this case, the observed spectral lines in the spectrum are H_α and H_β lines related to the hydrogen, atomic lines of Cu I 406.26 nm, In I 451.12 nm, In II 468.11 nm, Cu I 470.45 nm and a few molecular bands, such as the C_2 Swan bands of C_2 dimers, which can be attributed to the fragments of the dissociated ethanol molecules.

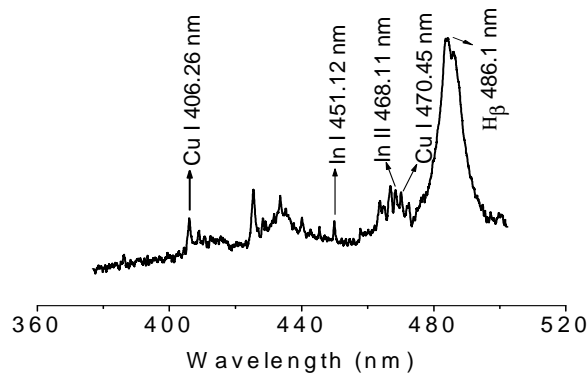


Figure 2. Typical emission spectrum of $CuInSe_2$ nanoparticles formed by plasma treatment of copper, indium and selenium powders mixture between tungsten electrodes submerged in ethanol.

The profiles of the H_α and H_β Balmer lines were used to measure the electron density of the electrical discharge plasma produced in ethanol with suspended copper, indium and selenium microparticles. Comparing the Stark widths obtained from the deconvolution of the H_α and H_β line profiles indicates they are valid within experimental precision for derivation of the electron densities although, the H_α line precision is not as good as in the case of H_β due to its sensitivity for self-absorption.

The measured values of the broadening of hydrogen Balmer H_α and H_β lines in the plasma formed during the electrical discharge processing of the suspension containing a mixture of copper, indium and selenium powders in ethanol were $\Delta\lambda = 2.1$ nm and 8.1 nm, for lines H_α and H_β , respectively, that correspond to the electron density $(29 \pm 5) \times 10^{16} \text{ cm}^{-3}$ and $(22 \pm 5) \times 10^{16} \text{ cm}^{-3}$. The plasma electron temperature in this case was estimated based on the ratio of

intensities of Cu I 406.26 nm and Cu I 470.45 nm atomic lines and was about 1 eV. As expected, the value of the electron density, determined from the width of the H_{α} line, was overestimated due to self-absorption hydrogen lines and can be used only for qualitative analysis.

The results of spectroscopic studies allowed to determine the component composition of plasmas formed in two developed types of electric discharge devices, as well as to estimate the concentration and temperature of the electrons in plasmas. The determined discharge parameters are significant factors influencing the nature of plasma-chemical reactions in EDL. It was demonstrated that the pulsed spark discharge between the bulk silicon electrodes immersed in the liquid (water, ethanol), provides the effective method for the synthesis of silicon NPs with an average size of about 5 nm, in result of the nucleation of the evaporated atoms from the electrodes in the decaying plasma channel and a growth of the embryonic particles, limited by the rate of cooling in the surrounding liquid. Morphology, the chemical and phase composition of the formed particles are determined by the mode of discharge, the electrode material and the composition of the liquid medium in which the discharge occurs. The Si-NPs synthesized exhibited a violet-blue photoluminescence at the room temperature through the mechanism of the radiative recombination via the defect centers formed in the surface oxide layer and can be used in light-emitting optoelectronic devices [1].

Processing of suspended powder mixture of copper, indium, and selenium, taken in the stoichiometrical proportions, in ethanol by pulsed electrical discharge initiated chemical reactions between powder components resulting in generation of compound chalcopyrite CuInSe_2 (CIS) nanocrystals with an average size of about 25 nm and a band gap of 1.2 eV. The optimal conditions for the CuInSe_2 nanocrystals formation are determined by the plasma temperature and particles concentrations. The method opens up new possibilities for creating absorbing layers for photovoltaic converters [2].

Acknowledgements

This work is partially financed by the Belarusian Foundation for Fundamental Researches under grant No. F 13K-086.

REFERENCES

- [1] M. Mardanian, A. A. Nevar and N. V. Tarasenko, *Appl. Phys. A Materials Science & Processing* 112, 437 (2013).
- [2] M. Mardanian, A. A. Nevar, M. I. Nedelko and N. V. Tarasenko, *The Eur. Phys. Journ. D.* 67, 208 (2013).

FORMATIVE TIME DELAY OF ELECTRICAL BREAKDOWN IN AIR

Aleksandar P. Jovanović¹, Biljana Č. Popović², Vidosav Lj. Marković¹,
Suzana N. Stamenković¹, Marjan N. Stankov¹

¹ *Department of Physics, Faculty of Sciences and Mathematics, University of Niš, Višegradska 33, P.O. Box 224, 18001 Niš, Serbia*

² *Department of Mathematics, Faculty of Sciences and Mathematics, University of Niš, Višegradska 33, P.O. Box 224, 18001 Niš, Serbia*

Abstract. The determination of the formative time delay of breakdown is a complex problem because it is determined indirectly as a minimal value of total time delay. This method can be hazardous due to possible existence of outliers. In this paper we will use the common statistical method for detection of outliers in order to justify the use of this method. In addition, we propose a new method for determination of the formative time delay and compare it to commonly used ones.

1. INTRODUCTION

The electrical breakdown in gases is not instantaneous process. Upon application of the voltage to the discharge tube some time delay exists. This time is known as time delay to breakdown. The breakdown time delay consists of statistical time delay (time that elapses between application of the voltage greater than static breakdown voltage to the discharge tube and appearance of free electron initiating breakdown) and formative time delay (time from appearance of initiating electron to the collapse of applied voltage and occurrence of self sustained current) [1]. The common approximation of formative time is minimal value of total time delay to breakdown [2]. This could be hazardous due to existence of possible outliers in distribution. In this paper we will use the method for identification of the outlier. Also, the new method for formative time determination is proposed and compared to commonly used ones.

2. EXPERIMENTAL DETAILS

The time delay measurements were carried out on a gas tube filled with synthetic air at the pressure of 3 mbar . The tube of the volume $V \approx 300 \text{ cm}^3$ is made of borosilicate glass (8245, Schott technical glass). Electrodes are made of stainless steel (AISI 304) with diameter $D = 6 \text{ mm}$ and inter-electrode distance

$d = 6 \text{ mm}$. The electrodes are in shape of cylinder with mildly rounded edges in order to avoid the edge effect and to obtain homogeneous electric field between the electrodes. Prior to the installment, electrodes were lapped and polished with polishing paste with the grain size $1 \mu\text{m}$ and after that cleaned in ultrasonic bath in methanol solution and further in distilled water. The synthetic air used in the experiment is a mixture of (21–23) % vol. oxygen with less than 3.5 ppm of impurities and remaining percentage of nitrogen with less than 5 ppm of impurities. The gas tube was pumped down to the pressure of 10^{-5} mbar , degassed at 650 K and then filled with the synthetic air at the pressure of 3 mbar . The measurements were carried out in series in which the sequence of rectangular pulses is applied to the discharge tube [3], with 100 data in a single series at working voltage $U_w = 750 \text{ V}$, glow current $I_g = 800 \mu\text{A}$ and glow time $t_g = 1 \text{ s}$. The rise and fall times of the voltage pulses are approximately $0.18 \mu\text{s}$. The static breakdown voltage was $U_s = 396 \text{ V}$. Measurements were carried out with the Tektronix FCA 3000 counter with 100 ps resolution with total number of 10000 measurements. During the measurements, the tube was protected from the external light.

3. RESULTS AND DISCUSSION

The main purpose of this work was to reliably determine formative time delay of breakdown. Usually as a reasonable estimation of the formative time minimal value of the breakdown time delay is used [2]. This is assumed on the premise that in series of measurements, there is at least one case where the initiating electron is emitted immediate after the application of voltage, hence the statistical time delay is negligible. This choice of approximation for the formative time delay can be hazardous in the case when outlying values can be found in the distribution. Therefore, the distribution has to be tested for possible outliers. Outliers are the data that fall out of distribution i.e. that are statistically inconsistent with the rest of data [4]. The possible outliers are extreme values i.e. minimum and maximum value in a sample distribution. The statistical method used to test the possible outliers is modified Thompson tau test [4]. Modified Thompson tau test is based on the following test statistics:

$$\delta = (x - \bar{x}) / s \quad (1)$$

where x is random variable, \bar{x} is the mean of random variable x and s is standard deviation of the same variable. This value is compared to τ value calculated by the following relation:

$$\tau = \frac{t_{\alpha/2}(n-1)}{\sqrt{n} \sqrt{n-2 + t_{\alpha/2}^2}} \quad (2)$$

where n is the number of data, $t_{\alpha/2}$ is $\alpha/2$ quintile of student's t distribution with $n-2$ degrees of freedom and α is a significance level. The following criterion is used to determine whether particular data is outlier:

if $\delta \leq \tau$ the point is not outlier and it should not be rejected

if $\delta > \tau$ the point is outlier and it should be rejected.

If outlier is detected, it should be removed from sample and test should be repeated until there are no more outliers. Previously described test is applied to experimental data measured at small relaxation times $\tau = 0.1 \text{ ms}$ in conditions defined previously in the paper. These conditions are chosen to secure the high electron yield in order to maximize occurrence of initiating electron. On the sample of 100 measurements, the formative time is determined by the usual method, as the minimal value of t_d and it was determined that $t_f = 6.491 \mu\text{s}$. In order to test whether this value is outlier, the previously mentioned test was used. The modified Thompson tau test at the significance level $\alpha = 0.05$ showed that the minimal value of t_d is not an outlier and that it is safe to use it as an approximation of formative time.

The alternative method for determination of formative time is to use the mean value of the minimal class of histogram of t_d , i.e., to use sample data which is in the first interval that is used to build the histogram of t_d [2]. According to this method formative time is calculated to be $t_f = 6.496 \mu\text{s}$.

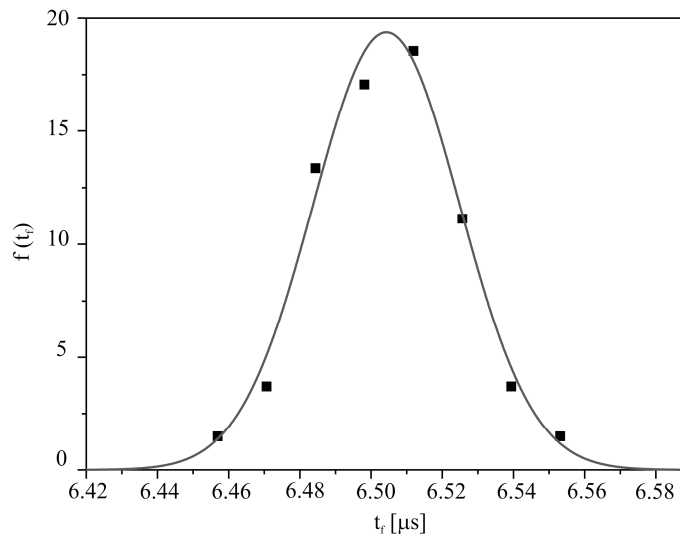


Figure 1. Probability distribution function of the formative time delay in synthetic air fitted by the Gaussian distribution function.

The third method for determination of formative time is proposed as an extension of the previously described method based on the minimal value. The large number of series, containing 100 data each, is measured. The minimal value in the single series is chosen as the approximation of the formative time. In this way the large number of formative time delay values is obtained. In this particular case, the 10000 measurements were carried out with 100 data in one series and from every series the minimal value is detected. In this way the 100 values of potential t_f are determined. In Fig. 1 the probability density function of formative time obtained in this way is presented fitted by Gaussian distribution with following parameters $\overline{t_f} = 6.504 \mu s$ and $\sigma = 0.02 \mu s$. Finally, we chose the mean value $\overline{t_f} = 6.504 \mu s$ as the formative time.

The comparison of formative time determined in three different ways is given in the table 1. It can be seen that minimal value can be satisfactory approximation of the formative time but the newly proposed method has the advantage because it takes in account the whole distribution of the formative time delay.

Table 1. The values of formative time delay determined by different methods

<i>Methods</i>	t_f [μs]
Minimal value	6.491
Average of the minimal class	6.496
Mean value of t_f distribution	6.504

Acknowledgements

This work is supported by Ministry of Education, Science and Technological development of the Republic of Serbia under the grants ON171025 and ON174007.

REFERENCES

- [1] C. G. Morgan., in *Electrical Breakdown of Gases*, edited by J. M. Meek and J. D. Craggs p. 656–688 (John Wiley & Sons, Chichester, 1978)
- [2] V. Lj. Marković, Z. Lj. Petrović and M. M. Pejović, *Plasma Sources Sci. Technol.* 6, 240–246 (1997).
- [3] V. Lj. Marković, A. P. Jovanović, S. N. Stamenković and B. Č. Popović, *EPL*, 100, 45002 (2012).
- [4] V. Barnett and T. Lewis, *Outliers in Statistical Data*, p. 17, (John Wiley and Sons Chichester, 1980)

TWO-DIMENSIONAL GLOW DISCHARGE MODELLING IN ARGON

M. N. Stankov¹, M. D. Petković², V. Lj. Marković¹, S. N. Stamenković¹,
A. P. Jovanović¹

¹*Department of Physics, Faculty of Sciences and Mathematics, University of Niš,
Višegradska 33, PO Box 224, 18001 Niš, Serbia*

²*Department of Computer Science, Faculty of Sciences and Mathematics,
University of Niš, Višegradska 33, PO Box 224, 18001 Niš, Serbia*

Abstract. Numerical modelling of stationary DC glow discharge in argon at pressure $p = 2\text{mbar}$ is performed and for this purpose the two-dimensional simple fluid model and the fluid model with nonlocal ionization source are applied. The two-dimensional profiles of ion and electron number densities obtained from the fluid model with nonlocal ionization source are presented. The number densities of ion and electron at axis of discharge tube obtained from those models are compared for the discharge current of $120\mu\text{A}$ and $160\mu\text{A}$.

1. INTRODUCTION

Numerical models are widely used for gas discharge modelling and better understanding of physical processes in various types of gas discharges. Among different models, the most common are fluid and particle models or their combinations. The fluid model with nonlocal ionization source shows good agreement with results from experiments and particle models [1]. Even in 1971. computer modelling was applied for the simulation of rapidly developing gaseous discharge [2]. In addition to the DC discharges, computer modelling is also used for the analysis of other types of discharges, such as RF [3].

The one-dimensional fluid model is often used for the analysis of the physical processes and mechanisms in the glow discharge [4]. In this paper the two-dimensional simple fluid model and fluid model with nonlocal ionization source are applied for the modelling of stationary DC glow discharge in argon at pressure $p = 2\text{mbar}$ for discharge currents of $120\mu\text{A}$ and $160\mu\text{A}$. The applied models are solved by the finite difference method and the system of equations obtained by the discretization of fluid equations is solved by applying the SOR method [5]. The theoretical description of models along with the short numerical analysis is given in section 2, while in section 3 the results of modelling are presented and discussed.

2. FLUID MODELS

The simple fluid model is based on continuity equation for charged particles (1) coupled with Poisson's equation (2) for electric field:

$$\frac{\partial n^{ele,ion}}{\partial t} + \nabla \Gamma^{ele,ion} = S, \quad (1)$$

$$\nabla^2 \varphi = -\frac{\rho}{\epsilon_0}, \quad (2)$$

where n is the number density of electrons and Ar^+ ions, Γ is the flux of particles, S is a source term, φ is a potential, ρ is the charge density and ϵ_0 is the dielectric constant. The source term S is determined by the electron impact ionization process and the process of electron and Ar^+ ions recombination:

$$S = \alpha \Gamma^{ele} - \beta n^{ele} n^{ion},$$

where α is Townsend ionization coefficient and β is the coefficient of recombination.

The simple fluid model with nonlocal ionization source term is applied in the paper [1] and the main idea of this model is to incorporate ionization of fast electrons in the fluid model. The source term has the following form:

$$S_{fast}(x) = \begin{cases} \Gamma^{ele}(0) \alpha \exp(\alpha x) & \text{for } x < d \\ \Gamma^{ele}(0) \alpha \exp(\alpha d) \exp(-(x-d)/\lambda) & \text{for } x \geq d, \end{cases}$$

where $\Gamma^{ele}(0)$ is the electron flux at cathode, x is the distance from cathode, λ is the decay constant and d is the length of cathode sheath region where the electric field is strong. The decay constant can be obtained from the relation [1]:

$$\lambda = \frac{\varphi(d)/(pB-d)}{\alpha d},$$

where $\varphi(d)$ is the cathode sheath voltage and B is the constant from Townsend ionization coefficient.

The equations (1), (2) are partial differential equations which are solved in cylindrical geometry using the finite difference method. In order to apply this numerical method two-dimensional mesh is generated between the electrodes and tube walls. After applying the finite difference method, the equations (1, 2) have the following form:

$$\frac{n_{ij}^{k+1} - n_{ij}^k}{\Delta t} + \frac{1}{r_j} \frac{\Gamma_{ij+1/2}^{k+1} - \Gamma_{ij-1/2}^{k+1}}{\Delta r} + \frac{\Gamma_{i+1/2j}^{k+1} - \Gamma_{i-1/2j}^{k+1}}{\Delta z} = S_{ij}, \quad (3)$$

$$\frac{1}{r_j} \frac{\phi_{i,j+1}^{k+1} - 2\phi_{i,j}^{k+1}}{\Delta r} + \frac{\phi_{i+1,j}^{k+1} - 2\phi_{i,j}^{k+1} + \phi_{i-1,j}^{k+1}}{\Delta z^2} + \frac{\phi_{i,j+1}^{k+1} - 2\phi_{i,j}^{k+1} + \phi_{i,j-1}^{k+1}}{\Delta r^2} = -\frac{\rho}{\epsilon_0}, \quad (4)$$

where k is a time index, i is a spatial index at z axis and j is a spatial index at r axis. The time step Δt is the time between two time moments j and $j+1$, while Δz and Δr are spatial steps. The fluxes for electron and ion number densities are discretized by the exponential scheme of Scharfetter-Gummel [6]. The equations (3-4) are the system of linear equations which are solved by SOR method [5].

3. RESULTS AND DISCUSSION

Numerical modelling is performed for DC glow discharge in *Ar* at the pressure of 2mbar . The discharge tube has a cylindrical shape with the electrode diameter $D = 2.2\text{cm}$ and the inter-electrode distance $d = 1\text{cm}$. The modelling was performed for applied voltage of 400V and for discharge currents of $120\mu\text{A}$ and $160\mu\text{A}$.

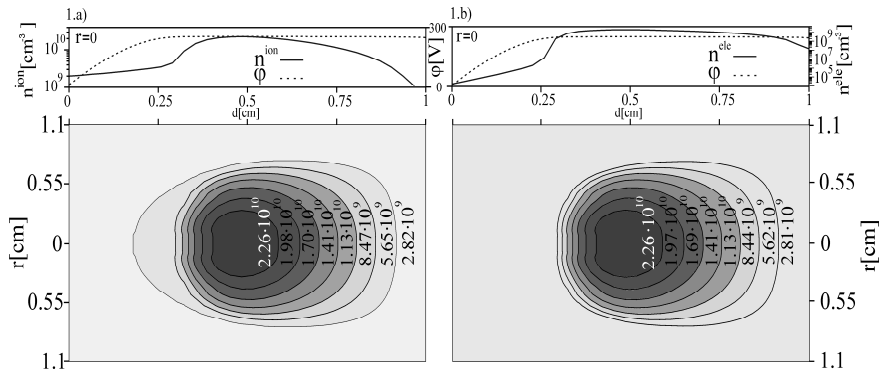


Figure 1. The profiles of particle number density and potential for current $I = 160\mu\text{A}$ obtained from fluid model with nonlocal ionization source.

In Fig.1 two-dimensional spatial profiles of electron and ion number densities for the current of $160\mu\text{A}$ are presented. These profiles were obtained by using the fluid model with nonlocal ionization source. Two-dimensional profiles of ion number densities along with the profile at axis of the gas tube ($r = 0$) are presented in Fig.1a, while these profiles for electron are presented on Fig.1b. The difference of ion and electron number density near the cathode in the glow discharge leads to the formation of the cathode voltage drop (Fig.1).

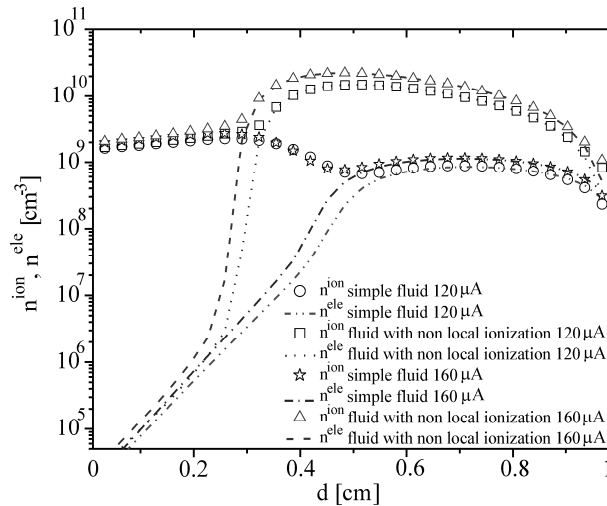


Figure 2. Ion and electron number densities at tube axis ($r = 0$) obtained from fluid models.

The number densities of ions and electrons at the axis of the tube ($r = 0$) obtained from the simple fluid and fluid model with nonlocal ionization source are presented in Fig.2. It can be noticed that the number densities of ions and electrons obtained from the simple fluid model are about one order of magnitude lower than the number densities from the fluid model with nonlocal ionization source. Although the simple fluid model is very suitable for the implementation because of its simplicity, this model is not good enough for the calculation of particles number densities in these conditions.

Acknowledgments

The authors are grateful to the Ministry of Education, Science and Technological development of the Republic of Serbia (projects 171025 and 174013).

REFERENCES

- [1] I. Rafatov, E. Bogdanov and A. Kudryavtsev, Phys. Plasmas 19, 093503 (2012).
- [2] A. Davies, C. Davies and C. Evans, Proc. Inst. Elect. Eng. 118, 816 (1971).
- [3] D. P. Lymberopoulos and D. J. Economou, J. Appl. Phys. 73, 3668 (1993).
- [4] M. Stankov, M. Petković, V. Marković, S. Stamenković, A. Jovanović, Rom. J. Phys. 59,328 (2014).
- [5] R. L. Burden and J. D. Faires, Numerical Analysis, p. 450 (Brooks/Cole, Cengage Learning Canada, 2011).
- [6] D. Scharfetter and H. Gummel, IEEE Trans. Electron. Devices 16, 64 (1969).

MEMORY EFFECT AND TIME CORRELATIONS IN AIR AND ARGON DC BREAKDOWN DELAY

V. Lj. Marković¹, A. P. Jovanović¹, S. N. Stamenković¹, M. N. Stankov¹
and B. Č. Popović²

¹*Department of Physics, Faculty of Sciences and Mathematics, University of Niš,
Višegradska 33, P. O. Box 224, 18 000 Niš, Serbia, vidosav@pmf.ni.ac.rs*

²*Department of Mathematics, Faculty of Sciences and Mathematics, University
of Niš, Višegradska 33, P. O. Box 224, 18 000 Niš, Serbia*

Abstract. Electrical breakdown time delays in synthetic air and argon at low pressures, as well as the memory effect and correlations of the statistical t_s and formative time delay t_f , were studied. The memory coefficient (or memory effect ratio) was determined, ranging from unity at low relaxation times and vanishing at the saturation level of the memory curves. It was shown that the statistical t_s and the formative time delay t_f are dependent variables and the positive correlation between them was confirmed experimentally and theoretically.

1. INTRODUCTION

Memory effect in gases is caused by residual charged and neutral active particles remained from the preceding glow and it is important for device operation in pulsed regime. From its discovery in 1953-6, the memory curve $\bar{t}_d(\tau)$ (where \bar{t}_d is the mean value of breakdown time delay and τ relaxation time or afterglow period) has been used for tracing the active particle decay in afterglow of AC and DC discharges in inert and molecular gases, their mixtures and vapours (including air) [1,2]. Memory effect in nitrogen and hydrogen was explained by charged particle decay and after that, by surface recombination of nitrogen and hydrogen atoms, respectively [3-7]. Also, the memory effect in inert gases was explained by the surface recombination of nitrogen atoms present as impurities [8-10]. In the ramp experiments with linearly rising voltage pulses, the memory effect was observed to influence the determination of the static breakdown voltage U_s . In order to determine U_s precisely, it is necessary and sufficient that the rate of voltage rise $k \rightarrow 0$ and the relaxation time $\tau \rightarrow \infty$ (residual states should vanish down to the cosmic rays and natural radioactivity level) [11,12].

Also, the negative point-to-plane Trichel pulse corona in nitrogen-oxygen and neon-oxygen mixture shows the memory effect and correlations of subsequent with previous discharge pulses. The memory and correlation coefficients were calculated from amplitude and pulse-time-separation distributions [13]. Recently, the memory effect in argon was confirmed in pulsed radio frequency atmospheric pressure glow discharges [14], as well as, in high power microwave dielectric window discharges [15]. The established correlations of the formative and statistical time delay in neon DC discharge [16] were confirmed recently on AC plasma display panels [17].

2. EXPERIMENTAL DETAILS

The measurements were carried out on gas tubes filled with synthetic air and argon at the pressures of 3 and 2 mbar, respectively. The tubes were made of borosilicate glass (8245, Schott technical glass) and the electrodes were made of stainless-steel (AISI 304) and OFHC cooper, respectively. The measurements were carried out in the series of 100 data. During the measurements, the tube was protected from external light. More details about experimental procedure and tube preparation can be found in [16,18].

3. RESULTS AND DISCUSSION

The memory curves measured in synthetic air and argon are shown in Fig.1a and b, respectively. The statistical $\bar{t}_s(\tau)$ and the formative time $\bar{t}_f(\tau)$ memory curves are separated in order to calculate the statistical and formative time memory coefficients (or memory effect ratios) by $M_{ts} = \bar{t}_{s0} / \bar{t}_s(\tau)$ and $M_{tf} = \bar{t}_{f0} / \bar{t}_f(\tau)$, respectively (Fig. 2a). Here, \bar{t}_{s0} and \bar{t}_{f0} designate interceptions of extrapolated memory curves at $\tau = 0$.

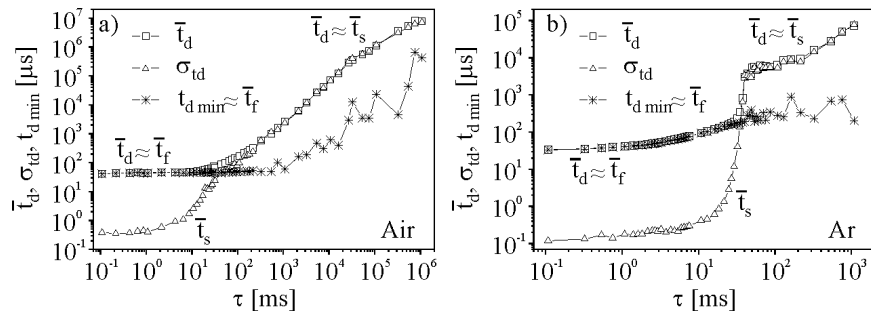


Figure 1. Memory curves for a) synthetic air and b) argon, separated into statistical and formative time memory curves

If the relaxation time τ is at the saturation region of the memory curve, i.e. $\tau \geq \tau_{sat}$ (Fig. 1), then residual active states (nitrogen atoms) from the preceding glow cease to influence the subsequent breakdown, the memory effect disappears and the breakdown time delay is determined only by the background ionization (cosmic rays and natural radioactivity) [4,9,14].

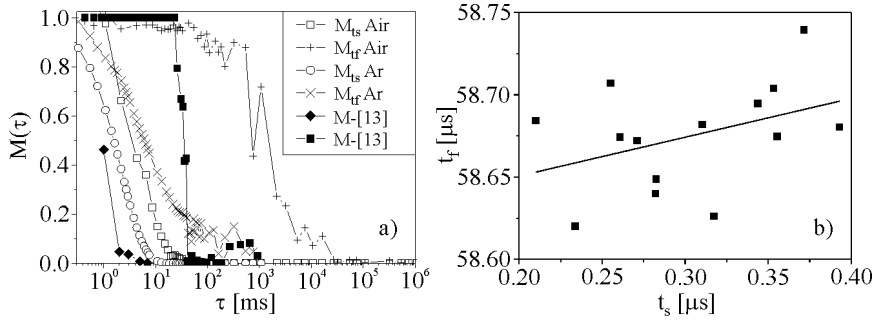


Figure 2. a) Memory coefficients (memory effect ratios) compared to calculated ones from [13] and b) the correlation of t_s and t_f for argon.

It is clear that statistical t_s and formative time delay t_f are dependent variables by plotting the mean values of the statistical and formative time delay $\bar{t}_s = 1/YP$ and $\bar{t}_f = \frac{qt_i}{q-1} \ln \frac{1+(q-1)(Y_g/Y)}{q}$ [16], as a function of electron yield Y. Here, P is the breakdown probability [3], $q = \gamma[\exp(\alpha d) - 1]$ is the electron multiplication factor and t_i is the ion transit time [16]. A positive correlation means that t_f decreases as t_s decreases and vice versa (Fig. 3a,b), while the sample correlation coefficient for argon at $\tau = 30 \text{ ms}$ is determined to be $\rho \approx 0.4$ (Fig. 2b).

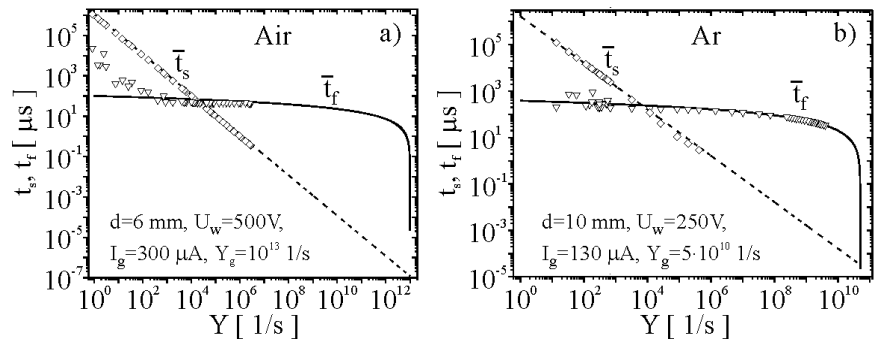


Figure 3. The statistical and formative time for a) air and b) argon show simultaneous decreasing behavior vs. Y and positive correlation.

Memory coefficient as defined in [13] was calculated for the sake of comparison with our definitions (Fig. 2a). Thus, memory and correlation coefficients tend to unity at low relaxation times and to zero at the saturation region of the memory curve (when residual active states from the preceding glow ceases to influence the subsequent breakdown and the memory effect and correlations disappear).

Acknowledgements

This work is supported by the Ministry of Education, Science and Technological Development, Republic of Serbia under the grants ON 171025 and ON 174007.

REFERENCES

- [1] Dj. A. Bošan, Proc. 5th Int. Conference on Gas Discharges (Liverpool University, Liverpool, UK, Stevenage: IEE Conf. Publ. No 165) 273 (1978).
- [2] Dj. A. Bošan and M. M. Pejović, J. Phys. D: Appl. Phys. 12, 1699 (1979).
- [3] V. Lj. Marković, Z. Lj. Petrović and M. M. Pejović, J. Chem. Phys. 100, 8514 (1994).
- [4] V. Lj. Marković, M. M. Pejović and Z. Lj. Petrović, Plasma Chem. Plasma Process. 16, 195 (1996).
- [5] V. Lj. Marković, Z. Lj. Petrović and M. M. Pejović, Plasma Sources Sci. Technol. 6, 240 (1997).
- [6] V. Lj. Marković, M. M. Pejović, Z. Lj. Petrović and S. S. Manola, Proc. 3rd General Conf. Balkan Physical Union, Cluj-Napoca, Romania, 1997; Proceedings Supplement of Balkan Phys. Lett. 5, 133 (1997).
- [7] Z. Lj. Petrović, V. Lj. Marković, M. M. Pejović and S. R. Gocić, J. Phys. D: Appl. Phys. 34, 1756 (2001).
- [8] V. Kudrle, E. LeDuc, M. Fitaire, J. Phys. D: Appl. Phys. 32, 2049 (1999).
- [9] V. Lj. Marković, S. R. Gocić, S. N. Stamenković and Z. Lj. Petrović, Phys. Plasmas 12, 073502 (2005).
- [10] V. Lj. Marković, S. R. Gocić, S. N. Stamenković and Z. Lj. Petrović, Phys. Plasmas 14, 103504 (2007).
- [11] V. Lj. Marković, S. N. Stamenković, S. R. Gocić and Z. Lj. Petrović, Contrib. Plasma Phys. 45, No. 7, 476 (2005).
- [12] V. Lj. Marković, S. N. Stamenković, S. R. Gocić and Z. Lj. Petrović, Rev. Sci. Instrum. 77, 096104 (2006).
- [13] R. J. Van Brunt and S. V. Kulkarni, Phys. Rev. A 42, 4908 (1990).
- [14] W. G. Huo, S. J. Jian, J. Yao and Z. F. Ding, Phys. Plasmas 21, 053505 (2014).
- [15] B. Kupczyk, X. Xiang, J. Sharer and J. Booske, Int. Conf. on Plasma Science (Edinburgh, UK, Publisher: IEEE) p. 2B-6 (2012).
- [16] V. Lj. Marković, S. R. Gocić and S. N. Stamenković, J. Phys. D: Appl. Phys. 42, 015207 (2009).
- [17] K. Yoshino, T. Nagatomi, Y. Morita, T. Oue, N. Kosugi, M. Nishitani, M. Kitagawa and Y. Takai, Jpn. J. Appl. Phys. 50, 026201 (2011).
- [18] V. Lj. Marković, A. P. Jovanović, S. N. Stamenković and B. Č. Popović, EPL 100, 54002 (2012).

NONSTATIONARY STATISTICAL TIME DELAY DISTRIBUTIONS IN ARGON

S. N. Stamenković¹, V. Lj. Marković¹, A. P. Jovanović¹ and M. N. Stankov¹

¹ *Department of Physics, Faculty of Sciences and Mathematics, University of Niš, Višegradska 33, 18000 Niš, Serbia*

Abstract. The experimental distributions of the statistical breakdown time delay in argon DC discharges at low preionization levels, under unstable conditions are presented. The obtained distributions are fitted by nonstationary exponential distribution with time dependent parameter that reflects unstable experimental conditions. The Laue diagrams of the statistical time delay are also fitted by the stationary exponential and Weibull distributions for the sake of comparison.

1. INTRODUCTION

The electrical breakdown in gases always occurs with a certain delay in regard to the moment of voltage application to the gas tube. A time interval between the moment of application of voltage greater than the static breakdown voltage U_s and the electrical breakdown is the breakdown time delay t_d and it comprises statistical t_s and formative time delay t_f ($t_d = t_s + t_f$) [1]. The stochastic character of statistical time delay was experimentally proved by Zuber [2], while von Laue [3] had derived the exponential distribution for its theoretical description. However, the type of t_s distributions depends on the electron yields Y - the number of generated electrons in the inter-electrode space per second. The distributions of statistical time delay are exponential ones for the low Y (low preionization) and change to the Gauss-exponential and Gaussian ones when the electron yields increase [4,5].

The cumulative exponential distribution of t_s derived by von Laue:

$$F(t_s) = 1 - \exp(-t_s/\bar{t}_s) \quad (1)$$

has the mean value of the statistical time delay \bar{t}_s as a distribution parameter. The \bar{t}_s is the inverse of the effective electron yield $\bar{t}_s = 1/Y_{eff} = 1/YP$, where P is the breakdown probability of one electron to cause a breakdown [1]. In semi-logarithmic representation (Laue plot), the exponential distribution of the statistical time delay under stable conditions is straightened since the electron yield Y and the breakdown probability P are constant [4]. On the other hand,

under unstable conditions (desorption of adsorbed gasses and impurities, sputtering of nonhomogeneous layers or oxides) or time varying voltage pulses, Y and/or P are time dependent variables. In such cases, the Laue plots are curved to the lower or higher values of the statistical time delay and it is necessary to introduce the nonstationary distribution with time dependent parameters.

2. EXPERIMENTAL DETAILS

The measurements were carried out on a gas tube made of borosilicate glass with the plane-parallel cylindrical copper cathode with radius $R = 11 \text{ mm}$ and gap distance $d = 20 \text{ mm}$. The tube was filled with research purity argon at the pressure of 2 mbar (Matheson Co. with a nitrogen impurity below 1 ppm). The static breakdown voltage was $U_s = 250 \text{ V}$. The measurements were carried out by applying step pulses to the tube (with the unconditioned cathode surface) at glow current $I_g = 70 \mu\text{A}$, glow time $t_g = 1 \text{ s}$, afterglow period (time between the voltage pulses) $\tau = 1 \text{ s}$ and at different working voltages U . The experimental distributions of t_s are obtained by subtracting $t_f \approx t_{d \min}$ from the measured time delay values [4,6,7]. More details about the experimental procedure can be found in [6,8].

3. RESULTS AND DISCUSSION

As already mentioned, the statistical time delay is random variable with the distribution function $F(t_s)$ which is determined by the probability of occurrence at least one electron in the interelectrode space for the time interval t_s [4]. When the electron yield Y and the breakdown probability P are constant i.e. when conditions are stable (e.g. electrical breakdowns by step pulses with negligible sputtering), the process of electron appearance is a stationary and the statistical time delay distribution is the stationary exponential one (1). This distribution is linear in Laue representation and from the slope of the Laue diagram the electron yield can be derived as $Y = -(1/P) \ln(n/N)/t_s$.

When the electron yield and/or the breakdown probability are time dependent variables (sputtering of nonhomogeneous layers or oxides, desorption of adsorbed gasses and impurities, time varying voltage pulses), the statistics of the electrical breakdowns is a nonstationary one. Thus, when the electrical breakdown occurs under unstable conditions (i.e. Y and/or P are time dependent), it is necessary to introduce the nonstationary distribution of t_s with time dependent parameters:

$$F_E(t_s) = 1 - \exp \left[- \int_0^{t_s} Y(t) P(t) dt \right], \quad (2)$$

or in Laue representation:

$$\ln(n/N) = -\int_0^{t_s} Y(t)P(t)dt . \quad (3)$$

The nonstationary exponential distribution (3) is applied for theoretical description of nonstationarity during the measurements (curving of the Laue diagrams) and the good agreement with the experimental data is found (Fig. 1). At the lower voltage $U_1 = 260V$ (Fig. 1a), the Laue diagram is curved to the higher values of the statistical time delay (concave on the right), while at the higher values of the voltage $U_3 = 500V$ (Fig. 1b), the curving of the Laue diagrams to the lower statistical times is obtained (convex on the right). At the some intermediate voltage ($U_2 = 300V$) the Laue diagram is straightened and this distribution is fitted by the stationary exponential one (1) with the constant distribution parameter (Fig. 1a,b). The curving of the Laue diagrams indicates that Y and/or P are function of time. The time dependent electron yields can be represented by the linear approximation:

$$Y_i = Y_{0i} (1 \mp \lambda_i t) \quad (4)$$

which describes the decreasing or increasing electron yields due to smoothing or roughening effect of the cathode sputtering and λ_i are the decay/growth constants. The time dependence of the probability P is expressed through the time dependence of the secondary electron yields γ_s which correspond to the static breakdown voltage [7,8]. In the conditions of the experiment, variation of U_s is of the order of volts in a series. Therefore, we can assume that the variation of γ_s and the breakdown probability can be neglected, i.e. $P \approx const$.

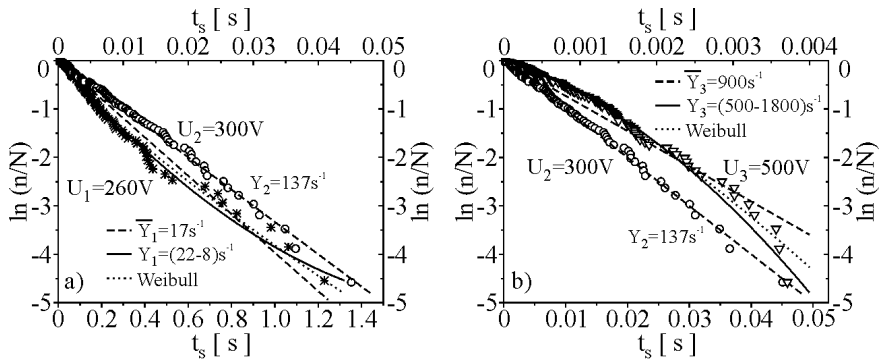


Figure 1. The Laue diagrams (symbols) and the fits based on nonstationary exponential distribution (solid line), stationary exponential distribution (dashed lines) and Weibull distribution (dotted line).

The fitting of the experimental data in Fig.1, for the voltage $U_1 = 260V$ is carried out using the linearly decreasing function of the electron yield:

$Y_1 = Y_{01} (1 - \lambda_1 t)$ with the fitting parameters $Y_{01} = 22s^{-1}$ and $\lambda_1 \approx 0.5s^{-1}$ (Fig. 1a, solid line). However, the experimental data in Fig. 1b for the voltage $U_3 = 500V$ are fitted by the linearly increasing yield: $Y_3 = Y_{03} (1 + \lambda_3 t)$ with the fitting parameters $Y_{03} = 500s^{-1}$ and $\lambda_3 \approx 700s^{-1}$ (Fig. 1b, solid line).

Since, Weibull distribution is often used for description of breakdown statistics in gases, the two-parameter Weibull distribution [9] is applied to the represented Laue diagrams in Fig. 1, as a comparison. The best fit of the data for $U_1 = 260V$ (dotted line in Fig. 1a) is obtained with parameters $\kappa = 0.835$ and $\eta = 0.262$, while for the voltage $U_3 = 500V$ the best agreement of the Weibull distribution with the experiment is accomplished with parameters $\kappa = 1.318$ and $\eta = 1.6 \cdot 10^{-4}$, but these parameters do not have physical meaning.

The curving of the Laue diagrams to the higher values of the statistical time delay at lower voltages is described by decreasing electron yield. However, the increasing electron yield is used to describe a trend of curving of the Laue diagrams to the lower values of the statistical time delay at higher voltages. Also, it should be noted that if the nonstationary exponential distribution is fitted by stationary one (dashed line at $U_1 = 260V$ and $U_3 = 500V$ in Fig. 1a,b), the parameter is incorrect, while in the case of applying Weibull distribution, the parameters do not have physical meaning.

Acknowledgements

The authors are grateful to Ministry of Education, Science and Technological Development of the Republic of Serbia for partial support (project 171025).

REFERENCES

- [1] C. G. Morgan, *Electrical Breakdown of Gases*, edited by J.M. Meek, J.D. Craggs (John Wiley & Sons, Chichester, 1978).
- [2] K. Zuber, *Ann. Phys.* 381, 231 (1925).
- [3] M. von Laue, *Ann. Phys.* 381, 261 (1925).
- [4] V. Lj. Marković, S. R. Gocić and S. N. Stamenković, *J. Phys. D: Appl. Phys.* 39, 3317 (2006).
- [5] V. Lj. Marković, A. P. Jovanović, S. N. Stamenković and B. Č. Popović, *EPL* 100, 45002 (2012).
- [6] V. Lj. Marković, M. M. Pejović and Z.Lj. Petrović, *Plasma sources Sci. Technol.* 6, 240 (1997).
- [7] V. Lj. Marković, S. R. Gocić and S. N. Stamenković, *J. Phys. D: Appl. Phys.* 42, 015207 (2009).
- [8] V. Lj. Marković, S. R. Gocić, S. N. Stamenković and Z. Lj. Petrović, *Phys. Plasmas* 12, 073502 (2005).
- [9] D. D. Wackerly, W. III Mendenhall and R. L. Scheaffer, *Mathematical Statistics with Applications*, (Belmont: Duxbury Press, 1996).

THE ESTIMATION OF ELECTRIC FIELD IN CATHODE FALL REGION OF NEON GRIMM GLOW DISCHARGE

N. V. Ivanović¹, G. Lj. Majstorović², N. M. Šišović³ and N. Konjević³

¹*University of Belgrade, Faculty of Agriculture, Nemanjina 6, 11080 Belgrade, Serbia*

²*University of Defence, Military Academy, 11105 Belgrade, Pavla Jurišića Šturma 33, Serbia*

³*University of Belgrade, Faculty of Physics, 11001 Belgrade, P.O. Box 368, Serbia*

Abstract. Ne I spectral lines were observed along the axis of cylindrical abnormal glow discharge parallel (side-on) and perpendicular to the cathode surface (end-on). The side-on spectra show spectral line shifting and sometimes simultaneous shifting and splitting in the cathode fall region of glow discharge. The results of measured line shift with available data for DC Stark effect are used for measurement of electric field strength in the cathode fall region of glow discharge.

1. INTRODUCTION

Glow discharges are successfully used as an excitation source for analytical spectroscopy of metal and alloy samples [1,2]. These glow discharge sources (GDS) are usually built on the basis of Grimm original design [3] with direct current (DC) and more recently with radio frequency (RF) excitation.

Recently, it has been noticed that the side-on spectra show spectral line shifting and sometimes simultaneous shifting and splitting in the cathode fall region of Grimm-type glow discharge [4]. The end-on recorded line profiles show up to 30% larger half-widths than the side-on recorded line profiles from the negative glow. This effect is a result of the superposition of line emission in the cathode fall region under the influence of the DC Stark effect on the line profile from the negative glow.

Since, neon is one of gases used for GDS operation, in this work we extended the study of Ne I line profiles started in Ref. [4]. An attempt will be made also to estimate electric field strength distribution in CF region of Ne GDS with iron cathode using Stark shift measurements of Ne I 511.368 nm.

2. EXPERIMENTAL

The discharge source, a modified Grimm GDS, was laboratory made after a Ferreira et al. design [5]. A hollow anode 30 mm long with inner diameter 8 mm has a longitudinal slot (16 mm long and 1.5 mm wide) for side-on observations along the discharge axis, see Figure 1. The water-cooled cathode holder has an iron electrode, 18 mm long and 7.60 mm in diameter, which screws tightly into its holder to ensure good cooling.

All experiments were carried out with neon (purity 99.999%). The continuous flow of about 300 cm³/min of neon (at room temperature and atmospheric pressure) was sustained in the pressure range 5-10 mbar by means of needle valve and two two-stage mechanical vacuum pumps. The reported results for gas pressure represent an average between gas inlet and outlet pressure measurements.

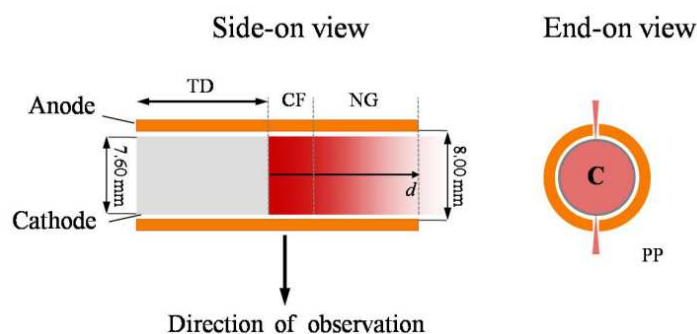


Figure 1. Schematic diagram of the central part of the Grimm GD for side-on and end-on observations. Symbols: MM – moving mechanism, CF – cathode fall region, NG – negative glow region, PP – protruding plasma, C – cathode.

To run the discharge a current stabilized power supply (0-2 kV, 0-100 mA) is used. A ballast resistor of 5.3 k Ω is placed in series with the discharge and the power supply. Spectroscopic observations of Grimm GD were performed end-on, while for axial intensity distribution of side-on radiation observed through the anode slot, the discharge tube was translated in ≈ 0.125 mm steps. The light from the discharge was focused with an achromatic lens (focal length 75.8 mm) with 1:1 magnification onto the 20 μ m entrance slit (height restriction 2 mm) of 2 m focal length Ebert type spectrometer with 651 g/mm reflection grating blazed at 1050 nm. For the line shape measurements the reciprocal dispersion of 0.37 nm/mm is used throughout this experiment. All spectral measurements were performed with an instrumental profile very close to Gaussian form with measured full width at half maximum (FWHM) of 0.0082 nm.

3. RESULTS AND DISCUSSION

In accordance with Figure 2, Ne I 511.368 nm line shifts are toward larger wavelengths (smaller wave numbers).

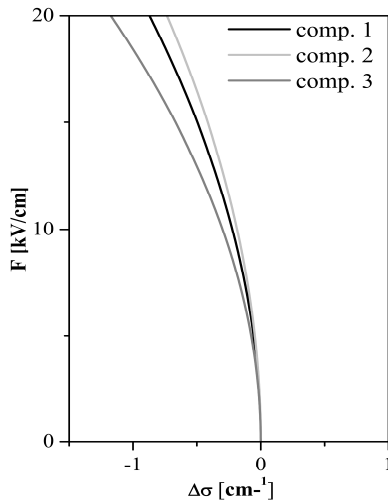


Figure 2. Behaviour of terms group 4d: Ne I 511.367 nm in a Stark field calculated using data from Table 2 in Ref. 7.

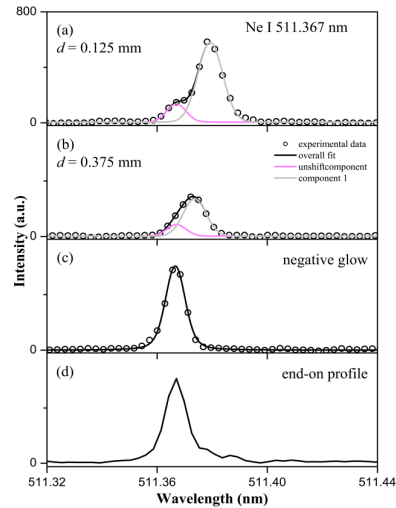


Figure 3. Spectral line shapes and best fits of Ne I 511.367 nm at different axial positions from cathode: (a), (b) and (c); and end-on experimental profile: (d) Discharge conditions: iron cathode, $p = 6.5\text{mbar}$; $I = 12\text{ mA}$; $U = 600\text{ V}$.

The change of the line shape along CF of neon GD is presented in Figure 3 where first three spectra recordings (a, b and c) depict spectral line shapes at three axial positions of GDS starting from the vicinity of the cathode surface and the fourth one, Figure 3d, shows line shape recorded end-on.

The sensitivity of line detection system and geometrical factors of the optical system are identical in Figures 3a, b and c, while for Figure 3d the discharge is setup for end-on observations and sensitivity scale is incomparable with preceding three.

Within spectra recorded closest to cathode surface, see Figure 3a, the line from discharge protruding through the anode slot in the vicinity of cathode surface is visible. In this case the line radiation emitted from discharge outside of electric field region with an unshifted wavelength and with the line shape having Gauss form of an instrumental profile. This phenomenon was noticed earlier in the study of He I lines in Grimm discharge of the same type [6].

Unshifted profile appears in side-on spectra recordings and was successfully used for line shift measurements induced by electric field. The line shapes along electric field, see Figures 3a and b are fitted with Gauss profiles to determine as precise as possible peak position within emitted feature. The width

of fitting profiles varies along discharge axis because the electric field and its gradient of changes as well while spatial resolution of our optical system remains constant. The exceptions of Gauss fitting procedure are profiles recorded from NG region, which were fitted with symmetric Voigt function. The end-profile in Figure 3 d was not fitted.

Using the results of line shift coefficients and applying analytical expression in [7] for line Ne I 511.368 nm it is possible to estimate the electric field strength distribution in the CF region of the GDS. Since the Stark shift for these lines is small, only estimate of maximum electric field strength ~ 15 kV/cm (close to the cathode surface) and CF length of about 0.9 mm is achieved. The voltage across the CF region calculated by integrating the measured field strength distribution agrees within 15% with the applied discharge voltage.

Another phenomenon is noticeable from Figure 3, line intensity closer to the cathode surface are stronger than at further position what is in contradiction with standard picture of CF region.

Acknowledgements

This work is supported by the Ministry of Education, Science and Technological Development of the Republic of Serbia under Project 171014.

REFERENCES

- [1] N. Jakubowski, A. Bogaerts and V. Hoffmann, *Atomic Spectroscopy in Elemental Analysis*, (Sheffield: Cullen M, Blackwell Publishing, 2003) Glow discharges in emission and mass spectrometry.
- [2] J. A. C. Broekaert, *Glow Discharge Plasmas in Analytical Spectroscopy*, p. 28, (eds R. K. Marcus and J. A. C. Broekaert, New York: Wiley, 2003).
- [3] W. Grimm, *Spectrochim. Acta B* 23, 443 (1968).
- [4] G. Lj. Majstorović, N. V. Ivanović, N. M. Šišović, S. Djurović and N. Konjević, *Plasma Sources Sci. Technol.* 22, 045015 (2013).
- [5] N. P. Ferreira, H. G. C. Human and L. R. P. Butler, *Spectrochim. Acta B* 35, 287 (1980).
- [6] M. M. Kuraica and N. Konjević, *Appl. Phys. Lett.* 70, 1521 (1997).
- [7] H. Jager and L. Windholz, *Phys. Scripta* 29, 344 (1984).

EFFECT OF METASTABLE NEON ATOMS IN COMPLEX PLASMA OF GLOW DISCHARGE

D. N. Polyakov, V.V. Shumova, L.M. Vasilyak

*Joint Institute for High Temperatures RAS, Izhorskaya 13 Bd.2, Moscow,
125412, Russia*

Abstract. The diffusion/drift model of the positive column of glow discharge in neon was used for the analysis of the role of neon metastable atoms in the interaction between neon plasma and dust particles. The radial profiles of electrons and metastable atoms were simulated in typical range of neon pressure and discharge current where dust particles may form dense dust structures changing the plasma properties.

1. INTRODUCTION

Usually the plasmas of noble gases contain a great quantity of metastable atoms. As the metastable atom concentration in a discharge may exceed the ion concentration by few orders and the metastable excitation energy is comparable to the ionization threshold, the interaction of metastable atoms with dust particles may work as one of the most significant channels of energy exchange between plasma and dust particles. From the other hand, metastable atoms participate in the processes of step-wise ionization and metastable-metastable ionization and give additional free electrons compensating the losses in a plasma bulk and on plasma reactor walls. The aim of the present study was to determine numerically the effect of metastable atoms in interaction of neon plasma with dust particles in a positive column of glow discharge depending on discharge parameters and number density of dust particles in the dust structure.

2. NUMERICAL MODEL

We have developed the diffusion/drift model of the positive column of glow discharge [1] as the basic model for the simulation of the effect of neon metastable atoms in the interaction between neon plasma and dust particles. We have considered the collision processes determining the metastable atom concentration: ground state ionization (W_i), step-wise ionization (W_{im}), metastable pooling (chemi-ionization W_{mm}), ground state excitation (W_{exc}) and metastable atom quenching in collisions with electrons and atoms. In addition to ion (G_{di}) and electron losses (G_{de}) on dust particles simulated according to the

collision enhanced collection model [2] we have also included the quenching of metastable atoms (G_{dm}) on dust particle surface as $G_{dm}=\pi a^2 n_d n_m V_m$, where V_m is the metastable atom thermal velocity. The ion and metastable atom temperatures were 295K. The mean electron energy and transport coefficients are obtained using the SIGLO Database and the electron Boltzmann equation solver BOLSIG+.

3. RESULTS AND DISCUSSION

We have applied our simulations to the experimental conditions described in [1]. The concentration of $2.55 \mu\text{m}$ dust particles was varied in the range observed in the experiments, and the size of dust structures was their mean radius $r_d=R/2$, where $R=8.25 \text{ mm}$ is the radius of the discharge tube.

It is observed that at low pressure of neon and low discharge current W_i and G_{de} exceed the rates of similar processes involving metastable atoms W_{im} and G_{dm} by order of magnitude and more. With increase in pressure and current significantly increase W_{im} and W_{mm} , so that they compensate for the losses of electrons on dust particles G_{de} . Figure 1(a) shows the rates of principal collision processes in the positive column of glow discharge in neon for dust particles number density $n_d=10^5 \text{ cm}^{-3}$ at $P=120 \text{ Pa}$, $I=3 \text{ mA}$. Note that in this case G_{dm} is only about three times less compared to G_{de} , and the latter even exceeds W_i within the dust structure. The competition of these processes leads to a change in equilibrium composition of neon plasma depending on discharge parameters and the dust structure density.

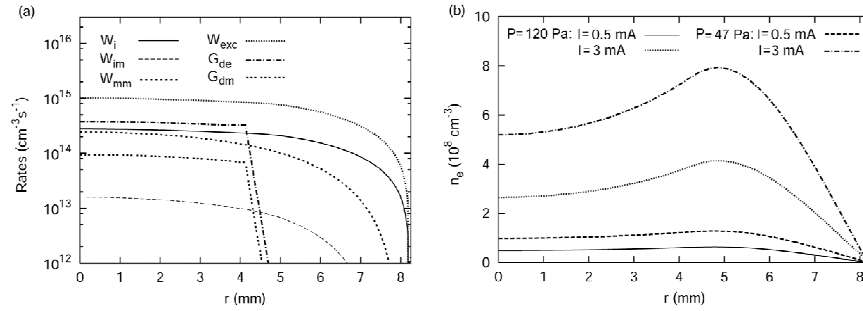


Figure 1. Radial profiles of (a) rates of principal collision processes in neon plasma with dust particles and (b) electron concentration

Simulations in pure neon show that the absolute values of the electron (n_e) and metastable atom (n_m) concentrations increase with discharge current and pressure. Nevertheless, n_e is the highest at higher discharge current, while n_m reaches a maximum at higher pressure. In pure neon the radial profiles of concentrations of plasma particles in the discharge tube are close to theoretical Bessel profiles. In presence of dust particles, the additional volume losses of electrons appear within the dust structure. The longitudinal electric field

increases to compensate for these losses and to maintain the ionization and the given total discharge current. As a result, n_e decreases within the dust structure, and the maximum n_e shifts beyond the dust structure (figure 1(b)).

The difference in mechanisms of electron and metastable atom losses on dust particles lead to the difference in relation of their concentrations in dusty plasma. The electron losses on dust particles increase exponentially with increase of mean electron energy determined by the longitudinal electric field strength, while the metastable atom losses do not depend. As a result, the ratio of concentrations of metastable atoms and electrons n_m/n_e significantly increases in the region of discharge with dust structure. Within the dust structure the value n_m/n_e increase few times with respect to the pure neon plasma. Beyond the bounds of dust structure n_m/n_e keep close to their values in the pure neon discharge. In other words, the temperature of the metastable atom excitation in the region with dust particles is higher than in the cross section of the discharge without dust particles. Note that at higher value of discharge current the effect of dust structure on n_m/n_e is more appreciable at the same value of n_d . Let us consider the effect of dust particle concentration on the discharge composition at fixed discharge pressure of 120 Pa and current of 3 mA (figure 2(a)). These parameters give the highest partial concentration of metastable atoms in pure neon plasma in the studied ranges of pressure and current.

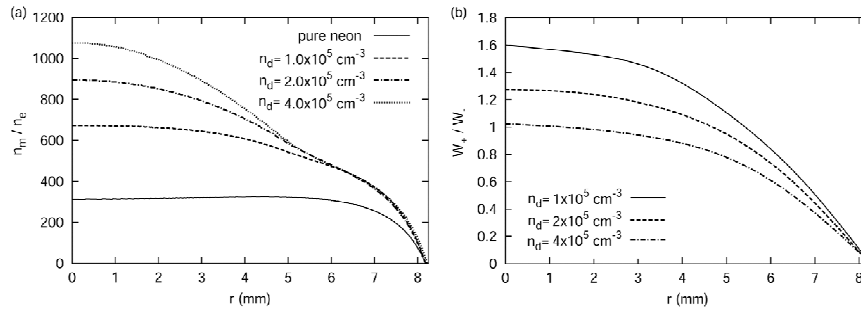


Figure 2. Radial profiles of (a) the ratio of concentrations of metastable atoms and electrons and (b) the value of metastable atom partial contribution to the ionization W_+ over metastable atom losses on dust particles W_- .

The absolute value of the metastable atom concentration behaves nonlinearly with the concentration of dust particles. It increases as compared to pure neon discharge, at least in some part of the discharge cross section for n_d increasing from 0 to 10^5 cm^{-3} and decreases as well for n_d increasing from 2 to $4 \times 10^5 \text{ cm}^{-3}$. Meanwhile, the ratio n_m/n_e , represented in figure 2(a), is definitely higher in the discharge with dust particles than in pure neon, and increases with increasing dust particle concentration. In figure 2(a) one can see the increased values of n_m/n_e beyond the bounds of the dust structure. This simulation confirms the non-local effect of dust cloud on the plasma glow observed in [3].

The role of metastable atoms in the interaction of plasma with dust particles may be quantified by comparing their partial contribution to the

ionization $W_+ = (W_{im} + W_{mm}) / (W_i + W_{im} + W_{mm})$ and in plasma losses on dust particles $W_- = (G_m^d) / (G_m^d + G_e^d)$. Simulations show that W_+ is higher than W_- and the ratio W_+ / W_- increases with increasing pressure, as well as the contribution of the metastable atoms to the ionization in pure neon. Figure 2(b) shows W_+ / W_- for three values of dust particle concentration at pressure of 47 Pa and current of 3 mA. One can see that metastable atoms give the higher partial contribution to the ionization, than in plasma losses on dust particles. At pressure of 120 Pa and the same value of discharge current the simulation shows more than double positive contribution of metastable atoms to ionization in presence of dust particles with concentration $4 \times 10^5 \text{ cm}^{-3}$. One may conclude that in spite of the fact that the rate of losses of metastable atoms on the dust particle surface may exceed the rates of their consumption in other plasma processes, their partial contribution to ionization is higher than in losses on the surface of dust particles. This result gives the quantitative representation of the effect of metastable atoms and their interactions with dust particles on the ionization balance in dusty plasma of positive column of glow discharge in neon.

4. CONCLUSION

The rate of losses of metastable atoms on the dust particle surface may exceed the rates of their consumption in other plasma processes. Nevertheless the partial contribution of metastable atoms to ionization is higher than their losses on the surface of dust particles and increases with the increase of neon pressure. Within the dust structure, the metastable atom concentration is higher than in discharge without dust particles at the same discharge parameters. The ratio of concentrations of metastable atoms and electrons is higher in presence of dust structures and may increase with increasing dust particle concentration in certain range of discharge parameters. The region of influence of dust structure on the ratio of concentrations of metastable atoms and electrons exceeds the size of dust structure that shows the nonlocal character of plasma particle interactions.

Acknowledgements

This work was supported by the RFBR grant №13-02-00641.

REFERENCES

- [1] L. M. Vasilyak, D. N. Polyakov and V. V. Shumova, *Contrib. Plasma Phys.* 53, 432 (2013).
- [2] L. G. D'yachkov, A. G. Khrapak, S. A. Khrapak and G. E. Morfill, *Phys. Plasmas* 14, 042102 (2007).
- [3] S. Mitic, M. Y. Pustynnik and G. E. Morfill, *New J. Phys.* 11, 083020 (2009).

INFLUENCE OF STREAMER DISCHARGE UPON THE EJECTION OF POLARIZATION CHARGING PARTICULATES FROM THE CATHODE

L. M. Vasilyak, V. I. Molotkov, V. Ya. Pecherkin and S. P. Vetchinin

JIHT RAS, Moscow, vasilyak@yandex.ru

Processes for charging of dust particles are well studied in various types of discharges [1-4]. The charge of micron size dust particles in such discharges can reach values of 10^3 - 10^4 elementary charges (e). Use of the electron beam in the vacuum or in the gas with a low pressure allows increasing the charge of dust particles up to the values of 10^6 - 10^7 e [3]. These ways for charging of dust particles in air at the atmospheric pressure do not allow getting high value of charge because of strong gas ionization. In this work we are shown the possibility for obtaining of extremely high value of charge on metal and dielectric particulates in air at atmospheric pressure in homogeneous electric field at the large field strength.

A plane capacitors of 5 cm and 15 cm diameters with air gap ($L_0=0.5$ -3 cm) were used. High speed video camera and laser were used to observe particulates. For definition of the charge of particulates the additional top electrode with an opening of 25 mm diameter was used. Three types of unequigranular metal particulates and three types of dielectric particulates were used (Table 1).

Table 1. Particulate types, sizes, average weight, dielectric permeability.

Material	Al	Brass	W	Diamond	Al ₂ O ₃	SiO ₂
a, μ	20-60	50-150	50-150	5-7	20-40	40-60
$\langle M \rangle$, μ g	0,7	34	77	3×10^{-3}	0,43	1,3
ϵ				16,5	8,5	6

A thin layer of particulates were poured on the bottom electrode of capacitor about its center. The DC voltage was applied to the electrodes of the capacitor. When the electric field strength had reached a certain value particulates started to eject from bottom electrode and accelerated in the gap

interval. The part of particulates took off through up the opening, and other part of particulates was recharged and reflected from the top electrode and moved down. The reflected particulates oscillated between electrodes. In the homogeneous electric field, we can calculate the particulate charge from its acceleration. Nevertheless we determined charge of particulates which have taken off through the opening by height of their lifting over the top electrode. Only the particulates which are taking off vertically up near an axis of the opening were considered. For definition of the maximum charge particulates with the greatest height of lifting were selected. The charge of particulates was defined according to the law of energy conservation. The ejection of heavy metal particulates occurred in case of electric field strength $E_0 > 5$ kV/cm. In that case formation of streamers is observed. Cathode-directional streamers are formed at first if the critical electric field strength is equal $E_{s+} = 4.7$ kV/cm. At approach of positively charged streamer to the polarized particulate on the cathode the local electric field near the particulate is increased. In this case the particulates can be ejected from cathode at the external electric field strength less than without streamers. The particulate is polarized by external electric field and on its surface there is a division of charges. If the polarized particulate is on the cathode a part of its charge flows on the cathode. Taking this into account the force acting on polarized particulate is calculated. The ejection of the particulate occurs, when the force operating on it from electric field side, surpasses particulate weight, $F > Mg$. Fig. 1 shows dependence of the reduced charge q/ea on particulates and potential drop on the particulate size $E_0 a$ a necessary for the ejection of particulates, from their weight.

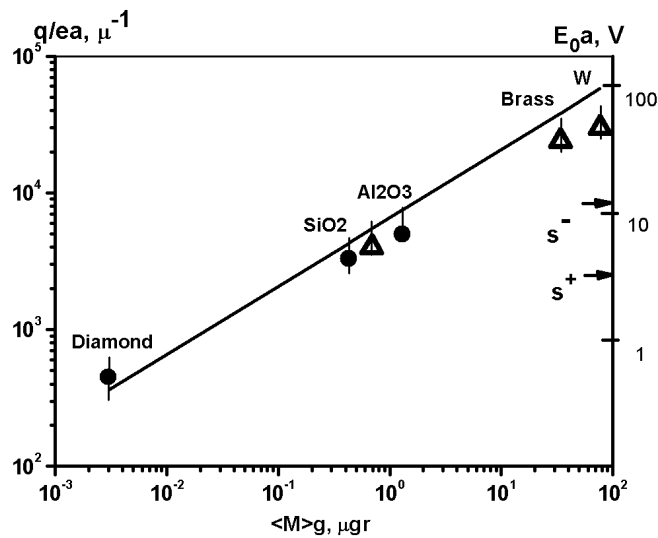


Figure 1. Dependence of particulate charge and potential drop at ejected moment versus particle weight. The continuous line – calculation curve, points – experimental values of the average charge q for various types of particulate.

From the offered mechanism of the polarization charging follows that the charge of particulates increases with increase in their weight at invariable size of particle, that is differ from all other ways of charging. The experimental values q for heavy metal particulates lie below calculation curve that is connected with that the ejection of heavy particulates occurs in rather strong electric fields when streamers are observed in the gap interval. Formation of streamers causes the particulate ejection from the cathode in electric fields E_0 of smaller strength (Fig. 2). From the Fig. 2 it is visible that particulates are ejected from electrode surface under action of higher electric field strength in small gap. This is the case of when streamers are not generated.

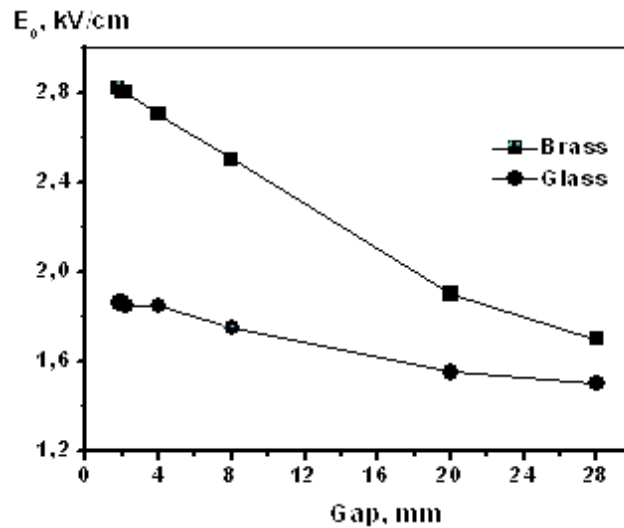


Figure 2. Dependence of electric field intensity at ejection of charged particulates versus gap value.

Critical values of electric field intensity E_s is specified on the right axes Fig. 1 by arrows for case when there are streamers in the gap.

The limiting charge value of metal particulates in size of some ten microns can reach values of $q \sim 10^6 - 10^7$ elementary charges. The charges of such values can be obtained in nonequilibrium low pressure plasma under action of electron beam with energy about 10 keV [5]. Formation of streamers is taken place at the electric field strength of $E_0 > 5$ kV/cm. The results of streamers are the reduction of the electric field strength needed to eject particulates from electrode and decrease of particulates charge.

REFERENCES

- [1] V. E. Fortov, G. E. Morfill, Complex and Dusty Plasmas. From Laboratory to Space, p. 418, (CRC Press, Taylor&Francis Group, Boca Raton, 2009).

- [2] A. Piel and A. Melzer, *Plasma Phys. Control Fusion*. 44, R1 (2002).
- [3] A. V. Phillipov, V. N. Babichev, N. A. Diatko et al. *JETF*. 119, 386 (2006).
- [4] A. I. Mesenyashin. *Sov. Phys. Tech.* 27, 327 (1982).
- [5] A. V. Phillipov, M. N. Vasilyev, A. V. Gavrikov et al. *Pisma v JETF*. 86, 1, 16 (2007).

OPTICAL DIAGNOSTICS OF DIFFUSE HELIUM COPLANAR DBD

Tomáš Morávek¹, Zdeněk Navrátil¹, Jozef Ráhel¹, Jan Čech¹

¹*DPE, Faculty of Science, Masaryk University, Kotlářská 2, 611 37 Brno*

Atmospheric pressure discharges are prone to streamer breakdown, which leads to their filamentation. Homogeneous discharges can be generated in helium, neon and nitrogen in volume configuration of electrodes. However the use of coplanar configuration typically leads to a filamentary discharge. We report observation of a stable homogeneous discharge in coplanar configuration in helium. Spatio-temporally resolved profile of electrical field was calculated from the intensity ratio of He lines 667.8 nm and 728.1 nm. The intensity distributions of the lines were measured using Time-Correlated Single Photon Counting. The results show two cathode and anode-directed ionizing waves with origin above the anode.

1. INTRODUCTION

Dielectric Barrier Discharges (DBD) are widely used for generation of atmospheric non-equilibrium plasma. They are usually observed in filamentary mode, with multiple microfilaments bridging the gap between the electrodes covered by dielectric barrier. In inert gases or for special geometries DBDs can be generated in a diffuse mode. These discharges are referred to as Atmospheric Pressure Glow Discharges (APGD) and due to their properties, they offer unique possibilities in the areas where homogeneity is required. This prompted the study of APGD by many research groups, which discovered its existence in various gas mixtures [1-3], obtained spatio-temporally resolved images of the discharge [4,5], and clarified the physical processes leading to the formation of APGD [1,5,6]. These works focused on the volume configuration of DBD. In this work we present our results on TCSPC (Time-Correlated Single Photon Counting) study on coplanar barrier discharge in helium at atmospheric pressure. By varying the parameters of a discharge in coplanar configuration, we managed to obtain a stable filament-free mode. Spatio-temporal emission patterns of several spectral lines (706.5 nm, 667.8 nm and 728.1 nm) were recorded. The ratio of intensities of spectral lines 667.8 nm and 728.1 nm can be used to estimate the

reduced electric field in the discharge [7]. In this paper spatio-temporally resolved distribution of the ratio $R_{667/728}$ is presented.

2. EXPERIMENTAL SET-UP

Presented measurements were carried out in a coplanar electrode configuration described in [8]. The metal electrodes with rectangular electrode gap of 4.65 mm, immersed into oil and covered with alumina dielectric, were placed into a small chamber equipped with a quartz window for discharge diagnostics. Helium with purity 5.0 was flowing through the chamber at flow rate of 555 sccm. The discharge was driven by an AC voltage of frequency 9.4 kHz, generated with function generator (Agilent 33220A) and amplified to a high voltage signal with amplitude of 1.6 kV. The applied voltage and the discharge current were measured by a digital oscilloscope (LeCroy WaveRunner 6100A). The discharge current was inferred from a voltage measured on a 3 k Ω resistor, connected in series with the electrodes.

The light coming out of the discharge was first monochromatized (Jobin Yvon HR-640) and then analyzed by single photon counter (Becker-Hickl SPC-150) equipped with photomultiplier working in photon counting mode (PMC-100-4). A time-resolution of 0.2 μ s was achieved by synchronization of the photon counter with the voltage signal. A spatial resolution of 0.1 mm was obtained by projecting the discharge by a quartz lens onto a movable slit, with optical fibre located beyond it. Using the TCSPC following transitions were measured: 706.5 nm ($3s^3S_1 \rightarrow 2p^3P$), 667.8 nm ($3d^1D_2 \rightarrow 2p^1P_1$) and 728.1 nm ($3s^1S_0 \rightarrow 2p^1P_1$). The pictures of the discharge were taken by digital camera Casio EXILIM F1.

3. RESULTS AND DISCUSSION

Figure 1 shows a typical oscillogram for He discharge. It can be seen that only one current peak per half period is recorded without any additional microdischarge pulses. The absence of any bright microfilaments can be also seen in Figure 2, showing the image of the discharge taken with digital camera. Figures 3a, 3b and 3c show the intensity distributions of three He lines. All of these lines exhibit similar behaviour. At first, a low intensity builds up near the anode. This pre-breakdown phase is attributed to the initial Townsend avalanching. After that a strong ionizing wave is started and propagates towards the cathode. At the same time a second less intense ionisation wave heading to the anode appears. It can be seen that the maximum intensity for triplet line 706 nm appears sooner than for the singlet lines 667 nm and 728 nm. Triplet states can be populated by stepwise excitation through metastables, efficient also at low electric field [7]. On the other hand the upper states of singlet transitions are populated from the ground state. Hence higher field strength is required.

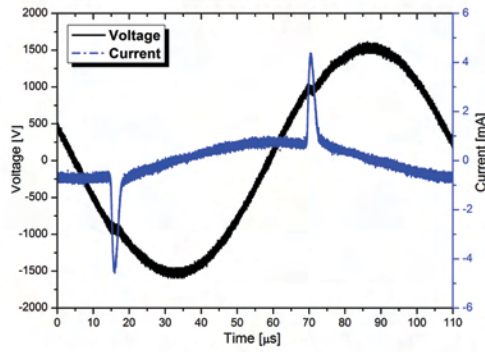


Figure 1. Evolution of the current and applied voltage in the diffuse APGD discharge in He.

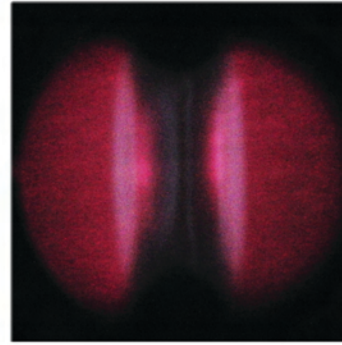


Figure 2. The visual appearance of the filament-free discharge in He. Exposure time was 1/6 s.

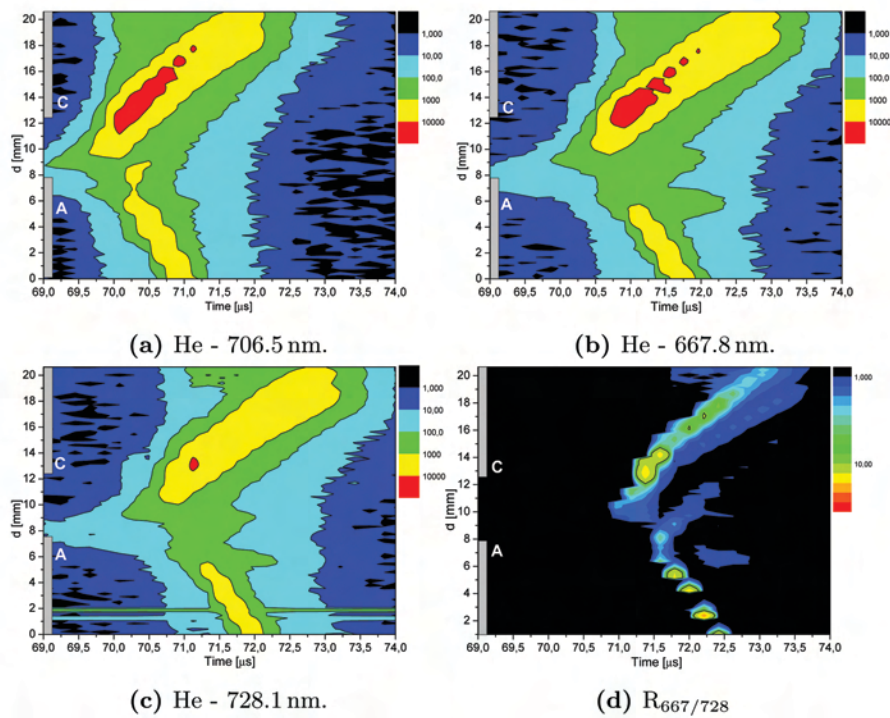


Figure 3. Spatio-temporally resolved intensity distributions of He lines and the ratio $R_{667/728}$ (E/N) for helium APGD with 4.65 mm gap. The positions of cathode and anode are denoted by letters C and A, respectively.

This expectation is supported by Figure 3d, which shows the ratio of intensities of spectral lines 667.8 nm and 728.1 nm. It can be seen

that the maximum of the ratio $R_{667/728}$ (E/N) occurs about $1.5 \mu\text{s}$ after the maximum of 706 nm line. The intensity distribution of $R_{667/728}$ (E/N) also shows two ionizing waves started between the electrodes heading for anode and cathode. The black areas represent the spatio-temporal coordinates, where the intensity was weak and the ratio could lead to misleading results.

4. CONCLUSION

In this work a stable filament-free discharge with coplanar configuration of electrodes in helium was investigated. Using the TCSPC a spatio-temporal spectroscopy was performed on three helium lines. From the ratio of intensities of 667.8 nm and 728.1 nm helium spectral lines the relative development of electric field was calculated. The $R_{667/728}$ ratio exhibits two maxima heading for the anode and cathode side of our experimental set-up.

Acknowledgements: The work was financially supported by the Czech Science Foundation, contract No. GA13-24635S and also by the project CZ.1.05/2.1.00/03.0086 funded by European Regional Development Fund.

REFERENCES

- [1] F. Massines et al., *J. Appl. Phys.*, 83 (1998)
- [2] D. Trunec et al., *J. Phys. D: Appl. Phys.*, 34 (2001)
- [3] N. Gherardi et al., *Plasma Sources Sci. Technol.*, 9 (2000)
- [4] Ricard et al., *Surf. Coat. Technol.*, 112 (1999)
- [5] K. Kozlov et al., *J. Phys. D: Appl. Phys.*, 38 (2005)
- [6] I. Radu et al., *J. Phys. D: Appl. Phys.*, 37 (2004)
- [7] S.S. Ivkovic et al., *J. Phys. D: Appl. Phys.*, 47 (2014)
- [8] J. Čech et al., *The European Physical Journal D*, 54 (2009)

SCALING OF THE NET EMISSION COEFFICIENTS

P. Kloc¹, V. Aubrecht¹ and M. Bartlova¹

¹*Department of Power Electrical and Electronic Engineering,
Faculty of Electrical Engineering and Communication,
Brno University of Technology, Technicka 10, 61600 Brno, Czech Republic*

Abstract. In this contribution we evaluated the net emission coefficients (NEC) of the air for several arc radii. We also calculated the divergence of radiation flux inside a infinite cylinder with fixed radius and fixed temperature profile using the same input data. We tried to find the reasonable correlation between the NEC and divergence of radiation flux to approximately describe the radiation transfer inside the infinite cylinder.

1. INTRODUCTION

The Net Emission Coefficient (NEC) was derived by Lowke [1] to easily predict the energy loss of plasma due to radiation and even predict the temperature profile. The way the NEC is derived limit its usage only to the center of infinite homogeneous cylinder or sphere. It is therefore not suitable for calculation of the radiation transfer inside the plasma.

To evaluate the radiation transfer inside the plasma the divergence of radiation flux is generally used. The associated radiation transfer equation (RTE) is however very computationally demanding. Thus several simplification approaches were developed including P_1 approximation, discrete ordinates methods (DOM) [2] or ray tracing [3]. All these methods can provide information about the divergence of radiation flux however they are still more complex compared to the simple calculation of NEC.

In this contribution we tried to correlate the NEC with the divergence of radiation flux. It is completely wrong in the sense of condition under which NEC was derived. Nevertheless it can provide quick estimation of the radiation transfer.

The NEC has two main parameters. Radius of the cylinder r and temperature of the plasma inside the cylinder. The plasma composition can be expressed as the function of temperature hence it is not directly included if known for entire temperature range. By varying these two parameters it is possible to match the NEC to the divergence of radiation flux.

2.RESULTS AND DISCUSSION

In this study we considered the air plasma at the pressure of 1 bar and calculated the plasma composition using the methods presented in [4]. Afterwards the absorption coefficients was calculated in the frequency range from 10^{13} Hz to 10^{16} Hz with frequency resolution of $2 \cdot 10^{10}$ Hz. The temperature was chosen between 3000 K and 25 000 K with 100 K temperature discretization.

The input data in the form of absorption coefficients was used to calculate the NEC. The results are depicted in the figure 1 for several selected arc radii. They are consistent with our previous results [5]. These coefficients were used to calculate the required temperature to match the divergence of radiation flux.

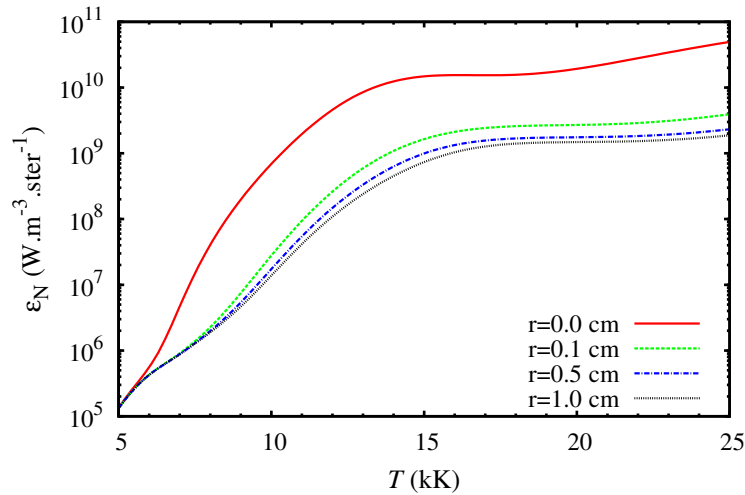


Figure 1. Net emission coefficients of the air plasma for various radius.

The divergence of radiation flux was calculated using one dimensional discrete ordinates method (DOM). The infinite long cylindrical computational domain was considered for the calculation with fixed axisymmetrical temperature profile. Three distinct temperature profiles as depicted on figure 2 were used.

The calculated divergence of radiation flux are presented in figure 3. The results were obtained taking into account 45 unique ordinates and taking advantage of the symmetry.

Given the way the NEC is derived it can not capture the absorption part of the radiation transfer. Thus only the part where the divergence of radiation flux is non negative was considered in the comparison. By comparing the divergence of radiation flux to the NEC we were able to produce a new set of temperature profiles. By using this supplementary

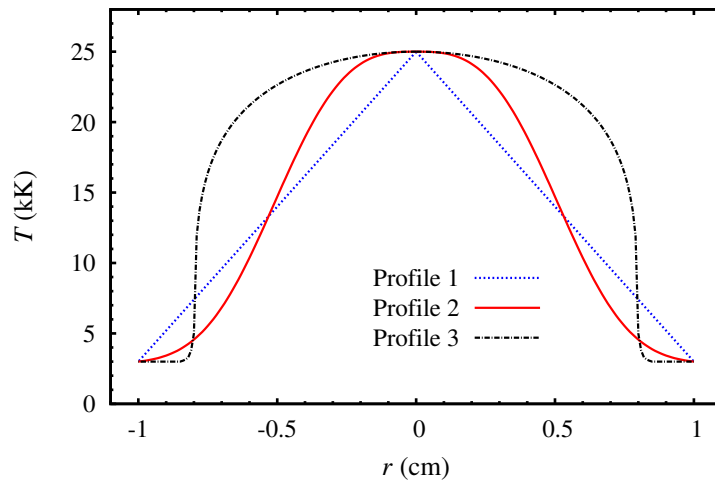


Figure 2. Various temperature profiles used to calculate the divergence of radiation flux.

temperature profile it is possible to scale the NEC to fit the emission part of the divergence of radiation flux.

The obtained supplementary temperature profiles seems quite similar, only shifted. It suggest there might be a formula to evaluate them from the original temperature profile.

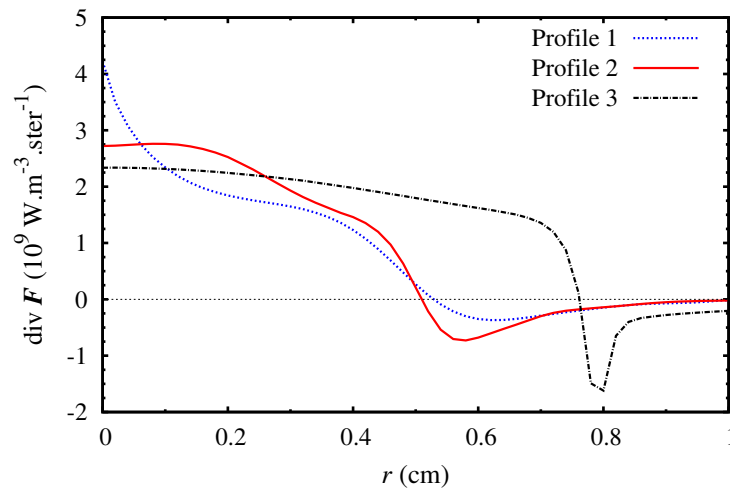


Figure 3. Divergence of radiation flux for different temperature profiles.

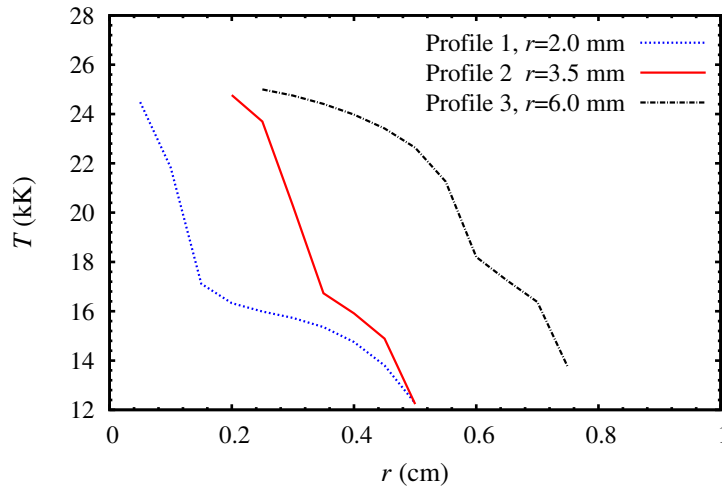


Figure 4. Final temperature profiles used to match the NEC with divergence of radiation flux. Radius r denotes the radius used for the NEC calculations.

3.CONCLUSION

We conclude that it might be possible to approximate the divergence of radiation flux by using net emission coefficients. However more investigation is needed to confirm this conclusion.

Acknowledgements

Authors gratefully acknowledge support from the Centre for Research and Utilization of Renewable Energy under project No. LO1210” and from the project No. CZ.1.07/2.3.00/30.0039 Excellent young scientist on Brno University of Technology.

REFERENCES

- [1] J. J. Lowke, *J. Quant. Spectrosc. Radiat. Transfer* 14, 111 (1974).
- [2] M. F. Modest, *Radiative Heat Transfer*, p. 498, (Oxford: Academic Press).
- [3] B. Peyrou, L. Chemartin, Ph. Lalande, B. G. Cheron, Ph. Riviere, M.-Y. Perrin and A. Soufiani *J. Phys. D: Appl. Phys.* 45, 455203 (2012).
- [4] O. Coufal, *J. Phys. D: Appl. Phys.* 40, 3371, (2007).
- [5] V. Aubrecht, M. Bartlova and O. Coufal, *J. Phys. D: Appl. Phys.* 43, 434007, (2010).

CALCULATION OF LIGHTNING CHANNEL LINE CHARGE DENSITY USING VERY CLOSE ELECTRIC FIELD MEASUREMENTS

Ignjatovic Milan¹, Cvetic Jovan¹, Taušanović Milica², Pavlovic Dragan¹, Djuric Radivoje¹, Ponjavic Milan¹, Sumarac Pavlovic Dragana¹ and Mijajlović Nikola¹

¹*School of Electrical Engineering Belgrade, Serbia*

²*PD Elektrodistribucija Beograd d.o.o, Srbija*

Abstract. A generalized lightning traveling current source (GTCS) model with the current reflections on both channel ends and the current partition has been used to examine the line charge density along the lightning channel just prior to the return stroke. Using very close vertical electric field waveforms measured at 0.1m and 15m from the channel core the values of the ground reflection as well as the current partition coefficient are calculated. As a result a new channel discharge function is obtained and the new distribution of the line charge density along the channel is calculated. The results agree well with the measured or estimated channel line charge profile in other studies.

1. THE GTCS MODEL

The GTCS model was established as a generalization of the traveling current source-type models [1]. The current impulses move upwards and downwards along the channel core, Fig. 1. The ratio between the current intensity of upward and downward impulse is defined by current partition coefficient $p = di_Q^{(u)} / di_Q^{(d)}$, where $-\infty \leq p \leq +\infty$. The reflections at the ground are taken into account with a constant ground reflection coefficient ρ .

The change of the line charge density in time $q(z,t)$ is introduced by the channel discharge function $f(t)$ with

$$q(z,t) = q_{tot}^-(z) f(t - z/v), \quad (1)$$

where $q_{tot}^-(z)$ is initial line charge density just prior to the return stroke.

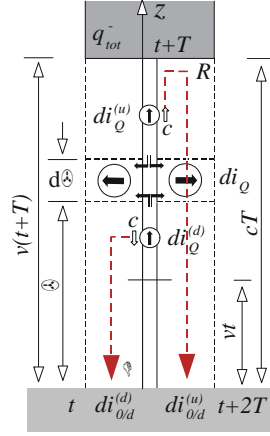


Figure 1. The upward $di_Q^{(u)}$ and the downward $di_Q^{(d)}$ propagating current pulses.

According to the extended GTCS model [2], the channel-base current is given by

$$i_0(t) = i_{0/d}(t) + i_{0/u}(t) = (1 + \rho)i_{0/d}(t), \quad i_{0/d}(t) = i_{0/d}^{(d)}(t) + i_{0/d}^{(u)}(t), \quad (2)$$

with the downward channel-base components given by

$$i_{0/d}^{(d)}(t) = (1 - p)^{-1} \left\{ \int_0^{v^*t} q_{tot}^-(z) \partial f(u) / \partial u dz + \sum_{\nu=1}^{\infty} (R\rho)^\nu \int_0^{v^*A^\nu t} q_{tot}^-(z) \partial f(u) / \partial u dz \right\}, \quad (3)$$

$$i_{0/d}^{(u)}(t) = R\rho / (1 - p) \left\{ \int_0^{v^*At} q_{tot}^-(z) f_1(u_1) dz + \sum_{\nu=1}^{\infty} (R\rho)^\nu \int_0^{v^*A^{\nu+1}t} q_{tot}^-(z) f_1(u_1) dz \right\}, \quad (4)$$

where $A = -R$, $u = A^\nu t - z / v^* \geq 0$, $f_1 = f(u_1) / \partial u_1$, $u_1 = Au \geq 0$ for $\nu \geq 1$, and for $A = 0$, $u = t - z / v^* \geq 0$. If one assumes that only one reflection has the dominant influence on the channel-base current, neglecting simultaneously the current reflections from the upper end of the channel that is. $R = 0$, it follows

$$i_0(t) = (1 / \beta) \int_0^{v^*t} q_{tot}^-(\xi) \partial f(t - \xi / v^*) / \partial t d\xi, \quad \beta = (1 - p) / (1 + \rho). \quad (5)$$

2. A NEW CHANNEL DISCHARGE FUNCTION

The vertical and radial electric field components E_z and E_r , respectively, in the vicinity of the straight, vertical, lightning channel, above perfectly conducting ground are given by ([3])

$$E_z = \frac{1}{4\pi\epsilon_0} \int_0^{+\infty} \frac{q_{tot}^-(\xi) f(t - \xi / v) (z_0 - \xi)}{[(z_0 - \xi)^2 + r_0^2]^{3/2}} d\xi, \quad E_r = \frac{r_0}{4\pi\epsilon_0} \int_0^{+\infty} \frac{q_{tot}^-(\xi) f(t - \xi / v)}{[(z_0 - \xi)^2 + r_0^2]^{3/2}} d\xi, \quad (6)$$

where (r_0, z_0) are the coordinates of the point of the field calculation in the cylindrical system. The influence of the channel image is taken into account substituting q_{tot}^- and z_0 with $-q_{tot}^-$ and $-z_0$, respectively, in (6). Theoretically, the channel discharge function can be calculated from the integral equations of the field components (6) if the electric field components E_z and E_r are measured and the channel line charge density distribution $q(\xi)$ is known. However, the channel-base current (5) is usually measured and the channel line charge distribution as well as the channel discharge function should be calculated from (5) and (6). This also implies the calculation of β in (5). This calculation could be simplified and solved if one notices that the time delay term in (6) can be neglected that is $\xi/v \ll t$. Therefore if one simplifies $f(t - \xi/v) \approx f(t)$, from (6) it follows

$$E_z(t) = f(t)E_0, \quad E_0 = (4\pi\epsilon_0)^{-1} \int_0^{+\infty} q_{tot}^-(\xi)(z_0 - \xi) / \left[(z_0 - \xi)^2 + r_0^2 \right]^{3/2} d\xi, \quad (7)$$

where E_0 is the value of electric field at time onset (measured value). The channel discharge function can be easily derived from (7)

$$f(t) = E(t) / E_0. \quad (8)$$

3. THE CHANNEL LINE CHARGE DENSITY

The channel discharge function can be determined from the measured electric field waveform. The results of the electric field measurements in the vicinity of the triggered lightning channel are given in [4], Table 1. The field measurement at the distance of 15m is denoted as $E_z^{15}(t)$ and used in the calculation in (8). Other two field measurements obtained at 10cm from the channel core are denoted as E_r^{10} (radial component) and E_z^{10} (vertical component) are used as references for the field matching at the time onset.

From (5), optimizing the values of parameters v and β in such a way to match the initial field value of E_r^{10} and E_z^{10} at the time onset, one obtains the results presented in Table 2. However, all results give approximately the same value for $v/c \approx 0.52$ whereas $\beta \approx 0.4$. If one accepted well grounded structure which is claimed in the measurements, [4], that is $\rho \approx 1$, it follows $p \approx 0.2$ indicating that about 17% of the current pulses injected in the channel core propagate upwards and about 83% propagate downwards. Using Eq.(5) one obtains the line charge density profile $q_{tot}^-(\xi)$, depicted in Fig.2.

Table 1. Measured values of the electric field components at the time onset, [4].

Electric field	E_r^{10} (at 10cm)	E_z^{10} (at 10cm)	E_z^{15} (at 15m)
Value [MV/m]	1.19	0.89	0.128

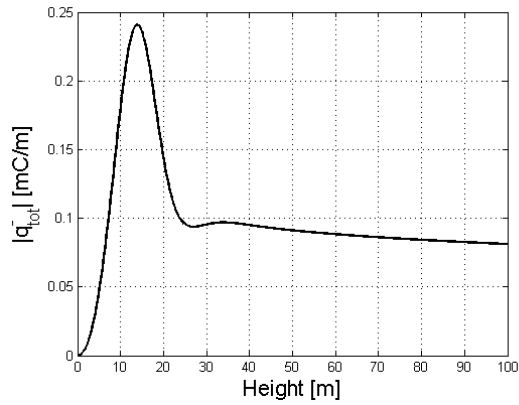


Figure 2. The initial line charge density along the lightning channel.

Table 2. Calculated values of the parameters the time onset

v/c	β	E_r^{10} [MV/m]	E_r^{10} [MV/m]	E_z^{15} [MV/m]
0.5211	0.4	-1.17	0.9	0.128
0.5158	0.4	-1.2	0.92	0.128
0.5316	0.418	-1.19	0.9	0.132

Acknowledgements

Ministry of Science and Technological Development of the Republic of Serbia supported this work under the contracts No. 171007 and 37019.

REFERENCES

- [1] J. M. Cvetić and B.V.Stanić, An improved return stroke model with specified channel-base current and charge distribution along lightning channel, International Conference on Electromagnetics in Advanced Application, Torino, 1995.
- [2] J. Cvetić, F. Heidler, A. Nesić and I. Tesnjak, The Generalized TCS Model with the Current Reflections at Ground and at the Upper End of the Lightning Channel, 4th International Symposium on Lightning Physics and Effects, European COST Action P18, Vienna, Austria, May, 2009.
- [3] V. A. Rakov and M. A. Uman, *Lightning, Physics and Effects*, Cambridge: Cambridge University Press, 2003.
- [4] M. Miki, V. A. Rakov, K. J. Rambo, G. H. Schnetzer, and M. A. Uman, *J. Geophys. Res.*, 107, D16, 4277 (2002).

THE INFLUENCE OF THE LIGHTNING CURRENT REFLECTIONS FROM THE GROUND ON ELECTRIC FIELD NEAR CHANNEL CORE

Tausanović Milica¹, Cvetic Jovan², Ignjatovic Milan², Pavlovic Dragan², Djuric Radivoje², Ponjavic Milan², Sumarac Pavlovic Dragana² and Mijajlović Nikola²

¹*PD Elektrodistribucija Beograd d.o.o, Srbija*
²*School of Electrical Engineering Belgrade, Serbia*

Abstract. The appearance of the overcompensated positive electric field in the most of very close vertical field measurements (0.1 m from the channel core) is explained using the generalized lightning traveling current source (GTCS) return stroke model with the current reflections from the ground. The channel-base current is separated into two components. The first one is fast component with a greater current peak and the second one is slower, with a smaller current peak. A new effect generated by the current pulse reflection from the ground is assumed. While the first current component, having a peak value over 15kA reflects from the perfect ground with the reflection coefficient equals one, the second current component, having a peak value well below 15kA reflects with the reflection coefficient smaller than one. As a result, uncompensated negative line charge density appears along the channel core near ground enhancing the negative radial electric field in the channel sheath. This field forces the overcompensated positive charges to move into the corona sheath where they remain after the return stroke current has ceased to flow.

1. THE LIGHTNING CHANNEL-BASE CURRENT

The calculations of channel charging function f^+ necessary for the calculations of the corona sheath dynamics involve the channel-base current. One analytical current waveshape involves Heidler's function [1]

$$i_0(t) = \sum_{i=1}^2 I_{mi} [(t/\tau_{i1})^{n_i} / (1 + (t/\tau_{i1})^{n_i})] \exp(-t/\tau_{i2}). \quad (1)$$

where I_m is the current magnitude, τ_1 and τ_2 are the time-discharge constants determining the leading and the trailing edge of the current, respectively, and n is

the current steepness factor. In Table 1 the parameters of the curves fit for the channel-base current according to the measurements [2] are presented.

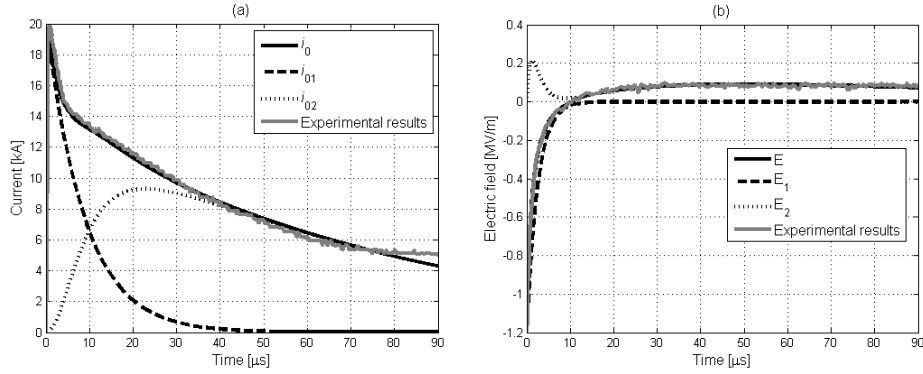


Figure 1. The channel-base current (a) and the measured electric field (b) (for stroke 1 in flash S0033, [2]) and their fit curves separated into two components.

The best fit of the measured current is obtained taking into account the existence of two channel-base current components, Fig. 1a.

Table 1. Parameters of the current fit curves according to measurements, [2].

Curve Fit	I_{mi} [kA]	n_i	τ_{i1} [μs]	τ_{i2} [μs]
(1) $i=1$	20.403	4	71.801	8.7766
(2) $i=2$	15.288	2	9.9791	0.19364

2. CLOSE ELECTRIC FIELD DURING RETURN STROKE

We used the measured value of the radial electric field for the same event (stroke 1 in flash S0033) in [2]. It means that the field waveform is adjusted so that the time onset is at the peak of the leader field, i.e., we considered only the trailing edge of the signal, Fig. 1b. The following mathematical expression for the field curves fit is used

$$E_1(t) = -E_{m1} \exp[-t / \tau_{21}], \quad (2)$$

$$E_2(t) = E_{m2} (t / \tau_{12})^n / [1 + (t / \tau_{12})^n] \exp(-t / \tau_{22}) + E_{m1} [\exp(-t / \tau_{11}) - \exp(-t / \tau_{21})],$$

where $\tau_{12} = 1.098 \mu\text{s}$, $\tau_{22} = 59.21 \mu\text{s}$, $\tau_{11} = 2.5 \mu\text{s}$ and $\tau_{21} = 50 \mu\text{s}$ are the time decay constants, $E_{m1} = 1.191 \text{ MV/m}$, $E_{m2} = 1.244 \text{ MV/m}$ and $n = 1.136$ are the constants of the electric field. In Fig. 1b the graph of the measured field and its curves fit are depicted. Remaining radial electric field waveshapes recorded in [2], although with smaller field magnitudes, show a more or less similar structure.

3. CHANNEL CORONA SHEATH DISCHARGE

The expression of the radial electric field closed to the negatively charged channel corona sheath during return stroke is overtaken from [3]

$$E = q_0^+ / (2\pi\epsilon_0 r) [f^+(u) - 1], \quad (3)$$

where $f^+(u)$ is the channel charging function defined in the GTCS model, $u = t - z/v (> 0)$ is the generalized time, z is the channel altitude, v is the return stroke speed and $q_0^+ = 6.67 \mu\text{C/m}$. Eq.(3) is derived without taking into account the transition line charge density along the channel core which could be neglected in the channel base if the ground is assumed to be perfectly conducting, that is the value of the ground reflection coefficient equals one, [3]. In aim to explain the positive overshoot of the electric field in the measurements [2], neglected in the previous study [3], we made some additional assumptions. The basic idea came after a review of other studies (e.g. [4], Ch.8) where the grounding resistance is considered. Based on the separation of the channel-base current into two components (Fig.1a) we assumed the following: for the current component i_{02} with smaller peak value (below 15 kA) the ground reflection coefficient ρ_2 is smaller than one, for the current component i_{01} with greater peak value (over 15 kA) this coefficient is $\rho_1 = 1$. In this case the reflection of the current i_{02} generates the transition line charge along the core near the channel bottom [5], but the current i_{01} does not (in both cases the current pulses travel along perfectly conducting channel core without attenuation). According to [5] additional field term caused by net negative transition line charge density in the core should be added in Eq.(3) which yields

$$E = q_0^+ / (2\pi\epsilon_0 r) \{ f^+ - 1 - i_{02}(1 - \rho_2) / [q_0^+ c(1 + \rho_2)] \}, \quad (4)$$

Rearranging the terms in Eq.(4) one obtains

$$f^+ = 1 + 2\pi\epsilon_0 r E / q_0^+ + i_{02}(1 - \rho_2) / [q_0^+ c(1 + \rho_2)]. \quad (5)$$

Since $f^+(0) = 0$, $i_0(0) = 0$ that is $2\pi\epsilon_0 r E(0) = -q_0^+$, it is clear from Eq.(5) that the channel charging function has a positive overshoot if $\rho_2 < 1$. The measured electric field is approximated with two functions, Fig.2a

$$E = E_1 + E_2. \quad (6)$$

Substituting Eq.(6) into Eq.(5) one obtains

$$f^+ = f_1^+ + f_2^+, \quad (7)$$

$$f_1^+ = 1 + 2\pi\epsilon_0 r E_1 / q_0^+, \quad f_2^+ = 2\pi\epsilon_0 r E_2 / q_0^+ + i_{02}(1 - \rho_2) / [q_0^+ c(1 + \rho_2)].$$

The charging function f_1^+ in Eq.(7) represents the classical charging function introduced previously in the GTCS model [3]. The charging function f_2^+ in Eq.(7) represents a new, additional function (charging the channel corona with an overcompensated positive charge) generated by the core line charge density. In Fig.2a both channel charging functions are depicted. The initial corona line

charge density distribution ($q_{tot}^-(z)$) and the return stroke speed (v) just prior to the return stroke can be found solving Eq.(8)

$$i_0(t) = [1/(1+\rho_2) + 1/2] \int_0^{v^*t} |q_{tot}^-(\xi)| \partial f_2^+(t-\xi/v^*) / \partial t d\xi. \quad (8)$$

where $v^* = vc/(v+c)$. Using Eqs.(7) and (8) in Figs. 2a and 2b, the channel charging functions and the line charge densities are depicted for different values of the ground reflection coefficient ρ_2 , respectively. The corresponding return stroke velocity is also calculated.

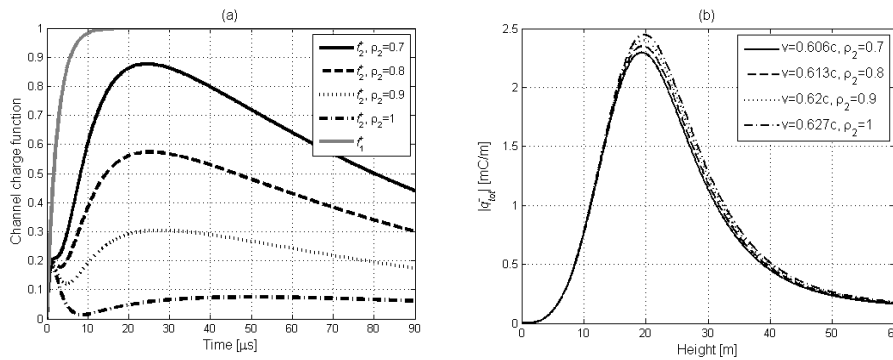


Figure 2. The channel charging function (a) and the initial channel line charge distribution (b) for different values of ground reflection coefficient according to Eqs. (7) and (8).

Acknowledgements

Ministry of Science and Technological Development of the Republic of Serbia supported this work under the contracts No. 171007 and 37019.

REFERENCES

- [1] F. Heidler, Journal of Lightning Research, 1, 40 (2007).
- [2] M. Miki, V. A. Rakov, K. J. Rambo, G. H. Schnetzer and M. A. Uman, J. Geophys. Res., 107 (D16), 4277 (2002).
- [3] M. Tausanovic, S. Markovic, S. Marjanovic, J. Cvetic and M. Cvejic, IEEE EMC, Vol. 52, No.2, DOI: 10.1109/TEMC.2010.2044886, 2010.
- [4] J. He, R. Zeng and B. Zhang, Methodology and technology for power system grounding, John Wiley & Sons, Singapore, 2013.
- [5] R. Thottappillil, V. A. Rakov, M. A. Uman, JGR, 102 (D6),6987 (1997).

ABNORMAL GLOW DISCHARGE IN ETHANOL VAPOUR

J. Sivoš, D. Marić, N. Škoro, G. Malović and Z. Lj. Petrović

*Institute of Physics, University of Belgrade,
Pregrevica 118, 11000 Belgrade, Serbia
e-mail: sivosj@ipb.ac.rs*

Abstract. In this paper we present measurements of Volt-Ampere characteristic for low-pressure discharge in ethanol vapour, at pd (pressure x gap) of 0.2 Torr cm and electrode gap of 1.1 cm. We focused more closely to the abnormal glow regime in ethanol, in particular, to the observed changes in operation mode of discharge. The transition occurs after certain time and it is smooth, without any instability in V - A waveforms.

1. INTRODUCTION

Nowadays discharges in ethanol represent one of the most interesting and potentially most lucrative areas of research because of wide range of possible applications. Fuel industry, sensor development, food industry, nanotechnology are fields where discharges in ethanol finds its implementation [1,2]. However, there is a lack of relevant data in literature. Therefore, studying basic properties of these discharges is of great importance. Earlier, we reported on breakdown conditions and spatial profiles in low-current limit of the discharge [3]. Here we present V - A characteristic of ethanol vapour discharge measured at working conditions close to the minimum of the Paschen curve, with detailed analysis of unusual behaviour observed in abnormal glow regime of the discharge.

2. EXPERIMENTAL SET-UP

The parallel-plane system of electrodes is fitting tightly inside a cylindrical quartz tube, which prevents long-path breakdown. Cathode surface is polished copper, while anode is quartz glass coated with transparent conductive thin film of platinum. Electrodes are 5.4 cm in diameter, 1.1 cm apart. Ethanol vapour is obtained from 95 % ethanol. The V - A characteristic of the discharge is scanned by applying a pulse of current in addition to a very small dc current that keeps the discharge running. The pulses are long enough so the discharge can reach steady state in a higher current regime. This way of measurements enables

avoiding gas and cathode heating and conditioning of the cathode surface during the measurements. Axial discharge profiles are recorded using a fast sensitive ICCD camera (Andor IStar DH720-18U-03). More detailed information on the measurement technique can be found elsewhere [4,5].

3. RESULTS AND DISCUSSION

Volt-Ampere characteristic of the discharge in ethanol vapour is presented in Figure 1. The V - A characteristic exhibits behaviour typical for low-pressure dc discharges, with distinguished regions of different discharge modes: low-current Townsend regime, at moderate currents normal glow and high current abnormal glow regime [4]. Between Townsend and normal glow regime, for currents from $20\ \mu\text{A}$ to $300\ \mu\text{A}$, is the region of free-running oscillations where steady state values of current and voltage cannot be obtained. In Townsend regime, V - A characteristic shows slight negative slope, with negative differential resistance of $R_D = -84\ \text{k}\Omega$. Abnormal regime is characterized with a very steep positive slope for currents above $800\ \mu\text{A}$.

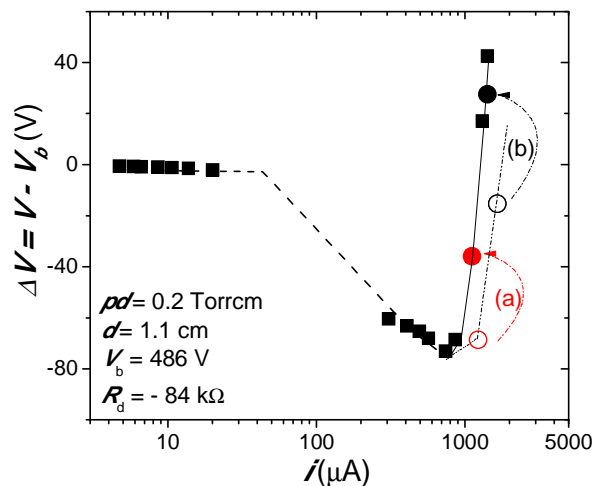


Figure 1. Volt-Ampere characteristic of ethanol vapour discharge for $pd = 0.2\ \text{Torr cm}$ and $d = 1.1\ \text{cm}$. Voltage is shown as a difference between discharge (V) and breakdown voltage (V_b). Circles indicate corresponding points shown in Figure 2.

Measurements in abnormal regime of discharge reveal changes in steady-state current and voltage values within single voltage pulse. The transition is noticed in the current range from the beginning of positive slope of V - A characteristic at around $860\ \mu\text{A}$ to around $1430\ \mu\text{A}$. In Figure 2 we show two examples of current and voltage waveforms with pronounced step-like shape due to the mode change. In Figure 2 a), where the initial current is $\sim 1240\ \mu\text{A}$, transition in operation mode occurs after approximately 2 ms. At the beginning of the pulse, the discharge operates at lower voltage and higher current, and then

it switches to ~ 40 V higher voltage and ~ 130 μA smaller current. The same effect is present at higher initial current of ~ 1680 μA , shown in Figure 2 b), just the transition happens here 30 μs after stable operation. By switching the operation mode the discharge continues to operate at ~ 70 V higher voltage and ~ 320 μA smaller current. It appears that the transition happens earlier within the pulse at higher currents.

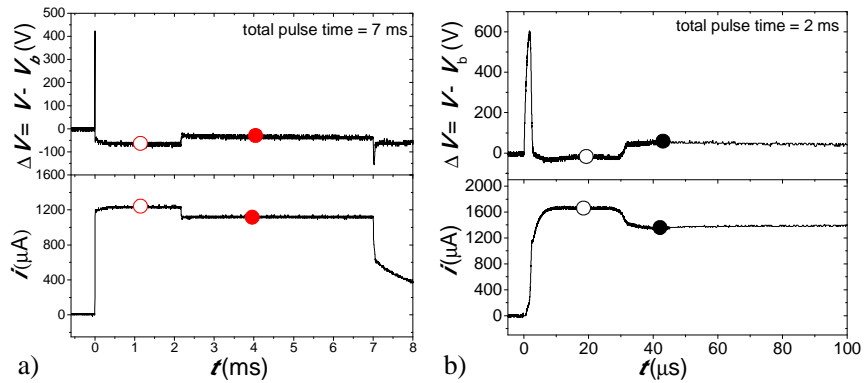


Figure 2. Waveforms of voltage and current obtained a) at lower current (initial $i_d \approx 1240$ μA) and b) higher current (initial $i_d \approx 1680$ μA). Values of the current and voltage before and after the transition are shown as open and closed circles in Figure 1.

In both cases, the transition is smooth, without any instabilities or oscillations in V - A waveforms. Moreover, there is no significant change in spatial structure of the discharge that could explain the mode change. Figure 3 shows axial profiles of emission recorded with a short exposure time (0.2 μs) at time points marked in Figure 2 b). Ratios of maximum intensities of profiles near the cathode and the anode, recorded before the step (open circles) and after the step (full circles), are the same (around 3). In both profiles, significant influence of heavy particles in excitation and ionization is visible (revealed through the peak of emission near the cathode). The profile recorded after the transition has higher overall intensity and the emission peak near the anode (negative glow) is shifted toward the cathode in comparison with the profile obtained before the transition, due to a change in electric field distribution.

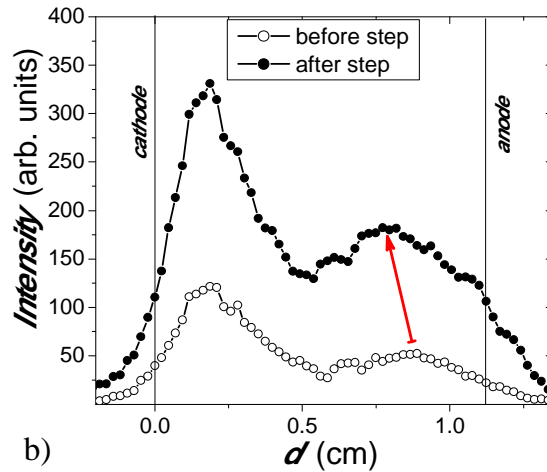


Figure 3. Axial profiles of emission from the discharge recorded before and after the step. Symbols correspond to points in Figure 2 b).

Apparently, after some time of stable operation, discharge slides into more preferable operating mode with lower current and higher voltage. We assume that there are changes in balance of charged or excited species: ions or electronically and vibrationally excited dissociation products of ethanol. Further experimental investigations and modelling should reveal processes behind the change in discharge regime. This effect is interesting from the point of basic discharge properties, but also for applications that operate in pulsed or high frequency glow regime.

Acknowledgements

This work is supported by the Serbian Ministry of Education, Science and Technological Development under project numbers ON 171037 and III 41011.

REFERENCES

- [1] G. Petitpas, J. D. Rollier, A. Darmonb, J. Gonzalez-Aguilar, R. Metkemeijer, L. Fulcheri, *International Journal of Hydrogen Energy*, 32, 2848 – 2867 (2007).
- [2] T. Hagino et al, *Appl. Phys. Express*, 5, 035101 (2012).
- [3] D. Marić, J. Sivoš, N. Škoro, G. Malović and Z. Lj. Petrović, 31st ICPIG (Granada, Spain, 14th-19th July 2013) PS4-048 (2013).
- [4] D. Marić, P. Hartmann, G. Malović, Z. Donko and Z. Lj. Petrović, *J. Phys. D: Appl. Phys.*, 36, 2639–2648 (2003).
- [5] N. Škoro, D. Marić, G. Malović, W. G. Graham and Z. Lj. Petrović, *Phys.Rev. E*, 84, 055401 (R) (2011).

ELECTRICAL BREAKDOWN IN LOW-PRESSURE METHANOL VAPOUR

J. Sivoš, D. Marić, N. Škoro, G. Malović and Z. Lj. Petrović

*Institute of Physics, University of Belgrade,
Pregrevica 118, 11000 Belgrade, Serbia
e-mail: sivosj@ipb.ac.rs*

Abstract. In this work we present measurements of dc breakdown voltages against pressure x electrode gap (pd) – Paschen curve in low-pressure methanol vapour. The discharge is established between parallel-plate electrode system at pd values between 0.1 Torr cm and 1.7 Torr cm. All measurements are carried out at electrode separation of 1.1 cm. Breakdown voltage measurements are supported with recordings of the axial profiles of the discharge emission with an ICCD camera. This enables us to verify the regime of the discharge and gives us the insight in elementary processes that participate in breakdown.

1. INTRODUCTION

A new realm in non-equilibrium discharges field, discharges in liquids and in contact with liquids, attract a considerable interest lately owing to the growing field of their possible applications. Despite of many developing applications and, in some cases, commercially operating devices, understandings and explanations of elementary processes taking place in these discharges is pervaded with inconsistencies and lack of experimental data. Since breakdown in liquids is quite complex issue [1], studies of breakdown in vapours of relevant liquids can provide initial information necessary for study important processes in the gas phase [2] and at surfaces [3].

In this work we show measurements on breakdown properties of methanol vapour at low pressure. Apart from measuring breakdown voltages in a wide range of pd (pressure x electrode gap) parameter, we show spatially and spectrally resolved emission from low-current discharge, which reveal information on elementary processes at different breakdown conditions.

2. EXPERIMENTAL SET-UP

Breakdown of methanol vapour is realized in a cylindrical quartz tube with plane-parallel electrodes: copper cathode and quartz anode with transparent and conductive platinum film (5.4 cm in diameter). Electrodes were separated at 1.1 cm. The electrical circuit with high resistance provided highly reproducible and reliable determination of breakdown voltages [4]. High reproducibility of measurements was also facilitated by cathode conditioning in moderate-current hydrogen prior to the measurements [5, 6] and tested by repeated measurements.

Quartz cylinder allowed side-on view on the discharge, i.e. recording of axial discharge profiles using a sensitive ICCD camera (Andor IStar DH720-18U-03). Time-integrated profiles of the discharge running in a steady state regime were integrated in visible spectra and with narrow band-pass filters at 425 nm and 656 nm ($H\alpha$). Methanol vapour is obtained from 99 % methanol using the same procedure as for water vapour [7].

3. RESULTS AND DISCUSSION

In Figure 1 we present Paschen curve for methanol vapour recorded for pd range from 0.1 Torr cm to 1.7 Torr cm, with the reduced electric field (E/N) indicated with dashed lines. The minimum of the Paschen curve is at $pd = 0.4$ Torr cm for breakdown voltage of 478 V. Up to $pd = 0.7$ Torr cm the discharge operation is stable. At higher pd , the discharge falls into relaxation oscillations. However it was possible to estimate breakdown voltages from oscillatory patterns [7].

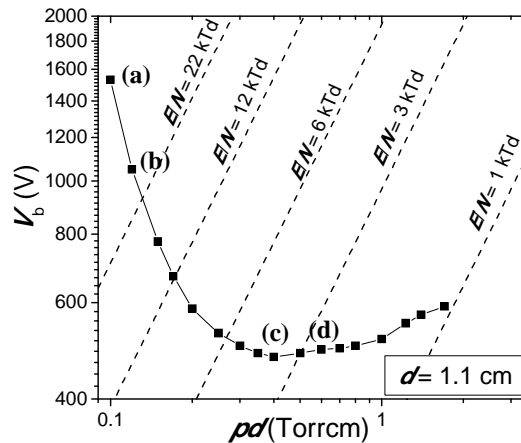


Figure 1. Paschen curve in methanol vapor recorded for electrode gap $d=1.1$ cm. Labels (a)-(d) correspond to profiles shown in Figure 2.

Distribution of emission intensity in methanol discharge running in the low-current limit of the V - A characteristics ($\sim 1\mu\text{A}$) are shown in Figure 2. The profiles are obtained from 2D side-on images of the discharge. For each pd a

profile obtained from emission integrated in visual spectra (full line) as well as profiles obtained with optical filters are shown. Optical filters are used to single out spatially resolved emission of CH band, with a bandhead at 431.2 nm (dashed line); and emission from Balmer excited hydrogen atoms ($H\alpha$ line at 656.28 nm) (dash-dot-dotted line).

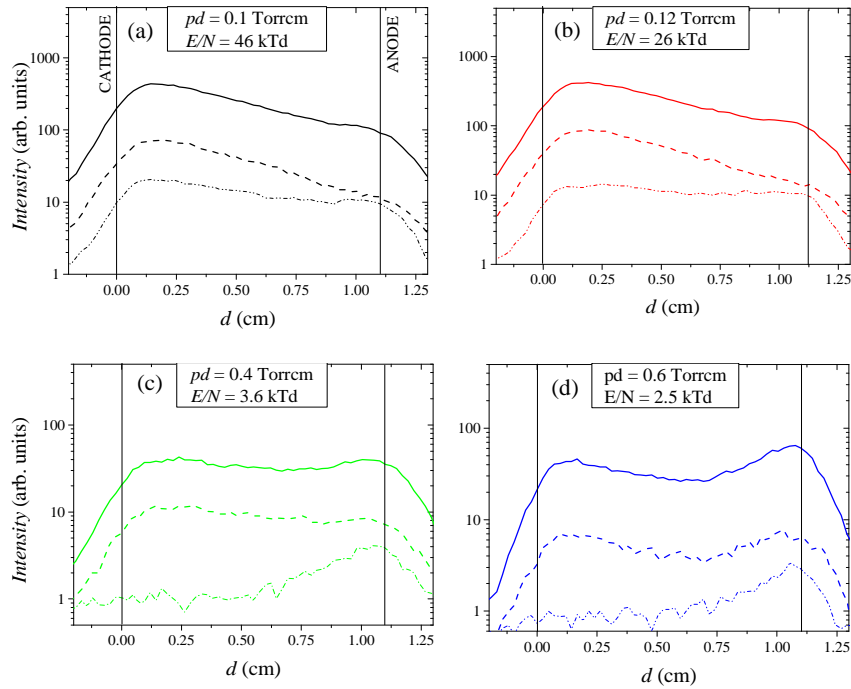


Figure 2. Axial profiles of Townsend discharge methanol vapour (close to the breakdown conditions $\sim 1\mu\text{A}$) for different values of pd (E/N) parameter. Emission integrated in visual spectra is shown – full lines, CH emission at 431.2 nm – dashed lines and $H\alpha$ emission (656 nm) – dash-dot-dotted lines.

Generally, CH emission follows the integrated emission profile in shape - all profiles show distinguished peak of emission near the cathode, which indicates that heavy-particles (positive ions and fast neutrals) have significant contribution in excitation [5]. At low pd (high E/N), this contribution becomes even dominant. The most important changes with operating pressure can be observed in $H\alpha$ emission. While at the highest E/N , $H\alpha$ emission mainly comes from heavy-particle induced processes of excitation, the profile levels off at $E/N = 26$ kTd. Below 10 kTd processes with electron induced excitation become dominant, which is revealed through the exponential increase of intensity from the cathode to the anode.

4. CONCLUSIONS

We have measured Paschen curve for methanol vapour and obtained the minimum voltage of 478 V at pd 0.4 Torr cm. Axial profiles of light emission show changes in excitation processes at different E/N values: from domination of heavy-particle processes at high E/N (at lower pressures) through equal contribution of electron and heavy-particle excitation around the minimum (0.4 Torr cm), while at higher pressure (lower E/N) electron excitation become significant. Spatially and spectrally resolved measurements of emission gave us some insight in elementary processes that participate in breakdown in methanol vapor. Further studies will include time resolved measurements of breakdown, to follow kinetics of the main elementary processes.

Acknowledgements

This work is supported by the Serbian Ministry of Education, Science and Technological Development under project numbers ON 171037 and III 41011.

REFERENCES

- [1] P. Bruggeman, C. Leys, J. Phys. D: Appl. Phys. 42 (no. 5), 053001 (2009).
- [2] V. Stojanović, J. Sivoš, D. Marić, N. Škoro, Z. Lj. Petrović, 26th SPIG (Zrenjanin, Serbia, August 27-31. 2012) 35-38 (2012).
- [3] M. Klas, S. Matejčik, M. Radmilović-Radjenović and B. Radjenović EPL 99, 57001 (2012).
- [4] D. Marić, M. Savić, J. Sivoš, N. Škoro, M. Radmilović-Radjenović, G. Malović, and Z. Lj. Petrović, Eur. Phys. J. D. 68, issue 6 155 ((2014).
- [5] D. Marić, P. Hartmann, G. Malović, Z. Donko, Z. Lj. Petrović, J. Phys. D: Appl. Phys. 36, 2639 (2003).
- [6] Z. Lj. Petrović and A.V. Phelps, Phys. Rev. E 47(4), 2806 (1993).
- [7] N. Škoro, D. Marić, G. Malović, W. G. Graham and Z. Lj. Petrović, Phys.Rev. E, 84, 055401 (R) (2011).

ON THE ELECTRIC POTENTIAL OF A DUSTY PLASMA IN THE PRESENCE OF THE ELECTRONEGATIVE GAS

K.Yasserian and A. Rahbarbinesh

Department of Physics, College of sciences, Karaj Branch, Islamic Azad University, Karaj, Iran

Abstract. Electronegative dusty plasma is investigated in the presence of the positively charged dust particles. For a different of negative ion temperatures, the electric potential of the dust as a function of positive ion mass are obtained. In addition, the dependence of the space charge around the dust on the electrons and negative ions temperature is studied. The results show that there is the critical value in which the sign of the dust potential changes.

1. INTRODUCTION

The dusty plasmas have wide applications in the industry and laboratories [1,2]. The dusty plasmas are quasi-neutral space containing small solid particles with a grain size of nanometers to micrometers. In the usual case, the electrons of the plasma are more mobile than the ion and therefore, the dust particles gain a negative charge. However, in the presence of photoemission, electron emission and thermionic emission, dust can gains positive charge [3, 4]. In addition, in the case of electronegative plasma, if the positive ions are lighter than the negative ions, dust particles acquire a positive charge [3].

Calculating of the electric potential of dust particle is still an open question. There are several articles which deal with investigation of electric potential of the dusty plasmas. In Ref [5, 6] a dusty plasma is considered when the positive ions have two temperatures In the current study, we focus on the dusty plasma which consists of the negative ions and electron as well as the positive ion in the case of positive dust particles. Using the convenient governing equations, the plasma potential and space charge profiles are obtained in different conditions.

1.1 Governing equations

It is assumed that the charge species are distributed according to the Boltzmann relation as:

$$n_n = n_{n0} \exp\left(\frac{e\phi}{T_n}\right) \quad n_e = n_{e0} \exp\left(\frac{e\phi}{T_e}\right) \quad n_i = n_{i0} \exp\left(-\frac{e\phi}{T_i}\right)$$

Far from the dust at the edge of plasma-sheath, the condition of the quasi-neutrality implies that $n_{i0} + z_d n_{d0} = n_{e0} + n_{n0}$, where n_{i0} , n_{e0} and n_{d0} denotes the ion, electron and dust number densities at the edge of plasma-sheath respectively and Z_{d0} is the number of electric charge accumulated on the dust grain. In addition, $dQ_d/dt = I_e + I_n + I_i$, where Q_d represents the electric charge of dust particles and I_e , I_n and I_i are the electric current caused by flows of electrons, negative ions and positive ions and can be written as:

$$I_e = -e\pi^2 \left(\frac{8T_e}{\pi m_e}\right)^{\frac{1}{2}} n_e \left(1 + \frac{e\phi}{T_e}\right) \quad I_n = -e\pi^2 \left(\frac{8T_n}{\pi m_n}\right)^{\frac{1}{2}} n_n \left(1 + \frac{e\phi}{T_n}\right)$$

$$I_i = e\pi^2 \left(\frac{8T_i}{\pi m_i}\right)^{\frac{1}{2}} n_i \exp\left(-\frac{e\phi}{T_i}\right)$$

At the equilibrium condition, the total current reaching to the dust vanishes. Therefore, it can be shown that:

$$-\frac{e\phi}{T_i} = \ln\left[\left(\frac{m_i T_e n_e^2}{m_e T_i n_i^2}\right)^{\frac{1}{2}} \left(1 + \frac{e\phi}{T_e}\right) + \left(\frac{m_i T_n n_n^2}{m_n T_i n_i^2}\right)^{\frac{1}{2}} \left(1 + \frac{e\phi}{T_n}\right)\right]$$

By the Matsoukas and Russell [4], an approximate solution can be found as:

$$-\frac{e\phi}{T_i} = \ln\left[\left(\frac{m_i T_e n_e^2}{m_e T_e n_i^2}\right)^{\frac{1}{2}} + \left(\frac{m_i T_n n_n^2}{m_n T_n n_i^2}\right)^{\frac{1}{2}}\right]$$

2. RESULTS

In the Figure 1 the normalized dust potentials are drawn as a function of positive ion mass for three values of negative ion temperature when $T_i = 0.1T_e$. As can be seen from that figure, by increasing the positive ion mass, the dust potential decreases and at the higher positive ion masses, the potential becomes negative.

From Figure 2, it is observed that increase electron temperature results to increase of dust potential. By increase of the temperature of electrons and negative ions, electrons and negative ions will enhance its energy and result to increase the value of Debye length which in turn leads to increase of electrical potential of the dust.

Figure 3 shows the normalized electric potential as a function of number density of electrons and negative ions. The figure illustrates that if the

numbers of electron and negative ions in plasma environment are sufficiently low, the potential will be positive. If the number density of electrons becomes high, the charge of the dust particles becomes negative which cannot be included in our model.

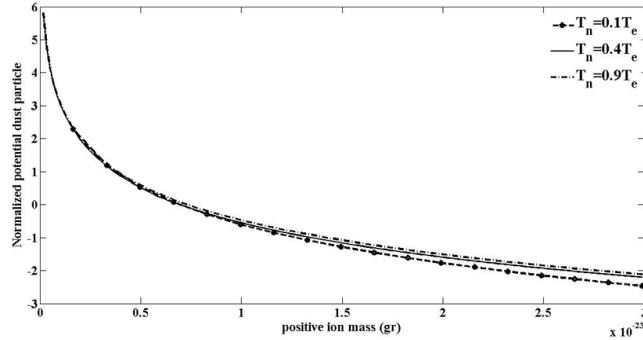


Figure 1. Normalized potential versus positive ion mass in three values for negative ion temperature.

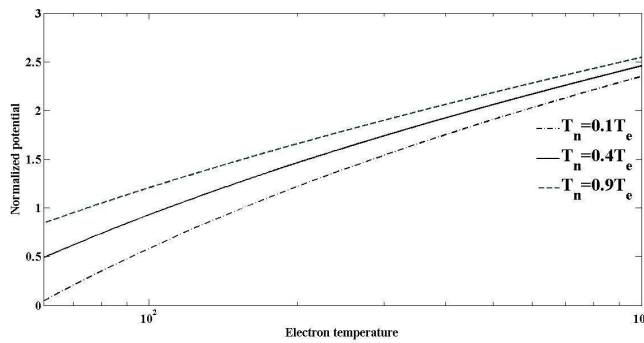


Figure 2. Normalized potential versus electron temperature ($T_i=0.1T_e$).

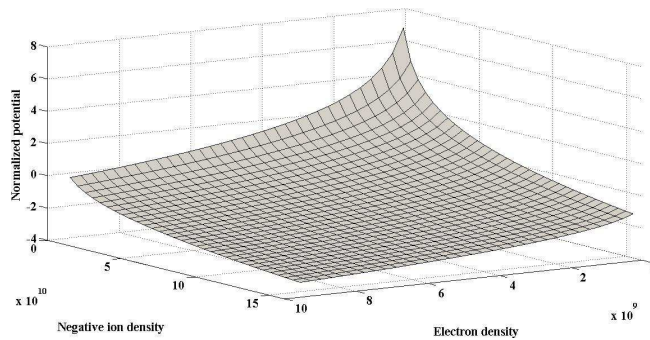


Figure 3. Normalized electric potential versus the number density of electrons and the number density of negative ions.

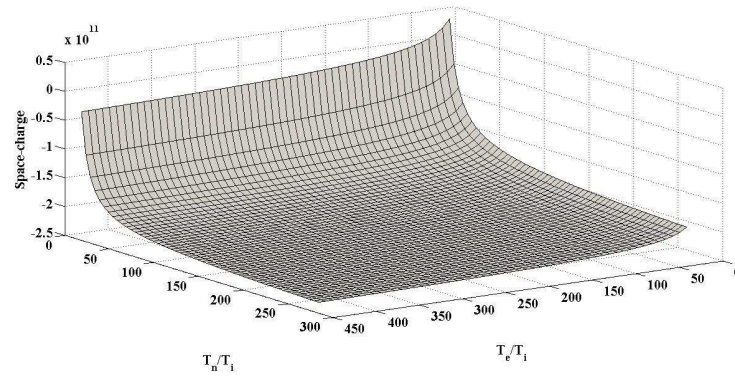


Figure 4. Space-charge versus ratio electrons and negative ions temperature on the positive ion temperature.

The Figure 4 shows space-charge around the dust particle as a function of ratio of negative ion temperature and electron temperature to positive ion temperature. As the case of positive dust particle is consider herethe space-charge formed around the dust is negative. However, by decreasing the electron and negative ion temperature, the space-charge can have a positive value which is equivalent to those conditions where the dust potential is negative.

3. CONCLUSIONS

We have considered the electronegative dusty plasma. It is shown that for sufficiently light positive ion, the electric potential of dust increases while in the presence of cold negative ion, that potential reduces. In addition, by rising up the negative ion, the dust potential increases. Furthermore, for low enough positive ion mass and high electronegativity, it is shown that the space-charge around the dust particle is negative.

REFERENCES

- [1] A. A. Samarian, O. S. Vaulina, A. P. Nefedov, V. E. Fortov, B. W. James and O. F. Petrov, *Phys. Rev.* 64, 056407
- [2] M. Cavarroc, M. C. Jouanny, K. Radouane, M. Mikikian and L. Boufendi, *J. Appl. Phys.* 99, 064301 (2006).
- [3] R. L. Merlino and Su-Hyun Kim, *Appl. Phys. Lett.* 89, 091501 (2006).
- [4] Themis Matsoukasa and Marc Russell. *J. Appl. Phys.* 77 (9) (1995).
- [5] D. Dorrnian, F. Shahbaz Tahmasebi, A. H. Sari and Y. Golian, *J Fusion Energ*, DOI 10.1007/s10894-010-9324-9.
- [6] Hamiz Reza Pakzad, *Solitons and Fractals* 42, 874 (2009).

PROPAGATION OF NEGATIVE PLANAR STREAMER FRONTS IN NOBLE GASES

S. Dujko¹, A.H. Markosyan² and U. Ebert³

¹*Institute of Physics, University of Belgrade,
Pregrevica 118, 11080 Belgrade, Serbia*

²*Electrical Engineering and Computer Science Department,
University of Michigan, Ann Arbor, MI 48109, USA*

³*Centrum Wiskunde & Informatica (CWI),
P.O. Box 94079, 1090 GB Amsterdam, The Netherlands*

Abstract. In this work we use our recently developed high order fluid model for streamer discharges to study the propagation of negative planar streamer fronts in noble gases. Values of streamer velocity, ionization level behind the front and average electron energy are presented for a range of the applied reduced electric fields. We found that the propagation of fronts is the fastest in helium while the ionization level behind the streamer front depends strongly on the applied reduced electric fields. The non-local effects in the profile of the average energy are present both in the PIC/MC (Particle in cell/Monte Carlo) model and in the high order fluid model, but are missing in the first order model due to the local field approximation.

1. INTRODUCTION

Streamers are transient filamentary plasmas produced by an ionization front that moves through non-ionized matter. Streamers occur in the initial stages of lightning and in sprite discharges above thunderclouds [1] as well as in industrial applications such as lighting [2] and gas cleaning [3]. Further optimization and understanding of such application is dependent on an accurate knowledge of the streamer properties, including the streamer velocity, spatiotemporal evolution of the particle densities and electric field and physical and chemical processes involved. Various techniques employed in this problem, for example fluid equation treatments, PIC/MC simulations and hybrid techniques have been recently reviewed [4, 5].

The most popular streamer model is the so-called classical fluid model for the densities of different particle species in the discharge. This simple model encompasses only the equations of conservations of density and momentum. If the effects due to the thermal motion of the particles and the force due to the divergence of the pressure tensor are neglected, then the simplified momentum balance equation, e.g., the drift-diffusion approximation follows. Fluid equations are closed in the local field approximation. This means that transport and rate coefficients for electrons (and ions) are functions of local electric field.

In this work we apply our recently developed high order fluid model to investigate propagation of negative planar ionization fronts in noble gases. The aims of this work are: (1) to provide fluid based calculations of the streamer properties, including the front velocity, ionization level behind the front and average electron energy for various noble gases; (2) to investigate the non-local effects of the average electron energy in three distinct spatial regions: the streamer head, the streamer channel and region ahead of streamer head, and (3) to test the classical fluid models and various types of second order models against the advanced high order and PIC/MC models.

2. THEORETICAL METHODS

In our recent papers [5, 6] we have developed a high-order fluid model for streamer discharges. The balance equations were obtained as velocity moments of the Boltzmann equation while the collisional terms were evaluated using momentum transfer theory. We have truncated the system of fluid equations at the level of energy flux balance by reducing the pressure tensor to a scalar kinetic pressure and by neglecting the high order terms associated with the flux of thermal motion. The energy flux of the drift motion, however, is included. The derived model consists of a set of differential equations for the electron density, for the average electron velocity, for the average electron energy and for the average electron energy flux. This system of differential equation is coupled to the Poisson equation for the electric field calculation. For more details we refer to [5, 6].

Results of simulations with the high order model are compared with those obtained by a PIC/MC model and with the classical fluid model (LFA). In addition, we include the results obtained from the fluid approach based on a two term theory for solving the Boltzmann equation. In this model the energy balance equation is obtained by the integration of the isotropic part of the distribution function over the energy and the system of fluid equations is closed in the so-called local-energy approximation (LEA). Electron transport data required as input in various fluid models are calculated from the solution of the non-conservative Boltzmann equation [5].

3. RESULTS AND DISCUSSIONS

As an illustrative example of transport data for electrons required as input in our fluid models, in figure 1 we show the variation of the electron mobility and ionization coefficient with E/n_0 in noble gases.

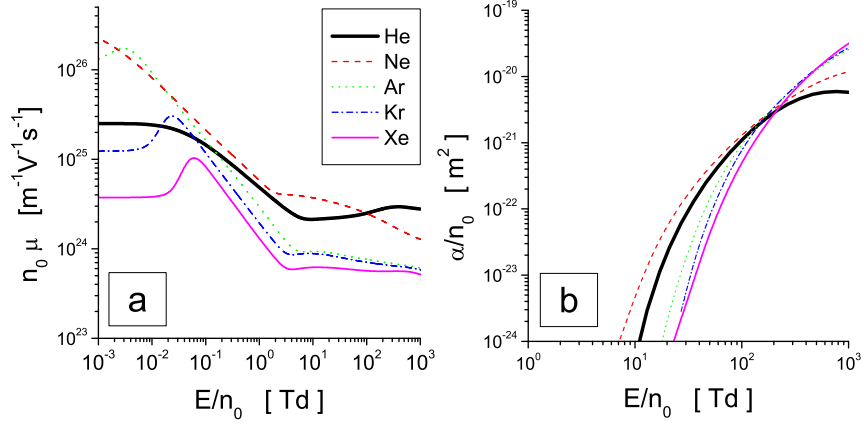


Figure 1. Variation of the mobility (a) and ionization coefficient (b) with E/n_0 for electrons in noble gases.

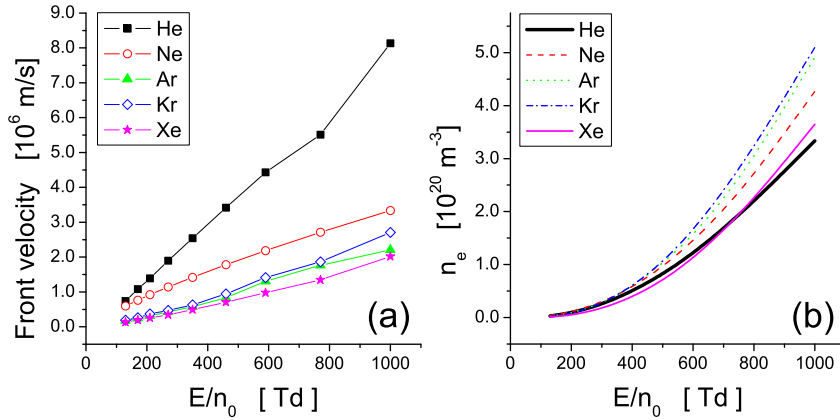


Figure 2. Variation of the front velocity (a) and ionization level behind the front (b) with E/n_0 for negative planar streamer fronts in noble gases.

Figure 2 shows the front velocity and ionization level behind the front as a function of E/n_0 . We observe that the propagation of planar

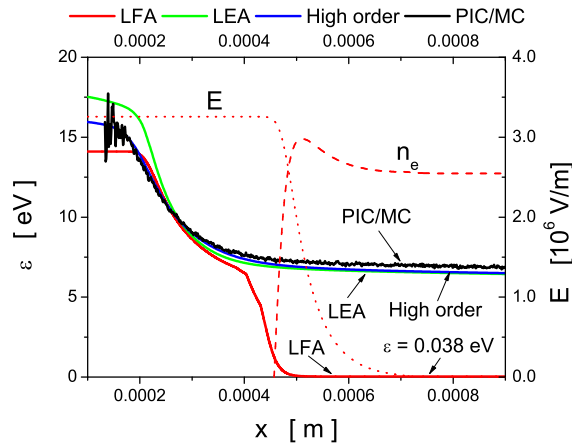


Figure 3. The average electron energy in four different models in Ne at time 1.2 ns and E/n_0 of 130 Td. Profiles of the electric field and the electron number density from the high order fluid model are also included to indicate the location of the front.

fronts is the fastest in He while the ionization level behind the front depends strongly on the applied reduced electric fields. As an example of non-local behavior of the average energy for noble gases, in figure 3 we show the averaged electron energy in four different models in Ne at time 1.2 ns. We see that the LFA model completely fails to describe the energy in the streamer channel. In this region the electric field is totally screened and hence LFA predicts the electron energy to take the thermal value of 38 meV.

REFERENCES

- [1] U. Ebert, S. Nijdam, C. Li, A. Luque, T.M.P. Briels and E.M. van Veldhuizen, *J. Geophys. Res. A* 115, A00E43 (2010).
- [2] G.G. Lister, J.E. Lawler, W.P. Lapatovich and V.A. Godyak, *Rev. Mod. Phys.* 76, 541 (2004).
- [3] E.M. van Veldhuizen, *Electrical discharges for Enviromental Purposes: Fundamentals and Applications* (Huntington, NY: Nova Science, 2000).
- [4] C. Li, J. Teunissen, M. Nool, W. Hundsdorfer, U. Ebert, *Plasma Sources Sci. Technol.* 21, 055019 (2012).
- [5] S. Dujko, A.H. Markosyan, R.D. White and U. Ebert, *J. Phys. D: Appl. Phys.* 46, 475202 (2013).
- [6] A.H. Markosyan, S. Dujko and U. Ebert, *J. Phys. D: Appl. Phys.* 46, 475203 (2013).

ELEMENTARY PHYSICAL PROCESSES OF ELECTRONS IN PLANETARY ATMOSPHERIC DISCHARGES

I. Adžić, Z.Lj. Petrović and S. Dujko

*Institute of Physics, University of Belgrade,
Pregrevica 118, 11080 Belgrade, Serbia*

Abstract. In this work we discuss the elementary physical processes of electrons in the mixtures of gases used to model planetary atmospheric discharges. Electron transport coefficients required as input in fluid models of these discharges are calculated as a function of electric and magnetic fields, and gas temperature using a multi term theory for solving the Boltzmann equation and Monte Carlo simulation technique. In particular, we present the results of our theoretical calculations for expected heights of occurrence of sprites above lightning discharges in atmospheres of planets in our Solar system.

1. INTRODUCTION

Sprites are large luminous discharges, which appear in the mesosphere at 40 to 90 km altitude above large thunderstorms [1, 2]. They represent one of the most spectacular forms of the so-called transient luminous events (TLEs) in the atmosphere of our planet. Sprites are always associated with positive cloud-to-ground lightning discharges which lower positive charge from clouds to the ground. After removal of positive charges from the cloud by a lightning stroke, the remaining negative charges in the thundercloud produces a large quasi-electric field above the thundercloud up to the conducting ionosphere. This field appears at all altitudes above the thundercloud, and endures for a time equal to approximately the local relaxation time at each altitude. The local relaxation time depends on the local conductivity and can be calculated from the profile of electron density and electron mobility. This temporarily existing electric field heats the electrons and controls transition from avalanches into streamers.

High speed telescopic images of sprites have revealed that sprites are collections of many individual streamers. In addition to sprites, other forms of TLEs are possible. These include the blue jets, the gigantic jets and elves. Though physical mechanisms behind of these TLEs are different comparing to sprites, the knowledge of electron transport properties for their modeling is of an essential importance.

The aims of this work are (1) to provide a database of electron transport coefficients in the mixtures of gases used to model planetary discharges, (2) to investigate the possibility of sprites in the atmosphere of other planets, and (3) to investigate the effects of planetary magnetic fields on electron kinetics and development of planetary atmospheric discharges.

2. THEORETICAL METHODS

2.1 The method of image charges

In this section we briefly discuss the quasi-electrostatic (QE) model used to calculate the electric field above the cloud after an intensive positive cloud-to-ground lightning discharge. Following some aspects of previous works [1, 2], our model assumes a dipole charge structure within a thundercloud where positive point charge is located above the negative one. When a positive point charge is removed, the remaining negative charge produces an instantaneous large QE monopole field. The conducting surface of the Earth immediately screens this electric field; the surface-thundercloud system at the altitude of the mesosphere can then be approximated by a dipole field. If a point positive charge is positioned at the thundercloud altitude z_s , the field E_s produced at z ($\gg z_s$) by this charge and its mirror below the ground is written as

$$E_s = \frac{Q}{4\pi\epsilon_0} \left[\frac{1}{(z - z_s)^2} - \frac{1}{(z + z_s)^2} \right] \approx \frac{Qz_s}{\pi\epsilon_0 z^3}, \quad (1)$$

where ϵ_0 is the vacuum permittivity. Pressure and altitude in our model are simply related by the hydrostatic equation. This suggests that the pressure of the atmosphere drops-off vertically like an exponential function. We assume an isothermal atmosphere: the vertical variation of the temperature is not taken into account.

2.2 Boltzmann equation and Monte Carlo method

Electron transport coefficients presented in this work are calculated from the solution of the non-conservative Boltzmann equation and using a Monte Carlo simulation technique [3]. Calculations are performed for electrons drifting and diffusing through a neutral gas under the influence of spatially homogeneous electric and magnetic fields, using cross sections for electron scattering as input.

3.RESULTS AND DISCUSSIONS

3.1 Expected heights of sprites in the atmosphere of Jupiter and Saturn

Jupiter and Saturn are gas giants with a $\text{H}_2\text{-He-CH}_4$ atmosphere. They lack a solid surface; the ionosphere is around 1000 km above the 1-bar level for both planets. For Jupiter, we placed a single charge center within the deep H_2O thundercloud which is supposed to reside between 5 and 3 bars, e.g., 30 km below the 1-bar level. For Saturn a single charge was placed 130 km below the 1-bar level.

In figure 1 we show the expected heights of sprites after lightning strokes in the atmosphere of Jupiter and Saturn. Calculations have been performed for different amount of charge Q . Conventional breakdown electric fields, E_k , for Jupiter and Saturn are, 10.6 and 11.5 kV/cm, respectively [4]. For selected values of Q , E_k is exceeded by the quasi-electrostatic field after a lightning stroke between 280 and 350 km above 1-bar level. These values are in good agreement with Yair *et al.* [2]. For Saturn, however, the expected heights of sprites are much higher, between 680 and 880 km above the 1-bar level.

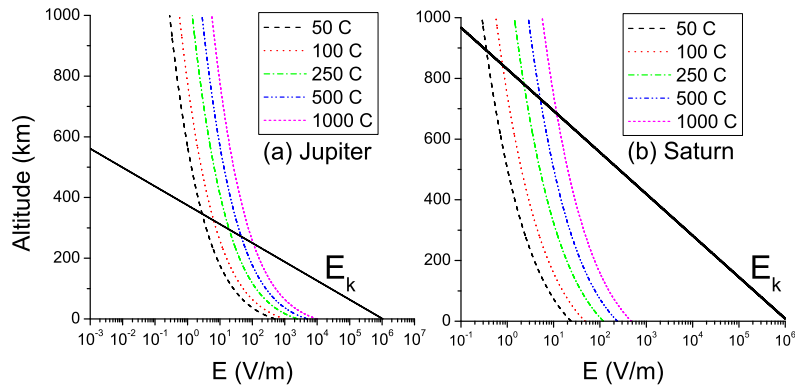


Figure 1. Electrostatic fields above Jupiter and Saturn thunderclouds possessing a negative charge located at -30 km for Jupiter and -130 km for Saturn below the 1-bar level. Where the conventional breakdown field E_k crosses the E field, a sprite can potentially occur.

3.2 Electron transport data for planetary atmospheres

Electron transport coefficients are calculated for all planetary atmospheres and the influences of specific physical processes on electron kinetics are identified. For example: (i) for Earth's atmosphere the effects of 3-body attachment on electron transport is studied; (ii) for Venusian atmosphere

the effects of the gas temperature is examined; and (iii) for gas giants, the influence of the electric and magnetic field strengths and their orientation is investigated. As an example of our calculations, in figure 1 we show the variation of the mean energy and longitudinal diffusion coefficient with E/n_0 and gas temperature T for electrons in Venusian atmosphere. For lower E/n_0 we observe that the electrons are in thermal-equilibrium with the gas mixture for $T = 293$ and $T = 773$ K. For higher E/n_0 the swarm is far from thermal-equilibrium and the effects of the gas temperature are minimal.

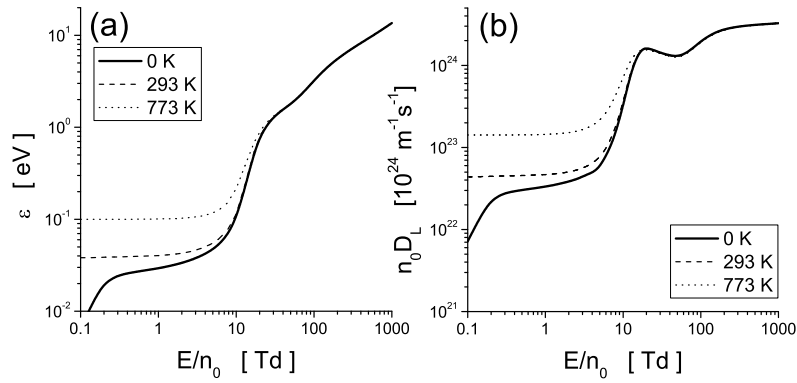


Figure 2. Variation of the mean energy (a) and longitudinal diffusion coefficient (b) with E/n_0 and gas temperature T for electrons in Venusian gas mixture ($\text{CO}_2:\text{N}_2=95:5$).

Acknowledgments

This work was supported by MPNTRRS Projects OI171037 and III41011.

REFERENCES

- [1] V. Pasko, in *Sprites, Elves and Intense Lightning Discharges* ed. M. Fullekrug (Berlin: Springer 2006) p. 253.
- [2] Y. Yair, Y. Takahashi, R. Yaniv, U. Ebert and Y. Goto, *J. Geophys. Res.* 114, E09002 (2009).
- [3] S. Dujko, R.D. White, Z.Lj. Petrović and R.E. Robson, *Phys. Rev. E* 81, 046403 (2010).
- [4] D.D. Sentman, 1st ISUAL scientific workshop, Taiwan, 08-O013-O016 (2004)

PARTICLE IN CELL SIMULATION OF THE ELECTRICAL ASYMMETRY EFFECT WITH A REALISTIC MODEL OF THE ION INDUCED SECONDARY EMISSION

Aleksandar Bojarov, Marija Radmilović-Radjenić
and Zoran Lj. Petrović

Institute of Physics, Pregrevica 11080, Belgrade, Serbia

Abstract. Capacitively coupled plasmas (CCP) have the possibility for separate control of ion flux and energy. Recently a technique was developed for improved separate control of ion flux and energy in a symmetric plasma reactor (B. G. Heil et al [1]). The electrical asymmetry effect (EAE) develops from a DC self bias which can be controlled, thus affecting the symmetry of the discharge. We examine the effect of different models of secondary emission from the electrodes on the characteristics of the EAE CCP discharges.

1. INTRODUCTION

Applicability of capacitively coupled radio frequency plasmas (CCP) in the electronic industry is governed by the efficiency of the separate control of the ion flux and energy. In application of these plasmas for etching of silicon wafers the ion energy is used to control the etching and deposition, while the ion flux is responsible for overall speed of these processes [2-3]. The flux of particles in asymmetric plasma reactor is different at the electrodes. A recently discovered electrical asymmetry effect (EAE) in dual frequency discharges can lead to improving the control of the ions [1,4]. The EAE effect was investigated using hybrid/fluid and Monte Carlo models [1,4] and also by PIC simulations [5]. When operated in higher pressures (starting from around 50Pa and above) the important source of ionization become electrons emitted from the bombarded surfaces. In this conditions a precise modeling of the ion induced secondary emission is required. To accomplish this we compute the probability for secondary electrons produced per impacting ion of energy ϵ according to the model of Phelps and Petrovic [6]

for a "dirty" electrode:

$$\gamma(\epsilon) = 0.002\epsilon/[1 + (\epsilon/30)^{1.5}] + 1.05 \times 10^{-4}(\epsilon - 80)^{1.2}/[1 + (\epsilon_i/8000)]^{1.5}, \quad (1)$$

where the second term is zero for ion energies ϵ below 80eV. We compare the effect of two models of secondary production ($\gamma(\epsilon)$ according to Equation (1) and a constant $\gamma = 0.1$) on the separate control of the ion energy and flux in EAE CCP.

2.SIMULATION CONDITIONS AND DISCUSSION

Simulations are performed using 1D PIC/MCC code in a plan parallel geometry with external circuit. The discharge gas is argon at 100Pa. Electron reflection coefficient is taken to be 0.2, secondary emission is as described before and background gas temperature is 350K. Electrode separation is 2cm in configuration where the right electrode is grounded and the left electrode is connected through a blocking capacitor ($C_b = 100nF/m^2$) on a voltage source of the form:

$$V(t) = 120[\cos(2\pi ft + \Theta) + \cos(4\pi ft)], \quad (2)$$

where the fundamental frequency is $f = 13.56\text{MHz}$. The phase Θ is varied from zero to $\pi/2$ in which the electrical symmetry goes from asymmetric at $\Theta = 0$, symmetric $\Theta = \pi/4$ and to opposite asymmetry at $\Theta = \pi/2$ i.e. the electrodes have switched roles (grounded electrode at $\Theta = 0$ behaves as the powered at $\Theta = \pi/2$ and vice versa). The induced asymmetry and the possibility to gradually change the role of the electrodes without physical changing the system is the main advantage in the EAE. In a working regime where the secondary electrons have ionization collisions in the sheath a precise model of their production on the electrodes is needed.

The difference in the ionization rate in the sheaths is present because of the different secondary electron production. Electronic ionization in the bulk plasma is smaller than in the sheaths due to the loss of energy in collisions before entering the bulk. On Figure 1 we see that this greatly affects the mean ion energy, a change in the effective gamma leads to shifting the mean ion energy. The relative change in the mean energy stays approximately the same, but in the absolute value the function is shifted significantly. One would also expect a change in the flux of ions, which is shown on Figure 2. In this case the same applies as the ion energy. We see that the separate control is greatly changed due to the change in the secondary production. This can decrease the possibility for separate control at higher pressures but EAE is still applicable with precise modeling of the secondary electron emission from the surface.

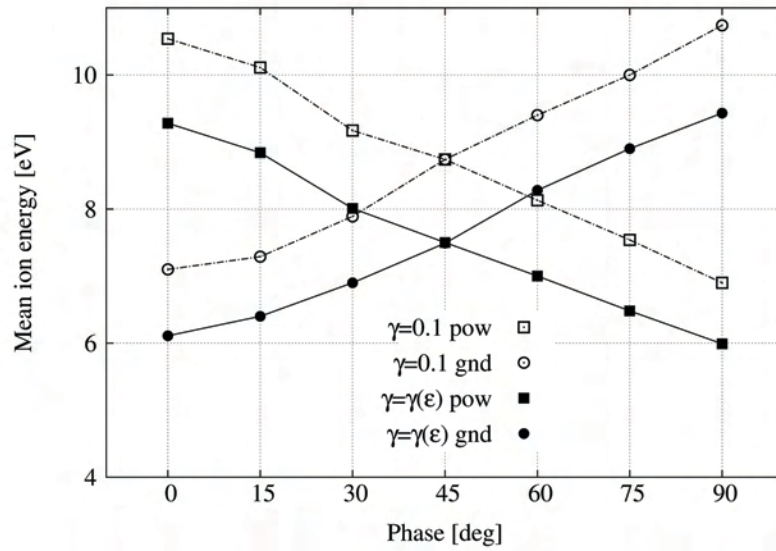


Figure 1. Mean ion energy at the grounded and powered electrode for two models of the secondary electron emission from the electrodes, in dependence of the phase angle Θ .

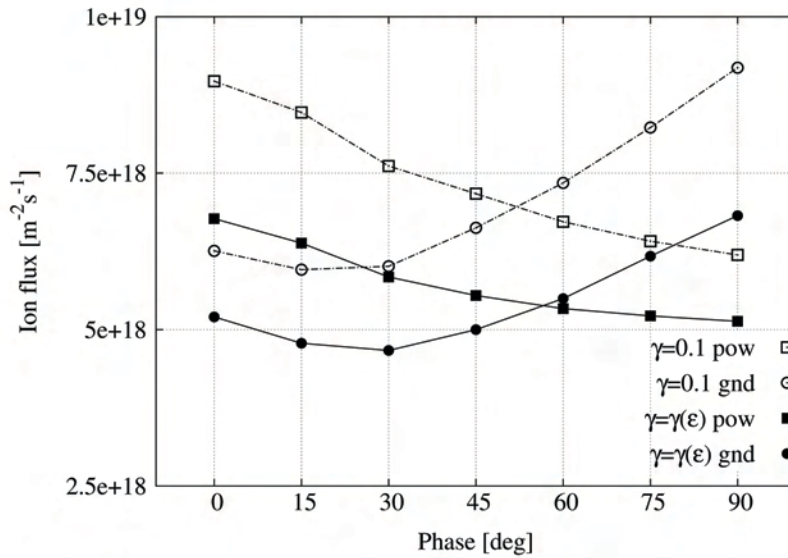


Figure 2. Flux of ions ions on the electrode and powered electrode for two models of the secondary electron emission from the electrodes, in dependence of the phase angle Θ .

Acknowledgements

This work is supported by Serbian Ministry of Education Science and Technological development under grants ON171037 and III41011.

REFERENCES

- [1] B. G. Heil, U. Czarnetzki, R. P. Brinkman and T. Mussenbrock, *J. Phys. D: Appl. Phys.* 41, 165202 (2008).
- [2] M. A. Lieberman and A. J. Lichtenberg, *Principles of Plasma Discharges and Materials Processing*, (Wiley Interscience, New Jersey, 2005).
- [3] T. Makabe and Z. Petrovic, *Plasma Electronics: Applications in Micro-electronic Device Fabrication*, (Taylor and Francis, CRC Press, 2006).
- [4] B. G. Heil, J. Schulze, T. Mussenbrock, R. P. Brinkmann and U. Czarnetzki, *IEEE Trans. Plasma Sci.* 36, 1404 (2008).
- [5] Z. Donkó, J. Schulze, B. G. Heil and U. Czarnetzki, *J. Phys. D: Appl. Phys.* 42, 025205 (2009).
- [6] A. V. Phelps and Z. Lj. Petrovic, *Plasma Sources Sci. Technol.* 8, R21-44 (1999).

MODELING OF THE RADIO FREQUENCY BREAKDOWN PASCHEN LIKE CURVES BY MONTE CARLO TECHNIQUE

Marija Savić, Marija Radmilović-Radjenović,
Milovan Šuvakov, Zoran Lj. Petrović

*Institute of Physics, University of Belgrade, Pregrevica 118, POB 68 Zemun,
11000 Belgrade, Serbia*

Abstract. The influences of the surface effects on the breakdown voltage curves of the radio frequency argon discharges are studied. A Monte Carlo code that was used follows transport of electrons only including surface effects. The obtained Monte Carlo results show a good agreement with the available experimental data.

1. INTRODUCTION

Study of the radio frequency (RF) discharges is of great importance for various applications such as biomedicine [1], microelectronics [2] and other plasma based technologies [3]. In order to optimize plasma technological processes it is often required to know gas breakdown conditions in a discharge device which can be determined from the breakdown voltage curve, known as Paschen curve. A necessary condition for a self sustained discharge is to have feedback between the electron growth toward instantaneous anode and their initialization at the cathode. We introduce a model for RF breakdown in electron dominated regime.

2. RESULTS AND DISCUSSION

For modeling of the RF discharges, we developed and tested a Monte Carlo code. In our calculations, well established cross sections data for argon was employed [4]. The breakdown voltage is determined in the same manner as explained in previous publications (see, for example, [5]). In this paper, we shall focus on the influence of the surface effects on the breakdown voltage curves.

When electron reaches the electrode, it can be reflected without any energy loss (elastic) or reflected with some energy loss (inelastic reflection). If inelastic reflection takes place, secondary electron can be ejected with Maxwellian energy distribution with peak at energy of 2 eV [6]. Finally, electron

can be absorbed by the electrode which may or may not be followed by secondary electron emission. Probability curves for elastic, inelastic reflection and secondary electrons emission are given in [7].

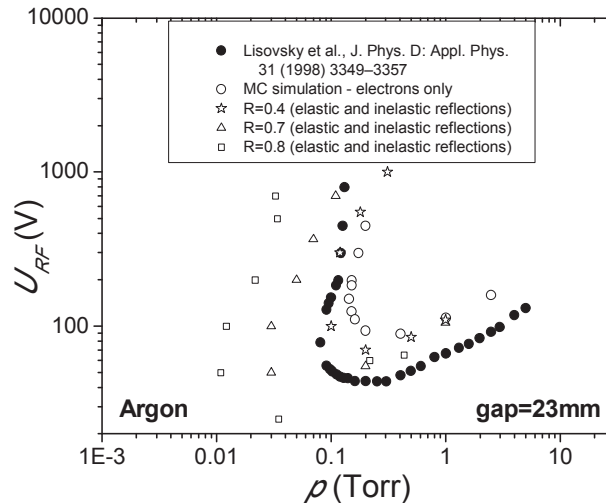


Figure 1. Paschen curves for different reflection coefficients: $R=0$ (open circles), 0.4 (stars), 0.7 (open triangles) and 0.8 (open squares). Experimental results taken from [8] are shown by solid circles. Distance between the electrodes is 23 mm and the frequency is 13.56 MHz.

The RF breakdown voltage curves are typically U-shapes as shown in Figure 1. Under certain circumstances, there is a region to the left of the minimum where a single gas pressure corresponds to two breakdown voltages (multi-valued nature of the RF Paschen curve [5,8]).

Figure 1 also contains Paschen curves obtained for different reflection coefficients, when the probability of the secondary electron emission is unchanged. As expected, with higher reflection coefficient, the breakdown voltage curve is shifted to lower pressures and voltages. One may notice that for $R=0.8$ at high voltages ($U > 400$ V) Paschen curve has tendency to straighten, which is in good agreement with the experimental data [8].

In order to examine the influence of the secondary electron emission on the shape of the Paschen curve, the probability curve was shifted to lower energies (for 120 eV) as shown in Figure 2.

As the number of secondary electrons emitted from the electrodes increases, the Paschen curve is shifted to lower pressure. Such shift is not so significant due to the low initial energies of emitted electrons and fast changing field so electrons do not have enough time to get away from the electrode and they are pushed back to it.

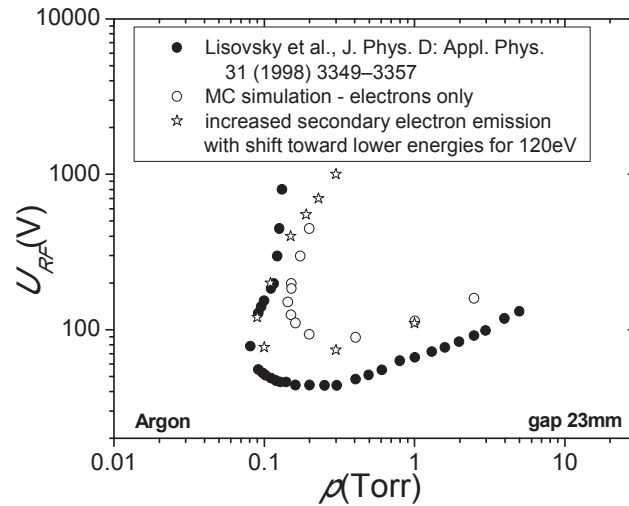


Figure 2. Paschen curves when the threshold for the secondary electron emission is shifted to lower energies for 120 eV. Simulation results (stars) are compared with the results of measurements taken from [8]. Distance between electrodes is 23 mm and frequency is 13.56 MHz.

Simulation results, presented here, confirm that there is a low-pressure region where a multi-valued dependence of the RF breakdown voltage on the gas pressure exists which is in agreement with previous experimental observations [8]. It was found that the multi-valued nature of the left hand branch of the RF breakdown voltage curve can be explained by the effect of electrons only. Also, behavior of Paschen like curve influenced by surface effects is analyzed.

Acknowledgements: The work has been carried out under Ministry of Education and Science Republic of Serbia ON171037 and III41011 projects.

REFERENCES

- [1] S. Lazović, N. Puač, M. Miletić, D. Pavlica, M. Jovanović, D. Bugarski, S. Mojsilović, D. Maletić, G. Malović, P. Milenković and Z. Lj. Petrović, *New Journal of Physics*, 12 083037 (2010).
- [2] T. Makabe and Z. Lj. Petrović, *Plasma Electronics: Applications in Microelectronic Device Fabrication*, (Taylor&Francis Group, 2006).
- [3] Z. Lj. Petrović, P. Maguire, M. Radmilović-Radjenović, M. Radetić, N. Puač, D. Marić, C. Mahony, G. Malović, *On Application of Plasmas in Nanotechnologies in Nanotechnology for Electronics, Photonics, and*

- Renewable Energy*, p.85 (Springer Series Nanostructure Science and Technology, Springer, New York, 2010).
- [4] Z.Lj. Petrović, M. Šuvakov, T. Nikitović, S. Dujko, O. Šašić, J. Jovanović, G. Malović and V. Stojanović, *Plasma Sources Sci. Technol.* 16 S1-S12 (2007).
 - [5] M. Savić, M. Radmilović-Radjenović, M. Šuvakov, S. Marjanović and Z. Lj. Petrović, *IEEE Transactions on Plasma Science*, 39 2556 (2011).
 - [6] S.B. Vrhovac, V.D. Stojanović, B.M. Jelenković and Z.Lj. Petrović, *Journal of Applied Physics*, 90 No12, 5871-5877 (2001).
 - [7] Z.Lj. Petrović and V.D. Stojanović, *J. Vac. Sci. Technol A*, 16 329-336 (1998).
 - [8] A. V. Lisovskiy, V. D. Yegorenkov, *J. Phys. D: Appl. Phys.* 31 3349–3357 (1998).

HYDROXYL RADICAL FORMATION IN LIQUID PHASE OF GAS-LIQUID DIELECTRIC BARRIER DISCHARGE REACTOR

V .V. Kovačević¹, B. P. Dojčinović², M. M. Aonyas³, M. Jović⁴, G. B. Sretenović¹, I. B. Krstić¹, G.M. Roglić³, B.M. Obradović¹ and M.M. Kuraica¹

¹ *University of Belgrade, Faculty of Physics, P.O. Box 44, 11000 Belgrade, Serbia*

² *IHTM, Center of Chemistry, Studentski trg 12-16, 11000 Belgrade, Serbia*

³ *University of Belgrade, Faculty of Chemistry, P.O. Box 158, 11000 Belgrade, Serbia*

⁴ *Innovation Center of the Faculty of Chemistry, University of Belgrade, Studentski trg 12-16, 11000 Belgrade, Serbia*

Abstract. Electrical discharges in and in contact with liquids are an emerging technique in water purification processes due to abundant production of chemically active species which play a key role in pollutant degradation. In this study generation of reactive species (ozone (O₃), hydrogen peroxide (H₂O₂), nitrite (NO₂⁻), nitrate (NO₃⁻) and hydroxyl radical (•OH)) in liquid phase of water falling film dielectric barrier discharge (DBD) in different gas atmospheres was investigated. Focus of the research was on quantification of hydroxyl radical using chemical probe dimethyl sulfoxide (DMSO), since it is considered to be the major reactive species which rapidly and non-selectively reacts with pollutant compounds.

1. INTRODUCTION

Non-thermal plasma sources have been widely used for biological decontamination and degradation of pollutants in water. However, complete understanding of water purification by plasma demands extensive knowledge on plasma-induced changes of liquid. In general, plasma treatment of water-based liquids leads to formation of reactive oxygen (ROS) and reactive nitrogen species (RNS) which strongly depends on reactor configuration and operating parameters. Therefore it is of great importance to have insight in plasma treated liquid chemistry for different types of electrical discharges and applications.

In this paper study of the formation of reactive species in water in contact with air plasma in water falling film dielectric barrier discharge reactor is presented. This plasma source has been successfully used in numerous water cleaning applications [1]. Here a number of parameters such as pH, conductivity,

concentrations of ozone (O_3), hydrogen peroxide (H_2O_2), nitrite (NO_2^-), nitrate (NO_3^-) and hydroxyl radical ($\bullet OH$) were determined in plasma treated distilled water depending on specific energy density (SED) and in different gas atmospheres (air, nitrogen, oxygen, argon, helium).

2. EXPERIMENTAL SETUP

The schematic diagram of experimental setup is shown in Fig. 1. Treated water forms a laminar flowing layer along the inner electrode of the coaxial DBD reactor. Special construction of the reactor with two glass barriers prevents impact of the electrode material on generation of reactive species. The reactor consists of two glass tubes and electrodes, placed concentrically. The inner glass tube, with an outer diameter of 20 mm, has double walls and it is silver plated on the inner side on a length of 370 mm. The silver layer was grounded inner electrode. The outer glass tube, with the inner diameter of 29 mm and length of 500 mm, was wrapped with aluminum foil on a length of 380 mm. Aluminum foil was connected to a high voltage. Gas flow rate was 5 L/min for all gases. Barrier discharge was generated within 4.5 mm gap between the inner and the outer glass tubes by applying voltage up to 20 kV at frequency of 300 Hz.

Electric parameters were monitored by a digital oscilloscope Tektronix TDS 3032 (300MHz bandwidth, 2GSamples/s) and a high voltage probe Tektronix P6015A. For current monitoring the grounded electrode was connected in series with 100 Ω non-inductive resistor. Lissajous figures (Q-U graphs) were used for determination of electric power dissipated in the plasma. To obtain these graphs a capacitor of 470 nF was connected in series with the discharge. Optical emission spectroscopy was performed using Ocean optics USB4000 spectrometer in range 200-900 nm

The solution is pumped by a peristaltic pump with a flow rate of 125 mL/min. In each experiment 2 L of distilled water / aqueous solution of DMSO (250 mmol/L, native pH) were treated. The specific energy density was increased by multiple passes, i.e. the solution passed ten times through the reactor. For pH and conductivity measurements of treated liquid monitors for pH (Microcomputer pH-vision 6071, JENCO Electronics Ltd., Taiwan) and conductivity (Cond. 330i/SET, WTW Wissenschaftlich, Germany) were used.

Immediately after each pass samples were analysed for estimation of nitrate [2], nitrite [3], hydrogen peroxide [4] and ozone [5] concentrations by methods based on color forming reaction with reagent. Photometric measurements were performed using the UV-Visible Cintra 6 spectrometer (GBC Scientific Equipment Pty Ltd., Australia). The $\bullet OH$ was measured by the method developed by Tai et al. [6], using trapping reaction of hydroxyl radicals and DMSO that generates formaldehyde which was analyzed by liquid chromatography-UV (HPLC Dionex UltiMate 3000).

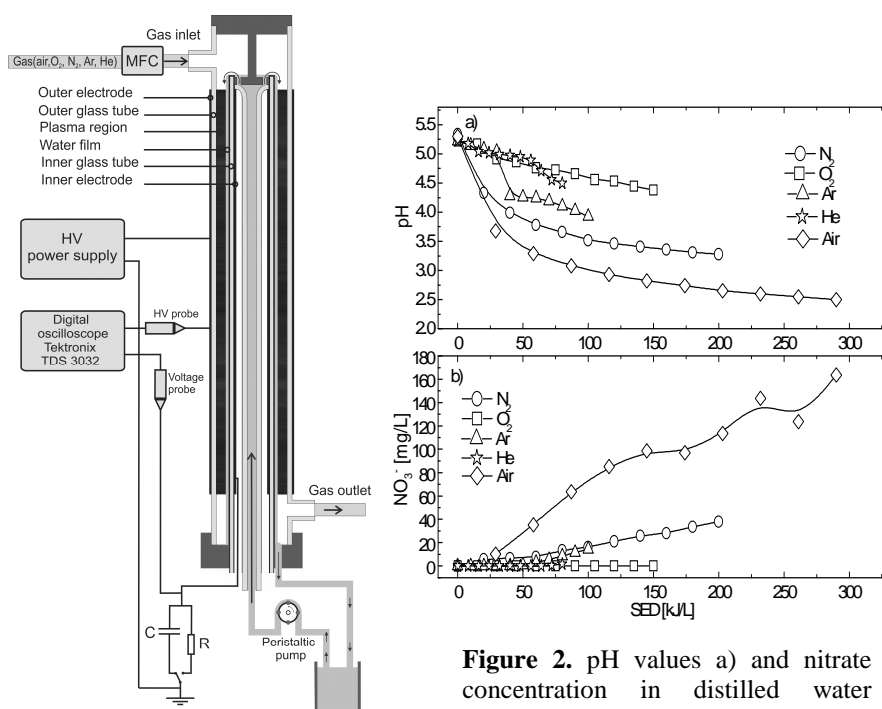


Figure 1. Schematic overview of the experimental set up

Figure 2. pH values a) and nitrate concentration in distilled water treated in different gases in DBD

3. RESULTS AND DISCUSSION

From voltage-current plots (not shown here) it can be seen that discharge had filamentary character in all gases. In order to estimate efficiency of formation of reactive species in different gases specific energy density (SED) was chosen as independent variable for comparison and calculated by dividing discharge power by liquid flow rate. Under selected experimental conditions measured discharge power was 60 W, 41 W, 32 W, 21 W and 16 W for air, nitrogen, oxygen, argon and helium, respectively.

In all gases acidification of treated water was observed (see Fig. 2), with the most pronounced effects in air and nitrogen. Measurements indicate that decrease of pH value is due to formation of nitrite (NO_2^-) and nitrate (NO_3^-) ions in water during treatment in air and nitrogen, which leads to formation of nitrous and nitric acid. In discharge in oxygen, argon and helium acidification is significantly lower compared to discharge in nitrogen and air due to much lower concentrations of nitrite and nitrate. The presence of ionic species increases conductivity of treated water, which linearly increases up to 850 $\mu\text{S}/\text{cm}$ and 200 $\mu\text{S}/\text{cm}$ in air and nitrogen, respectively, while in oxygen, argon and helium it reaches values of only 10 $\mu\text{S}/\text{cm}$. Hydrogen peroxide is formed in water treated

in discharge in all gases, with linear increase of concentration with SED, but with lower concentrations in oxygen and nitrogen. The highest production of ozone is recorded in discharge with oxygen, with a clear plateau value around 0.4 mg/L which stays constant with increase of SED. Ozone formation was negligible in discharge with argon and helium, while it slightly increases in nitrogen, and in air it reaches half of the value in oxygen (results for H_2O_2 and O_3 are not shown here). Trapping reaction of hydroxyl radicals and DMSO quantitatively and selectively generates formaldehyde, which then reacts with 2,4-dinitrophenylhydrazine (DNPH) to form the corresponding hydrazone (HCHO–DNPH), Fig. 3. Hydroxyl radical increases almost linearly with SED in all five gases, Fig. 4.

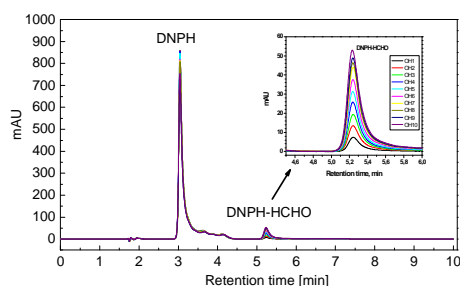


Figure 3. Chromatograms of the water containing 250 mmol/L DMSO after ten subsequent recirculation through the DBD reactor

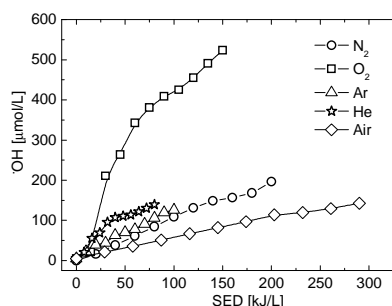


Figure 4. Effect of the gas composition on production of $\bullet\text{OH}$ in distilled water

Acknowledgements

This study was supported by the Ministry of Education, Science and Technological Development of the Republic of Serbia, under projects number OI 171034, TR 33022 and OI 172030.

REFERENCES

- [1] B. P. Dojčinović, G. M. Roglič, B. M. Obradović, M. M. Kuraica, M. M. Kostić, J. Nešić and D. D. Manojlović, *J. Hazard. Mater.* 192, 763 (2011).
- [2] <http://www.caslab.com/EPA-Methods/PDF/EPA-Method-3521.pdf>.
- [3] A. E. Greenberg, R. R. Trussell and L. C. Clesceri *Standard Methods for the Examination of Water and Wastewater*, Method 419, p. 404 (Washington: APHA & AWWA & WPCF, 1985)
- [4] G. M. Eisenberg, *Ind. Eng. Chem. Anal.* 15, 327 (1943).
- [5] L. S. Clescerl, A. E. Greenberg and A. D. Eaton, *Standard Methods for the Examination of Water and Wastewater* (Amer Public Health Assn, 1999)
- [6] C. Tai, J-F. Peng, J-F. Liu, G-B. Jiang and H. Zou, *Anal. Chim. Acta* 527, 73 (2004).

THE IMPREGNATION OF CORONA ACTIVATED POLYPROPYLENE NON-WOVEN FABRIC WITH THYMOL IN SUPERCRITICAL CARBON DIOXIDE

Darka Marković, Stoja Milovanović, Marko Stamenić, Bojan Jokić,
Irena Žižović and Maja Radetić

*Faculty of Technology and Metallurgy, University of Belgrade, Karnegijeva 4,
11120 Belgrade*

Abstract. This study discusses the possibility of impregnation of corona pre-treated polypropylene (PP) non-woven fabric with thymol in supercritical carbon dioxide. Corona treatment of PP fibers caused significant morphological changes. FTIR measurements revealed that ester bond between OH group of thymol and carbonyl group of corona treated PP fibers has been established. Antibacterial activity of corona activated PP non-woven fabrics impregnated with thymol was tested against Gram-negative bacteria *E. coli* and Gram-positive bacteria *S. aureus*. Maximum bacteria reduction was provided.

1. INTRODUCTION

Thymol (2-isopropyl-5-methylphenol) is a natural monoterpene phenol abundantly present in essential oils of thyme, oregano and winter savory [1]. It is natural antimicrobial agent which exhibits extraordinary antimicrobial activity against various microorganisms including methicillin-resistant staphylococci [2-3]. Taking into account that thymol can be exploited in the treatment of inflammatory processes and wound healing as well as growing interest for medical textiles, the idea was to impregnate polypropylene (PP) non-woven fabric with thymol in supercritical carbon dioxide. However, PP as a very hydrophobic material often requires surface activation. In this study corona discharge was used for the activation of PP fibers surface, i.e. hydrophylisation through formation of polar groups prior to impregnation with thymol.

2. EXPERIMENTAL

Polypropylene non-woven fabric (PP, 42 g/m²) was used as a substrate. Thymol (purity > 99%) was supplied by Sigma-Aldrich Chemie GmbH,

Germany. Commercial CO₂ (purity 99%) was purchased from Messer-Tehnogas, Serbia.

Corona treatment of PP non-woven fabric was performed at atmospheric pressure using a commercial device Vetaphone CP-Lab MK II. Samples were placed on the electrode roll covered with silicon coating, rotating at the minimum speed of 4 m/min. The distance between electrodes was 2.3 mm. The power was 700 W and the number of passages was set to 30.

Impregnation of CPP material with thymol was performed in the apparatus for supercritical fluid extraction previously described [4]. Thymol was placed at the bottom of the vessel and the substrate fitted in stainless steel support that was placed above it. CPP/thymol ratio was $0,3 \pm 0,05$ g/g. Operational pressure and temperature were 35 °C and 15.5 MPa. Time of impregnation was 4 hours. A slow decompression (3,8bar/min) was applied at the end of process.

The morphology of PP and CPP fibers was followed by field emission scanning electron microscopy (FESEM, Mira3 Tescan).

Fourier transform infrared (FT-IR) spectra of non-woven fabrics were recorded in the ATR mode using a Nicolet 6700 FT-IR Spectrometer (Thermo Scientific) at 2 cm⁻¹ resolution, in the wavenumber range 500–4000 cm⁻¹.

Antibacterial activity of the non-woven materials was evaluated against Gram-negative bacteria *E. coli* ATCC 25922 and Gram-positive bacterial strains *S. aureus* ATCC 25923 using the standard test method ASTM E 2149-01.

3. RESULTS AND DISCUSSION

Morphology of PP fibers was assessed by FESEM. FESEM images of untreated PP fiber, corona pre-treated PP fiber (CPP) and CPP fiber impregnated with thymol are presented in Figure 1. PP fibers have characteristic smooth surface. Bombardment of PP fibers with plasma species during corona treatment led to significant morphological changes. Figure 1b shows droplet-like surface topography which is typical for PP fibers that have undergone corona or DBD treatment [5]. Such droplet-like surface structure is attributed to plasma oxidation and polymer chain scission on the fiber surface i.e., the creation of low-molecular-weight oxidized materials [6]. These oligomers agglomerate on the PP fiber surface causing the formation of globules which result in specific droplet-like topography.

After impregnation in supercritical carbon dioxide, thymol is unevenly distributed over the surface of the CPP fiber (Figure 1c). In addition, droplet-like structure disappeared indicating that poor bound oligomers were likely removed during the processing in supercritical carbon dioxide.

The oxidation of PP fiber surface induced by corona treatment was confirmed by FTIR analysis. Compared to FTIR spectrum of untreated PP (not shown) two new peaks appeared at 1740 and 1638 cm⁻¹ (Figure 2). Broad band at 1740 cm⁻¹ is assigned to carbonyl groups in ketones, aldehydes and carboxylic acids [5]. A peak at 1638 cm⁻¹ can be attributed to hydrogen bonds established between aldehydes, carboxylic acids and alcohols on the fiber surface [5].

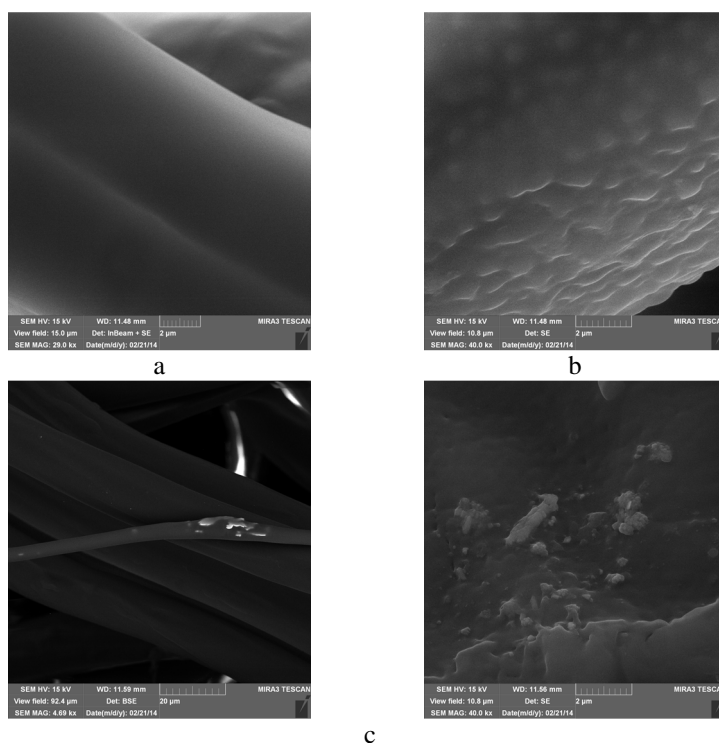


Figure 1. FESEM images of untreated PP fiber (a), CPP fiber (b) and CPP fiber impregnated with thymol in supercritical carbon dioxide (c).

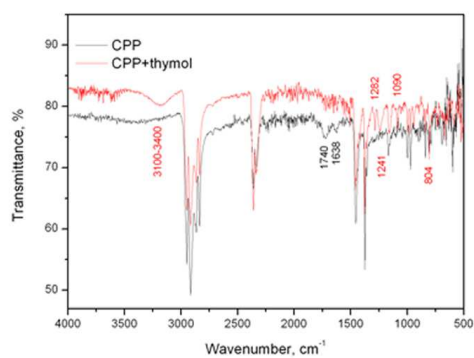


Figure 2. FTIR spectra of CPP and CPP non-woven fabric impregnated with thymol in supercritical carbon dioxide.

Impregnation of CPP material with thymol brought about the appearance of bands characteristic for thymol: a broad band between 3400 and 3100 cm⁻¹ due to phenolic -OH stretching, band at 1241 cm⁻¹ attributed to in-

plane bending vibration and C-O stretching in phenol, and band at 804 cm^{-1} due to out of plane aromatic C-H wagging vibrations. However, the peaks at 1282 cm^{-1} and 1090 cm^{-1} indicate the formation of ester bond between -OH group of thymol and carbonyl group of CPP fiber. Simultaneously, the bands at 1740 cm^{-1} and 1638 cm^{-1} disappeared likely due to creation of ester bonds. [7].

The rate of thymol impregnation after 4 hours long process was around 6.34 %. Impregnated amount of thymol provided maximum reduction of bacteria colonies of *E. coli* and *S. aureus* (99.9 %). Such high bacterial reduction indicates that thymol imparted excellent antibacterial activity to CPP non-woven fabric.

4. CONCLUSIONS

Corona pre-treated PP non-woven fabric can be efficiently impregnated with natural antimicrobial agent thymol in supercritical carbon dioxide. Corona treatment caused considerable morphological and chemical changes that could be utilized for better binding efficiency of thymol. The presence of thymol on PP fiber surface ensured excellent antibacterial activity against Gram-negative bacteria *E. coli* and Gram-positive bacteria *S. aureus*.

Acknowledgements

Financial support of the Serbian Ministry of Education, Science and Technology Development (Projects 172056 and III 45017) is gratefully acknowledged.

REFERENCES

- [1] M. Sokovic and L. J. L. D. van Griensven, *Eur. J. Plant Pathol.* 116, 211 (2006).
- [2] S. Cosentino, C. I. Tuberoso, B. Pisano, M. Satta, V. Mascia, E. Arzedi, F. Palmas, *Lett. Appl. Microbiol.* 29, 130 (1999).
- [3] A. Nostro, A. R. Blanco, M. A. Cannatelli, V. Enea, G. Flamini, I. Morelli, A. S. Roccaro, V. Alonzo, *FEMS Microbiol. Lett.* 230, 191 (2004).
- [4] S. Milovanovic, M. Stamenic, D. Markovic, M. Radetic, I. Zizovic, *J. Supercrit. Fluid.* 84, 173 (2013).
- [5] R. Morent, N. De Geyter, C. Leys, L. Gengembre, E. Payen, *Surf. Interface Anal.* 40, 597 (2008) 597.
- [6] N. Radic, B. M. Obradovic, M. Kostic, B. Dojcinovic, M. M. Kuraica, M. Cernák, *Surf. Coat. Technol.* 206, 5006 (2012).
- [7] G. Socrates, *Infrared and Raman characteristic group frequencies - Tables and Charts*, p. 137-138 (John Wiley & Sons, Ltd, Chichester, UK (2007)).

DNA STRAND BREAK FORMATION IN CELLS BY ATMOSPHERIC PRESSURE PLASMA JET

Sylwia Ptasinska and Xu Han

*Radiation Laboratory and Department of Physics, University of Notre Dame,
Notre Dame, 46556 IN, USA*

Abstract. In the present study, a nitrogen Atmospheric Pressure Plasma Jet (APPJ) was used for irradiation of SCC25 oral cancer and OKF oral healthy cells. The APPJ has significantly induced double strand breaks in DNA of cancer cells but no significant damage was observed in DNA of healthy cells. By using the immunofluorescence assay, the DNA damage was visualized, identified and quantified, thus the effective damage area and damage level were determined

1. INTRODUCTION

Atmospheric Pressure Plasma Jets (APPJs) offer many opportunities for applications at the interface of plasma physics, radiation chemistry and medicine. Currently, much of scientific effort is put on acquiring effects of plasmas interacting with cancer cells, understanding the fundamental mechanisms, and finding optimal conditions for cancer treatment. These studies aim to explore the plasma radiation as an alternative tool for antitumor therapy at the later stage.

In biology, it is known that reactive oxygen and nitrogen species (ROS and RNS) are highly reactive ions or molecules involved in cellular signaling. However, high levels of oxidative stress are known to be detrimental to cell survival and leads to either senescence or apoptosis [1-4]. Interestingly, normal cells have a higher tolerance to oxidative stress than cancer cells which have a higher basal level of intracellular ROS/RNS. While current cancer therapies utilize this ROS effect for treatment, they have low efficacy, drug resistance-associated problems and detrimental side effects.

Since electrical plasma, considered as the fourth state of matter, is an ionized gas composed of charged particles (ions, electrons), radicals and neutral species (excited atoms and molecules). Therefore, our aim is to investigate if APPJs, which produce a cocktail of ROS and RNS upon reaction with air and liquid, can be controlled and targeted to selectively destroy cancer cells causing little damage to the healthy tissue. We believe that this study will enable development of improved therapeutic technique.

2. EXPERIMENTAL SET-UP

An APPJ source used in this study operates based on dielectric barrier discharge and consists of a dielectric tube (inner $\text{Ø}=2$ mm, outer $\text{Ø}=3$ mm) with two thin copper electrodes alternatively wrapped around in a spiral configuration [5-6], with one electrode connected to a high voltage (HV) power supply and the other to the ground (Figure 1). A nitrogen gas flows through the dielectric tube at a flow rate of a few liters per minute. The gas discharge is ignited inside the tube by a relatively low frequency (a few kHz) DC pulse voltage. Once a plasma jet is launched outside the reactor, it forms an almost cylindrical shaped jet.

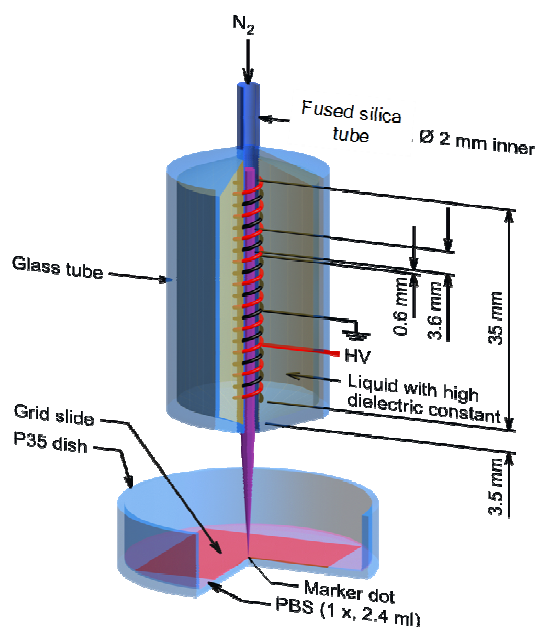


Figure 1. Scheme of the nitrogen APPJ source used for treating cells. A P35 culture dish with cells attached on the grid slide is placed at the vertical distance of 20 mm from the orifice of the plasma source.

SCC-25 oral cancer cells grown on gridded coverslips were irradiated by a nitrogen APPJ plasma source to determine its effectiveness in inducing DNA damage [5]. Double-strand breaks (DSBs) in the DNA were used as a surrogate marker for high level DNA damage in cells. To visualize DSB, treated and control cells were probed with H2AX primary antibody followed by secondary antibody and imaged by fluorescence microscopy. By comparing the number of cells with positive green fluorescence to the total number of DAPI-stained nuclei, a ratio of cells with DSB in comparison to all cells was obtained.

3. RESULTS AND CONCLUSION

Our previous studies showed that isolated DNA molecules, which were extracted from the cell, can be damaged by plasma radiation [7-10]. Damage levels in DNA were evaluated in terms of various exposure distances from the source and plasma treatment durations. In the present study, we investigated damage to cellular DNA. Since the diameter of the plasma jet tip is relatively small (~1 mm), we were interested in exploring how large an area can be treated by plasma irradiation. This could provide significant information about a precision of plasma therapy when only a tumor area is expected to be targeted. In this case, visualization of damaged cells distinguishable from intact cells is the key reason for choosing an immunofluorescence microscopy as the technique to analyze treated areas after plasma irradiation. In order to explore an effective area of plasma irradiation, the ratio of counted cells with DSB versus total cells (damage ratio) was plotted in terms of spatial parameters for four different plasma treatment durations. Figs. 2 a) and b) show spatial distribution of DNA damage for two grids with cancer cells treated by APPJ irradiation of 30 and 120 s, respectively.

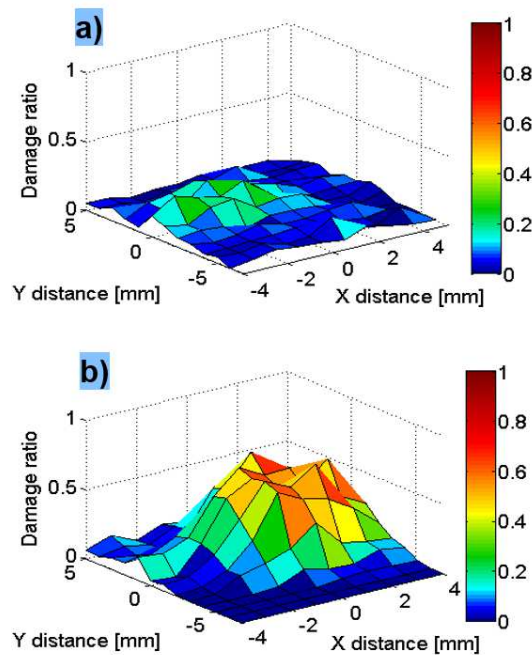


Figure 2. Spatial distributions of double strand breaks in DNA of cancer cells irradiated by APPJ irradiation of 30 (a) and 120 s (b).

The trends of all measured distributions suggest a lower number of cells with DSB farther from the irradiation center. A comparison of the peak widths indicates a direct correlation of plasma effective area with treatment time. Since the plasma jet diameter is small, the damaging effects observed away from the center are likely due to secondary interactions as a result of diffusion of ROS/RNS.

From the comparison of plasma effects on cancer and healthy cells, after conducting the same procedure on OKF oral healthy cells, a different conclusion was obtained. The damage ratio for all treatment durations is relatively constant and below 10% in the case of healthy cells, which indicates a selectivity of APPJ treatment for tumors.

Acknowledgements

The research described herein was supported by the Division of Chemical Sciences, Geosciences and Biosciences, Basic Energy Sciences, Office of Science, United States Department of Energy through grant number DE-FC02-04ER15533. This project has been performed in collaboration with Harper Cancer Research Institute at the University of Notre Dame.

REFERENCES

- [1] Q. Chen, B.N. Ames, *Proc. Nat. Acad. Sci.* 10, 4130 (1994).
- [2] Q. Chen, A. Fischer, J.D. Reagan, L.J. Yan, B.N. Ames, *Proc. Nat. Acad. Sci.* 92, 4337 (1995).
- [3] M.L. Circu, T.Y. Aw, *Free Radic Biol Med.* 48, 749 (2010).
- [4] H.U. Simon, A. Haj-Yehia, F. Levi-Schaffer, *Apoptosis.* 5, 415 (2000).
- [5] X. Han, M. Klas, Y. Liu, S.M. Stack, S. Ptasińska, *Appl. Phys. Lett.* 102, 233703 (2013).
- [6] M. Klas, S. Ptasińska, *Plasma Sources. Sci. Technol.* 22, 025013 (2013).
- [7] S. Ptasińska, B. Bahnev, A. Styczynska, M.D. Bowden, N.J. Mason, N.St.J. Braithwaite, *Phys. Chem. Chem. Phys.* 12, 7779 (2010).
- [8] A. Styczynska, S. Ptasińska, B. Bahnev, M.D. Bowden, N.St.J. Braithwaite, N.J. Mason, *Chem. Phys. Lett.* 500, 313 (2010).
- [9] X. Han, W.A. Cantrell, E.E. Escobar, S. Ptasińska, *Eur. Phys. J. D* 68, 46 (2014).
- [10] B. Bahnev, M.D. Bowden, A. Styczynska, S. Ptasińska, N.J. Mason, N.St.J. Braithwaite, *Eur. Phys. J D* 68, 140 (2014).

THE RADIAL BALANCE IN DUSTY PLASMA OF GLOW DISCHARGE WITH JOULE HEATING

D. N. Polyakov, V. V. Shumova and L. M. Vasilyak

*Joint Institute for High Temperatures RAS, Izhorskaya 13 Bd.2, Moscow,
125412, Russia*

Abstract. The forces determining the radial sustenance of dust structures in plasma of dc glow discharge in neon are simulated on the base of diffusion/drift model of the positive column of glow discharge with Joule heating. Radial profiles of electron number density, electric field strength and dust particle potential are represented for various values of dust particle concentration in dust structures.

1. INTRODUCTION

The current interest in interaction of plasma with dust particles is stimulated by numerous applications of dusty plasmas in technology and in fundamental science. Plasma with condensed dispersed phase is applied in synthesis of nanoparticles, surface modification and plasma coating [1]. The dust particles may be loaded in plasma from the outside or be formed in the course of technological process and change both local and integral plasma parameters [2]. Plasmas of noble gases are widely used in technique. In present paper we analyze the influence of dust structures on the electric field of a discharge considering the heat release, and the reverse influence of discharge electric field on the radial balance of dust structures in plasma.

2. NUMERICAL MODEL

In this study we follow the basic points of drift/diffusion model of the positive column of glow discharge which proved the reliability for simulations in neon plasma with micron size dust particles [3]. We consider neon plasma consisting of neutrals, electrons, ions and metastable neon atoms of 1-s configuration with the energy of 16.62 eV. The ionization by single electron collision with neon atom in the ground state, and the step-wise ionization through the metastable state are considered. Molecular ions and negative ions are neglected. In addition to the specific ion and electron losses in dusty plasma, we have also considered the quenching of metastable atoms on dust particle surface. The ion and metastable temperatures were supposed to be equal to gas

temperature, the mean electron energy and transport coefficients were obtained using the SIGLO Database and the electron Boltzmann equation solver BOLSIG+. Using this approach, we have found the radial distributions of ions, metastable atoms and electrons and the electric field for the given dust particle distribution $n_d(r)$, the total discharge current I and pressure P .

To find the radial gas temperature profile in a discharge tube, we have neglected the convective and electron heat conduction terms and solved the steady-state one-dimensional heat conduction equation with the appropriate boundary conditions considering the rate of Joule heat release as $Q(r)=n_e(r)\mu eE_1^2$, where $n_e(r)$ and μ are the electron concentration and mobility, E_1 is the longitudinal electric field strength. Simulations were carried out for the discharge tube radius $R=8.25$ mm, dust particle size $a=2.55$ micron, the temperature of the wall of the discharge tube $T_w=295$ K. The dust particle distribution $n_d(r)$ was given by an axially symmetrical flat profile of size $r_d=R/2$ with dust particle concentration on the axis of the discharge tube n_d and exponential end blurring as in [2]. The forces acting on the dust particle were considered as in [4]. The resulting force $F(r)$ is considered to be the superposition of the electric field force $F_e(r)$, thermophoretic force $F_{th}(r)$ and ion drag force $F_i(r)$.

3. RESULTS AND DISCUSSION

In free discharge the undisturbed radial concentration profiles of plasma particles are close to Bessel distribution. Dust particles cause the additional electron losses in the plasma bulk, changing the plasma ionization balance. For the maintenance of the discharge current, these losses should be compensated by increase in the ionization frequency through the increase of E_1 and electron temperature. The increase of dust particle concentration leads to the case when the electron concentration on the outer face of dust cloud becomes higher than in the center of the tube, i.e. the maximum of electron profile shifts towards the tube wall, forming a local minimum in the center of discharge tube (figure 1a). While the longitudinal electric field increases with the increase of dust particle concentration, there appears the smoothing of electron concentration over the discharge cross section under the action of dust cloud and even the essential inverse electron concentration gradient at high values of n_d . At high n_d the strong depletion of electron concentration within the dust cloud causes the reverse flow of electrons from free discharge towards the tube axis and results in the inversion of the radial electric field E_r (figure 1b). Following from this point, there appear the change of the electric force acting on the dust particles. The increased electric field strength leads to the increase of Joule heat release, while the redistribution of electron concentration over the cross section of discharge tube causes the shift of its maximum towards the tube walls.

The simulation of temperature profiles have shown that the increment of gas temperature on the axis of a discharge tube increases by about 50% in the presence of dust particles. Due to rather high value of thermal conductivity of neon the temperature profile seems to be smoother than the Joule heat release profile which is proportional to $n_e(r)$. However, the additional temperature

gradient caused by increased E_l in presence of dust structures may have the reverse influence on the dust structures and cause the transformations of its shape.

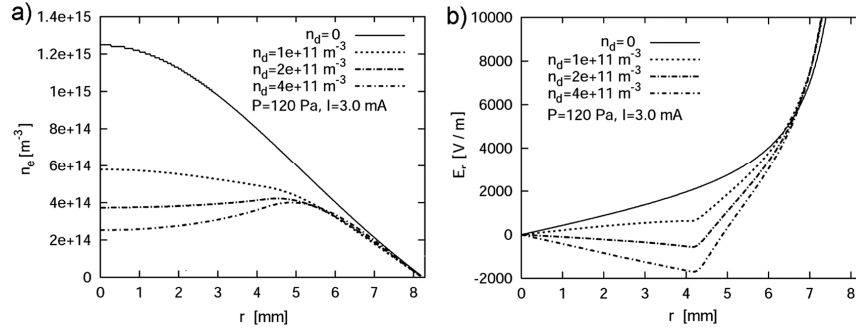


Figure 1. Radial profiles of: (a) electron concentration n_e and (b) radial electric field E_r at various values of dust particle concentration n_d .

The ion drag force magnitude is less than thermophoretic and electric forces, and the later are comparable in magnitude, except the region close to the tube wall, where the electric force strongly increases. The resulting force $F(r)$ is represented in figure 2a for three values of $n_d(r)$ and in pure neon plasma with test particle with charge of $5000 e^-$. The charge of the test dust particle was supposed to be independent on radial position of dust particle, in other cases the dust particle charge depended on the radial coordinate, being determined by the flows of ions and electrons to its surface.

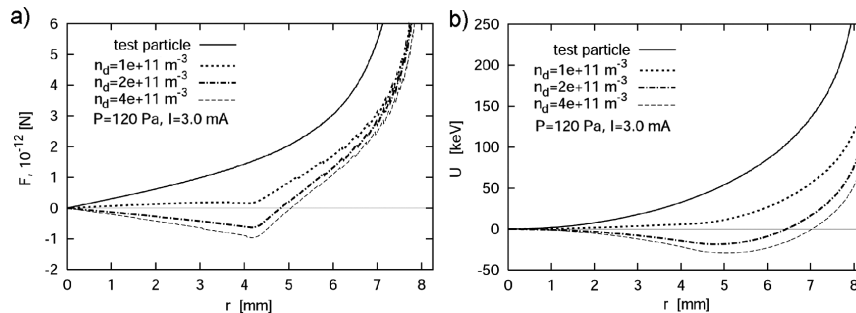


Figure 2. Radial profiles of: (a) resulting force $F(r)$ acting on the dust particle and (b) the dust particle potential $U(r)$ for various values of dust particle concentration n_d .

One can see that in the result of the redistribution of electrons and the corresponding self-organizing of dust structures, there appears the electric force directed inside the dust structure, which keeps dust particles in equilibrium in a radial direction. The magnitude of this force increases with the concentration of dust particles. The resulting force acting on a dust particle in a discharge is determined, for the most part, by the electric field force. One may conclude, consequently, that the mechanism of radial sustenance of dust particles in the discharge realizes through the self-consistent influence of dust particles on the discharge electric field configuration. The radial motion of a dust particle is

defined by its potential energy. In figure 2b the potential energy of a charged dust particle as a function of the particle position is represented. Note that the high value of the potential energy of dust particle appear due to high value of its negative charge on the order of several thousands the elementary charges and the radial electric field strength of several tens volts per centimeter. One can see that the arising additional force represented in figure 2a, leads to the shift of the minimum of potential energy towards the wall of the discharge tube with the increase of the dust particle concentration. This should result in the formation of the ring dust structures (voids) observed earlier in air [4], and in the increase of the concentration of dust particles near the outer border of the dust structure.

4. CONCLUSION

The introduction of dust particles in the positive column of glow discharge in neon was shown to lead to the noticeable increase in the longitudinal electric field strength and Joule heat release in the discharge. The arising additional temperature and concentration gradients result in the arising of the resulting force acting on the dust particle. This force changes the position and the shape of dust structure. The self-consistent electric field force and thermophoretic force are shown to play the major role in the formation of voids in dense dust structures.

Acknowledgements

This work was supported by the RFBR grant №13-02-00641.

REFERENCES

- [1] K. Ostrikov, U. Cvelbar, A. B. Murphy, *J. Phys. D: Appl. Phys.* 44, 174001 (2011).
- [2] D. N. Poliakov, L. M. Vasilyak, V. V. Shumova, V. E. Fortov, *Phys. Lett. A.* 375(37), 3300 (2011).
- [3] L. Vasilyak, D. Polyakov, V. Shumova, *Contrib. Plasma Phys.* 53(4-5), 432 (2013).
- [4] V. V. Balabanov, L. M. Vasilyak, S. P. Vetchinin, A. P. Nefedov, D. N. Polyakov, V. E. Fortov, *J. Exp. Theor. Phys.* 92(1), 86 (2001).

IN SITU OES MONITORING OF PLASMA ENHANCED ATOMIC LAYER DEPOSITION OF ALUMINIUM AND HAFNIUM OXIDE

A. Miakonkikh, K. Rudenko and A. Orlikovsky

*Institute of Physics and Technology, Russian academy of sciences,
Nakhimovsky av. 34, 117218, Moscow, Russia*

Abstract. Atomic layer deposition (ALD) of Al_2O_3 and HfO_2 was studied in situ by means of optical emission spectroscopy and spectral ellipsometry. Kinetics of spectral lines of plasma optical emission of radicals O^* , CO , OH were observed during plasma oxidation of chemisorbed monolayer layers of TMA and TEMA precursors, showing saturation of surface reaction. Dependence of surface reaction rate on plasma parameters measured by Langmuir probe and optical actinometry is studied. Method was used for optimization of process of atomic layer deposition of dielectrics.

1. INTRODUCTION

Atomic layer deposition technique became the most prominent method for deposition of ultrathin metal and dielectric layers in semiconductor applications [1].

Decrease of the gate dielectric electrical thickness providing physical thickness which is enough for suppressing tunneling current lead to implementation of high-k metal oxides as the gate dielectric, for example HfO_2 [2].

Due to its excellent dielectric properties, its good adhesion to many surfaces, barrier properties and its high thermal and chemical stability, Al_2O_3 is a very relevant material for a wide range applications.

ALD can be defined as a cyclic process which relies on sequential self-terminating reactions between gas phase precursor molecules and a solid surface. The self-terminating nature of the chemical reactions ensures precise film thickness control and excellent step coverage.

ALD allows to produce ultrathin films with atomic level control of film thickness (only monatomic layer is deposited in each step of process), low level of volume and surface defects, and excellent conformal coverage.

2. EXPERIMENT

Al_2O_3 and HfO_2 films were deposited in FlexAl ALD tool from Oxford instruments plasma technology. 2-50 nm thick films were deposited on 5% HF dipped Si(100) wafers. The films were deposited in plasma assisted ALD process with TEMAH ($\text{Hf}(\text{N}(\text{C}_2\text{H}_5)(\text{CH}_3))_4$) and TMA ($\text{Al}(\text{CH}_3)_3$) as metal precursors and O_2 as non-metal plasma precursor.

These processes are truly self limited and hence process dependence on external parameters (stage temperature, duration of the processes, pressure, plasma parameters) is flat in wide interval. That provides “process window”, in which stable and reproducible film properties can be achieved, including high homogeneity over 200mm wafer. ALD cycle consists of precursor dosage step (10-1000 ms), precursor purge step, plasma oxidation step (1-3 sec), and oxygen purge step.

Spectral ellipsometry was performed *in situ* by 65 degrees ellipsometer Woollam Co M2000X in 245-998 nm range. Measurements were done on every half of ALD cycle (after metalorganic precursor dosage and after oxygen plasma exposure as well).

Optical emission spectroscopy was used to detect excited species in oxygen plasma on plasma enhanced oxidation step. Plasma radiation was measured by two-channel acoustooptic spectrometer in range 300-850 nm through two quartz window. One port located on the axis of chamber collects light from ICP source, and the other on the wall of chamber collected light from close to wafer region. We measured lines of CO (519 nm), O^* (777 nm), H (656 nm), and OH (309 nm) with temporal resolution of less than 0.2 sec.

Plasma parameters with different external discharge conditions were measured by Langmuir probe which gives values of electron concentration of $\sim 10^9 \text{ cm}^{-3}$. Oxygen radicals concentration was measured by optical actinometry in comparison of lines O(777 nm) and Ar(750 nm) with typical values of 10^{12} cm^{-3} .

3. RESULTS AND DISCUSSION

The measurements reveal that lines of OH and H are the most sensitive to changes of plasma composition during plasma oxidation step. Figure 1 shows that intensity of OH line corrected for changes in wide-band molecular radiation intensity in this region of spectra changes two times during the plasma time in TMA+ O_2 ALD process.

Completeness of plasma oxidation reaction was proven by spectral ellipsometry measurements showing saturation of oxide thickness for plasma durations longer than 2 sec. Oxygen intensity remains unchanged during plasma step. Remaining intensity of OES signals of reaction products could be ascribed to residence time of species in reactor volume, which is estimated from pump rate and inflow of purge gas to be equal to approximately 2 sec.

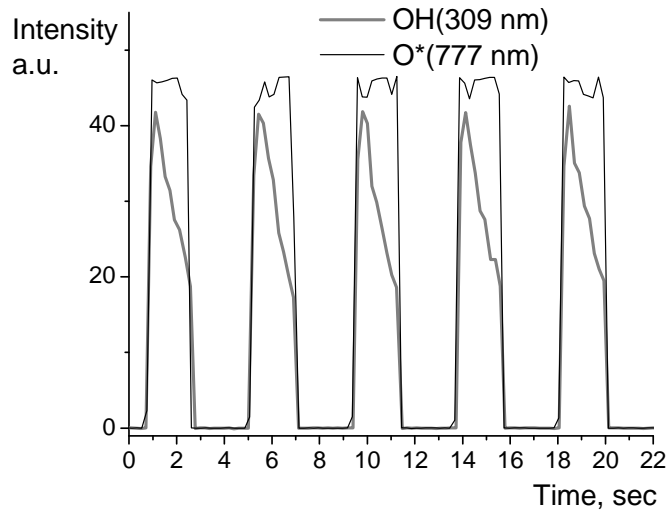


Figure 1. Plasma OES signals of OH and O* species during deposition of aluminum oxide in TMA+O₂ ALD process. Plasma duration is 2 sec.

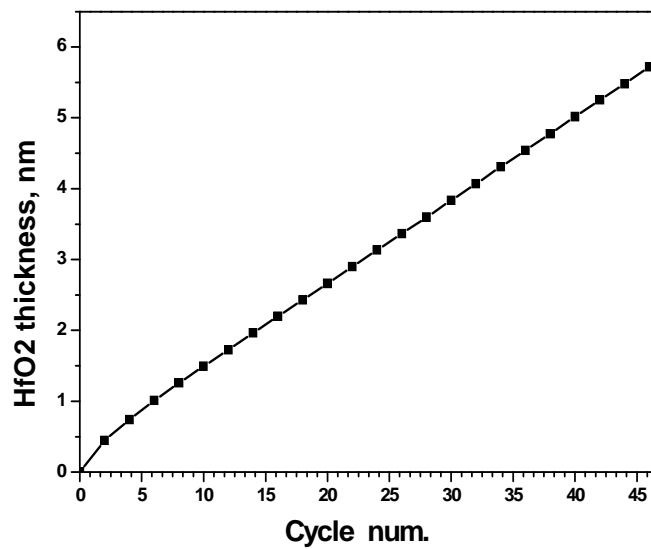


Figure 2. Thickness of HfO₂ deposited film in TEMAH/O₂ plasma process measured by in situ spectral ellipsometry, growth rate is about 1.05 nm/cycle

Spectral ellipsometry was used to determine initial nucleation lag of film growth (see Figure 2). It can be seen that there is no zero-rate period at the initial stage of growth. The light overestimation of growth rate on the first step could be attributed to measurement error of ellipsometry at extreme low thickness values.

Comparison of measured concentrations of charged particles and active radicals of oxygen shows that radical density is three times order of magnitude higher than ions density.

4. CONCLUSION

The in situ OES and SE monitoring of plasma enhanced ALD processes of HfO_2 and Al_2O_3 deposition allows to control precisely stages of chemisorption of metalorganic precursor, and plasma oxidation step. Rate of surface plasma enhanced reactions in different process conditions were determined and time of process saturation was calculated which could help to optimize process.

Acknowledgements

This work is partially supported by Russian Foundation of Fundamental Research under grant # 14-07-00844 A.

REFERENCES

- [1] S. M. George, Chem. Rev. 110, 111 (2010).
- [2] J.H. Choi, Y. Mao and J. P. Chang, R 72, 97–136 (2011).

SENSITIVE OES-TECHNIQUE FOR ENDPOINT DETECTION APPLIED TO PLASMA ETCHING OF W/HfO₂/Si STACK

K. Kuvaev, A. Miakonkikh, K. Rudenko and A. Orlikovsky

*Institute of Physics and Technology, Russian Academy of Sciences,
34, Nakhimovsky av., 117218 Moscow, Russia*

Abstract. The possibilities for sensitive OES-detection of the process endpoint during F- and Cl-based plasma etching of advanced structures of nanoelectronic devices have been analyzed. OES-monitoring experiments were carried out with process of plasma etching of stack W/HfO₂/Si. It had shown the reliable determination of endpoint for etching of metal layer even at 0.6% area of wafer open to be etched.

1. INTRODUCTION

Optical emission spectroscopy (OES) is widely used method for the monitoring of plasma technologies utilizing low-temperature plasmas in micro- and nanoelectronics [1]. The technique for endpoint detection involves measuring the emission of chemically active particles in plasma which take part in surface reactions or measuring the emission signal of species entering to plasma from etched material. Problem of OES endpoint method concerns the implementation of this technique for small windows in mask opened for etching in comparing with full area of processed silicon wafer. Under such conditions the decreasing of quantity of etch products in plasma gives the drop of signal to noise ratio at endpoint step. This is a reason why endpoint detection method becomes noisy and unreliable when the etched area less than 5% of full wafer. The paper presents the results of investigation showing more reliable OES endpoint detection in etching process of stack W/HfO₂/Si in SF₆-based plasma even for small etching area. Some spectral lines of atomic tungsten owing low energy threshold for excitation makes the W atoms detectable at extremely low concentration in processing plasma.

2. BASIC PRINCIPLES

Plasma species under direct electron impact emits the optical radiation corresponding with optical transitions in excited particle. Level of light intensity (I) at characteristic wavelength is described by well known equation:

$$I \propto 4\pi n n_e \int_{E_{th}}^{\infty} \sigma(\varepsilon) \cdot \sqrt{\frac{2\varepsilon}{m_e}} \cdot f(\varepsilon) \cdot d\varepsilon, \quad \text{where} \quad (1)$$

n – excited species density in plasma; n_e – electron density,

$\sigma(\varepsilon)$ – cross-section of optical transition;

m_e , ε , $f(\varepsilon)$ – electron mass, electron energy, and EEDF, respectively;

E_{th} – electron energy threshold for exciting of upper emitting level.

The value of E_{th} is in the range of 10 – 15 eV for spectral lines of species F*, Cl*, O*, H*, SiCl*, SiF*, N₂* conventionally used for OES-monitoring of plasma etching of silicon based structures except of lines of Si ($\lambda=288.2$ nm) with $E_{th} = 5.08$ eV and Al ($\lambda=309.3$ nm) with $E_{th} = 4.02$ eV. New materials involved in silicon nanoelectronics as gate stack elements are presented by d- and f- metals and its compounds. In the atomic state many of these metals in plasma has intensive spectral lines with low E_{th} , the examples are given in Table 1.

Table 1. Data on intensive atomic spectral lines of materials included in metal gate stacks of modern nanotransistors.

Gate stack material	Detectable atom in plasma	λ (nm)	I (a.u.)	E_{th} (eV)	Ref.
TiN	Ti	521.0	2100	2.43	[2,3]
TaN	Ta	360.7	750	3.68	[2,3]
W	W	400.9	1000	3.45	[2,3]
Pt	Pt	265.9	2000	4.66	[2,3]
ZrO ₂	Zr	360.1	400	3.59	[2,3]
HfO ₂	Hf	368.2	2200	3.36	[2,3]

From (Eq. 1) there is significant advantage in emission intensity for species with low energy threshold of excitation because of Maxwellian character of EEDF in plasma. Spectroscopic monitoring of processing of materials containing such metals potentially could be more effective through emission of atomic species in plasma releasing due to deep dissociation of initial molecular etch products up to atoms.

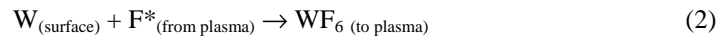
3. EXPERIMENTAL

The experiments on plasma etching of tungsten gate stack were performed at Dual PlasmaLab 100 etch System (Oxford Instruments, UK) equipped with 2 MHz ICP plasma source and 13.56 MHz bias source.

Anisotropic etch of tungsten layer was made by plasma $\text{SF}_6 + \text{O}_2$ gases at the pressure of 7 mTorr, gas flows 40.5 sccm (SF_6) and 4.5 sccm (O_2), power of RF $P_{\text{ICP}} = 1000$ Watt, and bias power $P_{\text{bias}}=100$ Watt. The temperature of wafer chuck was maintained at -30 °C. For etch process it was used 200 mm wafer with stack $\text{W}(80 \text{ nm})/\text{HfO}_2(4 \text{ nm})/\text{Si}$ -substrate. Open area for etching was in the range 0.6 – 30 % of full wafer. Optical spectra of plasma were measured by fast acousto-optical spectrometer Quartz-2000 model (Russia). Spectral range is 300 – 850 nm with resolution 0.15 – 0.3 nm, time for measuring each spectral point is 16 msec.

4. RESULTS

Surface reaction of plasma assisted etching is:



As follows from emission spectrum (Fig.1) the molecules of WF_6 is subjected to deep dissociation in plasma up to W atoms.

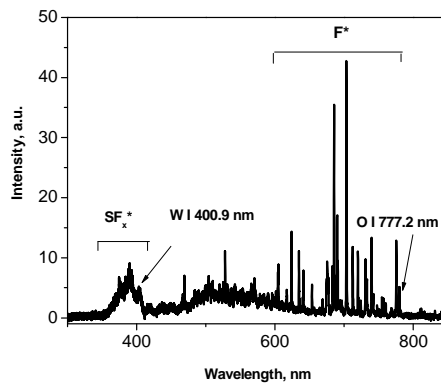


Figure 1. Emission spectrum of processing plasma $\text{SF}_6 + \text{O}_2$. Atomic line of etched tungsten is detected. Etching area is 10% of full wafer.

This is confirmed by detail spectrum in region of wavelength 399-402 nm which was acquired in period when tungsten was etched and immediately after that (Fig.2). The moment of endpoint is observed as sharp changing of signal intensity at $\lambda=400.9$ nm with negative slope at the moment when interface of etched layer of W and underlayer of HfO_2 has reached (Fig.3). Trace of spectral signal has no significant noise even at very small area of open windows. Despite of the chain of dissociation reactions for initial etch product WF_6 in plasma volume and small plasma concentration of atomic tungsten, the low energetic threshold for excitation of analytical line 400.9 nm in emission spectrum of W atoms gives significant advantage for its detection in plasma and for monitoring of etch process of tungsten in gate stack $\text{W}/\text{HfO}_2/\text{Si}$.

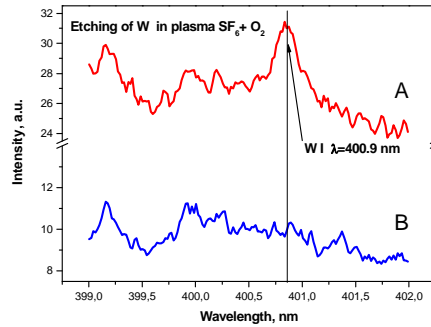


Figure 2. Observation of line W I (400.9 nm) in processing plasma when tungsten layer is under etching (A) and spectrum after full removing tungsten layer (B). Open etching area is 0.6% of full wafer.

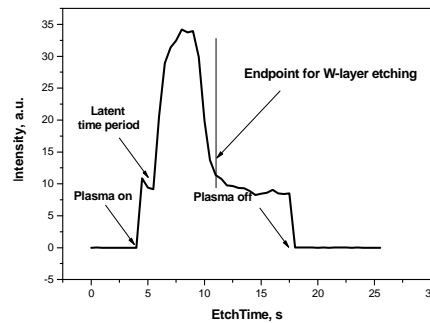


Figure 3. Evolution of spectral intensity at $\lambda=400.9$ nm during the process of plasma etching of gate stack W(80 nm)/HfO₂(4 nm)/Si-substrate. Open etched area is 2% of full wafer.

Acknowledgements

This work is supported by Russian Federal Agency of Scientific Institutions and Russian Academy of Sciences.

REFERENCES

- [1] V. M. Donnelly and A. Kornblit. *J. Vac. Sci. Technol. A* 31, p. 050825-1 – 050825-48 (2013).
- [2] A. N. Zaidel' et al., *Tables of spectral lines*, p. 782, (IFI/Plenum Press, London, 1970).
- [3] <http://physics.nist.gov>

ION ENERGY DISTRIBUTION AND LINE INTENSITIES IN ASYMMETRICAL OXYGEN RF DISCHARGE

Kosta Spasić, Nikola Škoro, Nevena Puač, Gordana Malović and
Zoran Lj. Petrović

*Institute of Physics, Pregrevica 118, 11080 Belgrade, Serbia,
Belgrade University*

Abstract. Asymmetric 13.56 MHz CCP plasma reactor of large area was developed for purpose of continuous plasma treatment of sensitive samples like polymers, textile and seeds. In order to maximize efficiency of plasma treatment and to get well acquainted with relevant plasma chemistry, plasma diagnostic by using mass spectrometer and optical emission recordings was performed. Supplied RF power was from 100 W to 600 W at 600 mTorr pressure of O₂ with 1% of Ar gas mixture. Distribution of O₂⁺ ions had much higher counts than O⁺ and for both species higher power resulted in more available high energy ions. Emission spectroscopy revealed an increase in oxygen 777 nm and argon 750 nm line intensity with the increase of power.

1. INTRODUCTION

In everlasting struggle for energetic efficiency and always needed cost reduction, numerous industries can find their solution in applications of low pressure plasmas. We have already shown some benefits for agriculture, because plasma treated seeds have higher germination rate and, in some cases, plants whose seed was treated develop significantly faster [1-3]. It is also important to emphasize possibility to use plasma as sterilization agent [1-3]. Positive effects of this technology are of great importance in textile industry [4], where they can improve quality of products and decrease ecological impact. Low pressure plasmas are used in various large scale industries, in processes like etching and deposition, where any reduction in used energy can make them more cost effective and environmentally friendly

Investigation of role of ions in plasma chemistry is of paramount importance both for general science and for industrial applications. In this paper we present measurements of ion energy distributions for singly ionized molecule and atom of oxygen (32 and 16 amu). Moreover, we have employed optical emission spectroscopy (OES) to obtain information about relevant lines of O and Ar.

2. EXPERIMENT

Large volume asymmetric CCP plasma reactor was developed as a prototype for industrial scale treatment of sensitive samples. Its asymmetric geometry allows stable plasmas to be formed without possibility of streamer formation. Stainless steel cylindrical chamber, 2.5 m in length and 1.17 m in width, serves as grounded electrode, while powered electrode is 1.5 m long axially placed aluminum rod (3 cm in diameter). Power is supplied at 13.56 MHz by Dressler Cesar 1310 supply through Variomatch matching network.

Spectrally resolved emission from plasma was recorded in a part of visible spectrum (720-790 nm) through a side window positioned at level of the rod electrode. We have used monochromator Oriel MS127i with i-Star Andor ICCD camera as detector. By using a lens at the entrance slit, the spectrometer collected all light originating from the part of the plasma volume at the side-on region of the electrode. Recording time of several hundred ms contains integrated light emission from many RF periods. Two characteristic lines for atomic oxygen (777 nm) and argon (750 nm) were traced at different powers

HIDEN EQP mass spectrometer was positioned side-on and the distance of the mass spectrometer orifice from the powered electrode was 30 cm. The orifice of the mass spectrometer was at ground potential. Ion energy distribution was measured for energies between 4 and 100 eV with resolution of 0.1 eV. The working gas mixture was 99% of oxygen and 1% of argon at a pressure of 600 mTorr which is suitable for treatments. Measurements were done in the range of powers from 100 to 600 W.

3. RESULTS AND DISCUSSION

In Fig. 1 a) we have presented ion energy distributions for positive ions of molecular oxygen (O_2^+) recorded at 600 mTorr for powers 400, 500 and 600 W. For powers lower than 400 W we could not obtain valid signal of ion energy distributions. At 400 W maximum ion counts can be observed at 4 eV and after that distribution rapidly decreases 5 orders of magnitude. For this power given by RF power supply maximum of ion energy is around 20 eV. With the increase of the power we can see that ions with higher energies can be collected. For the power of 500 W maximum ion energy goes up to 70 eV and for 600 W this energy is higher than 100 eV.

Situation is somewhat similar for distribution of singly ionized atomic oxygen (O^+) shown in Fig. 1 b). However, in case of O^+ we can see two peaks present for the powers of 400 and 500 W. In case of 600 W we can only assume that there is the second peak around 100 eV since the signal started to increase at around 90 eV.

Notwithstanding that we could not obtain valid ion signal for the powers lower than 400 W, plasma was ignited for the lower powers. In order to investigate if there is some change in plasma behavior at 400 W we have performed OES and recorded oxygen and argon line intensities.

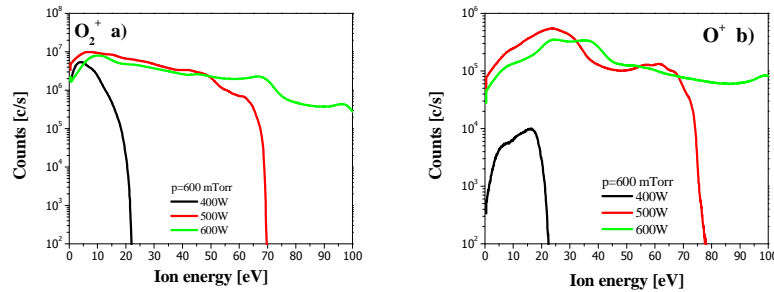


Figure 1. Ion energy distributions of O_2^+ (a) and O^+ (b), recorded at 600 mTorr for three different powers given by RF power supply.

Measurements of line intensity dependence for two oxygen and argon lines are shown in Fig. 2 for different powers (full symbols). Line intensities are relatively scaled and show similar intensities and rising tendency with power increase. For both lines the increase in intensity is larger, almost exponential, at higher powers. Additionally, the ratio between obtained line intensities is shown in the right-hand-side axis (crosses) and exhibits small increase with power. Also, interesting observation is that at 400 W there is decrease in line intensity ratio.

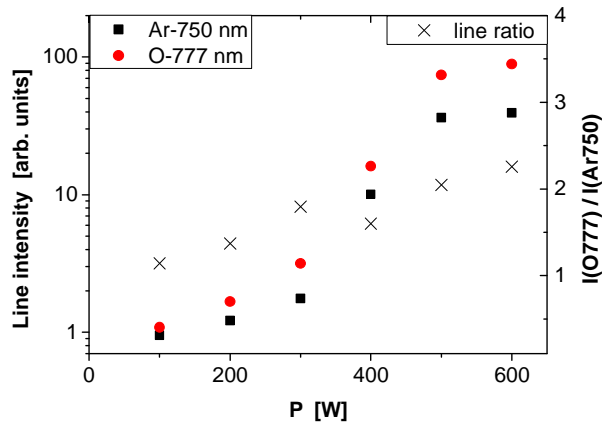


Figure 2. Left axis: oxygen 777 nm (circles) and argon 750 nm (squares) line intensities, right axis: line intensity ratio (crosses) at different powers at 600 mTorr.

Generally, in cases where emission originating from dissociative excitation is not dominant, the line intensity ratio could be used for an estimation of the dissociation extent in plasma through a method of optical actinometry [5]. However, in plasmas with low dissociation extent and where dissociative excitation channel is dominant, results of actinometry can provide only qualitative description of change in oxygen dissociation with plasma parameters

[6,7]. Thus, in this case the intensity ratio provides only general trend in dissociation of oxygen.

4. CONCLUSION

We have measured ion energy distribution and performed spectroscopic measurements of large volume asymmetric CCP plasma reactor. No valid ion signal could be detected at powers lower than 400 W, and even at that power distribution reaches minimal values at just over 20 eV. With increased RF powers, we were able to detect ions at energies higher than 100 eV. Optical emission spectroscopy, in this range of plasma parameters, could only provide us with general information that dissociation of oxygen molecules is rising with powers.

Acknowledgements

This research is supported by the Serbian Ministry of Education, Science and Technological Development under project numbers ON171037 and III41011.

REFERENCES

- [1] I. Filatova, V. Azharonok, V. Lushkevich, A. Zhukovsky, G. Gadzhieva, K. Spasić, S. Živković, N. Puač, S. Lazović, G. Malović, Z.Lj.Petrović, “*Plasma seeds treatment as a promising technique for seed germination improvement*”, (31st ICPIG, 2013).
- [2] N. Puač, Z. Lj. Petrović, S. Živković, Z. Giba, D. Grubišić, A. R. Djordjević, *Plasma Process Polym*, pp 193 (2005).
- [3] I. I. Filatova, V. V. Azharonok, S. V. Goncharik, V. A. Lushkevich, A. G. Zhukovsky, G. I. Gadzhieva, *J Appl Spectrosc*, 81 2 250 (2014).
- [4] M. Gorenšek, M. Gorjanc, V. Bukošek, J. Kovač, Z. Petrović, N. Puač, *Text. Res. J.* 80, 1633, (2010).
- [5] J. W. Cobrun, M. Chen, *J. Appl. Phys.* 51, 3134 (1980).
- [6] H. M. Katsch, A. Tewes, E. Quandt, A. Goehlich, T. Kawetzki, H. F. Doebele, *J. Appl. Phys.* 88 6232 (2000).
- [7] L. Zhongwei, L. Sen, C. Qiang, Y. Lizhen, W. Zhengduo, *Plasma Sci Technol*, 13 458 (2011).

REMOVAL OF REACTIVE ORANGE 16 FROM WATER BY PLASMA NEEDLE

Tatjana Mitrović^{1,2}, Dejan Maletić¹, Nataša Tomić¹, Saša Lazović¹, Gordana Malović¹, Tanja Nenin², Uroš Cvelbar³, Zorana Dohčević-Mitrović¹ and Zoran Lj. Petrović¹

¹*Institute of Physics, University of Belgrade, Pregrevica 118, 11080 Belgrade, Serbia*

²*Institute for development of water resources "Jaroslav Černi", Jaroslava Černog 80, 11226 Belgrade, Serbia*

³*Jožef Stefan Institute, Jamova Cesta 39, Ljubljana, SI-1000, Slovenia
email: lazovic@ipb.ac.rs*

Abstract. In this article we present the results of decolourisation and degradation of Reactive Orange 16 dye in the water by a plasma needle. Argon flow rates are varied in order to improve the removal efficiency. We find that the complete decolourization and a considerable percent of mineralization are achieved after 60 min of plasma treatment for the flow rates higher than 4 slm. The decolourisation and mineralization effects are measured by UV/VIS spectrophotometry and total organic carbon content.

1. INTRODUCTION

Plasma technologies are used in wastewater treatment because of a high removal efficiency of organic pollutants. Besides the capability to abundantly generate chemically active species, plasma is used for water decontamination because of convenient operating conditions (atmospheric pressure and relatively low temperature) [1].

There are various types of non-thermal plasma devices such as plasma jets, plasma needle, gliding arc, etc. [2-4]. These plasmas can produce high concentrations of radicals [5]. Plasma generated radicals enable numerous biomedical applications. In our previous research we have used plasma needle for treatment of biological samples like bacteria, human stem cells, plant stem cells (calli) [2, 6-8]. Besides the biomedical applications, radicals are important in advanced oxidation processes [1]. OH radicals have a particularly large oxidation potential. They interact with organic pollutants and can decompose them into less or non-harmful components.

In this paper we present the results of decolourisation of Reactive Orange 16 (RO 16) azo dye recorded using the UV/VIS spectroscopy.

Furthermore, we present degradation curves for two different argon flow rates (4 and 8 slm) obtained by total organic carbon measurements (TOC).

2. EXPERIMENTAL SETUP

The experimental setup is given on Figure 1. Plasma needle consists of a body made of Teflon, a central electrode made of copper, and a glass tube. A dye sample is prepared with distilled water (50 mg/l, 25 ml). The needle tip is immersed into the solution as presented in Figure 1. Magnetic stirrer (300 rpm) preserved the homogeneity of the sample. We use different argon flow rates (1, 4, and 8 slm). Decolourisation is monitored by measuring absorbance after plasma treatments at 493.7 nm (which corresponds to the $-N=N-$ bond). A complete dye spectra and absorbance at a fixed wavelength are measured by UV/VIS spectrophotometry. Degradation is recorded based on the total organic carbon content.

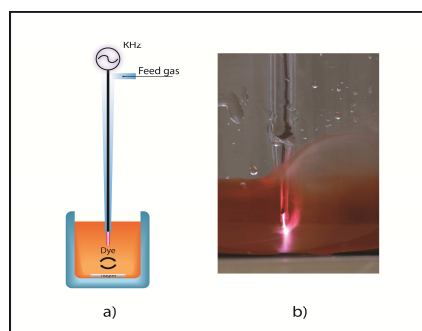


Figure 1. a) Experimental setup, b) Plasma in the dye solution.

3. RESULTS AND DISCUSSION

The degradation rate of RO 16 is determined following two different processes: the colour loss and oxidation. The colour loss gives evidence that the chromophore group which is responsible for the absorption of the dye molecule in the visible region of the spectral range is eliminated. This colorant is characterized by azo group as a chromophore ($-N=N-$) which has a maximum absorption at 493.7 nm. Decolourisation is presented on Figure 2. For the given set of experimental conditions we observe a decrease of absorbance and that the total decolourisation is achieved after 60 min of plasma treatment for the flow rates of 4 and 8 slm. However, for the lowest flow rate of 1 slm the colour loss is not complete even after 60 min of treatment, but it is obvious that there is a decreasing trend. In this case, longer treatment times could lead to the total decolourisation. It is very interesting to compare the decolourisation kinetics for 4 and 8 slm flow rates in the first 30 min and beyond that time. We can see that when we double the flow rate, the degradation rate significantly increases for the

first 30 min. For example, after 10 min of treatment the absorbance ratio (A/A_0) is reduced to 20 and 40 % for 8 and 4 slm flow rates of argon, respectively. However, after 30 min, the increase in flow rate does not contribute that much to the decolourisation rate as compared to the previous case.

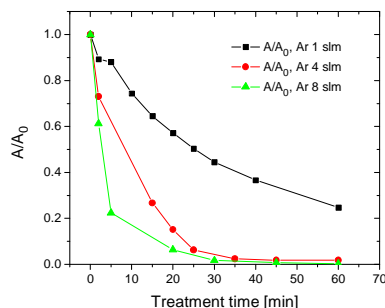


Figure 2. Decolourisation of Reactive orange 16 for three different argon flow rates (1, 4, 8 slm).

In order to demonstrate that the colorant is not just decolourised, but also degraded to some extent, we have performed TOC measurements. Although a full decolourisation is achieved after 60 min of plasma treatment, there is a possibility that hazardous by-products may appear as a result of incomplete decomposition of the molecule. To verify this, total organic carbon content, which concerns bond breaking in the aromatic part of the dye (C–C, C=C, C–N, C–S) is measured.

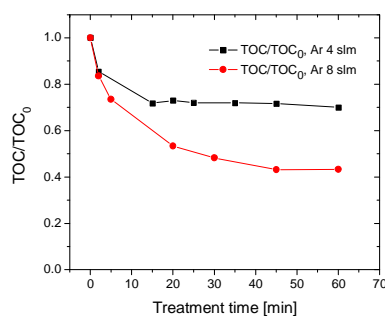


Figure 3. Degradation of Reactive Orange 16 for two different argon flow rates (4 and 8 slm)

We can see that the total organic carbon is reduced by about 60 % for 8 slm and only 30 % for 4 slm after 60 minutes of plasma treatment (Figure 3). As in the case of decolourisation, mineralisation rate also depends on the flow rate. For smaller flow rates the oxidation process is typically slower as compared to the

higher flow rates. Unlike decolourisation, full degradation was not reached after 60 min of plasma treatment.

4. CONCLUSION

In this paper we show the results of decolourisation and degradation of Reactive Orange 16 dye in aqueous solution. We find that complete decolourisation and a considerable percent of degradation are achieved after 1 hour of plasma treatment. As expected, degradation is much slower than decolourisation and both processes are dependent on treatment conditions such as the gas flow rate. We can conclude that the plasma needle can be a promising device for removal of organic pollutants from water and that further optimization of treatment parameters is needed to obtain high removal rates.

Acknowledgements

MESTD, Republic of Serbia, project no. III 41011 and ON 171037.

REFERENCES

- [1] B. Jiang, J. Zheng, S. Qiu, M. Wu, Q. Zhang, Z. Yan and Q. Xue, *Chem. Eng. J.*, 236, 348–368 (2014).
- [2] S. Lazović, N. Puač, M. Miletić, D. Pavlica, M. Jovanović, D. Bugarški, S. Mojsilović, D. Maletić, G. Malović, P. Milenković and Z. Petrović, *New J. Phys.*, 12, 8, 083037 (2010).
- [3] M. R. Ghezzar, F. Abdelmalek, M. Belhadj, N. Benderdouche and a Addou, *J. Hazard. Mater.*, 164, 2–3, 1266–74 (2009).
- [4] N. Puač, D. Maletić, S. Lazović, G. Malović, A. Đorđević and Z. Lj. Petrović, *Appl. Phys. Lett.*, 101, 2, 024103 (2012).
- [5] G. Malović, N. Puač, S. Lazović and Z. Petrović, *Plasma Sources Sci. Technol.*, 19, 3, 034014 (2010).
- [6] M. Miletić, D. Vuković, I. Živanović, I. Dakić, I. Soldatović, D. Maletić, S. Lazović, G. Malović, Z. Lj. Petrović and N. Puač, *Cent. Eur. J. Phys.*, 12, 3, 160–167 (2014).
- [7] M. Miletić, S. Mojsilović, I. Okić Đorđević, D. Maletić, N. Puač, S. Lazović, G. Malović, P. Milenković, Z. Lj. Petrović and D. Bugarški, *J. Phys. D: Appl. Phys.*, 46, 34, 345401 (2013).
- [8] N. Puač, S. Živković, N. Selaković, M. Milutinović, J. Boljević, G. Malović and Z. Lj. Petrović, *Appl. Phys. Lett.*, 104, 21, 214106 (2014).

CAPACITIVELY COUPLED RADIO-FREQUENCY DISCHARGES IN C₂H₂-Ar-N₂ MIXTURES: ENHANCING THE HEMOCOMPATIBILITY OF METALLIC SUBSTRATES

M. Santos^{1,2}, J. Hung², P. Michael², E. Filipe², A. Kondyurin¹, Martin K. C. Ng², S. G. Wise² and M. M. M. Bilek¹

¹*Applied & Plasma Physics Group, Physics School, University of Sydney, NSW 2006, Australia*

²*Heart Research Institute, Sydney, NSW 2042, Australia*

Abstract. We report the production of capacitively coupled radio-frequency plasma discharges generated in C₂H₂-Ar-N₂ atmospheres to create carbon-polymer-like coatings for metallic substrates. Optical emission spectroscopy diagnostics are used for quality control, by monitoring the radiation emitted by the plasma in each deposition. Hemocompatibility results show that the coating dramatically reduces thrombus weight, under both static and in flow conditions. Further, when translated to a stainless steel stent platform, our coating is robust, resisting cracking and delamination following stent expansion. This approach has strong potential for improving the biocompatibility of all metallic vascular implant, in particular coronary stents.

1. INTRODUCTION

In recent years, an increasing amount of research has aimed to improve the biocompatibility of metallic stents used in percutaneous coronary interventions. However, while current commercial devices have addressed the over-proliferation of smooth muscle cells, leading to vessel re-narrowing, long-term stent hemocompatibility remains a significantly issue. Current stent platforms carry on ongoing risk of thrombosis, requiring patients to be on dual anti-platelet therapies, which can result in bleeding and is not feasible for patients requiring additional surgery.

To address this issue, we used capacitively coupled radio-frequency (ccrf) discharges produced in C₂H₂-Ar-N₂ atmospheres to create a novel *plasma-activated coating (PAC)* [1, 2] that can be used to improve the hemocompatibility and facilitate the bio-integration of metallic vascular implants into the human vasculature. PAC was deposited onto 316L stainless steel (SS) flat sheets in a similar fashion to plasma enhanced chemical vapour deposition, a method widely used in both research and industry for thin film deposition. To evaluate the

hemocompatibility of *PAC* coatings, samples were exposed to heparinized whole blood in both static and flow conditions. The coatings were then delivered onto SS coronary stents, where the integrity of the carbon-polymer-like thin films was evaluated by means of SEM imaging post crimping and expansion of the stent.

2. EXPERIMENTAL DETAILS

PAC deposition was performed inside a stainless steel cylindrical (with a 10.5 cm radius and 35 cm height) ccrf reactor (see Figure 1.). The system was pumped down to a base pressure of $\sim 10^{-6}$ - 10^{-5} Torr and a reactive mixture of argon, nitrogen and acetylene was introduced in the upper part of the reactor. The flow, Q , of each gas ($Q_{\text{Argon}} = 3$ sccm, $Q_{\text{Acetylene}} = 2$ sccm and $Q_{\text{Nitrogen}} = 10$ sccm) was individually controlled using Allicat Scientific mass flow controllers and was maintained constant during the deposition. The plasma was sustained at a total pressure of 80 mTorr and the rf-power ($P_{\text{rf}} = 50$ W) was supplied by a 13.56 MHz frequency generator and delivered to the rf electrode through a matching box. During the deposition, all samples to be coated were electrically biased by means of a second electrode, which was driven by a high voltage dc pulse generator. The applied pulse voltage, frequency and duration was chosen to be, after process optimization, $V_{\text{bias}} = -1$ kV, $f_{\text{bias}} = 3$ kHz and $t_{\text{bias}} = 20$ μ s, respectively. The deposition time ranged from 5 – 10 min resulting in extremely thin films with deposited thicknesses (measured by profilometry) ranging 20 – 30 nm.

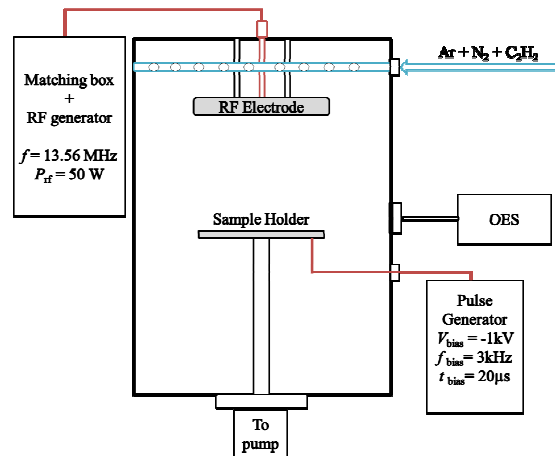


Figure 1. Schematic diagram of the plasma chamber used for *PAC* deposition.

For each deposition, the radiation emitted by the plasma was collected by an optical fibre, pointing directly to the area of the plasma above the sample holder. This optical emission spectroscopy (OES) set-up is used to estimate the relative density ratios and the vibrational temperatures of $N_2(C^3\Pi_u)$, $N_2^+(B^2\Sigma_u^+)$

and $N_2(B^3\Pi_g)$ states by measuring the emission intensities of the second positive system (SPS), the first negative system (FNS) and the first positive system (FPS) of nitrogen molecules. Figure 2. shows a typical emission spectrum of the C_2H_2 -Ar- N_2 plasma, recorded during *PAC* deposition. The monitoring of the radiation emitted by the plasma by means of OES diagnostics is a useful non-invasive technique, and is used in this work to control the reproducibility of the deposited *PAC* in subsequent depositions.

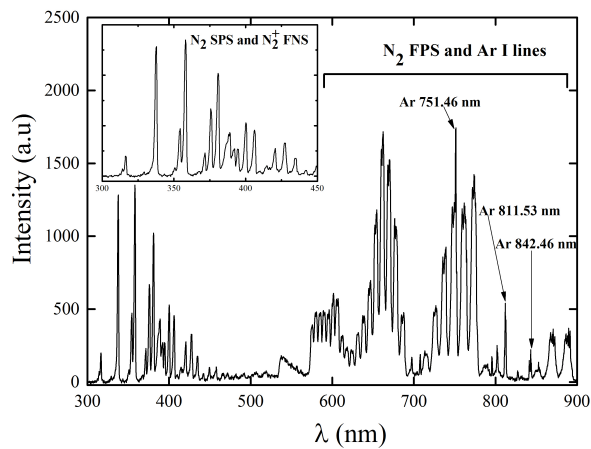


Figure 2. Typical emission spectrum of the C_2H_2 -Ar- N_2 plasma (300-900 nm) recorded during *PAC* deposition.

3. RESULTS

To evaluate the hemocompatibility of *PAC* surfaces, SS and *PAC* treated flat sheets were incubated in heparinized whole blood in both static and under flow conditions (for a more detailed description the reader is referred to [1]) for 30 and 60 minutes, respectively. Results show that *PAC* surfaces significantly reduce thrombus formation when compared to bare SS by 35-fold under static conditions and 43-fold under flow conditions (see Figure. 3a and 3b). Furthermore, SEM imaging *PAC* treated surfaces after 20 minutes of static blood contact clearly show the low thrombogenicity of *PAC*, noted by the reduced adhesion of erythrocytes and fibrin fibers when compared to SS (see Figure 3c).

The *PAC* platform described in this work was also applied to custom laser-cut stents, previously prepared with a graded interface between the SS stent surface and *PAC* coating [3]. The stents were then subjected to extreme stress by a balloon expansion, simulating the forces applied to these devices during a coronary intervention. SEM imaging of the expanded coated stents (see Figure. 3d) show that the coating has sufficient adhesion, undergoing stent expansion

without cracking or delamination. Results indicate that *PAC* could potentially be used on bare metal stents to enhance the hemocompatibility of these biomedical devices.

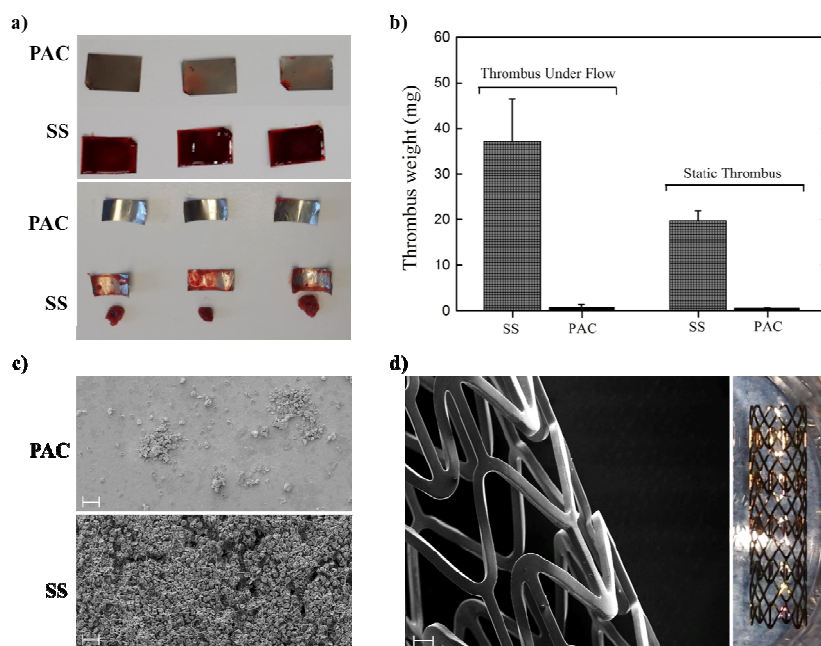


Figure 3. a) Image showing the results of the hemocompatibility assay under static (top) and flow conditions (bottom). b) Thrombus weight for the same conditions as in a). c) Representative SEM images of *PAC* treated surface and non-treated *SS* (scale bar = 20 μm). d) Representative SEM image (left) of expanded *PAC* coated stent (scale bar = 200 μm) and image of *PAC* coated stent (right).

Acknowledgements

The authors acknowledge the support of the Australian Research Council, National Health and Medical Research Council, and also the facilities as well as scientific and technical assistance at the Australian Centre for Microscopy and Microanalysis.

REFERENCES

- [1] A. Waterhouse *et al*, *Biomaterials* 31, 8332 (2010).
- [2] A. Waterhouse *et al*, *Biomaterials* 33, 7984 (2012).
- [3] Y. Yin *et al*, *Biomaterials* 33, 1675 (2012).

METHICILIN RESISTANT *STAPHYLOCOCCUS AUREUS* INHIBITION ZONE AREAS OBTAINED BY A PLASMA NEEDLE TREATMENT

Nenad Selaković¹, Nevena Puač¹, Maja Miletić², Irena Živanović³, Ivana Dakić³, Gordana Malović¹, Dragana Vuković³ and Zoran Lj. Petrović¹

¹*Institute of Physics, University of Belgrade, Pregrevica 118, 11080 Belgrade, Serbia*

²*Faculty of Dental Medicine, University of Belgrade, dr Subotića, 11000 Belgrade, Serbia*

³*Institute of Microbiology and Immunology, Faculty of Medicine, University of Belgrade, dr Subotića 1, 11000 Belgrade, Serbia*

Abstract. Plasma needle, nonequilibrium plasma source that operates at atmospheric pressure, was used for treatments of methicilin resistant *Staphylococcus aureus* (MRSA). Free radicals and other ion species formed inside the gas mixture of helium and air in the plasma needle discharge are cause for the inactivation of bacteria. In this paper we will show how the inhibition zone areas depend on the applied plasma power, distance of the plasma source relative to the sample and the exposure time.

1. INTRODUCTION

The expansion of the relatively new field of medicine, plasma medicine, is reflected in the development of new plasma devices operating at atmospheric pressure that can be used in the treatment of biological samples. Some of these atmospheric plasma sources, such as plasma jet, plasma needle, DBD and plasma torch [1-4] have been already used and investigated for possible application in sterilization of wounds and medical equipment, treatment of dental caries, faster coagulation of blood, inactivation of cancer cells [5-8], etc.

Plasma needle, originally introduced by Stoffels [9], is atmospheric pressure plasma source suitable for the treatment of biological samples. We have developed slightly advanced version of the plasma needle and, so far, used it for sterilization of planctonic samples of bacteria, differentiation of human periodontal stem cells into osteogenic line and for plant stem cells – calli. [10-12]. Plasma needle is mild source of plasma, but with abundant chemistry that is essential for successful treatments. One of the most important limits that has to be determined is the area of the treatment i.e. the range of the radical and ion species from the plasma. Therefore, we have used MRSA samples in order to determine

zone of inhibition for different treatment times, powers and distances of the source from the sample.

2. EXPERIMENT

Plasma needle is made of glass tube with o.d. of 6 mm and i.d. of 4 mm. Ceramic tube (o.d. ~1 mm) with tungsten wire is placed inside the glass tube. Tungsten wire serves as powered electrode. Helium flows between the ceramic and glass tube. During all experiments helium flow was kept constant at 1 slm. The plasma appears on the tip as a faint glow with a diameter around 1 mm. We power this plasma device with sine wave signal at 13.56 MHz. Electrical circuit of plasma needle contains signal generator, linear amplifier and matching box.

The MRSA isolate used in this study was recovered from a surgical wound and identified as MRSA by BD Phoenix Automated Microbiology System (Becton Dickinson Diagnostic Systems, Sparks, MD). Bacterial suspension were prepared by suspending overnight grown culture in sterile physiological saline. The turbidity of bacterial inoculum was adjusted to 0.5 McFarland standard ($\approx 10^8$ CFU/mL) by using a Densimat photometer (BioMeriex, France). After that suspension was spread evenly on the surface of a solid growth media in Petri dishes and exposed to the plasma needle.

We divided each Petri dish into the 9 areas and each area was exposed to the treatment. The experimental parameters that we varied were distance between tip of the needle and sample surface (2 mm and 4 mm), exposure time (60 s, 180 s and 300 s) and power delivered to the plasma (1.5 W-3 W). All treatments were done in triplicate. As control we have used untreated samples and helium treated samples when there was no ignition of the discharge.

3. RESULTS AND DISCUSSION

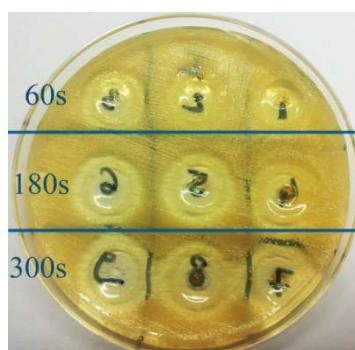


Figure 1. Treated samples of MRSA placed in Petri dish

In the Fig. 1 we can see inhibition zone areas obtained for the power of 1.5 W. Three upper fields were treated for exposure time of 60 s, the middle three fields 180 s and three fields below for 300 s. The needle in this plasma

treatment was set at a distance of 2 mm and it can be seen that the inhibition zone areas have larger diameter compared to the plasma needle.

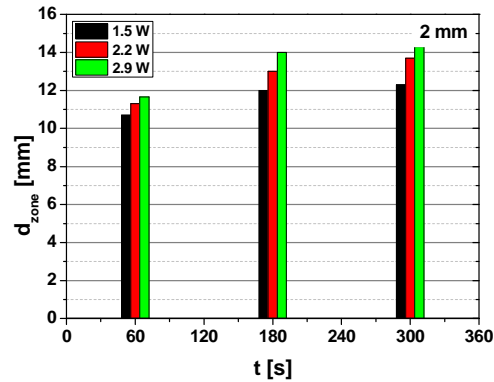


Figure 2. Comparison of MRSA inhibition area diameter for three different applied power of plasma needle and three different exposure times. The distance from plasma to sample was 2 mm.

Fig. 2 shows that the inhibition zone areas expand with the increase of the plasma power and the exposure time. Diameters of the obtained areas are in the range of 10-15 mm. We can see that there is no linear dependence of the measured diameters versus treatment time. With the increase of the treatment time diameters of the inhibition zones saturate at certain values. The higher the power saturation will occur for shorter treatment times. The largest inhibition area is obtained for maximum power 2.9 W, exposure time 300 s and the minimum distance of 2 mm.

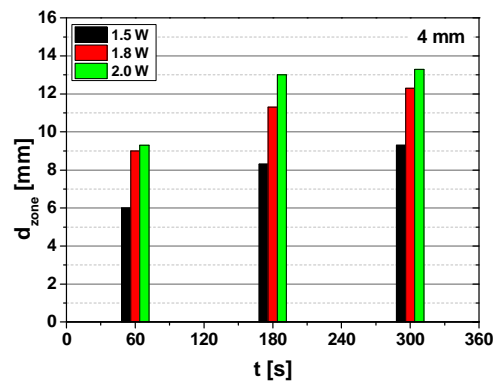


Figure 3. Comparison of MRSA inhibition area diameter for three different applied power of plasma needle and three different exposure times. The distance from plasma to sample was 3 mm.

For treatments with a distance of 4 mm we have observed smaller inhibition zones (see Fig. 3). This can be explain by following. Increase in the distance between the tip of the plasma needle and sample leads to a reduction in power and consequently we have reduced production of chemically reactive species. As in case for 2 mm distance increase in treatment time leads to saturation values of inhibition zones diameters.

4. CONCLUSION

We used the plasma needle in order to determine the surface area of the sample where the plasma makes inhibition effects. It was shown that the obtained inhibition zone areas are much larger than the size of the plasma needle.

Acknowledgements

This study was supported by Grant Nos. III41011, ON171037 and ON173024, MESTD, Republic of Serbia.

REFERENCES

- [1] N. Puač, D. Maletić, S. Lazović, G. Malović, A. Đorđević, and Z. Lj. Petrović, *Appl Phys. Lett.*, 101, 24103, (2012).
- [2] E. Stoffels, I. E. Kieft, R. E. J. Sladek, E. P. Van Der Laan, and M. Steinbuch, *Plasma Sources Sci. Technol.* 15, 169, (2006).
- [3] I. A. Shkurenkov, Y. A. Mankelevich, and T. V Rakhimova, *Eur. Phys. J. D.* 62, 213, (2011).
- [4] S. Yonson, S. Coulombe, V. Léveillé, and R. L. Leask, *J. Phys. D: App. Phys.* 39, 3508, (2006).
- [5] M. Laroussi, *Plasma Processes Polym.* 2, 391, (2005).
- [6] E. Stoffels, A. J. Flikweert, W. W. Stoffels, and G. M. W. Kroesen, *Plasma Sources Sci. Technol.* 11, 383, (2002).
- [7] G. Fridman, G. Friedman, A. Gutsol, A. B. Shekhter, V. N. Vasilets, and A. Fridman, *Plasma Processes Polym.* 5, 503 (2008).
- [8] B. Gweon, M. Kim, D. Bee Kim, D. Kim, H. Kim, H. Jung, J. H. Shin, and W. Choe, *Appl. Phys. Lett.* 99, 63701 (2011).
- [9] E. Stoffels, Y. A. Gonzalvo, T. D. Whitmore, D. L. Seymour, and J. A. Rees, *Plasma Sources Sci. Technol.* 15, 501, (2006).
- [10] S. Lazović, N. Puač, M. Miletić, D. Pavlica, M. Jovanović, D. Bugarski, S. Mojsilović, D. Maletić, G. Malović, P. Milenković, and Z. Petrović, *New J. Phys.* 12, 83037, (2010).
- [11] M. Miletić, S. Mojsilović, I. Okić Đorđević, D. Maletić, N. Puač, S. Lazović, G. Malović, P. Milenković, Z. Lj Petrović, and D. Bugarski, *J. Phys. D: Appl. Phys.* 46, 345401, (2013).
- [12] N. Puač, S. Živković, N. Selaković, M. Milutinović, J. Boljević, G. Malović, and Z. L. Petrović, *Appl. Phys. Lett.*, 104214106, (2014).

SURFACE WAVE AND OPERATION MODES OF PLASMA ANTENNA

N. N. Bogachev^{1,2}, I. L. Bogdankevich^{1,2}, N. G. Gusein-zade^{1,2} and
A. A. Ruhadze²

¹*Moscow State Technical University of Radio Engineering, Electronics and
Automation (MSTU MIREA), Russia, Moscow*

²*Prokhorov General Physics Institute, Russian Academy of Sciences (GPI RAS),
Russia, Moscow*

Abstract. Characteristics of a surface wave on a plasma column with a finite radius and operation modes of a plasma antenna are studied in this work. The dispersion equation of the surface wave has been solved for various values of plasma parameters. The numerical model of plasma based on Drude's theory. Distributions of the electric fields in near zone of the antenna and radiation patterns were obtained by the numerical simulation. These characteristics showed operation modes of the plasma antenna that correspond to modes of the surface wave.

1. INTRODUCTION

Nowadays plasma antennas are studied in many countries [1-6]. In a plasma antenna a metallic tube is replaced by a plasma column. Main attention is paid to study a Plasma Asymmetric quarter-wave Dipole (monopole) antenna (PAD) with a discharge tube [1, 3-6]. This antenna (see fig.1) was researched in this work. We studied the surface wave along PAD and operations modes of PAD. Properties of the surface wave and operations modes are interrelated. They are defined by plasma parameters.

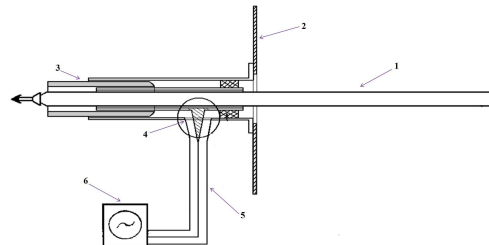


Figure 1. Plasma asymmetric dipole antenna: 1 – plasma discharge tube, 2 – metal screen, 3 – coaxial line, 4 – coaxial tee, 5 – coaxial cable, 6 – transmitter.

2. DISPERSION EQUATION SOLUTIONS

The surface wave plays important role in operation of the plasma antenna. The dispersion equation of the surface wave for cylindrical plasma with finite radius is formula (1). This equation follows from conditions of a tangential components continuity of the field E_z and H_ϕ .

$$\varepsilon(\omega_0) \tau_1 \frac{K_0(r_0 \tau_2)}{K'_0(r_0 \tau_2)} + \tau_2 \frac{I_0(r_0 \tau_1)}{I'_0(r_0 \tau_1)} = 0 \quad (1)$$

where plasma dielectric permittivity defined by

$$\varepsilon(\omega_0) = \varepsilon_0 - \frac{\omega_p^2}{\omega_0(\omega_0 + i\nu_e)} \quad (2)$$

and $\tau_1 = \sqrt{k^2 - \frac{\omega_0^2}{c^2}}$, $\tau_2 = \sqrt{k^2 - \varepsilon(\omega_0) \frac{\omega_0^2}{c^2}}$, $\omega_p = \sqrt{\frac{n_e e^2}{m_e \varepsilon_0}}$ - plasma

frequency, ν_e - electron collision frequency, ε_0 - vacuum dielectric permittivity, n_e - electron plasma density, m_e and e - mass and charge of electron, k - wave vector, $\omega_0 = 2\pi f_0$ - frequency of electromagnetic wave, c - velocity of light, r_0 - radius of cylindrical plasma, K_0 , I_0 and K'_0 , I'_0 - Bessel modified functions and their derivatives respectively.

Characteristics of the surface wave are defined by a plasma dielectric permittivity, which depends on the ratio of ω_0 and ω_p . The real parts of solutions of the dispersion equation are given on fig. 2 for various plasma density values.

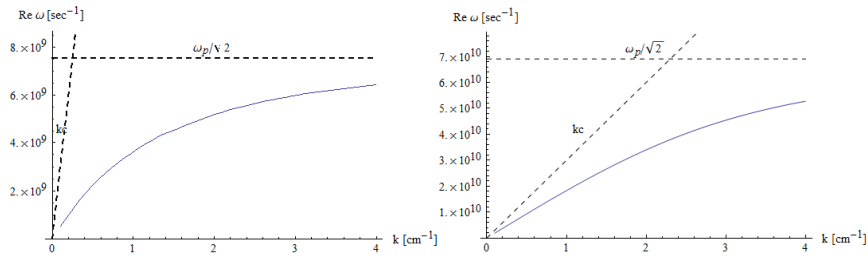


Figure 2. Solutions of dispersion equation for the plasma density values: $n_e = 8,0 \cdot 10^{10} \text{ cm}^{-3}$ (left) and $n_e = 3,6 \cdot 10^{12} \text{ cm}^{-3}$ (right).

The left dispersion curve on fig. 2 strongly differs from the kc line and represents non-linear dependence for the small plasma density $n_e = 8,0 \cdot 10^{10} \text{ cm}^{-3}$, when ω_p is near ω_0 . At such plasma density the antenna will work either in non-linear or nonradiating mode. For a case when ω_p is ten times more than ω_0 ($n_e = 3,6 \cdot 10^{12} \text{ cm}^{-3}$) the plasma antenna has two modes linear and non-linear. In

the linear mode the efficient length of the plasma antenna is smaller than at the similar metal antenna.

3. NUMERICAL MODEL, SIMULATION RESULTS AND DISCUSSION

The model of the plasma antenna conforms to scheme on fig. 1. It consists of the coaxial cable, the metal screen, the plasma antenna (the length - 4 cm, the radius - 0,5 cm) and the perfect matching layer on boundaries of calculating area. The electromagnetic wave with the frequency of 1,7 GHz moved through the coaxial cable to the plasma antenna. Model of plasma is based on Drude's theory where the dielectric permittivity of plasma is defined by formula (2). The model is created in the KARAT code (author is V.P. Tarakanov) [7]. The KARAT code solves Maxwell's equations by FDTD method.

We received electric field distributions in the near zone of the antenna. Distributions of the E_r component on z are presented on fig. 3, a), and radiation patterns are presented on fig. 3, b). Curves 1-3 are distributions for the plasma antenna with parameters from the table 1, curve number 4 is the same for the similar metal antenna.

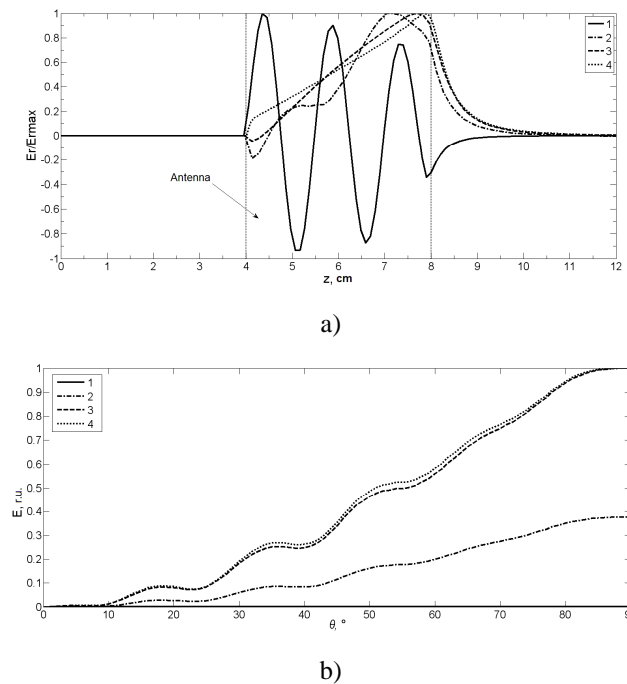


Figure 3. Distributions of $E_r(z)$ (picture a) and radiation patterns (picture b): 1-3 – modes of the plasma antenna, 4 – the metal antenna.

The curve 1 shows that along the plasma antenna the surface electromagnetic wave extends. It is a nonradiating mode. The curve 2 is transitional operation mode. The curves 3 and 4 coincide. Both curves show distribution of $E_r(z)$ for the quarter wave asymmetrical dipole antenna. These distributions are proportional to a charge distribution along the dipole. Radiation patterns show that the mode 1 is nonradiating, the mode 2 is non-linear (or transition), and mode 3 is the linear mode that is near to mode of the metal antenna.

Table 1. Plasma parameters of various modes.

No	Ratio ω_p vs ω_0	ω_p, s^{-1}	n_e, cm^{-3}
1	$\omega_p \approx \sqrt{2} \omega_0$	$1,58 \cdot 10^{10}$	$8,0 \cdot 10^{10}$
2	$\omega_p \approx 5 \cdot \omega_0$	$5,35 \cdot 10^{10}$	$9,1 \cdot 10^{11}$
3	$\omega_p \approx 10 \cdot \omega_0$	$1,07 \cdot 10^{11}$	$3,6 \cdot 10^{12}$

Acknowledgements

This work is supported by Russian Foundation of Based Research (RFBR) project number 14-08-31336. Authors express huge gratitude to professor A. M. Ignatov for discussion and valuable remarks.

REFERENCES

- [1] G. G. Borg, J. H. Harris, D. G. Miljak, and N. M. Martin // Appl. Phys. Lett. 74, 22, 3272 (1999).
- [2] I. Alexeff, T. Anderson, S. Parameswaran, et. al., IEEE Trans. on plasma science 34, 2, 166 (2006).
- [3] E. N. Istomin, D. M. Karfidov, I. M. Minaev, A. A. Rukhadze, K. F. Sergeichev et al., Plasma Physics Reports 32, 5, 388 (2006)/
- [4] C. Liang, Y. Xu, Z. Wang, Chin. Phys. Lett 25, 10, 3712 (2008).
- [5] Z. Chen, A. Zhu, J. LV, WSEAS Trans. on Com. 12, 2, 63 (2013).
- [6] N. N. Bogachev, I. L. Bogdankevich, N. G. Gusein-zade, V. P. Tarakanov, Acta Polytechnica 53, 2, 110 (2013).
- [7] V. P. Tarakanov, *User's Manual for Code KARAT* (VA, Springfield, 1992).

THE EFFECT OF A DC ELECTRIC FIELD ON THE DYNAMICS OF CHARGED SUBMICRON PARTICLES IN THE AFTERGLOW OF DUSTY PLASMA

I. Filatova¹, N. Chubrik¹ and F. Truhachev²

¹*Institute of Physics NAS of Belarus, Nezavisimosti Ave. 68, 220072 Minsk, Belarus*

²*State Institution of Higher Professional Education "Belarusian-Russian University", Mira Ave. 43, 212005, Mogilev, Belarus*

Abstract. The decay of dust structures formed in dusty plasma of a capacitively coupled radio frequency (RF) discharge is investigated in the afterglow stage. The dynamics of the submicron sized dust particles controlled by applying an external DC electric field is studied. The numerical simulations are performed for estimation of charge and velocity of particles after the extinction of plasma.

1. INTRODUCTION

Dusty plasmas find numerous industrial applications in growth and processing of nanomaterials, surface modification, plasmachemical devices cleaning, separation of macroparticles by size, etc. [1, 2]. It is known that micron and submicron dust particles acquire a large negative charge (from $10^2 e$ to $10^4 e$) in dusty plasma and form ordered structures [3]. Recent studies have shown that dust grains can preserve their residual charge in the afterglow phase [4–7]. It was shown that the decay of dust clusters in the afterglow can be accompanied with an explosion provided an efficient acceleration of micron sized particles [8]. This phenomenon can be used for deposition of dust particles on substrates to enhance physical and chemical properties of various materials such as catalysts [9].

In this paper, the effect of an external DC electric field on the dynamics of negatively charged dust particles in the afterglow of dusty plasma has been studied.

2. EXPERIMENTAL

The discharge was operated at a frequency of 5.28 MHz between two plane-parallel electrodes with the diameter of 120 mm separated by a distance of $L = 21$ mm. The experimental setup is described in detail in [7]. Ambient air was

used as a working gas in a pressure range of 40 and 100 Pa. Under the experimental conditions, the electron density and the electron and ion temperatures were $n_e \sim 10^8 \text{ cm}^{-3}$, $T_e \sim 2 \text{ eV}$, and $T_i \sim 0.03 \text{ eV}$, respectively.

A positive dc voltage (37 V) from stabilized power supply was applied to the upper electrode instead of the RF voltage, after the discharge was switched off to estimate the value of a residual charge on dust grains and their velocities. The strength value E of the established electric field between the electrodes was 1760 V/m. It was assumed that grains having a negative residual charge would shift toward the upper electrode.

Polydisperse Al_2O_3 grains with the diameter of $r_p \sim 0.1\text{--}10 \text{ }\mu\text{m}$ were externally injected into the plasma volume and levitated in the vicinity of the bottom electrode. Photographs of grains illuminated by a narrow laser sheet ($\lambda = 635 \text{ nm}$) with a thickness of about 1 mm and height of 20 mm were taken in the plane perpendicular to the electrode surface using a standard video camera with a frame rate of 25 s^{-1} . The velocities of grains were estimated using a series of frames, which reflected the dynamics of grains over a time interval of $\Delta t \sim 0.4 \text{ s}$ after switching-off of the discharge and termination of plasma recombination.

3. RESULTS AND DISCUSSIONS

The ordered structures consisted of several layers of particles were formed at the edge of plasma column near the electrode sheath. A dust structure formed at pressure of 40 Pa had the form of a truncated cone with the upper/lower diameter of nearly 4/21 mm and the height of 7 mm (Fig. 1). The largest grains from the lower layers precipitated onto the electrode just after the discharge was switched off. The phase corresponded to Fig.1c (in 1.32 s after the discharge switching off) is associated with an explosion of the dust cluster consisted of small particles ($\sim 200 - 100 \text{ nm}$) from the upper layers.

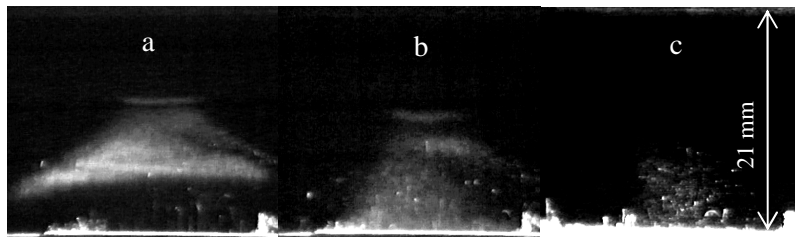


Figure 1. The dust structure decay in the afterglow of dusty plasma at pressure of 40 Pa: in 2 ms (a), 160 ms (b) and 1.32 s (c) after the discharge switching-off.

At $P = 93.3 \text{ Pa}$ we observed two layers (I) and (II) formed at a distance of 12 and 9 mm from the bottom electrode accordingly (Fig. 2). The dynamics of particles from the upper layers (I) and (II) was analyzed. In the absence of the dc voltage grains from layers I and II moved downward with

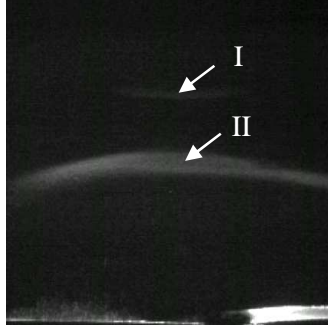


Figure 2. The dust structure decay in the plasma afterglow at pressure of 93.3 Pa: in 2 ms after the discharge switching-off.

velocities of $v_{DI} \approx 2.2$ mm/s and $v_{DII} \approx 5$ mm/s, respectively. After applying a positive dc potential, grains from both layers moved upward with the same velocities $v_{DI} = v_{DII} \approx 2.2$ mm/s. The radii r_D of grains from layers I and II were found to be $0.1 \mu\text{m}$ and $0.25 \mu\text{m}$, correspondingly, and the residual charge of particles can vary in the range from $-1e$ to $-10e$, depending on the grain size [7].

The dynamic parameters of dust particles were estimated from the balance of forces acting on the dust grain in the post-discharge phase:

$$\vec{F}_G + \vec{F}_{ND} + \vec{F}_E = m_D \vec{a}, \quad (1)$$

where m_D and a – mass and acceleration of dust grain, F_G , F_{ND} , F_E – the gravity force, the friction force against the neutral gas and the electric force, correspondingly. The velocity v_D of grain accelerating in the applied dc electric field was estimated using the expressions obtained in [8]:

$$v_D = \frac{kT(3QE - 4\pi r_D^3 \rho g)}{\sqrt{2\pi} r_D^2 m_n p_n v_{Tn} (8 + \pi)}, \quad (2)$$

where $Q = Ze$ is the dust grain charge, e is the elementary charge, $E = \varphi/L$ is the external dc electric field, r_D and ρ are the grains effective radius and their mass density, m_n , p_n and $v_{Tn} = \sqrt{8T_n / \pi m_n}$ are the mass, pressure and thermal velocity of buffer gas molecules, correspondingly. The velocity of grains (with the radius of $0.25 \mu\text{m}$) as a function of buffer gas pressure for two E values (1000 and 2000 V/m) is shown in Fig. 3.

At a gas pressure of 93.3 Pa and the electric field strength of 2000 V/m, we obtained a velocity value of grains with the size of $0.25 \mu\text{m}$ of ~ 2 mm/s which agrees with the experimentally observed value.

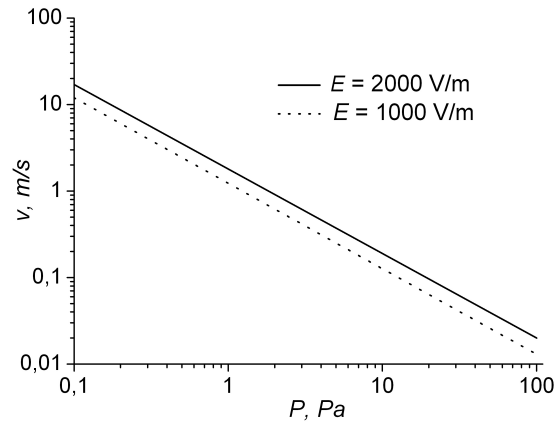


Figure 3. Dust grain velocity in the afterglow of RF dusty plasma in dependence on gas pressure at different strength E of applied DC electric field (for particle with the size of $0.25 \mu\text{m}$).

The grain velocity essentially increases with the decrease of pressure and the increase of strength value of the applied electric field. This result is in agreement with the results of model simulations of dust cluster explosion in the afterglow phase of the complex plasma discharge [10].

Acknowledgements

This work is partially supported by State Committee on Science and Technology of the Republic of Belarus under the grant No $\Phi 14\text{KA}3\text{-}004$.

REFERENCES

- [1] A. Bouchoule, *Dusty Plasmas: Physics, Chemistry and Technological Impacts in Plasma Processing*, p. 418 (Wiley, New York, 1999).
- [2] E. Stoffels, W. W. Stoffels, H. Kersten, et al. *Phys. Scr. T* 89, 168 (2001).
- [3] H. M. Thomas and G. E. Morfill. *Nature*. 379, 806 (1996).
- [4] S. Khrapak, A.V. Ivlev, G. Morfill et al. *Phys. Rev. Lett.* 90, 225002 (2003).
- [5] M. A. Childs and A. Gallagher. *J. Appl. Phys.* 87, 1086 (2000).
- [6] L. Couëdel, A. A. Samarian, M. Mikikian and L. Boufendi. *Europhys. Lett.* 84, 35002 (2008).
- [7] I. I. Filatova, N. I. Chubrik and F. M. Truhachev. *Plasma Phys. Rep.* 37, 1042 (2011).
- [8] A. Barkan and R. L. Merlino. *Phys. Plasmas*. 2, 3261 (1995).
- [9] F. K. Urban III, A. Hosseini-Tehrani, P. Griffiths, et al., *J. Vac Sci Technol. B* 20, 995 (2002).
- [10] A. Barkan and R. L. Merlino. *Phys. Plasmas*. 2, 3261 (1995).

POWERFUL MICROWAVE CONTROL BY THE 1D EBG PLASMA STRUCTURE IN A WAVEGUIDE

V.I. Arkhipenko¹, Th. Callegari², L.V. Simonchik¹, J. Sokoloff², M.S. Usachonak¹

¹*Stepanov Institute of Physics NAS of Belarus, pr. Nezavisimosti 68, 220072 Minsk, Belarus*

²*LAPLACE, UPS-CNRS, 118 route de Narbonne, 31062 Toulouse, France*

Abstract. The possibilities for 1D EBG plasma structures creation by using the positive column of glow discharges at low and atmospheric pressures and their utilization for controlling powerful electromagnetic wave propagation through plasma parameters variation are demonstrated.

1. INTRODUCTION

Most devices, which are based on the electromagnetic band gap (EBG) effect, are realized using the metallic or dielectric elements, have fixed parameters and do not allow fast reconfiguration and adjustment. It may create critical problems for high speed, large scale or complex systems such as, for instance, PCs, servers or automotive application, leading to significant time delay or extra development cost. Electric way of changing the characteristics of the EBG structures is considered to be more promising now. Glow discharge plasmas have a great potential for the application in the function of control elements [1, 2]. In our investigations, waveguide filter, which is widely used in microwave technique, serves as an example of 1D EBG structure. The use of gas discharge plasma as a reconfigurable element in a waveguide filters seems attractive because it can support a high incident microwave power.

2. DESIGN OF THE 1D EBG PLASMA STRUCTURES IN WAVEGUIDE

In our experiments we use typical X-band waveguide ($23 \times 10 \text{ mm}^2$) of about 20 cm long (Fig. 1, *a*). The periodical structure is formed by inserting plasma columns (positive columns of low pressure neon lamps GSh-6 or GSh-5 (Fig. 1, *b*) or atmospheric pressure glow discharge in argon) inside 3 holes of 4 mm in diameter that were drilled through the opposite wide waveguide walls. These plasma inhomogeneity configurations form resonators. The holes are separated by $l = \Lambda_g/2$, where Λ_g is a wavelength in the waveguide, which is expressed by relation

$$\Lambda_g = \lambda_{0m}(1 - (\lambda_{0m}/2a)^2)^{-1/2} \quad (1)$$

where λ_{0m} is the free space wavelength corresponding to the middle of the pass band; a is the wide waveguide wall dimension ($a = 23$ mm). Thus, for the frequency $f_0 = 10.2$ GHz ($\lambda_{0m} = 29$ mm), the resonator length is $l = \Lambda_g/2 = 19$ mm.

Such periodic structure forms a typical waveguide filter, which can be regarded as a four-pole and which can be characterized by the wave scattering matrix [S]. The calculations of the wave S-matrix elements were performed using Ansoft HFSS software [3].

3. TRANSMISSION OF 1D EBG PLASMA STRUCTURE FORMED BY LOW PRESSURE PLASMAS

In Fig. 1, *c* the experimental transmission spectra of waveguide section for three regimes of GSh-6 lamps are shown (symbols). No evident transmission band is observed at the DC current of 25 mA (Fig. 1, *c*, circles). The decrease on about 5 dB in the transmission level takes place around frequency of 8 GHz. However, we cannot say that a periodic structure in waveguide is created. In the pulsing lamp regimes, when the current reaches 1 A and 2 A, the EBG structure clearly appears (Fig. 1, *c*, triangles).

The magnitude of electric field changes weakly for these regimes (from 0.7 Td to 1 Td). Therefore, the electron collision frequency, which depends on E/N changes weakly as well. Estimations lead to the electron collision frequency $\nu_m \sim 3 \times 10^{10} \text{ s}^{-1}$ and to the electron density from $1.5 \times 10^{13} \text{ cm}^{-3}$ to 10^{15} cm^{-3} .

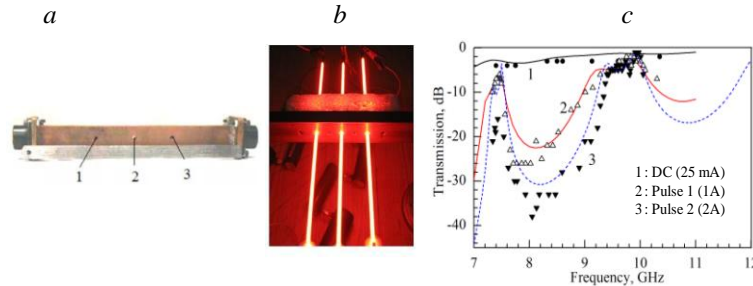


Figure 1. Photos of the waveguide section with holes (a), with inserted GSh-6 lamps (b) and transmission spectra at different currents (c).

The calculation results are shown in the same figure (curves). The electron collision frequency is assumed to be equal to $1.5 \times 10^{10} \text{ s}^{-1}$ and the electron density is varied in order to fit the experimental curve. We obtained the following electron concentrations: $1 \times 10^{13} \text{ cm}^{-3}$ (curve 1), $2 \times 10^{14} \text{ cm}^{-3}$ (2) and $5 \times 10^{14} \text{ cm}^{-3}$ (3). These magnitudes are about two times less than the experimental one estimated above. However, taking into account the features of the experimental and calculation procedures (average values of discharge lamp parameters, fixed value of electron collision frequency, homogeneous plasma,

negligible skin layer etc.) one can state a satisfactory agreement of both the calculated and experimental results.

As it follows from Fig. 1, *c*, the forbidden band exists in the range 8-9 GHz. Let an incident pulse microwave power at frequency of 8.5 GHz be 10 μ s in duration. This duration can be controlled through changing the delay time between the leading edge of microwave pulse and the lamps ignition time. In Fig. 2, *a*, curve 1 represents the waveform of the transmitted microwave pulse with initial duration of 10 μ s when the lamps are turned off. Curves 2, 3, and 4 correspond to the lamp ignition with time delay of 7 μ s, 3 μ s and 50 ns respectively.

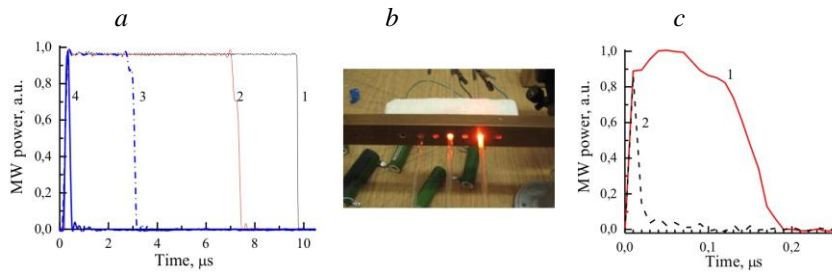


Figure 2. Pulse durations at different ignition delays (*a*), image of microwave discharges at high power (*b*) and waveforms of initial (1) and transmitted (2) high power microwave pulses (*c*).

Let's consider the interaction of powerful microwave radiation with a 1D EBG plasma structure formed by three GSh-5 lamps. We use generator with output power about 50 kW at a frequency $f_0 = 9.15$ GHz and a pulse duration of about 150 ns. This microwave power is enough for gas breakdowns in the lamps. As a result of this breakdown we observe in lamps the microwave discharges with different luminosities (Fig. 2, *b*). Therefore, the 1D EBG plasma structure in waveguide can be formed solely under influence of this power. Simultaneously, we register a reduction in pulse duration transmitting through 1D EBG waveguide structure from 150 ns down to about 20 ns (Fig. 2, *c*). In this case, the 1D EBG plasma structure acts as a passive device for reducing the duration of a transmitted powerful microwave pulse.

4. THE 1D EBG PLASMA STRUCTURE FORMED BY ATMOSPHERIC PRESSURE GLOW DISCHARGES

In order to carry out an active control of the transmitted powerful microwave it is needed to increase the threshold of microwave gas breakdown. That can be realized by an increase in the gas pressure in discharge tube. The array from three atmospheric pressure glow discharges (APGD) in argon is used for this purpose. The discharges are ignited in glass tubes (inner diameter is 3 mm) located in the waveguide holes (see Fig. 1, *a*). Interelectrode gap is about

11 mm and it is larger than a size of a narrow waveguide wall. Argon is used as a working gas at total flow of 1 l/min through the three tubes. Due to the large heat release in the APGD, pulse regimes of discharges will be more preferable. Homemade pulse voltage power supply is used in the experiments. Output voltage is 2.5 kV and maximal discharge currents in separate tubes are reached 15-20 μs later than ignition. Image of the discharge in waveguide is show in Fig. 3, *a*.

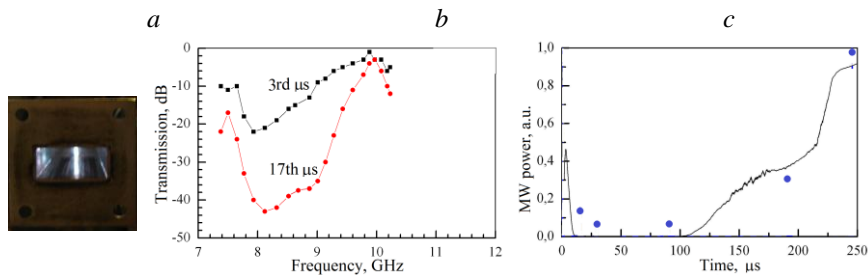


Figure 3. Image of discharge (*a*), transmission spectra at 3rd μs and 17th μs (*b*) and time behavior of microwave signal at frequency of 9.15 GHz (*c*).

Transmission spectra of the 1D EBG plasma structure formed by the three discharges in argon at 3rd and 17th μs are presented in Figure 3, *b*. Clearly, the transmission spectrum at 17th μs is more contrasting due to higher discharge current and, respectively, electron density. The microwave signal level in a suppressed frequency band is less than -40 dB in this moment while its attenuation in pass band does not exceed 4 dB.

In Fig. 3, *c*, waveform (solid curve) of a microwave signal at frequency of 9.15 GHz and at power of about 5 mW is shown. As it is seen, a good suppression is observed during the first hundred microseconds. In next hundred microseconds, transmission increases and recovers fully at around 250 μs , when discharges are out. When we use the powerful (~50 kW) microwave pulses, their suppression is significant during the first hundred microseconds. That is shown by circles in Fig. 3, *c* at frequent time points.

Acknowledgements

This work is supported under the BRFFR-CNRS grant F13F-005.

REFERENCES

- [1] O. Sakai, K. Tachibana, Plasma Sourc. Sci. Techn. 21, 013001 (2012).
- [2] J. Lo, J. Sokoloff et al., Applied Physics Letters 96, 251501 (2010).
- [3] Ansoft HFSS, <http://www.ansys.com/Products/Simulation+Technology/Electromagnetics/High-Performance+Electronic+Design/ANSYS+HFSS>.

PLASMA METHODS IN DEPOSITION AND EVALUATION OF NANO-SIZED CARBON FILMS

Branko Tomcik¹, Bratislav P. Marinkovic^{1,2} and Branko Predojevic³

¹ *Institute of Physics, University of Belgrade. PO Box 68. 11080 Belgrade, Serbia*

² *College for Electrical Engineering and Computing for Vocational Studies, Vojvode Stepe 283, 11000 Belgrade, Serbia*

³ *Faculty of Natural Sciences, University of Banja Luka, Republic of Srpska, B&H*

Abstract. For the deposition of ultrathin carbon overcoat with thicknesses below 2 nm the carbon precursors from the gas phase have advantages over the solid carbon targets. The surface carbon marks (micro and nano sized dust) that are part of deposition process can be minimized by the gas plasma composition. Introduction of ion and plasma sources over the traditional sputtering and cathodic arc solid carbon sources can improve the surface smoothness and continuous coverage of the disk. Optical emission spectroscopy from the gas excited species as well as micro Raman spectroscopy of deposited carbon film can be used to track the carbon dust formation on the surface.

1. INTRODUCTION

For the deposition of ultrathin diamond like carbon films with thicknesses below 5 nm a uniform surface deposition, carbon micro and nano dust-free coverage and controlled protective film properties are essential for the magnetic recording discs [1-3]. Cyclic incorporation of atomic and ionized oxygen or hydrogen in the process gas mixture, (e.g. C₂H₄ with noble and reactive gases), as well as effective pump-out time for the produced long living oxygen metastables and hydrogen atoms, can minimize deposition and adherence of carbon nano dust particles. DC sputtering technology is particularly vulnerable to creation of carbon dust and target poisoning. Improvements on the sputtering targets (better heat removal from the target surface, small grain size of the hot-pressed carbon particles during the target production, bipolar self-bias, controlled gas channel supply) are some of the measures in improving the carbon film properties [4,5].

Deposition of DLC film with a thickness below 2 nm is extremely challenging. Also, to prevent cross-contamination it is necessary for the sources to operate in separate vacuum chambers. Number of surface marks and defects, along with other protective properties, is a key parameter in the effectiveness of

the plasma method used. Introduction of the Plasma Beam Source (PBS) in carbon film deposition opens a door for the further optimization of the disk smoothness (e.g. by ion beam polishing, milling, disk buffing under vacuum for subsequent vacuum lubrication) with variable incident angle ion beam deposition and minimization the magnetic dead layer thickness.

2. RESULTS AND DISCUSSION

In Fig.1 is shown how a disk surface may look like after the carbon film deposition with sputtering or filtered cathodic arc deposition method. The optical surface analyzer and a standard Nomarsky polarization interference type optical microscope have been used.

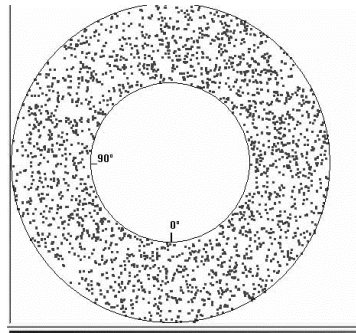


Figure 1. Pits and surface marks on the magnetic substrate (deposition conditions: 3 mTorr, $V_b = -120$ V; $N(\text{at}\%) = 11.2$ in $\text{Ar} + \text{C}_2\text{H}_4 + \text{N}_2$ gas).

The surface marks (hills) were not evenly distributed. Almost all surface marks in size over 1 micron were located close to the inner diameter. Majority of observed surface marks have a lateral size around 6 μm .

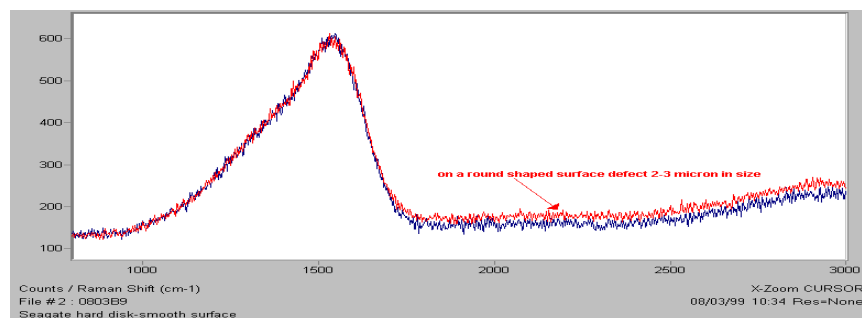


Figure 2. Micro Raman spectra of carbon films and the surface marks. Bottom curve: aside from the surface mark, on matrix. Upper curve: on a surface defect.

Increased background signal on the right side of the carbon peak with respect to the left side indicates higher hydrogen content in the surface mark.

Micro Raman analysis of the surface marks on a non-textured disk deposited with a new graphite target at different hydrocarbon concentration is shown in Fig.2 and Fig.3. Poisoning of the sputtering targets takes place very quickly, even after 15 minutes of operation.

The hydrogen can originate also from the water vapor occluded on the chamber wall as well as from the residual hydrogen of the target surface.

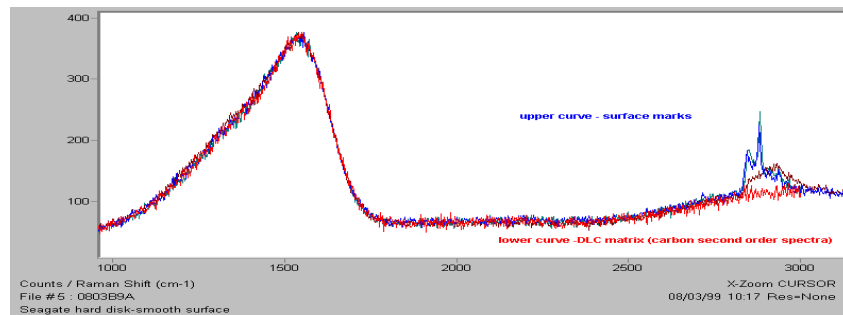


Figure 3. Several micro Raman spectra on different surface marks on a same substrate. An origin of the maximum at 2847 cm^{-1} and at 2880 cm^{-1} is not yet clarified. Both feature a sudden rise of a signal at 2840 cm^{-1} surpassing the carbon second order spectrum. Surface marks have a linear dimension ~ 5 micrometers.

Surface marks observed on the substrate as well as white and black appearing nodulus formation on the target are “rich” in hydrogen. Instead of introducing a gas mixture close to the target surface it is worth to consider a separate gas channel for hydrogen/hydrocarbon and nitrogen gas channel close to the disc. In order to estimate how long a target should be exposed to the cleaning process in pure Ar, a hydrogen H_{β} -line (486.1 nm) was acquired during the removal of the hydrogenated DLC formation on the target. A new target was “contaminated” by a gas mixture containing Ar (33 sccm), C_2H_4 (1.5 sccm) and N_2 (3 sccm) at a DC discharge power of 760 W (3.4 W/cm^2) for 20 minutes. This measurement may bring us to conclusion that even after 11 minutes of discharge cleaning, a leveled off hydrogen signal coming from the target surface can not be achieved. Because of numerous parameters that influence the emission intensity (e.g. electron energy distribution function, local electron density, energy of sputtered hydrogen atoms), that may change simultaneously, this time interval is only a rough prediction. Obviously, a solution for the carbon dust particle contamination should be searched in the gas phase carbon precursor deposition methods.

3. CONCLUSIONS

Ultrathin DLC carbon overcoat with a small number of surface defects-marks can be obtained in plasma discharges using hydrocarbon gas as a carbon precursor, rather than a solid, and in a controlled gas mixture. By adding a pure hydrogen or oxygen in a cyclic gas operation on dedicated deposition chambers the amount of carbon nano-dust and micro particles deposited on the substrate surface can be controlled. Non contact methods such as optical emission spectroscopy should be used for optimizing the carbon film deposition process. Additional tube with the holes of proper size looking at the substrate should be mounted in the vicinity of protective shields. In that way a reaction of hydrogen with the target surface can be minimized. On all micro Raman spectra due to the small defect size and low instrumental lateral resolution ($\sim 3 \mu\text{m}$) the influence of the matrix is predominant.

Acknowledgements

Authors would like to thank A*STAR, Singapore Agency for Science, Technology and Research and National University of Singapore for providing the capabilities for the experimental work.

REFERENCES

- [1] Bharat Bhusan, (*Tribology and Mechanics of Magnetic Storage Devices*, Second edition, Springer, New York, 1996)
- [2] C. Denis Mee, Eric D. Daniel, editors in (*Magnetic Recording Handbook: Technology and Applications*, New York. Mc Graw-Hill, 1990)
- [3] A.C. Ferrari, J.C. Robertson, Phys. Rev. B61, 1409 (2000).
- [4] J. Robertson, Tribology International 36, 405-415 (2003).
- [5] J. Robertson, Mat. Sci. Eng. R37, 129 (2002).

Section 4.

GENERAL PLASMAS

FIFTY YEARS OF QUASARS: PHYSICAL INSIGHTS AND POTENTIAL FOR COSMOLOGY

J. W. Sulentic¹, P. Marziani², D. Dultzin³, M. D'Onofrio⁴ and A. del Olmo¹

¹*IAA (CSIC), Spain*

²*INAF, Oss. Astronomico Padova, Italy*

³*IA-UNAM, Mexico*

⁴*Dipartimento di Fisica & Astronomia, Universita di Padova, Italy*

Last year (2013) was the 50th anniversary of the discovery of quasars. It is an appropriate time to review what we know about them both empirically and theoretically. These compact plasma sources show luminosities in the range of log bolometric luminosity 44.0 - 49.0 ergs/s and yet the emitting region can be no larger than a few Solar Systems (i.e. 1-3 light months in diameter). The advent of 8-10 meter class telescopes enable us to study them spectroscopically in ever greater detail.

In 2000 we introduced a 4D Eigenvector parameters space involving optical, UV and X-ray measures designed to serve as the 4D equivalent of the 2D H-R diagram so important for depicting the diversity of stellar types and evolutionary states. This diagram has revealed a principal sequence of quasars distinguished by Eddington ratio (proportional to the accretion rate per unit mass). While stellar differences are primarily driven by the mass of a star, the quasar differences are primarily driven by the ratio luminosity-to-mass.

Out of this work has emerged the concept of two quasars populations A and B separated at Eddington ratio around 0.2 which maximizes quasar multispectral differences. The mysterious 8 are lowest accretors with the largest black hole masses. Finally we consider the most extreme population A quasars which are the highest accretors and in some cases belonging to the youngest quasar population. We describe how we propose to use them as standard candles for cosmology.

STUDY OF A HIGH-PERFORMANCE PLASMA IN THE LARGE HELICAL DEVICE

Akio Komori¹, Tomohiro Morisaki¹ and LHD Experiment Group¹

¹*National Institute for Fusion Science
Toki 509-5292 Japan*

For more than 16 years, the Large Helical Device (LHD) has led fusion science and plasma physics, as the largest heliotron device in the world. With great effort and resulted discoveries, LHD has produced some significant outcome [1], especially in the steady-state operation and three-dimensional edge/divertor physics [2], which are caused by the advantage of the heliotron system for its currentless plasma [1]. In this lecture, recent results from LHD experiments are presented, together with the progress of the related fusion technology supporting the experiment.

In order to realize the fusion reactor, it is necessary to maintain the high performance plasma for more than one year, thus establishment of the steady-state operation and innovation of the technology are mandatory. Recently an ultra-long pulse discharge with central electron and ion temperatures of 2 keV and electron density of $1.2 \times 10^{19} \text{m}^{-3}$ was successfully maintained for 48 minutes. Such a high performance plasma was heated and sustained by newly developed gyrotrons and ICRF antennas. Due to the continuous heating with relatively high power of 1.2 MW, the total heating energy during the long pulse discharge was 3.36 GJ, which is the world highest record.

The highest central ion temperature of 8.1 keV was also recorded in the last experimental campaign. In this experiment, it is essential to reduce the edge electron density. If the edge density is low, heating beams can penetrate deeper into the core region without significant attenuation in the edge plasma. Careful discharge cleaning with low RF power was performed to evacuate neutrals in the vessel wall, between main discharges with high heating power. These processes realize the quite low recycling for particle, which results in the reduction of the edge plasma density.

Based on the knowledge and experiences obtained from LHD experiments for 16 years, LHD is now ready to start the deuterium-deuterium (DD) experiment. It is expected for LHD to explore the future aspect of helical reactors.

REFERENCES

- [1] A. Komori, et al., Nucler Fusion, **49**, 104015 (2009).
- [2] T. Morisaki, et al., Nucler Fusion, **53**, 063014 (2013).

ANION CHEMISTRY IN TITAN

Ján Žabka¹, Miroslav Polášek¹, Christian Alcaraz² and Véronique Vuitton³

¹*J. Heyrovský Inst. of Phys. Chem. of the ASCR, Dolejškova 3, Praha, CZ*

²*Lab. de Chimie Physique, UMR 8000 CNRS - Univ. Paris Sud 11, Orsay, Fr*

³*Inst. de Planétologie et d'Astrophys. de Grenoble, CNRS, Univ J. Fourier, Fr*

The Saturnian magnetosphere is dominated by neutrals originating from the icy satellites and ring system. These neutrals are ionized in the magnetosphere producing a plasma composed of protons, H_2^+ , and so-called “water group” ions O^+ , HO^+ , H_2O^+ and H_3O^+ [1]. A precipitation of these ions with energies of 1-4 keV was found at Titan by the Cassini CAPS spectrometer [2]. It has been suggested [3] that a few percent of the oxygen ion flux is converted to O^- ions that may play a role in the Titan’s negative ion chemistry, which was found unexpectedly rich, but is still rather poorly understood. The objective of this study was to measure the relative cross-sections for the formation of O^- and HO^- ions by charge reversal processes of O^+ , HO^+ , H_2O^+ and H_3O^+ ions in collisions with Xe, and major constituents of Titan’s atmosphere.

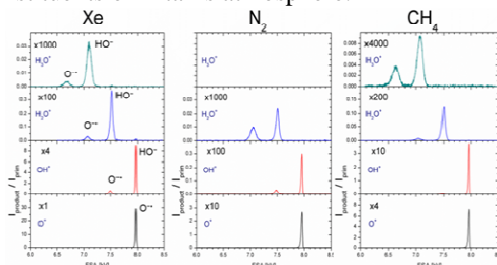


Fig. 1. Charge reversal mass spectra of “water group” ions colliding with Xe, N_2 , CH_4 .

Our results show that oxygen containing negative ions as well as neutral species can be formed by the high-energy collisions of positive “water group” ions impacting the Titan’s upper atmosphere. These species may interact with the components of the Titan’s atmosphere in many different ways and can, for example, initiate numerous ion/neutral-, neutral/neutral-, and collision-induced unimolecular reactions.

Acknowledgements: This work was supported by the Czech Science Foundation (project 14-19693S) and by the french national program of planetology (PNP).

REFERENCES

- [1] C. S. Arridge, N. André et al, *Space. Sci. Rev.* 162, 25, (2011).
- [2] R. E. Hartle, E. C. Sittler et al, *Planet. Space Sci.* 54, 1211 (2006).
- [3] T. E. Cravens et al. *Geophys. Res. Lett.* 35, L03103 (2008).

ELECTRON EXCITATION AND AUTOIONIZATION CROSS SECTIONS FOR ELEMENTS OF CHEMICALLY PECULIAR (CP) STARS: STUDY OF BISMUTH

B. Predojević^{1,2}, V. Pejčev², D. Šević² and B. Marinković²

¹*Faculty of Natural Sciences, University of Banja Luka, Republic of Srpska,
Bosnia and Herzegovina*

²*Institute of Physics, University of Belgrade, POB 68, 11080, Belgrade, Serbia*

Electron impact excitation from the ground state of bismuth atoms has been studied. A beam of electrons was scattered from a beam of atoms and intensity of scattered electrons was measured for scattering angles up to 150° and incident electron energies of 10, 20, 40, 60, 80 and 100eV. Obtained intensities were used for the calculation of relative differential cross sections (DCS). In addition, we recorded energy loss-spectra at different incident electron energies and scattering angles. These spectra were analyzed to determine the energy levels of bismuth atom below and above (autoionization) the first ionization limit.

The apparatus, described earlier [1], was used in the present measurements to record electron energy-loss spectra and to determine direct angular distribution of elastically and inelastically scattered electrons. Spectroscopic data of autoionizing region had been recently published [2].

The presence of bismuth was confirmed in spectra of the chemically peculiar (CP) Hg-Mn stars 73Dra and HR 7775 [3], [4] and more recently in χ Lupi [5]. The obtained results for relative DCS and identified autoionized energy levels of bismuth were analyzed and compared with previous experimental and theoretical data. The connection between our investigations of bismuth and astrophysical measurements are discussed.

Acknowledgements: This work is partly supported by the project MESTD RS OI 171020 and COST Action MP1002.

REFERENCES

- [1] B. P. Marinković et al, Rad. Phys. Chem. 76, 455, (2007).
- [2] B. P. Marinković et al, Int. J. Mass Spectrom. 271, 76-79 (2008).
- [3] B. N. G. Guthrie, Ap&SS 15, 214, (1972).
- [4] J. M. Jacobs and Dworetzky, Nature 299, 535, (1982).
- [5] G. M. Wahlgren et. al. ApJ 435, L67, (1994).

LANGMUIR WAVES IN INTERPLANETARY PLASMA

Sonja Vidojević

IHIS – techno experts d.o.o., Belgrade, Serbia

STUDYING THE COMPLEX ABSORPTION PROFILES OF Si IV IN 21 HiBALQSO SPECTRA

D. Stathopoulos^{1,2}, E. Danezis¹, E. Lyratzi^{1,2}, A. Antoniou¹, L. Č. Popović³,
D. Tzimeas¹ and M.S. Dimitrijević³

¹*University of Athens, Faculty of Physics Department of Astrophysics,
Astronomy and Mechanics, Panepistimioupoli, Zographou 157 84, Athens,
Greece*

²*Eugenides Foundation, 387 Sygrou Av., 17564, Athens, Greece*

³*Astronomical Observatory of Belgrade, Volgina 7, 11160 Belgrade, Serbia*

⁴*Laboratoire d' Etude du Rayonnement et de la Matière en Astrophysique,
Observatoire de Paris*

We investigate the physical conditions and kinematics of broad absorption line region clouds of Si IV in 21 HiBAL Quasars. We use the Gauss-Rotation model in order to fit and analyze the broad absorption troughs of Si IV resonance lines in the UV region of the electromagnetic spectrum. We find that the BAL flow is not smooth but instead plasma clouds are formed in it. BAL troughs present multicomponent structure which indicates the existence of more than one absorbing clouds in the line of sight, where every absorbing cloud produces a Si IV doublet (i.e. a system of resonance lines). We show that the blending of these doublets produces the apparent broad absorption troughs we observe. One of our main achievements is that we managed to decompose and deblend each complex absorption trough to the individual systems that it consists of. Apart from that, we succeeded in deblending the resonance lines between every system. By achieving accurate fits to the BAL troughs we calculated some physical and kinematical parameters that describe the plasma clouds in the line of sight. These parameters are: the radial outflow velocities of the clouds, the rotational velocities of the clouds around their own axes, the random velocities of ions inside each plasma cloud, the optical depth in the center of every absorption component, the FWHM, the Gaussian typical deviation, the absorbed energy and the column density. As a final step we correlate these physical parameters in order to draw useful conclusions.

DYNAMIC CHARACTERISTICS OF EXCITED ATOMIC SYSTEMS

N. N. Bezuglov^{1,2}, M. S. Dimitrijevic³, A. N. Klyucharev^{1,2} and A. A. Mihajlov⁴

¹*Department of Physics, St. Petersburg State University, 198504, Russia*

²*University ITMO, St. Petersburg, 197101, Russia*

³*Astronomical Observatory, Volgina 7, Belgrad, Serbia*

⁴*Institute of Physics, P.O. Box 57, 11001, Belgrad, Serbia*

The dynamics of excited atom interactions with other atoms, which often lead to associative ionization, is largely governed by stochastic diffusion of the valence electron through Rydberg states prior to the ionization [1]. Such processes are associated with random changes of the energy state of the highly excited electron, and they are likely to influence the nuclear dynamics, especially at ultracold collision energies. Possibilities of manipulation of the chaotic dynamics of Rydberg states require a detailed exploration. For an electron in a given Rydberg state moving in a microwave field, which can be generated via interaction with another atom or molecule, there exists a critical field strength, above which motion of the electron in the energy space is chaotic. Recently it was shown a way [2] to block the dynamic chaos regime if a given Rydberg state is located somewhat above the middle between two other states with orbital quantum number differing by one, whereby level shifts can be controlled by employing Stark/Zeeman shifts in external DC electric/magnetic fields. The stochastic effects in collisions involving Rydberg particles, in which the initial and final reaction channels are connected via intermediate highly excited collision complexes with multiple crossings of energy levels, can be treated using the dynamic chaos approach (Chirikov criterion, Standard and Keppeler mapping of time evolution of the Rydberg electron, solution of the Fokker-Planck- and Langevin-type of equations, etc.). Such approach to obtain dynamics characteristics is a natural choice, since the treatment of Rydberg electron dynamics as a kind of diffusion process allows one to bypass the multi-level-crossing problem, which can hardly be solved by the conventional quantum chemistry methods.

Acknowledgements: This work was supported by Government of Russian Federation, Grant 074-U01 and by EU FP7 Centre of Excellence FOTONIKA-LV (REGPOT-CT-2011-285912-FOTONIKA).

REFERENCES

- [1] K. Miculis et al, J. Phys. B: At. Mol. Opt. Phys. 38, 1811 (2005).
- [2] M. Yu. Zakharov et al, Russian Journal of Phys. Chem. B 5, 537 (2011).

THE NON-SYMMETRIC ION-ATOM ABSORPTION PROCESSES IN THE HELIUMRICH WHITE DWARF ATMOSPHERES IN UV AND EUV REGION

V. A. Srećković¹, A. A. Mihajlov¹, Lj. M. Ignjatović¹ and M. S. Dimitrijević^{2,3}

¹*University of Belgrade, Institute of Physics, Zemun, Serbia*

²*Astronomical Observatory, Volgina 7, 11160 Belgrade 74, Serbia*

³*IHIS-Technoexperts, Bežanijska 23, 11080 Zemun, Serbia*

The processes of absorption charge-exchange and photo-association in He+H⁺ collisions together with the process of ion HeH⁺ photo-dissociation are considered as factors of influence on the opacity of the atmospheres of helium-rich white dwarfs in the far UV and EUV region. The considered nonsymmetric ion-atom absorption processes are treated as one of the important channels of influence on the opacity of the atmospheres of helium-rich white dwarfs in the far UV and EUV region. The main result of this research is the establishment of the fact that in the cases of helium-rich white dwarfs with H:He > 10⁻⁵, and particularly with H:He = 10⁻⁴, these non-symmetric ion-atom absorption processes have to be included *ab initio* in the models of the corresponding atmospheres, since in the greater part of the considered far UV and EUV region they could be completely dominant with respect to the referent electron-atom and symmetric ion-atom absorption processes [1,2]. Besides, attention has been paid again in this paper to the role of the hydrogen component in the atmospheres of helium-rich white dwarfs [3].

Acknowledgements: This work is partially supported by our Ministry under the grant NO 176002 and III4402.

REFERENCES

- [1] A. A. Mihajlov, Lj. M. Ignjatović, V. A. Srećković, M. S. Dimitrijević and A. Metropoulos, MNRAS, 431(1), 589 (2013).
- [2] V. A. Srećković, A. A. Mihajlov, Lj. M. Ignjatović and M. S. Dimitrijević, Adv. Space Res. 4, eprint arXiv:1312.0094, (2014).
- [3] Lj. M. Ignjatović, A. A. Mihajlov, V. A. Srećković and M. S. Dimitrijević MNRAS 439, 2342 (2014).

GRAVITY WAVES IN STRATIFIED SOLAR ATMOSPHERE

Gordana Jovanović

University of Montenegro, Džordža Vašingtona bb

Abstract. We study analytically propagation properties of gravity waves in gravitationally stratified solar atmosphere. The main aim of this paper is derivation of reflection coefficient for gravity waves and its application to the boundary between the solar photosphere and solar corona. It is shown that reflection coefficient for gravity waves is very high, $R \approx 1$. Therefore these waves can not transfer the wave energy from photosphere towards the corona.

1. INTRODUCTION

Observations and measurements of solar oscillations have been carried out with high precision for decades in helioseismology studies Ref.[1], aiming to enlighten the internal structure of the Sun. The standard mathematical procedures in that field are based on solving eigenvalue problem for various models of solar interior and atmosphere Ref.[2]. We consider a problem of driven waves. This means, we assume the waves are generated in one of the two regions¹, they propagate in a two region model with constant temperatures- solar photosphere and solar corona. In this model waves experience both-reflection and transmission on the plane boundary $z = 0$. Stratified atmospheres can support not only acoustic waves but also gravity waves. We study propagation and reflection of gravity waves in order to understand what part of the gravity waves energy will be reflected back in the photosphere, and what part of the energy will be transmitted in the corona (the transmission coefficient is $T = 1 - R$). This is important for the energetics of the solar atmosphere.

2. EQUATIONS

The standard set of non-linear hydrodynamic equations describe the dynamics of a fully ionized plasma with properties of a perfect gas. These equations are: continuity equation, momentum equation and adiabatic law

¹How these waves are generated is not the primary task of this work.

for a perfect gas. The initial basic state is defined by the model itself which implies a stationary, static (i.e. the hydrostatic equilibrium), gravitationally stratified isothermal plasma with constant acceleration. Thus, in Cartesian coordinates, we have:

$$\vec{g} = -g\vec{e}_z, \quad g = \text{const}, \quad \rho_0 = \rho_0(z), \quad p_0 = p_0(z). \quad (1)$$

The unperturbed plasma is initially in hydrostatic equilibrium and assumed to be stepwise isothermal $T_0 = \text{const}$, i.e. with constant temperature in each of the two regions separated by the boundary $z = 0$. The basic state is given by:

$$\frac{d}{dz} \ln \rho_0 = -\frac{1}{H}. \quad (2)$$

Here, $H = v_s^2/\gamma g$ is the constant scale height. The solution of the above equation is:

$$\rho_0(z) = \rho_{00}e^{-z/H}. \quad (3)$$

In the model used in this paper there is a constant sound speed: $v_s^2 = \gamma p_0(z)/\rho_0(z) = \gamma RT_0 = \text{const}$, where $\gamma = c_p/c_v = 5/3$ is the ratio of specific heats, $R = R_0/\bar{M}$ and $R_0 = 8.3145 \text{ JK}^{-1}\text{mol}^{-1}$ is the universal gas constant while $\bar{M} = 0.5 \times 10^{-3} \text{ kg mol}^{-1}$ is the mean particle molar mass of the considered e-p plasma.

2.1 Perturbations

The dynamics of small amplitude waves is described by the standard set of HD equations for ideal plasma which are perturbed by taking any unknown physical quantity $\Psi(x, y, z, t)$ as a sum: $\Psi(x, y, z, t) = \Psi_0(z) + \delta\Psi(x, y, z, t)$. Perturbations $\delta\Psi(x, y, z, t)$ have the following form $\delta\Psi(x, y, z, t) = \Psi'(z)e^{i(k_x x + k_y y - \omega t)}$, with $|\Psi'| \ll |\Psi_0|$. Unperturbed quantities $\Psi_0(z)$ satisfy the basic state equation Eq.(2). The standard set of ideal hydrodynamic equations linearized according to these perturbations can be reduced to a sistem of two coupled ordinary differential equations:

$$\frac{d\xi'_z}{dz} = \frac{g}{v_s^2}\xi'_z - \frac{(\omega^2 - k_p^2 v_s^2)}{\rho_0(z)v_s^2\omega^2}p', \quad \frac{dp'}{dz} - g\frac{d\rho_0}{dz}\xi'_z = \rho_0(z)\left(\omega^2 + \frac{g^2}{v_s^2}\right)\xi'_z - \frac{g}{v_s^2}p', \quad (4)$$

where $\xi'_z = iv'_z/\omega$ is the z-component (i.e. the vertical component) of the fluid displacement, while p' is the pressure perturbation. The density distribution $\rho_0(z)$ is given by Eq.(3) and $k_p^2 = k_x^2 + k_y^2$ designates square of the horizontal wavenumber. The Eq.(4) allows the following solutions for the vertical fluid displacement ξ'_z and the pressure perturbation p' :

$$\xi'_z(z) = \xi'_z(0)e^{\frac{z}{2H}}e^{ik_z z}, \quad p'(z) = p'(0)e^{\frac{-z}{2H}}e^{ik_z z}. \quad p'(z) = p'(0)e^{\frac{-z}{2H}}e^{ik_z z}. \quad (5)$$

Eq.(4) with solutions in Eq.(5) finally yields the dispersion equation:

$$k_p^2 = \frac{\omega^2(\omega^2 - \omega_{co}^2 - v_s^2 k_z^2)}{v_s^2(\omega^2 - \omega_{BV}^2)}, \quad (6)$$

where $\omega_{co}^2 = \gamma^2 g^2 / 4v_s^2 = v_s^2 / 4H^2$ is the square of the acoustic wave cutoff frequency and $\omega_{BV}^2 = (\gamma - 1)g^2 / v_s^2 = (\gamma - 1)v_s^2 / \gamma^2 H^2$ is the square of the Brunt-Väisälää frequency. Eq.(6) corresponds to gravito-acoustic dispersion equation. Physical quantities in dispersion equation can be made dimensionless by appropriate scalings: $K_p = k_p H$, $K_z = k_z H$ and $\Omega = \omega H / v_s$. Here, K_p and K_z are dimensionless horizontal and vertical wavenumbers scaled to $1/H$ and Ω is dimensionless frequency scaled to v_s/H . Dimensionless form of dispersion equation (6) is:

$$K_z^2 = \Omega^2 - \Omega_{co}^2 - \frac{K_p^2(\Omega^2 - \Omega_{BV}^2)}{\Omega^2}, \quad (7)$$

with $\Omega_{co} = 0.5$ and $\Omega_{BV} = \sqrt{(\gamma - 1)/\gamma^2} = 0.489$. Dispersion equation (7) is bi-quadratic in Ω and its solutions present two wave branches-acoustic branch (solution with plus sign) and gravity branch (solution with minus sign). In the limit of very low frequencies, $\Omega \ll 1$, dispersion equation (7) has a form $\Omega^2 \approx K_p^2 \Omega_{BV}^2 / (K^2 + \Omega_{co}^2)$. This is a dimensionless dispersion equation for gravity waves. Note that K_p must be nonzero and, unlike the acoustic waves, there is no vertical gravity waves. For $K_z = 0$, but $K_p \gg \Omega_{co}$, gravity wave dispersion equation yields $\Omega \approx \Omega_{BV}$. Brunt-Väisälää is cutoff frequency and gravity waves cannot propagate above it.

3. REFLECTION COEFFICIENT

Harmonic wave which propagate through regions (1) and (2) does not changes its frequency Ω and horizontal wavevector component K_p parallel to the boundary $z = 0$. Normal wavevector component K_z has a discontinuity at $z = 0$ where it changes from K_{z1} to K_{z2} according to the dispersion equation (7). An incident gravity wave with unit amplitude in region (1)-photosphere is partially reflected at the boundary $z = 0$ with amplitude A_r and partially transmitted into the region (2)-corona with amplitude A_t . Applying equality of the unperturbed pressures at $z = 0$ and continuity of the fluid displacement ξ'_z and pressure perturbation p' the equations for complex amplitudes A_r and A_t can be obtained Ref.[3]. Reflection coefficient for gravity waves is defined as $R = |A_r|^2$ and it is presented in Fig.1. Dimensionless horizontal phase velocity is $V_h = \Omega / K_p$. Parameter $s = T_1 / T_2$ is constant because photosphere and corona are isothermal with temperatures $T_1 = 6 \times 10^3 K$ and $T_2 = 10^6 K$. Reflection coefficient for gravity waves is very high $R \approx 1$. It could be concluded that gravity waves are strongly reflected back to the photosphere from the photosphere-corona boundary Ref.[4]. A very small part of their energy could be transmitted in the solar corona. Indeed, there is no observational data to support the existence of gravity waves in the solar corona yet.

4. FIGURES

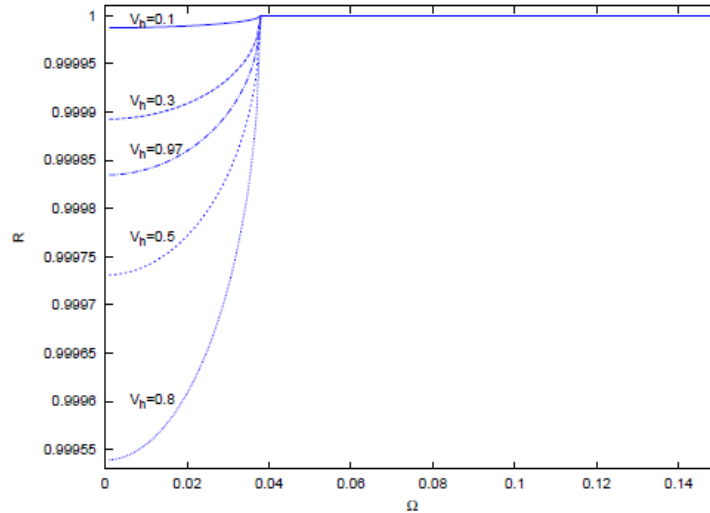


Figure 1. Reflection coefficient R for gravity waves that propagate from the solar photosphere to corona, when $s = 0.006$. It is a function of the frequency Ω . Allowed values of horizontal phase velocities are $V_h < 0.98$. Frequency $\Omega = \sqrt{s}\Omega_{BV} \approx 0.038$ is characteristic frequency that separates regions of propagating ($\Omega < \sqrt{s}\Omega_{BV}$) and evanescent gravity waves ($\Omega > \sqrt{s}\Omega_{BV}$). This means that $\Omega = \sqrt{s}\Omega_{BV}$ is a frequency above which the total internal reflection of gravity waves occurs and reflection coefficient is equal to unity.

Acknowledgements: This work is done in the framework of montenegrin national project Physics of Ionized Gases and Ionized Radiation.

REFERENCES

- [1] Christensen-Dalsgaard, J., Stellar Oscillations (Aarhus, Lecture Notes, Astronomisk Institut), Aarhus Universitet, 1989.
- [2] Goedbloed, H., Poeds, S., Principles of Magnetohydrodynamics, Cambridge University Press 2004, Cambridge, UK.
- [3] Jovanović, G., Romanian Reports in Physics, Vol. 65, No. 4, P. 13981406, 2013.
- [4] Lou, Y.Q., Gravitational-acoustic wave transformation in stellar atmospheres, Mon. Not. R. Astron. Soc. 276, 769-784, 1995.

SHAPE OF THE Fe $K\alpha$ LINE EMITTED FROM A RELATIVISTIC ACCRETION DISK WITH AN EMPTY GAP

P. Jovanović¹, V. Borika Jovanović² and D. Borika²

¹*Astronomical Observatory, Volgina 7, 11060 Belgrade, Serbia*

²*Atomic Physics Laboratory (040), Vinča Institute of Nuclear Sciences,
University of Belgrade, P.O. Box 522, 11001 Belgrade, Serbia*

Abstract. Here we study the shape of the Fe $K\alpha$ line emitted from a relativistic accretion disk with an empty gap, which could be formed in the binary systems of the supermassive black holes (SMBHs) when a secondary black hole is embedded in the accretion disk around a primary. We modeled X-ray emission in the Fe $K\alpha$ line from such a disk using numerical simulations based on ray-tracing method in the Kerr metric. The obtained results show that such a gap or cavity in the disk could leave the imprints in form of ripples in the emitted Fe $K\alpha$ line profile. If observed, the Fe $K\alpha$ line profiles with these imprints could be therefore used for studying the properties of such SMBH binaries and plasma physics in their relativistic accretion disks.

1. INTRODUCTION

Binary systems of supermassive black holes are formed in galactic mergers, and at some stage when two SMBHs become gravitationally bound and start to orbit around their center of mass, accretion of the surrounding matter on both SMBHs could be expected and as a result, a strong X-ray emission in the broad Fe $K\alpha$ line at 6.4 keV might be observed [1]. This line is emitted from a very compact region in the accretion disk near the central SMBH, and therefore, it represents a powerful diagnostic tool for studying plasma physics and space-time geometry in this region (see e.g. [2] for an overview and [3] for a case study).

In the case of the SMBH binaries, the Fe $K\alpha$ line emitting regions could have different structures, depending on the mass ratios of the components, separation between them and properties of their accretion disks [1]. In some cases, the Fe $K\alpha$ line emission could arise from both accretion disks around primary and secondary SMBHs, located in a central low density cavity of a circumbinary disk, and this emission is then affected by the Doppler shifts due to the orbital motion of the binary (see [1, 4] and

references therein).

However, sometimes the secondary SMBH could be embedded in the accretion disk around the primary SMBH, causing an empty annular gap in it [5]. Here we study whether the profiles of Fe $K\alpha$ line emitted from such a disk with an empty gap could be used to study some of the properties of these SMBH binaries.

2. RESULTS AND DISCUSSION

In order to obtain the simulated profiles of the Fe $K\alpha$ line emitted from such relativistic accretion disk with an empty annular gap, we performed numerical simulations of the disk emission based on ray-tracing method in Kerr metric, taking into account only those photon trajectories reaching the observer's sky plane [6, 7, 8].

In these simulations we assumed a rotating (Kerr) SMBH with spin $a = 0.1$, surrounded by the disk with inclination $i = 60^\circ$ which extends from $R_{ms} = 5.67 R_g$ up to $50 R_g$ (where R_{ms} is radius of the innermost stable circular orbit or so called marginally stable orbit, $R_g = GM/c^2$ is gravitational radius of SMBH with mass M , and G and c being the well known constants). We studied the following two cases for annular gap: i) $5 R_g$ wide gap extending between 20 and $25 R_g$ and ii) $10 R_g$ wide gap extending between 20 and $30 R_g$ from central SMBH. Two illustrations of an accretion disk with the above parameters and for the above two cases of an empty gap are presented in the left panels of Fig. 1. The comparisons between the simulated profiles of the Fe $K\alpha$ line corresponding to these two cases, as well as to the disk without a gap are presented in the right panels of Fig. 1 for two different power law emissivity indices p .

As it can be seen from Fig. 1, an empty annular gap in the accretion disk could have significant influence on the emitted Fe $K\alpha$ line shape, leaving the detectable imprints in it in form of a pair of dips which ripple blue-ward and red-ward from the line core, which is in good agreement with the results of some previous studies (see e.g. [5]). Our results also show that the amplitudes of these ripple effects depend on the width of an empty gap and its distance from the central SMBH, as well as on the disk emissivity law (see Fig. 1). The first two quantities, on the other hand, depend on the parameters of the secondary SMBH, such as its mass, accretion rate and separation from the primary, while the disk emissivity law of the primary SMBH mostly depends on its accretion rate, as well as on the plasma conditions in its accretion disk itself (see e.g. [9]).

Therefore, the obtained results demonstrate that such ripple effects, if observed in the profiles of the Fe $K\alpha$ line emitted from the SMBH binaries, could be used for electromagnetic monitoring of these systems, as well as for studying their properties and plasma physics of their accretion disks. However, it should be also taken into account that in the case of SMBH binaries in which the Fe $K\alpha$ line emission arises from both accretion disks

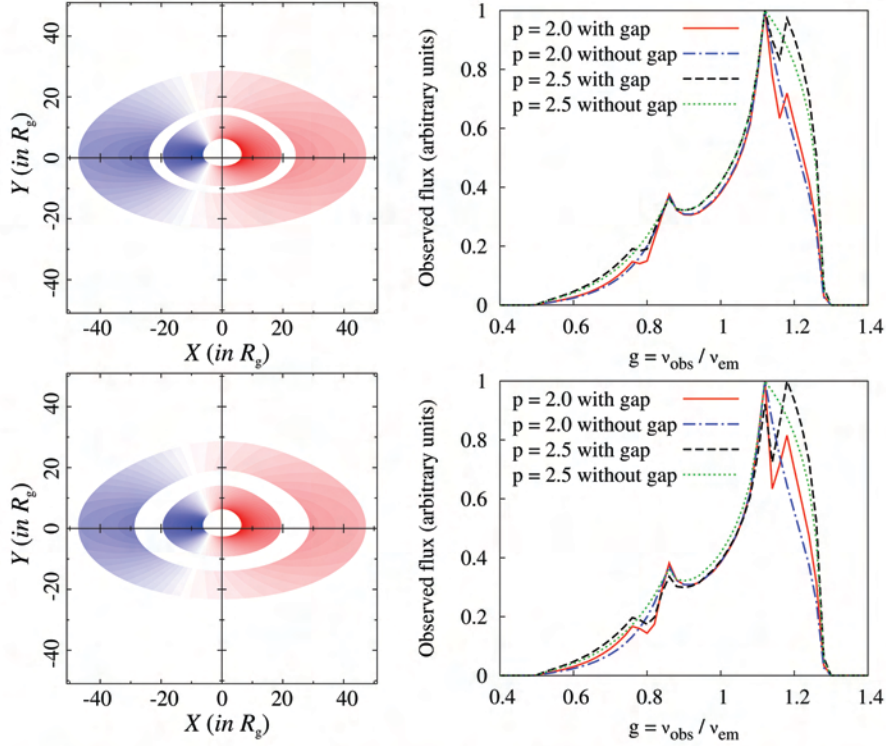


Figure 1. Illustrations of an accretion disk with an empty gap of two different widths (left panels), and the comparisons between the profiles of the Fe $K\alpha$ line emitted from the disk with and without the gap for two different power law emissivity indices p (right panels). The case of annular gap between 20 and 25 R_g is presented in the top panels, while the bottom panels present the case of gap between 20 and 30 R_g . The disk is extending from $R_{ms} = 5.67 R_g$ up to $50 R_g$ around Kerr SMBH with spin $a = 0.1$ and the disk inclination is $i = 60^\circ$.

around primary and secondary components, their Doppler shifts could leave similar signatures in the observed line profiles [1].

3. CONCLUSIONS

We simulated the profiles of the Fe $K\alpha$ spectral line emitted from a relativistic accretion disk with an empty gap, formed in the SMBH binaries when a secondary SMBH is embedded in the accretion disk around a primary. From our investigations we can outline the following conclusions:

1. An empty gap (or cavity) cleared by the secondary SMBH in the accretion disk around primary SMBH could leave detectable imprints

- in form of ripples in the emitted Fe $K\alpha$ line profile;
2. The amplitudes of these ripple effects strongly depend on the width and distance of the empty gap from the central SMBH, and hence such effects could be used for constraining the mass ratios and separations between the components in these type of SMBH binaries;
 3. Besides, the resulting Fe $K\alpha$ line profiles with such ripple effects are also significantly affected by the emissivity of the accretion disk around the primary, which on the other hand depends on its accretion rate and plasma conditions;
 4. Therefore, if detected, such ripple effects in the observed Fe $K\alpha$ line profiles could represent signatures of the SMBH binaries in which the secondary SMBH is embedded in the primary's accretion disk, and these effects could be used for electromagnetic monitoring of such systems, as well as for studying their properties and plasma physics in their relativistic accretion disks.

Acknowledgements

This work is supported by the Ministry of Education, Science and Technological Development of the Republic of Serbia through the project 176003 "Gravitation and the large scale structure of the Universe".

REFERENCES

- [1] P. Jovanović, V. Borka Jovanović, D. Borka and T. Bogdanović, *Adv. Space Res.* <http://dx.doi.org/10.1016/j.asr.2013.10.028> (2014).
- [2] P. Jovanović, *New Astronomy Reviews*, 56, 37, (2012).
- [3] P. Jovanović, V. Borka Jovanović and D. Borka, *Baltic Astron.* 20, 468 (2011).
- [4] E. Bon, P. Jovanović, P. Marziani, A. I. Shapovalova, N. Bon, V. Borka Jovanović, D. Borka, J. Sulentic and L. Č. Popović, *Astrophys. J.* 759, 118 (2012).
- [5] B. McKernan, K. E. S. Ford, B. Kocsis and Z. Haiman, *Mon. Not. R. Astron. Soc* 432, 1468 (2013).
- [6] C. Fanton, M. Calivani, F. Felice and A. Cadez, *Publ. Astron. Soc. Jpn* 49, 159 (1997).
- [7] A. Cadez, C. Fanton and M. Calivani, *New Astron.* 3, 647 (1998).
- [8] P. Jovanović and L. Č. Popović, *Fortschr. Phys.* 56, 456 (2008).
- [9] N. I. Shakura and R. A. Sunyaev, *Astron. Astrophys.* 24, 337 (1973).

THE LOCATION OF THE UV Fe II EMITTING REGION IN THE STRUCTURE OF THE ACTIVE GALACTIC NUCLEI

Kovačević Dojčinović Jelena and Popović Luka Č.

Astronomical Observatory, Volgina 7, 11060 Belgrade

Abstract. Active Galactic Nuclei (AGNs) consist of a supermassive black hole in their center, surrounded by accretion disk of ionized gas. In the process of accretion, a large amount of energy is produced which photoionize the gas in surrounding of the black hole, and results in rich and complex spectra with strong emission lines. The dominant mechanism of broadening of the emission lines in AGN spectra is Doppler broadening, caused by random moving of emitting clouds, while the shift of the lines is caused by the systematic motion of the gas. We try to locate where UV Fe II emission lines arise in the AGN structure, using the comparison between the kinematical properties (widths and shifts) of the different emission lines in the sample of the 293 AGN spectra. We found that UV Fe II lines arise mostly in the outer layer of the Broad Line Region (Intermediate Line Region - ILR), the same emission region where the optical Fe II and the cores of the Mg II 2800 Å and H β arise.

1. INTRODUCTION

Active Galactic Nucleus (AGN) is present in the center of 5-10% of all galaxies. It is assumed that an AGN consists of a supermassive black hole in the center, surrounded by accretion disk of gas. In the process of accretion, a large amount of energy is produced which photoionize the gas in surrounding of the black hole. It results in rich and complex spectra, which consist of the continuum emission and strong broad and narrow emission lines. The emission region of gas closer to the black hole and accretion disk is called the Broad Line Region (BLR), because it produces the broad emission lines in spectra. Further from the black hole and BLR, there is the region in which the narrow lines are produced (the Narrow Line Region - NLR). We assume that dominant mechanism of broadening of the emission lines in the AGN spectra is Doppler broadening, caused by turbulent, random or gravitational bounded motion of the emitting gas, while the shift of the lines is caused by the systematic motion of the gas. Therefore, the widths and shifts of the lines reflect the kinematical properties of the emitting regions, and they are given in km/s. In this work we analyze the iron emission lines. Generally, the Fe II emission lines are very interesting for investigation in

the AGN spectra, because there are many open questions about location of their emission region in the AGN structure, mechanisms of their excitation and unexplained correlations with some other lines (see review in [1], [2]). Previously, we investigated the optical Fe II lines [1]. Now, we extend our research to the Fe II lines in the UV band, which have many different properties comparing the optical Fe II lines [2]. Here we are trying to locate where UV Fe II emission lines arise in the AGN structure, using the comparison between the kinematical properties of the different emission lines in the AGN spectra.

2. THE SAMPLE AND ANALYSIS

For this investigation we used the 293 AGN spectra type 1 (in UV and optical range), chosen from Sloan Digital Sky Survey (SDSS), Data Release 7. The spectra are corrected for Galactic extinction, de-redshifted and the continuum emission in optical range ($\Lambda\Lambda$ 4000-5500 Å) is subtracted using the continuum windows. All these procedures are described in [1] and [2]. The subtraction of the UV pseudocontinuum is more complex than the optical, because the UV pseudocontinuum consists of the Balmer continuum and power low. Therefore, we calculated the Balmer continuum using the model described in paper [3]. In this model, the intensity of the Balmer continuum is not the free parameter. It is calculated using the intensity, width and shift of the Balmer lines, which enables less uncertain determination of the UV pseudocontinuum. The analyzed UV and optical iron lines are in ranges $\Lambda\Lambda$ 2650-3050 Å and $\Lambda\Lambda$ 4000-5500 Å. Therefore, after continuum subtraction, all emission lines in these two spectral ranges are fitted with a model of multi-Gaussian functions, where each Gaussian represents the emission from the one emission region. We assume that the width and shift of each Gaussian reflects the kinematical properties of an emission region (see [1] and references therein). Therefore, Balmer lines are fitted with the three components, which are coming from the three emission regions: NLR component (from the Narrow Line Region) and ILR and VBLR components, which are coming from the two layers of the Broad Line Region (ILR - Intermediate Line Region, the layer further from the black hole and VBLR - Very Broad Line Region, the layer closer to the black hole). The optical iron lines (within $\Lambda\Lambda$ 4000-5500 Å) are fitted with the iron template described in [1], [4], [5], and the UV iron lines are fitted with template described in [6]. Mg II lines are fitted with two Gaussians: one which fit the core, and one which fit the wings of the lines. According to the model of the multi-Gaussian fit of the emission lines, the lines or the line components which are coming from the same emission region have the same kinematical properties. Therefore, all narrow lines from the spectra ([O III]4959, 5007 Å and NLR components of Balmer lines) are assumed to have the same velocity dispersion and velocity shift, since it is supposed that they are originating in the Narrow Line Region (NLR), i.e. their parameters of width and shift are the same. The same is for the ILR and VBLR components of the Balmer lines. Also, we assume that all optical Fe II lines originate from the same emission region, so all Fe II lines from the optical template have the identical width and shift. The same is for the UV Fe II lines.

Finally, the kinematical parameters of the lines which are the free parameters are the widths and shifts of the Balmer components which arise in the NLR, ILR, VBLR, Mg II core, Mg II wings, optical Fe II lines and UV Fe II lines. The line decomposition in optical part of spectra 4000-5500 Å is shown and explained in details in papers [1], [2], [4], [5], and the line decomposition in the UV part of spectra $\Lambda\Lambda$ 2650-3050 Å in [2] and [6].

3. RESULTS AND CONCLUSIONS

Since the kinematical properties of the lines (widths and shifts) reflect the motion of the emitting gas, similarities between them for the different emission lines may indicate a kinematical connection between their emission regions. Here we investigate if there are any correlations between kinematical parameters of the lines which are the free parameters. In this way, we are trying to find the kinematical connection of the UV Fe II lines with other emission lines, and to locate their emission region in the AGN structure.

As it can be seen from Table 1, the strongest kinematical connection (the correlation between the widths) is between the UV Fe II, optical Fe II, Mg II core and Balmer lines core (ILR component). This means that as the width of the Fe II UV increases, the widths of the optical Fe II, of the Mg II core and Balmer lines core (ILR component) increase as well. It seems that the correlation of the Fe II UV and Fe II optical widths are slightly higher with FWHMs of Mg II and H (core + wings included), than with Mg II core and H ILR components separately (see [2]). The shift of the UV Fe II lines is in the correlation only with the shift of the Mg II core ($r=0.41$, $P=3E-13$). No correlation is seen between the shift of the optical Fe II lines and some other analyzed emission lines.

Table 1. The correlations between widths (w) of the optical and UV lines. The broad Balmer line components are denoted as: ILR and VBLR. The Spearman coefficient of correlation (r) and P-value are given in bold print for correlations with $P < 1E-9$.

		w ILR	w VBLR	w MgII core	w MgII wings	w FeII opt	w FeII UV
w ILR	r	1	0.35	0.60	-0.28	0.58	0.39
	P	0	9.8E-10	0	1.4E-6	0	2.4E-12
w VBLR	r	0.35	1	0.21	-0.15	0.19	0.20
	P	9.8E-10	0	2.5E-4	8.6E-3	9.3E-4	7.0E-4
w MgII core	r	0.60	0.21	1	-0.3	0.57	0.49
	P	0	2.5E-4	0	2.2E-7	0	0
w MgII wings	r	-0.28	-0.15	-0.30	1	-0.37	-0.43
	P	1.4E-6	8.6E-3	2.2E-7	0	5.4E-11	6.4E-15
w FeII opt	r	0.58	0.19	0.57	-0.37	1	0.39
	P	0	9.3E-4	0	5.4E-11	0	4.1E-12
w FeII UV	r	0.39	0.20	0.49	-0.43	0.39	1
	P	2.4E-12	7.0E-4	0	6.4E-15	4.1E-12	0

On the other hand, the optical and UV Fe II lines have close average values for widths (optical Fe II: 2360 km s^{-1} , UV Fe II: 2530 km s^{-1}), while the average values for the widths of the Mg II and H cores are slightly smaller (Mg II: 1590 km s^{-1} and H β ILR: 1930 km s^{-1}).

According to the obtained results, we can conclude where the UV Fe II lines originate in the AGN structure. They arise close to emission regions where the optical Fe II lines, as well as the cores of the Mg II and H arise. That is in the outer layer of the Broad Line Region - the Intermediate Line Region, i.e. a region with velocities around $1500\text{-}2000 \text{ km s}^{-1}$. However, there is a small contribution in the Fe II UV/optical emission from the deeper layer of the Broad Line Region (Very Broad Line Region) (see [2]).

Acknowledgements

This work is a part of the project (146002) "Astrophysical Spectroscopy of Extragalactic Objects" supported by the Ministry of Science of Serbia.

REFERENCES

- [1] J. Kovačević, L. Č. Popović and M.S. Dimitrijević, The Astrophysical Journal Supplement 189, 15 (2010)
- [2] J. Kovačević Dojčinović and L. Č. Popović (2014), in preparation.
- [3] J. Kovačević, L. Č. Popović and W. Kollatschny, Advances in Space Research, DOI:10.1016/j.asr.2013.11.035 (2013).
- [4] L. Č. Popović, J. Kovačević and M.S. Dimitrijević, 2013arXiv1301.6941 (2013).
- [5] A. I. Shapvalova, L. Č. Popović, A. N. Burenkov et al., The Astrophysical Journal Supplement 202, 10 (2012).
- [6] L. Č. Popović, E. G. Mediavilla, E. Bon, N. Stanić and A. Kubičela, The Astrophysical Journal, 599, 185 (2003).

KINEMATIC PROPERTIES OF THE NITROGEN FIVE (N V) REGION IN 20 Oe-TYPE STARS

A. Antoniou¹, E. Danezis¹, E. Lyratzi^{1,2}, L. Č. Popović³, M. S. Dimitrijević³ and
D. Stathopoulos¹

¹ *Address: University of Athens, Faculty of Physics Department of Astrophysics,
Astronomy and Mechanics, Panepistimioupoli, Zographou 157 84, Athens,
Greece*

² *Address: Eugenides Foundation, 387 Sygrou Av., 17564, Athens, Greece*

³ *Address: Astronomical Observatory of Belgrade, Volgina 7, 11160 Belgrade,
Serbia*

Abstract. Using the GR model, we analyze the UV N V resonance lines in the spectra of 20 Oe stars of different spectral subtypes, in order to detect the kinematic properties of N V region.

1. INTRODUCTION

The N V resonance lines in the Oe stellar spectra have a peculiar and complex profile. Many researchers have observed the existence of absorption N V components shifted to the violet side of the main spectral line (e.g. Refs [2-6]). These component are named Discrete or Satellite Absorption Components (DACs: [1], SACs: [6]). DACs or SACs originate in separate density clouds, in the N V region and have different rotational and radial velocities. In any case, the whole observed feature of the N V resonance lines is not the result of a uniform atmospheric region, but results from different N V clouds with different physical parameters, which create a number of components.

In this paper, using the GR model ([3]), we analyze the UV N V ($\lambda\lambda$ 1238.821 Å, 1242.824 Å) resonance lines in the spectra of 20 Oe stars of different spectral subtypes taken with IUE satellite. From this analysis we can calculate the values of a group of physical parameters. We present the variation of the kinematical parameters of the clouds, which contribute to the formation of the observed N V complex profile, as a function of the stars' effective temperatures.

2. VARIATION OF THE KINEMATICAL PARAMETERS OF THE N V REGION AS A FUNCTION OF THE EFFECTIVE TEMPERATURE

In Fig. 1, we present the N V doublet of the O7.5 III ((f)) HD 24912, and its best fit. The best fit has been obtained using three absorption components. The graph below the profile indicates the difference between the fit and the real spectral line.

In Figures 2 and 3 we present the variation of the values of the rotational and the radial velocities of the independent N V clouds as a function of the stars' effective temperature.

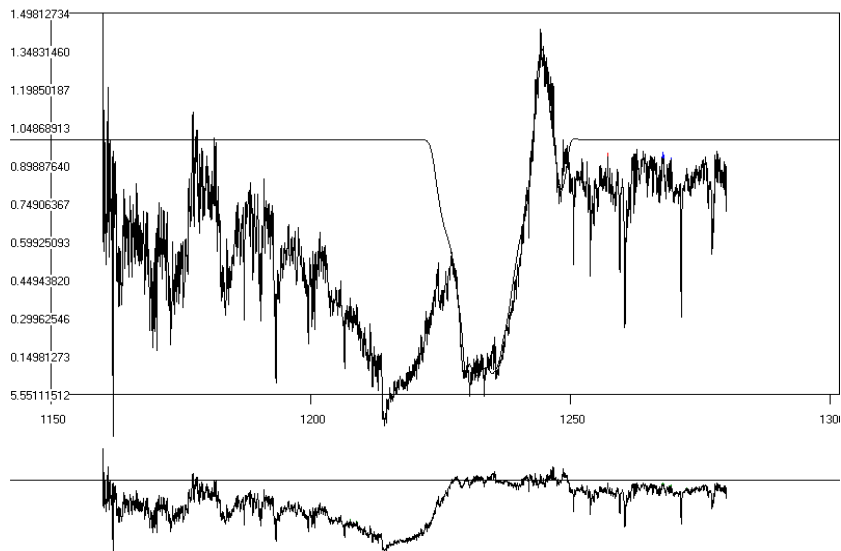


Figure 1. The N V $\lambda\lambda$ 1238.821, 1242.824 Å resonance lines in the spectrum of HD 24912. Each of N V spectral lines consists of three components. The graph below the profile indicates the difference between the fit and the real spectral line.

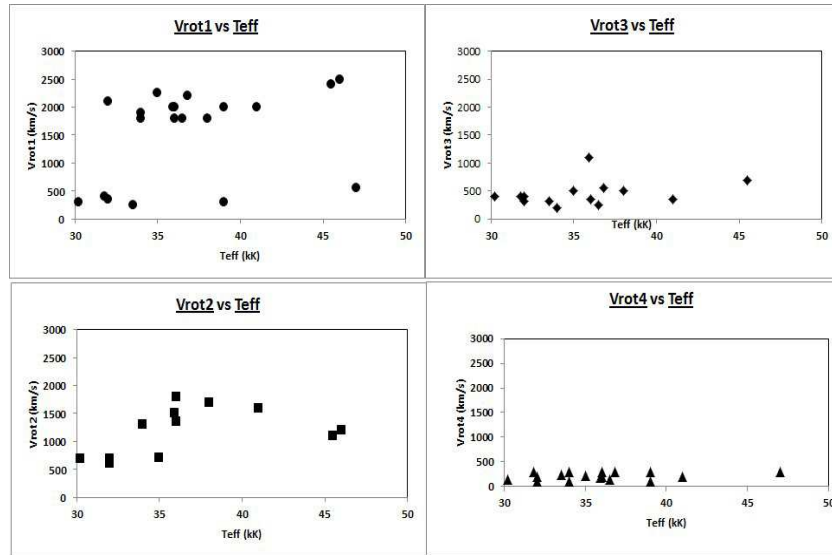


Figure 2. Variation of the values of the rotational velocities of the density clouds, which create the absorption components of the N V doublet (λ 1238.821, 1242.824 Å) as a function of the stars' effective temperature.

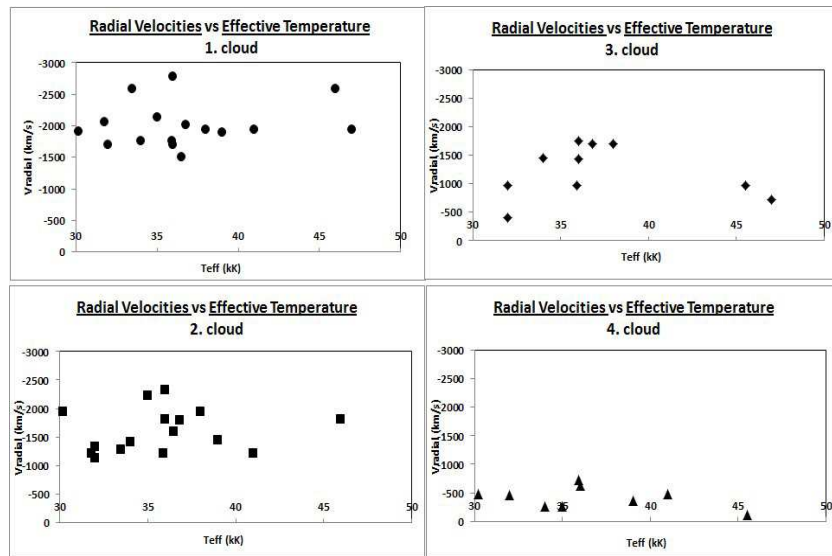


Figure 3. Variation of the radial velocities of the density clouds, which create the absorption components of the N V doublet (λ 1238.821, 1242.824 Å) as a function of the stars' effective temperature.

3. CONCLUSIONS

Rotational velocities: The kinematical independent clouds rotate with different mean velocities. We detected four levels of values. The 1st group of absorption clouds rotates with two levels of velocities (2200 and 500km/s). The 2nd group of absorption clouds rotates with a mean velocity of about 1200 km/s, the 3rd one with a mean velocity of about 300 km/s and the last one with a mean velocity of about 100 km/s. We note that the high values of the rotational velocities have to do with the environment of hot emission stars, where, apart from the density regions, the violent mass ejection may produce smaller regions due to micro-turbulent movements. These smaller regions produce narrow absorption components with different shifts that create a sequence of lines. The addition of all the lines of this sequence gives us the sense of line broadening. We also mention, as another possible explanation, the division of a spectral line which corresponds to not acceptable rotational velocities in two or more components with lower rotational velocities ([7]).

Radial velocities: Here we detected four levels of values. The first level has a mean value of about -2000 km/s, the second one has a mean value of -1600 km/s, the third one and has mean value of about -1200 km/s and the last one has a mean value of -400 km/s. The high values indicate eruptive phenomena in some of the studied stars. We have detected the same phenomenon in the C IV region of the studied stars ([7]).

Acknowledgements

This research project is progressing at the University of Athens, Department of Astrophysics, Astronomy and Mechanics, under the financial support of the Special Account for Research Grants, which we thank very much.

REFERENCES

- [1] B. Bates and D. R. Halliwell, MNRAS 223, 673 (1986).
- [2] E. Danezis, E. Theodosiou and P. G. Laskarides, Ap&SS 179,111 (1991).
- [3] E. Danezis, D. Nikolaidis, E. Lyratzi, L. Č. Popović, M. S. Dimitrijević, A. Antoniou and E. Theodosiou, PASJ 59, 827 (2007).
- [4] E. Lyratzi, E. Danezis, L. Č. Popović, M. S. Dimitrijević, D. Nikolaidis and A. Antoniou, PASJ 59, 357 (2007).
- [5] V. Doazan, G. Sedmak, M. Barylak and L. Rusconi, *A Be Star Atlas of Far UV and Optical High-Resolution Spectra* (ESA SP-1147, Paris: ESA Sci. Publ, (1991).
- [6] E. Danezis, E. Lyratzi, M. Stathopoulou, E. Theodosiou, D. Nikolaidis, C. Drakopoulos and A. Soulikias, "Spectral Lines Shapes", IV SCSLS, Arandjelovac, Serbia (2003).
- [7] A. Antoniou, E. Danezis, E. Lyratzi, L. Č. Popović, D. Stathopoulos and M. S. Dimitrijević, ASR (2014) (in press).

COMPARISON OF SPECTRAL ANALYSES OF X-RADIATION AND VLF SIGNAL AMPLITUDE DURING SOLAR X-FLARE

V. M. Čadež¹ and A. Nina²

¹*Astronomical Observatory, Volgina 7, 11060 Belgrade, Serbia*

²*Institute of Physics, University of Belgrade, Pregrevica 118,
11080 Belgrade, Serbia*

Abstract. In this paper, we present a comparison of Fourier spectral analyses of the X-radiation intensity and recorded VLF signal amplitude during a solar X-flare occurred on May 5th, 2010. The corresponding real time data were collected by the GOES-14 satellite for solar X-radiation in the energy domain between 0.1 nm and 0.8 nm, and by the VLF receiver located in Belgrade, Serbia for the VLF signal emitted at a fixed frequency by the DHO transmitter in Germany. The presented study points out first the existence of correlations between the analyzed signals, and second a shift in the two Fourier spectra that can be attributed to the ionization mechanism by the incoming X-radiation.

1. INTRODUCTION AND BASIC CONCEPTS

One of the most important sudden influences affecting the terrestrial ionosphere comes from the X-radiation emitted by solar X-flares. This radiation additionally ionizes the considered ambient plasma and its intensity I_X is being registered by the GOES-14 satellite in real time t . Consequently, the resulting electron concentration N_e in a general case can be considered as a complicated analytical function:

$$N_e = F(p_1^F, \dots, p_n^F; I_x, \vec{r}, t) \quad (1)$$

which is the solution of some model ionization rate equation that involves contributions from other possible ionization processes p_1^F, \dots, p_n^F (such as Ly α radiation, for example) and can also be explicitly time (t) and location (\vec{r}) dependent due to relaxation in electron recombination processes and variation of plasma parameters with location \vec{r} .

As to the time behavior of the registered VLF signal amplitude S_a , it certainly depends on the electron density N_e playing a major role

in the VLF radio wave reflection and propagation mechanism. Without going into details and models of the mechanism, we may state some general dependence:

$$S_a = G(p_1^G, \dots, p_n^G; N_e, t) \quad (2)$$

where quantities p_1^G, \dots, p_n^G symbolize other possible causes effecting the registered amplitude S_a .

In terms of Eqs. (1)-(2), traces of time variations in flux I_x can now be detected in behavior of the VLF signal S_a . As both quantities I_x and S_a are directly measured in real time by the satellite and the receiving antenna, respectively, we Fourier transform the corresponding data in search for similarities in their oscillation spectra in order to make conclusions about plasma processes in the considered part of the ionosphere based on correlations between I_x and S_a . Such a method to study behavior of plasma parameters in time and space is new (see, for example, [1-2]) and different from the existing procedures (see, for example, [3-8]).

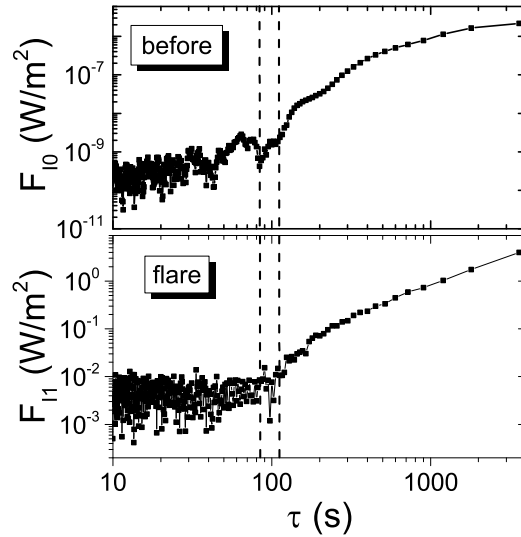


Figure 1. Fourier amplitude F_I of X radiation intensity in domain 0.1 nm to 0.8 nm recorded by the GOES-14 satellite in the period before (F_{I_0} , upper panel) and during (F_{I_1} , bottom panel) the solar X-flare on May 10, 2010.

This work shows an example with two Fourier spectra related to data recorded by the GOES-14 satellite for an X-flare that occurred on May 5, 2010, and the data obtained in [1] for the VLF signal (23.4 kHz) emitted by DHO transmitter located in Germany and recorded by the AWESOME (Atmospheric Weather Electromagnetic System for Observation Modeling and Education) receiver in the Institute of Physics, Belgrade, Serbia.

2.RESULTS AND CONCLUSION

The oscillation spectral amplitudes F_I and F_S related to I_x and S_a , respectively, are computed by the standard Fourier procedure given by:

$$F_I(\omega) = \frac{1}{\sqrt{2\pi}} \int e^{-i\omega t} I_x dt, \quad F_S(\omega) = \frac{1}{\sqrt{2\pi}} \int e^{-i\omega t} S_a dt \quad (3)$$

where $\omega \equiv 2\pi/\tau$ and τ are the oscillation frequency and oscillation period, respectively. The obtained spectral amplitudes F_I are computed for two time intervals of one hour before (10:45 - 11:45 UT) and during (11:45 - 12:45 UT) the flare occurrence. Fig. 1 shows $F_{I0} \equiv F_I(t \leq t_f)$ and $F_{I1} \equiv F_I(t \geq t_f)$ in the upper and lower panel, respectively, for $\tau > 10$ s and $t_f = 11:45$ UT.

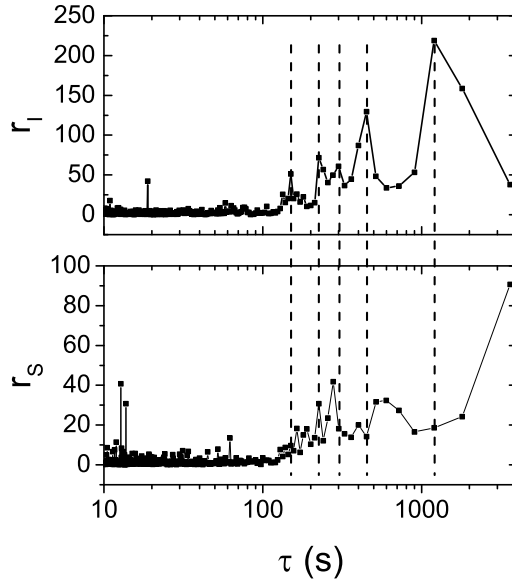


Figure 2. Normalized Fourier amplitudes r_I and r_S (the upper and lower panel, respectively) for the considered May 10, 2010 flare event.

Fig. 2 shows spectral amplitudes for the time interval during the flare normalized to their values before the flare occurred:

$$r_I = \frac{F_{I1}}{F_{I0}} \quad \text{and} \quad r_S = \frac{F_{S1}}{F_{S0}} \quad (4)$$

where the analogous data for the VLF signal, i.e. F_{S1} and F_{S0} , are taken from [2].

Comparing the upper and lower panel plots one can notice two facts: a similarity in their shapes, and a spectrum shift of r_S toward higher periods τ with respect to r_I .

Finally, this result allows for two conclusions. First, the similarity in shape of normalized spectra indicates the correlation between variations in the solar flare X-radiation and amplitude perturbations of the registered VLF signal. Second, the observed shift along the τ axis indicates a specific type of non-linear relationship between S_a and I_x through Eqs. (2)-(3) which can improve modeling and understanding plasma processes in the considered ionospheric D-region.

Acknowledgements

The authors would like to thank the Ministry of Education, Science and Technological Development of the Republic of Serbia for the support of this work within the projects III 44002, 176002, 176004.

REFERENCES

- [1] A. Nina, V. M. Čadež, Contributed papers and abstracts of invited lectures and progress reports of the 26th Summer school and international symposium on the physics of ionized gases, 379 (2012).
- [2] A. Nina, V. M. Čadež, Geophys. Res. Lett. 40 (18), 4803 (2013).
- [3] A. Nina, V. M. Čadež, V. A. Srećković, D. Šulić, Balt. Astron. 20, 609 (2011).
- [4] A. Nina, V. M. Čadež, D. Šulić, V. A. Srećković, and V. Žigman, Nucl. Instrum. Methods B 279, 106109 (2012)
- [5] A. Nina, V. M. Čadež, V. A. Srećković, D. Šulić, Nucl. Instrum. Methods B 279, 110 (2012).
- [6] A. Nina, V. M. Čadež, Adv. Space. Res., <http://dx.doi.org/10.1016/j.asr.2013.12.042>.
- [7] A. Kolarski, D. Grubor, D. Šulić, Balt. Astron. 20, 591 (2011).
- [8] A. Kolarski, D. Grubor, Adv. Space. Res. 53 (11), 1595 (2014).

SPECTRAL ANALYSES OF VLF SIGNAL VARIATIONS AND AGWs INDUCED BY SUNRISE IN LOW IONOSPHERE

A. Nina¹ and V. M. Čadež²

¹*Institute of Physics, University of Belgrade, Pregrevica 118,
11080 Belgrade, Serbia*

²*Astronomical Observatory, Volgina 7, 11060 Belgrade, Serbia*

Abstract. In this paper, we study the recorded VLF signal behavior before, during, and after the sunrise. The considered 23.4 kHz VLF signal is being emitted by the DHO transmitter in Germany, and recorded in real time by the VLF receiver located in Serbia. The recorded VLF amplitude data are then analyzed by the Fourier spectral procedure for three 30 min time intervals before, during and after the sunrise. The resulting oscillation spectra are related to AGWs (Acoustic-Gravity Waves) induced by the ST (Solar Terminator), and compared with theoretically obtained dispersion relation for an isothermal model of the ionosphere as explained in [1] in detail.

1. INTRODUCTION

The ionosphere is constantly influenced by numerous phenomena from the outer space and different parts of Earth's layers which makes the ionospheric plasma diagnostics rather complex. For this reason, the extraction of a particular influence requires additional study. In this paper our attention is focused on the sunrise induced amplitude variations of reflected VLF (very low frequency) radio waves that can be applied as a procedure for the low ionosphere monitoring. Thus, it is shown in [1] that the solar terminator (ST) induces acoustic and gravity waves (AGWs) in the low ionosphere. In that paper, the analysis is restricted to finite time intervals before and after the ST while the signal variation during the ST itself has a highly non-stationary behavior (explained in [2] and [3]) and cannot be used in investigations of linear AGWs. Consequently we study here total changes in the VLF signal propagation induced by the sunrise only. The considered VLF signal is emitted by the DHO transmitter in Germany at frequency of 23.4 kHz and is being recorded by the VLF receiver in Serbia in real time.

2.SIGNAL PROCESSING

In this work we analyze the described signal registered within the time interval 5:00 UT - 7:00 UT. Fig. 1 shows three distinct time sections of 30 min shaded and labeled by **n**, **sr** and **d**, respectively. They cover periods before (the entire signal path is at the nighttime), during, and after (whole signal path is at the daytime) the sunrise, respectively. Details of the applied procedure of signal analysis are explained [1]. The procedure consists of two steps. First, the Fourier transform is applied to the recorded amplitudes $A(t)$ during each of the considered time domains. The corresponding oscillation spectrum $A_F(\omega)$ follows from the Fourier transform:

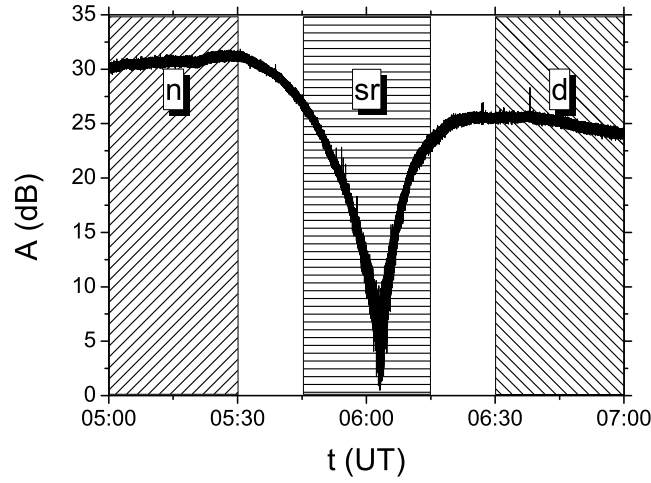


Figure 1. The time evolution of the VLF signal amplitude emitted by the DHO transmitter in Germany and recorded by the AWESOME VLF receiver in Serbia. The shaded domains designate the 30 min time intervals before, during and after the sunrise.

$$A_F(\omega) = \frac{1}{\sqrt{2\pi}} \int_{-\infty}^{+\infty} e^{-i\omega t} A(t) dt, \quad (1)$$

where $\omega \equiv 2\pi/\tau$ and τ are the oscillation frequency and oscillation period, respectively. The obtained values are shown in the Fig. 2 (left panels) for $\tau > 1$ min. Second, Fourier amplitudes A_F for relevant domains (as labeled in Fig. 1) are compared by scaling as follows:

$$\alpha_n^{sr}(\tau) \equiv \frac{A_F(\tau; sr)}{A_F(\tau; n)}, \quad \alpha_d^{sr}(\tau) \equiv \frac{A_F(\tau; sr)}{A_F(\tau; d)}, \quad \alpha_{dn}(\tau) \equiv \frac{A_F(\tau; d)}{A_F(\tau; n)}. \quad (2)$$

Resulting values are shown in Fig. 2 (right panels).

3.DISCUSSION AND CONCLUSIONS

The upper and middle right panels in Fig. 2 show that amplitude oscillations of VLF signals are more pronounced for the time interval that includes sunrise than for time intervals before and after the sunrise, respectively. The most intensive excitations appear for oscillation periods $\tau \approx 10$ min.

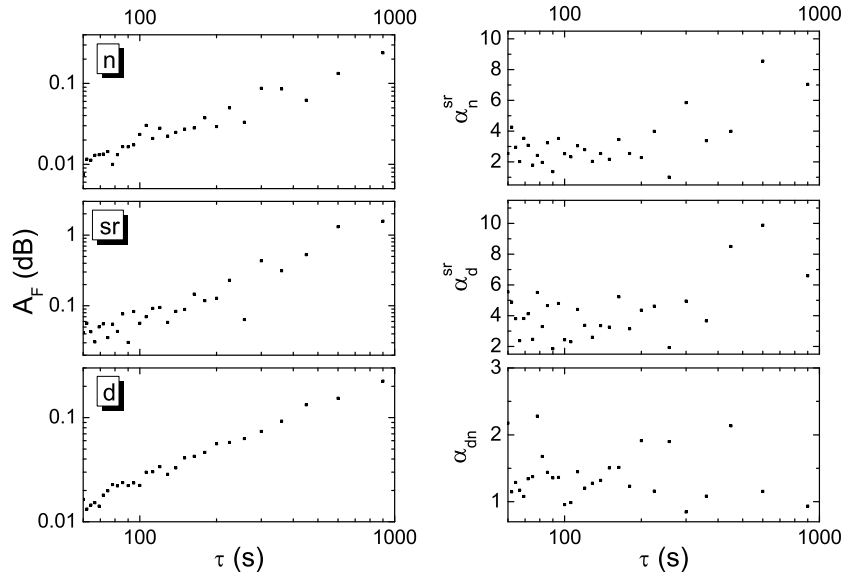


Figure 2. Fourier amplitudes of the VLF signal for domains **n**, **sr** and **d** (upper, middle and bottom left panels, respectively). The right panels show ratios of Fourier amplitudes related to domains **sr** and **n**, **sr** and **d**, and **d** and **n**, respectively.

For investigations of physical conditions in the low ionosphere, the most important information is the relation between signal properties in the **d** and **n** domains with quasi-stationary conditions which allows for detections of AGWs. Details of this analysis are explained in [1] where the extraction of waves excited by the ST was carried out by considering the following three typical characteristics of the phenomenon:

1. Perturbation AGW waves are excited during the ST and become attenuated to a certain degree afterwards.
2. These two processes occur both at the sunrise and sunset in spite of different daytime/nighttime conditions of the medium.

3. This repeats itself daily.

The peaks in the bottom right panel show the excitation of the Fourier amplitude of VLF signal after the sunrise. The obtained peaks values 60 s and 400 s for τ are in good agreement with results in [1] for the low ionosphere showing an enhanced induction of AGWs by the ST for oscillation periods τ within intervals 60 s - 100 s, 300 s - 400 s, and over 1000 s. Our results for the low ionosphere are very similar to those obtained for higher altitudes [4-7].

To conclude, the VLF signal propagation is definitely affected by the sunrise not only during its occurrence but the signal also remains perturbed for some time during the post sunrise relaxation period.

Acknowledgements

The authors would like to thank the Ministry of Education, Science and Technological Development of the Republic of Serbia for the support of this work within the projects III 44002, 176002, 176004.

REFERENCES

- [1] A. Nina, V. M. Čadež, *Geophys. Res. Lett.* 40 (18), 4803 (2013).
- [2] G. B. Carpenter, A. L. Whitson, *Radio Sci.* 69, 4621 (1965).
- [3] M. A. Clilverd, N. R. Thomson, C. J. Rodger, *Radio Sci.* 34, 939 (1999).
- [4] E. L. Afraimovich, *Earth, Planets and Space* 60, 895 (2008).
- [5] J. De Keyser and V. M. Čadež, *J. Geophys. Res.* 106, 29467 (2001).
- [6] J. De Keyser and V. M. Čadež, *J. Geophys. Res.* 106, 15609 (2001).
- [7] M. Hernández-Pajares, J. M. Juan and J. Sanz J. *Geophys. Res.* 111, 7 (2006).

REACTIONS OF O⁻ WITH H₂ AT LOW TEMPERATURES

T. D. Tran¹, R. Plasil¹, S. Roucka¹, D. Mulin¹, S. Rednyk¹, D. Gerlich^{1,2}
and J. Glosik¹

¹*Charles University in Prague, Faculty of Mathematics and Physics, Prague, Czech Republic*

²*Department of Physics, Technische Universität Chemnitz, 09107 Chemnitz, Germany*

Abstract. In order to fully understand the chemical evolution of the interstellar medium, it is necessary to study the interaction of molecules and grains. Our present concern is primarily reactions involving negative ions, since the first anions have been observed in interstellar space relatively recently. In the present contribution we concentrate on the interaction of the oxygen anion O⁻ with neutral H₂. Various reaction channels have been studied at different temperatures (from 10 K to 300 K). The temperature variable radiofrequency 22-pole ion trap has been used in present experiment.

1. INTRODUCTION

Besides neutral reactions and grain surface chemistry, ion-molecule reactions are crucial for understanding the formation of molecules in the interstellar medium. One type of such reactions are anion-molecule reactions, which have not been sufficiently explored yet. Herbst speculated already in 1981 that a substantial fraction of molecular species in the interstellar space might be in the form of anions. His estimates were based on large rate coefficients for radiative electron attachment [1].

The proof of the existence anions in interstellar space came in 2006, when the C₆H⁻ anion was identified in the molecular envelope of IRC+10216 and in the dense molecular cloud TMC-1 Ref. [2]. Moreover, 130 neutral molecules and 14 positive ions have been detected in interstellar space up to this time [2]. Afterwards other anions have been observed, e.g. C₂H⁻, C₄H⁻, C₆H⁻, C₈H⁻, CN⁻, C₃N⁻ and C₅N⁻ [3-5]. Anions have been discovered in many interstellar environments. As a result of prior observations, the need for studying the formation and destruction of anions and their involvement in astrochemistry has increased. Most experiments with anions were carried out at temperatures about 300 K [6-9] and exceptionally at temperatures down to 140 K [10,11]. These temperatures are higher than typical temperatures in interstellar space. To fully

understand processes in the interstellar space, it is necessary to examine anion-molecule reactions at low temperatures. Temperature variable ion traps can be used for such studies.

2. EXPERIMENTAL METHODS

The 22-pole ion trapping apparatus was developed by group of Dieter Gerlich [12]. The apparatus has been operated at Charles University in Prague since 2009. The trap may be operated at temperatures down to 10 K, which are typical in interstellar medium. The number density of neutral reactants in the trap may be as low as 10^8 cm^{-3} .

Primary ions are produced in a storage ion source via electron bombardment of neutral molecules. They are selected by the first mass filter and injected in pulses into the 22-pole trap subsequently. The trap consists of 2 sets of 11 rods, which are used to create an inhomogeneous radiofrequency field confining the ions in radial direction. Negative voltages, applied on the entrance and exit of the trap, confine the anions in axial direction. Details are depicted in Fig. 1. The trap is mounted onto a closed cycle helium refrigerator that may cool the trap down to 10 K. The ions are cooled in the collisions with helium buffer gas. Collisions of trapped ions with neutral reactant molecules lead to a change of the ion composition in the trap. We can choose the trapping time and after the extraction of the ions we count them using quadrupole mass filter and microchannel plate detector. Recorded time evolution of number of ions and the known density of reactants allow us to determine reaction rate coefficients.

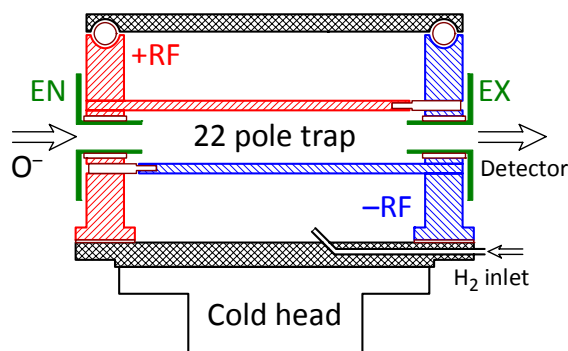


Figure 1. Schematic view of the 22-pole ion trap. Some thousand ions are injected into the ion trap. The ions are consequently stored and cooled in the ion trap and they react with neutral molecules. The entrance and the exit electrodes are marked as EN and EX. After leaving the trap the ions are analysed by the detector.

3. RESULTS

We decided to study the reactions of O^- with H_2 due to the occurrence of O_2 , H_2 and H_2O molecules in the interstellar space [13] and due to the electronegativity of oxygen. The reaction



where the anion reacts with neutral molecule via detachment of electron leading to the formation of a more complex molecule, is called associative detachment. Besides this process, the H atom transfer reaction



takes place in the ion trap.

We measured aforementioned reactions at two temperatures 38 K and 213 K. The measured data are plotted in Fig. 2.

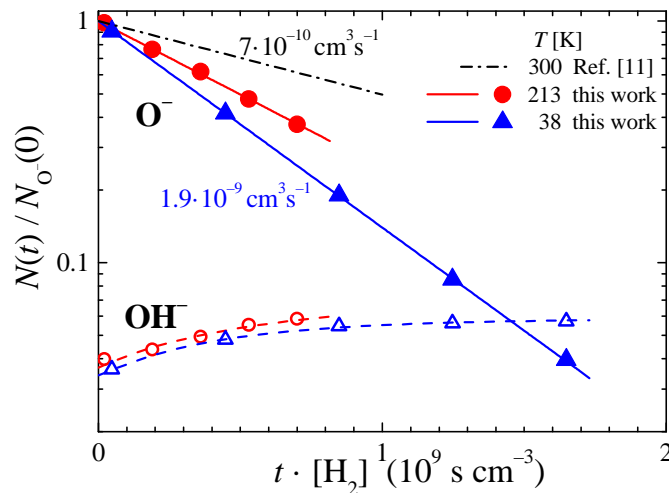


Figure 2. Reaction of stored O^- with normal H_2 at trap temperatures 38 K and 213 K and H_2 number densities $2 \cdot 10^{10} \text{ cm}^{-3}$ and $1 \cdot 10^{10} \text{ cm}^{-3}$. Plotted are the relative number of primary ions O^- and product ions OH^- as a function of the storage time multiplied by corresponding number density of H_2 . In this plot the slopes of solid lines (fits of the decrease of O^-) represent the rate coefficients. Dashed lines represent fits of the increase of OH^- . Dash-dotted line shows the value measured at 300 K [11].

As one can see, less than 10 % of reactive collisions lead to OH^- via reaction (2). The total reaction rate coefficient is proportional to the slope of the O^- decay in Fig. 2 and the coefficients are shown alongside the plots. Comparing the measured slopes we can see that with decreasing temperature, the rate of reaction is increasing. The observed increase was neither observed in previous experiments [11,14], nor predicted by simple theoretical considerations [14].

So far the initially prepared states of the collision system $O^- + H_2$ have not been mentioned. O^- is produced with a statistical population of the two fine structure states, the $^2P_{3/2}$ ground state and the 22 meV higher $^2P_{1/2}$ state. If one assumes adiabatic behaviour, four of the six asymptotic states lead to repulsive surfaces. The increase of the rate coefficients towards lower temperatures is most probably due to the increasing lifetime of the collision complex in the entrance channel, leading to non-adiabatic transitions to the attractive potential energy surface. In addition normal hydrogen has been used, i.e., the para and ortho configurations of nuclear spins of H_2 are populated with a weight of 1:3.

Future experiments aim at determining state specific rate coefficients for the collisions $O^- (^2P) + H_2 (j)$. An ambitious goal is to test whether the metastable H_2O^- anion can be formed via ternary and radiative association at the low temperatures of the ion trap.

Acknowledgements

We thank the Technical University of Chemnitz and the DFG for lending us this instrument. This work is partly supported by GACR P209/12/0233, by GACR 14-14715P, by GAUK 572214 and by GAUK 659112.

REFERENCES

- [1] E. Herbst, *Nature* 289, 656 (1981).
- [2] M. C. McCarthy, C. A. Gottlieb, H. Gupta and P. Thaddeus, *Astrophys. J.* 652, 141 (2006).
- [3] N. Sakai, T. Shiino, T. Hirota, T. Sakai, S. Yamamoto, *Astrophys. J. Letters* 718, 49 (2010).
- [4] M. Agúndez, J. Cernicharo, M. Guélin, C. Kahane, E. Roueff, J. Klos, et al., *A&A*, 517, L2 (2010).
- [5] M. A. Cordiner, S. B. Charnley, J. V. Buckle, C. Walsh and T. J. Millar, *Astrophys. J. Letters* 730, L18 (2011).
- [6] C. H. DePuy and V. M. Bierbaum, *Acc. Chem. Res.* 14, 146 (1981).
- [7] C. Barcholtz, T. P. Snow and V. M. Bierbaum, *Astrophys. J.* 547, 171 (2001).
- [8] B. Eichelberger, T. P. Snow, C. Barcholtz and V. M. Bierbaum, *Astrophys. J.*, 667 (2007).
- [9] R. Otto, J. Mikosch, S. Trippel, M. Weidemüller and R. Wester, *Phys. Rev. Lett.* 101, 063201 (2008).
- [10] A. A. Viggiano and J. F. Paulson, *J. Chem. Phys.* 79, 2241 (1983).
- [11] A. A. Viggiano, R. A. Morris, C. A. Deakyne, F. Dale and J. F. Paulson, *J. Phys. Chem.* 95, 3644 (1991).
- [12] D. Gerlich and S. Horning, *Chem. Rev.* 92, 1509 (1992).
- [13] D. H. Wooden, S. B. Charnley and P. Ehrenfreund, *Comets II*, p. 33–66, (The University of Arizona Press, Tucson, 2004).
- [14] M. McFarland, D. L. Albritton, F. C. Fehsenfeld, E. E. Ferguson and A.L. Schmeltekopf, *J. Chem. Phys.* 59, 6629 (1973).

LONG-TERM VARIABILITY IN THE CONTINUUM AND BROAD SPECTRAL LINES OF A NUMBER OF ACTIVE GALACTIC NUCLEI

Dragana Ilić¹, Alla I. Shapovalova², Luka Č. Popović^{1,3},
Alexander N. Burenkov², Vahram H. Chavushyan⁴, Andjelka Kovačević¹
and Wolfram Kollatschny⁵

¹*Faculty of Mathematics University of Belgrade, Studentski trg 16, 11000
Belgrade, Serbia*

²*Instituto Nacional de Astrofísica, Óptica y Electrónica, Apartado Postal 51, CP
72000, Puebla, Pue, Mexico*

³*Astronomical Observatory Belgrade, Volgina 7, 11000 Belgrade, Serbia*

⁴*Special Astrophysical Observatory of the Russian Academy of Science, Nizhnij
Arkhyz, Karachaevo-Cherkesia 369167, Russia*

⁵*Institut fuer Astrophysik, Universitat Goettingen, Friedrich-Hund Platz 1,
37077, Goettingen, Germany*

Abstract. We give a report of the on-going spectral long-term monitoring campaign of a number of active galactic nuclei (AGN) with the prominent broad emission lines. The aim of this campaign is to study the properties of the broad emission line regions of AGNs using the properties of the broad emission lines (e.g., fluxes, widths, line profiles, etc.) as well as their variability. These can be used to constrain the mass of the super-massive black hole believed to be in the center of every AGN.

1. INTRODUCTION

An important task of active galactic nuclei (AGN) investigations is the determination of the mass of the super-massive black hole (SMBH) that resides in the center of an AGN. The SMBH mass can be derived from the dynamics of the gas gravitationally bounded to an SMBH, and for this, the gas of the broad line region (BLR) can be used [see e.g. 1]. The broad emission lines (BELs), visible in the spectrum of Seyfert 1 galaxies and quasars (so-called type 1 AGN), are coming from the BLR and their properties (flux, profiles, widths, etc.) have been used for the investigations of the BLR structure (size, geometry, physics, etc.).

The BLR is a complex region, that very often shows multi-component emission [2-5], e.g. in AGNs with highly variable line profiles there may be an additional component (e.g. outflowing material) present in the BLR that greatly affects the BEL profiles [see e.g. 6]. Therefore, the estimates of the SMBH mass

are strongly influenced by the complex geometry and physics of the BLR, i.e. it is necessary to constrain as much as possible the BLR properties.

Here we give a report of our on-going spectral long-term monitoring of a number of AGNs as continuation of our two previous reports, see [7, 8]. We monitored a sample of type 1 variable AGNs with different spectral properties: (i) two Seyfert 1 (Sy1) AGNs - NGC 5548 and NGC 4151; (ii) two double-peaked broad line (DPL) AGNs - 3C 390.3 and Arp 102B, where 3C 390.3 is a radio-loud AGN while Arp 102B is a LINER like object; and (iii) one narrow line Seyfert 1 (NLSy1) AGN - Arp 564. We studied the dimension, geometry and kinematics in the BLR of these objects and Here we outline some of our main results, but give a detail list of references where all the analysis and results can be found.

2. DATA SAMPLES

The spectra were obtained with: (i) the 6-m and 1-m telescopes of Special Astrophysical Observatory, Russia; (ii) the 2.1-m telescope of Guillermo Haro Astrophysical Observatory at Cananea, Sonora, Mexico; (iii) the 2.1-m telescope of the Observatorio Astronomico Nacional at San Pedro Martir, Baja California, Mexico, and (iv) the 3.5-m and 2.2-m telescopes of Calar Alto, Spain. Details on the data acquisition, reduction and calibration, as well as on flux measurements can be found in [6, 9-12]. A summary of the data sample (object name, monitored period, object redshift and type, and references with our analysis and results) is given in Table 1.

Table 1. Summary of the data sample: object name, monitored period, object redshift and type, and references.

<i>Object</i>	<i>Period</i>	<i>z</i>	<i>AGN type</i>	<i>Ref.</i>
NGC 5548	1996-2002	0.0172	Sy 1.0-1.8	[9, 13, 14]
NGC 4151	1996-2006	0.0033	Sy 1.5-1.8	[6, 15, 19]
3C 390.3	1995-2007	0.0561	DPL Radio-loud	[10,16,17,18]
Ark 564	1999-2010	0.0247	NLSy1	[11]
Arp 102B	1987-2013	0.0242	DPL LINER	[12, 20]

3. MAIN RESULTS AND DISCUSSION

Figure 1 gives the light-curves of the H β flux for all five objects denoted in the upper left corner. Some main results are summarized below.

Sy1 AGNs NGC 5548 and NGC 4151 are exhibiting very strong variability in the broad spectral lines and continuum flux [6, 9], and their broad line profiles exhibit noticeable change in the line shape and intensity, resulting in

periods when these AGNs show the characteristics of Sy 2 spectra with very weak broad lines [6, 9, 15]. The line formation mechanism in these objects is probably not only governed by the photoionization [6, 13, 14].

The DPL AGNs 3C 390.3 and Arp 102B are having broad H β and H α lines with very large widths and with two distinguished peaks [10, 12], where in 3C 390.3 these lines are emitted from an accretion disc and an additional component (disk wind or outflowing component), while in case of Arp 102B the two peaks in BELs could not be explained with the disk-like geometry [20]. 3C 390.3 seems to have higher variability in the spectra [10], than Arp 102B [12] that can be clearly seen in Figure 1.

The NLSy1 AGN Ark 564 has strong Fe II emission lines and somewhat narrower broad lines (FWHM \sim 2000 km/s) with a prominent narrow component [11]. The variability of this AGN is weak, with flare-like outbursts (Figure 1), but the important conclusion is that the Fe II emission is originating further out from the BLR, in the so-called intermediate line region.

More results and detailed discussions can be found in the references listed in Table 1 for each object.

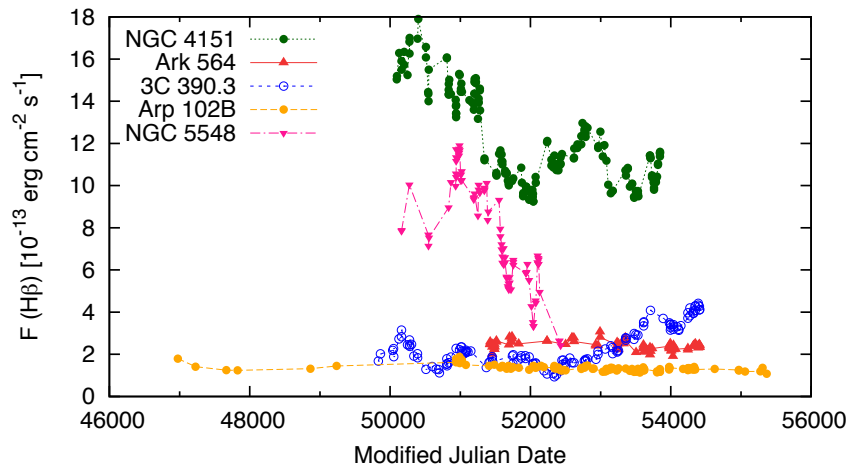


Figure 1. Light-curves of the H β flux for all five objects denoted in the upper left corner. In case of NGC 4151, the line flux was scaled by 1/10 and shifted for better comparison.

Acknowledgements

This work is partially supported by the project (176001) "Astrophysical Spectroscopy of Extragalactic Objects," of the Ministry of Education, Science and Technological Development of Serbia, by INTAS (grant N96-0328), RFBR

(grants N97-02-17625 N00-02-16272, N03-02-17123, 06-02-16843, N09-02-01136, 12-02-00857a, 12-02-01237a), CONACYT (research grants 39560, 54480, and 151494), and PROMEP/103.5/08/4722 grant.

REFERENCES

- [1] M. Gaskell, *ApJ* 325, 114 (1988).
- [2] J. W. Sulentic, P. Marziani, D. Dultzin-Hacyan, *ARA&A* 38, 521 (2000).
- [3] M. Gaskell, *New Astron. Rev.* 53, 140 (2009).
- [4] L. Č. Popović, E. G. Mediavilla, E. Bon, D. Ilić, *A&A* 423, 909 (2004).
- [5] D. Ilić, L. Č. Popović, E. Bon, E. Mediavilla, V. H. Chavushyan, *MNRAS* 371, 1610 (2006).
- [6] A. I. Shapovalova, L. Č. Popović, S. Collin et al., *A&A* 486, 99S (2008).
- [7] A. I. Shapovalova, L. Č. Popović, D. Ilić et al., *Baltic Astron.* 20, 476 (2011).
- [8] A. I. Shapovalova, L. Č. Popović, N. G. Bochkarev et al., *New Astron. Rev.* 53, 191 (2009).
- [9] A. I. Shapovalova, V. T. Doroshenko, N. G. Bochkarev et al., *A&A* 422, 925 (2004).
- [10] A. I. Shapovalova, L. Č. Popović, A. N. Burenkov et al., *A&A* 517, 42 (2010).
- [11] A. I. Shapovalova, L. Č. Popović, A. N. Burenkov et al., *ApJS* 202, 10 (2012).
- [12] A. I. Shapovalova, L. Č. Popović, A. N. Burenkov et al., *A&A* 517, 42 (2013).
- [13] L. Č. Popović, A. I. Shapovalova, V. H. Chavushyan, D. Ilić, A. N. Burenkov, A. Mercado, S. Ciroi, N. G. Bochkarev, *PASJ* 61, 1 (2008).
- [14] D. Ilić, *Ser. Astron. J.* 175, 15 (2007).
- [15] A. I. Shapovalova, L. Č. Popović, A. N. Burenkov et al., *A&A* 509, 106 (2010).
- [16] A. I. Shapovalova, A. N. Burenkov, L. Carrasco et al., *A&A* 376, 775 (2001).
- [17] L. Č. Popović, A. I. Shapovalova, D. Ilić et al., *A&A* 528, 130 (2011).
- [18] P. Jovanović, L. Č. Popović, M. Stalevski, A. I. Shapovalova, *ApJ* 718, 168 (2010).
- [19] E. Bon, P. Jovanović, P. Marziani, A. I. Shapovalova, N. Bon, V. Borka Jovanović, D. Borka, J. Sulentic, L. Č. Popović, *ApJ* 759, 118 (2012).
- [20] L. Č. Popović, A. I. Shapovalova, D. Ilić et al., *A&A* submitted (2014).

INVERSE BREMSSTRAHLUNG ABSORPTION COEFFICIENTS FOR DENSE HYDROGEN PLASMA IN CUT-OFF COULOMB POTENTIAL MODEL

N. M. Sakan¹, A. A. Mihajlov¹ and V. A. Srećković¹

¹ *Institute of Physics, University of Belgrade,
Pregrevica 118, Zemun, 11080 Belgrade, Serbia*

Abstract. The inverse Bremsstrahlung process play important role in modeling of continuous electromagnetic absorption in plasmas and as such should be investigated with more details. Here it is shown that this process can be successfully described in the frames of cut-off Coulomb potential model within the broad area of electron concentrations and temperatures. The corresponding quantum mechanical method of determination of the spectral coefficient for the considered processes is presented. The results discussed here are for the plasma with electron densities $N_e \sim 10^{19} \text{cm}^{-3}$ and temperatures $T \approx 2 \cdot 10^4 \text{K}$. The calculation method is applied to wavelength region $200 \text{nm} < \lambda < 500 \text{nm}$. The presented results can be of interest for dense laboratory plasmas as well as for partially ionized layers of different stellar atmospheres.

1. INTRODUCTION

Recently, in [1] it was shown that so-called cut-off Coulomb potential could be successfully applied in the case of dense highly ionized plasmas for the description not only transport processes (see [2]) but also the relevant photo-ionization processes. Here we keep in mind the model potential which is described by the relations

$$U_{cut}(r) = \begin{cases} -\frac{e^2}{r} + \frac{e^2}{r_c} & : 0 < r \leq r_c \\ 0 & : r_c < r \end{cases}, \quad (1)$$

where r_c is the cut-off radius, and $-e^2/r_c$ - the average potential energy of the electron in the considered plasma. Let us note that such potential was introduced in the considerations in [3] investigated in detail in [4]. Here we will show that in case of highly ionized non-ideal plasmas this potential could be successfully applied also for determination of spectral coefficients for the electron-ion inverse Bremsstrahlung processes.

2. THEORY

Since the cut-off Coulomb potential has radial symmetry, the adequate wave functions of the free electron could be taken in form $\Psi(r, \theta, \varphi) = (P_{nl}(r)/r) \cdot Y_{lm}(\theta, \varphi)$, where $P(r)$ is the solutions of the radial Schroedinger equation

$$\frac{d^2 P(r)}{dr^2} + \left[\frac{2m}{\hbar^2} (E - U(r)) - \frac{l(l+1)}{r^2} \right] P(r) = 0. \quad (2)$$

Accordingly to [5] the cross section for the inverse Bremsstrahlung process is given by the relations

$$\sigma(E; E') = \frac{8\pi^4 \hbar e^2 k}{3 q^2} \sum_{l'=l\pm 1} l_{max} |\hat{D}_{E,l;E'l'}|^2, \quad \hat{D}_{E,l;E'l'} = \int_0^\infty P_{E'l'} \cdot r \cdot P_{El} dr. \quad (3)$$

Because of the well known properties of the free electron wave functions the direct calculation of the dipole matrix element \hat{D} is very difficult and in practice, all until now, cross section was calculated with the help of approximate formulas (see e.g. [5]) based on the model of binary electron-ion interaction in the absence of any external perturbers. Because of that such approximations are valid only in cases of electron-ion plasmas that could be treated practically as ideal ones. Non-ideal plasmas were also discussed in literature (see e.g. [6], [7]), but only with the help of partial, and also approximative expressions. On the other hand, cut-off Coulomb potential model gives the possibility of direct determination of the cross section for the inverse Bremsstrahlung process without any additional approximations. Namely in the frames of presented model, with that purpose in mind, it is simple change from the dipole matrix element in Eq. 3 to the gradient of the potential energy ([5]) given by

$$|\hat{D}(r)_{ab}|^2 = \frac{\hbar^4}{m^2 (E_a - E_b)^4} |\nabla U_{ab}|^2, \quad (4)$$

$$\nabla_r U_{ab} = \int_0^{r_{cut}} P_b(r) \cdot \nabla_r U(r) \cdot P_a(r) dr. \quad (5)$$

The given method enabled the fast and reliable calculation of the discussed cross section and, consequentially, the corresponding spectral absorption coefficient which is given by

$$\kappa_{ff}(\varepsilon\lambda; N_e, T) = N_i N_e \int_0^\infty \sigma(E; E') v f_T(v) dv \left(1 - \exp \left[-\frac{\hbar\omega}{kT} \right] \right), \quad (6)$$

where N_i and N_e are the ion and free electron densities, and $f_T(v)$ - the Maxwell distribution (over electron speeds) with given temperature T .

It is obvious that this model could be used even in case $r_{cut} \rightarrow \infty$, i.e. in case of the Coulomb potential.

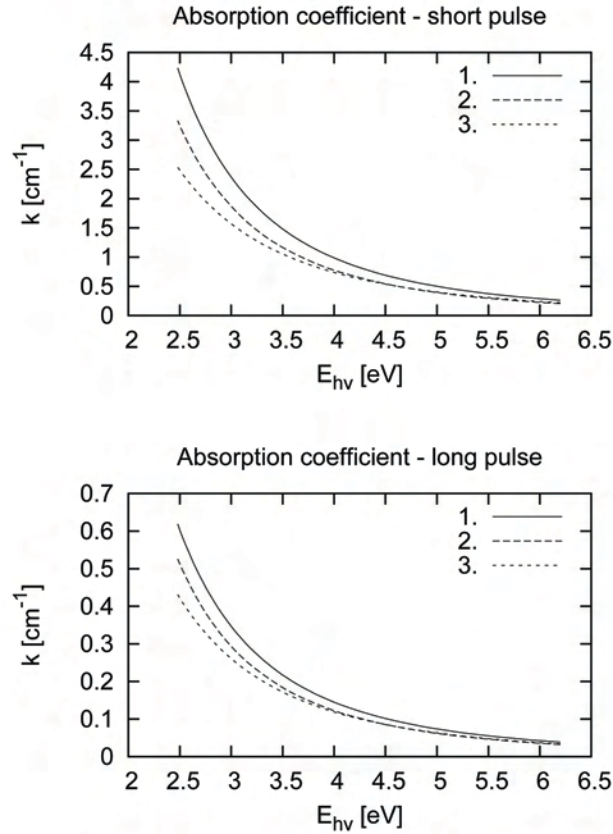


Figure 1. Absorption coefficient for the inverse Bremsstrahlung, **1.** - the gradient method - Coulomb potential, **2.** - the gradient method -cut-off Coulomb potential, **3.** - formula (7) from [5]. The presented data are calculated for the short and long pulse from [8].

3.RESULTS AND DISCUSSION

Here the described gradient method is applied for determination of the spectral coefficients for the inverse Bremsstrahlung process in two cases of non-ideal highly ionized hydrogen plasma [8] ($N_e = 1.8 \cdot 10^{19} \text{cm}^{-3}$, $T = 23650 \text{K}$ - short and $N_e = 6.5 \cdot 10^{18} \text{cm}^{-3}$, $T = 17960 \text{K}$ - long pulse) and considered later in [1]) in relation with photo-ionization processes. The results are presented on the Fig. 1. On this figures are presented also the

calculations of the same coefficients with the help of approximate expression from [5], namely

$$\kappa_{ff}^{Sob}(\varepsilon_\lambda; N_i, N_e, T, Z) = \frac{16\pi^{5/2}\sqrt{2}e^6}{3\sqrt{3}c\hbar m^{3/2}\omega^3} \frac{Z^2 N_i N_e}{(kT)^{1/2}} \left(1 - \exp\left[-\frac{\hbar\omega}{kT}\right]\right). \quad (7)$$

It could be observed that, as expected, three investigated methods of determination of the spectral coefficients for the inverse Bremsstrahlung process generate different values. The difference between the results grows significantly with the lowering of the absorbed photon energy, less than 4eV.

4. CONCLUSION

The presented exact quantum mechanical method could be used to obtain the spectral coefficients for inverse Bremsstrahlung process for the broad class of gaseous highly ionized plasmas. It is expected that the cut-off Coulomb potential model results are more accurate in comparison with other methods, developed primarily for either ideal or fully ionized plasma. Let us emphasize here, for now, that the described gradient method, based on the cut-off Coulomb potential model, at least formally could be applied on the plasmas with any N_e and T as long as such plasmas could be treated as non-relativistic objects. The presented method can be of interest for dense partially ionized layers of different stellar atmospheres.

REFERENCES

- [1] A. A. Mihajlov, N. M. Sakan, V. A. Srećković and Y. Vitel, *J. Phys. A* 44, 095502 (2011).
- [2] A.A.Mihajlov, D.Djordjević, M.M.Popović, T.Meyer, M.Luft, W.D.Kraeft, *Contrib.Plas.Phys.* vol.29, no.415, p.441-446 (1989).
- [3] K. Suchy, *Beitr. Plasmaphys.* 4, 71 (1964).
- [4] A.A.Mihajlov, D.Djordjević, S.Vučić, W.D.Kraeft, M.Luft, *Contrib. Plasma Phys.* vol.26, no.1, p.19-35 (1986).
- [5] I. I. Sobel'man, *Atomic Spectra and Radiative Transitions*, Springer Verlag, Berlin, 1979.
- [6] V. E. Fortov, I. T. Iakubov, *Physics of Nonideal Plasma*, Hemisphere, New York, 1989.
- [7] G. Kobzev, I. Jakubov, M. Popovich (Eds.), *Transport and Optical Properties of Non-Ideal Plasmas*, Plen.Press, New York, London, 1995.
- [8] Y. Vitel, T. V. Gavrilova, L. G. D'yachkov, Y. Kurilenkov, *JQSRT* 83 387-405 (2004).

The Workshop on Dissociative Electron Attachment (DEA)

ELECTRON ATTACHMENT TO MOLECULES STUDIED BY ELECTRON-MOLECULAR CROSSED BEAM EXPERIMENT

Janina Kopyra

Chemistry Department, Siedlce University, 3 Maja 54, 08-110 Siedlce, Poland

Among the various methods and techniques to study electron attachment processes one of the most frequently used is electron-molecular crossed beam technique. From electron beam experiments in combination with mass spectrometry information on the negative ions formed following electron attachment can be obtained (parent anion/fragment anions) [1,2].

In the present contribution I will review recent results obtained by means of crossed beam experiments from interaction of low energy electrons with biomolecules in the gas phase with respect to DNA damage. Particular attention will be paid to dissociative electron attachment to nucleosides (e.g., derivatives of 2'-deoxycytidine [3]) and nucleotides (2'-deoxycytidine-5'-monophosphate [4]). It has been recently proposed, on the basis of these results that both *direct electron attachment to the DNA backbone and electron transfer from the base to the backbone contribute to single strand breaks* [4].

Acknowledgements: This work has been supported by the Polish Ministry of Science and Higher Education.

REFERENCES

- [1] E. Illenberger and J. Momigny, *Gaseous Molecular Ions. An Introduction to Elementary Processes Induced by Ionization* (Steinkopff Verlag, Darmstadt/Springer-Verlag, New York, 1992).
- [2] J. Langer, R. Balog, M. Stano, H. Abdoul-Carime, E. Illenberger, *Int. J. Mass Spectrom.* 233, 267 (2004) (Review Article).
- [3] J. Kopyra, A. Keller, and I. Bald, *RSC Advances* 4, 6825 (2014).
- [4] J. Kopyra, *Phys. Chem. Chem. Phys.* 14, 8287 (2012).

ELECTRON ATTACHMENT TO UNSTABLE MOLECULES

Tom A. Field and Tom D. Gilmore

Centre for Plasma Physics, School of Maths and Physics, Queen's University Belfast, Belfast, BT7 1NN, N. Ireland, UK

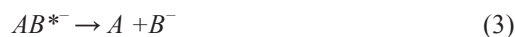
Novel experiments to investigate electron attachment to molecular radicals and unstable molecules will be described [1, 2]. In the process of electron attachment a free electron, e^- , attaches to a molecule, e.g. AB, to form a superexcited negatively charged molecular ion, AB^{*-} :



The lifetimes of the superexcited anions is frequently very short, of the order of a few vibrational periods. The anions can decay by autodetachment of the extra electron



and by dissociation to give a neutral and negatively charged fragment



This second process is dissociative electron attachment.

Experiments to measure the lifetimes of long lived molecular anions will also be discussed [3] and compared to lifetimes of doubly charged molecular ions such as CO_2^{2+} [4].

REFERENCES

- [1] S. A. Haughey, T. A. Field, J. Langer, N. S. Shuman, T. M. Miller, J. F. Friedman and A. A. Viggiano, *J. Chem. Phys.* 137, 054310 (2012).
- [2] K. Graupner, T. A. Field and C. A. Mayhew, *N. J. Phys.* 12, 083035 (2010).
- [3] K. Graupner, T. A. Field, A. Mauracher, P. Scheier, A. Bacher, S. Denifl, F. Zappa and T. D. Maerk, *J. Chem. Phys.* 128, 104304 (2008).
- [4] A. E. Slattery et al., *J. Chem. Phys.* 122, 084317 (2005).

DISSOCIATIVE ELECTRON ATTACHMENT STUDIES WITH POTENTIAL RADIOSENSITIZERS

Katrin Tanzer¹, Linda Feketeova², Benjamin Puschnigg¹, Paul Scheier¹, Eugen Illenberger³ and Stephan Denifl¹

¹*Institut für Ionenphysik und Angewandte Physik, Leopold Franzens Universität
Innsbruck, Technikerstrasse 25, A-6020 Austria*

²*ARC Centre of Excellence for Free Radical Chemistry and Biotechnology,
School of Chemistry and Bio21 Institute of Molecular Science and
Biotechnology, University of Melbourne, 30 Flemington Road, Victoria 3010,
Australia*

³*Institut für Chemie und Biochemie-Physikalische und Theoretische Chemie,
Freie Universität Berlin, Takustrasse 3, D-14195 Berlin*

Nitroimidazolic molecules are presently under investigation as potential radiosensitizers for so-called hypoxic tumors which are characterized by the deprivation of oxygen [1]. The effect of radiosensitizers, i.e. enhanced damage of tumor cells, is also ascribed partially to the action of low-energy secondary electrons which are formed in abundant amounts during the irradiation of biological tissue. The kinetic energy distribution of secondary electrons formed finds its maximum below 10 eV, where the (dissociative) electron attachment may significantly contribute to the damage cross section. In the present study we investigated low energy electron attachment to nitroimidazole and a methylated derivative in the electron energy range between about zero eV and 8 eV. The setup used was a high resolution electron monochromator combined with a quadrupole mass spectrometer. The resulting negative ion mass spectra as well as anion efficiency curves showed distinct differences between the two compounds. For example, while for nitroimidazole no parent anion was observable on mass spectrometric timescales, the parent anion was observed at about zero eV for the methylated compound. In addition, the ion yield of fragment anions formed upon DEA to nitroimidazole show a sharp peak structure below 2eV which is not present for the molecule in its methylated form.

Acknowledgements: The present research was supported by FWF (P22665) and ARC CoE program.

REFERENCES

- [1] G. E. Adams et al, Rad. Res. 178, 183 (2012).

(TIME-DEPENDENT) DENSITY FUNCTIONAL THEORY FOR UNDERSTANDING DISSOCIATIVE CHEMISTRY OF ORGANOMETALLIC COMPOUNDS

Matija Zlatar

Institute of Chemistry, Technology and Metallurgy, University of Belgrade

Organometallic compounds, e.g. $\text{Pt}(\text{PF}_3)_4$, $\text{W}(\text{CO})_6$, $[\text{Co}(\text{CO})_3\text{NO}]$, well-known precursors in Focused Electron Beam Induced Processing used to create metal nanostructures, are widely explored [1]. Further insight into their dissociative chemistry is given by Density Functional Theory (DFT), i.e. by calculations of electronic structure, bond-dissociation energies, and mechanistic pathways. Role of relevant excited states is elucidated by TD-DFT. Taking into account relativistic effects, in the case of $\text{Pt}(\text{PF}_3)_4$, is found to be crucial for a good agreement with the experimental findings, Fig. 1.

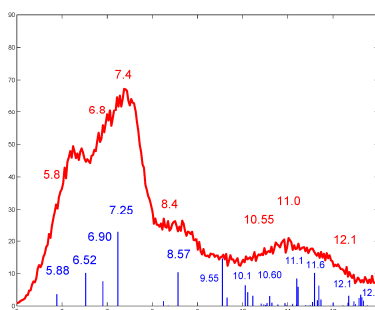


Figure 1. Electronic excitations of $\text{Pt}(\text{PF}_3)_4$ by Electron Energy Loss spectroscopy (red curve) [1a] and TD-DFT calculations (blue bars)

Acknowledgements: This work is partially supported by the Serbian Ministry of Science under project 172035 and COST action CM1301 (CELINA).

REFERENCES

- [1] a) M. Allan, *J. Chem. Phys.*, 134, 204309 (2011); b) O. May, D. Kubala, M. Allan, *PCCP*, 14, 2979 (2012) c) S. Engmann, et al. *Angew. Chem. Int. Ed.*, 50, 9475 (2011).

ROLE OF SYMMETRY IN ELECTRON-IMPACT RESONANT VIBRATIONAL EXCITATION OF POLYATOMIC MOLECULES

Roman Čurík¹, Petr Čárský¹ and Michael Allan²

¹*J. Heyrovsky Institute of Physical Chemistry, ASCR, Dolejskova 3, Prague, Czech Republic*

²*Department of Chemistry, University of Fribourg, Chemin du Musee 9, CH-1700 Fribourg, Switzerland*

Recent developments in Discrete momentum representation (DMR) method opens a possibility of fairly accurate computations for vibrational excitation of polyatomic molecules by electron impact. Our studies of smaller hydrocarbon molecules (cyclopropane, diacetylene) indicate that well-established symmetry selection rules [1] for resonant vibrational excitation are too restrictive as they do not cover all the possible mechanisms during the inelastic collision. One of these mechanisms is shown in Fig. 1 for resonant vibrational excitation (left panel) of non-symmetric HCH twist mode ν_4 of cyclopropane molecule.

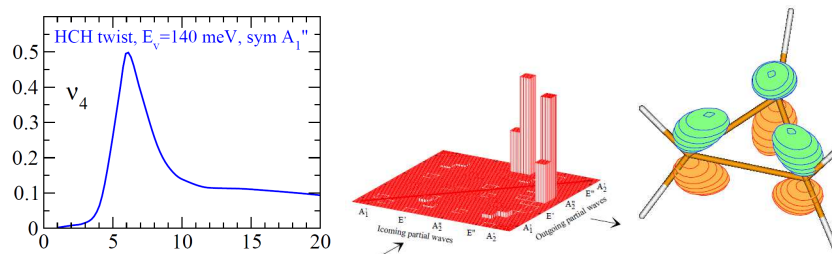


Figure 1. Left panel shows the energy dependence of inelastic integral cross section for excitation of ν_4 mode. Middle panel displays square of inelastic T-matrix elements separated to symmetry contributions in incoming and outgoing channels. On right panel we show the angular shape of the outgoing partial wave of A_2'' symmetry.

Acknowledgements: We acknowledge the funding by the Grant Agency of the Czech Republic (grant P208/11/0452).

REFERENCES

- [1] S. F. Wong and G. J. Schulz Phys. Rev. Lett. 35, 1429 (1975).

ROLE OF SYMMETRY LOWERING IN DEA

Juraj Fedor¹, Radmila Janečková¹ and Jaroslav Kočíšek¹

¹*Department of Chemistry, University of Fribourg, Chemin du Musée 9, CH-1700 Fribourg*

In this contribution we discuss several qualitatively different mechanisms of dissociative electron attachment at low energies and imprints of these mechanisms in absolute cross sections. All data were acquired using a quantitative spectrometer that combines trochoidal electron monochromator and an ion time-of-flight analyzer [1]. We have recently upgraded the setup by implementing a time-and-position sensitive delay-line detector that allows for effective separation of background signals and thus significantly improves the signal-to-noise ratio.

Perhaps the simplest DEA mechanism – electron attachment mediated by a σ^* resonance followed by dissociation has usually very low cross sections due to absence of the reverse barrier for autodetachment. The prototype case for this type of behavior is the 3.9 eV resonance in hydrogen and deuterium molecules H_2 and D_2 . We have examined the isotope effect in this benchmark system and found that it is considerably stronger than previously reported.

The DEA cross section at σ^* resonance is usually much larger if the molecule has a dipole moment, due to nonlocal effects and nonadiabatic processes. The prototypes in this class are hydrogen halides [2]. The second class of molecules with large DEA cross sections are those in which a π^* resonance acts as a doorway and a substantial distortion of a molecular framework (symmetry lowering) is required, the prototype case being acetylene [1]. We have probed the competition of these two processes in molecules where both of them can in principle occur. Both in methylacetylene $HCCCH_3$ [3] and in formic acid $HCOOH$ [4] it is the first process which is operative.

REFERENCES

- [1] O. May, J. Fedor, M. Allan, *Phys. Rev. A* 80, 012706 (2009).
- [2] J. Fedor, O. May, M. Allan, *Phys. Rev. A* 78, 032701(2008).
- [3] R. Janečková, O. May, J. Fedor, *Phys. Rev. A* 86, 052702 (2012).
- [4] R. Janečková, D. Kubala, O. May, J. Fedor, M. Allan, *Phys. Rev. Lett.* 111, 213201 (2013).

VELOCITY SLICE IMAGING STUDY ON DISSOCIATIVE ELECTRON ATTACHMENT

Ewelina Szymanska-Skolimowska¹, E Krishnakumar² and Nigel J Mason¹

¹*Department of Physical Sciences, The Open University, Walton Hall, Milton Keynes, MK7 6AA, United Kingdom*

²*Tata Institute of Fundamental Research, Homi Bhabha Road, Colaba, Mumbai, 400005, India*

Dissociative electron attachment (DEA) leads to the formation of anionic and neutral fragments due to the interaction of low energy electrons with a neutral molecule. DEA is a resonance driven process such that the production of such anions occurs primarily within limited (low) energy regions as the result of the decay of a transient negative ion formed by the capture of the electron by the neutral target. The DEA process may be summarised as: $e^- + ABC \rightarrow ABC^{*-} \rightarrow AB + C^-$. The decay of these transient negative ion states (ABC^{*-}) leads to the formation of vibrationally and electronically excited molecules, radicals and anions. All of these products may be highly reactive and may strongly influence the local chemistry inducing both secondary chemical and physical processes. Anions formed by DEA play an important role in many applications and techniques such as: high-voltage discharges, plasma chemistry, atmospheric reactions (both in terrestrial and planetary atmospheres), radiation chemistry and biology, and recently have been identified as playing a key role in astrochemistry.

To investigate this process we use a time of flight spectrometer coupled with the velocity slice imaging (VSI) technique. Briefly, this apparatus consists of a magnetically collimated low energy pulsed electron gun, a molecular beam, a pulsed ion extraction field, a time of flight analyser and a position sensitive detector consisting of microchannel plates and a phosphor screen. The VSI technique provides direct information about (i) the internal energies of the fragments and the dissociation limits of a transient negative ion involved, and (ii) the symmetry of a transient negative ion responsible for the DEA process. Kinetic and angular distribution measurements also provide an understanding of the overall dissociation dynamics of the anion resonance.

At the conference I will present DEA measurements for some illustrative small organic molecules.

DISSOCIATIVE ELECTRON ATTACHMENT TO ORGANOMETALLIC COMPOUNDS

Peter Papp, Michal Lacko and Štefan Matejčík

Department of Experimental Physics, Faculty of Mathematics, Physics and Informatics, Comenius University, Mlynska dolina, 84248 Bratislava, Slovakia

Combined experimental and theoretical studies of dissociative electron attachment (DEA) to gas phase molecules will be presented in this work. The experiment of crossed electron/molecular beams technique [1] equipped with the quadrupole mass analyzer has been used for the recent studies of DEA to organometallic compounds, Cobalt tricarbonyl nitrosyl [2] and Iron pentacarbonyl. Theoretical calculations on the level of Density Functional Theory have been used to interpret the DEA processes and products, evaluate the bond dissociation energies of sequential ligand losses and the electron affinities of the fragments. The electron attachment processes are typical with formation of a so called transient negative ion which is stabilized with detachment of the incident electron or dissociation to a more stable negative ion. In many cases the transient negative ions cannot be described by the standard quantum chemical calculations like the DFT methods used above. More sophisticated treatments are needed to find the resonant energy [3] of electron attachment to molecule.

Acknowledgements: This work was supported by the Slovak Research and Development Agency under Contract No. APVV-0733-11, the Slovak grant agency VEGA V/0514/12. This work was conducted within the framework of the COST Action CM1301 (CELINA).

REFERENCES

- [1] M. Stano, Š. Matejčík, J. D. Skalný and T. D. Märk, *J. Phys. B - At. Mol. Opt. Phys.* 36, 261 (2003).
- [2] S. Engmann, M. Stano, P. Papp, M. J. Brunger, Š. Matejčík and O. Ingólfsson, *J. Chem. Phys.* 138, (2013).
- [3] P. Papp, Š. Matejčík, P. Mach, J. Urban, I. Paidarová and J. Horáček, *Chem. Phys.* 418, 8 (2013).

**The Workshop on X-ray
Interaction with Biomolecules in
Gas Phase (XiBiGP)**

STUDY OF SINGLE PHOTON MULTIPLE IONISATION PROCESSES WITH A MAGNETIC BOTTLE SPECTROMETER

P. Lablanquie¹, F. Penent¹, L. Andric¹, J. Palaudoux¹, P. Selles¹, S. Carniato¹, J. M. Bizau, D. Cubaynes, M. Nakano, T. P. Grozdanov, M. Žitnik, S.-M. Huttula, M. Huttula, K. Jänkälä, S. Sheinerman, E. Shigemasa, M. Tashiro, H. Iwayama, Y. Hikosaka, K. Soejima, I. H. Suzuki, and K. Ito

¹*CNRS &UPMC, LCPMR, 11 rue Pierre et Marie Curie, 75231 Paris 05, France*

Our studies deal with single photon multiple ionization of atoms and molecules. Experiments are performed at Photon Factory (Japan) and at SOLEIL (France) using a magnetic bottle time-of-flight spectrometer. The peculiar properties of this apparatus, including its very high detection efficiency (up to 70%) and good energy resolution ($\Delta E/E= 1.5\%$) allows the detection in coincidence of all the ejected electrons (up to 5) and provides an efficient method to observe in details the weak multiple photoionization pathways. Energy levels of multiply ionized atomic or molecular ions are obtained accurately with the branching ratio of all the possible processes that provide a deep understanding of the different mechanisms in play. We will present some recent results including:

- Observation of double K shell ionization in simple molecules [1] and of the associated simultaneous K-shell ionization and K-shell excitation [2]
- Double photoionization of the cyclic molecules benzene and pyrrole and its connection to Cooper-pairs formation [3]
- In atoms, core-valence double ionization in Argon offers a powerful method to obtain the Auger spectra following inner-shell ionization of Ar^+ ions [4]. In Mercury we obtained the spectroscopy of Hg^{3+} and Hg^{4+} states and the mechanisms of the $5p$ and $4f$ Auger decays. [5]

REFERENCES

- [1] P. Lablanquie, et al, Phys. Rev. Lett. 106, 063003 (2011), P. Lablanquie et al, Phys. Rev. Lett. 107, 193004 (2011), M. Nakano *et al*, Phys. Rev. Lett. 110, 163001 (2013).
- [2] M. Nakano, et al, Phys. Rev. Lett. 111, 123001, (2013).
- [3] K. Jänkälä, et al, Phys. Rev. Lett. 112, 143005 (2014).
- [4] S.-M. Huttula, et al, Phys. Rev. Lett. 110, 113002 (2013).
- [5] M. Huttula, et al, Phys. Rev. A. 83, 032510 (2011), M. Huttula, et al, Phys. Rev. A 89, 013411 (2014), J. Palaudoux, et al, submitted (2014).

**SYNCHROTRON RADIATION STUDIES OF
BIOMOLECULES: PHOTOABSORPTION, AND
CORE AND VALENCE PHOTOIONIZATION**

Kevin C. Prince

Sincrotrone Trieste, Trieste, Italy

ELECTRON-ION COINCIDENCE SPECTROSCOPY AS A TOOL TO STUDY RADIATION-INDUCED MOLECULAR DYNAMICS

Edwin Kukk

*Department of Physics and Astronomy, University of Turku,
20014 Turun yliopisto, Finland*

Electron-ion coincidence experiments of free molecules are a very efficient experimental means of extracting information about quantum mechanical events following ionization by radiation or particle impact. Multicoincidence experiments in particular, together with kinetic energy resolved electron detection, provide deep insight into dissociation processes and dynamics. This presentation demonstrates, how physically significant quantum information is contained in coincidence datasets and what are the aspects of molecular dynamics that can be revealed by the analysis of coincidence experiments. The case is illustrated by several examples of recent synchrotron-radiation-based electron-ion coincidence measurements of molecules such as thiophene, uracil and methionine.

BIOMOLECULAR IONIZATION AND FRAGMENTATION DYNAMICS STUDIED WITH ENERGETIC PHOTONS FROM SYNCHROTRONS AND FREE ELECTRON LASERS

Thomas Schlathöler

*Zernike Institute for Advanced Materials, University of Groningen, Nijenborgh 4
9747AG Groningen, The Netherlands*

Gas phase studies of biomolecular systems allow to study fundamental problems, inaccessible in the condensed phase. Intrinsic biomolecular properties can be distinguished from effects of the chemical environment, fundamental interactions and microsolvation can be studied on the level of isolated molecules and a direct comparison to quantum chemical calculations is possible. Very recently, two teams have begun to employ tandem mass spectrometers equipped with electrospray ionization sources and radiofrequency ion traps for spectroscopic studies using energetic photons [1,2]. We found, that in contrast to conventional mass spectroscopic techniques, where mainly backbone scission is observed, VUV photon induced fragmentation of the peptide leucine enkephalin induce mainly sidechain losses [1,3]. For protonated YGnF peptides, VUV spectroscopy as a function of peptide length revealed that sidechain loss is due to fast hole migration from the backbone to the Y and F termini [3]. K-edge soft X-ray photoionization even allows to assign fragmentation channels to electronic transitions some of which are site specific. For instance, C 1s \rightarrow π^* excitations in the aromatic side chains induce little fragmentation, whereas such excitations along the peptide backbone are more destructive [4]. Interestingly, in larger protonated proteins, the respective fragmentation channels are quenched. Femtosecond multiple absorption of 90 eV photons opens these channels also in large proteins, as we observed recently at the free electron laser facility FLASH.

REFERENCES

- [1] S. Bari et al. *J. Chem. Phys.* 134 024314 (2011).
- [2] A. R. Milosavljevic et al. *Phys. Chem. Chem. Phys.* 13 15436 (2011).
- [3] O. Gonzalez-Magaña et al. *Phys. Chem. Chem. Phys.* 14 4351 (2012).
- [4] O. Gonzalez-Magaña et al. *J. Phys. Chem. A* 116 10745 (2012).

ACTION SPECTROSCOPY OF STORED BIOMOLECULAR IONS IN THE SOFT X-RAY RANGE

A. R. Milosavljević¹, C. Nicolas², F. Canon³, C. Miron² and A. Giuliani^{2,4}

¹*Institute of Physics, University of Belgrade, Pregrevica 118, Belgrade, Serbia*

²*Synchrotron SOLEIL, L'Orme des Merisiers, Saint-Aubin, B.P. 48,
91192 Gif-sur-Yvette, France*

³*UAR 1008 Cepia, Institut National de la Recherche Agronomique (INRA), BP
71627, 44316 Nantes Cedex 3, France*

⁴*INRA, U1008, CEPIA, Rue de la Géraudière, 44316 Nantes, France*

Inner shell action spectroscopy of multiply protonated protein ions formed by electrospray has been systematically studied as a function of the charge state. The experiment has been performed by coupling a commercial linear quadrupole ion trap ("Thermo scientific LTQ XL"), fitted with an electrospray ion source (ESI), to the PLEIADES beamline at the SOLEIL facility, France [1]. The series of charge states that could be formed by ESI for the ubiquitin and cytochrome *c* protein have been studied around the C-, N- and O-edges. Surprisingly, we observe no effect in our experimental conditions of the charge state on the position of the single photoionization spectra, related to resonant K-shell excitation. In contrast, the ionization yields derived from the double ionization of the target, exhibit a trend very similar to that observed under VUV experiments [2]. The present experiment offers an exciting possibility to probe the correlation between the physicochemical properties of an isolated gas-phase protein and its secondary structure.

Acknowledgements: Data collection was performed at the PLEIADES beamline at the SOLEIL Synchrotron (Proposal 20130382). Work supported by ANR France (#BLAN08-1_348053). A.R.M. acknowledges the support by the MESTD RS OI 171020.

REFERENCES

- [1] A. R. Milosavljević, F. Canon, C. Nicolas, C. Miron, L. Nahon and A. Giuliani, *J. Phys. Chem. Letters* 3, 1191 (2012).
- [2] A. Giuliani, A. R. Milosavljević, C. Hinsén, F. Canon, C. Nicolas, M. Réfrégiers and L. Nahon, *Ang. Chem. Int. Ed.* 51, 9552 (2012).

ULTRAFAST PROTON AND ELECTRON DYNAMICS IN CORE-IONIZED AQUEOUS SOLUTION

Bernd Winter

*Joint Laboratory for Ultrafast Dynamics in Solution and at Interfaces (JULiq),
Helmholtz-Zentrum Berlin, Albert-Einstein-Strasse 15, D-12489 Berlin,
Germany*

Photo- and Auger electron spectroscopy from liquid water reveals a novel electronic de-excitation process of core-level ionized water in which a pair of two cations, either $\text{H}_2\text{O}^+\cdot\text{H}_2\text{O}^+$ or $\text{OH}^+\cdot\text{H}_3\text{O}^+$. These reactive species are the delocalized analogue to the localized Auger decay, leading to H_2O_2^+ , and are expected to play a considerable role in water radiation chemistry. Both cationic pairs form upon autoionization of the initial ionized water molecule, and we are particularly interested in the situation where autoionization occurs from a structure that evolves from proton transfer, from the ionized water molecule to a neighbor molecule, within few femtoseconds. The actual autoionization is either through intermolecular Coulombic decay or Auger decay. Experimental identification of the proton dynamics is through isotope effect. A question that arises is whether such so-called proton-transfer mediated charge separation (PTM-CS) processes [1] occur in other hydrogen-bonded systems as well. This is indeed the case, and is illustrated here for ammonia as well as glycine in water, and for hydrogen peroxide in water, where characteristic differences are detected in the Auger-electron spectra from the light versus heavy species, i.e., NH_3 in H_2O versus ND_3 in D_2O , and H_2O_2 in H_2O versus D_2O_2 in D_2O .

Acknowledgements: This work is supported by the Deutsche Forschungsgemeinschaft (DFG), Research Unit FOR 1789.

REFERENCES

- [1] S. Thürmer, M. Oncak, N. Ottosson, R. Seidel, U. Hergenhahn, S. E. Bradforth, P. Slavicek and B. Winter, *Nat. Chem.* 5, 590 (2013).

**The 3rd International Workshop
on Non-Equilibrium Processes
(NonEqProc)**

NON-EQUILIBRIUM TRANSPORT OF CHARGED PARTICLES IN GASEOUS AND DISORDERED MATERIALS

G. Boyle¹, W. Tattersall^{1,2}, B. Philippa¹, R.E. Robson^{1,2}, M.J. Brunger³, G. Garcia⁴, S. Dujko⁵, Z.Lj. Petrovic⁵, R. McEachran², S. J. Buckman², J. de Urquijo⁶ and R.D. White¹

¹*School of Engineering and Physical Sciences, James Cook University, Townsville, Australia*

²*Research School of Physics and Engineering, ANU, Canberra, Australia*

³*Flinders University, Adelaide, South Australia*

⁴*CSIC, Madrid, Spain*

⁵*Institute of Physics, Belgrade, Serbia*

⁶*Universidad Nacional Autónoma de México, Cuernavaca, Mor., Mexico*

An understanding of charged particle transport under highly non-equilibrium conditions finds application in many areas, from low-temperature plasmas, to positron emission tomography, radiation damage and organic semiconductors. This presentation explores analytic framework and numerical techniques for a multi-term solution of Boltzmann's equation for both electrons/positrons/holes and ions, and associated fluid equation models. We will highlight:

- (i) recent advancements in the testing/validation of complete cross-section sets for electrons in water vapour, including mixtures with noble gases;
- (ii) recent studies of electron/positron transport in dense gases and liquids disordered materials, accounting for coherent scattering effects and modifications to the scattering environment.
- (iii) recent development of a generalized Boltzmann equation for charge carrier transport in disordered systems accounting for trapping events, including a fractional Boltzmann equation and associated fractional diffusion equation.

Acknowledgements: This work is supported by the Australian, Spanish, Mexican and Serbian governments.

FIRST PRINCIPLES CALCULATION OF THE EFFECT OF COULOMB COLLISIONS ON ELECTRON

Z. Dónko

*Wigner Research Centre for Physics, H-1121 Budapest,
Konkoly-Thege Miklós str. 29-33, Hungary*

At appreciable electron densities, Coulomb collisions may significantly influence the velocity distribution function (VDF) in electron swarms. Boltzmann equation solutions conventionally adopt a binary approach for handling such collisions. To overcome this approximation, a new, first principles computational method is proposed here, for the calculation of the VDF and the swarm parameters in a spatially homogeneous system, at arbitrary electron density to gas density ratio [1]. The method is based on a combination of the classical Monte Carlo (MC) technique and a Molecular Dynamics (MD) method. The MD simulation (based on the PPPM method of [2]) describes the many-body interactions within the electron gas. The motion of the (classical) electrons is followed inside a cubic box, with periodic boundary conditions. Their phase space trajectories are derived via the integration of their Newtonian equations of motion, which take into account the Coulomb forces and the effect of a homogeneous external electric field. The electron gas and the background gas interact via electron – atom collisions; these events are accounted for via adopting the standard procedures of Monte Carlo transport calculations. The capabilities of the method are illustrated via computation of electron swarm characteristics in Ar, at low reduced electric fields (with ionization taken as a conservative process). The simulations make it possible to follow the modifications of the VDF across the different regimes of the electron to neutral density ratio. Besides calculating the “usual” swarm characteristics, the method also allows to study the onset of pair correlations and the emergence of a collective mode (electrostatic oscillations) in the electron gas, with increasing density.

REFERENCES

- [1] Z. Dónko, *Phys. Plasmas* 21, 043504 (2014).
- [2] R. W. Hockney and J. W. Eastwood, *Computer Simulation Using Particles* (New York: McGraw-Hill, 1981).

RECENT PROGRESS IN THE NEWTONIAN THREE-BODY PROBLEM

V. Dmitrašinović and Milovan Šuvakov

*Institute of Physics, Belgrade University, Pregrevica 118,
Zemun, P.O.Box 57, 11080 Beograd, Serbia*

The three-body problem dates back to the 1680s, when Isaac Newton tried to solve it following the lines of his solution to the two body-problem [the periodic two-body orbit, such as a star and a planet held together by gravity, is always an ellipse (sometimes turning into a circle)]. Newton couldn't come up with a similar solution for the case of three bodies orbiting one another. About one century later (1772) Lagrange and Euler came up with their analytic solutions. For another century, scientists tried different tacks until the German mathematician Heinrich Bruns (1887) showed that the search for a general solution for the three-body problem was futile, and that the only specific solutions that work only under particular conditions, were possible. Only three families of such collisionless periodic orbits were known until recently: 1) the (analytic) Lagrange-Euler (1772); 2) the (numerical) Broucke-Henon (1975); and 3) the (numerical) Cris Moore's (1993) "figure-8" periodic orbit of three bodies moving on a single trajectory. Here we review the recent progress in this field: the discovery of 13+11 new periodic orbits, bringing the total up to 27. We discuss the methods used to find and distinguish them, as well as their application to gravitational wave research.

EMISSION SPECTROSCOPY OF DENSE PLASMAS IN LIQUIDS: A WINDING ROAD FROM LIGHT TO CHEMISTRY

T. Belmonte^{1,2}, C. Noël^{1,2} and G. Henrion^{1,2}

¹*Université de Lorraine, Institut Jean Lamour, UMR CNRS 7198, NANCY, F-54011 France*

²*CNRS, Institut Jean Lamour, UMR CNRS 7198, NANCY, F-54011, France*

Optical emission spectroscopy of streamers and spark discharges in liquids is the most straightforward diagnostics to investigate chemical pathways in these complex media. However, correlating the collected light with plasma chemistry is submitted to many pitfalls that can lead to misinterpretation. For instance, pressure broadening and Stark broadening can be easily swapped by assuming either a low electron density and a high pressure or conversely, a high electron density and a low pressure. This situation arises from the difficulty to estimate accurately these parameters independently. A similar issue is commonly encountered to determine the origin of the background emission. It is either due to bremsstrahlung, electron-ion recombination or black-body emission. The line broadening makes it hard to find an accurate baseline over the whole wavelength range of the spectrometer, which brings large uncertainties in the respective weights of broadening sources.

An important aspect of spectra interpretation lies in the consideration of strong concentration gradients which affect the transport of light within the plasma that behaves as an optically thick medium. Several models are available to describe self-absorbed lines but they rely on strong hypotheses that are not always fully satisfied. Furthermore, more complex phenomena are to be taken into account. For instance, the quasi-static approximation can be under a stay of default. The lowering of the ionization energies is a precious help to estimate the pressure range in discharges.

We shall see that a reliable analysis of optical emission spectra must be based on time-resolved measurements together with coherent multiple sets of data deduced from different lines. Time-resolved measurements are mandatory to follow the drift of line shifts and widths along the pressure drop. However, time evolutions of lines intensities commonly suffer from a low signal-to-noise ratio, not only because of the difficulty to subtract a correct baseline, but also because of the stochastic behaviour of discharges in liquids. Using high voltage nanosecond-pulsed power generators is the most appropriate response to this issue. Chemical reactions can thus be investigated at the expense of all these conditions.

PICOSECOND-TALIF TO PROBE ATOMIC OXYGEN IN THE PLUME OF AN RF DRIVEN ATMOSPHERIC PRESSURE PLASMA JET IN AMBIENT AIR

J. Bredin, J. Dedrick, K. Niemi, A. West, E. Wagenaars, T. Gans and
D. O'Connell.

*York Plasma Institute, Department of Physics, University of York, YO10 5DD,
York, U.K.*

Picosecond resolution is required for direct measurements, without assumptions, of radicals under the highly collisional environment of atmospheric pressure. Quenching of two-photon absorption laser induced fluorescence (TALIF) excited states is very efficient and the lifetime of approximately a few ns is in the order of a typical ns laser pulse width. To determine radical densities, challenges include knowing the quenching partners and calculating associated quenching rates to obtain the effective lifetime. Using ps-TALIF (32 ps pulse width) it is possible to resolve the lifetime and therefore avoid quenching rate calculations. Spatially resolved measurements in the plume of an RF atmospheric pressure plasma with O₂ and dry air admixtures of the lifetime is shown in Figure 1. The excited state lifetime and ground state densities decrease at the extremities of the plume due to ambient air diffusion. Figure 1 shows that the lifetime with dry air admixtures is longer than with O₂ admixtures, as oxygen is a more efficient quencher than nitrogen. The lifetime in dry air admixture decreases closer to the centre compare with the O₂ admixture, which could be due to atomic oxygen densities that are smaller in the dry air admixture case and therefore more sensitive to quenching with ambient air. Measurements in O₂ admixtures show that the lifetimes obtained with ps-TALIF are shorter than those calculated as for the ns-TALIF measurements. Consequently, either quenching through plasma produced species and/or three body collisions may play a role.

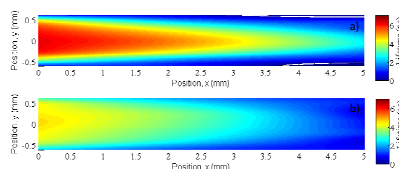


Figure 1. Excited state lifetime of oxygen as a function of the position in the plasma plume for a) dry air admixture and b) pure O₂ admixture.

Acknowledgements: The authors acknowledge support by the UK EPSRC EP/H003797/1 and EP/K018388/1.

VUV EMISSIONS FROM LOW TEMPERATURE ARGON AND ARGON-MOLECULAR GAS MIXTURES IN INDUCTIVELY COUPLED PLASMAS

Svetlana Radovanov¹, Harold Persing¹, Amy Wendt², John Boffard³, Chun Lin³
Cody Culver⁴ and Shicong Wang²

¹*Addresses: Applied Materials/Varian, 35 Dory Road, Gloucester, MA 01930, USA*

²*Department of Electrical and Computer Engineering, University of Wisconsin, Madison, WI 53706*

³*Department of Physics, University of Wisconsin, Madison, WI 53706*

⁴*Materials Science Program, University of Wisconsin, Madison, WI 53706*

In argon ICP plasmas, VUV emission is due to the decay of the $1s_4$ and $1s_2$ principal resonance levels, with emission wavelengths of 104.8 and 106.7 nm, respectively [1]. In this experiment, we have measured the number densities of atoms in the two resonance levels from radiation-trapping induced changes in the $3p^5 4p \rightarrow 3p^5 4s$ branching fractions measured via visible/near-ir optical emission spectroscopy as functions of pressure and power. From optical emission spectroscopy (OES) we derive the electron temperature and density in Ar, Ar/N₂ and Ar/H₂ plasmas. Real time measurements of the excited species and plasma parameters were performed using high and low resolution spectrometers.

The resonance level concentrations determined by means of OES were then used as inputs for the VUV surface flux analytical model. These calculations are compared with the real time VUV flux measurements made with the windowless UV vacuum photodiode and sodium salicylate fluorescence detection arrangement. The results include VUV flux measurements and model calculations obtained from argon plasmas plus VUV emissions from Ar/H₂ and Ar/N₂, at pressures from 2.5 to 15 mTorr and powers from 20 to 1000 W.

A VUV transport model from principal resonance level densities based upon the measured $1s_2$, $1s_4$ resonance level densities agree well with VUV measurements made with the vacuum photodiode in pure argon.

Acknowledgements: This work is partially supported by Applied Materials, CTO's Office.

REFERENCES

- [1] J. B. Boffard, C. C. Lin, C. Culver, Shicong Wang, Amy E. Wendt, Svetlana Radovanov and H. Persing, *JVST A* 6, 32 (2014).

SPECTRAL ANALYSIS FOR OPTIMIZATION OF MAGNETIC RESONANCE SPECTROSCOPY IN EARLY TUMOR DIAGNOSTICS

Karen Belkić and Dževad Belkić

Karolinska Institute, Oncology-Pathology, Stockholm, Sweden

Molecular imaging through magnetic resonance spectroscopy (MRS) can provide information about key metabolites. Conventional applications of MRS are hampered by data analysis via the fast Fourier transform (FFT). Most MRS studies for cancer detection have relied upon estimations of a mere handful or even a single composite metabolite, e.g. total choline. These have yielded incremental improvements in diagnostic accuracy. In vitro studies reveal much richer metabolic information for identifying cancer, particularly in the closely-overlapping components. Among these are phosphocholine, a marker of malignant transformation. The FFT cannot assess these congested spectral components. This can be done by the fast Padé transform (FPT), an advanced, high-resolution, quantification-equipped method, applied to MRS time signals encoded from patients with various cancers. The FPT unequivocally and robustly extracts the concentrations of all the metabolites, including phosphocholine, which completely underlies phosphoethanolamine. In sharp contrast, the FFT produces a rough envelope spectrum with only a few shortened, broadened peaks, and key metabolites altogether absent. The FPT clearly distinguishes noise from true metabolites whose concentrations are accurately computed. The efficiency and high resolution of the FPT translates directly into shortened examination time of the patient. These capabilities strongly suggest that by applying the fast Padé transform to time signals encoded in vivo from various cancers, MRS will fulfill its potential to, at last, become a clinically-reliable, cost-effective method for early cancer detection.

Acknowledgements: This work is supported by Radiumhemmets-forskningsfonden, FoUU & Cancerfonden.

MEASURING ELEMENTARY PLASMA PROCESSES: ELASTIC SCATTERING, VIBRATIONAL AND ELECTRONIC EXCITATION, DISSOCIATIVE ATTACHMENT

Michael Allan

Department of Chemistry, University of Fribourg, Fribourg, Switzerland

The talk will discuss the methods of, and the problems encountered in, measuring absolute cross sections useful for plasma simulations – as they are applied in the Fribourg laboratory. The discussion will be illustrated by several older and more recent examples (furan, acrylonitrile, Pt(PF₃)₄).

The threat of losing the know-how in the future will be brought up. It is related to the fact that the ‘modern’ bibliometric criteria applied to candidates for academic positions strongly disfavor this research – because it leads neither to publications in highly prestigious journals like Nature, nor to numerous citations and thus an excellent ‘*h*-factor’. A feedback of the plasma community in this question will be sought. The loss of the know-how of measuring the neutral dissociation cross sections by the method relying upon the efficient reaction of radicals with tellurium to yield volatile and stable organotellurides, developed by John H. Moore [1], is a warning precedent.

Acknowledgements: This work was supported by the Swiss National Science Foundation under the grant No. 200020-144367, and by the Cost Action CM1301 CELINA.

REFERENCES

- [1] J. H. Moore, P. Swiderek, S. Matejcek, M. Allan, in Nanofabrication Using Focused Ion and Electron Beams – *Principles and Applications*, I. Utke, S. Moshkalev, P. Russel, eds., chapter *Fundamentals of Interactions of Electrons with Molecules*, pp.184-225 (Oxford University Press, 2012).

**FUTURE STUDIES ON ELECTRON SCATTERING;
A RENAISSANCE?**

Nigel Mason

Department of Physical Sciences, The Open University, Milton Keynes, UK

Author Index

A

Acsente T.	165
Adoui L.	12
Adžić I.	403
Allan M.	78, 523, 544
Alcaraz C.	475
Aleksiy V.V.	106
Almeida D.	17
Alves L. L.	11
Anderson E.	8
Andrić L.	529
Antoniou A.	478, 493
Aoneas M. M.	110
Aonyas M. M.	415
Aparicio J. A.	303
Arkhipenko V. I.	463
Aubrecht V.	375
Avaldi L.	12
Aumayr F.	161

B

Bald I.	58, 74, 90, 163
Banković A.	118
Bartlova M.	375
Belić D. S.	62
Belkić Dž.	3, 543
Belkic K.	543
Belmonte M. T.	303
Belmonte T.	230, 540
Bereczky R. J.	210
Bezuglov N. N.	479
Bibić N.	194, 198, 202
Bilek M. M. M.	447
Bizau J. M.	529
Blahova L.	218, 252
Blanco F.	169
Boadle R.	8
Bogachev N. N.	455
Bogdankevich I. L.	455

Boffard J.	542
Bojarov A.	407
Bolognesi P.	12
Borka D.	168, 170, 485
Borka Jovanović V.	170, 485
Boscher N.	164
Bošnjaković D.	21, 114
Boyle G.	537
Božanić D. K.	202
Brablec A.	291
Brannaka J. A.	16
Bredin J.	541
Brunger M.	5, 8, 169, 537
Brykalova X. O.	30, 38
Buckman S.	5, 8, 537
Burakov V. S.	242, 339
Burenkov A. N.	509

C

Callegari Th.	463
Canon F.	54, 533
Carniato S.	529
Cassidy D.	6
Castillo F.	295
Chavushyan V. H.	509
Chekan P. V.	238
Chiari L.	5, 8
Choquet P.	164
Chubrik N.	459
Chumakov A.N.	234, 238
Cubaynes D.	529
Cullen P. J.	307
Culver C.	542
Cunha T.	17
Cvejić M.	261, 311, 315
Cvelbar U.	443
Cvetanović N.	263, 271
Cvetić J.	379, 383
Čadež V. M.	497, 501

Čarsky P.	523
Čech J.	371
Černák M.	167, 291
Čubrović V.	194
Čurík R.	523

D

Da Silva G. B.	5
Dakić I.	451
Daly S.	9
Dampc M.	15, 82
Danezis E.	478, 493
Danko M.	86
De Giacomo A.	162
De Urquijo J.	537
Del Olmo A.	473
Dedrick J.	541
Denifl S.	521
Delaunay R.	12
DellAglío M.	162
DePascale O.	162
Derzsi A.	262
Dias-Tendero S.	12
Dimitrijević M. S.	478, 479, 480, 493
Dinescu G.	165
Djoković V.	202
Djuric R.	379, 383
Djurović S.	303, 323, 327
Dmitrašinović V.	539
D'Onofrio M.	473
Dohčević-Mitrović Z.	443
Dojčilović R.	202
Dojčinović B. P.	415
Dojčinović I. P.	247, 347, 351, 279
Dohnal P.	335
Donko Z.	262, 538
Domaracka A.	12, 94
Dossmann H.	9
Draganić I. N.	202
Duday D.	164
Dujko S.	21, 114, 118, 122, 126, 130, 134, 138, 399, 403, 537
Dultzin D.	473
Dupljanin S.	146

Duque H. V.	5
Đorđević S.	42

E

Ebert U.	399
Eden S.	15, 82
Ellingboe A. R.	251
Elrashedy R.	162

F

Fairbrother H.	16
Fedor J.	14, 524
Feketeova L.	521
Ferreira da Silva F.	17
Field T.	520
Filatova I.	459
Filipe E.	447
Flores O.	295
Foitikova P.	252
Franck C. M.	154
Fridman A.	249
Fuss M. C.	169

G

Gajić R.	186
Gajo T.	327
Galijaš S. M. D.	174, 178, 182
Galmiz O.	291
Gans T.	541
Garcia G.	5, 8, 17, 169, 537
Garcia G. A.	9
Gaudiuso R.	162
Gavanski L.	323
Gavrilović M.	311, 315
Gerlich D.	505
Gilmore T. D.	520
Giuliani A.	54, 74, 94, 533
Glosík J.	335, 505
Goncharov V.	214, 226
Gordillo-Vazques F. J.	255
Gorfinkiel J.	10
Grozdanov T. P.	102, 529
Gusein-zade N. G.	455

H

Haefliger P.	154
Hambdan A.	230
Han Xu	423
Henrion G.	230, 540
Hikosaka Y.	529
Hilt F.	164
Hlochova L.	252
Hoder T.	255
Horak J.	252
Hoshino M.	5
Huber B. A.	12
Hung J.	447
Huttula M.	529
Huttula S.-M.	529

I

Ignjatović Lj.	480
Ignjatović M.	379, 383
Ilić D.	509
Illenberger E.	521
Ingolfsson O.	16
Ito A. M.	166
Ito K.	529
Ivanović N. V.	359
Ivanović S.	42
Ivković M.	319
Ivković S. S.	263, 271
Iwayama H.	529

J

Janečkova R.	14, 524
Jankala K.	529
Janova D.	252
Jevremović D.	42
Jokić B.	222, 419
Jones D. B.	5, 169
Jovanović A. P.	258, 343, 347, 351, 355
Jovanović G.	481
Jovanović J.	150
Jovanović P.	485
Jović M.	415
Jovičević S.	311, 315
Jovović J.	259, 283

Junkar I.	257
Jureta J.	50,

K

Kačarević-Popović Z. M.	206
Kálosi Á.	335
Kan Ye. S.	30, 38
Keller A.	163
Kiris V. V.	339
Kisić D.	190
Kloc P.	375
Klyucharev A	479
Kobilarov R.	323, 327
Kočišek J.	14, 524
Kollatschny W.	509
Komori A.	474
Kondratiev S.V.	38
Kondyurin A.	447
Konjević N.	283, 359
Kopyra J.	90, 519
Korica S.	206
Korolov I.	262
Kostov K. G.	299
Kotsikau D. A.	242
Kovačević A.	509
Kovačević	489
Dojčinović J.	
Kovačević V. V.	267, 415
Kozadaev K.	214
Kozakova Z.	252
Krčma F.	218, 252
Krishnakumar E.	525
Krivosenko Yu. S.	30, 34, 38
Krstić I. B.	267, 275, 415
Kukk E.	531
Kuraica M. M.	263, 267, 271, 275, 415
Kutasi K.	254
Kuvaev K.	435
Kuznechik O.	234

L

Lablanquie P.	529
Lacko M.	526

Lazea A. 165
 Lazić V. 311, 315
 Lazović S. 443
 Lazur V. Yu. 106
 Limao-Vieira P. 17
 Lin C. 542
 LHD Exp. Group 474
 Lopes M. C. A. 5
 Lyratzki E. 478, 493

M

Machacek J. 8
 Maclot S. 12
 Majkić M. D. 178, 182
 Majstorović G. Lj. 283, 359
 Makabe T. 138
 Maksić A. 198
 Maletić D. 331, 443
 Maletić S. 206
 Maljković J. B. 18, 210
 Malović G. 331, 387, 391, 439, 443, 451
 Mančev I. 98
 Mar S. 303
 Marascu V. 165
 Mardanian M. M. 339
 Marić D. 142, 387, 391
 Marinković B. P. 42, 46, 50, 210, 467, 476
 Marinković, D. B. 42
 Marjanović S. 13
 Markosyan A. H. 399
 Marković D. 419
 Marković V. Lj. 343, 347, 351, 355
 Marziani P. 473
 Martínez H. 295
 Mason N. J. 42, 86, 525, 545
 Matejčik Š. 86, 526
 Matković A. 186
 Mazankova V. 252
 McEachran, R. P. 46, 537
 McElwee-White L. 16
 Meneses G. 17
 Miakonkikh A. 431, 435
 Michael P. 447
 Migutskiy A. 214

Mihajlov A. A. 479, 480, 513
 Mijajlović N. 379, 383
 Mijatović Z. 323, 327
 Miletić M. 451
 Milićević M. 186
 Milojević N. 20, 98
 Milosavljević A. R. 50, 54, 58, 74, 94, 210, 533
 Milosavljević V. M. 307
 Milošević M. Z. 22
 Milovanović S. 419
 Mikithcuk H. 214
 Mirić J. 122, 126
 Mirković M. A. 174
 Miron C. 54, 533
 Mišković Z. L. 168
 Mitrović T. 443
 Mítu B. 165
 Molotkov V. I. 367
 Morisaki T. 474
 Morávek T. 371
 Mozejko P. 66, 70
 Mulin D. 505
 Munoz A. 169

N

Nahon L. 9
 Naidis G. 250
 Nakano M. 529
 Nakamura H. 166
 Navrátil Z. 371
 Nedeljkić N. N. 26, 174, 178, 182
 Nedelko M. I. 339
 Nenadović M. 190, 222
 Nenin T. 443
 Ng M. K. C. 447
 Nicolas C. 54, 533
 Niemi K. 541
 Nikitović Ž. 150
 Nikonchuk I. 234
 Nina A. 497, 501
 Noël C. 230, 540
 Novaković M. 194, 198
 Novikau A. 214

O

O'Connell D.	541
Obradović B. M.	263, 267, 271, 275, 415
Orlikovsky A.	431,435

P

Pajović J.	202
Palaudoux J.	529
Pandey R.	15, 82
Pankov V. V.	242
Papp P.	526
Parra-Rojas F. C.	255
Pavličák D.	291
Pavlović D.	379, 383
Pavlović S. S.	307
Pavlychev A. A.	30, 34, 38
Pecherkin V. Ya.	367
Pejčev V.	46, 476
Peláez R. J.	303
Penent F.	528
Persing H.	542
Petković M. D.	347
Petrenko A. M.	238
Petronijević I.	206
Petrović Z. Lj.	8, 21, 114, 118, 122, 126, 130, 134, 138, 142, 146, 150, 331, 387, 391, 403, 407, 411, 439, 443, 451, 537
Pettifer Z.	5
Philippa B.	537
Piekarski D.G.	12
Plašil R.	335, 505
Polašek M.	475
Polyakov D. N.	363, 427
Ponjavić M.	379, 383
Poparić G. B.	110, 307
Popović B. Č.	343, 351
Popović M.	194, 198, 222
Popović L. Č.	478, 489, 493, 509
Potočnik J.	222
Powis I.	9
Predojević B.	467, 476
Prikryl R.	252

Prince K. C.	530
Prinz J.	74
Prlina I.P.	26, 178
Prochazka M.	218, 252
Prukner V.	255
Prysiazhnyi V.	167, 299
Ptasinska S.	256, 423
Ptasińska-Denga E.	70
Puač N	331, 439, 451
Purić J.	279
Puschnigg B.	521
Puzyrev M.	226

R

Rabasović M.	19
Rabie M.	154
Rackwitz J.	58, 74, 90, 163
Radetić M.	475, 419
Radkova L.	252
Radmilović	407, 411
Rađenović M.	
Radosavljević A. N.	206
Radovanov S.	542
Radović I.	168
Rahbarbinesh A.	395
Ráhel J.	371
Rakočević Z.	190, 222
Ranitović P.	7
Ranković M. Lj.	54, 58, 210
Raspopović Z. M.	138, 142, 150
Rednyk S.	505
Regeta K.	78
Reyes P. G.	295
Ribar A.	86
Ricci A. H. C.	299
Ristić M. M.	110
Robson R. E.	537
Roglić G. M.	415
Rostov D.A.	30, 38
Roucka S.	505
Rousseau P.	12, 94
Rubović P.	335
Rudenko K.	431,435
Ruhadze A. A.	455
Ryszka M.	15, 82

S

Saito S.	166
Sakan N. M.	513
Santos M.	447
Savić I.	323, 327
Savić M.	411
Sazavska V.	252
Scheier P.	521
Schlathölter T.	532
Schulze J.	262
Schüngel E.	262
Schürmann R.	74, 163
Selaković N.	451
Selles P.	529
Shapovalova A. I.	509
Sheinerman S.	529
Shigemasa E.	529
Shirai N.	253
Shumova V. V.	363, 427
Simonchik L. V.	463
Simonović I.	130, 134
Simonović N.	22
Sivoš J.	387, 391
Soejima K.	529
Sokoloff J.	463
Solov'ev E. A.	102
Spasić K.	439
Spencer J.	16
Srećković V. A.	480, 513
Sretenović G. B.	267, 271, 415
Stamenić M.	419
Stamenković S. N.	343, 347, 351, 355
Stankov M. N.	260, 343, 347, 351, 355
Stathopoulos D.	478, 493
Stauffer A.D.	46
Steflekova V.	287
Stoica D.	165
Stojanović D.	190
Stojanović V.	142, 150
Sulentic J.	473
Sullivan J.	8
Suzuki I. H.	529
Swiderek P.	4
Szmytkowski Cz.	70
Szymańska-	86, 525

Skolimowska E.	
Šašić O.	122, 146
Šević D.	46, 476
Šiljegović M.	206
Šimek M.	255
Šišović N. M.	359
Škoro N.	387, 391, 439
Šumarac Pavlović D.	379, 383
Šuvakov M.	411, 539

T

Tanaka H.	5
Tanzer K.	521
Takayama A.	166
Tapalaga I.	279
Tarasenko N. N.	242
Tarasenko N. V.	242, 339
Tashiro M.	529
Tattersall W.	8, 537
Taušanović M.	379, 383
Thorman R.	16
Tochikubo F.	253
Tökési K.	210
Tomčik B.	467
Tomić N.	443
Tošić S. D.	46
Tran T. D.	505
Truhachev F.	459
Tzimeas D.	478

U

Uchida S.	253
Usachonak M. S.	463

V

Vasicek M.	252
Vasić B.	186
Vasilyak L. M.	363, 367, 427
Vetchinin S. P.	367
Vičić M. D.	110
Vidojević S.	477
Villa M.	295
Vizireanu S.	165
Vogel S.	74, 163
Vojnović M. M.	62, 110

Vuitton V.	475
Vujčić V.	42
Vuković D.	451

W

Wagenars E.	541
Wang S.	542
Warneke J.	4
Wendt A.	542
West A.	541
Winter B.	534
Wise S. G.	447
White R. D.	8, 118, 126, 138, 537

Y

Yasserian K.	395
Yasuhiro O.	166

Z

Zawadzki M.	70
Zemánek M.	291
Zhang K.	194
Zlatař M.	522
Żywicka B.	66
Žabka J.	475
Žitnik M.	529
Žižović I.	419
Živanović I.	451

**POST-DEADLINE
CONTRIBUTIONS**

INSIGHTS INTO ANIONIC STATES OF ACETOACETIC ACID FROM PHOTOELECTRON AND ELECTRON ENERGY-LOSS SPECTROSCOPES AND THEORY

M. Gutowski¹, Z.G. Keolopile^{1,2}, A. Buonaugurio³, E. Collins³, X. Zhang³,
J. Erb³, T. Lectka³, K.H. Bowen³, M. Allan⁴

¹*Institute of Chemical Sciences, Heriot-Watt University, Edinburgh EH14 4AS,
United Kingdom*

²*Department of Physics, University of Botswana, Private Bag 0022, Gaborone,
Botswana*

³*Department of Chemistry, Johns Hopkins University, Baltimore, MD 21218,
USA*

⁴*Department of Chemistry, University of Fribourg, chemin du Musee 9, 1700
Fribourg, Switzerland*

Abstract. The anion photoelectron and electron energy-loss spectroscopies probe different regions of the anionic potential energy surface. The former probes the potential energy surface close to the minimum energy structure of the anion. The latter probes the anionic potential energy surface close to the minimum energy structure of the neutral. Both experimental techniques and theory have been engaged to study anionic states of acetoacetic acid (AA). The keto tautomer of AA, equipped with neighboring carboxylic and *keto* groups, is a promising system for studies of intramolecular proton transfer (*keto-ol*) driven by an excess electron. The anion photoelectron spectra are consistent with our theoretical prediction that the valence anion has the *ol* structure, i.e., the COOH proton is transferred to the *keto* group. However, the electron energy-loss spectra do not provide evidence for the ultrarapid proton transfer capable of competing with the spontaneous electron detachment. The computational results allow rationalizing these experimental findings in terms of the co-existence of various tautomers and conformers of the neutral AA. Only one, and not the most stable, keto conformer is prearranged for intramolecular proton transfer, and apparently it is not present in the gas of neutral AA with significant concentration. This conclusion is confirmed by vibrational spectrum of AA obtained in the electron energy-loss experiments: the carboxylic OH is not involved in intramolecular hydrogen bond, and thus the molecule is not prearranged for intramolecular proton transfer.

27th SPIG

Particle and Laser Beam Interaction with Solids
Progress Report

INTERACTION OF CHARGED PARTICLES WITH CAPILLARIES

Károly Tökési

*Institute for Nuclear Research, Hungarian Academy of Sciences, Debrecen,
Hungary*

LANGMUIR WAVES IN INTERPLANETARY PLASMA

Sonja Vidojevic¹, Arnaud Zaslavsky², Milan Maksimovic², Olga
Atanackovic³, Milan Drazic³

¹*IHS techno-experts, Belgrade, Serbia* ²*Observatoire de Paris, France*

³*Faculty of Mathematics, Belgrade, Serbia*

Radio observations of the waves in a range of 4 – 256 kHz from the WAVES experiment onboard the Wind spacecraft have been statistically analyzed. A subset of 36 events with Langmuir waves and type III radio bursts occurred at the same time, has been selected. The Langmuir waves electric field observed as a function of time actually appears as a series of short-duration (\sim tens of millisecc.) wave packets. They are separated from each other by a time interval difficult to evaluate since the waveform data available onboard the spacecraft are usually limited to samples of \sim 100 ms. The question then naturally arises whether the statistics performed on the electric field spectral power provided by the Thermal Noise Receiver onboard Wind spacecraft, and integrated over \sim 4 s time-windows, reflects, or not the statistics of the amplitude of these wave packets. The answer to this question is crucial for the interpretation of the *in situ* observations of Langmuir waves that has been performed in a number of previous publications. Thus, we investigate the question by performing numerical simulations of the response of the TNR to series of Langmuir wave packets, and adapt the input parameters in order to recover results similar to the Wind's observation. By comparing the amplitudes of variations of the simulated output distributions and their shapes with the ones derived from the actual Wind observations, we can conclude that the best agreement between simulations and observations is achieved when: (1) the shape of the input distributions is rather Pearson I or lognormal than a power law which should be definitively excluded; (2) the parameter λ (number of packages in one second) in Poisson distribution lies between 0.1 and 1; (3) the maximum value of the input wave packet amplitude is about $5 \times 10^{-3} \text{V m}^{-1}$. Therefore, there is a clear need to measure Langmuir waves energy distributions directly at the waveform level and not *a posteriori* in the spectral domain.



Ministry of Education,
Science and Technological Development
Republic of Serbia



IOP Conference Series

austrijski kulturni forum^{beg}

INSTITUT
FRANÇAIS
SERBIE

